SciTech
PUBLISHING
an imprint of the IET

Multidimensional Radar Imaging

Edited by
Marco Martorella

Multidimensional
Radar Imaging

Related titles on radar:

Advances in Bistatic Radar Willis and Griffiths
Airborne Early Warning System Concepts, 3rd Edition Long
Bistatic Radar, 2nd Edition Willis
Design of Multi-Frequency CW Radars Jankiraman
Digital Techniques for Wideband Receivers, 2nd Edition Tsui
Electronic Warfare Pocket Guide Adamy
Foliage Penetration Radar: Detection and characterisation of objects under trees Davis
Fundamentals of Ground Radar for ATC Engineers and Technicians Bouwman
Fundamentals of Systems Engineering and Defense Systems Applications Jeffrey
Introduction to Electronic Warfare Modeling and Simulation Adamy
Introduction to Electronic Defense Systems Neri
Introduction to Sensors for Ranging and Imaging Brooker
Microwave Passive Direction Finding Lipsky
Microwave Receivers with Electronic Warfare Applications Tsui
Phased-Array Radar Design: Application of radar fundamentals Jeffrey
Pocket Radar Guide: Key facts, equations, and data Curry
Principles of Modern Radar, Volume 1: Basic principles Richards, Scheer and Holm
Principles of Modern Radar, Volume 2: Advanced techniques Melvin and Scheer
Principles of Modern Radar, Volume 3: Applications Scheer and Melvin
Principles of Waveform Diversity and Design Wicks *et al.*
Pulse Doppler Radar Alabaster
Radar Cross Section Measurements Knott
Radar Cross Section, 2nd Edition Knott *et al.*
Radar Design Principles: Signal processing and the environment, 2nd Edition Nathanson *et al.*
Radar Detection DiFranco and Rubin
Radar Essentials: A concise handbook for radar design and performance Curry
Radar Foundations for Imaging and Advanced Concepts Sullivan
Radar Principles for the Non-Specialist, 3rd Edition Toomay and Hannan
Test and Evaluation of Aircraft Avionics and Weapons Systems McShea
Understanding Radar Systems Kingsley and Quegan
Understanding Synthetic Aperture Radar Images Oliver and Quegan
Radar and Electronic Warfare Principles for the Non-specialist, 4th Edition Hannen
Inverse Synthetic Aperture Radar Imaging: Principles, algorithms and applications Chen and Marotella
Stimson's Introduction to Airborne Radar, 3rd Edition Baker, Griffiths and Adamy
Test and Evaluation of Avionics and Weapon Systems, 2nd Edition McShea
Angle-of-Arrival Estimation Using Radar Interferometry: Methods and applications Holder
Biologically-Inspired Radar and Sonar: Lessons from Nature Lessons from Nature Balleri, Griffiths and Baker
The Impact of Cognition on Radar Technology Farina, De Maio and Haykin
Novel Radar Techniques and Applications, Volume 1: Real aperture array radar, imaging radar, and passive and multistatic radar Klemm, Nickel, Gierull, Lombardo, Griffiths and Koch
Novel Radar Techniques and Applications, Volume 2: Waveform diversity and cognitive radar, and target tracking and data fusion Klemm, Nickel, Gierull, Lombardo, Griffiths and Koch
Radar and Communication Spectrum Sharing Blunt and Perrins
Systems Engineering for Ethical Autonomous Systems Gillespie
Shadowing Function from Randomly Rough Surfaces: Derivation and applications Bourlier and Li

Photo for Radar Networks and Electronic Warfare Systems Bogoni, Laghezza and Ghelfi

Multidimensional Radar Imaging

Edited by

Marco Martorella

The Institution of Engineering and Technology

Published by SciTech Publishing, an imprint of The Institution of Engineering and Technology, London, United Kingdom

The Institution of Engineering and Technology is registered as a Charity in England & Wales (no. 211014) and Scotland (no. SC038698).

© The Institution of Engineering and Technology 2020

First published 2019

This publication is copyright under the Berne Convention and the Universal Copyright Convention. All rights reserved. Apart from any fair dealing for the purposes of research or private study, or criticism or review, as permitted under the Copyright, Designs and Patents Act 1988, this publication may be reproduced, stored or transmitted, in any form or by any means, only with the prior permission in writing of the publishers, or in the case of reprographic reproduction in accordance with the terms of licences issued by the Copyright Licensing Agency. Enquiries concerning reproduction outside those terms should be sent to the publisher at the undermentioned address:

The Institution of Engineering and Technology
Michael Faraday House
Six Hills Way, Stevenage
Herts, SG1 2AY, United Kingdom

www.theiet.org

While the authors and publisher believe that the information and guidance given in this work are correct, all parties must rely upon their own skill and judgement when making use of them. Neither the authors nor publisher assumes any liability to anyone for any loss or damage caused by any error or omission in the work, whether such an error or omission is the result of negligence or any other cause. Any and all such liability is disclaimed.

The moral rights of the authors to be identified as authors of this work have been asserted by them in accordance with the Copyright, Designs and Patents Act 1988.

British Library Cataloguing in Publication Data
A catalogue record for this product is available from the British Library

ISBN 978-1-78561-807-9 (hardback)
ISBN 978-1-78561-808-6 (PDF)

Typeset in India by MPS Limited
Printed in the UK by CPI Group (UK) Ltd, Croydon

Contents

About the editors **xi**
Foreword **xiii**

1 Introduction **1**
Marco Martorella and David Greig

1.1 Background 1
1.2 Multidimensional radar 4
1.2.1 Multistatic radar imaging systems 5
1.2.2 Multichannel radar imaging systems 6
1.2.3 Multi-polarisation radar imaging systems 7
1.2.4 Multi-frequency radar imaging systems 7
1.2.5 Systems design considerations 8
1.2.6 Concluding remarks 9
1.2.7 Book organisation 10

Part I Multidimensional radar imaging algorithms **13**

2 Three-dimensional inverse synthetic aperture radar **15**
Daniele Staglianò, Federica Salvetti, Elisa Giusti and Marco Martorella

2.1 Introduction 15
2.2 Algorithm description 17
2.2.1 Multichannel ISAR signal model 18
2.2.2 System geometry 18
2.2.3 Received signal modelling 18
2.2.4 Multichannel CLEAN algorithm 21
2.2.5 3D reconstruction processing 23
2.3 Performance analysis 28
2.3.1 Scatterers realignment 28
2.3.2 Soft assignment 29
2.3.3 Performance indicators 29
2.4 Results 30
2.4.1 Simulated results 30
2.4.2 Experimental results 37
2.5 Conclusion 42
References 43

3 STAP–ISAR **47**
Samuele Gelli, Alessio Bacci and Marco Martorella

3.1 Mathematical background 47
 3.1.1 Multichannel ISAR signal model 48
 3.1.2 High-resolution imaging of noncooperative moving targets 51
 3.1.3 Clutter model 55
3.2 Space–time adaptive processing for clutter suppression 60
 3.2.1 Joint SDAP ISAR 61
 3.2.2 Joint E-SDAP ISAR 68
3.3 Results 73
 3.3.1 SDAP–ISAR results 73
 3.3.2 E-SDAP ISAR results 88
3.4 Conclusion 105
References 105

4 Wide-band multi-look passive ISAR **109**
Elisa Giusti, Marco Martorella, Fabrizio Berizzi and Amerigo Capria

4.1 Introduction 109
4.2 Data pre-processing 111
 4.2.1 Target extraction 112
 4.2.2 Merging of RD maps and ISAR data formation 115
4.3 ISAR image processing 119
 4.3.1 Conventional ISAR imaging 119
 4.3.2 CS-based ISAR imaging 121
4.4 Results 123
 4.4.1 Cooperative targets – WUT system 123
 4.4.2 Non-cooperative targets – SMARP 130
4.5 Conclusions 137
References 139

5 Radar tomography **141**
Hai-Tan Tran and Lorenzo Lo Monte

5.1 Introduction 141
 5.1.1 Adaptability 146
 5.1.2 Modularity 146
 5.1.3 Graceful degradation 146
5.2 Tomographic image formation 147
 5.2.1 Signal models 147
 5.2.2 Fourier-based methods 150
 5.2.3 Matrix-based methods 164
 5.2.4 Multistatic Doppler–radar tomography 171

5.3 Practical considerations 179
  5.3.1 Considerations with system geometry 179
  5.3.2 Considerations for signal processing 182
5.4 Concluding remarks 182
Appendix 184
  A Theoretical image resolution limits 184
References 185

6 Multistatic PCL–SAR 189
Diego Cristallini, Philipp Wojaczek and Ingo Walterscheid

6.1 Introduction 189
6.2 Signal processing for PCL–SAR based on DVB-T 191
  6.2.1 Structure of DVB-T signal 192
  6.2.2 Received DVB-T signal model 192
  6.2.3 Synchronization and reference signal reconstruction 193
  6.2.4 Range compression in PCL–SAR 196
  6.2.5 Image formation 198
  6.2.6 Challenges for airborne PCL 200
6.3 Multi-PCL–SAR for improved range resolution 207
  6.3.1 Range resolution improvement principle 207
  6.3.2 Scenario for multi-PCL–SAR 211
  6.3.3 Simulation of DVB-T range pulse response 212
  6.3.4 Optimal trajectories for multi-PCL–SAR 219
6.4 Experimental verification 222
  6.4.1 Scenario definition 222
  6.4.2 Image results of PCL–SAR 225
6.5 Conclusions 227
Acknowledgments 229
Glossary 229
References 230

7 Sparsity-driven multistatic ISAR image reconstruction 235
Stefan Brisken

7.1 Constraints 236
  7.1.1 Spatial decorrelation 236
  7.1.2 Foreshortening effect 238
7.2 Problem formulation 238
7.3 Reconstruction 241
7.4 A simulated example 244
7.5 Experimental results 247
7.6 Conclusion 249
References 250

Part II Practical feasibility and applications **253**

8 Rotor blade parameter estimation with multichannel passive radar **255**
Marcin Kamil Bączyk and Jacek Misiurewicz

8.1 Introduction 255
8.1.1 Problem formulation 255
8.1.2 Methods for helicopter classification 256
8.1.3 Recognition of the propeller aircraft or other rotary-wing aircraft 257
8.2 A geometric model of the helicopter 257
8.2.1 The echo of the helicopter's fuselage 257
8.2.2 The main rotor 258
8.2.3 The tail rotor 261
8.2.4 The rotor parameters 262
8.3 A model of the received echo signal 262
8.3.1 A generic model of the echo signal 262
8.3.2 A model of the main rotor blade echo 263
8.3.3 A tail rotor blade echo model 268
8.4 Method for determining rotor parameters 269
8.4.1 Main rotor parameters 271
8.4.2 Tail rotor parameters 275
8.5 Main rotor imaging algorithm based on the target echo spectrogram 276
8.6 Live signal processing experiment 279
8.6.1 Measurement campaign 279
8.6.2 Data pre-processing 279
8.6.3 Results 281
8.7 Conclusions and result discussion 284
References 284

9 Multistatic 3D ISAR imaging of maritime targets **287**
Federica Salvetti, Elisa Giusti, Daniele Staglianò and Marco Martorella

9.1 Multiview 3D InISAR image fusion 289
9.1.1 3D fusion 292
9.2 Multiview 3D InISAR image fusion in experimental scenarios 295
9.2.1 Application of multiview 3D to multitemporal data 296
9.2.2 Application of multiview 3D to multistatic data 304
9.2.3 Application of multiview 3D to a combination of multistatic and multitemporal data 305
9.3 Conclusion 308
References 308

10 Challenges of semi-cooperative bi/multistatic synthetic aperture radar (SAR) using Cosmo-SkyMed as an illuminator 311
Claire Stevenson, Matthew Nottingham, Darren Muff and David Blacknell

10.1 Introduction 311
10.2 Semi-cooperative bi/multistatic data collection 312
10.3 Hardware considerations 313
10.3.1 Analogue-to-digital convertors (ADCs): bulk delay offset 313
10.3.2 Clock drift 314
10.4 Semi-cooperative bistatic SAR signal processing 315
10.5 Effect of errors in transmitter position 317
10.6 Image formation 319
10.7 Experimental validation of semi-cooperative bistatic SAR signal processing 321
10.8 Conclusions 322
References 323

11 Lesson learnt from NATO SET-196 RTG on 'multichannel/ multi-static radar imaging of non-cooperative targets' 325
Marco Martorella and David Greig

11.1 The role and impact of NATO SET-196 RTG within and outside NATO 325
11.2 Progress made by NATO SET-196 within multidimensional radar imaging 326
11.3 Lesson learnt and open issues 328
11.4 The way ahead for multidimensional radar imaging systems 328
11.4.1 Towards affordable multidimensional radar imaging systems 329
11.4.2 Clusters and swarms 330

Index 333

This page intentionally left blank

About the editors

Marco Martorella has received his Laurea degree (bachelor+masters) in Telecommunication Engineering in 1999 (cum laude) and his PhD in remote sensing in 2003, both at the University of Pisa. He is now an associate professor at the Department of Information Engineering of the University of Pisa where he lectures on 'fundamentals of radar' and 'digital communications' and an external professor at the University of Cape Town where he lectures on 'high resolution and imaging radar' and 'introduction to radar' within the 'masters in radar and electronic defence'. Prof. Martorella is also Director of the CNIT's National Radar and Surveillance Systems Laboratory. He has authored more than 200 international journals and conference papers, more than 10 book chapters, a book entitled *Inverse Synthetic Aperture Radar Imaging: Principles, Algorithms and Applications* and another book entitled *Radar Imaging for Maritime Observation*. He has presented several tutorials at international radar conferences, has lectured at NATO Lecture Series and organised international journal special issues on radar imaging topics. He is a member of the IET Radar Sonar and Navigation Editorial Board, a senior member of the IEEE and a member of AFCEA. He is also a member of the IEEE AES Radar Systems Panel, a member of the NATO SET Panel, where he sits as co-chair of the Radio Frequency Focus Group, and a member of the EDA Radar Captech. He is currently the chair of the research task group NATO SET-250 on 'Multidimensional Radar' and co-chair of NATO SET-236 on 'Robust compressive sensing techniques for radar and ESM applications'. He was also chair of the SET-196 on 'Multichannel/Multistatic radar imaging of non-cooperative targets' and of the specialist meeting NATO SET-228 on 'Radar Imaging for Target Identification'. He has been the principal investigator of more than 20 research projects. He has been the recipient of the 2008 Italy-Australia Award for young researchers, the 2010 Best Reviewer for the IEEE GRSL, the IEEE 2013 Fred Nathanson Memorial Radar Award, the 2016 Outstanding Information Research Foundation Book publication award for the book *Radar Imaging for Maritime Observation* and the 2017 NATO Set Panel Excellence Award. He is co-founder of a radar systems-related spin-off company, namely ECHOES.

This page intentionally left blank

Foreword

Radar was originally developed as a system for detecting objects and determining their positions by means of echo-location, and this remains the principal function of modern radar systems. However, radar systems have evolved over more than seven decades to perform a variety of very complex functions; one such function is imaging. Radar-based imaging is a technology that has been developed mainly within the engineering community. There are good reasons for this: some of the critical challenges are (1) transmitting microwave energy at high power, (2) detecting microwave energy and (3) interpreting and extracting information from the received signals. The first two problems have to do with the development of appropriate hardware; however, these problems have now largely been solved, although there is ongoing work to make the hardware smaller and lighter. The third problem is essentially a set of mathematical challenges, and this is the area where most of the current effort is taking place. Existing imaging methods rely on very specific simplifying assumptions about radar scattering phenomenology and data collection scenarios:

(i) They assume that the target or scene behaves as a rigid body. This assumption is obviously inadequate for scenes that include multiple moving objects.
(ii) They also assume a linear relationship between the data and scene. In many situations, this is also inadequate.[1]

Nowadays, target classification and imaging are used in a variety of defence and civil applications; for example, in Medicine Tomography, development of automatisation in industry transport, self-driving transport vehicles in air and space and other domains. Radar imaging often responds to the need to see, sense and identify what is around the sensing machine. Also, it is a means for artificial intelligence applications where it is crucial to estimate the shape of a target even in a dynamic and complex environment. A pivotal technique for radar imaging is based on synthetic aperture radar (SAR). This technique has made radar imaging applicable to remote sensing from air and space and it represents today one of the most important technologies for Earth observation, including civil and military applications. Signal and image processing associated with SAR has evolved greatly in the last few decades and has been making use of classical and new mathematical tools, including Fourier analysis, statistical inference, array processing and the more recent compressive sensing (CS) to mention a few.

Classic radar configurations have a single channel. This is a good compromise in terms of benefits and costs. Single channel radar can achieve good performance and perform a large variety of tasks, from detection to tracking and imaging. Nevertheless, it shows its limitations when it comes to pushing the performances and improving target imaging and classification. NATO SET-196, a Research Task Group (RTG) that was active within the Sensor and ElectronicsTechnology (SET) Panel, carried out a thorough gap analysis of imaging systems, especially when performed with single channel radar. Such an analysis clearly identified the limits associated with such type of radar systems. SET-196 took off then to exploring systems and algorithms that were based on multi-channel and multi-static types of radar systems, with specific attention to their ability to outperform single channel radar in terms of imaging capabilities and performances. Results from that work were impressive as they were also supported by extensive trials executed both in the Netherlands and in Italy, with the participation of more than ten multi-channel and multi-static radar systems. The research within the NATO framework is continuing along these lines with a follow-on RTG, namely SET-250 on multidimensional radar imaging. SET-250 extended the vision of SET-196 by including additional dimensions, such as multi-frequency and multi-polarisation (full-pol radar systems). Most of the results achieved within SET-196 and SET-250 are now contained in this book, which is offered to open literature.

---

[1] 10.1088/0266-5611/25/12/123005

The results contained in this book are very important to the NATO. Radar technology is a long-term effort within the NATO Science and Technology Organisation (STO) and radar imaging is included as a specific case. Imaging is a critical function for command and control (C2) systems where there is the need to visually interpret what various types of sensors acquire. A commander in charge of a C2 system must have a timely and clear view of the dynamical changes of a scenario and imaging systems are dedicated to supporting domain awareness in all its various declinations: maritime, land, air and space.

We can track numerous STO SET Panel activities that have investigated the problem of imaging and its applications, not only by means of radar. A non-exhaustive list is as follows:

- Sub-terahertz radar imaging;
- vKHS Optronic 3D Imaging Systems;
- Computational imaging and compressive sensing for EO/IR systems;
- Compressive sensing applications for radar, ESM and EO/IR imaging;
- Quantum structures for non-cryogenic infrared imaging;
- Military applications of millimetre wave imaging;
- High-performance passive/active radiometric millimetre-wave imaging using thinned arrays;
- Adaptive Optics for laser beam delivery and passive and active imaging and turbulence mitigation; and
- Computational imaging.

I would strongly encourage researchers from academia, industry and government institutions to read this book as it presents the leading state-of-the-art of radar imaging, with a strong focus on multi-dimensionality. For those who seek knowledge in and answers to multidimensional radar imaging and its benefits (and costs) with respect to classical imaging would find a great deal in this book.

Dr. Pavel Zuna
NATO Collaborative Support Office (CSO) Director

Chapter 1

Introduction

Marco Martorella[1] *and David Greig*[2]

The year 2015 saw the 50th anniversary of the famous paper by Gordon E. Moore, which led to the now often-quoted Moore's law. The last word of that paper was 'Radar', which predicted that modern computer (and by inference signal processing) technology would revolutionise the world of radar. When that paper was written, the abundance of coherent RF emissions was relatively rare. Now in the twenty-first century, we find ourselves surrounded (and penetrated) by wideband coherent energy from a broad range of sources. The combination of these multiple sources is highly challenging but has the potential to revolutionise the capabilities and technologies of this planet from individual environmental awareness, through the automotive and autonomous transport industry, to high-end intelligence and military awareness. Radar was originally invented as a detection system. However, modern operations increasingly require that the system can also identify the detected object. Imaging an object is the basis of most identification methods and, for this reason, radar imaging systems have increasingly been improved and extended. More specifically, the inclusion of additional dimensions into the image can improve the identification system in terms of accuracy and robustness and, in some cases, enable target recognition where it was not possible with standard imaging systems. The purpose of this book is to frame the current state-of-the-art in the subject of multidimensional RF signal processing with specific application to radar imaging. Most of the findings enclosed in the following chapters are the result of a NATO Research Task Group (RTG), namely the NATO SET-196 on *Multichannel and Multistatic Radar Imaging of Non-Cooperative Targets*.

1.1 Background

In many scenarios, one of the most challenging tasks is target classification as important decisions are often based on such knowledge. Radar is a sensor that can provide this capability in all-weather and day/night conditions. With reference to Figure 1.1, it can be seen that the classification process is a black box with radar data as input and

---

[1] Department of Information Engineering, University of Pisa and Radar and Surveillance Systems, CNIT, Pisa, Italy
[2] Leonardo, Edinburgh, UK

a classified target as output. A classification process can be accomplished either by a human operator or a machine or both. In any case, such a problem is very complex as radar data is not easily interpretable in its raw format.

One way to overcome the problem of radar data interpretability/presentation is through the formation of radar images. Radar images are much more easily interpretable than raw data as they present a map of a target in a similar way as an optical image does. This aspect makes the classification process more intuitive either in the case of a direct use of the image by an operator or in the case of supervised automatic target classification. In any case, the image formation process is, in most cases, a lossless transformation that does not limit the effectiveness of any subsequent classifier. The reader may refer to Figure 1.2, where radar data is first transformed into a radar image and then processed by a classifier.

In recent decades, many radar imaging systems have been designed, which are capable of producing images of targets and, as a result, image-based classifiers have been developed. Nevertheless, the overall process is still not able to produce satisfactory outcomes. The main reason behind that is that the system performance is target-driven and therefore not fully under the operator's control. To give an example of the target-dependence, a sequence of radar images of a non-cooperative target is shown in Figure 1.3. In this specific example, the radar is fixed (ground-based) and the target's motion is the only component that produces a radar synthetic aperture and therefore a radar image. The target's image changes dramatically from one frame to another

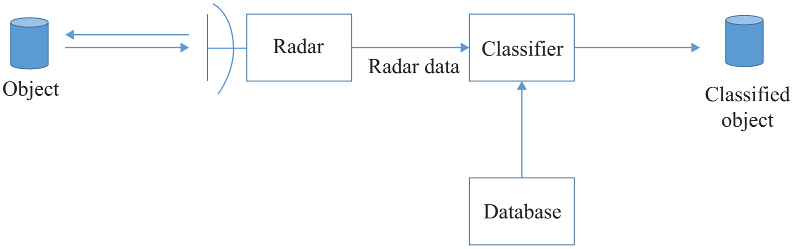

Figure 1.1 Pictorial view of a classification system based on radar data

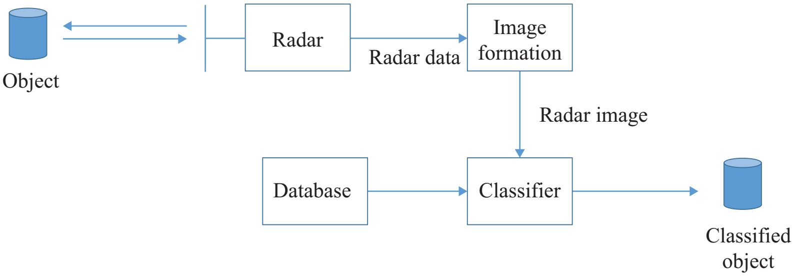

Figure 1.2 Pictorial view of a classification system based on radar images

within a time span of a few seconds highlighting its variability due to the target's dynamics. All the image resolution, target-to-sensor aspect and the image projection plane are in this case determined by the motion of the target, which makes the imaging system performance unpredictable. The system that produced the images in Figure 1.3 is a monostatic single channel and single sensor radar imaging system. Although this is the simplest and most economical case, it suffers from a number of limitations:

- The radar image projection plane is not entirely controlled by the radar operator as it depends on the target's dynamics. This makes the image interpretation hard as a three-dimensional (3D) object is projected onto an unknown plane. This is because

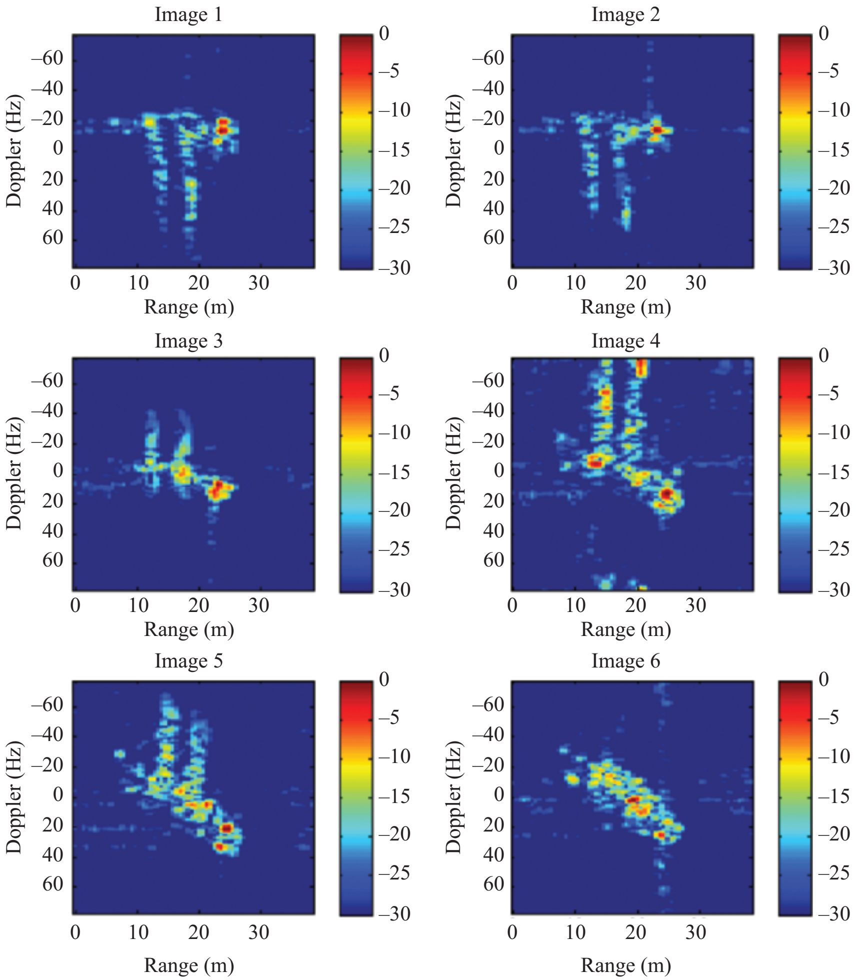

Figure 1.3 Sequence of ISAR images data from MECORT Radar (CSIR, South Africa)

the 2D projection of a 3D object cannot produce features that are invariant under, for example, transformations of aspect angle or image projection plane. Aspect angle and image projection plane are therefore additional degrees of freedom in classification and lead to the requirement for massive (and impractical) databases.
- In the general case, it is not possible to access the full target motion with a single sensor. This leads to the necessity of assumptions on the target motion, which is limited to short observation times. This in return limits the achievable resolution.
- The radar-target dynamics may be unfavourable when it comes to producing an effective synthetic aperture. A simple but effective example is a target (e.g. a missile) that is pointing directly at the radar. In this case, there would not be any synthetic aperture formed and therefore the resultant radar image would only produce a 1D profile (not a 2D image).
- Self-occlusion: A target viewed from an angle may mask part of target itself, therefore hiding important information that may be used for classification purposes.
- Single-perspective: Even a good radar image taken from a given view angle may present limited information about the target, which may be enriched if the same target was viewed from other angles.
- Low-observable targets: These can be made more covert to conventional radars.
- Jamming: Monostatic/single sensor radar imaging systems are vulnerable to jamming as they may be easily discovered.
- Resilience: Single-sensor radars are in general not very resilient as a system failure would result in capability loss.

All these shortcomings can be mitigated by the introduction of multistatic and multichannel radar-sensing techniques.

1.2 Multidimensional radar

Radar information is rich enough to allow for images to be formed. The way radar images are formed may vary depending on the sensor characteristics and the signal processing used. One of the most effective ways of producing radar images is through synthetic aperture. This technique allows for high-resolution images to be formed with relatively small antennas and ‘independently’ of range. Nowadays, high-resolution radar images (below 1×1 m) are regularly produced from space by an increasing number of systems. Nevertheless, as pointed out in the previous section, limitations occur that cannot be overcome with radar imaging systems in their simplest form. A radar operating with a single frequency, a single antenna, a single polarisation and as a single node produces what we can see as a limited ‘vision’ of the world. From an information content point of view, we may argue that, by increasing the number of antennas (spatial channels), frequencies, polarisations and by increasing the number of nodes, therefore creating a radar network (or multistatic radar system), we may enrich the information content and therefore produce much more effective radar images and overcome limitations that are set by single channel, single frequency, single polarisation and node radars.

We would like to introduce the concept of *multidimensional radar system* as a radar that has either multiple spatial channels (antennas) or multiple frequencies (dual- or multi-frequency radar) or multiple polarisation (polarimetric radar) or multiple nodes (radar network or multistatic radar) or a combination of those. Conversely, a radar that offers no such a diversity may be addressed as a monodimensional radar.

Multidimensionality brings in more information as a target is interrogated with different sets of *stimuli* and it may respond differently to such stimuli, therefore revealing some aspects that were not appearing using a different stimulus. On the other end, though, multidimensionality comes at a cost as it requires a higher system complexity. Therefore, the seemingly obvious conclusion that all radar should be multidimensional finds its cost as a trade-off. For this reason, multidimensionality must be considered an option and its cost/benefit should be analysed carefully before an efficient and even optimal radar system is designed. The goal of a recent NATO RTG, namely SET-196 RTG, was to investigate benefits coming from the use of multichannel and multistatic radar imaging systems and many aspects were studied, starting from modelling and algorithms, through to system feasibility, trials and data analysis and finishing with some recommendations regarding the design and use of such systems. An even more recent NATO RTG, namely SET-250 RTG, has been looking at a broader spectrum, including multi-frequency and multi-polarisation, which increases the degrees of freedom with which we can play around to design an effective radar imaging system. At this stage, a natural question arises that should be somehow answered: ‘In a budget-constrained scenario, how should a radar be designed in terms of number of spatial channels, frequencies, polarisations and nodes?’. The answer is not straightforward as it strongly depends on the specific radar application(s) and can only come from a thorough modelling and performance analysis. In the following subsections, we will singularly analyse each of the above-mentioned degrees of freedom.

1.2.1 Multistatic radar imaging systems

Imaging of targets from multiple directions produces multiple views of the target, which can be either fused to form richer images or directly fed to an ATR system for target classification/recognition/identification. NATO SET-163 RTG proved in operational conditions that multi-perspective synthetic aperture radar (SAR) images obtained from multiple angles produce better ATR performances than having a single-perspective SAR image. In the more specific case of inverse synthetic aperture radar (ISAR) case, the resulting image is dependent on the relative motion of the target with respect to the radar. There are cases where imaging is not always possible in a monostatic ISAR system if such a motion is unfavourable, such as the case of a missile directly pointing at the radar.

- Solution to the problem of obtaining persistent imaging. The time on target may be significantly reduced by simultaneously looking at the same target from different angles.

- Multistatic imaging is naturally multi-aspect, therefore also increasing the chances of forming high-quality images (image fusion, coherent and incoherent).
- Increases the probability to obtain at least one effective ISAR image for ATR purposes in a given time interval.
- Reduces the effects of shadowing and self-occlusion.
- Increases classification performances in case shadows are used to classify the target as multiple shadows are created from different aspect angles.
- Wide area coverage single wide area illuminating source and network of passive receiving radars can be a lower cost solution compared to multiple monostatic systems and would make a more efficient use of the spectrum.
- Covert surveillance/counter jamming: ESM/ECM would be directed at the illuminating source rather than at the passive receivers, therefore increasing the signal-to-interference ratio and the resulting image quality.
- Possible advantages against clutter (in maritime scenarios, clutter less spiky in bistatic configurations).
- Multi-aspect imaging produces 3D images to support target classification.
- Multistatic geometry opens up new possibilities in target motion estimation (multilateration).
- Possible advantages by means of the reduction of imaging time and/or bandwidth.
- Increased system resilience, i.e. failure of one or two components may reduce system performance but do not completely bring down the imaging system.

Ready application to totally passive operations using illuminators of opportunity (IO): passive ISAR using multiple IOs could enable a multistatic radar imaging system that could defeat target low-observability and therefore allow for such targets to be imaged. Some results have been shown in the following RTGs: SET-164, SET-186, SET-195.

1.2.2 Multichannel radar imaging systems

Multichannel radar systems allow for spatial signal processing. More specifically, digital multichannel systems enable adaptive spatial signal processing, such as digital beamforming. Regarding radar imaging, multichannel systems have been used to add the following important capabilities:

- Additional data from multiple channels produce extra dimensions to be exploited to form 3D images, which in turns may prove useful to increase ATR performances.
- Clutter suppression methods for detection of small targets become more effective with multichannel systems as modern GMTI techniques that make use of multiple channels can be implemented. The elimination of strong clutter contributions may enable effective imaging of ground targets.
- Multiple beamforming for imaging radar (simultaneous imaging of multiple targets) may allow for a better integration and usage of imaging functions into multifunction radars.
- MIMO radar imaging may lead to an increase of performances in 3D image formation and consequently in ATR.

1.2.3 Multi-polarisation radar imaging systems

Radar polarimetry has been studied and used in the last decades as it provides means to discriminate among different scattering mechanisms. The way different polarisations interact with targets and the environment allow for additional degrees of freedom to be used for a number of applications. Some important applications of interest where polarimetry provides the means for improved performance or additional capabilities are as follows:

- Effective detection: Polarimetry can be used to enhance the target RCS and to remove clutter. Evidences can be found in the detection of small ships in heavy sea clutter as well as the detection of targets under foliage.
- Automatic target classification and recognition: Targets are seen by radar as complex scattering phenomena. Such scattering mechanisms can be discriminated and classified by using fully polarimetric radar systems. Decomposition methods that are able to classify different types of scattering have been devised, which can be associated with specific targets of parts of them. Such an ability allows for ATR system to become more effective than those based on single-polarisation radar systems.
- Classification of natural scenes: Natural scenes, similarly to man-made targets, are characterised with different types of scattering. More specifically, various types of natural surfaces exhibit different behaviour from an e.m. point of view. Such characteristics can be sensed by polarimetric radar, which can use it to classify the type of scene. Such capability can be used for both civil- and military-driven Earth observation.

1.2.4 Multi-frequency radar imaging systems

As scattering mechanisms strongly depend on frequency, frequency diversity can be used to enhance and enable radar capabilities. More specifically, for what concerns radar imaging, a number of applications benefit from dual and multiple frequency radar systems. As a general rule, higher frequencies open the possibility of using wider bandwidth, which, in turn, allow for finer resolutions to be achieved. On the other hand, lower frequencies may have limited bandwidth and therefore coarser resolution, which limits the amount of details that may be visible. Although higher frequencies should be preferred in this matter, they suffer of a few drawbacks, such as limited range and scarce foliage penetration capability. For these reasons, lower frequencies still play an important role in radar imaging. We may summarise some benefits that descend from the use of multi-frequency radar systems, as follows:

- Multi-frequency radars are able to take advantage of both low-frequency and high-frequency characteristics and guarantee effectiveness in a variety of scenarios.
- The use of multi-frequency systems should also be regarded as multispectral systems that are able to obtain spectral signatures of targets, which appear differently at various frequencies. This dimension should be considered as an additional

degree of freedom to be exploited to enhance diversity and therefore separate a target from another.

- Target detection within SAR images should be benefitted from the use of multiple frequencies as the signal-to-clutter ratio may depend on the utilised frequency and maxima may be found at given frequencies that guarantee higher target detectability.

1.2.5 Systems design considerations

More channels or nodes cost more; hence there needs to be a strong justification in performance benefit to justify the cost, such as more coverage and more timely information. By timely we mean detecting something further away but also taking less time to be able determine what it is and decide what to do about it. This is where enhanced identification through target imaging is most likely to be of benefit. It is more likely that a technique discussed in this book will be adopted if it can be implemented as an additional capability in an existing system or system of systems than if a new system has to be built to implement the method. Despite much research into multichannel systems, the most numerous radar systems available remain monostatic and single channel, although more of these are coherent than would have been the case 20 years ago. This suggests that multistatic methods will have a more readily available user base than multichannel; however, these systems need to be able to communicate information between them, which might not always be the case. Many radars, particularly mobile or relocatable military systems, are used stand-alone with only the operators privy to the information produced. Some of the data may be shared, sometime this can still be via verbal communication over radio or a radio data-link, such as MIDS, which has limited bandwidth and is therefore generally restricted to target-track information. Multistatic systems may therefore require an enhancement of communications networks in terms of bandwidth and data-rates, which could be as complex as upgrading the radars. The move to network-enabled capability is likely to make the comms infrastructure more readily available. Multi-frequency systems could be similar to multistatic systems, if they comprise a distributed network of sensors operating at different frequencies so that data and/or imagery needs to be shared around the system. A platform could also have multiple co-located sensors providing imagery in different radar bands, which reduces the complexity of distributing the data, but would mean that the imagery has a single perspective. It is also conceivable that an ultra-wideband radar can produce imagery at differing frequencies from a single sensor and possibly even over a single aperture or data-collection period (by processing different parts of the bandwidth separately or interleaving pulses at different frequencies). Note that hyperspectral systems that can produce multiple images at varying frequencies simultaneously have not yet appeared in the RF domain and, while not beyond the realms of possibility, the technology would be exceedingly complex to develop. Multichannel systems get around the problem of synchronisation and between spatially separated nodes but make the individual sensor more complex and increase the processing demands. For these reasons, most multichannel systems in operation have a modest number of channels (two, three or four) and most are dedicated to the convention approach of sum, difference and guard channels formed at RF and then digitised. Radars with larger numbers of channels, based on individually digitised ‘subarrays’ of a phased array antenna, are becoming more numerous, though many remain as experimental or development systems. Systems with a small number of channels will however remain the most numerous for a long time to come, hence techniques based around conventional set-ups of channels are most likely to be immediately exploited. Of all the techniques considered here, it is probably fair to say that radar systems that can measure polarisation are the least numerous, being limited to a few experimental airborne systems and satellite radars for Earth observation. Operational radar systems generally have an antenna with a fixed polarisation, or more accurately an antenna provides no measurement of the polarisation state of the received signal. Polarisation is a neglected subject in radar-signals analysis because of this, with the variation in polarisation due to interaction with the structure of the target most often subsumed into statistical models of radar cross-section and clutter backscatter. The incorporation of polarisation measurement into the antenna and receiver hardware of an operational system, as well as the additional processing required, would be technologically challenging, especially for phased array antennas that would need transmit/receive elements with selectable polarisation. Such technology is feasible, which is why it is important to consider the application of polarimetry here and understand whether the performance benefits justify the investment in technology development. The previous sentence sums up the ethos of the analysis provided in this book. If the science tells us that a technique provides a major advance in performance then when we as engineers are asked ‘can we build it?’ The answer is most often ‘yes we can’.

1.2.6 Concluding remarks

Without any doubt, multidimensional radar systems are more complex and costly than monodimensional ones. Nevertheless, the advantages offered by such systems may be such to justify the effort. As described in the previous sections, multidimensionality embraces several degrees of freedom, which may lead to optimal combinations in dependance of the scenario and application at hand. The question to ask (and to answer) is, therefore, not just a matter of deciding whether a multidimensional radar is better or not than a monodimensional one, but what combination of dimensions (radar characteristics, such as polarimetry, channels and frequencies) better responds to certain needs. In this book, we have tried to collect contributions that explore multidimensional radar in many aspects, including multichannel, multistatic and multi-frequency systems with the aim to provide a grasp of the results that are achievable with such systems. The answer to what configuration provides the optimal system is not contained in this book as it is not unique, and it depends on a number of variables. Nevertheless, having some notions of what can be achieved in terms of capability and performance with a certain type of multidimensional radar system surely helps when deciding what type of radar to build for a specific scenario or combination of scenarios.

1.2.7 Book organisation

This remainder of this book is composed of two parts. Part I will deal with multidimensional radar imaging algorithms, whereas Part II will focus on practical feasibility and applications. More specifically,

- Part I
  - Chapter 2 describes a method for 3D reconstruction of moving targets based on ground-based dual-interferometric ISAR system. ISAR systems form 2D images of targets, which results in a filtered projection of a 3D target onto an image plane. Such an image plane is dependent on the radar-target geometry and dynamics that are generally unknown. 3D ISAR images eliminate the problem of having to deal with an unknown projection. The interferometric phases measured from two orthogonal baselines are used to jointly estimate the effective rotation vector and the scattering centre heights. The scattering centre extraction from the ISAR image is performed by applying a multichannel CLEAN technique. Theoretical approach and results from simulated and real datasets are presented to demonstrate the effectiveness of 3D ISAR imaging.
  - Chapter 3 provides an overview of space-time adaptive processing (STAP)–ISAR processing for clutter suppression and high-resolution imaging of non-cooperative moving targets. In particular, an alternative version of conventional STAP processing for the imaging of moving targets in SAR images is described. Results based on simulated and real data acquired with a multichannel airborne radar system are shown. Specifically, results of the STAP–ISAR processing both on monostatic and bistatic system configurations are presented.
  - Chapter 4 provides the mathematical fundamentals of passive ISAR. Particular attention is given to passive radar systems that make use of multi-frequency broadcast signals, including the possibility to use heterogeneous IO (e.g. DVB-T, UMTS and others). The exploitation of a signal composed of multiple broadcast signals allows for finer spatial resolutions to be obtained and effective radar images to be generated. On the other hand, spectral gaps in broadcasted signals may exist, which would require a system's ability to deal with them. Such issue and other constraints will be analysed in this chapter and solutions will be provided. Results are finally shown based on theoretical, simulated and experimental analysis.
  - Chapter 5 discusses the principles and applications of radar tomography in the more traditional areas of SAR and spotlight SAR as well as the more novel Doppler radar tomography, which are fundamentally related to the so-called fast- and slow-time spatial frequency spaces. The system requirement, data collection requirement and challenges for each application are discussed; various image formation techniques are described; predictions for expected imaging performance in terms of image resolution and image contrast are given. Lastly, the advantages and disadvantages of radar tomography are also

  discussed, with the objective giving the radar engineer tasked with designing such a system some realistic options to consider.
  - Chapter 6 gives an overview of potentials and limitations of SAR based on passive radar systems. Particular attention is devoted to the exploitation of digital broadcasting signals as IO. This chapter defines multistatic operations and presents a validation based on experimental setups available at Fraunhofer FHR.
  - Chapter 7 introduces a technique for multistatic/multiband ISAR image fusion. Special regard is given to the facts that coherence between separated sensors cannot be assumed and that the fusion has to be performed in all three spatial dimensions. The result is a 3D ISAR image that mitigates the problem of aspect angle dependence of ISAR images used for classification. The presented method is furthermore a solution to fuse heterogeneous signals (e.g. multiband). The functionality of the technique is illustrated by results using both simulated and real data.
- Part II
  - Chapter 8 presents an analysis of micro-Doppler signatures of helicopters obtained using a network of passive radar receivers in a multistatic system geometry. Methods for rotor blades imaging, such as inverse synthetic aperture, and rotor parameter estimation using a multiband/multi-receiver passive radar system, are described. Relevant performance comparisons between passive and active radar systems are presented and discussed where appropriate.
  - Chapter 9 discusses the use of data collected from multiple interferometric systems to enhance the system capability to reconstruct 3D non-cooperative target images effectively. In particular, a method for multistatic 3D target reconstruction that is based on an incoherent technique is described, and results based on real data are shown.
  - Chapter 10 describes the acquisition and processing of semi-cooperative bistatic SAR data using the Italian space-based Cosmo-SkyMed SAR system as an illuminator and ground-based receivers that were designed and built at DSTL. Exploiting illumination sources designed for SAR image formation has a number of advantages, including desirable waveform ambiguity functions and suitable power spectral density on the ground. The aim of the work was to assess the performance of the receiver hardware and image formation algorithms. In particular, the impact of errors in transmitter location is addressed and the resulting spatially variant geometric distortions in imagery are explored.
  - Chapter 11 encloses the experience learnt during the 4-year NATO SET-196 RTG on 'multichannel/multistatic radar imaging of non-cooperative targets'. Considerations on the achievements obtained, practical implementations experimented, remaining challenges and future trends are reported in this final chapter to conclude this book.

This page intentionally left blank

Part I

Multidimensional radar imaging algorithms

This page intentionally left blank

Chapter 2

Three-dimensional inverse synthetic aperture radar

Daniele Staglianò[1], Federica Salvetti[1], Elisa Giusti[1] and Marco Martorella[1]

Inverse synthetic aperture radar (ISAR) has proven capabilities for non-cooperative target recognition applications. This sensing imaging technique has been able to provide operational information in a robust manner.

Multichannel/multi-static ISAR systems are of emerging interest as they can exploit spatial diversity, enabling improved performance and new applications. Such systems differ from typical monostatic ISAR systems through consisting of multiple spatially diverse transmitter and receiver sites. Due to this spatial diversity, these systems present challenges in managing their operation as well as in usefully combining the multiple sources of information to give an output to the radar operator.

As we know, the conventional ISAR imaging approach produces two-dimensional (2D) images of targets by projecting the reflectivity function onto the so-called image projection plane (IPP). This means that the same target may produce very different projections and then appear very different when the IPP changes. 3D ISAR imaging can, therefore, be seen as a logical solution to such a problem as it produces 3D target reconstructions and, therefore, can avoid the target's projection onto planes.

This chapter introduces the development of a method for 3D reconstruction of moving targets. This method is based on the use of a dual interferometric ISAR (InISAR) system. The interferometric phases measured from two orthogonal baselines are used to jointly estimate the target's effective rotation vector and the heights of the scattering centres with respect to the image plane. The algorithms are tested on a variety of simulated and real datasets.

2.1 Introduction

The evaluation of radar data of non-cooperative targets that have been acquired using a multichannel or a multi-static radar system needs proper algorithms to recover all available target information. ISAR has been studied for more than three decades

---

[1] CNIT Radar and Surveillance System (RaSS) National Laboratory, Pisa, Italy

and several demonstrations have proven its effectiveness in forming electromagnetic images of non-cooperative targets [1,2]. In its most simple form, ISAR systems produce 2D images of targets. A 2D-ISAR image can be interpreted as a filtered projection of a 3D target's reflectivity function onto an image plane. Given the dependence of the image plane orientation on the radar-target geometry and dynamics (which are typically unknown), such projection cannot be predicted. This often results in a difficult interpretation of an ISAR image. Not knowing the projection of the target onto the image plane necessarily causes difficulties when attempting to classify or recognize the target by using ISAR images. 3D ISAR imaging can, therefore, be seen as a logical solution to such a problem as it produces 3D target reconstructions. 3D ISAR imaging has been a subject for research for many years. In [3], a 3D imaging algorithm based on tomography was developed that extended the synthetic aperture both along the azimuth and the elevation. A key factor in achieving accurate 3D images is precise control over the radar line of sight (LoS) and the incident angle. Such accuracy can be achieved in controlled experiments, such as in the case of turntables [4]. The use of ISAR image snapshots to form 3D images of fast rotating objects when the spinning velocity is much higher than the precession velocity has been proposed in [5]. The effectiveness of this method was proven in the case of ballistic missile 3D imaging. Another way of forming 3D ISAR images was proposed in [6–8], where a sequence of ISAR images is used to track scattering centre range histories. The 3D location of such scatterers is then estimated by using such tracks and by using geometrical constraints induced by rigid bodies. Such methods rely on long observation of the target and their performance strongly depends on the target's motion. Meanwhile, techniques based on the use of multichannel sensors and interferometry have been proposed [9–12] to obtain 3D ISAR images. It should be pointed out sooner rather than later that the 3D target reconstruction is not a full 3D image, as the scatterer's elevation with respect to the IPP is obtained as a result of an estimation problem and not as an output of an imaging algorithm. Nevertheless, a direct advantage of using such techniques is that no a priori knowledge of the target's rotational motion is required and their effectiveness does not depend on such a motion.

The authors of [6,7] proposed a novel algorithm for producing 3D ISAR images of targets by combining ISAR image sequences and interferometry, as detailed in [7].

Problems related to the baseline length in InISAR for 3D target reconstruction were discussed in [13]. A method for compensating the baseline length variation was also proposed in the same paper. In any case, in order to avoid the phase wrapping, by keeping valid the following constraint:

$$d < \frac{\lambda R_0}{D} \tag{2.1}$$

where d is the baseline length, λ is the wavelength of the transmitted waveform, R_0 is the radar-target distance in the phase centre and D is the maximum size of the target. However, the baseline length should be set close to the above-mentioned upper bound since the longer the baseline length, the finer the accuracy results.

A technique for co-registering ISAR images prior to applying interferometry was discussed in [14], whereas the use of two perpendicular antenna arrays was proposed in [9] to form target 3D images. Target motion effects in InISAR were investigated in [15] by using a realistic 3D target model. The problem of 3D target reconstruction is addressed and solved in this work by introducing a new estimation problem, which involves the joint estimation of the target's effective rotation vector (modulus and phase) and the height of the scattering centres by using a dual InISAR system. The estimation of the effective rotation vector allows the ISAR image plane to be estimated.

A partial theoretical foundation of this approach has been introduced in [16,17]. Nevertheless, some critical aspects still remain either unchallenged or not well defined. In particular, the scattering centre extraction and the 3D reconstruction alignment need particular attention. The main goal of this work is to provide a solid theoretical foundation for 3D-InISAR imaging paying particular attention to such problems. The scattering centre extraction is a fundamental step as it allows the computation burden to be greatly reduced. In fact, by extracting a number of bright scatterers from an ISAR image, the target information can be significantly compressed. As a consequence, the 3D reconstruction reduces into the localization of bright scattering points in a 3D space. The scattering centre extraction is carried out in this work by applying an extended version of the CLEAN technique [18], namely the multichannel CLEAN (MC-CLEAN) technique. Once the target 3D reconstruction is accomplished, it is important to align the 3D cloud of points with respect to a preset reference system. This operation is fundamental as it allows reconstructed targets to be compared directly with the target's models. In this work, a 3D target alignment process is proposed that is based on the estimation of the effective rotation vector.

Simulated data are finally used to verify the assumptions made and to confirm the effectiveness of the proposed technique. The simulated data used in this work are obtained by generating the backscattered signal from two point-like scatterer models: an airplane and a boat. By varying the target's motion and the system geometry, several scenarios can be produced to test the proposed algorithm. Also, a real dataset from NATO Joint Trial within RTG SET-196 has been used to test the proposed method in an experimental environment.

2.2 Algorithm description

In this section, the signal processing chain and the system geometry are described. The overall flowchart is depicted in Figure 2.1.

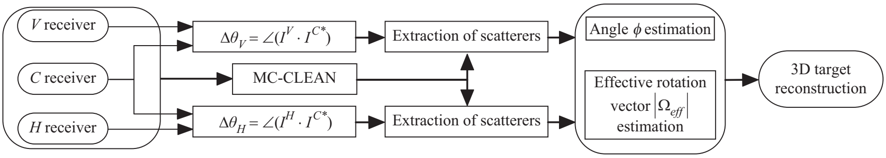
V receiver
C receiver
H receiver
$\Delta\theta_V = \angle(I^V \cdot I^{C*})$
MC-CLEAN
$\Delta\theta_H = \angle(I^H \cdot I^{C*})$
Extraction of scatterers
Extraction of scatterers
Angle ϕ estimation
Effective rotation vector $|\Omega_{eff}|$ estimation
3D target reconstruction

Figure 2.1 Overall flowchart of 3D reconstruction processing

2.2.1 Multichannel ISAR signal model

This section is devoted to present the geometry of an InISAR system and to introduce the multichannel signal model.

2.2.2 System geometry

The system described in Figure 2.2 consists of three antennas arranged in an L-shape configuration with vertical baseline d_V and horizontal baseline d_H. Having to deal with three reference systems, we will denote points in the 3D space by using a subscript according to the specific reference system coordinates, e.g. $\mathbf{C}_\xi$ and $\mathbf{C}_y$ denote the same point expressed with the reference system coordinates T_ξ and T_y , respectively. The point $\mathbf{C}_{\xi'}$ corresponds to the origin of the reference system T'_ξ, which is the antenna array phase centre. The antennas located at points $\mathbf{V}_{\xi'}$ and $\mathbf{H}_{\xi'}$ lie on the ξ'_3 and ξ'_1 axis, respectively. The reference system T'_ξ is embedded on the radar system while T_y is the time-varying reference system embedded on the target and T_x is coincident with T_y at time $t = 0$. The reference system T_ξ corresponds to T'_ξ, but it is centred on the target. For simplicity of representation, let us consider the three antennas to be both transmitting and receiving. Such a configuration would require the use of orthogonal waveforms in order to separate the three channels. However, equal effectiveness could be achieved by considering the use of one transmitter and a certain number of co-located receivers.

Finally, the target is described as a rigid body fixed with respect to T_x, composed of K point-like scatterers with complex amplitude σ_k and with position $\mathbf{x} = \left[x_{1_k}, x_{2_k}, x_{3_k}\right]$ at time $t = 0$ for the generic kth scatterer.

2.2.3 Received signal modelling

As well known, the signal in the frequency/slow time domain at the output of the matched filter after the application of the *straight iso-range* approximation can be expressed as

$$S^{(i)}(f,n) = C \cdot W(f,n) \int_V f'(\mathbf{x}) \exp\left\{-j\frac{4\pi f}{c}\left[R_0^{(i)}(n) + \left(\mathbf{x} \cdot \mathbf{i}^{(i)}_{LOS_x}(n)\right)\right]\right\} d\mathbf{x} \tag{2.2}$$

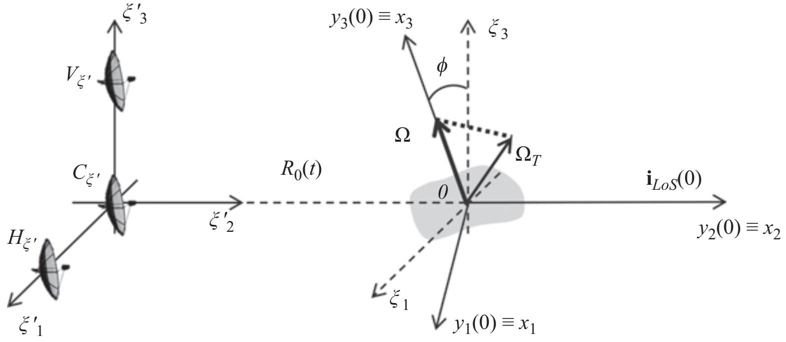

Figure 2.2 ISAR system geometry

where

$$W(f,n) = \mathrm{rect}\left[\frac{n}{N}\right]\mathrm{rect}\left[\frac{f-f_0}{B}\right] \tag{2.3}$$

defines the domain where the 2D Fourier transform (2D-FT) of the reflectivity function $f'(\mathbf{x})$ is defined, C is the complex amplitude, f_0 is the carrier frequency, B is the transmitted signal bandwidth, N is the number of pulses transmitted by the radar, $R_0^{(i)}(n)$ is the modulus of vector $\mathbf{R}_0^{(i)}(n)$ which locates the position of the focusing point O, $\mathbf{i}_{LOS_x}^{(i)}(n)$ is the LOS unit vector of $\mathbf{R}_0(n)$ expressed with respect to T_x and $i \in \{V, C, H\}$. The function rect(x) is equal to 1 for $|x| < 0.5$, 0 otherwise.

For an ideal point scatterer, (2.2) is modified as follows:

$$S^{(i)}(f,n) = \sigma_k^{(i)} \exp\left\{-j\frac{4\pi f}{c}R_0^{(i)}(n)\right\} \exp\left\{-j\frac{4\pi f}{c}\left[\mathbf{x}\cdot\mathbf{i}_{LOS_x}^{(i)}(n)\right]\right\} W(f,n) \tag{2.4}$$

When the baselines are short compared to the radar-target distance, the reflectivity functions $\sigma_k^{(i)}$ can be considered the same for all the channels, i.e. $\sigma_k^{(i)} = \sigma_k$. The received signal after motion compensation can be written as follows:

$$S_C^{(i)}(f,n) = \sigma_k \exp\left\{-j\frac{4\pi f}{c}\left[\mathbf{y}(n)\cdot\mathbf{i}_{LOS_y}^{(i)}(n)\right]\right\} W(f,n) \tag{2.5}$$

where $\mathbf{y}(n)$ is the position of an arbitrary target's point scatterer and $\mathbf{i}_{LOS_y}^{(i)}(n)$ is the LoS unit vector expressed with respect to T_y. The distance between the focusing point O and the projection of the scatterer onto the LoS is mathematically expressed by the scalar product $\mathbf{y}(n)\cdot\mathbf{i}_{LOS_y}^{(i)}(n)$. Under the assumption of a small observation time, the total rotation vector can be considered as constant and the image plane fixed with respect to T_ξ:

$$\boldsymbol{\Omega}_T(n) \cong \boldsymbol{\Omega}_T, \quad 0 \le nT_R \le T_{obs} \tag{2.6}$$

processing interval.

In this case, the position of the target's point scatterer $\mathbf{y}(n)$ can be calculated by solving the following differential equation system:

$$\begin{cases} \dot{\mathbf{y}}(n) = \boldsymbol{\Omega}_T \times \mathbf{y}(n) \\ \mathbf{y}(0) = \mathbf{x} \end{cases} \tag{2.7}$$

The resulting closed form solution is as follows [17,19,20]:

$$\mathbf{y}(n) = \mathbf{a} + \mathbf{b}\cos(\Omega_T nT_R) + \frac{\mathbf{c}}{\Omega_T}\sin(\Omega_T nT_R) \tag{2.8}$$

where $\mathbf{a} = ((\boldsymbol{\Omega}_T\cdot\mathbf{x})/\Omega_T^2)\boldsymbol{\Omega}_T$, $\mathbf{b} = \mathbf{x} - ((\boldsymbol{\Omega}_T\cdot\mathbf{x})/\Omega_T^2)\boldsymbol{\Omega}_T$, $\mathbf{c} = \boldsymbol{\Omega}_T \times \mathbf{x}$ and $\Omega_T = |\boldsymbol{\Omega}_T|$ and $\boldsymbol{\Omega}_T = \left(0, \Omega_{T_2}, \Omega_{eff}\right)$ in the chosen reference systems. Since Ω_{T_2} is aligned along the radar LoS, it does not produce any aspect angle variation and, therefore, does not contribute to the ISAR image formation. The projection onto the plane orthogonal to the LOS defines the effective rotation vector $\boldsymbol{\Omega}_{eff}$. The plane orthogonal to $\boldsymbol{\Omega}_{eff}$ is the imaging plane. The assumption of a small T_{obs} allows also to approximate the term $\mathbf{y}(n)$ in (2.8) by its first-order Taylor series around $t = 0$. The result is expressed in (2.9):

$$\mathbf{y}(n) \cong \mathbf{a} + \mathbf{b} + \mathbf{c}nT_R = \mathbf{x} + \mathbf{c}nT_R \tag{2.9}$$

Under this approximation, the ISAR image can be successfully reconstructed by the range-Doppler (RD) technique [2,21,22] because the Doppler frequency of each scatterer is considered as constant. When the effective rotation vector is sufficiently constant and when the total aspect angle variation is sufficiently small, the RD technique provides focused images. Consequently, a 2D-FT can be used to form the ISAR image. The matrix $\boldsymbol{M}_{\xi y}$ in (2.10) describes the rotation of the reference system T_y of an angle ϕ with respect to T_ξ:

$$\boldsymbol{M}_{\xi y} = \begin{bmatrix} \cos\phi & 0 & \sin\phi \\ 0 & 1 & 0 \\ -\sin\phi & 0 & \cos\phi \end{bmatrix} \tag{2.10}$$

By means of the rotation matrix $\boldsymbol{M}_{\xi y}$, the LoS unit vectors $\mathbf{i}_{LOS_y}^{(i)}(n)$ can be written as the normalized difference between the positions of each sensor and the origin of T_x:

$$\begin{aligned}
\mathbf{i}_{LOS_y}^{V}(n) &\triangleq \frac{\mathbf{y}(n)-\mathbf{V}_y(n)}{|\mathbf{y}(n)-\mathbf{V}_y(n)|} = \left[\frac{-d_V\sin\phi}{\sqrt{R_0(n)^2+d_V^2}} \;\; \frac{R_0(n)}{\sqrt{R_0(n)^2+d_V^2}} \;\; \frac{-d_V\cos\phi}{\sqrt{R_0(n)^2+d_V^2}}\right] \\
\mathbf{i}_{LOS_y}^{C}(n) &\triangleq \frac{\mathbf{y}(n)-\mathbf{C}_y(n)}{|\mathbf{y}(n)-\mathbf{C}_y(n)|} = [0 \;\; 1 \;\; 0] \\
\mathbf{i}_{LOS_y}^{H}(n) &\triangleq \frac{\mathbf{y}(n)-\mathbf{H}_y(n)}{|\mathbf{y}(n)-\mathbf{H}_y(n)|} = \left[\frac{-d_H\cos\phi}{\sqrt{R_0(n)^2+d_H^2}} \;\; \frac{R_0(n)}{\sqrt{R_0(n)^2+d_H^2}} \;\; \frac{d_H\sin\phi}{\sqrt{R_0(n)^2+d_H^2}}\right]
\end{aligned} \tag{2.11}$$

where $\mathbf{V}_y(n)$, $\mathbf{C}_y(n)$ and $\mathbf{H}_y(n)$ are the positions of the antennas with respect to T_y and d_V and d_H represent the vertical and horizontal baseline lengths, respectively. Therefore, the scalar product in (2.5) can be written as [22]

$$\begin{aligned}
\mathbf{y}(n)\cdot\mathbf{i}_{LOS_y}^{V}(n) &\cong (\mathbf{x}+\mathbf{c}nT_R)\cdot\mathbf{i}_{LOS_y}^{V}(n) = (x_1+c_1nT_R)\left(\frac{-d_V\sin\phi}{\sqrt{R_0(n)^2+d_V^2}}\right) \\
&\quad + (x_2+c_2t)\left(\frac{R_0(n)}{\sqrt{R_0(n)^2+d_V^2}}\right) + (x_3+c_3nT_R)\left(\frac{-d_V\cos\phi}{\sqrt{R_0(n)^2+d_V^2}}\right) \\
&\cong x_2+c_2nT_R-\frac{d_V}{R_0}\left[(x_1+c_1nT_R)\sin\phi+(x_3+c_3nT_R)\cos\phi\right] \\
&= K_0^V+K_1^VnT_R
\end{aligned} \tag{2.12}$$

where

$$K_0^V \triangleq x_2 - \frac{d_V}{R_0}\left(x_1\sin\phi + x_3\cos\phi\right) \tag{2.13}$$

$$K_1^V \triangleq c_2 - \frac{d_V}{R_0}\left(c_1\sin\phi + c_3\cos\phi\right) \tag{2.14}$$

The term $R_0(t)$ can be reasonably approximated with $R_0(0) = R_0$ when considering a small observation time. Equivalently, the denominators $\sqrt{R_0(n)^2 + d_V^2}$ and $\sqrt{R_0(n)^2 + d_H^2}$ are approximated as R_0. The terms c_1, c_2 and c_3 are the three components of the vector $\mathbf{c}$ introduced in (2.8). The scalar products for the other two elements can be similarly computed as follows:

$$\mathbf{y}(n) \cdot \mathbf{i}^{C}_{LOS_y}(n) \cong K_0^C + K_1^C nT_R \tag{2.15}$$

$$\mathbf{y}(n) \cdot \mathbf{i}^{H}_{LOS_y}(n) \cong K_0^H + K_1^H nT_R \tag{2.16}$$

where

$$K_0^C \triangleq x_2 \tag{2.17}$$

$$K_1^C \triangleq c_2 \tag{2.18}$$

$$K_0^H \triangleq x_2 + \frac{d_H}{R_0}\left(x_3 \sin\phi - x_1 \cos\phi\right) \tag{2.19}$$

$$K_1^H \triangleq c_2 + \frac{d_H}{R_0}\left(c_3 \sin\phi - c_1 \cos\phi\right) \tag{2.20}$$

By substituting the scalar products of (2.12), (2.15) and (2.16) into (2.5), the received signal model can be written as follows:

$$\begin{aligned} S_C^{(i)}(f,n) &= \sigma_k \exp\left\{-j\frac{4\pi f}{c}\left[K_0^{(i)} + K_1^{(i)} nT_R\right]\right\} W(f,n) \\ &= \sigma_k \exp\left\{-j\frac{4\pi f K_1^{(i)}}{c} nT_R\right\} \operatorname{rect}\left(\frac{n}{N}\right) \exp\left\{-j\frac{4\pi K_0^{(i)}}{c} f\right\} \operatorname{rect}\left(\frac{f-f_0}{B}\right) \end{aligned} \tag{2.21}$$

In the case of small aspect angle variations, the standard procedure for obtaining ISAR images is the RD technique. A 2D-FT is applied and the analytical form of the complex ISAR image in the delay-time (τ) and Doppler (ν) domain is obtained. The result is shown in (2.22).

$$\begin{aligned} I^{(i)}(\tau,\nu) &= RD_{\substack{f\to\tau \\ n\to\nu}}\left\{S_C^{(i)}(f,n)\right\} = BNT_R\sigma_k e^{j2\pi f_0\left(\tau - \frac{2}{c}K_0^{(i)}\right)} \\ &\qquad \operatorname{sinc}\left[T_{obs}\left(\nu + \frac{2f_0}{c}K_1^{(i)}\right)\right] \operatorname{sinc}\left[B\left(\tau - \frac{2}{c}K_0^{(i)}\right)\right] \end{aligned} \tag{2.22}$$

where $\operatorname{sinc}(x) \triangleq (\sin(\pi x)/\pi x)$ and $RD_{\substack{f\to\tau \\ n\to\nu}}\{\cdot\}$ indicate the operation of image formation by means of the RD approach.

2.2.4 Multichannel CLEAN algorithm

In this section, a spatial MC-CLEAN technique is proposed. The CLEAN technique can be used to extract target features, such as position and complex amplitude of dominant scattering centres. Being the system at hand a multichannel system, the single-channel CLEAN technique is here modified. The modification made stems from similar concept discussed in [23], where a POLCLEAN technique was presented. The MC-CLEAN works iteratively using a genetic algorithm [24] by

- locating the brightest scattering centre in one of the multichannel ISAR images and finding its coordinates in the time delay-Doppler image plane;
- estimating the scattering centre point spread function (PSF) which corresponds to the extracted coordinates of each ISAR image and
- removing the estimated PSFs from the ISAR images in order to extract the next brightest scattering centre.

The algorithm stops when the residual energy in the ISAR image at the kth iteration is lower than a preset threshold λ. Such a threshold is typically set to a percentage of the initial energy. The block diagram describing the MC-CLEAN is depicted in Figure 2.3.

Figure 2.4 shows an example with a target that resembles the shape of an aircraft. An example of a simulated 2D-ISAR image, the output of the MC-CLEAN technique and the residual ISAR image is shown in Figure 2.4. The input ISAR image resembles

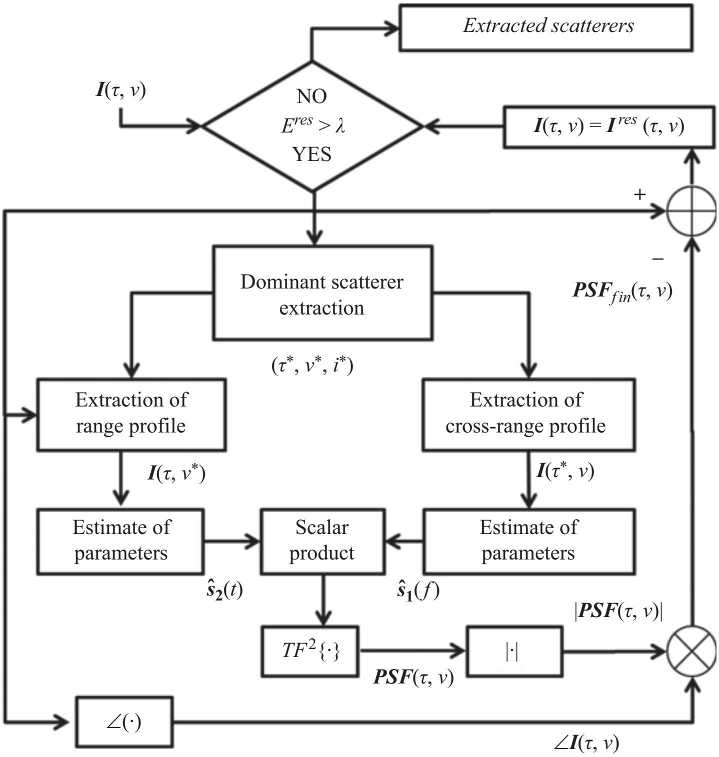

Figure 2.3 MC-CLEAN block diagram

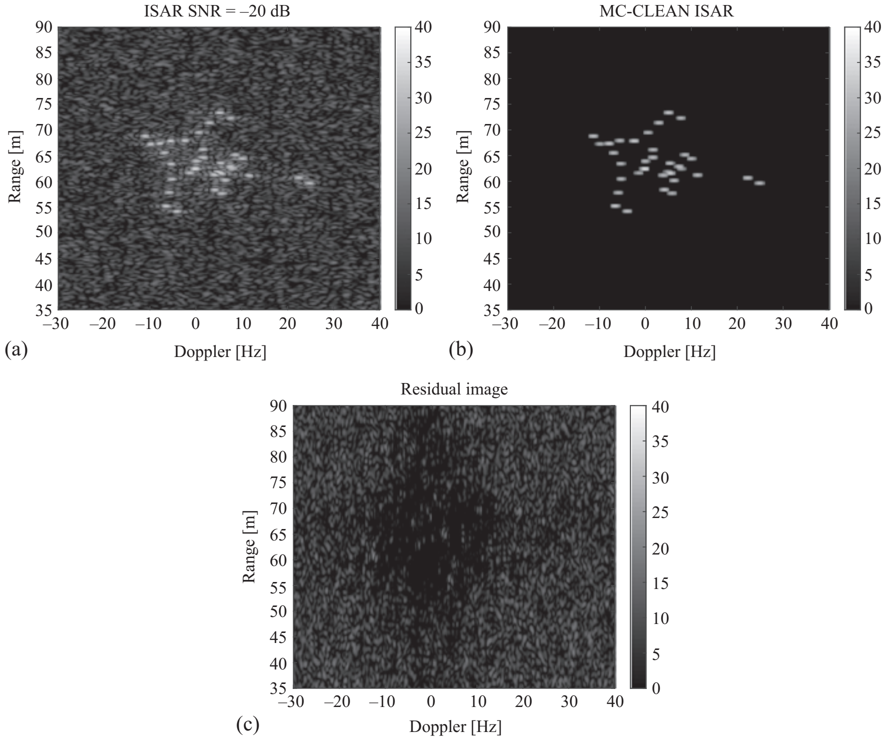

Figure 2.4 MC-CLEAN results: (a) ISAR image as input, (b) output and (c) residual ISAR image

the shape of an aircraft with 35 scatterers. Additive white Gaussian noise has been added in data domain so as to have a signal-to-noise ratio (SNR) equal to −20 dB. All the scatterers are extracted in the right coordinates.

2.2.5 3D reconstruction processing

According to [17,25], the height of each scatterer with respect to the image plane depends on the angle ϕ and on the phase differences between the antennas along the vertical and horizontal baselines. We also assume that the IPP is the same and that the target is located in the far field region. The phase differences, i.e. *interferograms*, for the horizontal and vertical configurations, can be calculated from the ISAR images by exploiting both the vertical and horizontal interferometers as

$$\triangle\theta_V = \angle\left\{I^V(\tau,\nu)\cdot\mathrm{conj}\left[I^C(\tau,\nu)\right]\right\} \tag{2.23}$$

$$\triangle\theta_H = \angle\left\{I^H(\tau,\nu)\cdot\mathrm{conj}\left[I^C(\tau,\nu)\right]\right\} \tag{2.24}$$

where conj$(\cdot)$ represents the conjugate operator. By considering the ISAR images calculated at the peaks of the sinc functions in (2.22), the interferograms in (2.23) and (2.24) can be expressed as follow:

$$\triangle\theta_V = \frac{4\pi}{c} f_0 \left(K_0^C - K_0^V\right) = \frac{4\pi}{c} f_0 \frac{d_V(x_1 \sin\phi + x_3 \cos\phi)}{R_0} \tag{2.25}$$

$$\triangle\theta_H = \frac{4\pi}{c} f_0 \left(K_0^C - K_0^H\right) = \frac{4\pi}{c} f_0 \frac{d_H(x_1 \cos\phi - x_3 \sin\phi)}{R_0} \tag{2.26}$$

The point $\mathbf{x} = \mathbf{y}(0)$ is first mapped onto the point $\boldsymbol{\xi} = [\xi_1, \xi_2, \xi_3]$ from the reference system T_x to the reference system T_ξ. In order to obtain the analytical expression of its coordinates with respect to T_ξ, the following transformation is applied:

$$\boldsymbol{\xi} = \mathbf{M}_{\boldsymbol{\xi}\mathbf{y}}^{-1} \cdot \mathbf{y}(0)^T = \mathbf{M}_{\boldsymbol{\xi}\mathbf{y}}^{-1} \cdot \mathbf{x} \tag{2.27}$$

where the symbol $(\cdot)^T$ is the transpose operator and the rotation matrix $\mathbf{M}_{\boldsymbol{\xi}\mathbf{y}}^{-1}$ is defined as in (2.10). In details:

$$\boldsymbol{\xi} = \begin{bmatrix} \cos\phi & 0 & -\sin\phi \\ 0 & 1 & 0 \\ \sin\phi & 0 & \cos\phi \end{bmatrix} \cdot \begin{bmatrix} x_1 \\ x_2 \\ x_3 \end{bmatrix} \tag{2.28}$$

Therefore, the coordinates of the point $\mathbf{y}_\xi$ can be expressed as

$$\begin{cases} \xi_1 = x_1 \cos\phi - x_3 \sin\phi \\ \xi_2 = x_2 \\ \xi_3 = x_1 \sin\phi + x_3 \cos\phi \end{cases} \tag{2.29}$$

These coordinates can be expressed as a function of the phase differences. This can be done after rewriting $\triangle\theta_V$ and $\triangle\theta_H$ by substituting (2.27) in (2.30) and (2.31) and then by inverting the obtained equations, as shown in the following equation:

$$\triangle\theta_V = \frac{4\pi}{c} f_0 \frac{d_V \xi_3}{R_0} \Rightarrow \xi_3 = \frac{c}{4\pi f_0} \frac{R_0}{d_V} \triangle\theta_V \tag{2.30}$$

$$\triangle\theta_H = \frac{4\pi}{c} f_0 \frac{d_H \xi_1}{R_0} \Rightarrow \xi_1 = \frac{c}{4\pi f_0} \frac{R_0}{d_H} \triangle\theta_H \tag{2.31}$$

Finally, the expression of the coordinates of $\mathbf{x}$ can be obtained by remapping the coordinates from T_ξ to T_x as follows:

$$\mathbf{x} = \mathbf{M}_{\boldsymbol{\xi}\mathbf{y}} \cdot \boldsymbol{\xi} \tag{2.32}$$

In details:

$$\mathbf{x} = \begin{bmatrix} \cos\phi & 0 & \sin\phi \\ 0 & 1 & 0 \\ -\sin\phi & 0 & \cos\phi \end{bmatrix} \cdot \begin{bmatrix} \xi_1 \\ \xi_2 \\ \xi_3 \end{bmatrix} \tag{2.33}$$

Therefore, the coordinate of $\mathbf{x}$ can be written as

$$\begin{cases} x_1 = \xi_1 \cos\phi + \xi_3 \sin\phi \\ x_2 = \xi_2 \\ x_3 = \xi_3 \cos\phi - \xi_1 \sin\phi \end{cases} \tag{2.34}$$

In particular, by substituting (2.30) and (2.31) into the component x_3 of (2.34), which represents the height of the scatterer with respect to the image plane, it can be expressed as a function of the phase differences and the angle ϕ as follows:

$$x_3 = \frac{c}{4\pi f_0} R_0 \left(\frac{\Delta\theta_V}{d_V} \cos\phi - \frac{\Delta\theta_H}{d_H} \sin\phi \right) \tag{2.35}$$

In order to completely define the component x_3, the angle ϕ needs to be estimated. In fact, all of the other parameters are known or measured. In particular, the range distance R_0 can be evaluated from the RD map and the interferograms $\Delta\theta_V$ and $\Delta\theta_H$ are measured from the ISAR images as shown in (2.23) and (2.24).

It should be reminded that ϕ represents the angle between the third component of the T_ξ reference system and $\mathbf{\Omega}_{\mathit{eff}}$. Since $\mathbf{\Omega}_{\mathit{eff}}$ is aligned with respect to the axis x_3 in the T_x reference system, the angle ϕ corresponds to rotation angle between the reference systems T_ξ and T_x.

$\mathbf{\Omega}_{\mathit{eff}}$ and ϕ can be jointly estimated by expressing the term $\mathbf{c}$ in (2.8) with respect to the reference system T_y:

$$\mathbf{c} = \mathbf{\Omega_T} \times \mathbf{x} \Rightarrow c_2 \simeq x_1 \Omega_{\mathit{eff}} \tag{2.36}$$

where $\mathbf{\Omega_T} = \left(0, \Omega_{T2}, \Omega_{\mathit{eff}}\right)$, Ω_{eff} is the modulus of $\mathbf{\Omega}_{\mathit{eff}}$ and Ω_{T2} is the coordinate of $\mathbf{\Omega_T}$ along the y_2 axis. It should be noted that this is the result of the selection of T_y. In fact, this reference system is chosen in order to have the y_3 axis aligned with $\mathbf{\Omega}_{\mathit{eff}}$ at $t = 0$, the y_2 axis aligned with the LoS and the y_1 axis to complete a Cartesian triplet. It should also be pointed out that Ω_{T2} does not produce any aspect angle variation, as it is aligned with the LoS. Thus, the first component Ω_{T1} must be zero since Ω_{eff} is the only component that gives the contribution to changing the aspect angle.

The term c_2 can also be expressed by taking into account the Doppler component as follows:

$$\nu_C \triangleq -\frac{2f_0}{c} K_1^C \cong -\frac{2f_0}{c} c_2 \Rightarrow c_2 = -\nu_C \frac{c}{2f_0} \tag{2.37}$$

After some algebra, a relation between ν_C, $\Delta\theta_H$, $\Delta\theta_V$ and ϕ can be obtained. In particular, by substituting the component x_1 of (2.34) and (2.36) into (2.37), the following equations can be derived:

$$c_2 = x_1 \Omega_{\mathit{eff}} = (\xi_1 \cos\phi + \xi_3 \sin\phi) = -\nu_C \frac{c}{2f_0} \tag{2.38}$$

Thus, by using the relations in (2.31) and (2.30):

$$\frac{cR_0 \Delta\theta_H}{4\pi f_0 d_H} \Omega_{\mathit{eff}} \cos\phi + \frac{cR_0 \Delta\theta_V}{4\pi f_0 d_V} \Omega_{\mathit{eff}} \sin\phi = -\nu_C \frac{c}{2f_0} \tag{2.39}$$

After some simplifications, the following equation is derived:

$$\nu_C = -\frac{R_0\Omega_{eff}}{2\pi}\left(\frac{\triangle\theta_H}{d_H}\cos\phi + \frac{\triangle\theta_V}{d_V}\sin\phi\right) \tag{2.40}$$

Equation (2.40) can be also expressed as follows:

$$Z = aY + bX \tag{2.41}$$

where

$$\begin{cases} Z \triangleq \nu_C \\ Y \triangleq -\dfrac{R_0}{2\pi d_H}\triangle\theta_H \\ X \triangleq -\dfrac{R_0}{2\pi d_V}\triangle\theta_V \\ a \triangleq \Omega_{eff}\cos\phi \\ b \triangleq \Omega_{eff}\sin\phi \end{cases} \tag{2.42}$$

Consequently, by considering the contribution of K independent scatterers, the parameters Z, Y and X can be expressed as vectors. In particular,

$$\mathbf{Z} = [Z_1, Z_2, \ldots, Z_K]^T \tag{2.43}$$

$$\mathbf{Y} = [Y_1, Y_2, \ldots, Y_K]^T \tag{2.44}$$

$$\mathbf{X} = [X_1, X_2, \ldots, X_K]^T \tag{2.45}$$

Therefore, (2.41) can be rewritten by considering only the contribution due to the kth scatterer as follows:

$$Z_k = aY_k + bX_k \qquad k = 1, \ldots, K \tag{2.46}$$

In other words, Z_k corresponds to the Doppler value of the kth scatterer for the central receiver. Therefore, the interferometric phases are calculated from the matrices $\triangle\theta_H$ and $\triangle\theta_V$ only in the range and Doppler bins where the scatterers are extracted. In this way, the terms X_k, Y_k and Z_k are real values and (2.46) represents the equation of a plane.

Then, the estimates of Ω_{eff} and ϕ can be calculated by estimating a and b. This can be done by evaluating the regression plane, that is the plane that minimizes the sum of the square distances of the points $P_k = (X_k, Y_k, Z_k)$ from the plane itself.

The problem can be mathematically solved by minimizing the function:

$$\Upsilon(a,b) = \sum_{k=1}^{K}[Z_k - (aY_k + bX_k)]^2 \tag{2.47}$$

The minimization of $\Upsilon(a,b)$ in (2.47) can be done by demonstrating that $\Upsilon(a,b)$ is a convex function. In fact, a twice differentiable function of several variables is convex on a convex set if and only if its Hessian matrix is positive semidefinite on the interior of the convex set. Any local minimum of a convex function is also a global minimum. A strictly convex function will have at most one global minimum. The latter condition is verified when convex set corresponds to the whole domain.

Let the following quantities be defined as follow:

$$\begin{cases} S_{XX} = \mathbf{X}^T\mathbf{X} \\ S_{YY} = \mathbf{Y}^T\mathbf{Y} \\ S_{XY} = \mathbf{X}^T\mathbf{Y} \\ S_{XZ} = \mathbf{X}^T\mathbf{Z} \\ S_{YZ} = \mathbf{X}^T\mathbf{Z} \end{cases} \tag{2.48}$$

By solving the minimization problem with respect to the variables (a, b), the following result can be derived:

$$\begin{cases} a = \dfrac{S_{XZ}S_{XY} - S_{YZ}S_{XX}}{S_{XY}^2 - S_{XX}S_{YY}} \\ b = \dfrac{S_{YZ}S_{XY} - S_{YY}S_{XZ}}{S_{XY}^2 - S_{XX}S_{YY}} \end{cases} \tag{2.49}$$

Finally, the estimation of Ω_{eff} and ϕ can be derived from the estimates $\tilde{a}$ and $\tilde{b}$ as described in the following equations:

$$\hat{\Omega}_{eff} = \sqrt{\tilde{a}^2 + \tilde{b}^2} \tag{2.50}$$

$$\hat{\phi} = \arctan\left(\frac{\tilde{b}}{\tilde{a}}\right) \tag{2.51}$$

An example of the function $\Upsilon(a, b)$ is depicted in Figure 2.5.

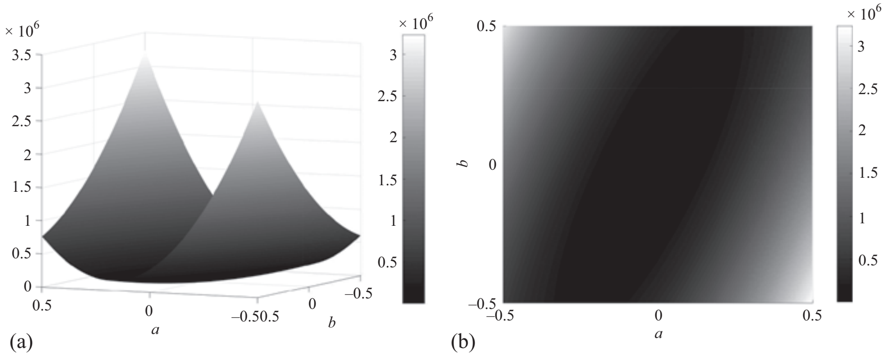

Figure 2.5 Υ convex function: (a) 3D view and (b) top view

2.3 Performance analysis

It is very important to evaluate the performances of the interferometric processing in order to better interpret the results of the 3D reconstruction.

Consider to analyse simulated data where Gaussian noise has been added to the raw data in order to obtain a given SNR (in the data domain).

As described in the previous sections, the inputs of the interferometric processing are the interferometric phases and the RD positions of the scattering centres extracted by the MC-CLEAN technique. The height of each scatterer with respect to the image plane is then obtained through the estimation of the mentioned parameters. Consequently, the resulting 3D shape is composed of several scattering centres. In order to analyse the performances of this method, the first step is then to realign the reconstructed target, expressed with respect to the image plane, with the reference model, expressed with respect to T_ξ. In this way, each scatterer of the reconstructed target can be consistently compared with each scatterer of the reference model.

The performance analysis block diagram is shown in Figure 2.6.

First, the reference model is rotated so that its heading coincides with the assigned trajectory and the reconstructed target is rotated so that the image plane coincides with the horizontal plane where the reference model is expressed.

Second, each scatterer of the 3D reconstructed target is associated to the correspondent scatterer of the model through a soft assignment processing. Finally, performance indicators are defined in order to verify the effectiveness of the method.

2.3.1 Scatterers realignment

1. **Rotation of the model along the trajectory**: The model is rotated along the trajectory by means of the rotation matrix $\boldsymbol{R}_t$ as follows:

$$\begin{aligned} \boldsymbol{C}_{rt} &= \boldsymbol{R}_t \cdot \boldsymbol{C}_m \\ \boldsymbol{R}_t &= \boldsymbol{R}_\mu \cdot \boldsymbol{R}_\nu \cdot \boldsymbol{R}_\phi \end{aligned} \tag{2.52}$$

   where $\boldsymbol{C}_m$ is the matrix of dimensions $3 \times K_M$ describing the coordinates of the model; $\boldsymbol{R}_\mu, \boldsymbol{R}_\nu$ and $\boldsymbol{R}_\xi$ are the yaw, pitch and roll rotation matrices, respectively. Finally, $\boldsymbol{C}_{rt}$ is the matrix representing the 3D coordinates of the model after being rotated.
2. **Image plane rotation**: The reconstructed target is rotated in order to have the image plane coincident with the horizontal plane. This can be done by remapping

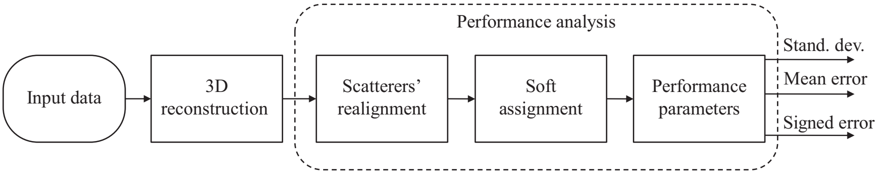

Figure 2.6 Performance analysis flowchart

the coordinates of the reconstructed target from the reference system T_x to the reference system T_ξ, as defined in (2.27).

2.3.2 Soft assignment

The adopted soft assignment method is based on a probabilistic least squares approach [26,27]. A soft assignment procedure associates each model scatterers to each reconstructed scatterers. Each of these assignments is weighted by a coefficient that is defined as a probability. In fact, the sum of all possible assignments for a given scatterer adds to the unity. Thus, the optimization problem can be expressed as

$$\hat{\boldsymbol{\alpha}} = \arg\{\min\{J(\boldsymbol{\alpha})\}\} \tag{2.53}$$

where

$$J(\boldsymbol{\alpha}) = \sum_{i=1}^{K_M} \sum_{k=1}^{K} \alpha_{i,k} \boldsymbol{\varepsilon}_{i,k}^T \boldsymbol{\varepsilon}_{i,k} \alpha_{i,k} \tag{2.54}$$

is the cost function; K is the number of the extracted scattering centres, K_M is the number of scatterers which composes the target model and $\boldsymbol{\varepsilon}_{i,k}$ is the distance between the ith scatterer of the model and the kth scatterer of the reconstructed target; $\boldsymbol{\alpha}$ is the matrix of dimensions $K_M \times K$ containing the soft assignments:

$$\boldsymbol{\alpha} = \begin{bmatrix} \alpha_{1,1} & \cdots & \alpha_{1,K} \\ \vdots & \vdots & \vdots \\ \vdots & \alpha_{i,k} & \vdots \\ \vdots & \vdots & \vdots \\ \alpha_{K_M,1} & \cdots & \alpha_{K_M,K} \end{bmatrix} \tag{2.55}$$

Each element of the matrix $\alpha_{i,k}$ represents the probability that the kth extracted scatterer belongs to the ith model's scatterer and is expressed as follows:

$$\begin{cases} \alpha_{i,k} = \dfrac{\left(\boldsymbol{\varepsilon}_{i,k}^T \boldsymbol{\varepsilon}_{i,k}\right)^{-1}}{\sum_{p=1}^{K_M} \left(\boldsymbol{\varepsilon}_{p,k}^T \boldsymbol{\varepsilon}_{p,k}\right)^{-1}}, \\ \sum_{i=1}^{K_M} \alpha_{i,k} = 1 \quad \forall k = 1, \ldots, K \end{cases} \tag{2.56}$$

Finally, each extracted scatterer is assigned to the model's scatterer with the highest $\alpha_{i,k}$.

2.3.3 Performance indicators

Two different kinds of errors could affect the results: the assignment error and the scatterers height estimation error.

The assignment error is related to the identification of unreliable assignments and, therefore, it allows for an accurate evaluation of the scatterers' height estimation error. An unreliable assignment is declared when a scatterer's height error ϵ_h is greater than a fixed threshold Λ, which is expressed as follows:

$$\Lambda = A_v[\bar{\epsilon}_h(s)] + \gamma \cdot \sigma_{\epsilon_h} \tag{2.57}$$

where $A_v[\cdot]$ indicates the expectation operator calculated by considering S Monte Carlo runs of the simulation and $\bar{\epsilon}_h(s)$ is defined as follows:

$$\bar{\epsilon}_h(s) = \frac{1}{K}\sum_{k=1}^{K} \epsilon_h(k,s) \tag{2.58}$$

The height error of the single kth scatterer of the sth Monte Carlo step is defined as

$$\epsilon_h(k,s) = |h_m(k,s) - h_r(k,s)| \tag{2.59}$$

where $h_m(k,s)$ and $h_r(k,s)$ are the heights with respect to the image plane referring to the model and to the reconstructed target, respectively. The parameter σ_{ε_h} is the standard deviation of ϵ_h and $\gamma \in \mathbb{R}$ is a parameter that can vary to empirically adjust the threshold Λ. Simulations with different values of γ have demonstrated that this parameter does not affect the final result.

The scatterers' height estimation error is then computed using the same procedure, after having discarded all the unreliable assignments.

Finally, the error on the estimates of the angle $\hat{\phi}$ and the effective rotation vector $\hat{\Omega}_{eff}$ are calculated by using the expectation operator as follows:

$$A_v[\epsilon_\Omega(s)] = \frac{1}{S}\sum_{s=1}^{S} \epsilon_\Omega(s) \tag{2.60}$$

and

$$A_v[\epsilon_\phi(s)] = \frac{1}{S}\sum_{s=1}^{S} \epsilon_\phi(s) \tag{2.61}$$

where $\epsilon_\Omega(s)$ and $\epsilon_\phi(s)$ are defined as follows:

$$\epsilon_\Omega(s) = |\hat{\Omega}_{eff}(s) - \Omega_{eff}| \tag{2.62}$$

$$\epsilon_\phi(s) = |\hat{\phi}(s) - \phi| \tag{2.63}$$

where Ω_{eff} and ϕ are a priori known.

2.4 Results

2.4.1 Simulated results

The analysis of simulated data aims at testing the effectiveness of the 3D reconstruction algorithm. In particular, we tested the algorithm performance for three different baseline lengths with the increasing of the SNR. It is worth pointing out that Gaussian noise has been added to the raw data in order to have the selected SNR (in the data domain). Two tests have been run, either in the presence or in the absence of unreliable assignments.

The target is assumed to be a rigid body moving in a rectilinear trajectory (defined by roll, pitch and yaw directions) with respect to the radar LoS. The target resembles the shape of a boat and it is composed of $K_M = 36$ ideal scatterers.

In this simulation, perfect motion compensation has been applied. The target is in a non-squinted configuration and the performance analysis is carried out with the increase of the baseline length and SNR. The target motion is characterized by its own motion components.

The target is shown in Figure 2.7. For a clearer and simpler visualization, their principal axes coincide with the X–Y–Z Cartesian coordinates.

The threshold Λ selected for both the simulations has been tested by varying the parameter γ. Results do not show significant variations. Table 2.1 shows the

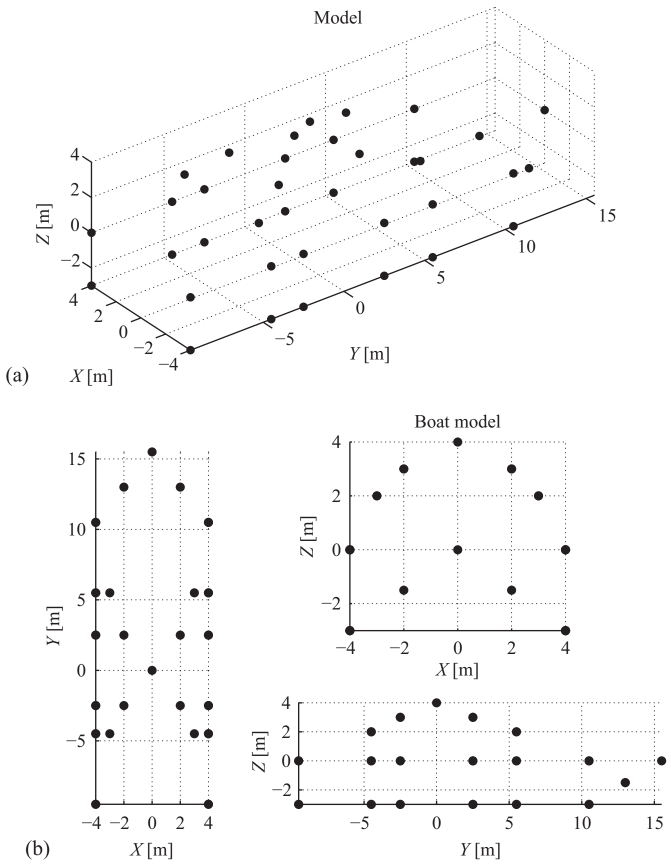

Figure 2.7 Model targets composed of ideal point-like scatterers. (a) target from a 3D view; (b) target projected onto X–Y, X–Z and Y–Z planes

parameters used in the simulation. The backscattered signal is simulated by using a stepped frequency continuous waveform and its characteristics are described in Table 2.1.

The final result obtained with a $SNR = -10$ dB is shown in Figures 2.8 and 2.9, where the reconstructed targets are superimposed onto the models.

Figures 2.10 and 2.11 show the behaviour of the height error and the standard deviation of the height error as the SNR and the baseline length change. The height error and the standard deviation of the height error are expressed in metres. Both the performance indicators are shown with and without unreliable assignments. The baseline lengths are chosen in order to avoid the ambiguity of the interferometric phases. Short baselines produce larger phase error measurement and, therefore, larger height estimation errors occur. On the other hand, as the baseline length exceeds the upper bound of the ambiguity of the interferometric phases, the height error tends to increase since the target is not contained in the unambiguous window.

Figure 2.12 depicts the height error $E[\bar{\epsilon}_h(k)]$ calculated by preserving the positive or negative sign of ϵ_h when unreliable assignments are discarded. It can be noted that the estimator is unbiased.

Table 2.1 Parameters of simulation

Number of freq.	256	γ	1.2
Radar sweeps	128	Target position	$[0, 10, 0]$ km
Bandwidth	300 MHz	Target velocity	10 m/s
Carrier freq.	10 GHz	Roll/pitch/yaw	0°/0°/60°
T_{obs}	0.8 s	Baselines	$[1, 3, 5]$ m

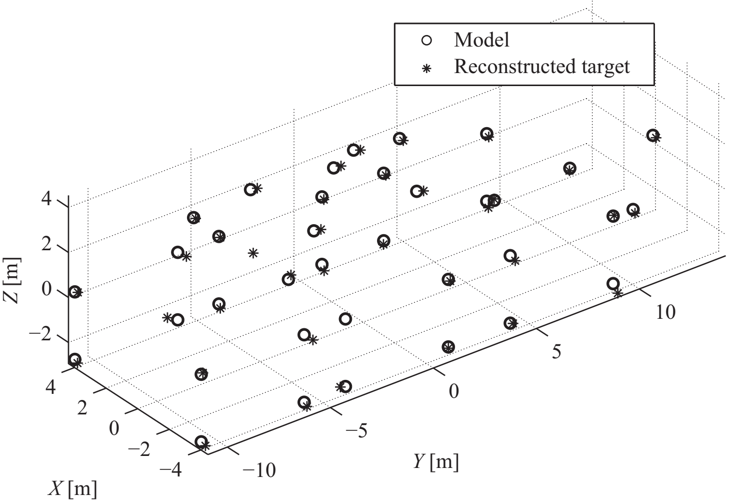

Figure 2.8 Results of the target reconstruction

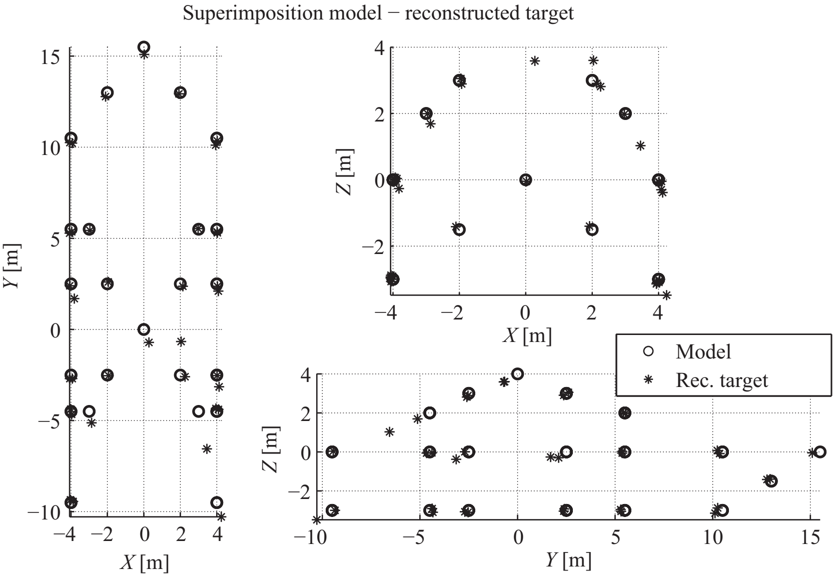

Figure 2.9 Results of the target reconstruction along three different planes

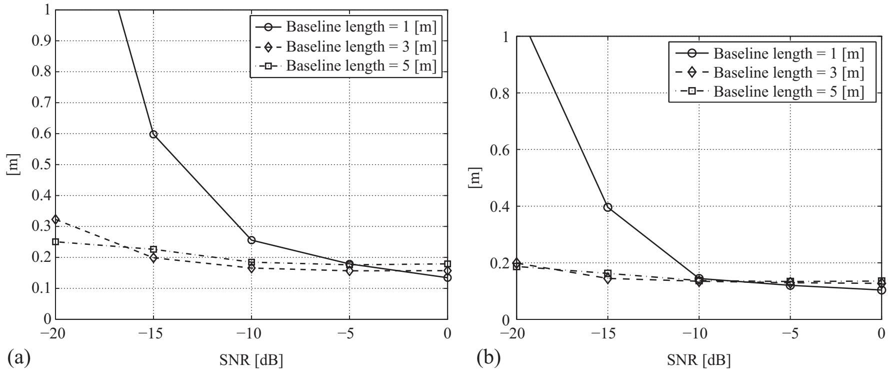

Figure 2.10 Height error – boat: (a) height error with unreliable assignments and (b) height error without unreliable assignments

The same descendant pattern can be observed in Figures 2.13–2.16, where the mean error and the standard deviation of the estimates of Ω_{eff} and ϕ are depicted when unreliable assignments are discarded.

It can be observed that this pattern changes in the case of a baseline length equal to 5. This is because the baseline length exceeds the unambiguous window of the interferometric phase.

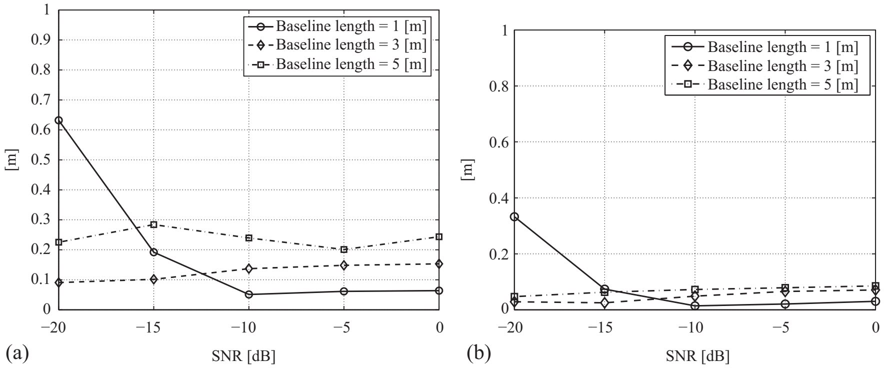

Figure 2.11 Standard deviation of the height error – boat: (a) standard deviation of the height error with unreliable assignments and (b) standard deviation of the height error without unreliable assignments

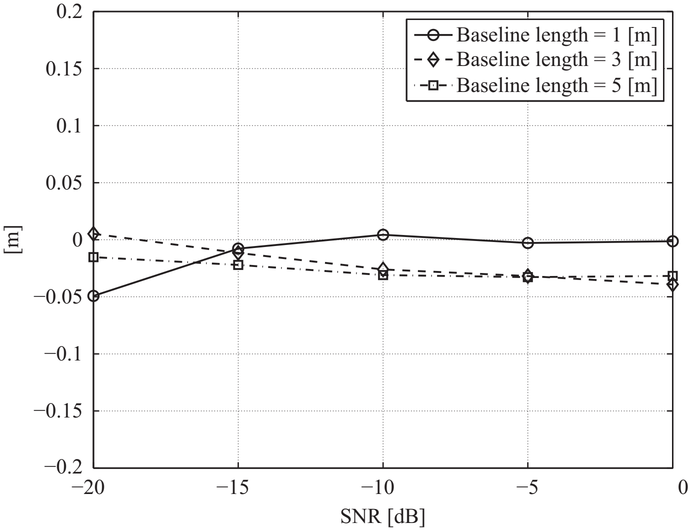

Figure 2.12 Signed error without unreliable assignments

It is worth pointing out that, when the unreliable assignments are discarded, the values of the height error and the standard deviation decrease significantly. Furthermore, in this case, the curves follow a decreasing trend as the SNR increases and as the baseline length increases, accordingly with the theory. Thus, it can be deducted that the correct identification of the unreliable assignments, and consequently the choice of an appropriate threshold, is fundamental in order to obtain reliable results.

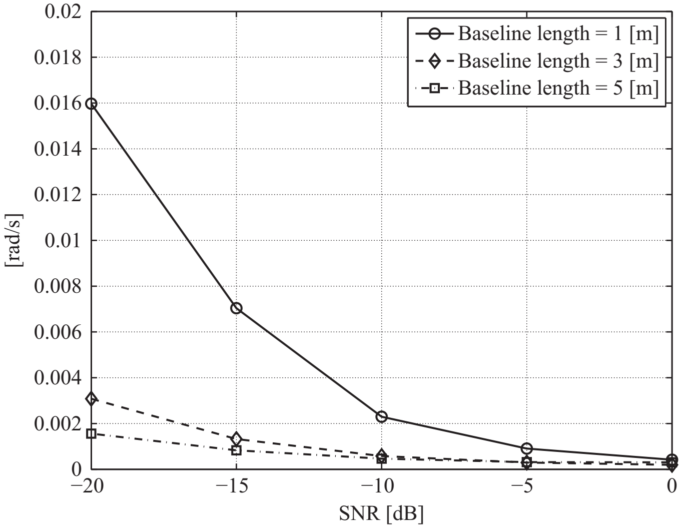

Figure 2.13 Mean error of the estimate of Ω_{eff}

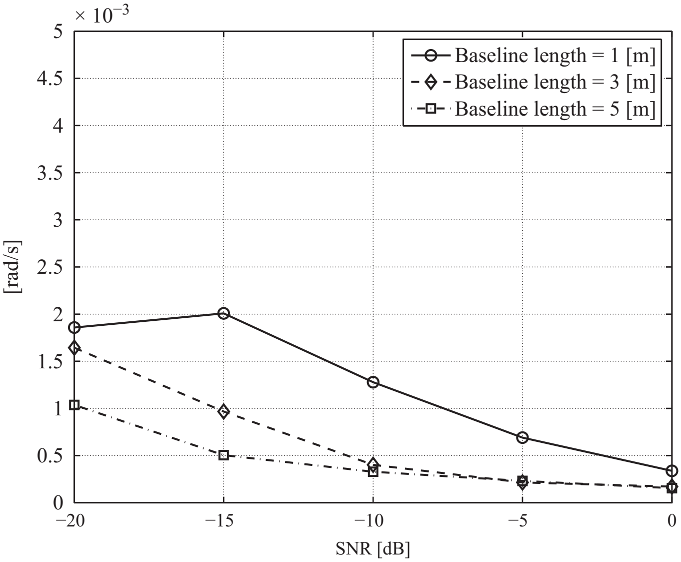

Figure 2.14 Standard deviation of the estimate of Ω_{eff}

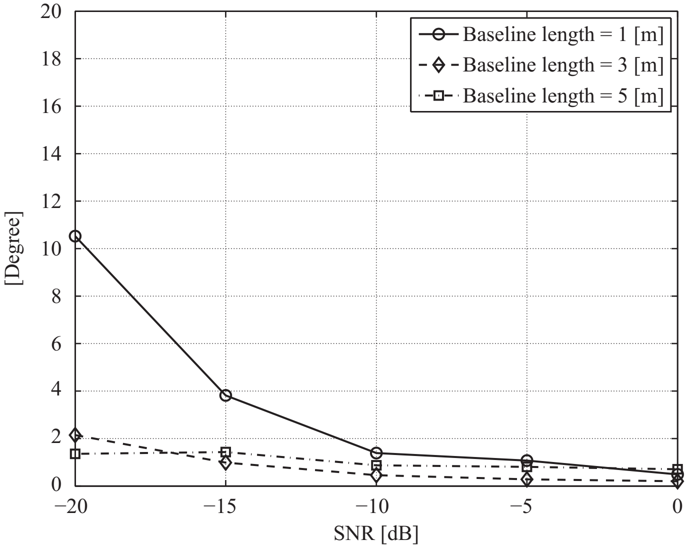

Figure 2.15 Mean error of the estimate of ϕ

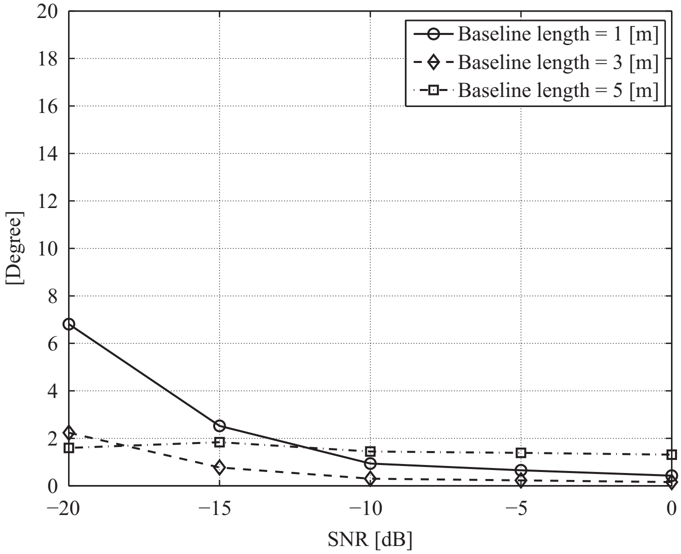

Figure 2.16 Standard deviation of the estimate of ϕ

2.4.2 Experimental results

An acquisition campaign was carried out at the beginning of October 2014 at the Institute 'G. Vallauri' in Livorno, Italy, in occasion of the NATO SET-196 Joint Trials. The goal of these Joint Trials is to prove the effectiveness of multi-static/multichannel radar imaging systems. In particular, the real data presented in this chapter were collected by means of a X-band interferometric ground-based linear frequency modulated continuous wave radar, namely PIRAD, designed and developed with the collaboration of RaSS laboratory of CNIT and University of Pisa. PIRAD was aiming at the sea region in front of the site and Figure 2.17 shows the acquisition scenario highlighting the location of the radar and the surveillance area.

A picture of such system is shown in Figure 2.18. The specifications of the PIRAD transceiver are summarized in Table 2.2.

The acquisition parameters are listed in Table 2.3.

The RD map is obtained by processing $T_{obs} = 1$ s of data. Two vessels were moving during the acquisition and one sailing ship was stationary. The targets are shown in Figure 2.19 and their brief description is in Table 2.4.

Some numerical results are shown in Table 2.5. The targets can be seen in the RD map in Figure 2.20: target A at around 1,350 m of distance and positive radial speed, target B at around 600 m and negative radial speed and target C stationary (only motion due to the sea state) at around 600 m. The ISAR images of the selected targets, before and after the motion compensation, are shown in Figure 2.21(a) and (b), Figure 2.22(a) and (b), Figure 2.23(a) and (b) for target A, B and C, respectively.

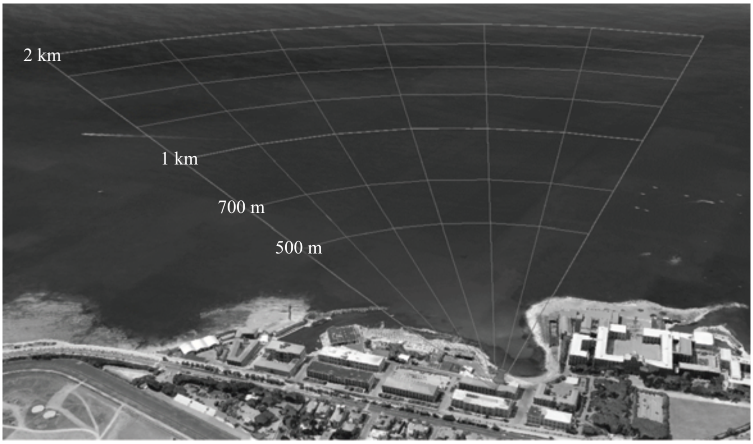

Figure 2.17 Acquisition scenario

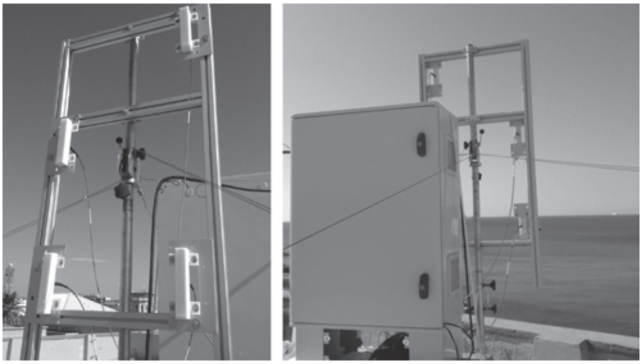
(a) (b)

Figure 2.18 PIRAD system: (a) frame of the antennas and (b) cabinet and frame installed on a lifting structure

Table 2.2 Radar transceiver specifications

TX power	Up to 33 dB m	Operative frequency	10.55 ÷ 10.85 GHz
Chirp rate	Up to 1.5 THz/s	Dynamic range	−132 ÷ −38 dB m
Noise figure	4.2 dB	SFDR	65 dB c
System losses	8 dB	Receiver gain	29 dB
Sampling freq.	12.5 MHz	ADC resolution	14 bit

Table 2.3 PIRAD's acquisition parameters

TX power	33 dB m
Bandwidth	300 MHz
PRF	1,000 Hz
T_{obs}	1 s
Range resol.	0.5 m
Baselines	H: 0.41 m V: 0.47 m

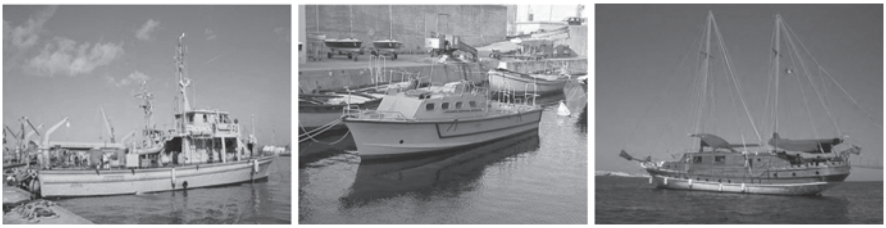
(a) (b) (c)

Figure 2.19 Targets for the trial with PIRAD: (a) target A: Astice, (b) target B: MBN and (c) target C: sailing ship

Table 2.4 Targets

Target A	Astice	Target B	MBN	Target C	Sailing ship
Length	33.25 m	Length	8.50 m	Length	13.2 m
Width	6.47 m	Width	2.30 m	Width	–
Height	–	Height	1.75 m	Height	13 m

Table 2.5 Numerical results for trial with PIRAD

Target	A	B	C
R_0	1,324 m	567 m	3,065 m
Length	19.4147 m	7.6586 m	11.7928 m
Height	6.2310 m	1.5500 m	12.8190 m
Ω_{eff}	0.0452 rad/s	0.1810 rad/s	0.0290 rad/s
ϕ	43.0559°	4.8931°	89.4960°
v_r	−2.6135 m/s	3.5159 m/s	0.3520 m/s
a_r	0.0206 m/s^2	0.0189 m/s^2	0.0448 m/s^2

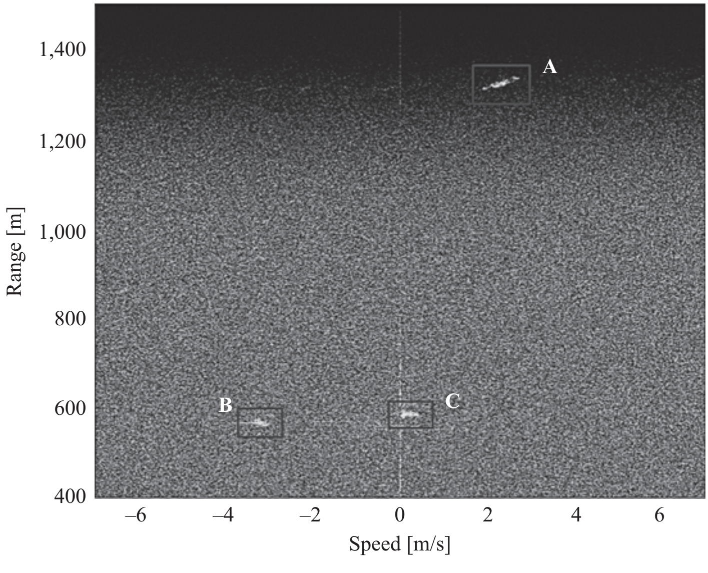

Figure 2.20 Range-Doppler map

The 3D reconstruction results are shown in Figures 2.24, 2.25 and 2.26. It should be noticed that the size of all of the targets under test match the actual ones except for the target A. This is because the MC-CLEAN cannot extract some scatterer, in particular the weak scatterers on the bow. In fact, it is possible to see that in Figure 2.24(a), the scatterers in the pow are missing. This fact underestimates the measure of the

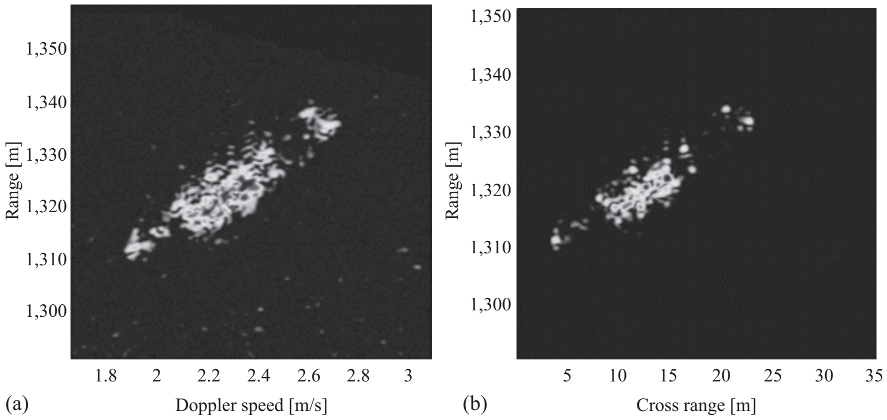

Figure 2.21 ISAR results for target A: (a) crop of the RD map and (b) ISAR image

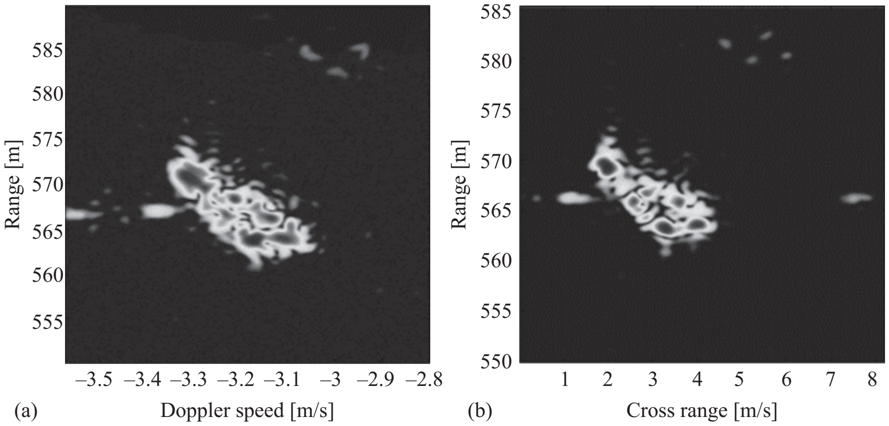

Figure 2.22 ISAR results for target B: (a) crop of the RD map and (b) ISAR image

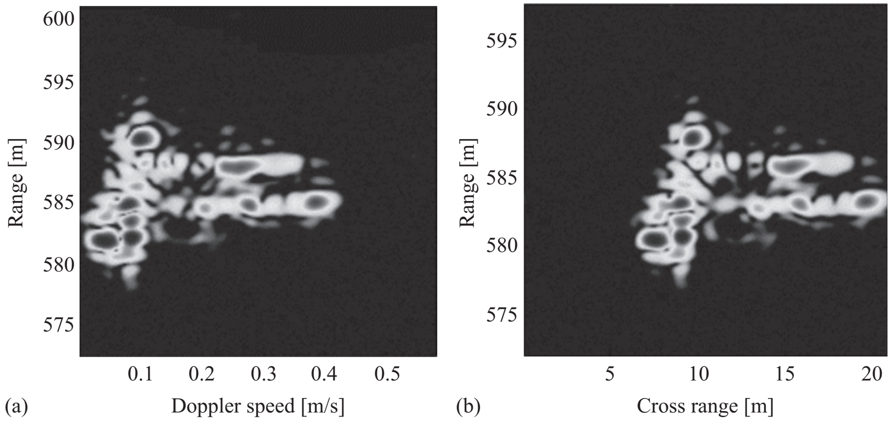

Figure 2.23 ISAR results for target C: (a) crop of the RD map and (b) ISAR image

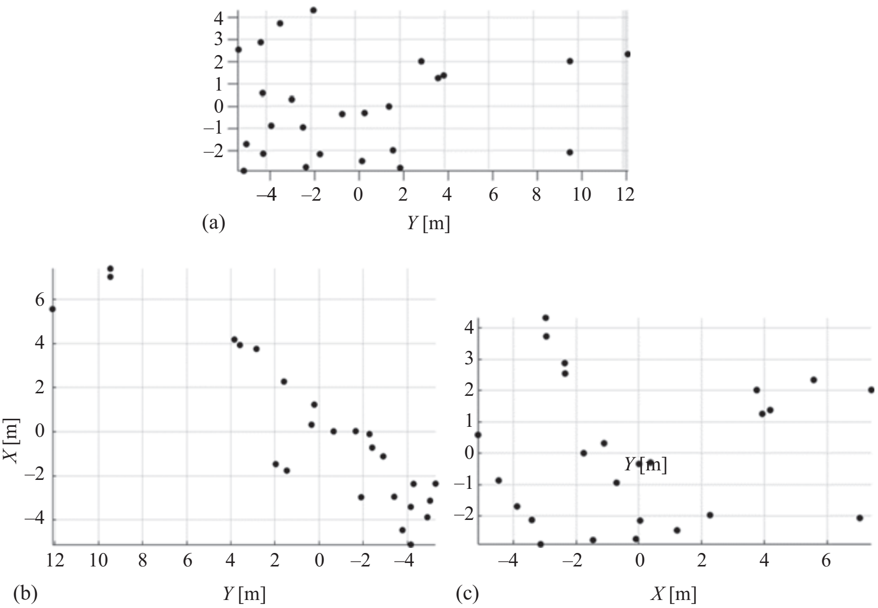

Figure 2.24 3D reconstruction results for target A: (a) range-height plane, (b) range-crossrange plane and (c) height-crossrange plane

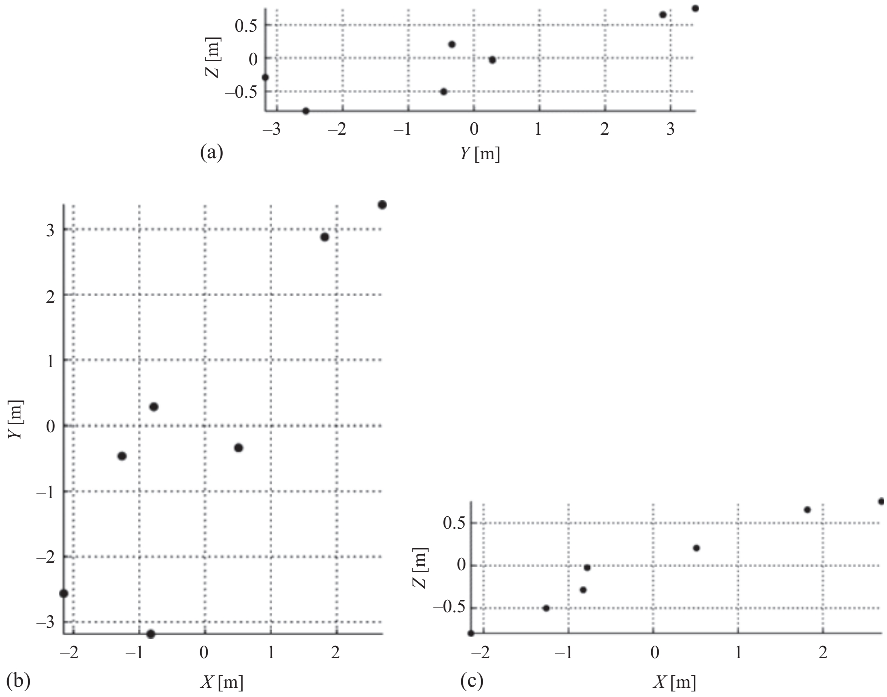

Figure 2.25 3D reconstruction results for target B: (a) range-height plane, (b) range-crossrange plane and (c) height-crossrange plane

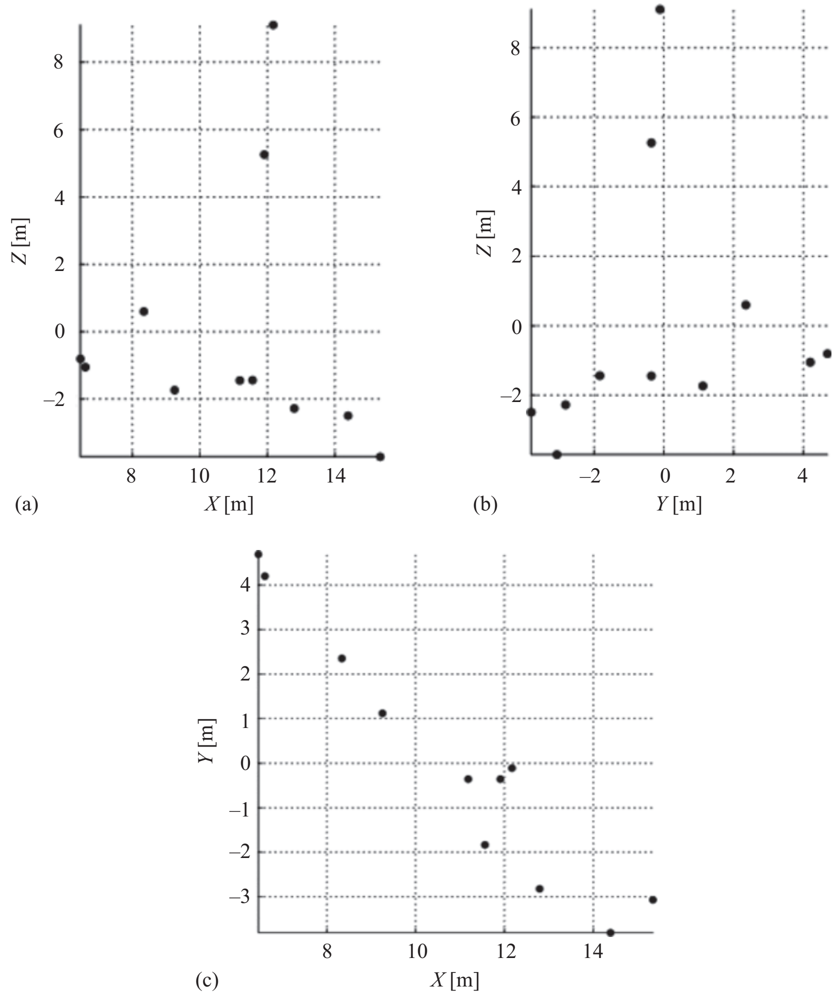

Figure 2.26 3D reconstruction results for target C: (a) range-height plane, (b) height-crossrange plane and (c) range-crossrange plane

vessel's length. For the target C, it is very interesting how the estimate of the IPP corresponds to a side view. This is confirmed by the estimate of the angle ϕ that is equal to 89°. This result matches with the ISAR image of target C since the two masts are visible in the Doppler direction.

2.5 Conclusion

In this chapter, an interferometric approach for a multichannel ISAR system for the reconstruction of non-cooperative moving targets has been described. First, the multichannel received signal model has been defined and the 3D InISAR processing has been introduced. 3D InISAR processing allows for the estimate of the height of the dominant scatterers and the estimate of the IPP as well. The phase differences between the signal received from different channels are exploited with an interferometric approach to provide information on the height of the scatterers. An approach for selecting these dominant scatterers has been described. Such technique, namely MC-CLEAN, is based on a iterative estimate of the PSF of the dominant scatterer which is removed from the ISAR image at each step. Finally, both simulated and real dataset have been used to carry out a performance analysis and to test the effectiveness of this 3D reconstruction processing. Simulation results have shown that the algorithm achieves better results when both the SNR and the baseline lengths are increased. This is consistent with the theory. Real data analysis exploiting a multichannel dataset provided within the activities of the NATO SET-196 has been performed. Results have demonstrated the effectiveness of the proposed processing chain and its applicability in real systems for surveillance purposes.

References

[1] Ausherman, D. A., Kozma, A., Walker, J. L., Jones, H. M., and Poggio, E. C. Developments in radar imaging. In *Aerospace and Electronic Systems, IEEE Transactions on AES-20*, 4 (1984), 363–400.

[2] Wehner, D. *High-Resolution Radar*. Artech House Radar Library. Norwood, MA, Artech House, Inc., 1987.

[3] Knaell, K., and Cardillo, G. Radar tomography for the generation of three-dimensional images. *IET Proceedings Radar, Sonar and Navigation 142*, 2 (1995), 54–60.

[4] Kempf, T., Peichl, M., Dill, S. and Suess, H. 3D tower-turntable ISAR imaging. 2007 European Radar Conference, Munich, 2007, pp. 114–117.

[5] Mayhan, J., Burrows, M., Cuomo, K., and Piou, J. High resolution 3D "snapshot" ISAR imaging and feature extraction. *IEEE Transactions on Aerospace and Electronic Systems 37*, 2 (2001), 630–642.

[6] Suwa, K., Yamamoto, K., Iwamoto, M., and Kirimoto, T. Reconstruction of 3-D target geometry using radar movie. 7th European Conference on Synthetic Aperture Radar, Friedrichshafen, Germany, 2008, pp. 1–4.

[7] Suwa, K., Wakayama, T., and Iwamoto, M. Three-dimensional target geometry and target motion estimation method using multistatic ISAR movies and its performance. *IEEE Transactions on Geoscience and Remote Sensing 49*, 6 (2011), 2361–2373.

[8] Stuff, M., Biancalana, M., Arnold, G., and Garbarino, J. Imaging moving objects in 3D from single aperture synthetic aperture radar. In *Radar Conference, 2004. Proceedings of the IEEE* (Apr 2004), 94–98.

[9] Ma, C. Z., Yeo, T. S., Zhang, Q., Tan, H. S., and Wang, J. Three-dimensional ISAR imaging based on antenna array. *IEEE Transactions on Geoscience and Remote Sensing 46*, 2 (2008), 504–515.

[10] Given, J., and Schmidt, W. Generalized ISAR – Part II: Interferometric techniques for three-dimensional location of scatterers. *IEEE Transactions on Image Processing 14*, 11 (2005), 1792–1797.

[11] Given, J. A., and Schmidt, W. R. Generalized ISAR – Part I: An optimal method for imaging large naval vessels. *IEEE Transactions on Image Processing 14*, 11 (2005), 1783–1791.

[12] Xu, X., and Narayanan, R. Three-dimensional interferometric ISAR imaging for target scattering diagnosis and modeling. *IEEE Transactions on Image Processing 10*, 7 (2001), 1094–1102.

[13] Shen, N., Yin, Z. P., and Chen, W. D. A compensation method for baseline length variation in InISAR imaging. 2009 2nd Asian-Pacific Conference on Synthetic Aperture Radar, Xian, Shanxi, 2009, pp. 1034–1038.

[14] Zhang, Q., and Yeo, T. S. Novel registration technique of InISAR and InSAR. IGARSS 2003. 2003 IEEE International Geoscience and Remote Sensing Symposium. Proceedings (IEEE Cat. No.03CH37477), Toulouse, 2003, vol. 1, pp. 206–208.

[15] Felguera-Martin, D., Gonzaalez-Partida, J. T., Almorox-Gonzalez, P., Burgos-García, M.-G., and Dorta-Naranjo, B. P. Interferometric inverse synthetic aperture radar experiment using an interferometric linear frequency modulated continuous wave millimetre-wave radar. *IET Radar, Sonar Navigation 5*, 1 (2011), 39–47.

[16] Wang, G., Xia, X.-G., and Chen, V. Three-dimensional ISAR imaging of maneuvering targets using three receivers. *IEEE Transactions on Image Processing, 10*, 3 (2001), 436–447.

[17] Battisti, N., and Martorella, M. Intereferometric phase and target motion estimation for accurate 3D reflectivity reconstruction in ISAR systems. In *Radar Conference, 2010 IEEE* (May 2010), 108–112.

[18] Sun, Y., and Lin, P. An improved method of ISAR image processing. In *Circuits and Systems, 1992, Proceedings of the 35th Midwest Symposium on*, 2 (Aug 1992), 983–986.

[19] Berizzi, F., Dalle Mese, E., Diani, M., and Martorella, M. High-resolution ISAR imaging of maneuvering targets by means of the range instantaneous Doppler technique: modeling and performance analysis. *IEEE Transactions on Image Processing 10*, 12 (2001), 1880–1890.

[20] Scaglione, A., and Barbarossa, S. Estimating motion parameters using parametric modeling based on time-frequency representations. In *Radar 97 (Conf. Publ. No. 449)* (Oct 1997), 280–284.

[21] Martorella, M., Berizzi, F., and Haywood, B. Contrast maximisation based technique for 2-D ISAR autofocusing. *IEE Proceedings Radar, Sonar and Navigation 152*, 4 (2005), 253–262.

[22] Berizzi, F., and Diani, M. Target angular motion effects on ISAR imaging. *IEE Proceedings Radar, Sonar and Navigation 144*, 2 (1997), 87–95.

[23] Martorella, M., Cacciamano, A., Giusti, E., Berizzi, F., Haywood, B., and Bates, B. CLEAN technique for polarimetric ISAR. *International Journal of Navigation and Observation 2008* (2008), 1–13.

[24] Martorella, M., Berizzi, F., and Bruscoli, S. Use of genetic algorithms for contrast and entropy optimization in ISAR autofocusing. *EURASIP Journal on Advances in Signal Processing 2006*, 1 (2006), 087298.

[25] Martorella, M., Stagliano, D., Salvetti, F., and Battisti, N. 3D interferometric ISAR imaging of noncooperative targets. *IEEE Transactions on Aerospace and Electronic Systems 50*, 4 (2014), 3102–3114.

[26] Krieg, M., and Gray, D. Comparison of probabilistic least squares and probabilistic multi-hypothesis tracking algorithms for multi-sensor tracking. In *Acoustics, Speech, and Signal Processing, 1997. ICASSP-97, 1997 IEEE International Conference on*, 1 (Apr 1997), 515–518.

[27] Giusti, E., Martorella, M., and Capria, A. Polarimetrically-persistent-scatterer-based automatic target recognition. *IEEE Transactions on Geoscience and Remote Sensing 49*, 11 (2011), 4588–4599.

This page intentionally left blank

Chapter 3

STAP–ISAR

Samuele Gelli[1], *Alessio Bacci*[1] *and Marco Martorella*[1,2]

The aim of this chapter is to develop a processing chain that exploits multichannel information provided by a multichannel synthetic aperture radar (SAR) system to obtain high-resolution images of noncooperative moving target within SAR images. There are two steps of the proposed processing chain. Clutter suppression and platform motion compensation are first performed through the space–time adaptive processing (STAP) processing by exploiting the multichannel information in order to improve target detection capability within SAR image. At this point, inverse synthetic aperture radar (ISAR) autofocusing is required in order to compensate the residual target own motion and to reduce the defocusing effect due to that unknown motion component. The study of moving target detector (MTD)/Moving Target Indicator (MTI) techniques and the development of clutter mitigation algorithms are the aims of this chapter together with the study of the applicability of ISAR processing to refocus moving target detected within SAR images. The integration of the proposed algorithms with ISAR techniques leads to the final processing chain. All the developed techniques are tested on simulated and real dataset.

3.1 Mathematical background

This section focuses on the definition of the signal and the clutter model exploited in this chapter. First, the attention on the monostatic multichannel ISAR signal model leading to the formulation of a multichannel version of the range–Doppler image formation technique will be paid. High-resolution imaging of noncooperative moving targets is also treated. A solution based on the application of the ISAR processing is described. Finally, the monostatic and bistatic clutter model is provided and the spatial and temporal decorrelation effects induced by the bistatic geometry that degrades the STAP performance in clutter suppression is analyzed.

---

[1] National Inter-University Consortium for Telecommunications – Radar and Surveillance System Laboratory (CNIT-RaSS), Pisa, Italy
[2] Department of Information Engineering, University of Pisa, Pisa, Italy

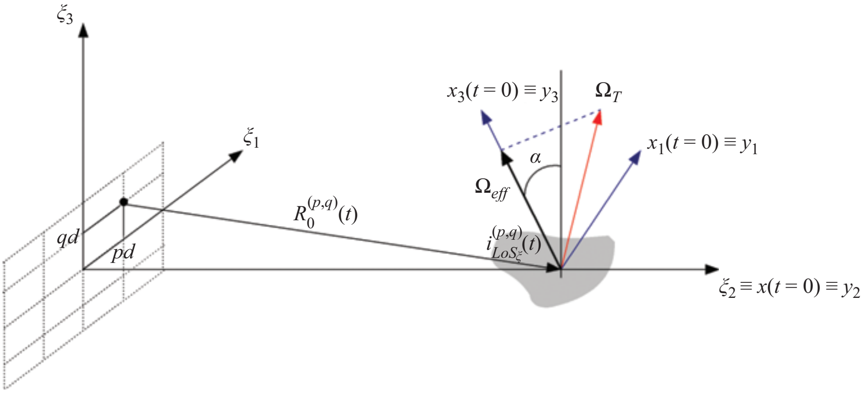

Figure 3.1 Multichannel ISAR geometry

3.1.1 Multichannel ISAR signal model

The introduced multichannel ISAR signal model is a generalization of the model present in [1], in which the configuration with two orthogonal baselines is presented. Consider the geometry shown in Figure 3.1 where a two-dimensional array illuminates a noncooperative moving target. The bidimensional array can be installed on an airborne or spaceborne platform that moves along a trajectory. The center of the reference system T_ξ is placed in the phase center of the transmitter. The reference system T_ξ is oriented so that the axes ξ_2 are parallel to the radar line of sight (LoS) while ξ_1 and ξ_3 correspond to the horizontal and the vertical baseline, respectively. As stated in [2], the target motion can be seen as the superimposition of the translational motion of the reference point $R_0(t)$ and the rotational motion denoted by the rotation vector $\Omega_T(t)$ applied to the reference point. The projection of $\Omega_T(t)$ on the plane orthogonal to the LoS is the effective rotation vector $\Omega_{eff}(t)$. The reference system T_x is embedded in the target with the axes x_2 oriented along the LoS and the axes x_3 oriented along $\Omega_{eff}(t)$. The reference system T_y is embedded on the target, its orientation is fixed and coincides with T_x for $t = 0$. The angle α is the angle between ξ_3 and x_3.

In the considered configuration, all the antennas are both transmitter and receiver. It has been demonstrated in [3] that if only one antenna acts as a transmitter and all the others are receivers, an equivalent monostatic configuration for each bistatic couple of transmitter and receiver can be considered.

Assuming that the inter-element spacing d is the same in both the dimensions, the couple (p, q) denotes the array elements placed in $\xi_1 = pd$ and $\xi_2 = qd$ where $p = -(P/2), \ldots, (P/2) - 1$ and $q = -(Q/2), \ldots, (Q/2) - 1$ are the indexes that identify the element position in the array.

As in monostatic ISAR where a single transmitter/receiver embedded in the center of the reference system T_ξ is considered and assuming the straight iso range approximation holds [2], the phase of the received signal can be written as follows:

$$\phi(\mathbf{y}, t, f) = \frac{4\pi f}{c}(R_0(t) + \mathbf{y} \cdot \mathbf{i}_{LoS}(t)) \tag{3.1}$$

where $R_0(t)$ is the distance between the radar and the reference point on the target at the time t, $\mathbf{y}$ is the scatter position in the T_y reference system and $\mathbf{i}_{LoS}(t)$ is the unit vector in the direction of the LoS at time t. As a consequence, the received signal from the generic element (p, q) can be written as

$$S_R^{(p,q)}(f,t) = W(f,t) \int_V \sigma(\mathbf{y})^{(p,q)} \, e^{-j(4\pi f/c)\left[R_0^{(p,q)}(t)+\mathbf{y}\cdot\mathbf{i}_{LoS_\xi}^{(p,q)}(t)\right]} d\mathbf{y} \tag{3.2}$$

The rotation of T_x of an angle θ with respect to T_ξ can be defined by a rotation matrix $\mathbf{M}_{\xi x}$:

$$\boldsymbol{M}_{\xi x} = \begin{bmatrix} \cos\alpha & 0 & \sin\alpha \\ 0 & 1 & 0 \\ -\sin\alpha & 0 & \cos\alpha \end{bmatrix} \tag{3.3}$$

By means of the rotation matrix $\boldsymbol{M}_{\xi x}$, the LoS unit vector $\mathbf{i}_{LoS_x}^{(p,q)}(t)$, expressed with respect to T_x, can be written as the normalized difference between the positions of each sensor and the origin of T_x:

$$\mathbf{i}_{LoS_x}^{(p,q)}(t) = \boldsymbol{M}_{\xi x}\mathbf{i}_{LoS_\xi}^{(p,q)}(t) = \frac{1}{C}\begin{bmatrix} -pd\cos\alpha - qd\sin\alpha \\ R_0(t) \\ pd\sin\alpha - qd\cos\alpha \end{bmatrix} \tag{3.4}$$

where

$$C = \sqrt{R_0^2(t) + (pd)^2 + (qd)^2} \approx R_0(t) \tag{3.5}$$

is the normalization factor. The approximation in the right-side term can be done because the radar target distance is much bigger than the distance between the generic array element and the array phase center. Moreover, $R_0(t) \approx R_0(0) = R_0$. As shown in [2], the position of a scatter in the T_x reference system can be approximated as in the following equation:

$$\mathbf{x}(t) \cong \mathbf{a} + \mathbf{b} + \mathbf{c}t = \mathbf{y} + \mathbf{c}t \tag{3.6}$$

where $\mathbf{a} = ((\Omega_T \cdot \mathbf{y})/\Omega_T^2)\Omega_T$, $\mathbf{b} = \mathbf{y} - ((\Omega_T \cdot \mathbf{y})/\Omega_T^2)\Omega_T$, $\mathbf{c} = \Omega_T \times \mathbf{y}$.

As a consequence, the inner product in (3.2) can be expressed as follows (more details can be found in [4]):

$$\mathbf{y} \cdot \mathbf{i}_{LoS_\xi}^{(p,q)}(t) = \mathbf{x}(t) \cdot \mathbf{i}_{LoS_x}^{(p,q)}(t) = K_0^{(p,q)} + K_1^{(p,q)}t \tag{3.7}$$

where

$$\begin{aligned} K_0^{(p,q)} &= y_2 - \tfrac{d}{R_0}[y_1(p\cos\alpha + q\sin\alpha) + y_3(q\cos\alpha - p\sin\alpha)] \\ K_1^{(p,q)} &= c_2 - \tfrac{d}{R_0}[c_1(p\cos\alpha + q\sin\alpha) + c_3(q\cos\alpha - p\sin\alpha)] \end{aligned} \tag{3.8}$$

in which, from [4,5], $c_2 = \Omega_{eff}y_1$.

The ISAR PSF relative to a single scatterer located at $y^{(k)}$ at the channel (p, q) can be obtained after a 2D-IFT of the compensated signal and can then be expressed as

$$I^{(p,q)}(\tau, \nu) = B \cdot T_{obs} \cdot \sigma(y_1^{(k)}, y_2^{(k)}) \cdot e^{j2\pi f_0\left(\tau-(2/c)K_0^{(p,q)}\right)} \\ \times \operatorname{sinc}\left[T_{obs}\left(\nu + \frac{2f_0}{c}K_1^{(p,q)}\right)\right] \cdot \operatorname{sinc}\left[B\left(\tau - \frac{2}{c}K_0^{(p,q)}\right)\right] \tag{3.9}$$

It is worth highlighting that under the assumption of array size much smaller than radar-target distance, the K_0 and K_1 terms within the sinc functions can be approximated as

$$\begin{aligned} K_0^{(p,q)} &= y_2 \\ K_1^{(p,q)} &= c_2 = \Omega_{eff} y_1 \end{aligned} \tag{3.10}$$

It is obvious that the model presented so far for 2D array is still valid for linear arrays. In particular, this section focuses on a system with a linear array, which is the case for $q = 0$.

In order to obtain an image by processing the images of all the P channels, those images should be summed. The sum can be done only if all the Ps are in phase, i.e., coherent sum. It is worth pointing out that since the focusing is performed with respect to a single focusing point, the P images are in phase only for this point. So, in order for the sum to be coherent, a bound for the phase difference among the other points of the images should be evaluated in order to find a condition to meet for coherently sum the images. This condition can be found by imposing an upper bound to the maximum phase difference among the images as

$$\frac{4\pi}{\lambda}(P-1)\frac{d}{R_0}(y_1 \cos\alpha - y_3 \sin\alpha) \leq \frac{\pi}{8} \tag{3.11}$$

That leads to

$$D_{array} \leq \frac{\lambda R_0}{32(y_1 \cos\alpha - y_3 \sin\alpha)} \tag{3.12}$$

where $(y_1 \cos\alpha - y_3 \sin\alpha)$ is the target size in the ξ_1 dimension. It is quite clear that this condition depends on the array size and the target size along the direction parallel to the array. It is worth pointing out that this method can still be applied when the target size along ξ_1 dimension is bigger than the bound expressed in (3.12). In this case, the whole region must be split into smaller regions (with dimension lower than the bound in (3.12)) and the focusing applied on each of this region. In order to better understand the distortions introduced when the requirement in (3.12) is not met, a closed form of the attenuation term can be evaluated.

Consider the summation along the p channels so that the resulting image can be expressed as

$$\begin{aligned} I(y_1, y_2) &= \sum_{p=-(P/2)}^{(P/2)-1} I^{(p)}(y_1, y_2) \\ &= I^{(0)}(y_1, y_2) \sum_{p=-(P/2)}^{(P/2)-1} e^{j(4\pi/\lambda)(d/R_0)y_1 p} \\ &= I^{(0)}(y_1, y_2) e^{+j(4\pi/\lambda)(dPy_1/2R_0)} \sum_{p=0}^{P-1} e^{j(4\pi/\lambda)(d/R_0)y_1 p} \end{aligned} \tag{3.13}$$

In order to simplify the notation, it has been considered the case in which $\alpha = 0$. After some mathematical manipulations, (3.13) becomes

$$I(y_1, y_2) = I^{(0)}(y_1, y_2) e^{j(2\pi Pd/\lambda 2R_0)y_1} \frac{\sin(2\pi dy_1 P/\lambda R_0)}{\sin(2\pi dy_1/\lambda R_0)} \tag{3.14}$$

The term $J(y_1) = (\sin(2\pi dy_1 P/\lambda R_0)/\sin(2\pi dy_1/\lambda R_0))$ produces a distortion in the amplitude of the image due to the fact that for cross-range region far away from the focusing point, the p images do not sum coherently as explained earlier. In order to evaluate the attenuation introduced by the noncoherent summation along the channel dimension, the term $J(y_1)$ can be evaluated. In Figure 3.2, the attenuation term $J(y_1)$ is shown for the radar center-scene distance, $R_0 = 5$ km, a carrier frequency, $f_0 = 10$ GHz, and an interelement distance obtained imposing the condition in (3.12) with $y_1 = 100$ m so that

$$d = \frac{\lambda R_0}{32 y_1 (P-1)} \tag{3.15}$$

As it can be noted, the condition in (3.12) is very restrictive leading to a loss of 0.2 dB within a distance of 100 m from the focusing point.

3.1.2 High-resolution imaging of noncooperative moving targets

High-resolution imaging of noncooperative moving targets in single channel SAR images is the aim of this section. A solution based on ISAR processing is introduced with a description of the ISAR image formation process.

In a typical SAR scenario, the radar moves along a trajectory that can be considered a-priori known and the observed area is assumed static or quasi-static. In this case, the perfect motion compensation due to the perfect knowledge of the geometry results in a coherent processing of the received signal producing a high-resolution imaging of the observed scene. A noncooperative moving target present in the observed area appear blurred and misplaced in the SAR image due to the lack of the relative motion compensation between the radar platform and the moving target [2,6]. Many techniques [7–10] have been proposed in the literature to compensate the phase difference between the platform and the moving target. Some of these are based on the restrictive

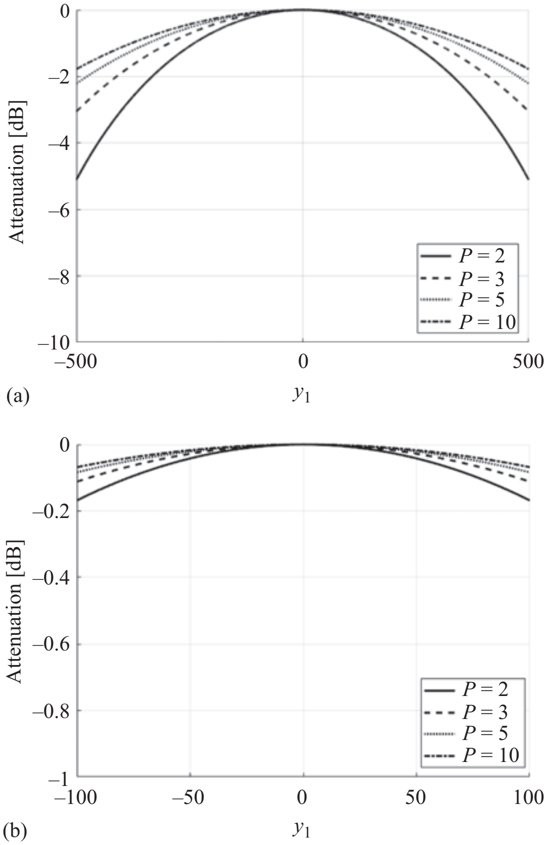

Figure 3.2 Attenuation factor. (a) Attenuation factor introduced by the non coherent summation along the channel dimension. (b) Zoom of the attenuation factor for a cross-range region of 100 m far away from the focusing point. A loss of 0.2 dB occurs within a distance of 100 m from the focusing point

assumption that moves along rectilinear trajectories or require some multiple prominent scatters on the target could be rather complex. ISAR processing offers another way to look into the problem of high-resolution imaging of noncooperative moving targets. Typically, in ISAR processing, the radar is assumed fixed on the ground and target motion is exploited to form the synthetic aperture obtaining a high cross-range resolution image [6]. In this case, any prior knowledge about the target or the geometry is not needed since the relative motion between the radar and the moving target is properly estimated and compensated during the image formation process. In recent years, a solution based on ISAR processing has been applied to refocus moving targets in SAR image both for monostatic and bistatic configurations [11,12]. In Figure 3.3,

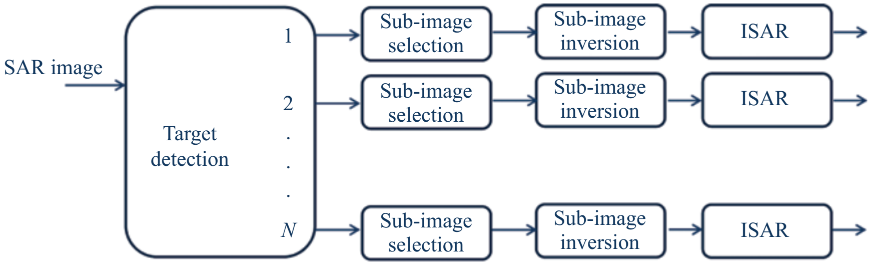

Figure 3.3 Block scheme of detection and refocusing processor

a functional block processing, referred to as ISAR from SAR, is depicted and is composed by the following main steps:

- **Target detection**: It is clear that in order to refocus moving target, the target must be first detected. Different from maritime application where the clutter return is lower compared to the target return, this step can be critical in the case of ground target due to both strong ground clutter return and because the unknown target motion leads to a target energy dispersion over wide region.
- **Subimage selection**: After target detection step, each detected target must be cropped and separated from the clutter and other targets contribution. This is a mandatory step since each target has its own translational and rotational motions and ISAR processing can estimate motion parameters only one target at time. A number of subimages equal to the number of detected targets are then obtained.
- **Subimage inversion**: Since ISAR processing considers raw data as input, an inversion from the image domain to the data domain is needed. It is worth pointing out that the raw data obtained from the inversion of the whole SAR image are not suitable for ISAR processing due to the fact that each target has its own motions. Different types of image inversion algorithms can be used depending on the image formation algorithm used to form the SAR image.

  If the straight iso-range approximation holds true, the total aspect angle variation is not too large and the effective rotation vector is approximately constant during the observation time. The polar grid, in which the received signal is defined, can be well approximated with a regular sampled rectangular grid. Under this approximation, the image can be reconstructed by a bidimensional fast Fourier transform (2D-FFT) through the conventional range–Doppler algorithm. In this case, the suitable inversion algorithm, call inverse range–Doppler, consists of a bidimensional inverse Fourier transform usually implemented by means of inverse 2D-IFFT.

  Thanks to the development in the digital signal processing capabilities, more accurate image reconstruction algorithm has been recently proposed. These algorithms, such as *Omega-k* also called *range migration algorithm* [13], *range stacking* [14] or *time domain correlation* [15], do not require the straight iso-range approximation but perform a wavefront reconstruction through a matched filter (MF).

- **ISAR processing**: After obtaining raw data from each selected subimage, ISAR processing can be applied in order to perform the motion compensation and the image formation. It is worth pointing out that the motion of the radar platform has already been compensated during the SAR image formation processing. Therefore, only the relative motion between radar platform and noncooperative moving target must be taken into account at the entry of the ISAR processing.

  Details about ISAR processing will be given in the next section.

3.1.2.1 ISAR processing

The main steps of the ISAR processing starting after subimage inversion step that allows to obtain a well-refocused image of noncooperative moving target starting from SAR image are shown in Figure 3.4 and are briefly recalled in this section:

- Motion compensation
- Time window selection
- Image formation
- Cross-range scaling

Motion compensation

The motion compensation technique (also called *autofocusing* technique) proposed here is known as image contrast (IC)-based autofocus (ICBA) algorithm and aims to estimate and compensate target own motions [16]. ICBA is a parametric autofocusing technique based on IC maximization.

Briefly, in the ICBA algorithm, the motion compensation problem, i.e., the estimation and the suppression of the term $R_0(t)$, can then be seen as an optimization problem where the IC is maximized with respect to an unknown vector that contains the motion parameters of the target. More details can be found in [16].

Time window selection

As previously shown, the RD algorithm can be applied when the effective target rotation vector is approximately constant during the observation time and when the total aspect angle variation is small. However, in some cases, this approximation does not hold true, for example, in the case of maneuvering target in which the aspect angle variation during the coherent processing interval (CPI) could be too large to apply properly the RD algorithm. A viable solution is to consider a temporal window along the CPI in which the aspect angle variation is not too large and the RD image formation processing can be applied properly.

In [17], a solution for time window selection is proposed. In particular, the length and the position of the window are chosen in order to obtain an image with the highest focus. The criterion used to define the highest focus is based on the IC.

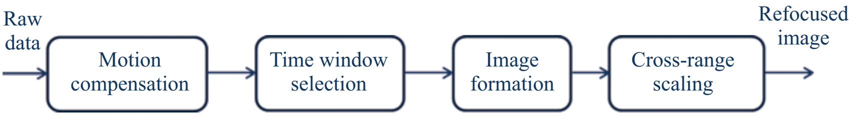

Figure 3.4 Block scheme of the ISAR processing

Image formation

The image formation process is based on the RD algorithm. The range–Doppler processing can be applied in the case in which the total aspect angle variation is small and the effective rotation vector of the target can be considered constant. Under these hypotheses, the polar grid in the spatial frequency domain where the received signal is defined can be well approximated with a regular sampled rectangular grid. The spatial frequencies can be assumed as independent variables and the bidimensional inverse FFT can be used to reconstruct ISAR image, $I(\tau, \nu)$, as follow:

$$I(\tau, \nu) = 2D - IFFT\left[S_{R,C}(f, t)\right] \tag{3.16}$$

where $S_{R,C}(f, t)$ is the received signal after motion compensation.

Cross-range scaling

After the RD image formation process, ISAR image in the time delay Doppler domain can be obtained, i.e., $I(\tau, \nu)$. In order to determine the size of the target, it is preferable to have fully scaled image, i.e., an image in the range cross-range domain. As explained in [6], the scaling from time delay domain to range domain is quite straightforward since it can be performed with the known relationship $y_2 = c\tau/2$ while the cross-range scaling requires the effective rotation vector of the target Ω_{eff}, that is not a priori known.

To solve this inconvenience, an algorithm has been recently proposed [18]. It is possible to demonstrate that when the target rotation vector can be considered constant during the observation time, the chirp rate produced by the scatters on the target can be related to the effective rotation vector. Therefore, it is possible to say that the scatters on the target carry information about the effective rotation vector. In conclusion, a number of scatters can be extracted from ISAR image and then an equal number of chirp rate estimates can be produced. Therefore, the problem of estimating the modulus of the effective rotation vector can be solved by exploiting the chirp rate estimations.

3.1.3 Clutter model

As from [19], conventional STAP techniques derive data depending on weight by calculation applied to a set of training data. Thanks to the estimation of clutter plus noise covariance matrix that includes the local clutter spectral characteristics, a superior performance compared to the conventional MTI can be obtained. Many of the past studies employed the familiar independent and identically distributed (IID) assumption considering the same statistical clutter property of the cell under test for each training data. Under such a hypothesis [20], the estimation of the covariance matrix used in the classical sample matrix inversion (SMI) approach is a maximum likelihood estimate that asymptotically converges to the exact one as the number of training data increases. In this case, the convergence issue is only related to the number of training data and not to the interference scenario. This situation is equivalent to the homogeneous clutter environment assumption which is, however, violated in some real scenario due to the heterogeneity of clutter that produces an alteration in covariance estimation, therefore, degrading STAP performance.

In general, the stationarity of training data is affected not only from clutter heterogeneity but also from the acquisition geometry. From [21], it is possible to observe that clutter return exhibits a Doppler shift that varies with the platform velocity as well as the direction and the width of the antenna beam. As a consequence, the acquisition geometry influences the clutter response at a given range cell and then the clutter angle/Doppler behavior shows some degrees of variation along the range dimension. Clutter range dependence breaks the IID assumption due to the fact that each training data shares a different covariance matrix producing a strong degradation of the STAP performance. Range dependence appears most severe in bistatic configurations [21]. A composite model that includes clutter heterogeneity which allows for amplitude and spectral fluctuation is considered in [22]. These models do not take into account temporal and spatial decorrelation effects introduced by the particular configuration used in the data acquisitions. These effects are considered in this subsection.

First of all, a statistical model for a covariance matrix for homogeneous environment and monostatic configuration is addressed.

The observation of the Earth's surface by a linear array gives rise to a particular temporal and spatial correlation between samples of the signal received from different antenna elements at different times, due to the fact that platform is moving. Temporal correlation is a pulse-to-pulse correlation that can be expected when a single channel observes a particular range cell at different time instants due to the changing of clutter characteristics in time while spatial correlation may be expected when two or more channels observe a scene at the same time instant. Under such considerations, the correlation between samples received from different antenna elements at different times can be expressed as [23]

$$\mathbf{R}_c = E\{u(k,n)u^*(i,m)\} = P_c\rho_t[(m-n)T_R]\,\rho_s\,[(k-i)d + (m-n)vT_R] \tag{3.17}$$

where $u(k,n)$ and $u(i,m)$ represent the received signal from the kth antenna channel at nth transmitted pulse and from ith antenna channel at mth transmitted pulse, respectively, while P represents the received signal power, d is the distance between the antenna elements and v represent the platform velocity. The temporal and the spatial correlation coefficients, $\rho_t(\Delta_t)$ and $\rho_s(\Delta_s)$, are typically considered as Gaussian coefficients [23]. It is worth pointing out that (3.17) cannot be considered as a cascade of single space and time correlation. This, therefore, makes it a bidemensional processing.

It is also worth pointing out that the correlation model in (3.17) has been obtained by assuming that the values of the backscattering coefficient corresponding to a different range of cell positions are statistically independent, whereas the values corresponding to the same cell position in different time instants are correlated by an amount depending on the time fluctuation of the surface. Another relevant assumption of this model is to consider a surface backscattering coefficient with constant statistical parameters, which is assuming the surface as homogeneous.

It is clear that this model does not take into account any type clutter heterogeneity and any distortion induced by the acquisition geometry. In Figure 3.5, an example

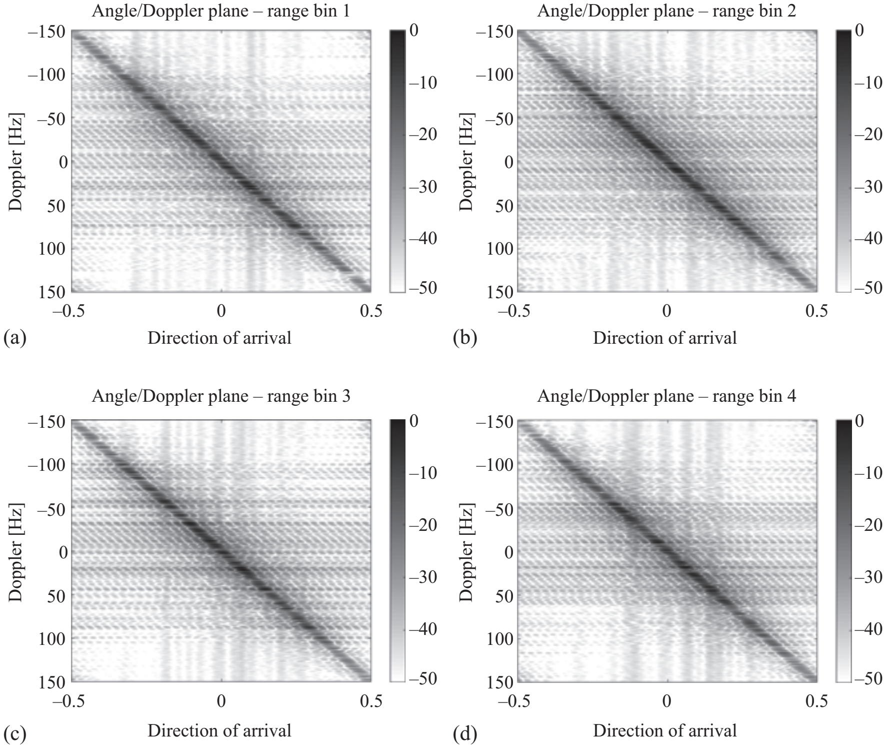

Figure 3.5 Monostatic homogeneous clutter angle/Doppler trajectories (dB scale) (a) range bin 1, (b) range bin 2, (c) range bin 3, (d) range bin 4

of the clutter ridge in the angle/Doppler plane is shown for four different range bins. The clutter has been generated exploiting the covariance matrix model previously described and the effects due to heterogeneity of the scene are not taken into account. From this figure, it is possible to see the classical two-dimensional clutter "ridge" due to the multichannel system. It can also be observed that the clutter is range independent since the clutter angle/Doppler trajectories are the same for different range cells. Bistatic geometry is in general more complex than monostatic. For a monostatic system, the clutter Doppler shift in a particular range cell varies with the look angle due to the platform motion resulting in the well-known clutter angle/Doppler ridge. In the case where transmitter and receiver are not collocated, the Doppler shift of clutter on the receiver still varies with the direction of arrival (DoA); however, in the case in which the transmitter and the receiver have different velocities, an additional Doppler shift will be expected. Moreover, in bistatic configurations, the transmitter and the receiver antenna beam pattern cannot be completely superimposed and then a new spatial decorrelation term must be taken into account. This term will depend on the range distance between the antenna patterns introducing a range dependence in the receiver clutter Doppler frequency. Under such considerations, a different model of the correlation function can be defined [12]:

$$\begin{aligned}\mathbf{R}_c &= E\{u(k,n)u^*(i,m)\}\\ &= P_c\rho_t(K_D(m-n)T_R)\\ &\quad\times \rho_s((k-i)d + K_D(m-n)vT_R)\rho_{b,s}\big((n_{r_{Rx}} - n_{r_{Tx}})\Delta r\big)\end{aligned} \tag{3.18}$$

where the symbol × indicates the multiplication operator, K_D represents the additional Doppler shift depending on the relative motion between the transmitter and the receiver while $n_{r_{Tx}}$ and $n_{r_{Rx}}$ are the transmitter and the receiver range cell position, respectively, defined by antenna beam patterns. The range cell index is related to the range cell position r' through the relation $r' = n_r\Delta r$ where $\Delta r = c/2B\cos\beta$ and β represents the bistatic angle.

In order to better examine the effects introduced by the bistatic configuration, the relation between the Doppler frequency and the DoA of the received signal and the clutter behavior in the angle/Doppler plane will be considered. In the monostatic sidelooking case, the Doppler frequency linearly depends on the DoA which leads to the bidimensional clutter ridge in angle/Doppler plane. The relationship is shown in the following equation:

$$f_d = \frac{2v_r}{\lambda}\sin\theta \tag{3.19}$$

where θ represents the DoA and v_r is the platform velocity. The relation can be normalized with respect to the pulse repetition frequency (PRF) and spacing between antennas as shown in the following equation:

$$F_{D_M} = 2\frac{v_r}{d}T_R\left(\frac{d}{\lambda}\cos\theta\right) = \mu\Theta \tag{3.20}$$

where θ represents the DoA and v_r is the platform velocity. In the bistatic case, the Doppler frequency is not a simple harmonic oscillation but it is a superimposition of the transmitter and the receiver terms:

$$\begin{aligned}F_{D_B} &= \frac{v_{r_{Tx}}}{d}T_R\left(\frac{d}{\lambda}\cos\theta_{Tx}\right) + \frac{v_{r_{Rx}}}{d}T_R\left(\frac{d}{\lambda}\cos\theta_{Rx}\right)\\ &= \mu_{Tx}\Theta_{Tx} + \mu_{Rx}\Theta_{Rx}\end{aligned} \tag{3.21}$$

In the case in which the transmitter and the receiver have different velocities, $v_{r_{Tx}} \neq v_{r_{Rx}}$, and the beam patterns are steered to the same observed area, $\theta_{Tx} \approx \theta_{Rx} = \theta$, an additional Doppler shift can be expected. This effect results in a changing of clutter angle/Doppler slope, as reported in the following equation:

$$\begin{aligned}F'_{D_B} &= \frac{v_{r_{Tx}}}{d}T_R\left(\frac{d}{\lambda}\cos\theta\right) + \frac{v_{r_{Rx}}}{d}T_R\left(\frac{d}{\lambda}\cos\theta\right)\\ &= (\mu_{Tx} + \mu_{Rx})\Theta_{Rx}\end{aligned} \tag{3.22}$$

Through (3.18), it is possible to include this effect in the angle/Doppler plane, as can be seen from Figure 3.6. In this figure, the bidimensional clutter ridge is relative to

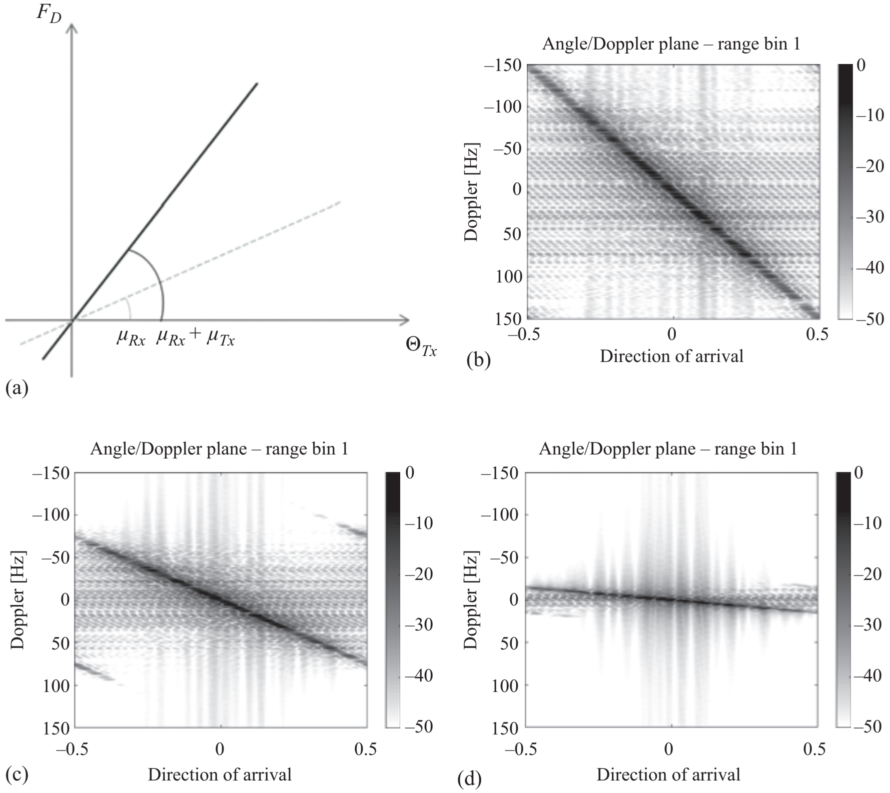

Figure 3.6 Temporal decorrelation effect in bistatic clutter angle/Doppler trajectories (dB scale): (a) clutter slope variation in angle/Doppler plane, (b) $K_D = 1$, (c) $K_D = 0.5$ and (d) $K_D = 0.1$

the same range cell and is obtained for a different value of the Doppler shift term K_D. The case in which the transmitter and the receiver fly at the same velocities, $v_{r_{Tx}} \approx v_{r_{Rx}} = v_r$, but observe two partially different areas, $\theta_{Tx} \neq \theta_{Rx}$, is reported in the following equation:

$$\begin{aligned} F''_{D_B} &= \frac{v}{d} T_R\left(\frac{d}{\lambda}\cos\theta_{Tx}\right) + \frac{v}{d} T_R\left(\frac{d}{\lambda}\cos\theta_{Rx}\right) \\ &= \mu_{Rx}\Theta_{Tx} + \mu_{Rx}\Theta_{Rx} \end{aligned} \tag{3.23}$$

In this case, the effect results in a particular clutter ridge shift by a quantity of $\mu_{Rx}\Theta_{Tx}$. From (3.18), it is possible to observe that the new spatial correlation term corresponds to a simple shift in the angle/Doppler domain depending on the range distance between antenna patterns. Clutter range dependence can be seen from Figure 3.7 where the clutter angle/Doppler trajectories are reported for different range of

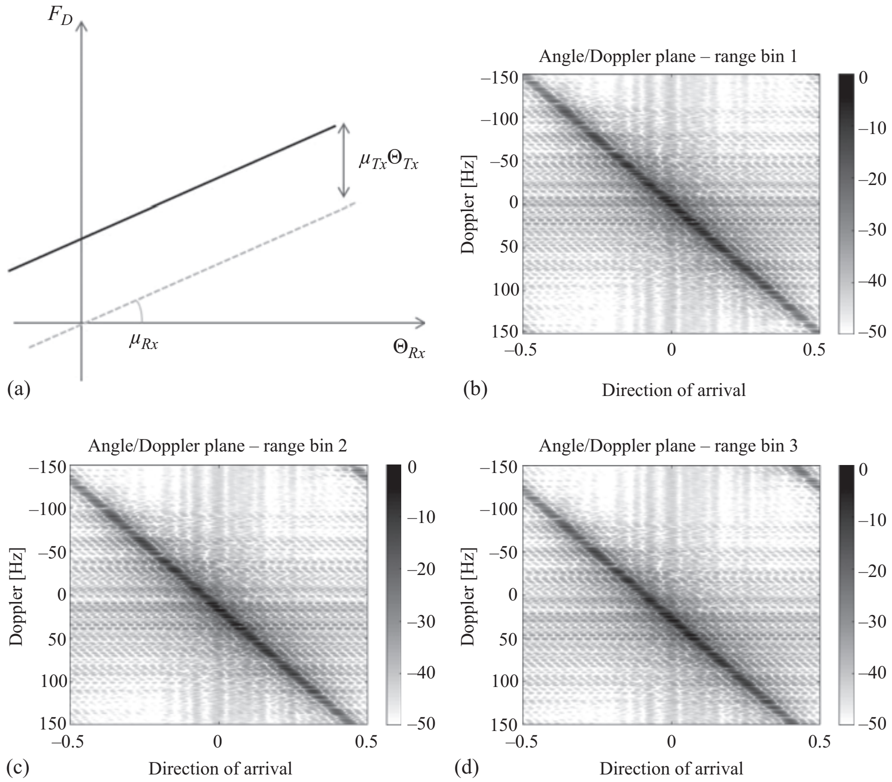

Figure 3.7 Spatial decorrelation effect in bistatic clutter angle/Doppler trajectories (dB scale): (a) clutter ridge shift in angle/Doppler plane, (b) range bin 1, (c) range bin 2 and (d) range bin 3

cells. It is worth pointing out that the received signal from stationary clutter can be completely described from its own clutter covariance matrix, as previously described. The introduced covariance clutter model does not claim to describe the physical reality in its completeness, for example, the described model does not take into account the difference in platform heights. The aim of this model is to show that, in addition to the heterogeneity of the environment, clutter non-stationarity is also caused by the acquisition geometry.

3.2 Space–time adaptive processing for clutter suppression

In this section, a modified version of conventional STAP processing termed space Doppler adaptive processing (SDAP) is presented. A technique that combined clutter suppression and ISAR processing to obtain high-resolution image of extended moving targets is investigated. The problem is addressed from an imaging point of view. Two principal issues are addressed. The applicability of ISAR processing after clutter mitigation and the need for suboptimum approach due to the difficulties in the estimation of the clutter covariance matrix. A modified version of SDAP processing, termed extended SDAP (E-SDAP), is proposed in order to take into account the distortion introduced by the bistatic configurations. Joint E-SDAP ISAR for bistatic clutter suppression and high-resolution imaging with its suboptimal approach are finally addressed.

3.2.1 Joint SDAP ISAR

In this section, a technique that combines clutter suppression and ISAR processing in order to obtain well-focused images of extended moving targets is investigated. The problem will be addressed from the imaging point of view. Two principal issues will be addressed. The applicability of ISAR processing after clutter mitigation first and then the need of suboptimal approach due to the difficulty in the estimation of the clutter space–time covariance matrix will be investigated. A modified version of the classical STAP, described in [19], is presented. This is derived from the range–Doppler image formation algorithm and works in the space Doppler domain. In the following, it will be addressed as SDAP.

The theoretical formulation will be derived both for optimum and suboptimum processing. It will be combined with the ISAR processing in order to obtain well-focused images of noncooperative moving targets embedded in strong clutter environments.

3.2.1.1 Optimum processing

Let us consider the same acquisition geometry shown in Figure 3.8 in which the radar system observes a moving target within a static background. The total Fourier transform of the received signal can be expressed as follows:

$$S(f,t) = S_t(f,t) + S_c(f,t) + N(f,t) \tag{3.24}$$

where $S_t(f,t)$ is the contribution due to the moving target, $S_c(f,t)$ is the contribution due to the static scene that in this case is considered clutter and $N(f,t)$ is the additive noise. $f \in [f_0 - (B/2), f_0 + (B/2)]$ and $t \in [(-T_{obs}/2), (T_{obs}/2)]$ denote the range frequency and the azimuth slow time, respectively. As shown in Section 3.1, the multichannel signal model can be easily obtained from the single channel model. The signal received relative to the target can be written as

$$S_t(f,t) = e^{-j(4\pi/\lambda)R_0(t)} \sum_{k=1}^{K} \sigma_k e^{-j(4\pi/\lambda)\left[K_{0,k}^{(p)} + K_{1,k}^{(p)} t\right]} \tag{3.25}$$

where the terms $K_0^{(p)}$ and $K_1^{(p)}$ are defined in (3.8).

It is worth pointing out that for array size much smaller than the radar-target distance, the LoS is the same for each antenna element and the terms $K_0^{(p)}$ and $K_1^{(p)}$ can be approximated as in (3.10).

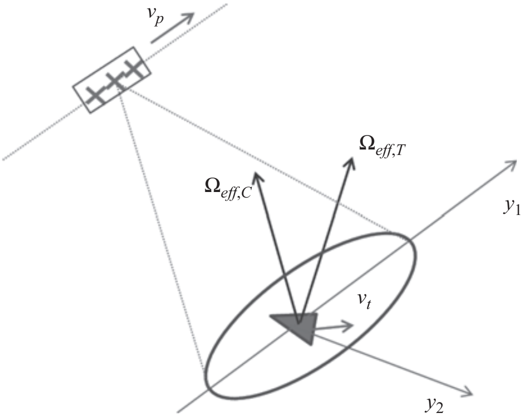

Figure 3.8 Acquisition geometry

Under this assumption, the received signal relative to a moving target, $S_{t(f,t)}$, and the static scene $S_c(f,t)$ can be expressed as

$$S_t(f,t) = e^{-j(4\pi/\lambda)R_{0t}(t)} \sum_{k=1}^{K} \sigma_k e^{-j(4\pi/\lambda)\left[y_2^{(k)}+\Omega_{eff,t}y_1^{(k)}t\right]} \tag{3.26}$$

$$S_c(f,t) = e^{-j(4\pi/\lambda)R_{0c}(t)} \iint_{(y_1,y_2)} \sigma(y_1,y_2) e^{-j(4\pi/\lambda)\left[y_2+\Omega_{eff,c}y_1t\right]} dy_1 dy_2 \tag{3.27}$$

where $R_{0t}(t)$ denotes the position of the reference point on the target at the time t and takes into account the superimposition of the target own motion and the platform motion, k is the scatterer index, $y_1^{(k)}$ and $y_2^{(k)}$ denote the cross-range and the range coordinates of the kth scatterer and $\Omega_{eff,t}$ is the total rotation vector due to the platform and the target motion projected on a plane orthogonal to the LoS.

These expressions are valid in case of *straight iso-range approximation*. It is worth pointing out that since the proposed SDAP is based on the range–Doppler image formation algorithm, the straight iso-range approximation is mandatory to apply this processing.

High resolution in range dimension is obtained by transmitting wideband signals and matched filtering the received signal. High resolution in azimuth can be obtained by applying the range–Doppler processing [4,6]. Considering $S_t(f,t)$, the signal received from a static scatterer placed in the generic position (y_1,y_2), the range–Doppler processing can be expressed as

$$u_D(f,\nu) = FT_t\left\{S_t(f,t)S_{ref}^*(f,t)\right\} \tag{3.28}$$

where $FT_t\{\}$ is the Fourier transform along the slow time dimension t. Equation (3.28) can be expressed in terms of convolution in the Doppler frequency domain as

$$u_D(f,\nu) = \tilde{S}_{ref}(f,-\nu) \otimes \tilde{S}_t(f,\nu) \tag{3.29}$$

where

$$\tilde{S}_t(f,\nu) = FT_t\{S(f,t)\} \tag{3.30}$$

and

$$\tilde{S}_{ref}(f,\nu) = FT_t\left\{S_{ref}(f,t)\right\} \tag{3.31}$$

are the Fourier transformed received signal and reference signal along the slow time dimension, respectively.

It is evident from (3.29) that the range–Doppler image formation processing, can be seen as a matched filtering in the frequency Doppler domain.

This formulation can be easily extended to a discretized version of the signal in which $S(n,m) = S(n\Delta f, mT_R)$. The indices $n = [(-N/2),\ldots,(N/2)-1]$ and $m = [(-M/2),\ldots,(M/2)-1]$ denote the discrete frequency and the pulse index, respectively, while δf and T_R denote the frequency sampling step and the pulse repetition interval, respectively. In this case, the range–Doppler image formation processing can be expressed as

$$u_D(n,m_\nu) = DFT_m\left\{S_t(n,m)S^*_{ref}(n,m)\right\} \tag{3.32}$$

where m_ν denotes the Doppler frequency index, or in term of Doppler matched filtering as

$$u_D(n,m_\nu) = \tilde{S}_t(n,m_\nu) \otimes_{m_\nu} \tilde{S}_{ref}(n,-m_\nu) \tag{3.33}$$

where

$$\tilde{S}_t(n,m_\nu) = DFT_m\{S_t(n,m)\} \tag{3.34}$$

$$\tilde{S}_{ref}(n,m_\nu) = DFT_m\left\{S_{ref}(n,m)\right\} \tag{3.35}$$

and $\otimes_{m_\nu}$ denotes the discrete convolution along the m_ν dimension and DFT_m is the discrete Fourier transform along the discretized slow time dimension.

The matched filtering operation in (3.33) can be expressed in a vectorial form after defining the signal vector, i.e., $\tilde{\mathbf{S}}(n)$, and the reference vector, i.e., $\tilde{\mathbf{G}}_D(n,m_\nu)$, as

$$\tilde{\mathbf{S}}(n) = [\tilde{S}(n,0),\tilde{S}(n,1),\ldots,\tilde{S}(n,M-1)]^T \in \mathbb{C}^{M\times 1} \tag{3.36}$$

$$\tilde{\mathbf{G}}_D(n,m_\nu) = [\tilde{S}_{ref}(n,m_\nu),\ldots,\tilde{S}_{ref}(n,m_\nu-(M-1))]^T \in \mathbb{C}^{M\times 1} \tag{3.37}$$

so that

$$u_D(n,m_\nu) = \tilde{\mathbf{G}}^H_D(n,m_\nu)\tilde{\mathbf{S}}(n) \tag{3.38}$$

This processing can be easily extended to the multichannel scenario. The formulation of the multichannel ranged Doppler can be expressed as

$$u_D(n,m_\nu) = \sum_{p=1}^{P} u_{D,p}(n,m_\nu) = \sum_{p=1}^{P} \tilde{S}_{t,p}(n,m_\nu) \otimes_{m_\nu} \tilde{S}_{ref,p}(n,-m_\nu) \tag{3.39}$$

Equation (3.39) can be expressed in a vectorial form after performing a stacking operation first along the channel dimension (3.40) and (3.41) and along the Doppler frequency dimension (3.42) and (3.43) as

$$\tilde{\mathbf{S}}(n, m_\nu) = \frac{1}{P}[\tilde{S}_1(n, m_\nu), \tilde{S}_2(n, m_\nu), \ldots, \tilde{S}_P(n, m_\nu)]^T \in \mathbb{C}^{P\times 1} \tag{3.40}$$

$$\tilde{\mathbf{S}}_{ref}(n, m_\nu) = \frac{1}{P}[\tilde{S}_{ref,1}(n, m_\nu), \tilde{S}_{ref,2}(n, m_\nu), \ldots, \tilde{S}_{ref,P}(n, m_\nu)]^T \in \mathbb{C}^{P\times 1} \tag{3.41}$$

$$\tilde{\mathbf{S}}(n) = [\tilde{\mathbf{S}}(n, 0), \tilde{\mathbf{S}}(n, 1), \ldots, \tilde{\mathbf{S}}(n, M-1)]^T \in \mathbb{C}^{MP\times 1} \tag{3.42}$$

$$\tilde{\mathbf{G}}_D(n, m_\nu) = [\tilde{\mathbf{S}}_{ref}(n, m_\nu), \ldots, \tilde{\mathbf{S}}_{ref}(n, m_\nu - (M-1))]^T \in \mathbb{C}^{MP\times 1} \tag{3.43}$$

The output of the Doppler MF is then expressed as

$$u_D(n, m_\nu) = \tilde{\mathbf{G}}_D^H(n, m_\nu)\tilde{\mathbf{S}}(n) \tag{3.44}$$

It is worth highlighting that in order to apply this image formation processing, the straight iso-range approximation must hold true. Moreover, in order to properly obtain the multichannel image, the sum along the spatial dimension must be performed (Equation (3.39)). In order to avoid distortions in the resulting image, this must be a coherent sum leading to limitation in the array and in the imaging area size. These limitations have been analyzed in Section 3.1 deriving the condition that must be met to properly process multichannel data via range–Doppler-based processing expressed in (3.12).

At this stage, to obtain the final image, a Fourier transform along the range frequency dimension is performed.

Space Doppler adaptive processing–ISAR

Optimum SDAP involves the replacement of the space–Doppler reference vector with the weight vector that maximizes the output signal to interference plus noise ratio (SINR) as

$$u_D(n, m_\nu) = \tilde{\mathbf{W}}_D^H(n, m_\nu)\tilde{\mathbf{S}}(n) \tag{3.45}$$

The expression of the optimum filter can be defined through the SMI implementation [20], expressed as

$$\tilde{\mathbf{W}}_D(n, m_\nu) = \gamma \hat{\mathbf{R}}_{Dc}^{-1}\tilde{\mathbf{G}}_D(n, m_\nu) \tag{3.46}$$

where γ is a scalar that does not affect the SINR at the output of the optimum filter and $\hat{\mathbf{R}}_{Dc}$ is the estimation of the interference cross-power spectral matrix $\mathbf{R}_{Dc}$ and it is obtained by averaging along N_r target-free range cells of training data as

$$\hat{\mathbf{R}}_{Dc} = \frac{1}{N_r}\sum_{n_r=0}^{N_r-1} \tilde{\mathbf{Z}}(n_r)\tilde{\mathbf{Z}}^H(n_r) \in \mathbb{C}^{MP\times MP} \tag{3.47}$$

The vector $\tilde{\mathbf{Z}}(n_r)$ denotes the target-free data in the nth range cell in the space–Doppler frequency domain.

It is worth pointing out that the optimum processing in (3.46) performs both clutter suppression and image formation by means of range–Doppler processing.

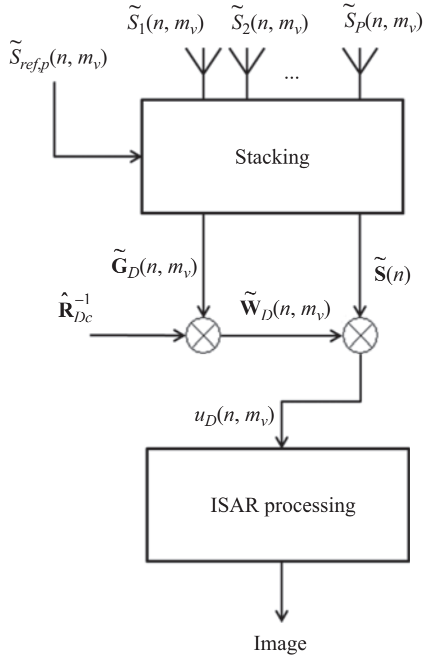

Figure 3.9 Optimum SDAP ISAR functional block

In order to obtain a well-focused image of the noncooperative moving target, the reference vector $\tilde{\mathbf{G}}_D(n, m_v)$ must compensate both platform and target own motion. Obviously, this is not a realistic situation since the target is noncooperative. So, a first motion compensation is performed in the SDAP processing considering only the known part of the relative radar target motion while high-resolution image of noncooperative target is obtained by applying the ISAR processing at the output of the SDAP. As stated before, ISAR processing must be applied separately at each target detected after clutter mitigation.

The functional block is depicted in Figure 3.9. Another issue to be addressed concern the estimation of the clutter covariance matrix $\hat{\mathbf{R}}_{Dc}$. As known from the Reed–Mallet–Brennan rule [20], in order to obtain an average performance loss of roughly 3 dB, a number of $N_r = 2MP$ target-free range cells are needed, while typical values of $PRF = 1$ kHz, $T_{obs} = 1$ s and $P = 3$, $N_r = 6{,}000$ range cells are needed. Assuming a range resolution of 0.5 m, this results in an area of homogeneous clutter of 3 km in the range dimension. In the next section, a suboptimum approach to overcome this issue and reduce the dimensionality of the clutter covariance matrix will be presented.

3.2.1.2 Suboptimum processing

The reduction in the dimensionality of the cross-power spectral matrix can be obtained by splitting the filtering operation in (3.46) in sub-windows as shown in Figure 3.10.

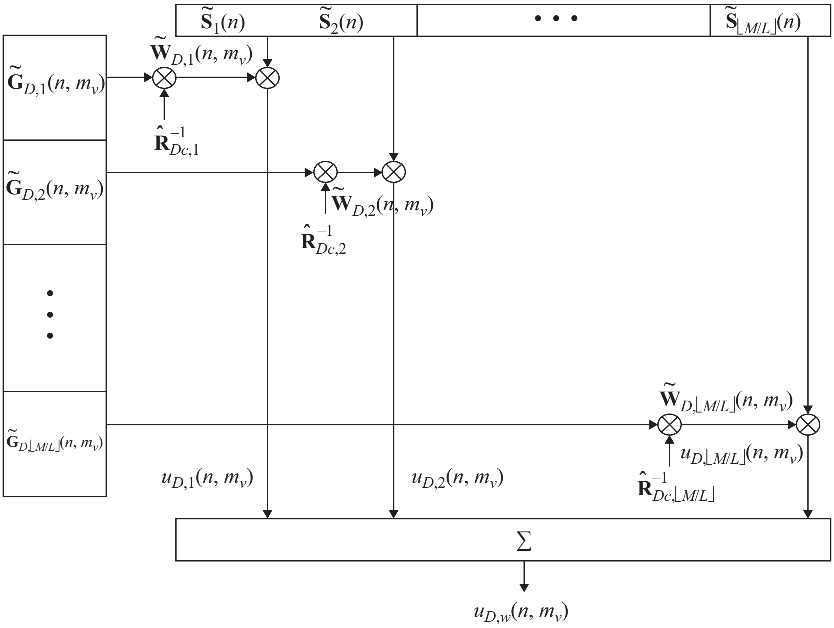
$\tilde{\mathbf{S}}_1(n)$
$\tilde{\mathbf{S}}_2(n)$
• • •
$\tilde{\mathbf{S}}_{\lfloor M/L \rfloor}(n)$
$\tilde{\mathbf{G}}_{D,1}(n, m_v)$
$\tilde{\mathbf{W}}_{D,1}(n, m_v)$
$\hat{\mathbf{R}}^{-1}_{Dc,1}$
$\tilde{\mathbf{G}}_{D,2}(n, m_v)$
$\tilde{\mathbf{W}}_{D,2}(n, m_v)$
$\hat{\mathbf{R}}^{-1}_{Dc,2}$
$\tilde{\mathbf{W}}_{D,\lfloor M/L \rfloor}(n, m_v)$
$\tilde{\mathbf{G}}_{D\lfloor M/L \rfloor}(n, m_v)$
$u_{D,\lfloor M/L \rfloor}(n, m_v)$
$\hat{\mathbf{R}}^{-1}_{Dc,\lfloor M/L \rfloor}$
$u_{D,1}(n, m_v)$
$u_{D,2}(n, m_v)$
Σ
$u_{D,w}(n, m_v)$

Figure 3.10 Suboptimum optimum SDAP ISAR functional block

This operation consists of splitting the Doppler dimension in sub-windows of length L and applying a reduced dimension SDAP in each subblock. The reduction in the dimensionality of the cross-power spectral matrix to be estimated is given by the length of the considered sub-window. It is worth pointing out that this windowing operation does not involve any losses if only the Doppler-matched filtering operation is performed, i.e., $\tilde{\mathbf{W}}(n, m_v) = \tilde{\mathbf{G}}_D(n, m_v)$. However, when the clutter mitigation is performed and the weigh vector assumes the structure in (3.46), the windowing operation involves an approximation in the considered cross-power spectral matrix, i.e., $R_{Dc,w}$, with respect to the ideal one R_{Dc}. This approximation consists of considering only a set of block of the overall cross-power spectral matrix aligned along the principal diagonal as shown in Figure 3.11. This suboptimum processing can be formalized as follows. Let i denote the window index and L the window length. The output of the filtering operation in the ith sub-block is

$$u_{D,i}(n, m_v) = \tilde{\mathbf{W}}^H_{D,i}(n, m_v)\tilde{\mathbf{S}}_i(n) \tag{3.48}$$

where $\tilde{\mathbf{W}}_{D,i}(n, m_v)$ and $\tilde{\mathbf{S}}_i(n)$ are the weight vector and the signal vector with respect to the ith block. The global output of the suboptimum SDAP filtering process is

$$u_{D,w}(n, m_v) = \sum_i u_{D,i}(n, m_v) \tag{3.49}$$

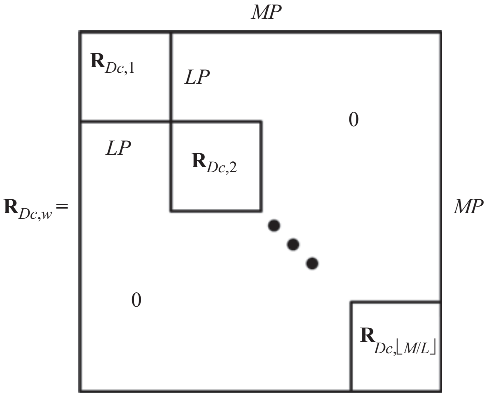

Figure 3.11 Approximated cross-power spectral matrix

The weight vector in the *i*th window is expressed as

$$\tilde{\mathbf{W}}_{D,i}(n,m_v) = \hat{\mathbf{R}}_{Dc,i}^{-1}\tilde{\mathbf{G}}_{D,i}(n,m_v) \tag{3.50}$$

where

$$\tilde{\mathbf{G}}_{D,i}(n,m_v) = \begin{bmatrix} \tilde{\mathbf{S}}_{ref}(n,m_v-(i-1)L) \\ \tilde{\mathbf{S}}_{ref}(n,m_v-((i-1)L+1)) \\ \tilde{\mathbf{S}}_{ref}(n,m_v-((i-1)L+2)) \\ \vdots \\ \tilde{\mathbf{S}}_{ref}(n,m_v-((iL-1)) \end{bmatrix} \in C^{LP\times 1} \tag{3.51}$$

and

$$\tilde{\mathbf{S}}_i(n) = \begin{bmatrix} \tilde{\mathbf{S}}(n,(i-1)L) \\ \tilde{\mathbf{S}}(n,(i-1)L+1) \\ \tilde{\mathbf{S}}(n,(i-1)L+2) \\ \vdots \\ \tilde{\mathbf{S}}(n,iL-1) \end{bmatrix} \in C^{LP\times 1} \tag{3.52}$$

The cross-power spectral matrix in the *i*th window, $\hat{\mathbf{R}}_{Dc,i}$, is estimated as

$$\hat{\mathbf{R}}_{Dc,i} = \frac{1}{N_r}\sum_{n_r=0}^{N_r-1}\tilde{\mathbf{Z}}_i(n_r)\tilde{\mathbf{Z}}_i^H(n_r) \in \mathbb{C}^{LP\times LP} \tag{3.53}$$

Since the dimension of the matrix to be estimated is reduced, a reduced number of training range cells are needed. In fact, to obtain a performance loss of 3 dB, only $N_r = 2LP$ target-free range cells are needed. It is quite obvious that the windowing operation may introduce some distortion in the resulting image since an approximated cross-power spectral matrix is used.

3.2.2 Joint E-SDAP ISAR

In this chapter, a technique that combines clutter suppression and ISAR processing to obtain high-resolution image of noncooperative moving targets for bistatic configuration is introduced. An extended version of conventional SDAP processing that aims to take into account clutter non-stationarity in order to restore conventional SDAP filtering performance is proposed. E-SDAP formulation is derived from multichannel RD algorithm and takes into account clutter range variations. Due to the specific properties of the RD algorithm, the proposed processing is structurally different from the STAP algorithm proposed in the literature for bistatic case. A suboptimum version of E-SDAP processing is then proposed in order to reduce both the computational load and the training data requirement.

3.2.2.1 Optimum processing

As previously shown, in optimal SDAP processing for monostatic configuration, target-free training data are assumed IID. In this case, the convergence issue of the clutter covariance matrix estimation is only related to the amount of training data and not to the interference scenario (see (3.47)). IID assumption can be often violated in some real scenarios due to the very high number of training data required to obtaining a proper estimation of the clutter covariance matrix.

Clutter range dependence is particularly strong in multichannel bistatic configurations. In past years, a modified version of conventional STAP algorithm that aims to restore detection performance under a strong clutter non-stationarity has been proposed [24–27]. These techniques fall in general under the class of bistatic STAP.

SDAP is an innovative formulation that is structurally and algorithmically different with respect to the conventional STAP approach. In this section, its extended version is derived.

Let us consider that the optimal SDAP weight vector derived in (3.46), an extension of conventional SDAP processing through the first-order Taylor expansion, is proposed to take into account linear Doppler variation of clutter along range dimension.

Assuming to consider only linear range variation on time, the SDAP weight vector can be modeled as the sum of a fixed component and a component varying linearly with fast time:

$$\mathbf{W}(n_r, m) = \mathbf{W}_0(n_r, m) + n_r \Delta\mathbf{W}(n_r, m) \tag{3.54}$$

where n_r is the range cell index and is related to the range cell position r through the relation $r = n_r \Delta_r$ in which $\Delta_r = c/2B\cos\beta$ is the bistatic range resolution where β defines the bistatic angle [28,29]. In order to avoid range cell migration, a MF operation is performed in range/frequency domain leading to a weight vector expressed in frequency/slow-time domain:

$$\mathbf{W}(n, m) = DFT_{n_r}\{\mathbf{W}(n_r, m)\} \tag{3.55}$$

It is then possible to perform E-SDAP processing simply by considering the Taylor expansion of the weight vector in the frequency/Doppler domain as

$$\mathbf{W}_D(n, m_\nu) = DFT_m\{\mathbf{W}(n, m)\} \tag{3.56}$$

It is worth pointing out that this formulation is different from conventional post-Doppler STAP algorithm [19,30] and bistatic STAP algorithms proposed in [27], due to the different definitions of the extended weight vector present in (3.56) that makes the approach different. Therefore, the beamformer output can be expressed as

$$\begin{aligned} u_D(n, m_\nu) &= \mathbf{W}_{D,0}^H(n, m_\nu)\tilde{\mathbf{S}}(n) + n_r \Delta\mathbf{W}_D^H(n, m_\nu)\tilde{\mathbf{S}}(n) \\ &= \mathbf{W}_D'^H(n, m_\nu)\mathbf{T}_{n_r}^H\tilde{\mathbf{S}}(n) = \mathbf{W}_D'^H(n, m_\nu)\tilde{\mathbf{S}}'(n, m_\nu) \end{aligned} \tag{3.57}$$

where the new doubled weight vector is defined as

$$\mathbf{W}'_D(n, m_\nu) = \begin{bmatrix} \mathbf{W}_{D,0}(n, m_\nu) \\ \Delta\mathbf{W}_D(n, m_\nu) \end{bmatrix} \in C^{2MP\times 1} \tag{3.58}$$

while $\mathbf{T}_{n_r} = [\mathbf{I}, n_r\mathbf{I}] \in C^{MP\times 2MP}$ is the matrix that includes range cell dependence and $\mathbf{I} \in C^{MP\times MP}$ represents the identity matrix. The new doubled vector of received signal is then defined as

$$\tilde{\mathbf{S}}'(n) = \begin{bmatrix} \tilde{\mathbf{S}}(n) \\ n_r\tilde{\mathbf{S}}(n) \end{bmatrix} \in C^{2MP\times 1} \tag{3.59}$$

Considering (3.58), it is possible to derive an expression for the optimum extended weight vector that maximizes the output SINR and follows the conventional SMI:

$$\mathbf{W}'_D(n, m_\nu) = \gamma'\hat{\mathbf{R}}_D'^{-1}\tilde{\mathbf{G}}'_D(n, m_\nu) \in C^{2MP\times 1} \tag{3.60}$$

where γ' does not affect the SINR and where $\tilde{\mathbf{G}}'_D(n, m_\nu) = \begin{bmatrix} \tilde{\mathbf{G}}_D(n, m_\nu) \\ 0 \end{bmatrix} \in C^{MP\times 1}$ defines the new doubled reference vector in which $\tilde{\mathbf{G}}_D(n, m_\nu)$ has been defined in (3.43). It is worth highlighting that in conventional SDAP processing, the choice of the weight vector can be subjected to a set of linear constraints. As known, one of the most common constraints is, for example, the minimum variance distortionless response that constrains the beam pattern to be unity in the steering direction. In the case of time-varying weight vector, there are several different ways in which it is possible to choose to constrain the gain of the adapted beam [31]. One strategy could be to constraint $\mathbf{W}_{D,0}$ to have unity gain in the steering direction and leave $\Delta\mathbf{W}_D$ unconstrained. This leads to the previous definition of the reference vector.

The estimation of the new clutter covariance matrix presented in (3.60) is obtained by still considering a set of N_r training data that must be target free to avoid the fact that the useful target return is considered as interference:

$$\hat{\mathbf{R}}'_D = \frac{1}{N_r}\sum_{n_r=1}^{N_r}\tilde{\mathbf{Z}}'(n_r)\tilde{\mathbf{Z}}'(n_r)^H \in C^{2MP\times 2MP} \tag{3.61}$$

where $\tilde{\mathbf{Z}}'(n_r)$ is the new doubled training data vector relative to the n_r range cell that is defined in the space/Doppler domain:

$$\tilde{\mathbf{Z}}'(n_r) = \begin{bmatrix} \tilde{\mathbf{Z}}(n_r) \\ n_r\tilde{\mathbf{Z}}(n_r) \end{bmatrix} \in C^{2MP\times 1} \tag{3.62}$$

where $\tilde{\mathbf{Z}}(n_r)$ is the space/Doppler snapshot used in SDAP processing in the clutter covariance matrix estimation defined in (3.47). The new doubled clutter covariance matrix can also be seen in a more compact form as represented earlier:

$$\hat{\mathbf{R}}'_D = \begin{bmatrix} \hat{\mathbf{R}}_D^{(0)} & \hat{\mathbf{R}}_D^{(1)} \\ \hat{\mathbf{R}}_D^{(1)} & \hat{\mathbf{R}}_D^{(2)} \end{bmatrix} \in C^{2MP\times 2MP} \tag{3.63}$$

in which the single elements represent the $MP \times MP$ estimated clutter covariance matrix used in conventional SDAP approach:

$$\hat{\mathbf{R}}_D^{(k)} = \frac{1}{N_r}\sum_{n_r=1}^{N_r} n_r^{(k)}\tilde{\mathbf{Z}}(n_r)\tilde{\mathbf{Z}}^H(n_r) \in C^{MP\times MP} \tag{3.64}$$

It is quite evident that the effect of modeling the first-order dynamic behavior of the weight vector is to increase the dimension of the estimation problem and consequently the dimension of the degrees of freedom. The increase in the adaptive weight vector dimension involves an increase of the computational load. This is the price that must be paid in order to take into account linear variation of clutter along the range dimension. It is clearly possible to extend this approach by using more terms from the Taylor series expansion to cope with any suitably smooth nonlinear time variation. The fundamental processing chain of E-SDAP ISAR algorithm is depicted in Figure 3.12. As in SDAP case, in order to compensate for the relative motion between platform and moving target, ISAR processing must be applied at the output of the E-SDAP processing.

3.2.2.2 Suboptimum processing

For a typical value of radar PRF and observation time, the required number of training data is very high corresponding to a wide area of homogeneous clutter. In some cases, especially in bistatic configurations, clutter heterogeneity leads to a degradation of SDAP performance. A reduction of the number of required training data is a desirable feature. In fact a reduction in training data means a smaller range area on which the clutter can be estimated. As a consequence, it is more reasonable to consider clutter range variation as linear [12]. In this section, a suboptimum approach for E-SDAP processing is derived. The reduction in the dimensionality of the clutter covariance matrix can be obtained by splitting the E-SDAP filtering operation, derived in (3.60), in sub-widows as shown in Figure 3.13. The suboptimum E-SDAP approach consists of applying a windowing operation onto the Doppler spectrum and applying the optimum filter on each window. The reduction in the dimensionality of the extended clutter covariance matrix to be estimated is given by the length of the considered sub-window.

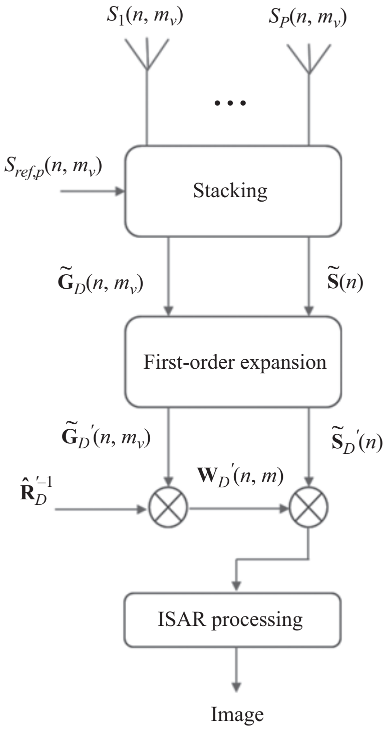

Figure 3.12 E-SDAP ISAR functional block processing

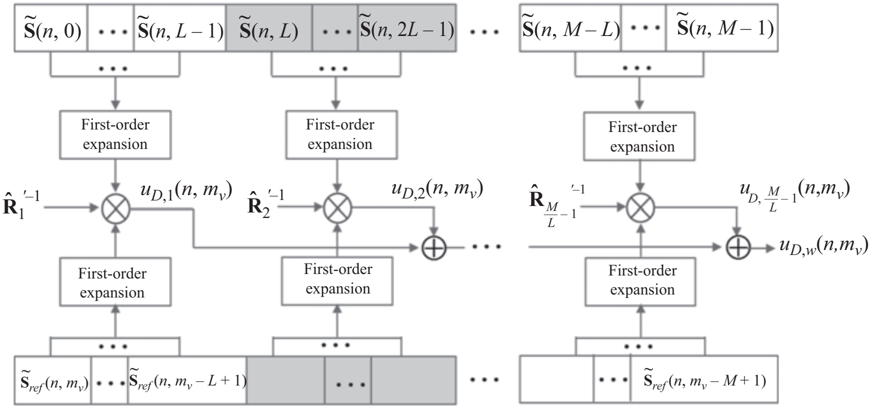
$\tilde{\mathbf{S}}(n, 0)$
$\tilde{\mathbf{S}}(n, L-1)$
$\tilde{\mathbf{S}}(n, L)$
$\tilde{\mathbf{S}}(n, 2L-1)$
$\tilde{\mathbf{S}}(n, M-L)$
$\tilde{\mathbf{S}}(n, M-1)$
First-order expansion
$\hat{\mathbf{R}}_1'^{-1}$
$u_{D,1}(n, m_v)$
$\hat{\mathbf{R}}_2'^{-1}$
$u_{D,2}(n, m_v)$
$\hat{\mathbf{R}}_{\frac{M}{L}-1}'^{-1}$
$u_{D,\frac{M}{L}-1}(n,m_v)$
$u_{D,w}(n,m_v)$
$\tilde{\mathbf{S}}_{ref}(n, m_v)$
$\tilde{\mathbf{S}}_{ref}(n, m_v-L+1)$
$\tilde{\mathbf{S}}_{ref}(n, m_v-M+1)$

Figure 3.13 Suboptimum E-SDAP ISAR functional block processing

Let's define $i = 0, 1, \ldots, \lfloor M/L \rfloor - 1$ as the window index and L as the window length across the Doppler spectrum. The output of the filtering operation in the ith subblock can be expressed as

$$u_{D,i}(n, m_v) = \mathbf{W}'^{H}_{D,i}(n, m_v)\tilde{\mathbf{S}}'_i(n) \tag{3.65}$$

where the $\mathbf{W}'_{D,i}(n, m_v)$ and the $\tilde{\mathbf{S}}'_i(n)$ represent the extended weight vector and extended received signal vector with respect to the ith block, respectively. The global output of the suboptimum E-SDAP filtering process can be obtained as

$$u_{D,w}(n, m_v) = \sum_i \mathbf{W}'^{H}_{D,i}(n, m_v)\tilde{\mathbf{S}}'_i(n) \tag{3.66}$$

The extended weight vector relative to the ith subblock can be clearly defined as follows:

$$\mathbf{W}'_{D,i}(n, m_v) = \gamma'_i \hat{\mathbf{R}}'^{-1}_{D,i}\tilde{\mathbf{G}}'_{D,i}(n, m_v) \in C^{2LP\times 1} \tag{3.67}$$

while $\tilde{\mathbf{S}}'_i(n)$ and $\tilde{\mathbf{G}}'_{D,i}(n, m_v)$ are obtained as follows:

$$\tilde{\mathbf{S}}_i(n) = \begin{bmatrix} \tilde{\mathbf{S}}(n, iL) \\ \tilde{\mathbf{S}}(n, iL+1) \\ \vdots \\ \tilde{\mathbf{S}}(n, (i+1)L-1) \end{bmatrix} \in C^{LP\times 1} \tag{3.68}$$

$$\tilde{\mathbf{S}}'_i(n) = \begin{bmatrix} \tilde{\mathbf{S}}_i(n) \\ n_r\tilde{\mathbf{S}}_i(n) \end{bmatrix} \in C^{2LP\times 1} \tag{3.69}$$

$$\tilde{\mathbf{G}}_{D,i}(n, m_v) = \begin{bmatrix} \tilde{\mathbf{S}}_{ref}(n, m_v - iL) \\ \tilde{\mathbf{S}}_{ref}(n, m_v - (iL+1)) \\ \vdots \\ \tilde{\mathbf{S}}_{ref}(n, m_v - ((i+1)L-1)) \end{bmatrix} \in C^{LP\times 1} \tag{3.70}$$

$$\tilde{\mathbf{G}}'_{D,i}(n, m_v) = \begin{bmatrix} \tilde{\mathbf{G}}_{D,i}(n, m_v) \\ \mathbf{0} \end{bmatrix} \in C^{2LP\times 1} \tag{3.71}$$

The signal vector of the ith block in (3.68) is obtained by applying a windowing operation along the Doppler dimension and the extended signal vector relative to the ith block can be obtained as in (3.69). The same concept holds true for the definition of the extended reference vector.

The extended clutter covariance matrix in the ith sub-window, $\hat{\mathbf{R}}'_{D,i}$, can be obtained in a similar way to (3.63):

$$\hat{\mathbf{R}}'_{D,i} = \begin{bmatrix} \hat{\mathbf{R}}^{(0)}_{D,i} & \hat{\mathbf{R}}^{(1)}_{D,i} \\ \hat{\mathbf{R}}^{(1)}_{D,i} & \hat{\mathbf{R}}^{(2)}_{D,i} \end{bmatrix} \in C^{2LP\times 2LP} \tag{3.72}$$

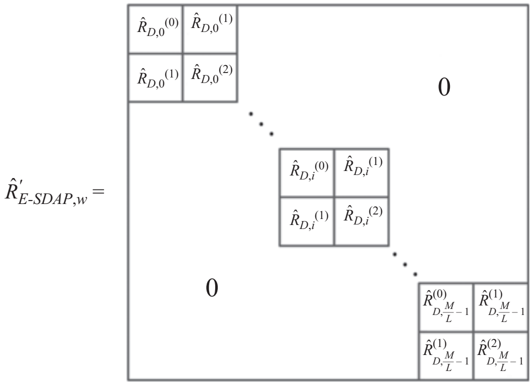

Figure 3.14 Extended clutter covariance matrix in the suboptimum E-SDAP approach

where the generic element, $\hat{\mathbf{R}}_{D,i}^{(k)}$, of the extended covariance matrix represents a $LP \times LP$ subblock relative to the ith window obtained by applying the windowing operation on the training data set:

$$\hat{\mathbf{R}}_{D,i}^{(k)} = \frac{1}{N_r}\sum_{n_r=1}^{N_r} n_r^k \tilde{\mathbf{Z}}_i(n_r)\tilde{\mathbf{Z}}_i^H(n_r) \in C^{LP\times LP} \tag{3.73}$$

where $\tilde{\mathbf{Z}}_i(n_r)$ represents the extended target-free space/Doppler snapshot of the n_r range cell relative to the ith subblock. The extended covariance matrix in suboptimum approach is reported in Figure 3.14.

3.3 Results

In this section, the SDAP processing and the E-SDAP processing previously described will be tested on real data and on simulated data, respectively. The real data have been provided by Metasensing and consist of the data acquired by a two-channel SAR system while simulated data have been provided by the Warsaw University of Technology (WUT). Both the real and simulated dataset are analyzed and the critical aspects for the application of the proposed processing are highlighted.

3.3.1 SDAP–ISAR results

In this section, the SDAP processing previously described will be tested on real data. The data have been provided by Metasensing and consist of the data acquired by a two-channel SAR system. As it will be explained in the following, the system setup is not optimal for the application of the algorithms described in the previous chapters, so some preliminary operations are needed to arrange the data in a manner that allows for the proposed processing to be applied. In Section 3.3.1.2, the multichannel range–Doppler (MRD) processing to obtain the SAR image will be tested and some conclusions will be drawn while in Section 3.3.1.3, the SDAP-ISAR processing will be applied exploiting the two available channels.

3.3.1.1 Dataset description

A measure campaign has been conducted within the activities of the NATO-SET 196. The campaign took place on the June 5, 2013 close to Teuge airport (NL). The platform used is a 208 Grand Caravan from Paracentrum Teuge (PH-SWP). The radar mounted on the platform is a dual-channel FMCW SAR system. A summary of the measures campaign conducted by Metasensing can be found in [32]. Details about the functioning of the FMCW system can be found in [33]. The acquisitions have been performed by flying over a highway in proximity of Teuge airport. The highway was perpendicular to the flight trajectory. The acquisition parameters are summarized in Table 3.1. The radar parameters are listed in Table 3.2 while the antenna specifications are in Table 3.3.

Figure 3.15 shows the transmitter (a) and receiver (b) antennas, respectively. The setup of the platform is shown in Figure 3.16 while a picture of the area under test is shown in Figure 3.17.

It is quite obvious that the measured setup described earlier is not optimal for the testing of the proposed method. The principal shortcomings are as follows:

- Small bandwidth ($B = 120$ MHz). This involves a slant-range range resolution $\Delta_{y_2} = 1.25$ m. This is poor resolution especially when dealing with ground target.
- Baseline $d > \lambda/2$. This is a problem from a beamforming point of view but also for the MRD image formation process.

Table 3.1 Acquisition parameters

Platform	208 Grand Caravan from Paracentrum Teuge (PH-SWP)
Look angle	55°
Flight altitude	1,200 m
Velocity	180 km/h
Mean range	2 km
Swath	1 km

Table 3.2 Radar parameters

Center frequency	9.6 GHz
TX bandwidth	120 MHz
PRF	5 kHz
ADC sampling frequency	25 MHz

- Only two channels resulting in a small number of spatial degrees of freedom.
- Highway parallel to the range dimension. This involves a difficult estimation of the interference space/slow time covariance matrix.

All these issues will be analyzed in the following.

3.3.1.2 Multichannel range–Doppler image formation

In this section, the performance of the MRD image formation processing will be discussed. In particular, the condition on the array size derived in Section 3.1 will be analyzed. The condition is here recalled for the sake of clarity

$$D_{array} \leq \frac{\lambda R_0}{32(y_1 \cos\alpha - y_3 \sin\alpha)} \tag{3.74}$$

It is worth pointing out that since in a SAR scenario $\alpha = 0$ (see Figure 3.1), (3.74) imposes a direct relationship between the image cross-range and the array size. The available data were acquired by a two-channel SAR system with baseline

Table 3.3 Antennas parameters

TX: horn	
Gain	19.6 dB
Antenna aperture (3 dB)	Elevation 20° Azimuth 20°
RX: microstrip patch	
Gain	21.4 dB
Antenna aperture (3 dB)	Elevation 22° Azimuth 7.5°
Baseline	15 cm

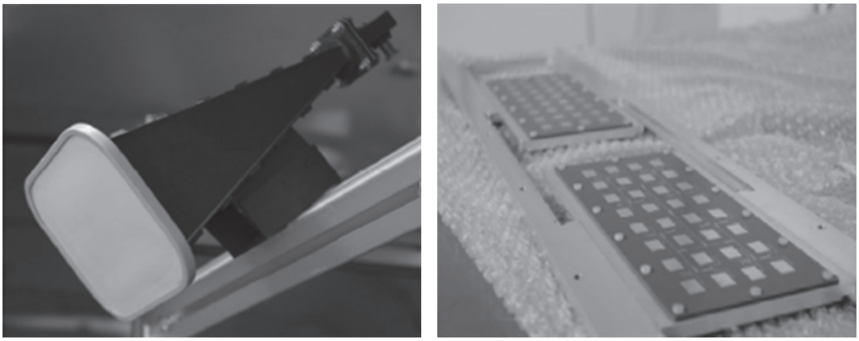
(a) (b)

Figure 3.15 TX antenna (a) and RX antennas (b)

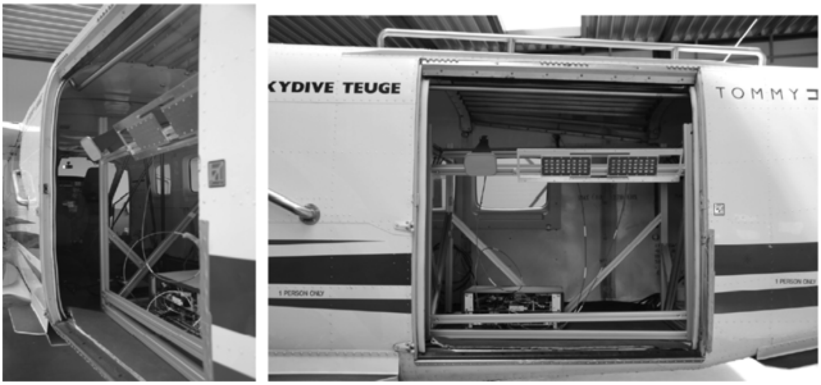

Figure 3.16 Platform set up

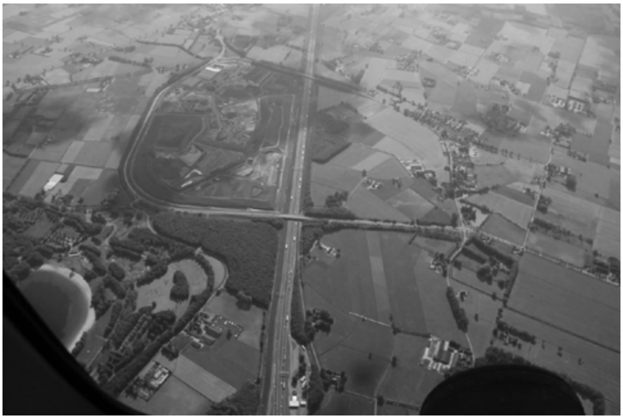

Figure 3.17 Optical image of the area under test

$d = 15\,\text{cm} \approx 5\lambda$. It is quite clear that such a distance is quite large and considering the cross-range y_1 imaging area, the array size, D_{array}, does not meet the condition in (3.74). In fact, considering the system parameters listed in Table 3.3, the cross-range imaging size can be roughly evaluated considering receiver antenna beamwidth as

$$D_{y_1} \approx R_0\theta_{az} = 262\,\text{m} \tag{3.75}$$

The results of the imaging processing are shown in Figure 3.18. In Figure 3.18(a) and (b), the images obtained by applying the RD processing on data acquired by channels 1 and 2, respectively, are shown. In Figure 3.19, the image obtained by applying MRD is shown. As can be noted, the distortions due to the abovementioned effects are evident. The array size is too large and the summation is coherent only in a small

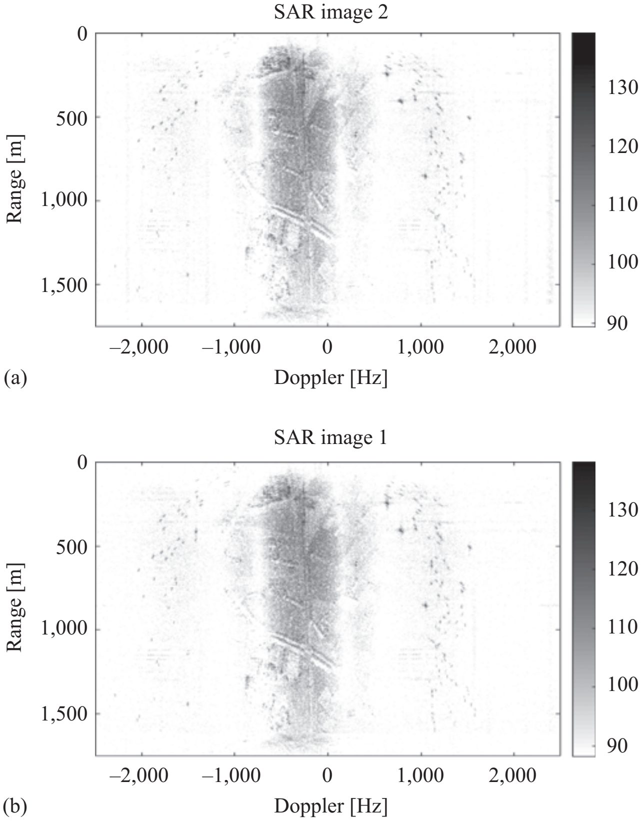

Figure 3.18 Range–Doppler image results (a) channel 1, (b) channel 2

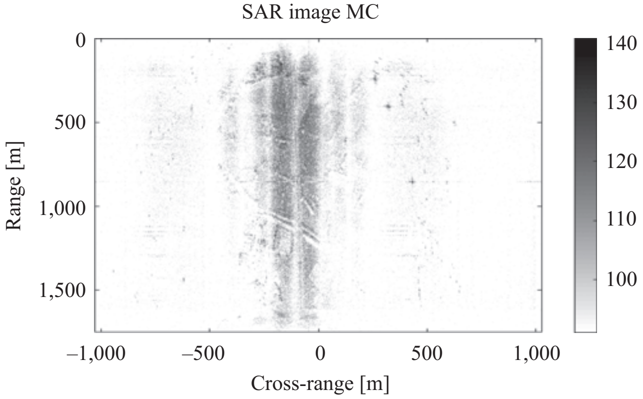

Figure 3.19 Multichannel range–Doppler image results

cross-range region. In order to reduce the baseline between the two antennas, the first N_d samples are discarded in the channel 1 data and the last N_d samples are discarded in the channel 2 data as in Figure 3.20. In this way, the equivalent baseline, d_{eq} between the two channels becomes

$$d_{eq} = d - N_d v_p T_R \tag{3.76}$$

It is quite obvious that in this case, the acquisitions are no longer contemporary. This is not an issue for the image formation processing but it can affect the performances when clutter suppression is performed. Considering the system parameters described in Section 3.3.1.1, the configuration in which the elements are as close as possible is obtained with $N_d = 17$. Result with $N_d = 17$ is shown in Figure 3.21.

3.3.1.3 Clutter suppression and imaging

In this section, the results of the application of SDAP ISAR processing will be presented. Some preliminary operations on the available data are needed before applying the clutter suppression and the imaging processing. Specifically, a baseline reduction is mandatory for multichannel RD imaging processing. However, it is worth pointing

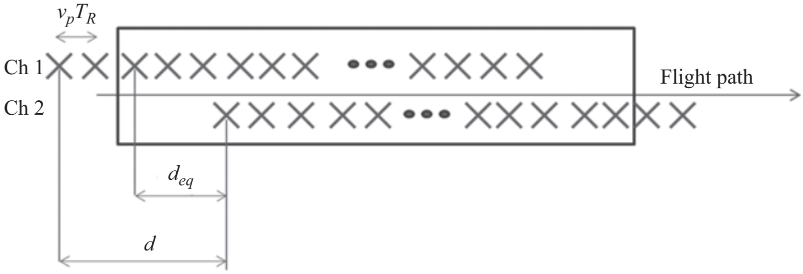

Figure 3.20 Baseline reduction

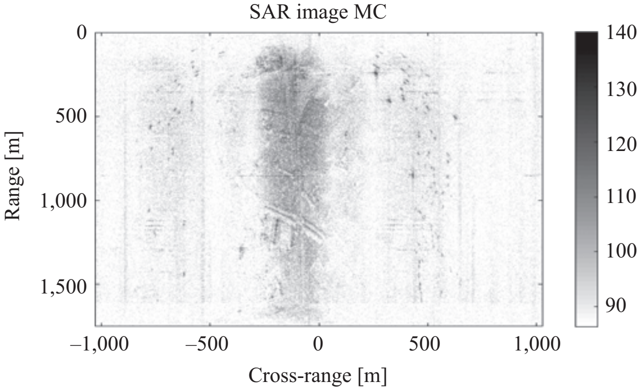

Figure 3.21 Multichannel range–Doppler image results $N_d = 17$

out that after this preprocessing, the data acquired by the two channels are no longer contemporary. Although this is not an issue in the multichannel RD processing, a time decorrelation is introduced which can affect the performance of the SDAP processing. Nevertheless, it is worth noting that the system PRF is very high, i.e., $PRF = 5$ kHz, and for such a high PRF, the scene can be considered static within the N_d pulses. Another shortcoming is due to the observed scene. As can be noted, a highway is present in the scene and is oriented along the range direction. This involves the presence of a number of moving targets along all the range dimension of the image. It is quite obvious that, in this particular situation, the estimation of the space–slow time covariance matrix of the disturbance becomes a difficult task because of the lack of the availability of target-free range cells. However, the signal-to-clutter ratio (SCR) is very low because the clutter region is significantly larger than the targets region so that the estimation can be reasonably performed. Moreover, as explained in previous section, the system has only two channels that result in a small number of spatial degree of freedom. It is worth pointing out that in order to evaluate the performances of the proposed clutter suppression and imaging process, a ground truth would be necessary. This would allow for a comprehensive performance evaluation. Unfortunately, the ground truth is not available.

In Figure 3.22, the region under test and the training region are highlighted with a solid line and with a dotted line, respectively. It is evident that moving targets are present in both the regions as stated before so that the estimation of the clutter covariance matrix will be affected. The situation of both the cases will be analyzed.

In the first case, the proposed SDAP–ISAR processing will be applied to the data collected by the two channels after the baseline reduction. As it will be evident after the analysis of the results, the clutter suppression seems to work properly. However, since the ground truth is not available, it is very difficult to assess the correct functioning of the proposed processing. In fact, all the moving targets appear outside of the clutter Doppler bandwidth. The clutter seems to be properly canceled, but it is very hard

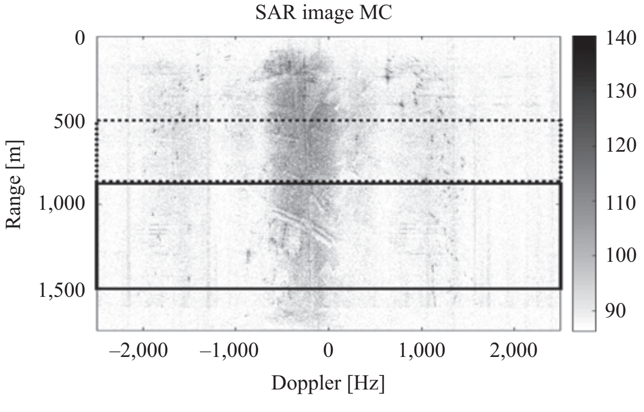

Figure 3.22 SAR image with region under test (red box) and training range cells (yellow box)

to state if some of the moving targets within the clutter bandwidth are canceled as well. In order to correctly evaluate the effectiveness of the proposed SDAP-ISAR algorithm, a case in which some moving targets are present in the clutter Doppler bandwidth should be considered. This is easily obtained performing a subsampling in the slow time dimension (in addition to the baseline reduction) as shown in Figure 3.23. A subsampling factor value of 3, $sf = 3$, has been chosen. In this way, the equivalent PRF is obtained as

$$PRF_{eq} = \frac{PRF}{3} = 1.67\,\text{kHz} \tag{3.77}$$

A fixed relationship between the Doppler frequency of a target in the image obtained considering the data without subsampling and the Doppler frequency of the same target in the image obtained by processing the data with PRF_{eq} exists and can be exploited to verify if some moving targets are canceled by the clutter suppression process. The relationship between the target Doppler frequency before and after the subsampling can be derived by considering Figure 3.24.

Specifically, a target with Doppler frequency $|f_D| < (PRF_{eq}/2)$ will appear in the same Doppler position within the images obtained by processing the data with the two PRF values. On the other hand, a target with Doppler frequency $(PRF_{eq}/2) < |f_D| < (PRF/2)$ will be wrapped in the image obtained by processing the data with PRF_{eq}. In this case, the target will appear in a Doppler position that can be expressed as

$$f_{D_{eq}} = -\text{sgn}(f_D)PRF_{eq} + f_D \tag{3.78}$$

In this way, a pseudo-ground truth is created and used to verify the effectiveness of the proposed algorithm.

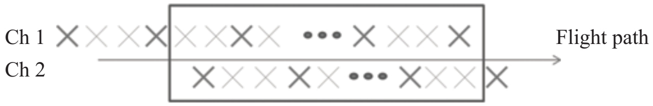

Figure 3.23 Baseline reduction and subsampling

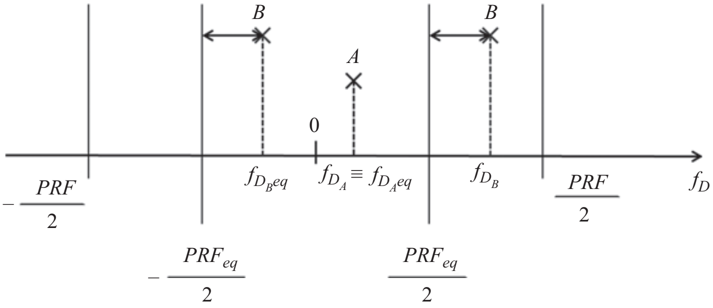

Figure 3.24 Doppler mapping

Case study 1

In the first case, an amount of data corresponding to an observation time $T_{obs} = 0.2$ s is used. This small value of observation time allows for the processing of an amount of data that can be easily processed with a general purpose PC. In fact, with $PRF = 5\,\text{kHz}$ larger T_{obs} corresponds to large amounts of data that cannot be treated. The suboptimum SDAP processing described in Section 3.2.1.2 is applied with window length $L = 32$ samples. In Figure 3.25, the images of the region under test without clutter suppression (a) and with clutter suppression (b) are shown. As can be noted after a visual inspection, the proposed SDAP processing performs the clutter cancellation very well. However, as stated before, it is not possible to assess the correct functioning of the method because of the lack of the ground truth. One crop cut from the images shown in Figure 3.25 is shown in Figure 3.26. As can be noted, the moving targets are present after the clutter suppression. Moreover, the image after clutter suppression seems to be more noisy but this is only a visualization issue. In fact, both the images are normalized with respect to its maximum value and a dynamic of 40 dB is represented. Since the image after clutter mitigation presents

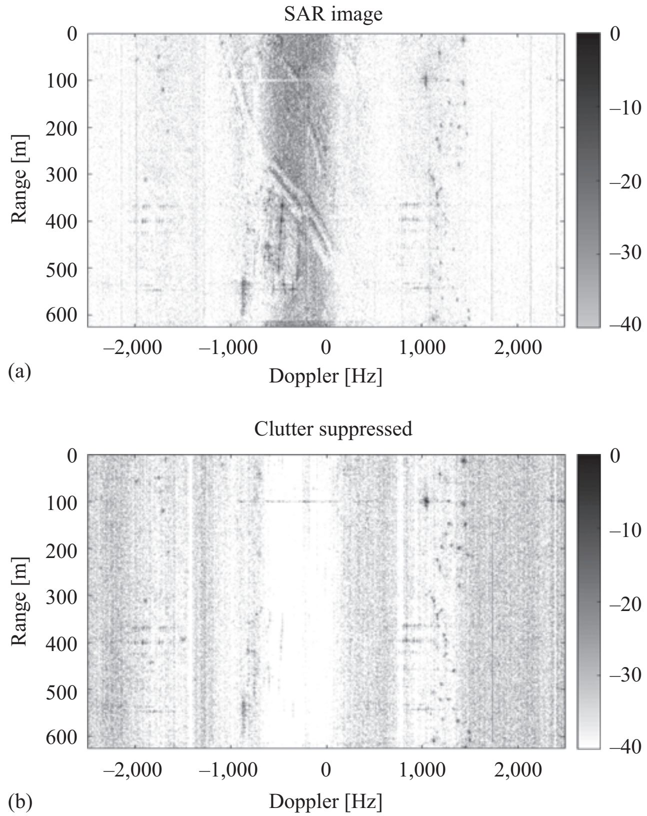

Figure 3.25 SAR image (a) and clutter suppressed SAR image (b)

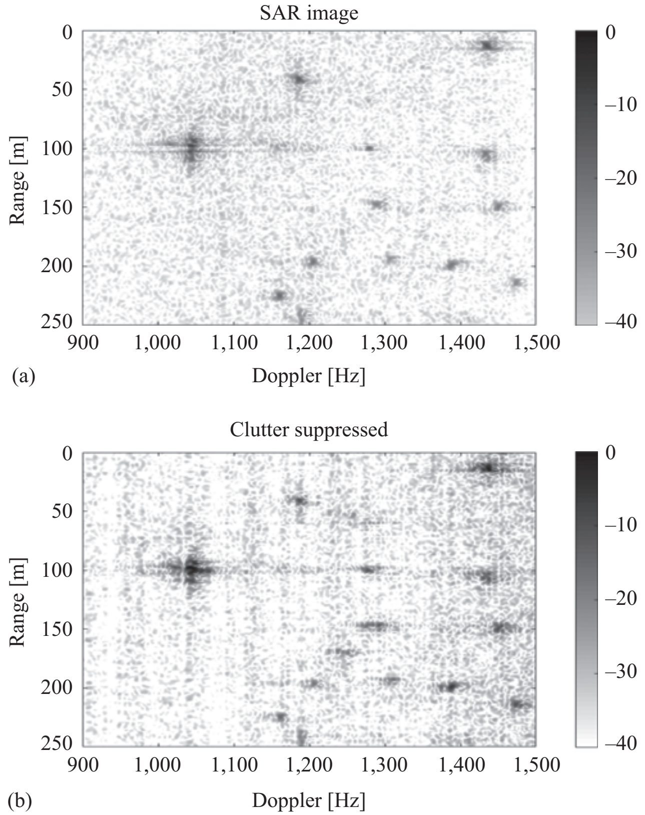

Figure 3.26 Detail 2: SAR image (a) and clutter suppressed SAR image (b)

a lower peak value than the SAR image (because of the cancellation of the static scene), more noise is visible within the 40-dB dynamic in Figures 3.25 and 3.26(b) with respect to Figure 3.25 and Figure 3.25(a). As stated before, no conclusions can be drawn by observing these results because all the moving targets seem to be outside of the clutter Doppler bandwidth. Another issue regards the application of the ISAR refocusing processing. In Figures 3.27 and 3.28 two target crops are shown before (a) and after the ISAR processing (b). As can be noted, the improvement in the image focus is almost irrelevant. This is due to the fact that with the considered CPI, the defocusing effect introduced by the uncompensated target own motion is negligible and the ISAR processing does not lead to any significant improvement. However, a little improvement in the image focus is present and can be measured by exploiting the IC values before and after the application of the ISAR processing that is summarized in Table 3.4.

Case study 2

As stated before, the second case study is obtained applying a subsampling operation to the acquired data along the slow time dimension. In this way, a data reduction is

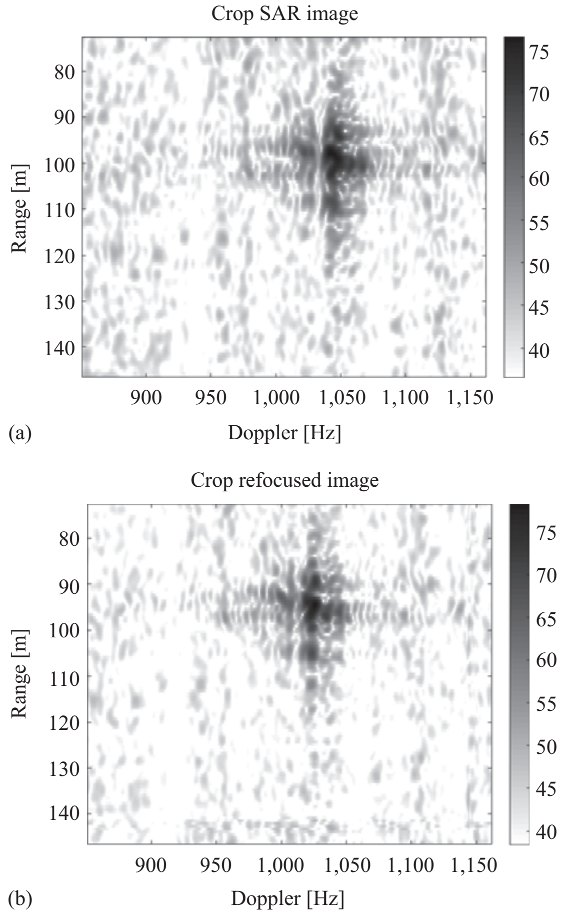

Figure 3.27 Crop 1: original SAR image (a) and refocused image (b)

obtained allowing for the processing of a larger CPI and, more important, the presence of moving targets within the clutter Doppler bandwidth is imposed. A subsampling factor $sf = 3$ has been chosen together with an observation time of $T_{obs} = 6$ s. The SAR image obtained by processing the subsampled data is shown in Figure 3.29. The region under test and the training range cells are highlighted with a solid line and with a dotted line, respectively. By comparing Figure 3.29 and Figure 3.22, it is evident that the moving targets that appear clearly visible in the image with full PRF are wrapped within the clutter Doppler bandwidth in the image with the reduced PRF. The SAR images of the region under test without clutter suppression and with clutter suppression are shown in Figure 3.30(a) and (b), respectively. As can be noted after a visual inspection, clutter suppression seems to work properly and a lot of targets that masked under the static scene in Figure 3.30 become clearly visible in Figure 3.30(b).

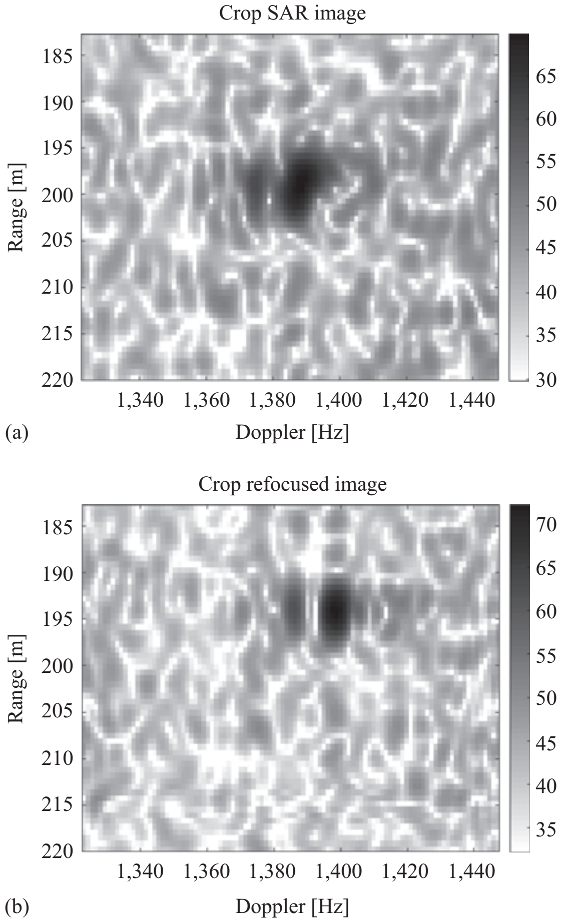

Figure 3.28 Crop 2: original SAR image (a) and refocused image (b)

Table 3.4 Case study 1: IC values

	IC SAR	IC ISAR
Crop 1	9.943	11.819
Crop 2	5.945	7.995

In order to better appreciate the moving target detection improvement, two subregions are represented in Figures 3.31 and 3.35. In Figure 3.31, the SAR image of the subregion 1 without application of the clutter mitigation processing (a) and with the application of the clutter mitigation processing (b) is shown. Moreover, the portion of the image obtained by processing the data without subsampling, $PRF = 5$ kHz, in

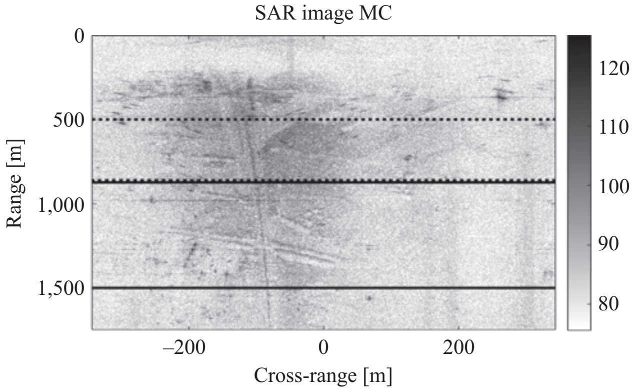

Figure 3.29 SAR image obtained processing subsampled data

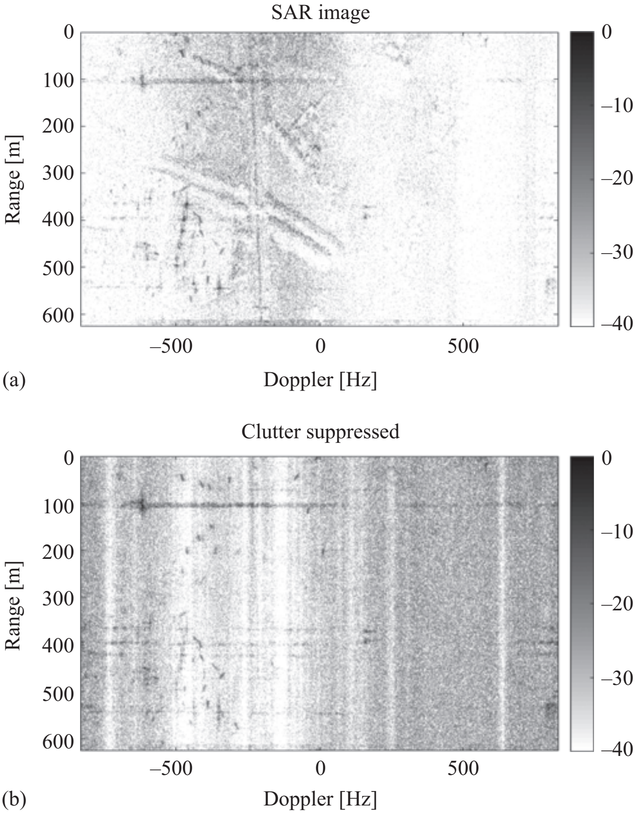

Figure 3.30 SAR image (a) and clutter suppressed SAR image (b)

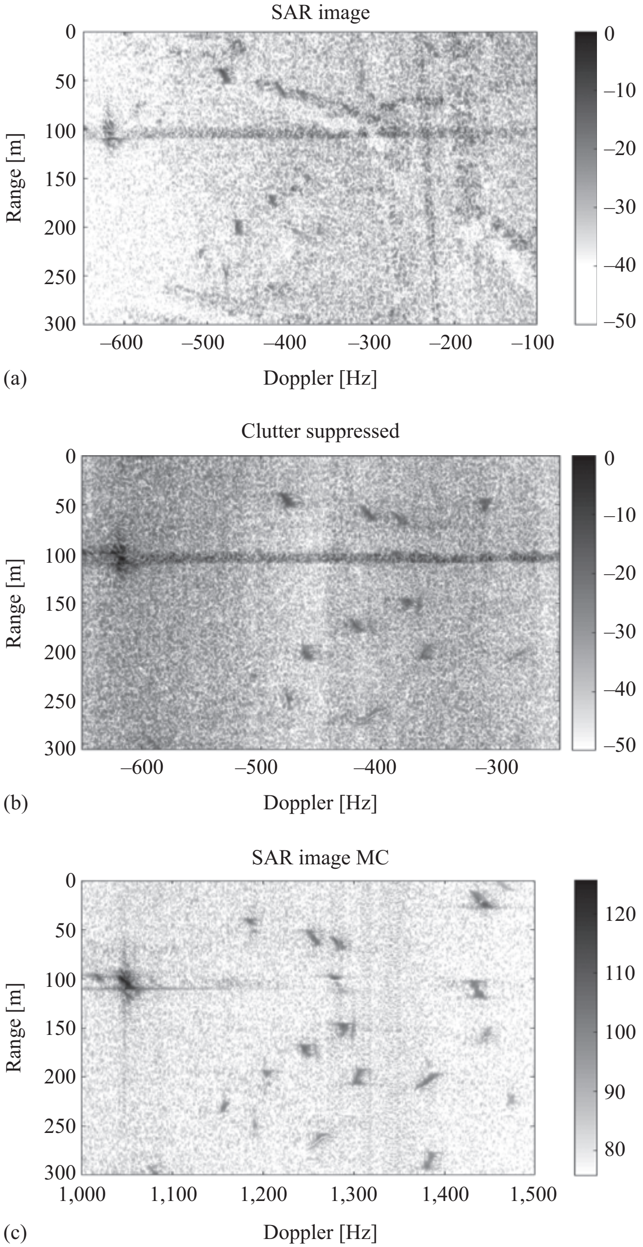

Figure 3.31 Subimage 1: SAR image (a), clutter suppressed SAR image (b), pseudo ground truth (c)

Table 3.5 Subregion 1: pseudo ground truth comparison

Target no.	f_D [Hz] ($PRF = 5$ kHz)	f_D [Hz] ($PRF = 1.67$ kHz)	Range [m]	Missing targets
1	1,187	−479	40	
2	1,257	−409	58	
3	1,284	−382	65	
4	1,047	−619	103	
5	1,288	−378	147	
6	1,250	−416	172	
7	1,203	−463	197	
8	1,305	−361	199	
9	1,383	−283	204	X
10	1,158	−504	227	X
11	1,440	−227	24	X
12	1,437	−230	110	X
13	1,474	−193	220	X
14	1,384	−283	282	X

which the same targets are present is shown in Figure 3.31(c). This last image represents the Doppler region that in the image obtained by processing the subsampled data is folded within the clutter Doppler bandwidth. As a consequence, it provides a pseudo-ground of truth that can be exploited to verify the effectiveness of the proposed method. The Doppler frequencies of every visible target in the pseudo-ground truth image (Figure 3.31(c)) are listed in Table 3.5 with the relative Doppler frequency evaluated considering the subsampling operation. The range coordinates are listed as well in order to locate the target within Figure 3.31(b) and (c). As can be noted, 6 targets out of 14 are canceled. It is worth pointing out that the target that can be clearly seen in Figure 3.31(b) with coordinates range and Doppler coordinates, $Range = 55$ m and $f_D = -310$ Hz, respectively, does not appear in Figure 3.31(c). This is not an artifact introduced by the processing but a target that in the pseudo-ground truth image has coordinates equal to $Range = 55$ m and $f_D = -1{,}976$ Hz and results folded in the right position. In Figures 3.32–3.34, the results of the application of the ISAR processing are shown. Specifically, three targets are selected (target no. 1, 2, 5) and for each of them, the SAR image (a) and the refocused ISAR image (b) are shown. The defocusing effect due to the uncompensated target own motion is evident by observing the target SAR images while the improvement in the image focus obtained by applying the ISAR autofocusing process can be clearly noticed by visual inspection of the results shown. In order to better evaluate the performance of the refocusing process, the IC values before and after the autofocusing are listed in Table 3.6 for all the targets detected in Figure 3.31(b). The improvement in the image quality is evident. The same analysis is performed in the other subregions of the scene under test. In Figure 3.35, subregion 2 is shown. The SAR images without clutter suppression and with clutter suppression are shown in Figure 3.35(a) and (b),

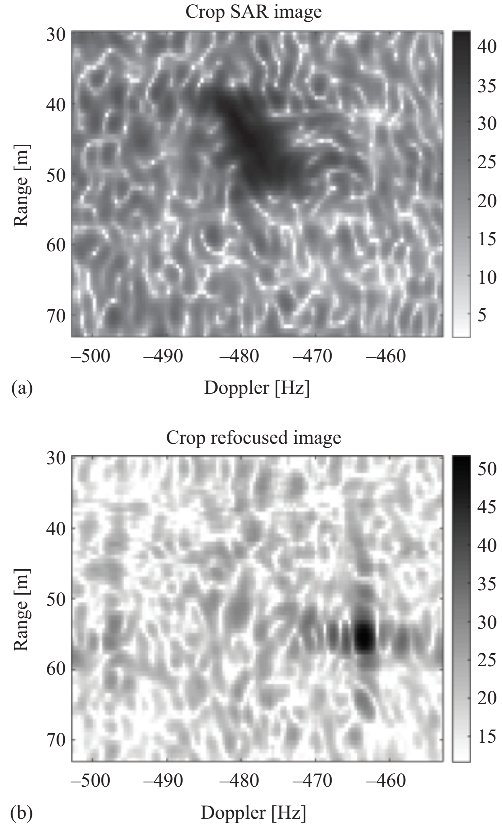

Figure 3.32 Subregion 1—Crop 1: original SAR image (a) and refocused image (b)

respectively. The pseudo-ground truth is shown in Figure 3.35(c). Also in this case, the improvement in the detection capability results is evident from the visual inspection. The results of the comparison between the pseudo-ground truth and the clutter suppressed image are listed in Table 3.7. Also in this case, a couple of targets out of 13 are canceled. It is worth pointing out that this second subregion is farther from the training range cells than the subregion 1 so the estimation of the space–slow time covariance matrix could be less accurate for this region with respect subregion 1. The IC values for each target before and after the application of ISAR processing are listed in Table 3.8. The improvement in the image focus is evident for all the considered targets. Three of them (specifically target number 1, 4, and 6) are shown in Figures 3.36–3.38.

3.3.2 E-SDAP ISAR results

In this section, the proposed algorithm for clutter suppression in bistatic geometry will be tested on simulated data. The data have been simulated by the WUT, Institute

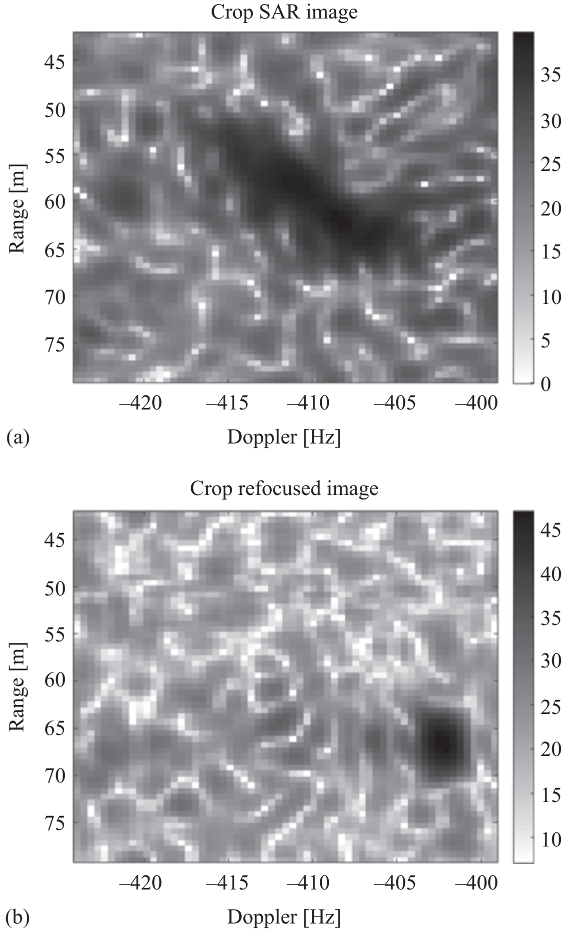

Figure 3.33 Subregion 1—Crop 2: original SAR image (a) and refocused image (b)

of Electronic System within the activity of the NATO-SET 196. A SAR raw data simulator has been used. This simulator is based on a hybrid analysis, based on geometrical optics enhanced with full-wave electromagnetic simulations of larger facets of the size of a few radar resolution cells. The scene under test can be defined using real digital elevation model (DEM) gathered using systems such as light detection and ranging systems [34]. This raw data SAR simulator allows a complex and realistic simulation of the scene under radar observation to be performed. The simulated dataset is referred to a particular bistatic configuration where a three-channel receiver is used. In Section 3.3.2.2, the MRD processing to obtain SAR images will be performed while in Section 3.3.2.3, the proposed E-SDAP ISAR processing will be tested and validated with a multichannel processing using simplified scenario with three channels.

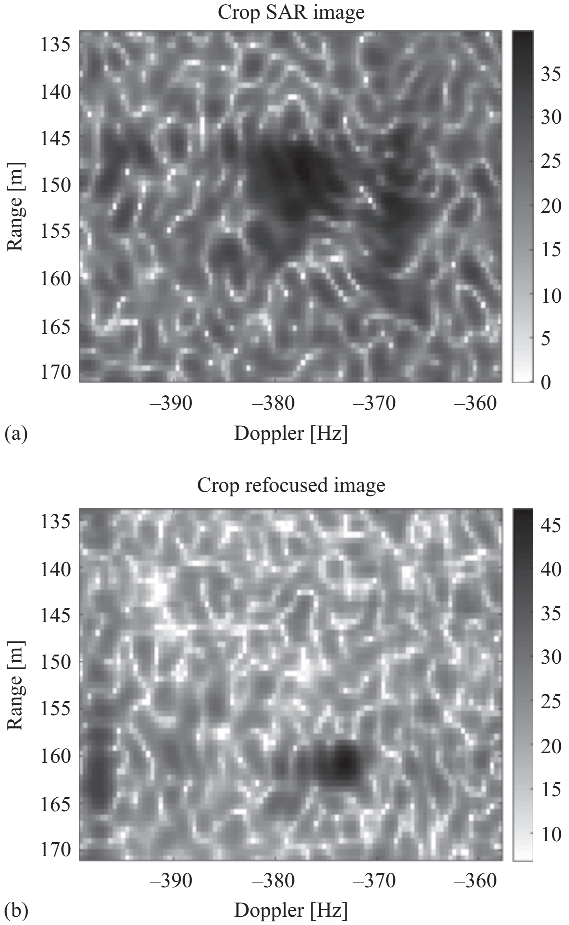

Figure 3.34 Subregion 1—Crop 5: original SAR image (a) and refocused image (b)

Table 3.6 Subregion 1: IC values before and after ISAR processing

Target no.	IC SAR	IC ISAR
1	2.673	10.174
2	1.472	4.84
3	0.83	3.344
4	2.80	5.326
5	1.345	3.698
6	1.161	4.165
7	1.879	6.502
8	1.072	4.92

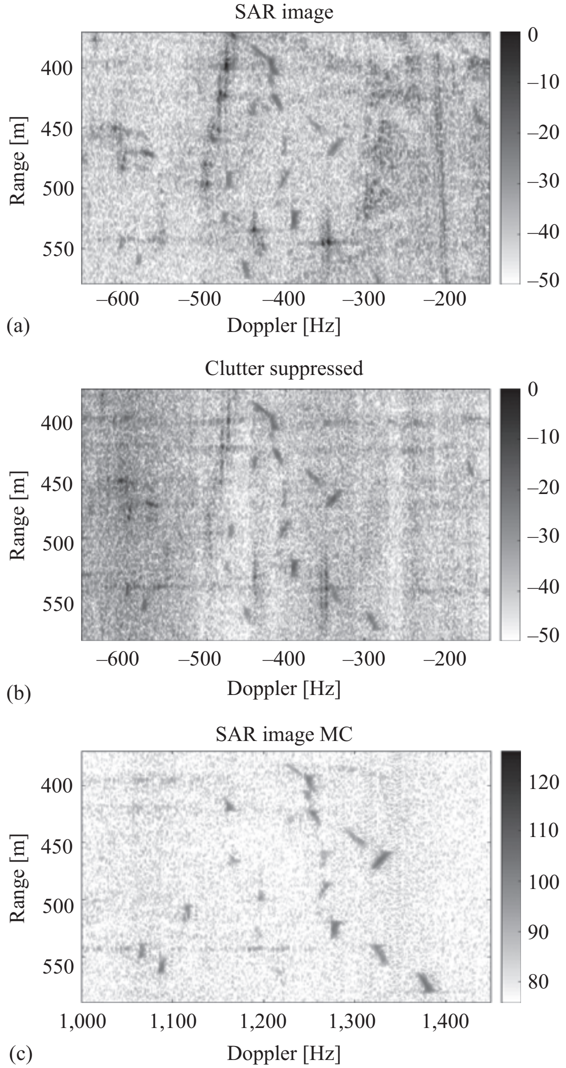

Figure 3.35 Subimage 2: SAR image (a), clutter suppressed SAR image (b), pseudo ground truth (c)

3.3.2.1 Dataset description

In this section, a description of the available dataset will be provided. In the available dataset, the terrain has been modeled by using a DEM with a dimension of 500 m × 500 m in which two slow noncooperative moving targets are present, specifically, a large trailer truck with a velocity of 10 m/s along the range direction and a GAZ 66 military truck with velocity of 5 m/s along the range direction. In order to better demonstrate the detection capabilities of the proposed processing, a point-like slow

Table 3.7 Subregion 2: pseudo-ground truth comparison

Target no.	f_D **[Hz] (*PRF* = 5 kHz)**	f_D **[Hz] (*PRF* = 1.67 kHz)**	**Range [m]**	**Missing targets**
1	1,255	−412	395	
2	1,165	−502	419	X
3	1,257	−410	427	
4	1,301	−366	445	
5	1,332	−355	465	
6	1,268	−399	489	
7	1,198	−469	498	
8	1,117	−550	510	
9	1,281	−386	524	
10	1,667	−600	543	X
11	1,329	−338	546	
12	1,090	−577	558	
13	1,379	−288	573	

Table 3.8 Subregion 2: IC values before and after ISAR processing

Target no.	**IC SAR**	**IC ISAR**
1	1.475	4.935
3	1.812	5.560
4		
5	1.856	7.673
6	1.455	4.694
7	1.028	3.703
9	1.615	6.327
10		
11		
12	0.882	2.755
13	1.426	5.774

moving target with a velocity of 3 m/s along the range direction has also been added in the scenario. In the simulated geometry, the transmitter and the receiver have different velocities and the fight paths are orthogonal. The geometry is depicted in Figure 3.39 while the radar parameters are summarized in Table 3.9 and the acquisition parameters are reported in Table 3.10. As it is possible to see from Table 3.9, different from the previous section, the measure setup is quite suitable for testing the proposed algorithms. The principal benefits are as follows:

- **High bandwidth**: The transmitter bandwidth is quite high, i.e., $B = 500$ MHz and allows for a sufficient fine bistatic range resolution, to be obtained. In the considered configuration in which $\beta = 44.3°$, the bistatic range resolution is $\delta_r = 0.42$ m.

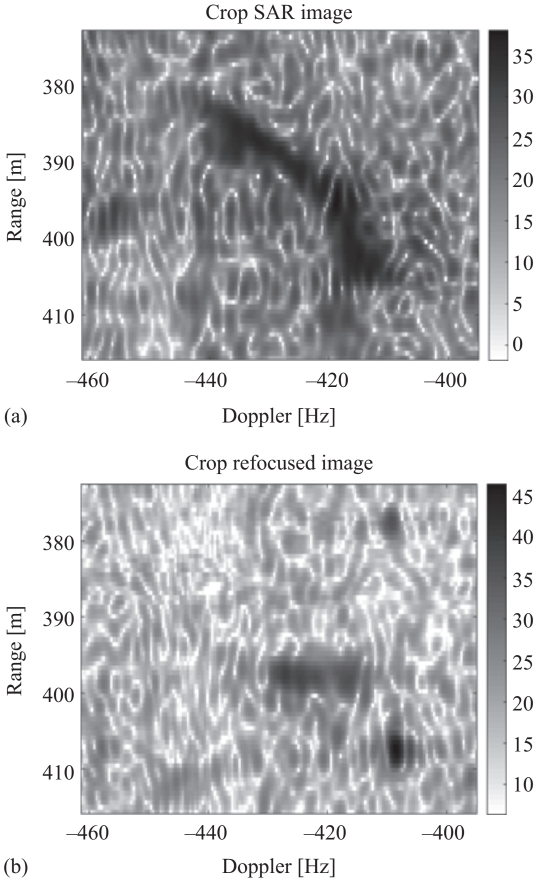

Figure 3.36 Subregion 2—Crop 1: original SAR image (a) and refocused image (b)

- **Distance between channels**: The baseline is set to $d = (\lambda/2) = 0.015$ m. This choice avoids any problem from both a beamforming point of view and from MRD image formation algorithm perspective, as it will be shown later.
- **Multichannel system**: A receiver with three channels has been simulated. This results in enough number of spatial degrees of freedom to properly apply the proposed algorithms.

3.3.2.2 Multichannel range–Doppler image formation

In this section, considerations about multichannel RD image formation algorithm will be discussed. The condition on the array size, introduced in Section 3.1, will be analyzed. This condition is recalled here for the sake of clarity:

$$D_{array} \leq \frac{\lambda R_{B,0}}{32(y_1 \cos(\alpha) - y_3 \sin(\alpha))} \tag{3.79}$$

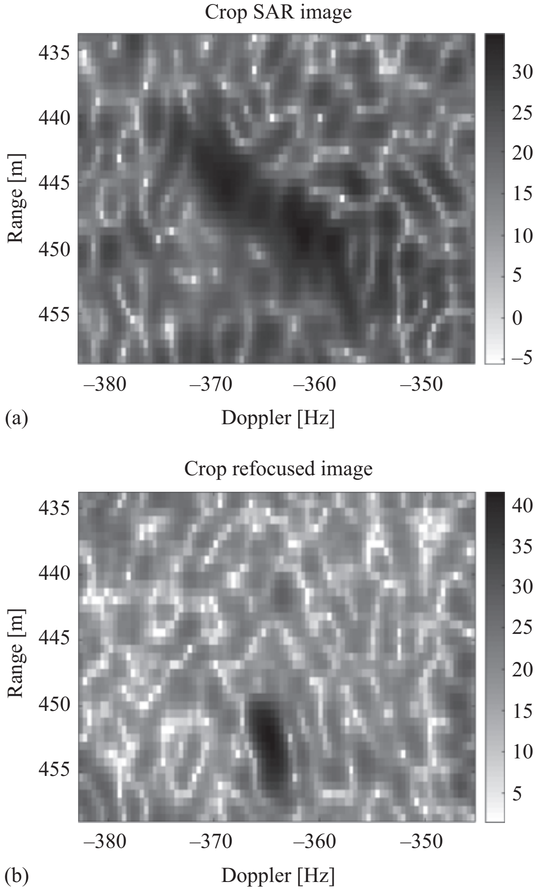

Figure 3.37 Subregion 2—Crop 4: original SAR image (a) and refocused image (b)

In (3.79), $R_{B,0}$ represents the bistatically equivalent monostatic (BEM) radar-target distance, i.e., $R_{B,0} = ((R_{tx,0} + R_{rx,0})/2)$ where $R_{tx,0}$ and $R_{rx,0}$ represent the transmitter-target and receiver-target distance, respectively [3]. This condition is derived for multichannel bistatic systems and allows for the coherent sum the images obtained by processing the data acquired by each of the P channels. Since in a SAR scenario $\alpha = 0$, [4], it is possible to obtain a direct relationship between the cross-range image dimension and the array size. As reported in Table 3.9, the multichannel receiver is composed of three channels separated by a distance of $d = (\lambda/2) = 1.5$ cm. The array dimension, $D_{array} = (P - 1)d = 3$ cm, is quite small considering that the BEM radar-target distance is about $R_{B,0} \approx 24.4$ km while the cross-range imaging area is about $D_{y1} \approx 500$ m. Therefore, the array dimension meets the condition in (3.79) and as a consequence, no image distortions appear when the multichannel RD image formation algorithm is applied. The results of the image processing are shown in Figures 3.40

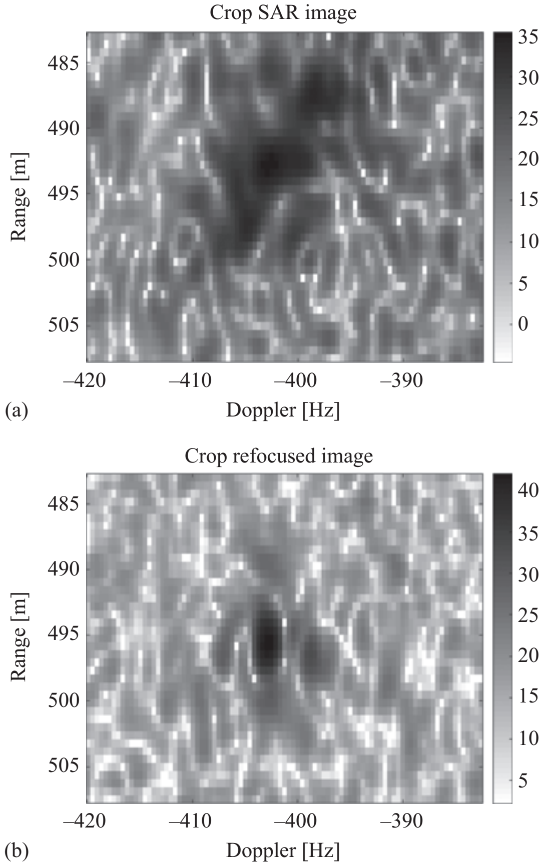

Figure 3.38 Subregion 2–Crop 6: original SAR image (a) and refocused image (b)

and 3.41. In Figure 3.40, the images obtained by applying the RD algorithm on the first channel (a) and on the third channel (b) are shown while in Figure 3.41, the result obtained after applying the multichannel RD algorithm is represented.

3.3.2.3 Clutter suppression and imaging

In this section, the results on the application of E-SDAP for clutter suppression in strong non-stationary clutter environment will be presented. After clutter suppression, ISAR processing will be exploited in order to obtain high-resolution images of non-cooperative moving targets present in the scene. In this case, the clutter suppression and the image formation processing can be applied without any particular preliminary operations on the available data since targets are in the clutter Doppler bandwidth. It is quite obvious that since target positions are unknown, training data might be not target free. However, the SCR is very low since the clutter region is significantly

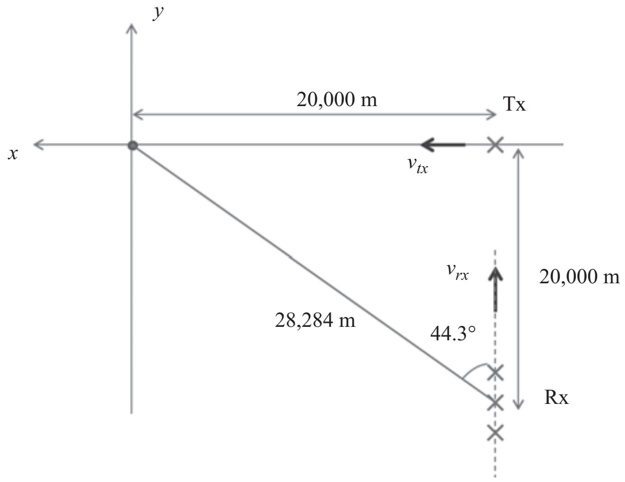

Figure 3.39 Multichannel bistatic acquisition geometry 2

Table 3.9 Radar parameters for geometry 1 and geometry 2

Center frequency	9.6 GHz
TX bandwidth	500 MHz
Observation time	0.2 s
ADC sampling frequency	25 MHz
Receiver channel distance	λ/2
Pulse repetition frequency (PRF)	5 kHz
Number of receiver channels	3

Table 3.10 Acquisition parameters

Bistatic angle	44.3°
Tx acquisition parameters	
Altitude	400 m
Platform velocity	50 m/s
Look angle	78.6°
Rx acquisition parameters	
Altitude	400 m/s
Platform velocity	60 m/s
Look angle	80.9°

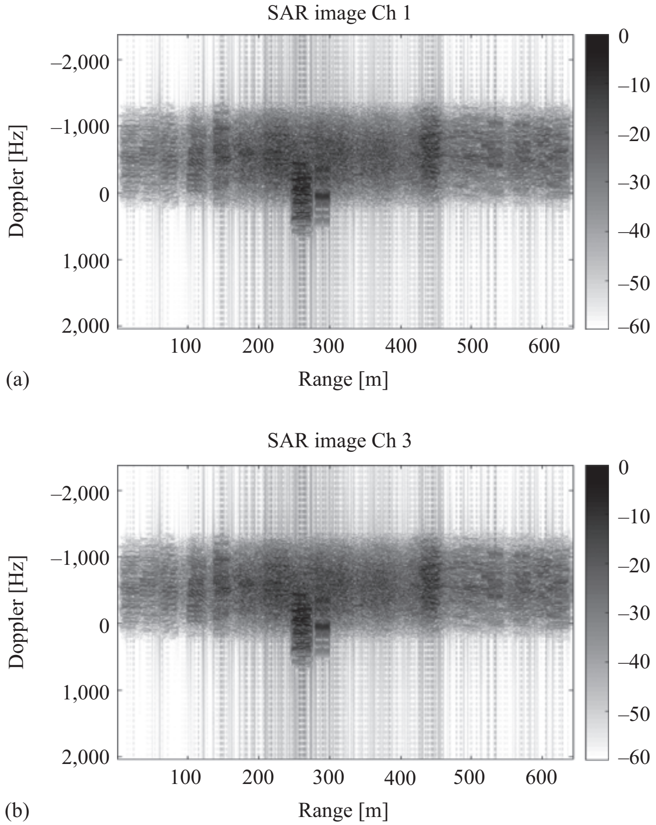

Figure 3.40 Range–Doppler image results: (a) range–Doppler algorithm on channel 1 and (b) range–Doppler algorithm on channel 3

larger than the target region, then the estimation of the clutter covariance matrix can be reasonably performed. It is worth also pointing out that in this situation, the ground truth would not be necessary for a comprehensive performance evaluation of the proposed processing since all moving targets fall within clutter region. In Figure 3.42, the region under test and the training region are highlighted with a solid line and with a dotted line, respectively. Due to the high number of required target-free training data, a suboptimum approach is applied. The suboptimum processing allows for the computational load and the dimension of the range area in which the clutter covariance matrix is estimated, to be reduced. In the case of E-SDAP approach, this allows to reasonably approximate the clutter range variation as linear exploiting only the first order of Taylor series to perform clutter suppression. An amount of data corresponding to an observation time of $T_{obs} = 0.2$ s is used. The suboptimum version of E-SDAP processing is applied with a window length of $L = 10$ samples. The performance in clutter suppression will be evaluated by comparing the bidimensional null filter in the

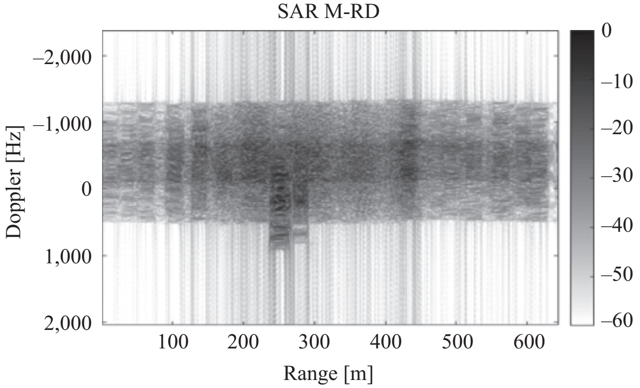

Figure 3.41 Result of multichannel range–Doppler algorithm

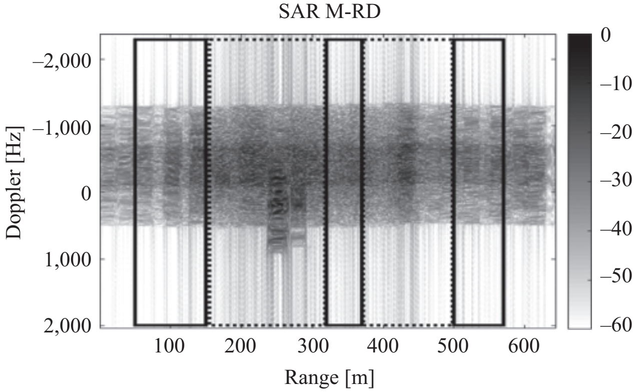

Figure 3.42 SAR image with region under test (solid line) and training region (dotted line)

angle/Doppler plane of the proposed E-SDAP processing with the conventional SDAP processing while the performance in target refocusing capabilities will be measured in terms of the IC.

In Figure 3.43, results for E-SDAP processing are shown. Specifically, in Figure 3.43(a), the original SAR image is represented and in Figure 3.43(b), the image obtained at the output of conventional SDAP processing is represented. As can be noticed, moving targets present in the scene are not visible neither in the original image nor in the image after SDAP processing. In the first case, this is due to both the presence of target in the static scene region and to the strong ground clutter return that completely masks the target return. In the second case, the strong clutter range dependence induced by the acquisition geometry produces a consistent mismatch between

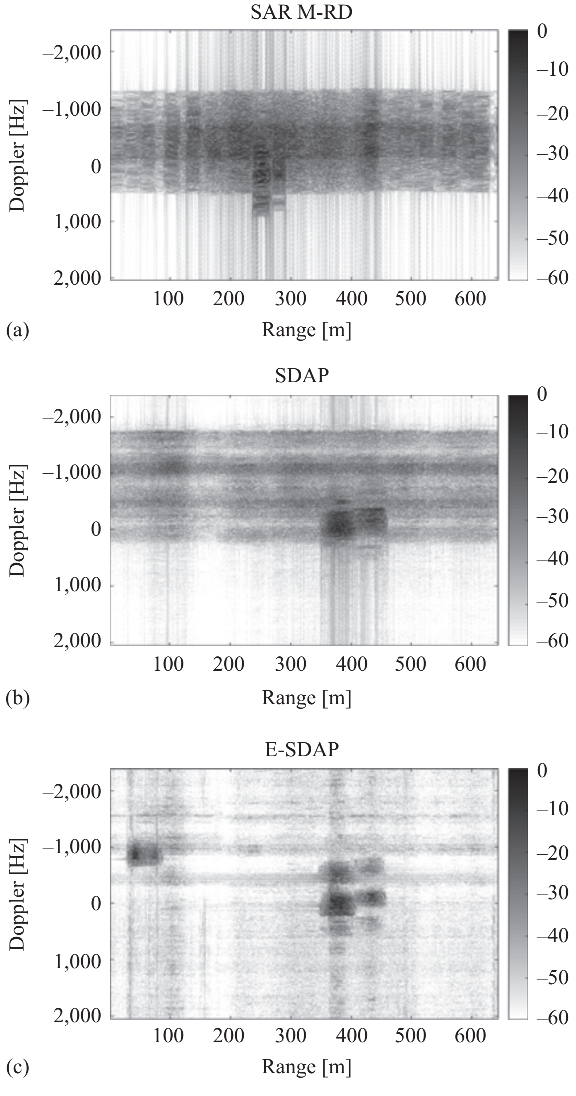

Figure 3.43 E-SDAP results: (a) original SAR image, (b) SDAP, (c) E-SDAP

the estimated and the exact clutter covariance matrix that degrades the conventional SDAP clutter filter performance. In Figure 3.43(c), the result for E-SDAP is shown. As can be noticed, the proposed algorithm seems to work properly and all moving targets can be detected. It is worth pointing out that for this geometry, the two targets in the scene do not completely fall in the static Doppler region and then appear partially visible both in the SAR image and in the image obtained after SDAP processing. However, the pointlike target that completely falls in the clutter Doppler region can be

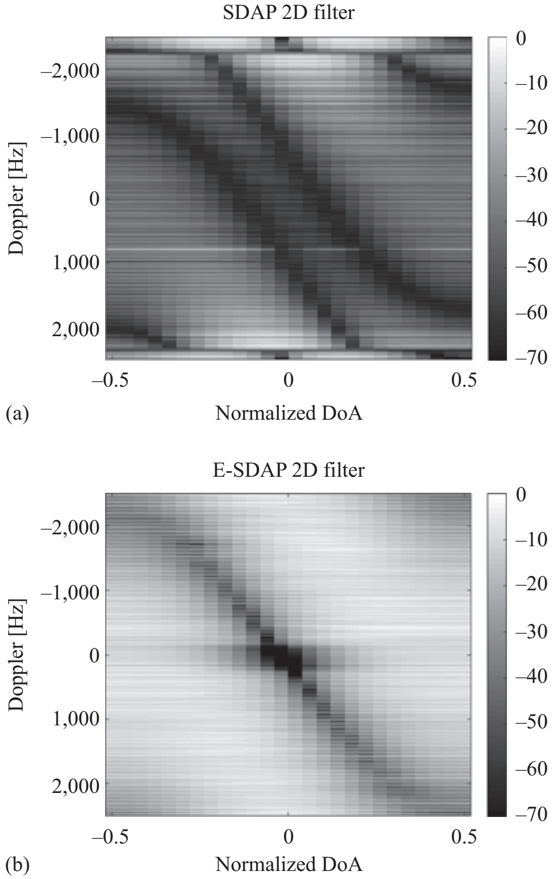

Figure 3.44 Null filter in the angle/Doppler plane: (a) SDAP filter, (b) E-SDAP filter

detected only with the E-SDAP processing. Another aspect that must be highlighted is that SDAP filter does not lead to a signal cancellation but to an increase of the interference residual with respect to its extended version. As known, the estimation errors in the clutter covariance matrix translate into a non-convergent adaptive filter response. By expressing the optimal weight vector that provides insight into the relationship between covariance matrix error and degraded filter response [35], it is possible to observe that the mismatch between the estimated clutter covariance matrix and the exact one caused by the clutter range dependence leads either to the overnulling or undernulling. The overnulling effect leads to potential signal cancellation, whereas undernulling effect results in increased interference residual. To better appreciate the performance in clutter suppression of the proposed processing, a comparison between the bidimensional null filters of the SDAP algorithm and its extended version has been

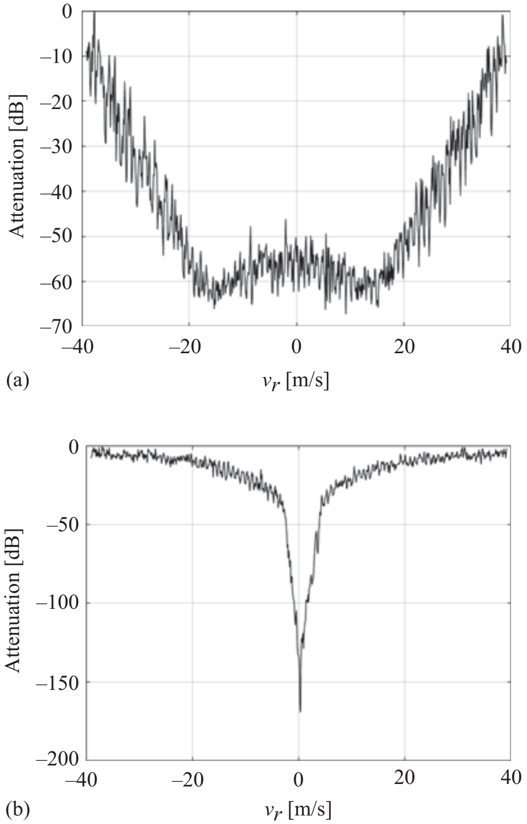

Figure 3.45 Null filter along Doppler frequency: (a) SDAP filter and (b) E-SDAP filter

done. Both the filters are represented in the angle/Doppler plane and are shown in Figure 3.44. As can be seen, both filters are centered along the clutter ridge that is due to the relation between the Doppler frequency and the DoA of the received signal. The difference between the two filters lies in the null bandwidth. In fact, the E-SDAP filter shows a narrower bandwidth that suppresses only clutter allowing slow-moving targets to be detected. A more accurate comparison can be obtained by representing both filters as function of Doppler frequency. This can be obtained by taking a slice from the bidimensional filter for $DoA = 0°$ as shown in Figure 3.45. As can be seen, the SDAP filter shows a large stop bandwidth that suppresses both the clutter and the target return, while the E-SDAP filter is centered on the zero Doppler frequency with a narrow bandwidth and allows only the interference to be suppressed while detecting the slow-moving targets present in the scenario. Another issue to be addressed is the application of ISAR processing at the output of the E-SDAP in order to refocus non-cooperative moving targets. As explained in Section 3.1.2.1 to properly apply ISAR

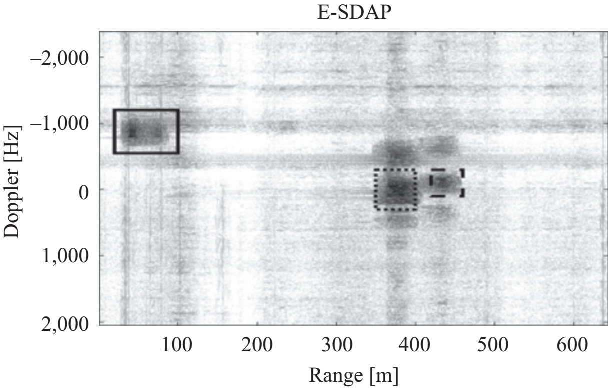

Figure 3.46 Detected targets crop (dB scale)

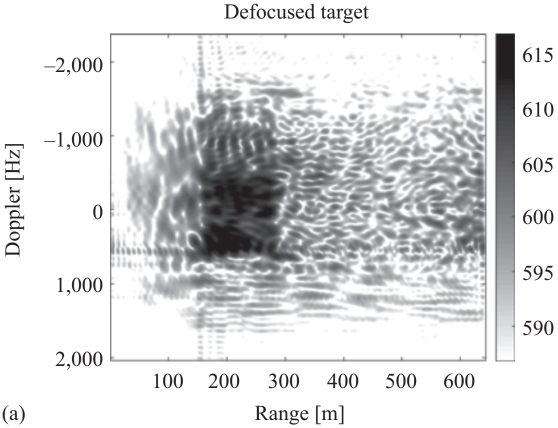

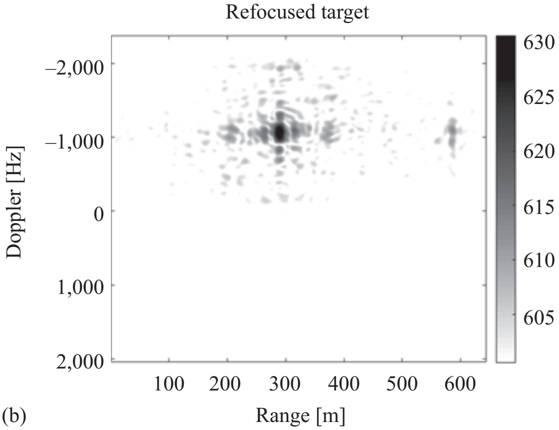

Figure 3.47 Target crop 1: (a) before ISAR processing and (b) after ISAR processing

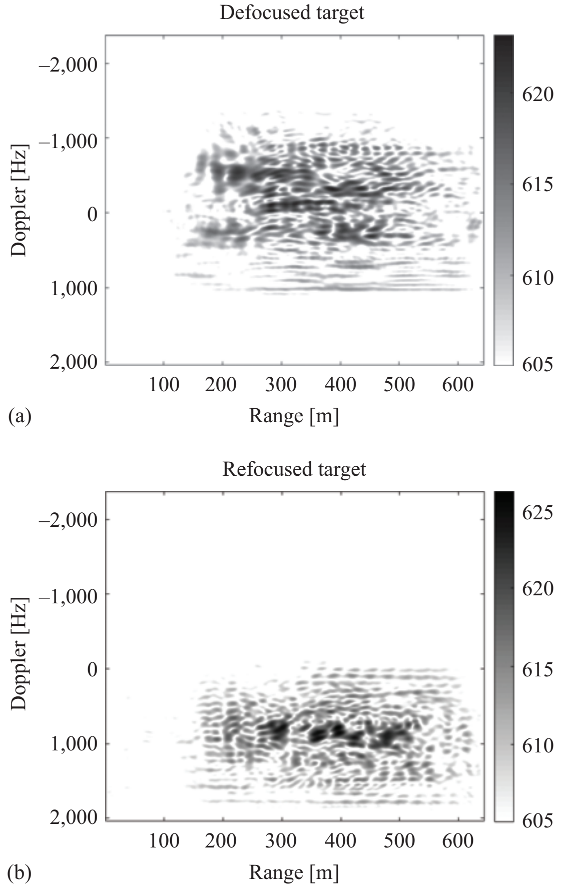

Figure 3.48 Target crop 2: (a) before ISAR processing and (b) after ISAR processing

processing, each detected target must be separated from both the contributions of the static scene and the other targets. In Figure 3.46, each target crop is highlighted. As can be seen, target crop 1 is within the solid line while target crop 2 is highlighted with dotted line and target crop 3 is in dashed box. It is worth pointing out that the geometry and systems parameter allow for the RD algorithm to be applied, and as a consequence, the inverse RD processing can be exploited to perform image crop inversion. In Figure 3.47, Figure 3.48 and Figure 3.49, the first, second and third target crops are represented before and after ISAR processing. As can be noted, the improvements in the image focus are more evident. The energy of the scatters is more concentrated in the refocused image and this results in a better IC as it is also possible to see from the Table 3.11 that shows the IC values before and after ISAR processing.

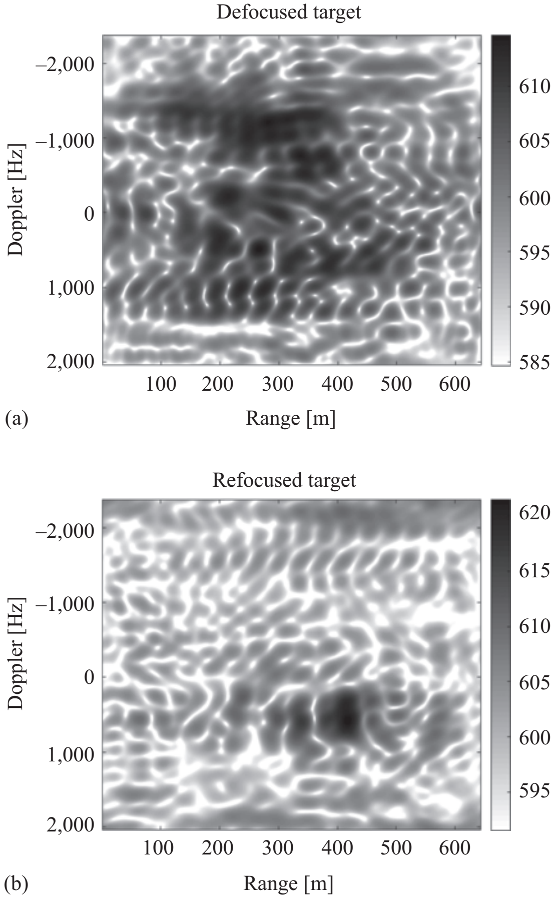

Figure 3.49 Target crop 3: (a) before ISAR processing and (b) after ISAR processing

Table 3.11 Image contrast before and after E-SDAP ISAR processing for geometry 2

	SAR IC	**ISAR IC**
Target crop 1	2.55	19.28
Target crop 2	0.85	2.62
Target crop 3	1.81	2.79

3.4 Conclusion

In this chapter, the problem of the imaging of noncooperative moving targets within SAR images has been addressed. The proposed solution is based on the applicability of the ISAR processing to compensate the unknown part of the relative radar-target motion. The applicability of ISAR processing to refocus moving targets within conventional single channel SAR images has been investigated. It is worth pointing out that in order to apply ISAR processing, each target to be refocused must be detected first. This is a critical aspect especially in case of ground target. In fact, ground clutter can be much stronger than the target return and can completely mask the target of interest. In order to overcome this issue, multichannel information has been exploited. In fact, spatial degrees of freedom can be used as well as the temporal degrees of freedom to mitigate the static clutter making improving detection capabilities. A review of the multichannel formulation of the commonly used (especially in ISAR imaging) range–Doppler image formation algorithm has been derived. A statistical description of the static ground clutter has also been presented. Then, joint SDAP-ISAR processing has been formalized and presented both for monostatic and bistatic configurations.

Optimal and suboptimal approaches have been developed and tested on simulated data and real data within the activities of the NATO-SET 196. The performances of the MRD image formation algorithm have been analyzed first. Then the monostatic and bistatic formulations of the SDAP-ISAR processing have been applied to obtain well-focused images of noncooperative moving targets. Results have demonstrated the effectiveness of the proposed processing chain and its applicability in real systems for surveillance purposes.

The main future direction will involve the reduction of the computational cost and the overcome of statistical issues due to the need of the disturbance covariance matrix estimation. Reduced rank techniques could be studied and applied to modify the proposed algorithms leading to near or better performances with respect to their full rank counterpart with a reduced computational load. Making the processing chain fully automatic avoiding the need of external inputs can be another aspect to investigate. A-priori knowledge can also be exploited to improve the clutter suppression performance of the conventional STAP/SDAP processing.

References

[1] Battisti, N., and Martorella, M. Intereferometric phase and target motion estimation for accurate 3d reflectivity reconstruction in ISAR systems. In *Radar Conference, 2010 IEEE* (2010), pp. 108–112.

[2] Berizzi, F., Martorella, M., and Giusti, E. *Radar Imaging for Maritime Observation*. CRC Press, Pisa, Italy, 2016.

[3] Martorella, M., Palmer, J., Homer, J., Littleton, B., and Longstaff, I. On bistatic inverse synthetic aperture radar. *Aerospace and Electronic Systems, IEEE Transactions on 43*, 3 (2007), 1125–1134.

[4] Bacci, A., Martorella, M., Gray, D. A., and Berizzi, F. Space–Doppler adaptive processing for radar imaging of moving targets masked by ground clutter. *IET Radar, Sonar Navigation 9*, 6 (2015), 712–726.

[5] Martorella, M., Stagliano, D., Salvetti, F., and Battisti, N. 3d interferometric ISAR imaging of noncooperative targets. *IEEE Transactions on Aerospace and Electronic Systems 50*, 4 (2014), 3102–3114.

[6] Chen, V., and Martorella, M. *Inverse Synthetic Aperture Radar Imaging: Principles, Algorithms and Applications*. Institution of Engineering and Technology, Stevenage, 2014.

[7] Perry, R., DiPietro, R., and Fante, R. SAR imaging of moving targets. *IEEE Transactions on Aerospace and Electronic Systems 35*, 1 (1999), 188–200.

[8] Zhu, S., Liao, G., Qu, Y., Zhou, Z., and Liu, X. Ground moving targets imaging algorithm for synthetic aperture radar. *IEEE Transactions on Geoscience and Remote Sensing 49*, 1 (2011), 462–477.

[9] Zhou, F., Wu, R., Xing, M., and Bao, Z. Approach for single channel SAR ground moving target imaging and motion parameter estimation. *IET Radar, Sonar Navigation 1*, 1 (2007), 59–66.

[10] Werness, S., Stuff, M., and Fienup, J. Two-dimensional imaging of moving targets in SAR data. In *Signals, Systems and Computers, 1990 Conference Record Twenty-Fourth Asilomar Conference on* (1990), vol. 1, 16 pages.

[11] Martorella, M., Giusti, E., Berizzi, F., Bacci, A., and Mese, E. D. ISAR based techniques for refocusing noncooperative targets in SAR images. *IET Radar, Sonar Navigation 6*, 5 (2012), 332–340.

[12] Gelli, S., Bacci, A., Martorella, M., and Berizzi, F. Clutter suppression and high-resolution imaging of noncooperative ground targets for bistatic airborne radar. *IEEE Transactions on Aerospace and Electronic Systems 54*, 2 (2018), 932–949.

[13] Carrara, W., Goodman, R., and Majewski, R. *Spotlight Synthetic Aperture Radar: Signal Processing Algorithms*. Artech House Signal Processing Library. Artech House, Incorporated, Boston, MA, 1995.

[14] Soumekh, M. *Synthetic Aperture Radar Signal Processing with MATLAB Algorithms*. Wiley-Interscience Publication. Wiley, New York, USA, 1999.

[15] Rosenberg, L. *Multichannel Synthetic Aperture Radar.* PhD thesis, University of Adelaide, Australia, 2007.

[16] Martorella, M., Berizzi, F., and Haywood, B. Contrast maximisation based technique for 2-d ISAR autofocusing. *IEE Proceedings – Radar, Sonar and Navigation 152*, 4 (2005), 253–262.

[17] Martorella, M., and Berizzi, F. Time windowing for highly focused ISAR image reconstruction. *IEEE Transactions on Aerospace and Electronic Systems 41*, 3 (2005), 992–1007.

[18] Martorella, M. Novel approach for ISAR image cross-range scaling. *IEEE Transactions on Aerospace and Electronic Systems 44*, 1 (2008), 281–294.

[19] Klemm, R. Institution of Engineering and Technology. *Principles of Space–Time Adaptive Processing, 3rd Edition*. IET radar, sonar, navigation and avionics series. Institution of Engineering and Technology, Stevenage, 2006.

[20] Reed, I. S., Mallett, J. D., and Brennan, L. E. Rapid convergence rate in adaptive arrays. *IEEE Transactions on Aerospace and Electronic Systems AES-10*, 6 (1974), 853–863.

[21] Klemm, R. Comparison between monostatic and bistatic antenna configurations for STAP. *IEEE Transactions on Aerospace and Electronic Systems 36*, 2 (2000), 596–608.

[22] Nitzberg, R. An effect of range-heterogeneous clutter on adaptive Doppler filters. *IEEE Transactions on Aerospace and Electronic Systems 26*, 3 (1990), 475–480.

[23] Barbarossa, S., and Farina, A. Space–time-frequency processing of synthetic aperture radar signals. *IEEE Transactions on Aerospace and Electronic Systems 30*, 2 (1994), 341–358.

[24] Himed, B., Michels, J. H., and Zhang, Y. Bistatic STAP performance analysis in radar applications. In *Radar Conference, 2001. Proceedings of the 2001 IEEE* (2001), pp. 198–203.

[25] Melvin, W. L., Callahan, M. J., and Wicks, M. C. Bistatic STAP: application to airborne radar. In *Radar Conference, 2002. Proceedings of the IEEE* (2002), pp. 1–7.

[26] Lapierre, F. D., Verly, J. G., and Droogenbroeck, M. V. New solutions to the problem of range dependence in bistatic STAP radars. In *Radar Conference, 2003. Proceedings of the 2003 IEEE* (May 2003), pp. 452–459.

[27] Melvin, W. L., and Davis, M. E. Adaptive cancellation method for geometry-induced nonstationary bistatic clutter environments. *IEEE Transactions on Aerospace and Electronic Systems 43*, 2 (2007), 651–672.

[28] Gelli, S., Bacci, A., Martorella, M., and Berizzi, F. Extended space Doppler adaptive processing for bistatic multichannel ISAR imaging of targets masked by strong clutter. In *Proceedings of EUSAR 2016: 11th European Conference on Synthetic Aperture Radar* (Jun 2016), pp. 1–4.

[29] Gelli, S., Bacci, A., Martorella, M., and Berizzi, F. A sub-optimal approach for bistatic joint STAP-ISAR. In *2015 IEEE Radar Conference (RadarCon)* (May 2015), pp. 0992–0997.

[30] Ender, J. H. G. Space–time processing for multichannel synthetic aperture radar. *Electronics Communication Engineering Journal 11*, 1 (1999), 29–38.

[31] Hayward, S. D. Adaptive beamforming for rapidly moving arrays. In *Radar, 1996. Proceedings, CIE International Conference of* (Oct 1996), pp. 480–483.

[32] Trampuz, C., Meta, A., Coccia, A., and Imbembo, E. Metasensing – the advanced solution for commercial and scientific sar imaging. In *Advances in Radar and Remote Sensing (TyWRRS), 2012 Tyrrhenian Workshop on* (2012), pp. 326–329.

[33] Meta, A., De Wit, J. J. M., and Hoogeboom, P. Development of a high resolution airborne millimeter wave FM-CW SAR. In *Radar Conference, 2004. EURAD. First European* (2004), pp. 209–212.

[34] Gromek, D., Gromek, A., Kulpa, K., Malanowski, M., Samczynski, P., and Tanski, G. SAR/InSAR raw data simulator using DTM scene definitions. In *2012 13th International Radar Symposium* (May 2012), pp. 153–156.

[35] Melvin, W. L., and Guerci, J. R. Knowledge-aided signal processing: a new paradigm for radar and other advanced sensors. *IEEE Transactions on Aerospace and Electronic Systems 42*, 3 (2006), 983–996.

Chapter 4

Wide-band multi-look passive ISAR

Elisa Giusti[1]*, Marco Martorella*[2]*, Fabrizio Berizzi*[1,2]
and Amerigo Capria[1,2]

This chapter discusses the passive inverse synthetic aperture radar (SAR) (ISAR) (P-ISAR) technique. Radar imaging, and in particular P-ISAR, is a new feature for passive radars (PRs) made possible by the recent technological advances. This chapter presents the theory of the P-ISAR algorithm. It also discusses the issues related to the application of the ISAR technique to passive coherent location (PCL) systems and in particular the obtainable spatial resolutions. How to deal with this problem is also discussed in this chapter. Finally, results on real data from two different PCL systems are presented to demonstrate the feasibility and effectiveness of P-ISAR. This chapter is organized as follows. Section 4.1 introduces the P-ISAR concepts and its main 'ingredients'. Section 4.2 deals with the data preprocessing that includes all the steps necessary to obtain data suitable for the application of ISAR technique. Section 4.3 presents the ISAR image processing algorithm. It also proposes a method for handling incomplete data, particularly data with frequency ranges, that occurs when a full bandwidth signal is not available. Section 4.4 presents the results obtained by processing two datasets gathered with two different PCL systems. Main conclusions are finally drawn in Section 4.5.

4.1 Introduction

The ever higher computational resources of commercial off-the-shelf (COTS) devices and the technological advances gave a strong push to the research on PR field. Such radar systems have drawn a lot of attention all over the world because of the advantages with respect to active radars (low cost, flexible configuration, reduced electromagnetic pollution, low vulnerability to electronic countermeasure and counter-stealth advantage). More specifically, the recent availability of high-performance and low-cost devices has increased the number of PR demonstrators and prototypes and this, in turn, has driven research into this field through the extensive use of experimental data [1–4]. As research in this field progresses, more radar techniques are added to

---

[1] National Inter-University Consortium for Telecommunications, Radar and Surveillance System Laboratory (CNIT-RaSS), Pisa, Italy
[2] Department of Information Engineering, University of Pisa, Pisa, Italy

PCL systems to make passive bistatic radar (PBR) handle several tasks. One such task is radar imaging of non-cooperative targets through ISAR imaging, which, in turn, may open the doors to non-cooperative target recognition capabilities. In [5], the authors have demonstrated that a multichannel Digital Video Broadcasting-Terrestrial (DVB-T) signal can be used to generate higher range resolution with respect to the resolution achievable by using a single DVB-T channel. Built on this work, a novel P-ISAR imaging scheme has been proposed in [4,6,7], which employs multiple adjacent channels' DVB-T signals to form a focused ISAR image.

Effective implementation of PR imaging of non-cooperative moving targets requires the following three main ingredients:

- **Fine spatial resolution**: Spatial resolutions depend on the transmitted waveform that, however, cannot be controlled in PBR systems. Nevertheless, to meet this requirement, we can exploit the fact that digital broadcast communication channels (DVB-T, DVB-S and Universal Mobile Telecommunications System (UMTS) to mention a few) are 'almost' spectrally adjacent. By coherently adjoining multiple frequency adjacent channels at the receiver, a wideband signal suitable for imaging purpose can be obtained. In truth, frequency gaps are in between adjacent frequency channels. Such gaps are meant to reduce the cross-channel interference and guarantee high-quality TV signal transmission but generate grating lobes in the ISAR image when the multichannel DVB-T signal is used in conjunction with Fourier-based imaging techniques. In addition to that, the VHF/UHF spectrum is not completely filled with digital broadcast transmissions, therefore, leaving gaps that are typically much larger than those existing between adjacent channels. In such circumstances, the use of compression sensing (CS) instead of Fourier-based imaging algorithms has proved effective in reducing grating lobes and in reconstructing a high-resolution ISAR image free of artefacts [8].
- **Bistatic ISAR theory** [9]: A PR is intrinsically bistatic. Therefore, bistatic ISAR must be considered and results obtained in this field can be exploited.
- **ISAR from SAR techniques**: A recently published paper has proposed an algorithm aiming at focusing on moving targets that appear unfocused in SAR images and that exploit target detection and data projection [10]. An RD map is obtained as the output of standard PR signal processing, which is usually addressed as the cross-ambiguity function (CAF). By interpreting such RD map as an unfocused target image, a similar processing to that adopted in [10] can be applied to refocus such targets.

All these ingredients are combined together to implement the passive bistatic ISAR whose block scheme is represented in Figure 4.1. 'PR processing' involves all the steps necessary to produce a range/Doppler map. It is typically composed of a 'reference signal pre-processing' aimed at generating a reference signal free of multipath, the 'zero Doppler filter' aimed at removing the zero Doppler clutter and the 'CAF calculation' that gives as output the RD map, $\chi^{(m)}(\tau, \nu)$, where m indicates the mth time burst of the whole received signal. Computational complexity of the 'PR processing' imposes some limitation on the maximum integration time, T_{int}. The detection is then performed onto the RD map, to detect moving targets.

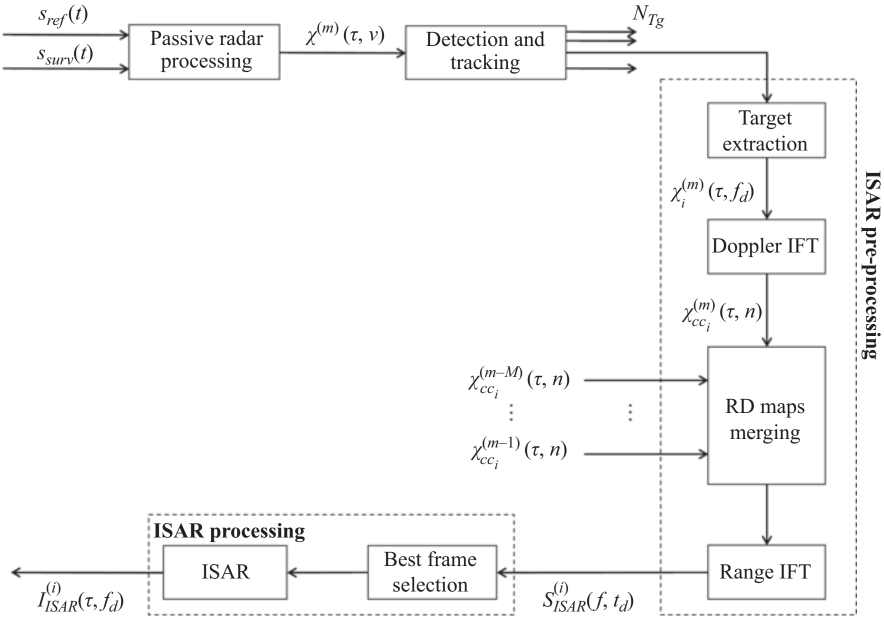

Figure 4.1 Block scheme of the ISAR processing

After detection, ISAR processing should be applied at each moving target to obtain a radar image of it. To accomplish this task, we have to deal with the fact that ISAR processing can be applied at a target at a time since each target has its own motions and that ISAR processors are typically designed to work in the frequency/slow-time domain. The 'ISAR pre-processing' has been designed to overcome these obstacles to ISAR application. The following subsections will focus on the 'ISAR pre-processing' and the 'ISAR processing' blocks while for more details on the 'PR processing' block, the reader may refer to [11,12].

The remainder of this chapter is organized as follows.

4.2 Data pre-processing

The 'ISAR pre-processing' block is all the signal processing in between the 'PR processing' and the 'ISAR processing' blocks and aims at generating a signal suitable for the application of ISAR techniques. After the target detection, a moving target is considered and its position in the range–Doppler map as well as its range and Doppler extent in term of resolution cells are input to the 'ISAR pre-processing' algorithm. By referring to Figure 4.1, the ISAR image pre-processing algorithm is composed of the following blocks:

1. **Target extraction**: This block aims at cropping the target sub-image from the RD map. The size of such sub-image should be properly chosen so as to retain

all the energy backscattered by the target. The received signal is the composition of all the signals backscattered by the targets (being them stationary or moving). Therefore, the signal corresponding to a particular target cannot be separated in the signal domain. After the image formation (SAR image or RD map), instead, even if unfocussed, the targets appear as separated objects. This allows the target radar sub-image and, as a consequence, its backscattered echo to be separated from the others.

2. **Doppler inverse Fourier transform (IFT)**: It aims at converting the Doppler frequency into the slow-time, thus proving range/slow-time maps of the target.
3. **RD map merging**: It is designed to obtain a signal of the target corresponding to an observation time T_{obs} as long as desired. The computational power of hardware devices may limit the maximum number of received signal pulses that can be processed at the 'PR processing' block to form the RD map online. The result is an RD map obtained by processing both the surveillance and the reference signals for an integration time, T_{int}, not long enough to get fine Doppler resolutions and, therefore, effective ISAR images. In such circumstances, a target echo corresponding to a longer observation time can be reconstructed by concatenating target sub-images corresponding to adjacent time intervals, T_{int}. In the event that the RD map has been obtained by processing the desired observation time, such step is not necessary.
4. **Range IFT**: It finally converts range/slow-time maps into frequency/slow-time signal, suitable to be processed by an ISAR algorithm.

4.2.1 Target extraction

The 'target extraction' block aims at isolating a target echo from the other targets, noise and clutter. It is performed in the image domain and acts as a two-dimensional (2D) filter onto the RD map, $\chi^{(m)(\tau,\nu)}$ at the output of the 'PR processing' block. The output of the 'target extraction' block is a RD sub-image centred onto the target of interest, namely $\chi_i^{(m)}(\tau,\nu)$, where $i = 1, 2, \ldots, N_{tg}$ indicates ith detected target and N_{Tg} is the number of tracked targets over M RD maps obtained by processing adjacent temporal bursts of the reference signal, $s_{ref}(t)$ and of the surveillance signal, $s_{surv}(t)$. The target extraction step can be implemented manually or automatically. The main issue of the automatic mode is to find a method to automatically choose the sub-image sizes, namely the 'bounding box (BB)' that contains the target. This is an important target attribute especially in the event of distributed targets that may occupy several resolution cells. Then, the detector will provide not only the target range and Doppler coordinates but also its range and Doppler extent. The minimum BB is defined as the minimum rectangular box which contains the target of interest and is an attribute of the detected target extracted by the 'detection and tracking' block. This is estimated through the 'discriminator' that aims to cluster together the detected pixels belonging to the same target. Figure 4.2 shows both an example of RD map obtained by processing a time-batch of 0.5 s, $\chi^{(m)}(\tau,\nu)$ and the detection result. The RD map in Figure 4.2(left) has been obtained by processing measurements acquired in a maritime scenario where four non-cooperative vessels were present. After detection clustering is applied to label the detected targets, as shown in Figure 4.2(right), where ten targets have been identified but only four are true targets. The minimum BB is the minimum rectangular box that contains all the target pixel. The BB of target 8 is highlighted with a dashed grey line in Figure 4.3(right).

As already said, the computational resources may limit the integration time T_{int}, needed to form an RD map. When this occurs, T_{int} is usually too short to get effective ISAR image of the target. In these circumstances, a number of RD maps, M, obtained by processing time-adjacent T_{int} are formed for ISAR processing. The BB size cannot be, therefore, determined from a single RD map but should be computed from an RD corresponding to the entire observation time, $t_{obs} = MT_{int}$. An easy way to get it is to incoherently sum the RD maps corresponding to each T_{int}. The results cannot be used for ISAR purposes (since the incoherent summation does not preserve the signal phase over time) but it is useful to estimate the target extent relative to the entire T_{obs}.

Figure 4.4 shows the detection maps relative to a single $T_{int} = 0.5$ s and to a $T_{obs} = 25 \times T_{int} \simeq 12.5$ s, respectively. Figure 4.5 shows a particular image of Figure 4.4 centred on the target 8.

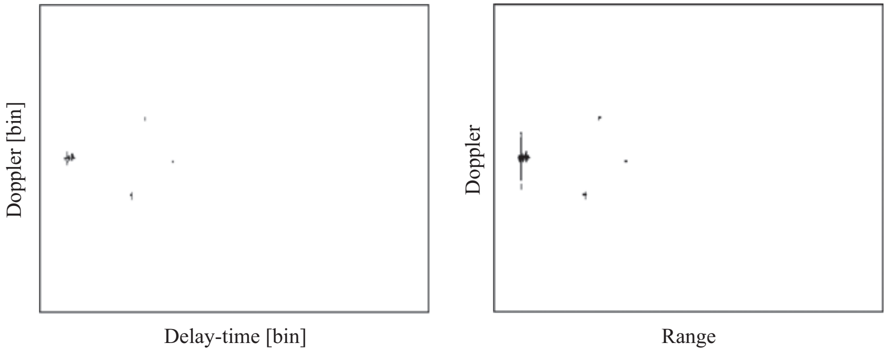

Figure 4.2 (left) RD map and (right) detection result

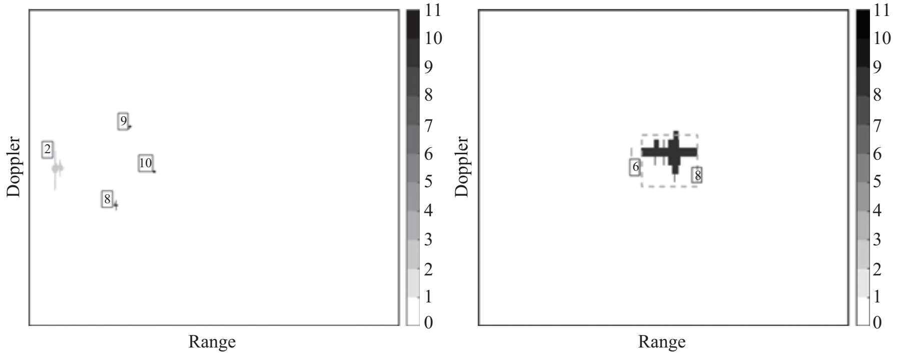

Figure 4.3 (left) RD image after labelling and (right) zoom on target 8. The dashed grey line represents the minimum BB of target 8

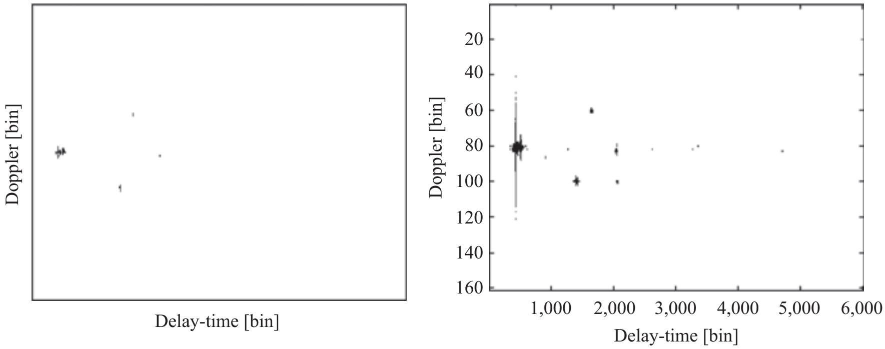

Figure 4.4 Detection maps obtained by processing a single T_{int} (left) and $T_{obs} = 25 \times T_{int}$ (right)

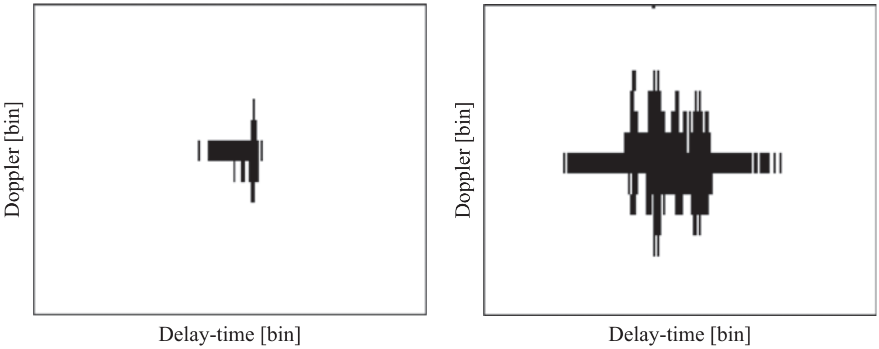

Figure 4.5 Zoom of images in Figure 4.4

The minimum BB is then determined by using the image on the right side of Figure 4.5. The BB can be chosen, for example, as twice the size of the minimum BB so computed. In this way, the BB is the same for each RD map and the target phase history is then preserved over the whole observation time.

It has been demonstrated in [12] that the CAF between the surveillance signal, $s_{surv}(t)$ and the reference signal, $s_{ref}(t)$, can be seen as a weighted sum of the ambiguity functions calculated within each batch intervals. When $T_b \nu_{\max} \ll 1$, where T_b is the temporal batch length and $\nu_{\max}$ is the maximum target Doppler frequency, the CAF can be computed as follows:

$$\chi^{(m)}(\tau, \nu) = \sum_{n=1}^{N_b} e^{-j2\pi \nu n T_b} \int s_s(t, n) s_r^*(t - \tau, n)\, dt \tag{4.1}$$

where $s_s(t, n)$ and $s_r(t, n)$ are portion of $s_{surv}(t, n)$ and $s_{ref}(t, n)$, respectively, and are obtained as represented in Figure 4.6.

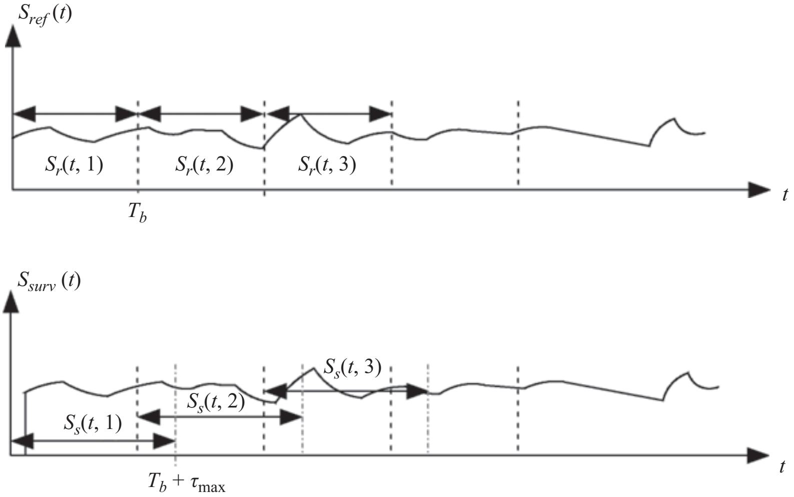

Figure 4.6 Graphical representation of how the surveillance and the reference signals are segmented in time-batches

Equation (4.2) can then be written as follows:

$$\chi^{(m)}(\tau, \nu) = \sum_{n=1}^{N_b} e^{-j2\pi\nu nT_b} \chi_{cc}^{(m)}(\tau, n) \tag{4.2}$$

where

$$\chi_{cc}^{(m)}(\tau, n) = \int s_s(t, n) s_r^*(t - \tau, n)\, dt \tag{4.3}$$

represents the CAF relative to the nth batch. This CAF implements the matched filter and, therefore, the pulse compression. It is, therefore, straightforward to conclude that $\chi_{cc}^{(m)}(\tau, n)$ represents the target range profiles over the slow-time variable n. After the 'target extraction', a sub-image of the target of interest, i, is obtained, namely $\chi_i^{(m)}(\tau, \nu)$. According to (4.2), the target range profiles, $\chi_{cc_i}^{(m)}(\tau, n)$, can be obtained by applying an IFT along the Doppler coordinate, as follows:

$$\chi_{cc_i}^{(m)}(\tau, n) = IFT\{\chi_i^{(m)}(\tau, \nu)\} \tag{4.4}$$

This is performed in the 'Doppler IFT' block.

4.2.2 Merging of RD maps and ISAR data formation

The target phase history is a continuous function of time and depends on the target bistatic distance over time. Because of the limited computational resources, a number of M RD maps are formed by processing adjacent time intervals of length T_{int}.

However, to reach finer Doppler resolutions and, therefore, get effective ISAR images, we should observe the target for a longer observation time, T_{obs}. This can be obtained by coherently concatenating along the slow-time domain the target echoes computed at each processing intervals. In other words, the target range profiles, $\chi_{cc_i}^{(m)}$ obtained at each processing interval, $m = 1, 2, \ldots, M$, are joined along the slow-time domain. Figure 4.7 shows an example of the merged range profiles of the target $i = 8$ in Figure 4.5 after the concatenation process.

Finally, the 2D ISAR data in the frequency/slow-time domain can be obtained by Fourier transforming the target range profiles, $\chi_{cc}(\tau, n)$. The ISAR data is derived hereinafter.

Let the geometry be represented by Figure 4.8, where T_x and T_ξ are the Cartesian reference systems embedded in the target and centred at the transmitter coordinates, respectively. R_{TxTg}, R_{TxRx} and R_{RxTg} represent the transmitter–target, transmitter–receiver and receiver–target distances. The receiver is composed of two antennas, one pointing towards the transmitter, A_{ref}, and the other pointing towards the area to be monitored. Being the PR working in a bistatic geometry, the bistatic ISAR theory can be applied in this framework. According to this theory, an ISAR image obtained in a bistatic geometry is the one that would be obtained by using a monostatic radar, namely the bistatically equivalent monostatic (BEM) radar located along the bistatic angle β bisector, unless the bistatic angle changes during the observation time are negligible as demonstrated in [9]. The target angular motion with respect to the BEM radar can be described by means of the effective target angular rotation vector $\mathbf{\Omega}_{eff}(t)$.

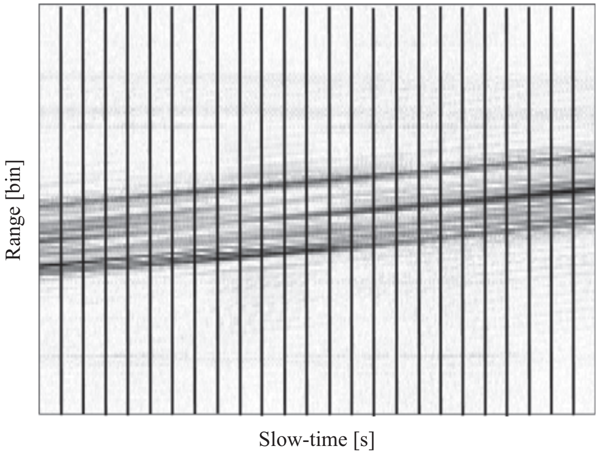

Figure 4.7 Range profiles of target 8 obtained by concatenating all the $\chi_{cc_8}^{(m)}$ for $m = 1, 2, 3, \ldots, 25$. The dark lines are meant to identify the target range profiles $\chi_{cc_8}^{(m)}$ extracted from each one of the 25 RD maps

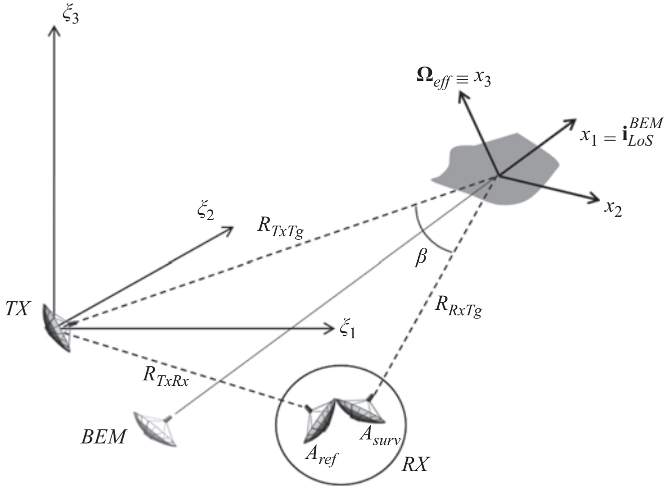

Figure 4.8 System geometry

The backscattered echo by a moving target can be written as follows:

$$s_{surv}(t) = \iiint_V g(\mathbf{x}) s_{ref}(t - \tau(t; \mathbf{x}))\, d\mathbf{x} \tag{4.5}$$

where $\tau(t; \mathbf{x}) = (R(t; \mathbf{x})/c)$, $R(t; \mathbf{x})$ is the bistatic distance between an arbitrary point on the target, the receiver and the transmitter, $\mathbf{x}$ is the vector locating the point of the target in the coordinates system embedded on the target, c is the light speed in vacuum $\left(c \simeq 3 \cdot 10^8 \text{ m/s}\right)$, V is the spatial domain where the target's reflectivity function $g(\mathbf{x})$ is defined.

By assuming the target stationary during the batch interval, T_b, the delay-time can be approximated as $\tau_{\mathbf{x}}(t; \mathbf{x}) \simeq \tau_{\mathbf{x}}(n; \mathbf{x})$. By referring to [7,12] and Figure 4.6, (4.5) can be reformulated as shown in (4.6).

$$s_{surv}(t) = \sum_{n=1}^{N_b} \iiint_V g(\mathbf{x}) s_r\left(t - \tau_{\mathbf{x}}(n; \mathbf{x}) - nT_b, n\right) d\mathbf{x} \tag{4.6}$$

According to (4.3), the target range profiles can be written as follows:

$$\chi_{cc}(\tau, n) = \iiint_V g(\mathbf{x}) \int_t s_r(t - \tau(n; \mathbf{x})) s_r^*(t - \tau, n)\, dt\, d\mathbf{x} \tag{4.7}$$

By inverse Fourier transforming $\chi_{cc}(\tau, n)$ with respect to the delay-time domain, the signal $X_{cc}(f, n)$ in the frequency/slow-time domain is obtained as follows:

$$
\begin{aligned}
X_{cc}(f,n) &= FT[\chi_{cc}(\tau,n)] \\
&= \iiint\limits_{V} g(\mathbf{x}) \int\limits_{t} s_r(t-\tau(n;\mathbf{x}),n) \int\limits_{\tau=-\infty}^{\infty} s_r^*(t-\tau,n)e^{-2j\pi\tau f} d\tau \; dt \; d\mathbf{x} \\
&= \iiint\limits_{V} \int\limits_{t} s_r(t-\tau(n;\mathbf{x}),n) S_r^*(f,n) e^{-j2\pi ft} dt \; d\mathbf{x} \\
&= \iiint\limits_{V} g(\mathbf{x}) S_r^*(f,n) S_r(f,n) e^{-j2\pi f\tau(n;\mathbf{x})} \, d\mathbf{x} \\
&= |S_r(f,n)|^2 \iiint\limits_{V} g(\mathbf{x}) e^{-j2\pi f\tau(n;\mathbf{x})} \, d\mathbf{x}
\end{aligned}
\tag{4.8}
$$

where $S_r(f, n)$ is the IFT of $s_r(\tau, n)$.

The delay-time of a scatterer of the target can be written as follows:

$$
\tau_{\mathbf{x}}(n;\mathbf{x}) = \frac{R_{\mathbf{x}}(n)}{c} = \frac{(R_{T\mathbf{x}}(n) + R_{R\mathbf{x}}(n))}{c}
\tag{4.9}
$$

where $R_{T\mathbf{x}}(n)$ and $R_{R\mathbf{x}}(n)$ are the distances between the scatterer and the transmitter and the receiver, respectively. When the target size is much smaller than both the target–transmitter and target–receiver distances, the straight-iso-range approximation can be applied, therefore both $R_{T\mathbf{x}}$ and $R_{R\mathbf{x}}$ can be approximated as shown subsequently:

$$
\begin{aligned}
R_{T\mathbf{x}}(n) &= R_{T0}(n) + \mathbf{x} \cdot \mathbf{i}_{LoS,T}(n) \\
R_{R\mathbf{x}}(n) &= R_{R0}(n) + \mathbf{x} \cdot \mathbf{i}_{LoS,R}(n)
\end{aligned}
\tag{4.10}
$$

where R_{T0} and R_{R0} are the distances between the centre of the reference system, T_x and the transmitter and the receiver, $\mathbf{i}_{LoS,T}$ and $\mathbf{i}_{LoS,R}$ are the unit vectors which identify the line of sight (LoS) of the transmitter and the receiver and · means the inner product.

Therefore, by exploiting (4.10), (4.9) can be reformulated as follows:

$$
\tau(n;\mathbf{x}) = \frac{2}{c}\left[R_{B,0}(n) + K(n)\mathbf{x} \cdot \mathbf{i}_{LoS,B}(n)\right]
\tag{4.11}
$$

where

$$
\begin{aligned}
R_{B,0}(n) &= \frac{R_{T0}(n) + R_{R0}(n)}{2} \\
K(n) &= \left|\frac{\mathbf{i}_{LoS,T}(n) + \mathbf{i}_{LoS,R}(n)}{2}\right| = \cos\left(\frac{\beta(n)}{2}\right) \\
\mathbf{i}_{LoS,B}(n) &= \frac{\mathbf{i}_{LoS,T}(n) + \mathbf{i}_{LoS,R}(n)}{\left|\mathbf{i}_{LoS,T}(n) + \mathbf{i}_{LoS,R}(n)\right|}
\end{aligned}
\tag{4.12}
$$

where $\beta(n)$ represents the value of the bistatic angle at time n (see Figure 4.8 for the geometrical interpretation of β). Equation (4.8) can then be rewritten as follows:

$$X_{cc}(f,n) = |S_r(f,n)|^2 \, e^{-j4\pi\frac{f}{c}R_{B,0}(n)} \iiint_V g(\mathbf{x}) e^{-j4\pi\frac{f}{c}K(n)\mathbf{x}\cdot\mathbf{i}_{LoS,B}(n)} \, d\mathbf{x} \tag{4.13}$$

4.3 ISAR image processing

As depicted in Figure 4.1, the ISAR processing is mainly composed of two blocks:

- The 'best frame selection' block that aims at finding the coherent processing interval (CPI) that gives the best ISAR image. When the target motions are too complex, the effective target rotation vector, $\mathbf{\Omega}_{eff}(t)$, may change over time. Under these circumstances, a well-focused ISAR image cannot be obtained by processing the entire T_{obs}. Therefore, a CPI smaller than the T_{obs} should be properly chosen to meet this requirement. How to choose the optimal CPI depends on what meaning is given to the term 'best frame'. As for example, in [13], 'best frame' means the time intervals that give the ISAR image with the higher image contrast (IC). In [14], instead the criteria to select the best time interval to process are based on a combined function of the ISAR image IC and Doppler spread.
- The ISAR processing is composed of the autofocusing and the image formation steps. The autofocusing aims at removing the phase term outside the integral in (4.13) that depends on $R_{B,0}(n)$. Numerous algorithms have been proposed in the literature to accomplish this task, for example the IC-based autofocus (ICBA) [15], the image entropy-based autofocus [16], the phase gradient autofocus [17,18] to cite a few. After autofocusing, the range–Doppler approach is typically used to reconstruct a 2D ISAR image. This algorithm makes use of a 2D fast Fourier transform (FFT). The FFT requires that data is uniformly sampled in the data domain. This in turn requires a small target aspect angle variation in the observation time (as it will be clarified in next subsections). The 'best frame selection' can be used to limit the CPI and then meet this requirement as well. When wide rotation occurs, different ISAR image reconstruction algorithm should be implemented that does not use FFT and that uses the a priori known or an estimate of the modulus of the target-effective rotation angle.

The following sections will focus on the ISAR image reconstruction algorithm.

4.3.1 Conventional ISAR imaging

Following [7], after target's motion compensation, by assuming that the effective target rotation vector can be approximated constant within the CPI and by choosing the Cartesian reference system T_x so that x_3 is aligned with $\mathbf{\Omega}_{eff}$, the ISAR data can be rewritten as follows:

$$X_{cc}(f,n) = W(f,n) \int_{x_1} \int_{x_2} \alpha(x_1,x_2) e^{-j4\pi(f/c)K(n)(x_1X_1+x_2X_2)}, \; dx_1 \, dx_2 \tag{4.14}$$

where $\alpha(x_1, x_2) = \int_{x_3} g(\mathbf{x})$ represents the projection of the target 3D reflectivity function onto a 2D plane, namely (x_1, x_2) that is called the image projection plane, $W(f, n) = |S_r(f, n)|^2 (u(n) - u(n - N))$ is the support band where the target echo is different from zero, $u(n)$ is the unit step function and

$$
\begin{aligned}
X_1 &= \frac{2f}{c} \cos(\Omega_{eff} n T_b) \\
X_2 &= \frac{2f}{c} \sin(\Omega_{eff} n T_b)
\end{aligned}
\tag{4.15}
$$

are the spatial frequencies. Under the hypothesis of small target aspect angle variation, namely $|\Omega_{eff} T_{obs}| \ll 1$, the functions in (4.15) can be approximated at the first order of their Taylor series and the target echo can be approximated as follows:

$$
X_{cc}(f, n) = W(f, n) \int\limits_{x_1} \int\limits_{x_2} \alpha(x_1, x_2) \exp -j2\pi \left(x_1 \frac{2f}{c} + x_2 \frac{}{2} f_0 \Omega_{eff} n T_b c \right), \; dx_1 \, dx_2
\tag{4.16}
$$

By substituting variables (x_1, x_2) with variables (τ, ν), (4.17) can be rewritten as follows:

$$
X_{cc}(f, n) = C \cdot W(f, n) \int\limits_{\tau} \int\limits_{\nu} \alpha(\tau, \nu) \exp -j2\pi (\tau f + \nu n T_b), \; d\tau \, d\nu
\tag{4.17}
$$

where

$$
\begin{aligned}
\tau &= \frac{2K_0 x_1}{c} \\
\nu &= \frac{2f_0 K_0 \Omega_{eff} x_2}{c}
\end{aligned}
\tag{4.18}
$$

$C = (c^2 / 4f_0 K_0^2 \Omega_{eff})$ is a constant term due to the change of variables in the integrals and $K(n) \simeq K_0$.

Differently from active radar systems, PR systems do not transit the same waveform over time but it changes from sweep to sweep since it depends on the transmitted information content. For example, DVB-T signals depend on the transmitted OFDM symbols. Because of that, the received signal cannot be modelled as a deterministic signal but rather as a random signal as it varies among different sweeps and acquisitions. This could be an issue for the evaluation and prediction of the P-ISAR performance. Only the statistical average of the algorithm performance can be estimated. To do that, the statistical average of the received signal is defined:

$$
\bar{X}_{cc}(f, n) = C \cdot \bar{W}(f, n) \int\limits_{\tau} \int\limits_{\nu} \alpha(\tau, \nu) \exp -j2\pi (\tau f + \nu n T_b), \; d\tau \, d\nu
\tag{4.19}
$$

where $\bar{X}_{cc}(f, n) = E\{X_{cc}(f, n)\}$, $\bar{W}(f, n) = E\{W(f, n)\}$ and $E\{\cdot\}$ represent the statistical average operator.

In a real scenario, both (f, n) and (τ, ν) are discrete variables. It is, therefore, appropriate to write the signal as a function of discrete variables, defined as follows:

$$\begin{aligned} f_r &= f_0 + r\Delta f & m &= 0, 1, \ldots, R-1 \\ \nu_q &= q\Delta_\nu & q &= 0, 1, \ldots, N-1 \\ \tau_p &= p\Delta_\tau & p &= 0, 1, \ldots, R-1 \end{aligned} \tag{4.20}$$

where Δf is the frequency step, $\Delta_\nu = (1/T_{obs})$ is the Doppler frequency resolution and $\Delta_\tau = (1/M\Delta f)$ is the delay-time resolution. Therefore, the signal in (4.17) can be rewritten as follows:

$$\bar{X}_{cc}(r, n) = C \cdot \exp -2\pi f_0 \tau \sum_{p=0}^{R-1} \sum_{q=0}^{N-1} \alpha(q, p) \exp -j2\pi \frac{rp}{M} \exp -j2\pi \frac{nq}{N} \tag{4.21}$$

where the term $\exp -j2\pi f_0 \tau$ is a nuisance phase term that only causes a range shift in the image domain and does not affect the ISAR image quality.

Equations (4.17) and (4.21) show that the P-ISAR data and the 2D target reflectivity function $\alpha(\tau, \nu)$ are linked by a 2D continuous and discrete Fourier transform, respectively. Therefore, under the hypothesis mentioned earlier, the P-ISAR image, which is an estimate of $\alpha(\tau, \nu)$, can be obtained by applying a 2D Fourier transform, as follows:

$$I(\tau, \nu) = 2D\text{-}FT\left\{\bar{X}_{cc}(f, n)\right\} \tag{4.22}$$

This method is typically called range/Doppler algorithm. Its standard output is an ISAR image in a hybrid domain, namely range/Doppler domain. To sizing the target, an ISAR image in a fully spatial domain is needed. This can be done by converting the Doppler axis in Hz to the cross-range axis in m. This operation resorts to a scaling operation. But the scale factor to convert Hz into m depends on the modulus of the target effective rotation vector, Ω_{eff}. An algorithm has been recently proposed [19] to estimate it directly from the acquired data, which also applies to the PR imaging scenario.

4.3.2 CS-based ISAR imaging

As already highlighted in Section 4.1, in this chapter, the CS theory is applied to reconstruct ISAR images by using incomplete data caused by spectral gaps, in frequency and/or slow-time domains, in which no signal is transmitted. From now on, it will be assumed that motion compensation has been correctly performed and only the image formation problem will be considered. From CS point of view, the Fourier transform represents the dictionary that projects the ISAR data onto a domain in which the data is sparse, namely the image domain. In ISAR framework, the sparsity degree is then represented by the number of scatterers composing the target. If this number is small compared to the image size, the ISAR data is said to be sparse. The fewer the scatterers, the higher the sparsity degree, and the more compressible the ISAR image.

Here, the input data is meant to be an incomplete version of the complete data (in which some entries are equal to zero). The data incompleteness can be either in the frequency or in the time domain or both and can be due to several factors: memory resources reduction, co-channel interferences avoidance, missing data, etc. The sensing process consists of discarding elements from the complete data so as to create an incomplete data. This can be done intentionally or can be an intrinsic property of the acquired data because of, for example, missing channels as in the case of DVB-T PR.

Hereinafter, the ISAR signal model will be presented in the framework of CS theory. Equation (4.21) can be written in a matrix form as follows:

$$\bar{\boldsymbol{X}}_{cc} = \boldsymbol{\Phi}_x \boldsymbol{\Omega} \boldsymbol{\Phi}_y^T \tag{4.23}$$

where $\bar{\boldsymbol{X}}_{cc}$ represents the averaged data matrix in the frequency/slow-time domain, $\boldsymbol{\Phi}_x$ and $\boldsymbol{\Phi}_y$ represent the Fourier dictionaries in frequency and slow-time, respectively, and $\boldsymbol{\Omega}$ is the P-ISAR image, where the value and the position of each element correspond to the reflectivity and location of a scattering centre.

An element $\boldsymbol{\Omega}_{p,q} \neq 0$ indicates that there is a scattering centre with coordinate (p, q) in the image.

A further refinement of the image grid can also be performed to reduce the pixels spacing in the ISAR image. Let the size of $\boldsymbol{\Omega}$ be $P \times Q$ and $P > R$ and $Q > N$. Therefore, the two matrices $\boldsymbol{\Phi}_x$ and $\boldsymbol{\Phi}_y$ are defined as follows:

$$\boldsymbol{\Phi}_x = \left[\boldsymbol{\Phi}_{x,0}\ \boldsymbol{\Phi}_{x,1}, \ldots, \boldsymbol{\Phi}_{x,P-1}\right] \tag{4.24}$$

$$\boldsymbol{\Phi}_y = \left[\boldsymbol{\Phi}_{y,0}\ \boldsymbol{\Phi}_{y,1}, \ldots, \boldsymbol{\Phi}_{y,Q-1}\right] \tag{4.25}$$

where $\boldsymbol{\Phi}_{x,p} = [\exp -j2\pi 0/P\ \exp -j2\pi 1/P\ \cdots\ \exp -j2\pi(P-1)/P]^T$ and $\boldsymbol{\Phi}_{y,q} = [\exp -j2\pi 0/Q\ \exp -j2\pi 1/Q\ \cdots\ \exp -j2\pi(Q-1)/Q]^T$, and $p = 0, 1, \ldots, P-1$ and $q = 0, 1, \ldots, Q-1$.

The signal as defined in (4.23) is the complete data, which is the data without spectral gaps. The actual acquired data can be interpreted as the signal at the output of a sensing process and can be rewritten as follows:

$$\bar{\boldsymbol{X}} = \boldsymbol{\Psi}_x \boldsymbol{\Phi}_x \boldsymbol{\Omega} \boldsymbol{\Phi}_y^T \boldsymbol{\Psi}_y^T = \boldsymbol{\Theta}_x \boldsymbol{\Omega} \boldsymbol{\Theta}_y^T \tag{4.26}$$

where $\boldsymbol{\Psi}_x$ and $\boldsymbol{\Psi}_y$ represent the sensing matrices along the frequency and slow-time domain, respectively, and $\boldsymbol{\Theta}_x$ and $\boldsymbol{\Theta}_y$ are the partial Fourier matrices.

In case only frequency gaps are present, the following equation becomes

$$\bar{\boldsymbol{X}} = \boldsymbol{\Psi}_x \boldsymbol{\Phi}_x \boldsymbol{\Omega} \boldsymbol{\Phi}_y^T = \boldsymbol{\Theta}_x \boldsymbol{\Omega} \boldsymbol{\Phi}_y^T \tag{4.27}$$

that means the sensing processing is only applied along the frequency domain. The partial Fourier matrices are obtained from the complete Fourier matrices, $\boldsymbol{\Phi}_x$ and $\boldsymbol{\Phi}_y$ by replacing the rows and/or columns corresponding to the gaps with zeros.

According to the CS framework and considering the influence of the noise, an estimate of the ISAR image, $\hat{\boldsymbol{\Omega}}$, can be obtained by solving the following optimization problem:

$$\hat{\boldsymbol{\Omega}} = \arg \underset{\Omega}{\max}\ {}_{\boldsymbol{\Omega}}\|\boldsymbol{\Omega}\|_0 \quad \text{s.t.} \quad \|\bar{\boldsymbol{S}} - \boldsymbol{\Theta}_x \boldsymbol{\Omega} \boldsymbol{\Theta}_y^T\|_F^2 \leq \varepsilon \tag{4.28}$$

where $\|\cdot\|_0$ denotes the l_0-norm and corresponds to the number of non-zero components in $\mathbf{\Omega}$, $\|\cdot\|_F$ denotes Frobenius norm of a matrix and ε is a small constant bounded by the noise level. The optimization problem in (4.28) can be solved via the 2*D-SL*0 algorithm [8].

It should be pointed out that the scope of the CS is not to recover the missing data but to reconstruct the ISAR image. Conversely, we are also interested to test the ability of the CS to extrapolate the received signal in a wider bandwidth. An extra step is necessary to estimate the complete data in the spectral domain (namely frequency/slow-time). This can be done by projecting the estimated ISAR image $\hat{\mathbf{\Omega}}$ back to the spectral domain as follows:

$$\hat{\bar{\boldsymbol{X}}} = \mathbf{\Phi}_x \hat{\mathbf{\Omega}} \mathbf{\Phi}_y^T \tag{4.29}$$

where $\hat{\mathbf{\Omega}}$ is the solution of $\mathbf{\Omega}$ provided by solving (4.28).

This extra step serves the purpose to form a Fourier-like ISAR image. Then a 2*D-FT* can be applied to $\hat{\bar{\boldsymbol{X}}}$ in order to obtain an ISAR image fairly comparable with the one that is obtained by applying the 2*D-FT* directly to the complete data, $\bar{\boldsymbol{X}}$.

4.4 Results

Results obtained by applying the proposed P-ISAR processing to real measurements are shown in this section. Two datasets are used to test both ‘conventional ISAR processing’ and ‘CS-based ISAR processing’ algorithms. Two different PR demonstrators have been used to acquire the two datasets used in the following subsections. The first one has been developed at the Warsaw University of Technology (WUT) in Poland. The latter has been developed at the Radar and Surveillance System (RaSS) Laboratory of the Italian National Inter-University Consortium for Telecommunications (CNIT) and is permanently installed at the Navy Academy in Livorno. Both PR demonstrators were installed at the facilities of the Vallauri Institute of the Naval Military Academy in Livorno. Both can operate in the VHF band. Both are able to acquire a multi-frequency channel DVB-T signal, but the WUT-demonstrator is able to acquire a signal with a larger instantaneous bandwidth. During experiments, both have used the DVB-T transmitter installed in Monte Serra near Pisa (Tuscany, Italy) as illuminator of opportunity (IO). The acquisition geometry for both systems was nearly the same and is depicted in Figures 4.10 and 4.11. Many targets were present during the measurements and some of them were cooperative, therefore quipped with GPS systems. Other targets were non-cooperative and were mainly cargo vessels leaving or approaching the Livorno harbour. The target pictures and target sizes are summarized in Figure 4.9 and Table 4.1.

4.4.1 Cooperative targets – WUT system

The first set of results has been obtained by using the PR system developed at WUT. The system is composed of five receivers realized with COTS components. One

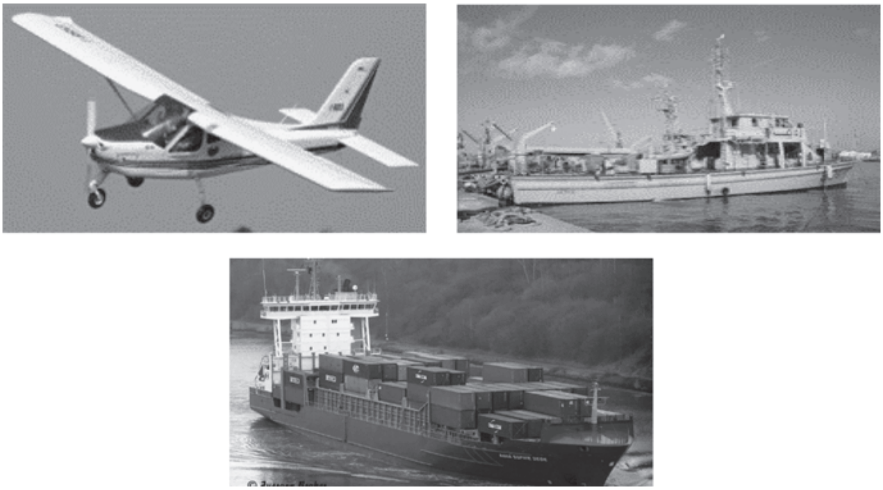

Figure 4.9 Targets pictures

Table 4.1 Targets sizes

	Length [m]	**Wide/wingspan [m]**	**Height [m]**
Astice	33.25	6.47	12
P92	7	15	–
Anna-Sophie	134	23	–

channel is the reference channel and the others are the surveillance channels located as shown in Figure 4.10.

More precisely, two antennas are at the site A and two others at the site B. The hardware was able to acquire up to 60 MHz of instantaneous bandwidth. GPS systems have been used to synchronized the data. Three cooperative targets were present during measurements, namely an aerial target P92 and two vessels, MBN and Astice. The targets' trajectories measured via GPS systems installed on board of such targets are shown in Figure 4.11.

The image in Figure 4.12 represents the RD map corresponding to an observation time of 500 s and obtained by superimposing RD maps relative to CPIs equal to 2 s and distant 5 s each.

The image in Figure 4.14 shows an example of a 2 s length time burst of acquired data, in the frequency/slow-time domain. As can be noted, each frequency channel has a different mean power. This may affect the range resolution. To avoid range resolution degradation, power equalization is required at each frequency channel. Moreover, it is possible to observe the gaps between frequency channels. These gaps give rise to grating lobes along the range domain. Two data bursts relative to two targets, namely 'Astice' and 'P92', have been analysed and results are shown in the following subsections.

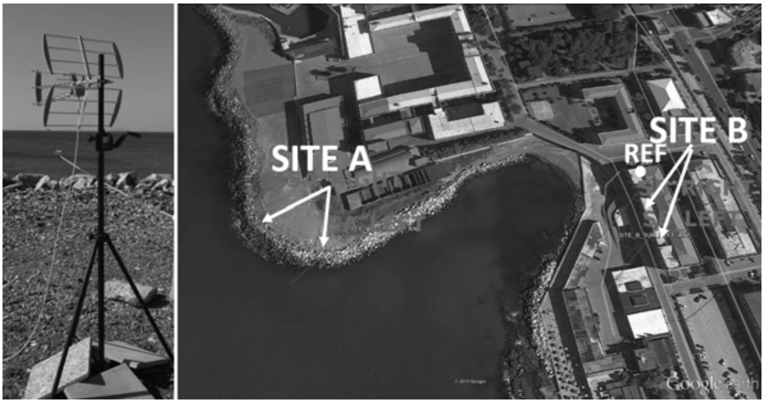

Figure 4.10 *Single antenna element (left) and system geometry (right)*

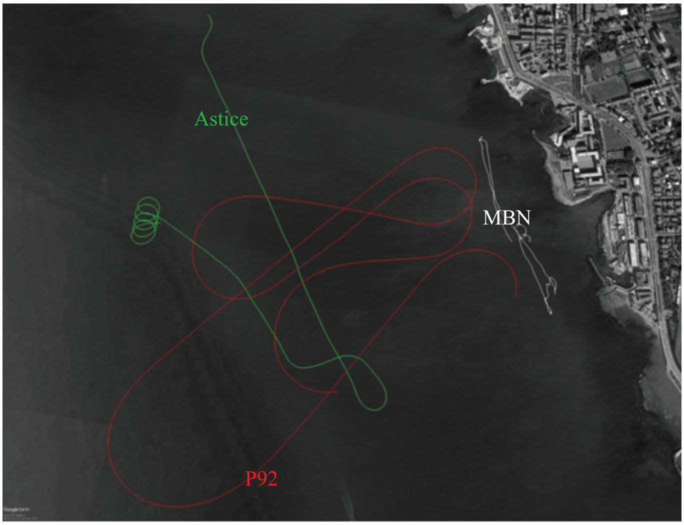

Figure 4.11 *Targets trajectory during measurements*

4.4.1.1 Passive-ISAR imaging results: Astice

Results shown in this section are obtained by processing the fourth 2 s length time batch. Figure 4.13 shows the RD map where the rectangle represents the cropped area around the target of interest, namely 'Astice'.

Images in Figure 4.14 represent the data after back projecting the cropped sub-image into the frequency/slow-time domain. The images on the left and on the right represent the data before and after the equalization, respectively.

Images in Figure 4.15 represent the range profiles before and after motion compensation performed via the ISAR processing. As can be noted, the target experiences

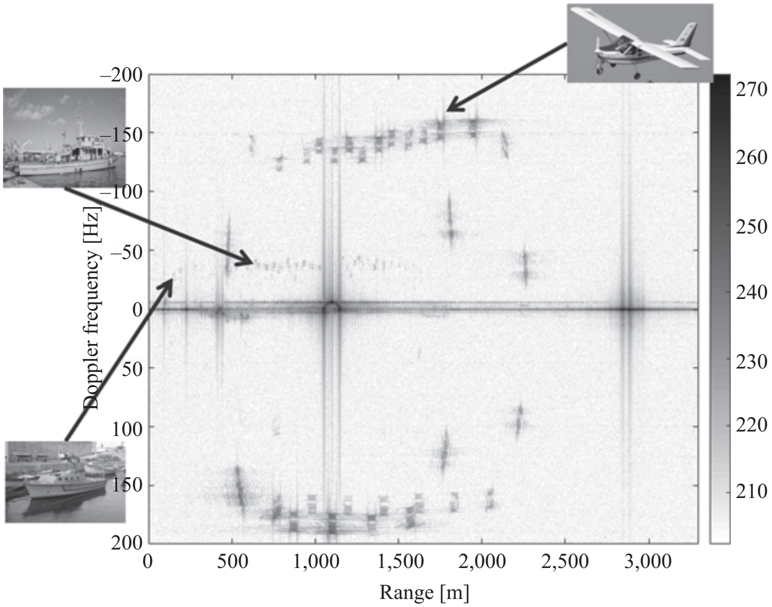

Figure 4.12 RD map relative to 150 s of data. This RD map has been obtained by incoherently sum in amplitude each RD map obtained at each CPI. The CPI length is 2 s. CPIs was separated by 5 s

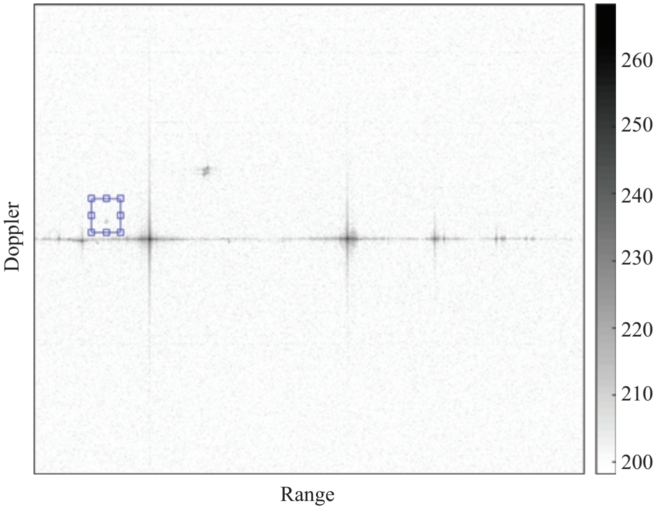

Figure 4.13 RD map relative to the fourth CPI. The rectangle represents the target sub-image extracted by the 'Target extraction' block

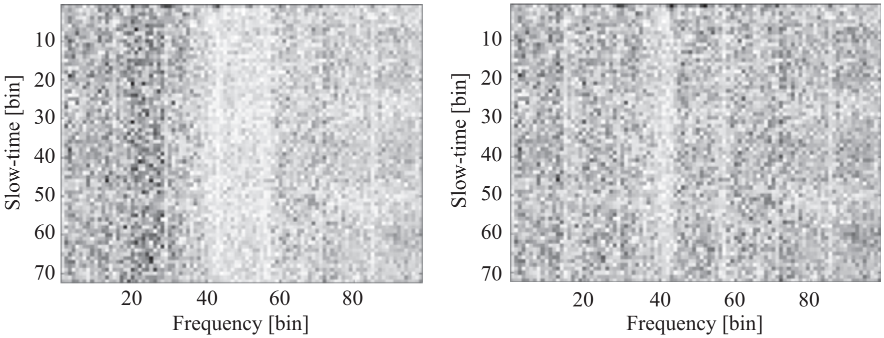

Figure 4.14 Target echo before (left) and after (right) power equalization

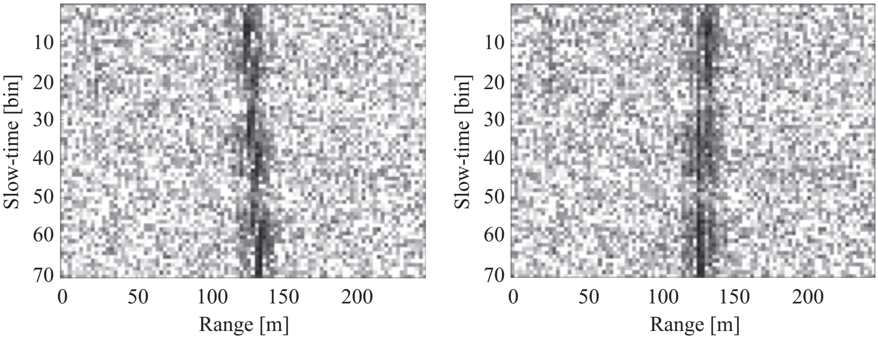

Figure 4.15 Target range profiles before (left) and (right) autofocusing

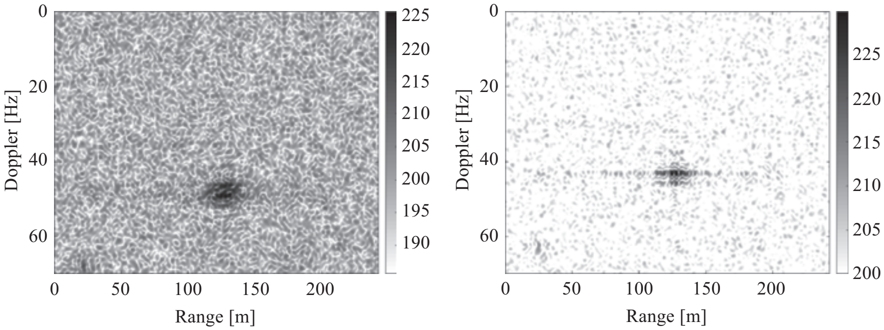

Figure 4.16 Target RD image before (left) and (right) ISAR processing

a range migration which is compensated by the autofocusing algorithm processing. Here, we have implemented the ICBA-based autofocusing technique.

Images in Figure 4.16 show the radar images of the target in the range/Doppler domain before and after the ISAR processing. These results have been obtained by using the entire bandwidth, namely $B = 60$ MHz.

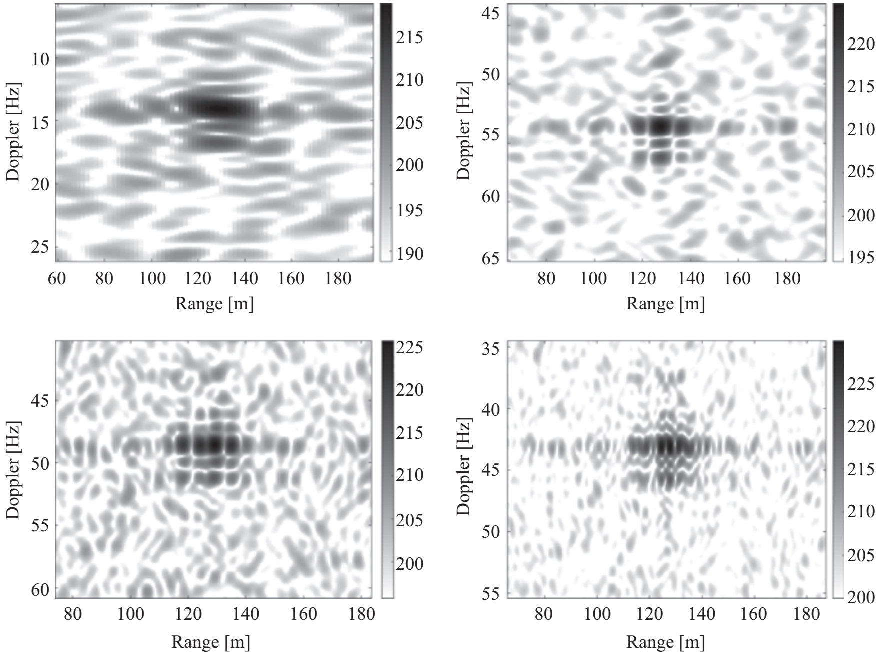

Figure 4.17 Target ISAR images at different range resolution levels. From top-left-hand corner B = 8 MHz, B = 24 MHz, B = 4 MHz and B = 56 MHz

As it can be noted, the target is focused and this is also confirmed by peak level that increases when ISAR processing is applied. To show the benefit in terms of range resolution of coherently adjoin adjacent DVB-T, ISAR images at lower range resolutions have been obtained by selecting a reduced number of frequency channels. The aim is to show the range resolution increase when multi-frequency P-ISAR is used.

Figure 4.17 shows ISAR images obtained by using one DVB-T channel ($B =$ 8 MHz), three DVB-T channels ($B = 24$ MHz), five DVB-T channels ($B = 40$ MHz) and seven DVB-T channels ($B = 56$ MHz).

4.4.1.2 Passive-ISAR imaging results: P92

Results shown in this section are obtained by processing the 16th, 2 s length time batch. Figure 4.18 shows the RD map where the rectangle represents the cropped area around the target of interest, namely ‘P92’.

Images in Figure 4.19 represent the data after back projecting the cropped sub-image into the frequency/slow-time domain. The image on the left and on the right represents the data before and after the equalization, respectively.

Images in Figure 4.20 represent the range profiles before and after motion compensation performed via the ISAR processing. As can be noted, the target experiences

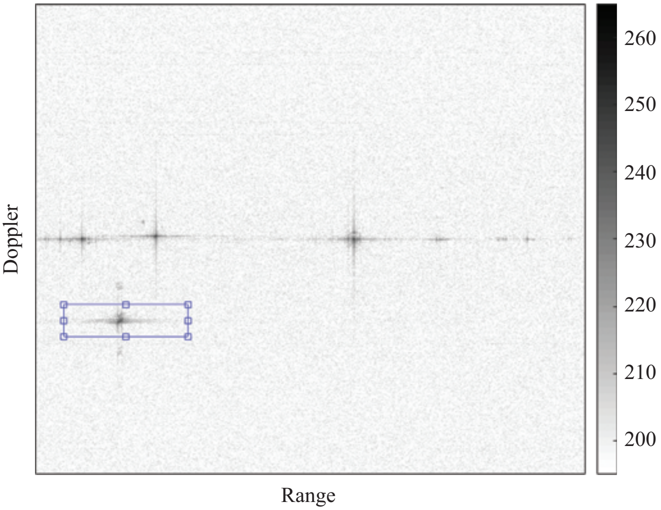

Figure 4.18 RD map relative to the fourth CPI. The rectangle represents the target sub-image extracted by the 'Target extraction' block

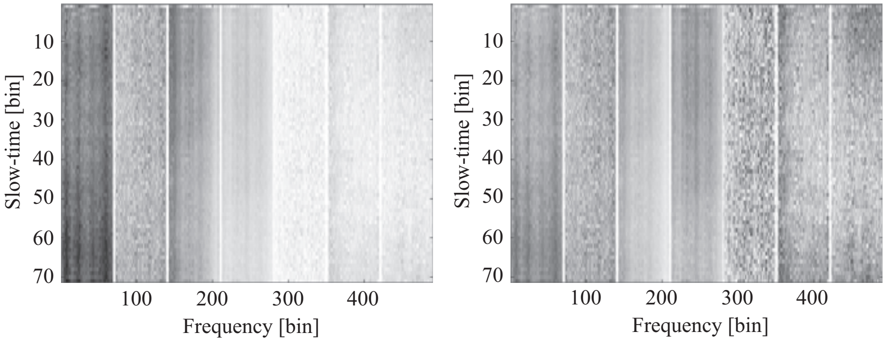

Figure 4.19 Target echo before (left) and after (right) power equalization

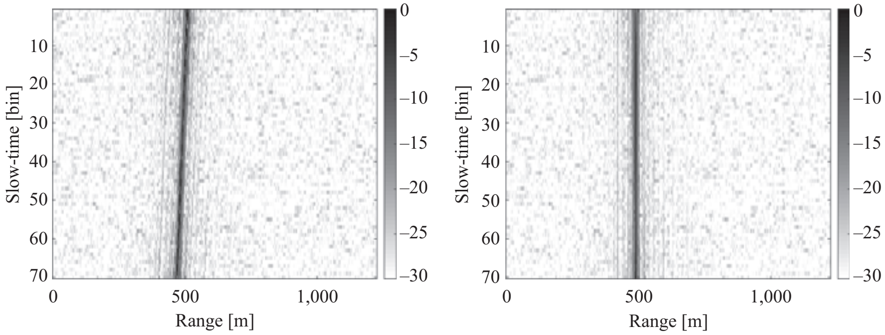

Figure 4.20 Target range profiles before (left) and (right) autofocusing

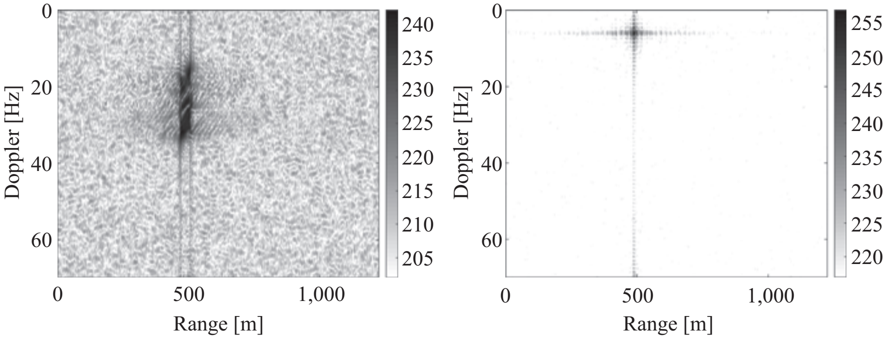

Figure 4.21 Target RD image before (left) and (right) ISAR processing

a range migration which is compensated by the autofocusing algorithm processing. Here, we have implemented the ICBA-based autofocusing technique.

Images in Figure 4.21 show the radar images of the target in the range/Doppler domain before and after the ISAR processing. These results have been obtained by using the entire bandwidth, namely $B = 60$ MHz.

Also, in this case, the improvement in the image focus degree is evident and confirmed by peak level that increases when ISAR processing is applied. To show the benefit in terms of range resolution of coherently adjoin adjacent DVB-T, ISAR images at lower range resolutions have been obtained by selecting a reduced number of frequency channels. The aim is to show the range resolution increase when multi-frequency P-ISAR is used.

Figure 4.22 shows ISAR images obtained by using one DVB-T channel ($B = 8$ MHz), three DVB-T channels ($B = 24$ MHz), five DVB-T channels ($B = 40$ MHz) and seven DVB-T channels ($B = 56$ MHz).

4.4.2 Non-cooperative targets – SMARP

The second set of results has been obtained by processing data acquired by means of SMARP PR demonstrator. The SMARP system has been developed by the RaSS Laboratory of the Italian CNIT in the framework of the Italian National Plan for Military Research. The SMARP particular features are listed as follows:

- It is equipped with a multiband receiving array antenna and operating at both UHF and S bands, with dual polarization reception.
- It makes use of software-defined receiver based on commercially available solutions.
- It implements digital array processing techniques and advanced radar signal processing algorithms implemented on COTS processing architectures.

Such features allow the use of both DVB-T and UMTS IOs for detection and tracking of targets in the range–Doppler map. Moreover, the use of array processing allows for the estimation of the target DoA thus allowing for accurate target

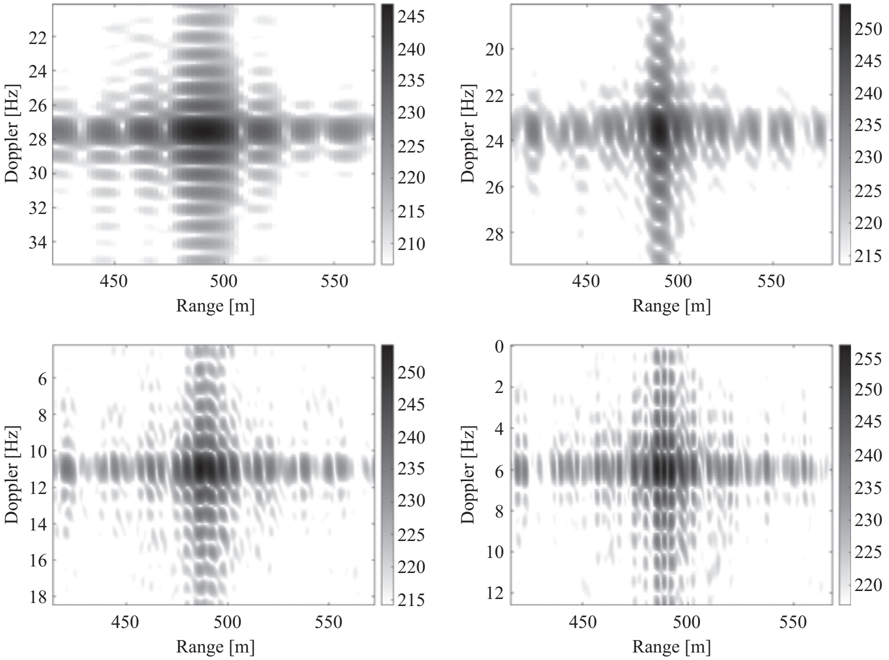

Figure 4.22 Target ISAR images at different range resolution levels. From top-left-hand corner B = 8 MHz, B = 24 MHz, B = 40 MHz and B = 56 MHz

localization. Radar imaging functionality is instead activated on demand by using a wider bandwidth signal. Signals with wide enough bandwidth may be obtained for example by coherently combining adjacent DVB-T or UMTS channels. A picture of the SMARP system is in Figure 4.23. SMARP is permanently installed at the Naval academy (CSSN-ITE) facilities in Livorno (Italy) and is located close to the reference antenna of the PR system developed at WUT and represented in Figure 4.10 as a white dot near the label 'REF'.

The antenna system is composed of a single element reference antenna and four linear arrays, two for each band, composed of eight path antennas each. The UHF- and S-band antennas operate in the frequency ranges 470–490 and 2,100–2,200 MHz, respectively. The synchronization signal generator provides a reference signal that permits a synchronous and coherent multichannel acquisition. The generation of the reference signals has been achieved in the SMARP demonstrator by using a clock distribution unit. Further technical details on SMARP can be found in [20].

During measurements, a cooperative target, namely 'Astice', was equipped with GPS system in order to track it along its trajectory. Non-cooperative targets were also present at the time of the measurements approaching or leaving the Livorno harbour. Non-cooperative targets were cargo vessels of large size. Subsequently, only results relative to a non-cooperative target are shown. The ISAR image of targets quite larger

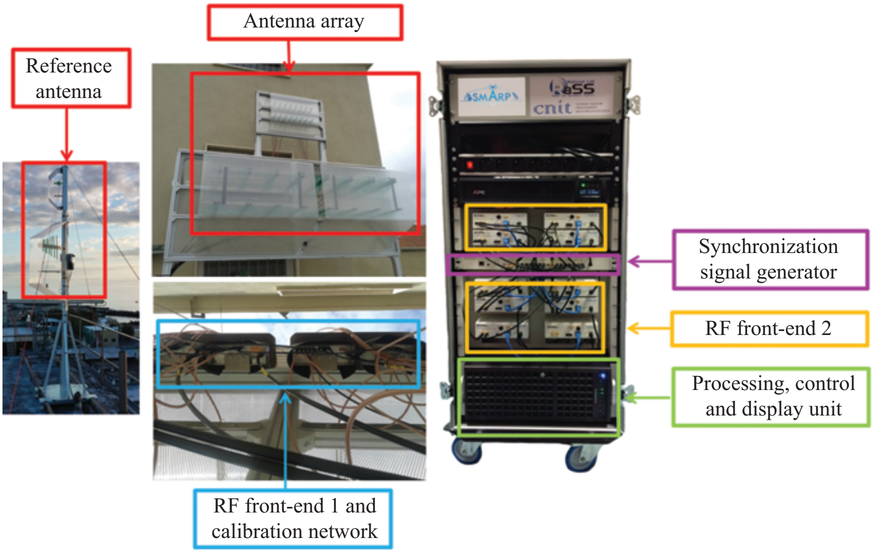
Antenna array
Reference antenna
Synchronization signal generator
RF front-end 2
Processing, control and display unit
RF front-end 1 and calibration network
SMARP
cnit

Figure 4.23 SMARP passive radar system and its main hardware component

than the range resolution appears as composed of a large number of scattering centres. When this occurs, the ‘cross-range scaling’ algorithm gives more accurate results and ISAR images in a fully spatial coordinate system can be generated. An automatic identification system receiver has been used at the PR location to gather information about the observed target and, more specifically, its Maritime Mobile Service Identity number so as to know target sizes and type and its trajectory that may help to test detection and tracking algorithms and target orientation with respect to the radar LoS during the observation time.

Effective ISAR images can be obtained by using large bandwidth signals and by observing the target for a long enough integration time. This is because the range resolution is inversely proportional to the signal bandwidth and the Doppler resolution is inversely proportional to the observation time. When the system operates in the ISAR mode, the data has to be acquired continuously for a long enough observation time. In these experiments, data is acquired for 40 s continuously. To reach fine-enough range resolution, a wideband signal needs to be acquired. In this experiment, the SMARP system acquires a signal composed of three adjacent DVB-T channels. The signal bandwidth was 24 MHz. All the moving targets underwent complex motion either because they were manoeuvring or because of the sea state that during the experiments was moderate. As a consequence, well-focused ISAR images are obtained by processing data in time intervals shorter than the whole observation time. Therefore, the ‘best frame’ selection has been applied that gives a sequence of ISAR images. The ‘best frame’ selection algorithm applied here is based on the IC value as described in [13].

Figure 4.24 shows a sequence of four ISAR images of the selected target. Each ISAR image has been obtained by processing a different CPI as detailed in the figure

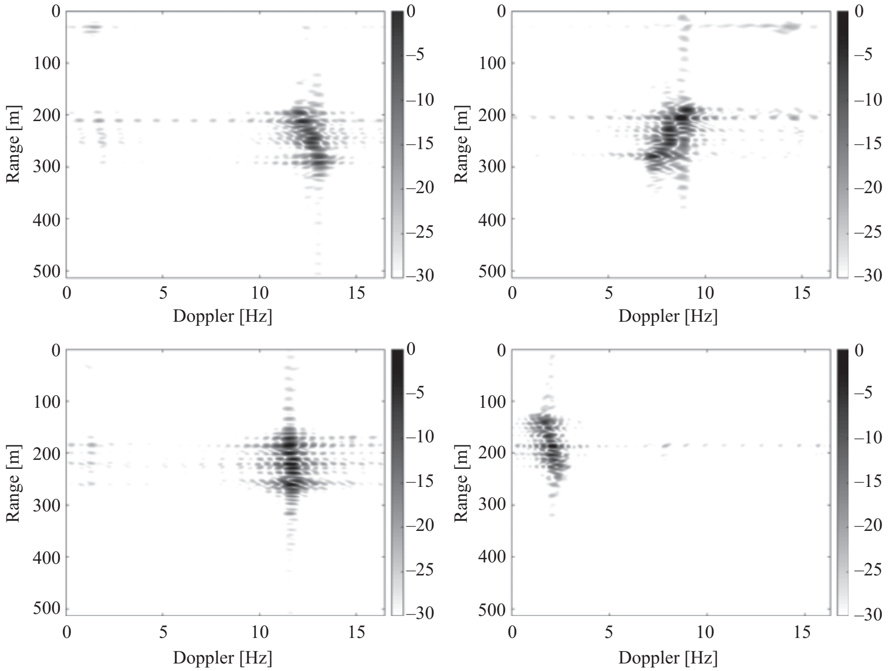

Figure 4.24 Passive ISAR images of target 'Anne-Sophie' obtained by processing (from top-left-hand corner), 21, 2, 2 and 4 s, respectively. Each frame of data is centred on a different time instant. The time intervals between two subsequent ISAR images are 2 s from the first and the second ISAR image, 6 s from the second to the third ISAR images and 12 s from the third and the fourth ISAR images

caption. As it can be noted, the target changes its orientation in the range/cross-range plane. This is caused by the target-effective rotation vector, $\mathbf{\Omega}_{eff}$, change in time.

The images in Figure 4.24 are in the range/Doppler domain. In such a domain, it is not possible to sizing the target. An ISAR image in a fully spatial coordinate system is then obtained by applying the cross-range scaling algorithm proposed in [19]. This algorithm aims at estimating the modulus of $\mathbf{\Omega}_{eff}$ in order to use (4.18) to convert Doppler coordinates into cross-range coordinates. This algorithm relies on the fact that the phase term of each scatterers contains information on Ω_{eff}. In particular, the chirp rate of each scatterer, namely the rate at which its Doppler frequency change over time, is a function of both its range coordinate and Ω_{eff}. More specifically, a scatterer range coordinate and chirp rate are linearly dependent and the slope of this straight line is a function of Ω_{eff}. The algorithm then works following this work-flow:

- Extract the brightest scatterers that compose the target. Each scatterer range coordinate is also estimated.

- Estimate the chirp rate of each scatterer by using for example a polynomial Fourier transform.
- Estimate the straight line that better approximates the cloud of points in the range/chirp-rate domain by using a least square error (LSE) approach.
- Estimate the straight line slope and then Ω_{eff}.

Figure 4.25 shows the results of the application of such a processing to the ISAR images in Figure 4.24. Images on the left represent the LSE results. Dots are the range/chirp-rate pair of each scatterer while the solid line is the straight line estimated by the LSE algorithm. Images on the right are instead the ISAR images in spatial coordinates.

CS-based ISAR reconstruction algorithm has been applied to this dataset to test its effectiveness to deal with incomplete data. Figure 4.26 shows the P-ISAR image in the range/Doppler domain obtained by using conventional RD algorithm and CS-based algorithm, respectively.

As it can be observed, the presence of frequency gaps generates grating lobes in the RD ISAR images (on the left side of Figure 4.26) that are slightly mitigating by using instead a CS-based algorithm (on the right side of Figure 4.26). Grating lobes along the Doppler dimension are due to the fact that the 'RD maps merging' block introduces slight discontinuities along the slow-time domain. These grating lobes are also reduced by applying the CS-based reconstruction algorithm.

The super-resolution capability of the CS-based ISAR algorithm has been also tested. To prove this capability, the full data has been reduced by replacing a number of data samples with zeros, as shown in Figure 4.27. The compression rate (CR) is the percentage of non-zero data samples after data reduction, with respect to the original number of data samples. Figure 4.27 shows data with different CR, namely 100% (which corresponds to the full data), 70%, 60% and 50%.

Conventional RD ISAR algorithm and CS-based ISAR algorithm have been applied to the data in Figure 4.27 and results are shown in Figure 4.28.

The benefit of using a CS-based algorithm is 2-fold:

- It may deal with incomplete data by preserving the spatial resolutions that would be reached with a complete data.
- It has super-resolution capability by extrapolating over the available spatial frequency. In fact, by comparing images on the right side of Figure 4.28 with the image in the top-left-hand corner of Figure 4.24, it can be noted that the main target scatterers are correctly reconstructed.

Obviously, the accuracy of this algorithm has some limits, among all the high-computational time and a limit on the maximum CR, that guarantee a proper image reconstruction that is linked to the data sparsity degree, which is however unknown. A more detailed analysis of the SR capability of the CS-based ISAR algorithm can be found in [21].

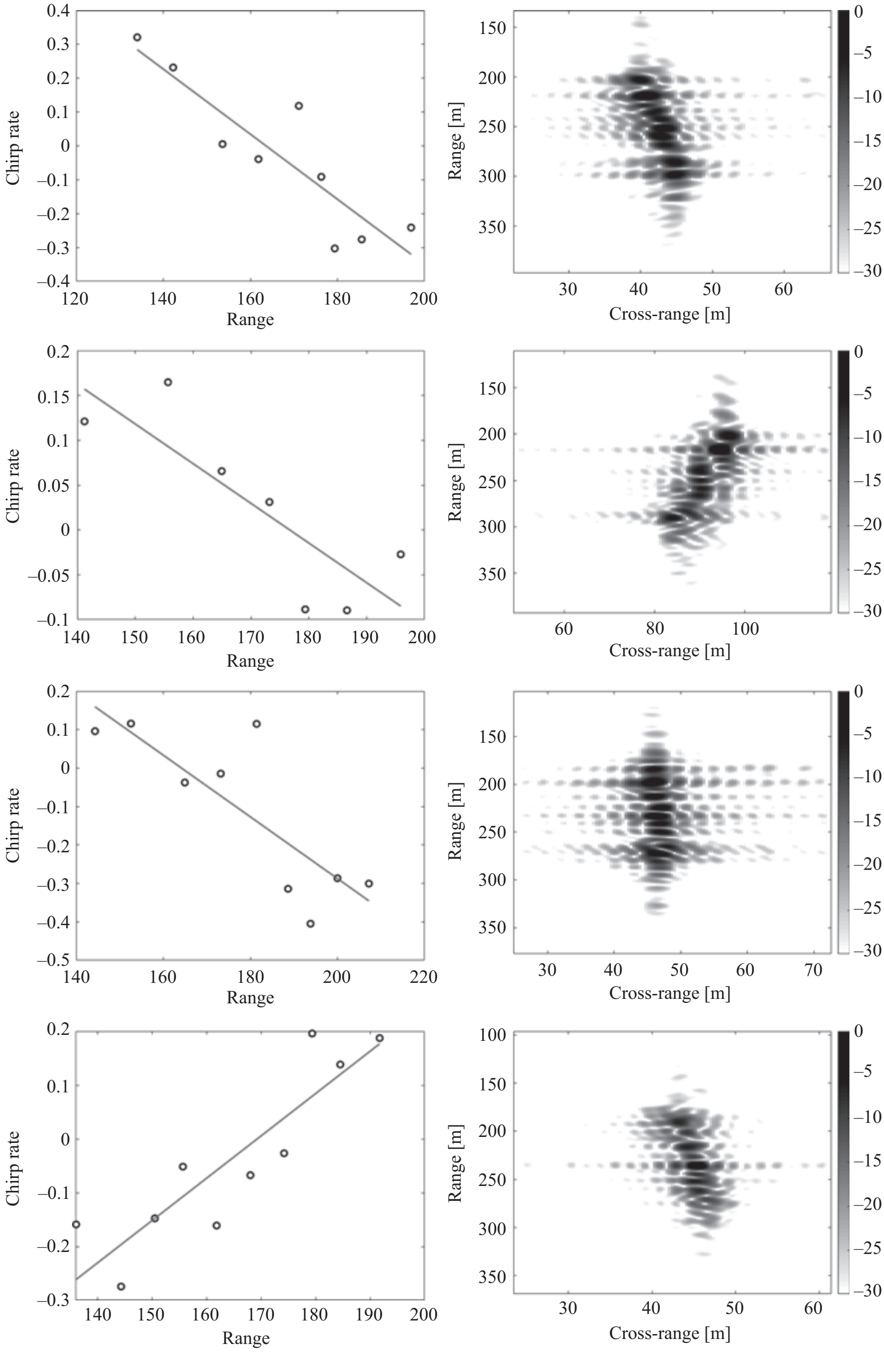

Figure 4.25 Fully scaled passive ISAR images

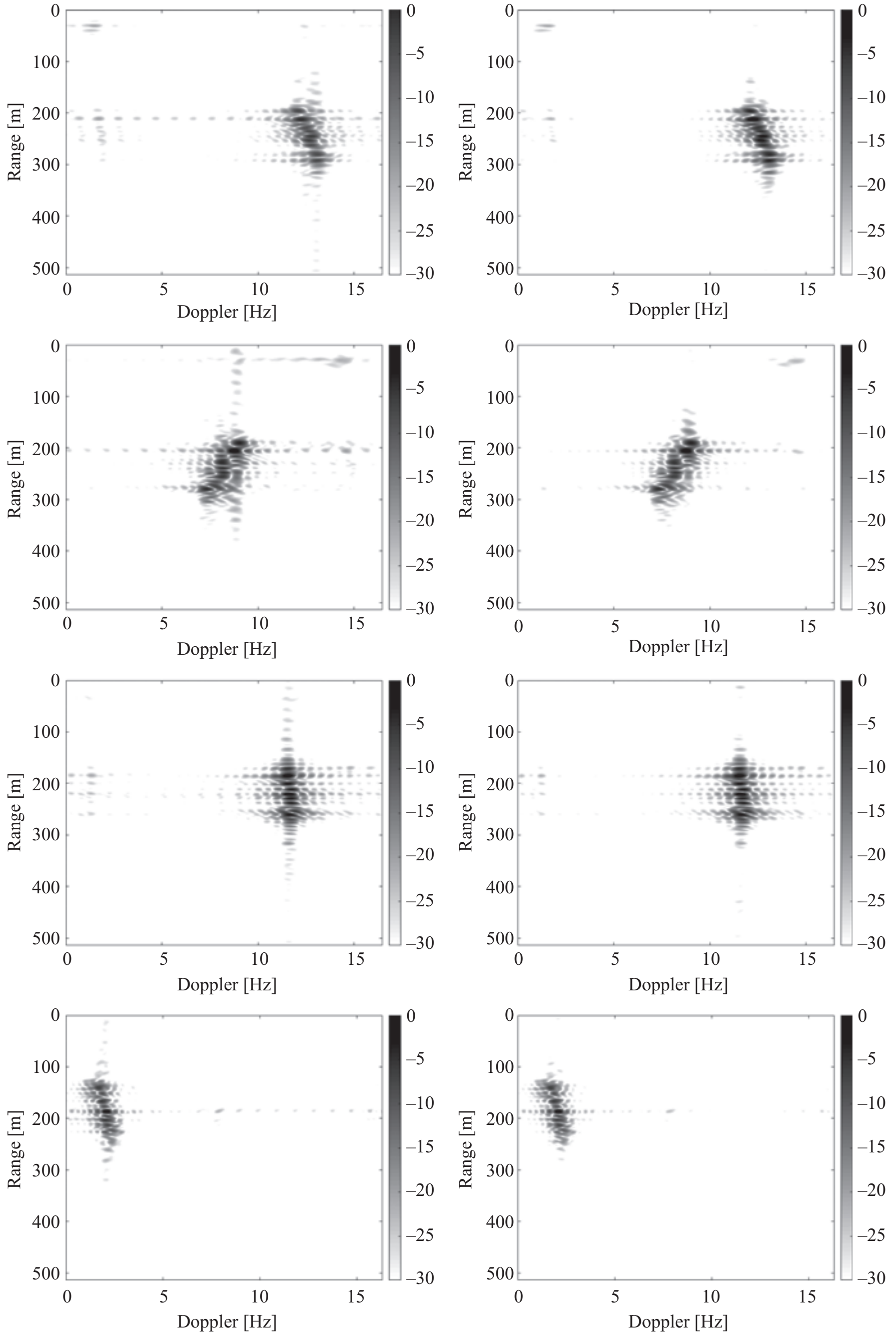

Figure 4.26 ISAR images obtained by using a 2D-FT (left) and ISAR images obtained by using a CS-based approach (right)

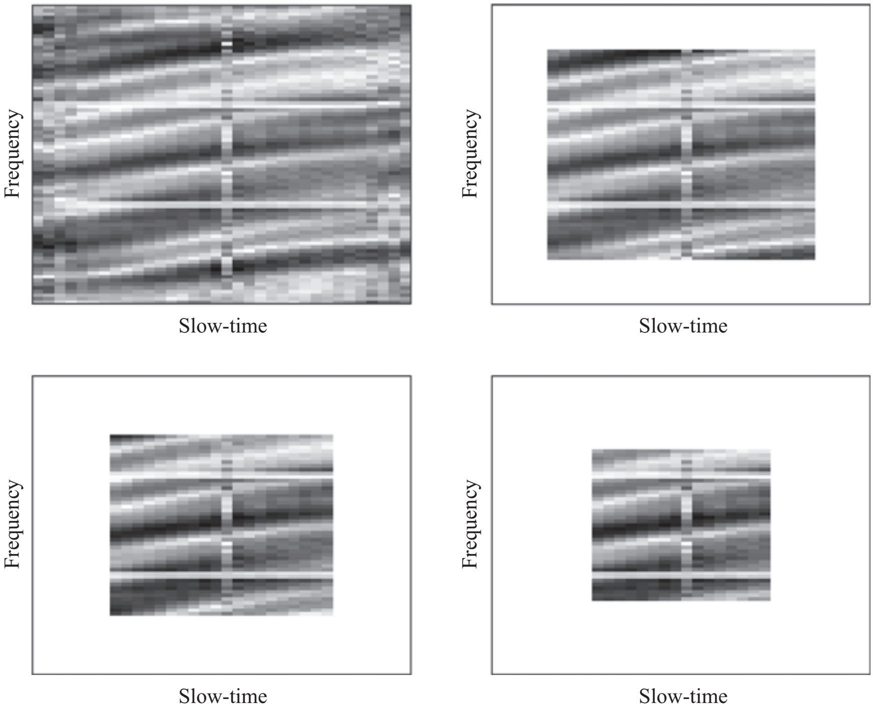

Figure 4.27 ISAR data after motion compensation and data reduction at different CR. From top-left-hand corner, CR = 100%, CR = 70%, CR = 60%, CR = 50%

4.5 Conclusions

The P-ISAR algorithm has been reviewed in this chapter. In particular, the theory behind the P-ISAR algorithm is provided to fully support the evidence of the PR imaging capability. In this chapter, the case of PR using broadcast transmitters as IO is addressed. However, the theoretical approach is valid independently on the transmitter type.

An extensive result analysis has been conducted that proves and validates the proposed algorithm. Two different PR systems have been used that make use of TV broadcast transmitters as IO. Measurements were gathered during trials at the Navy academy in Livorno in the framework of the research Task Group SET-196 on ‘Multichannel/Multistatic Radar Imaging of Non-Cooperative Targets’.

P-ISAR performance in terms of spatial resolutions is limited by the waveform bandwidth and by the operating frequencies. Nevertheless, wider bandwidth may be obtained by adjoining more channels, which may produce a resolution fine enough to enable automatic target classification. The VHF/UHF band is, however, not completely filled by broadcast signals. Therefore, P-ISAR has to deal with incomplete

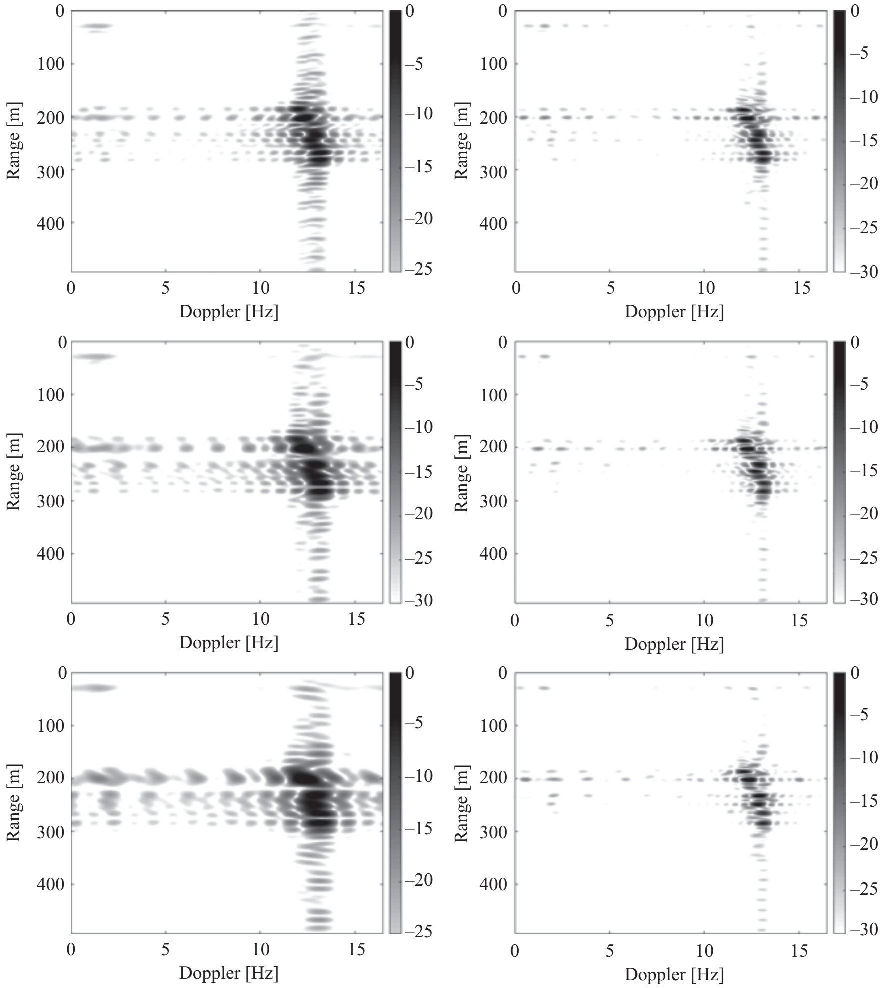

Figure 4.28 ISAR images obtained by processing the reduced data in Figure 4.27. Images on the left have been obtained by applying the RD algorithm, namely a 2D-FT, images on the right have been obtained by applying the CS-based algorithm

data. A CS-based ISAR approach has been proposed to account for this issue. CS-based ISAR algorithm has been proven efficient in case of both narrow and even large frequency gaps. The CS-based ISAR algorithm permits to estimate the missing data and then reconstruct a full-bandwidth P-ISAR image of the target, obviously, at some price and with some limits. The price is a higher computational cost with respect to conventional P-ISAR algorithm. But this allows to avoid the artefacts otherwise present when using standard techniques with incomplete data. The limit of the applicability of the CS-based ISAR algorithm is linked with the sparsity degree of an

ISAR image. The sparsity degree of an ISAR image is the number of scatterers that composes the target image. In general, the more the data is sparse, the less the number of the scatterer and the higher the probability to correctly reconstruct the ISAR image from a compressed or incomplete data.

Moreover, beside the well-known advantages of PR systems (among all the covertness), P-ISAR provides radar cross-section information of targets at low frequencies where active radar typically cannot transmit.

References

[1] Malanowski M, Mazurek G, Kulpa K, *et al.* FM based PCL radar demonstrator. In: Proceedings of the International Radar Symposium; 2007. pp. 1–5.

[2] Glende M, Heckenbach J, Kuschel H, *et al.* Experimental passive radar systems using digital illuminators (DAB/DVB-T). In: Proceedings of the International Radar Symposium; 2007. pp. 1–5.

[3] O'Hagan DW, Kuschel H, Ummenhofer M, *et al.* A multi-frequency hybrid passive radar concept for medium range air surveillance. IEEE Aerospace and Electronic Systems Magazine. 2012;27(10):6–15.

[4] Olivadese D, Giusti E, Petri D, *et al.* Passive ISAR with DVB-T signals. IEEE Transactions on Geoscience and Remote Sensing. 2013;51(8):1–10.

[5] Conti M, Petri D, Capria A, *et al.* Ambiguity function sidelobes mitigation in multichannel DVB-T passive bistatic radar. In: Proceedings of the International Radar Symposium; 2011. pp. 1–5.

[6] Olivadese D, Martorella M, and Berizzi F. Multi-channel P-ISAR grating lobes cancellation. In: IET International Conference on Radar Systems (Radar 2012); 2012. pp. 1–5.

[7] Martorella M, and Giusti E. Theoretical foundation of passive bistatic ISAR imaging. IEEE Transactions on Aerospace and Electronic Systems. 2014; 50(3):1647–1659.

[8] Qiu W, Giusti E, Bacci A, *et al.* Compressive sensing-based algorithm for passive bistatic ISAR with DVB-T signals. IEEE Transactions on Aerospace and Electronic Systems. 2015;51(3):2166–2180.

[9] Martorella M, Palmer J, Homer J, *et al.* On bistatic inverse synthetic aperture radar. IEEE Transactions on Aerospace and Electronic Systems. 2007;43(3):1125–1134.

[10] Martorella M, Giusti E, Berizzi F, *et al.* ISAR based technique for refocussing non-cooperative targets in SAR images. IET Radar, Sonar, Navigation. 2012;6(5):1–9.

[11] Petri D, Moscardini C, Martorella M, *et al.* Performance analysis of the batches algorithm for range–Doppler map formation in passive bistatic radar. In: IET International Conference on Radar Systems (Radar 2012); 2012. pp. 1–4.

[12] Moscardini C, Petri D, Capria A, *et al.* Batches algorithm for passive radar: a theoretical analysis. IEEE Transactions on Aerospace and Electronic Systems. 2015;51(2):1475–1487.

[13] Martorella M, and Berizzi F. Time windowing for highly focused ISAR image reconstruction. IEEE Transactions on Aerospace and Electronic Systems. 2005;41:992–1007.

[14] Cataldo D, and Martorella M. Optimal CPI selection based on Doppler spread and image contrast. In: 2018 19th International Radar Symposium (IRS); 2018. pp. 1–11.

[15] Martorella M, Berizzi F, and Haywood B. Contrast maximisation based technique for 2-D ISAR autofocusing. IEE Proceedings – Radar, Sonar and Navigation. 2005;152(4):253–262.

[16] Martorella M, Berizzi F, Palmer J, *et al.* Image contrast and entropy based autofocusing for polarimetric ISAR. In: 2007 International Waveform Diversity and Design Conference; 2007. pp. 245–249.

[17] Berizzi F, Martorella M, and Giusti E. Radar Imaging for Maritime Observation. Signal and Image Processing of Earth Observations. Taylor & Francis; 2016. Available from: https://books.google.it/books?id=3kaNMQEACAAJ.

[18] Nel W, Giusti E, Martorella M, *et al.* A time domain phase-gradient based ISAR autofocus algorithm. In: Proceedings of 2011 IEEE CIE International Conference on Radar. vol. 1; 2011. p. 541–544.

[19] Martorella M. Novel approach for ISAR image cross-range scaling. IEEE Transactions on Aerospace and Electronic Systems. 2008;44(1):281–294.

[20] Capria A, Giusti E, Moscardini C, *et al.* Multifunction imaging passive radar for harbour protection and navigation safety. IEEE Aerospace and Electronic Systems Magazine. 2017;32(2):30–38.

[21] Giusti E, Cataldo D, Bacci A, *et al.* ISAR image resolution enhancement: compressive sensing versus state-of-the-art super-resolution techniques. IEEE Transactions on Aerospace and Electronic Systems. 2018;54(4):1983–1997.

Chapter 5

Radar tomography

Hai-Tan Tran[1] *and Lorenzo Lo Monte*[2]

This chapter discusses the principles and applications of radar tomography (RT) in the areas of spotlight synthetic aperture radar (SAR), circular SAR, and Doppler–radar tomography (DRT). The applications are diverse, ranging from ground and terrain imaging, imaging of buried objects under the ground, to high-resolution imaging of a small airborne target, or concealed weapons on a human body. The theoretical foundation, however, can be elegantly described in the spatial frequency spaces, also known as the "k-spaces," of RT.

An emphasis of the chapter is on the centrally important role of the k-spaces in radar imaging as a design and analysis tool, including a novel type of k-space called the *"slow-time" k-space*. Another emphasis is on the practical aspects of using radar tomographic imaging systems. For instance, this chapter discusses the data collection requirement and challenges for typical applications, the various image formation techniques, and some imaging performance metrics in terms of image resolution and image contrast. The chapter also discusses the advantages and disadvantages of RT, with the objective of giving the radar engineer tasked with designing such a system some realistic options to consider.

5.1 Introduction

Radar imaging may be simply described as a spatial mapping of an object, commonly called a "target," by a radar, taking advantage of its well-known advantages: long-range operation under all-weather conditions. RT is one of the several possible approaches known to date for radar imaging. Historically, the term "tomography" originates from the Greek word "tomo" meaning "slice" or "section"; it reflects the close connection to the projection-slice theorem (PST) [1] that is the theoretical foundation of this mathematical science area. Nowadays, the term may refer to *any of several techniques for creating three-dimensional images of the internal structure of a solid object by analyzing the propagation of waves of energy, such as X-rays or seismic waves, through the object* [2]. RT makes use of radio signals, and the

---

[1] Department of Defence, Defence Science and Technology, Edinburgh, Australia
[2] Telephonics, New York, NY, USA

"slices" may refer to lower dimensional "cuts" in either the frequency domain or the spatial domain. Strictly speaking, these domains are defined fully only within the so-called far-field approximation; several authors have nevertheless extended the term "tomography" to include algorithms also in the near-field cases.

From a theoretical perspective, RT is not a new concept: pioneering works in the far-field approximation had been reported by a number of authors since the 1980s. Since then, related concepts and new applications have continued to be developed. The promising advantage of tomography is the exploitation of observations of a target from multitude views or aspects: each observation is a projection of a three-dimensional (3D) target onto a lower spatial domain. If such observations are sufficiently distributed in spatial aspects around the target, then tomography provides a method to reconstruct the target from such projections which are *coherently ensembled* in a spatial frequency space. The fundamental mathematical principles of tomographic imaging are well covered in [1], while some of the early applications to 2D radar imaging were reported in [3,4] for spotlight SAR imaging and Doppler tomography [5]. Generally, 3D measurements could be processed for 3D target imagery; similarly, 2D measurements would lead to 2D imaging.

The key "system resource" for RT imaging is the *spatial diversity* in a dynamical radar-target system geometry, in addition to any *spectral diversity* represented by the signal bandwidth. Spatial diversity may take the form of angular separations of the transmitting and/or receiving antennas, or changes in a target's aspect due to radar platform motion, or the target's own motion, either translational or rotational, relative to the radar antennas. The two system resources are complementary: a wideband radar can satisfactorily perform its target imaging function with minimal requirement on effective target rotation; and conversely a narrowband radar system must rely on sufficient rotational motion or spatial distribution of receivers for imaging. And when spatial diversities are required, precise knowledge of the motion or spatial distribution of the antennas relative to the target is required for image-focusing algorithms, which may present numerous challenges for the imaging radar, particularly in terms of channel calibration, synchronization, data communication between the receiver channels, and signal processing.

RT can be regarded as a general framework of radar imaging which reduces to "simpler" forms in certain limits, depending on the extent of effective rotational motion and the geometry of the transmitting and receiving antennas relative to the target. Effective rotational motion is defined by three possible factors: rotational motion by a target on its own (relative to its own inertial reference frame), translational motion relative to the bisector of the bistatic angle it makes with a radar transmitter–receiver system, and the 3D antenna beam widths and modes of illumination. For example, relative to a specific spot on the ground, a spotlight or circular SAR which continuously illuminate it can produce an effective rotation angle that is much larger than in the case of a strip-map SAR mode. Indeed, when effective rotation is restricted to small angles, RT becomes strip-map SAR or range–Doppler inverse SAR (ISAR); the relative motion can then be linearized, motion estimation is simplified (but may not be simple), and computationally efficient tools such as the fast Fourier transform (FFT) may be applied. When rotational motion is extended to wider angles, high-resolution imaging must rely on precise motion models; in this case, RT becomes spotlight SAR, circular SAR, or "polar-formatting ISAR imaging." Alternatively, processing techniques, such as Doppler cross-range profiling and sparse signal reconstruction, may be necessary, and RT may be called "augmented DRT."

Another important advantage of RT is that the underlying algorithms do not pose restrictions on the shape of a radiated waveform when adequate geometric diversity is available. This is in contrast with classical SAR/ISAR imaging algorithms, where the waveform should have good pulse compression properties to avoid range sidelobes. As such, RT is appealing to passive modes of operation and noncooperative scenarios, where the waveforms may not have good pulse compression properties. In favorable geometries, RT can achieve sub-wavelength resolution, regardless of the bandwidth, although additional higher bandwidths would lead to lower sidelobes in the point spread function (PSF) and hence better image contrast.

From a practical application perspective, extensive demonstrations have been reported in recent years, most of which serve to verify or validate the fundamental claims. The main driving factors and challenges prompting such developments are summarized in the following.

A first challenge is the fact that the *RF spectrum available to radar operation is becoming increasingly congested or denied*. The scenario may also be hostile with the presence of electronic support/electronic attack (EA) assets. Capabilities of generating high-quality SAR/ISAR imagery using traditional wideband radars may thus be compromised.

A second challenge is the use of imaging systems designed mainly for 2D objects for highly 3D terrains, with abrupt elevation changes, such as buildings and canyons. Existing commercial SAR systems usually offer both strip-map and spotlight modes of operation [4]. Circular SAR [6] provides exquisite image resolution as well as greater information concerning a threat due to reduced shadowing, foreshortening, and speckle effects. In their classical implementation, all of these SAR modalities often assume that the threat scenario lies over a roughly flat terrain so that the only retrievable information is the one of slant-range and cross-range; the elevation information is usually poor or unavailable. Asymmetric warfare has refocused attention from open fields to urbanized areas or mountainous regions, which requires situational awareness of the vertical dimension. As such, the full 3D information of targets and surrounding terrain becomes pivotal for intelligence analysis and informed decision-making. See illustration in Figure 5.1.

Specially designed SAR radars may exploit additional (interferometric) channels to provide information about the elevation angle of the terrain [7]. However, their 3D reconstruction capability is challenged when the terrain exhibits sharp vertical changes, due to the inability of current algorithms to properly unwrap the phase history of the interferometric data. Multi-pass SAR, i.e., SAR data collected at different heights, improves the 3D reconstruction capabilities: this technology also allows legacy single-channel SAR systems to retrieve (to some extent) the elevation information of targets.

A third challenge is the vulnerability of monostatic systems to EA. For classical ISAR [8], the illumination and observation points are usually colocated, i.e.,

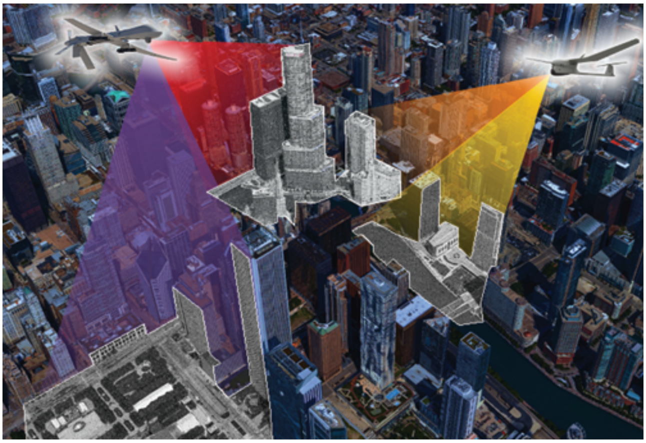

Figure 5.1 Abrupt changes in urban terrain elevation may pose problems for conventional SAR imaging

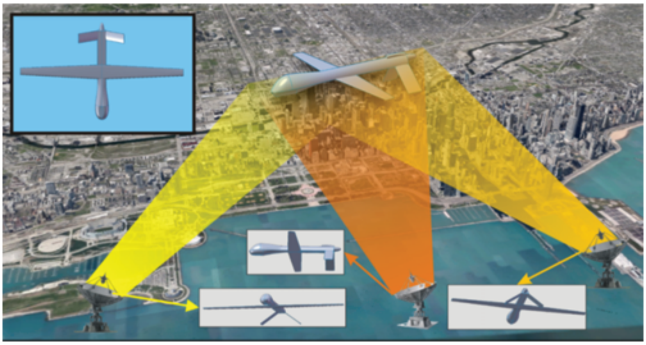

Figure 5.2 3D image reconstruction from 2D projections

monostatic, which may be readily located and jammed. The covertness of a bistatic receiver in a distributed ISAR system may be useful as an electronic protection. Furthermore, when a target does not change its aspect angle relative to the monostatic radar, by heading directly to it for example, ISAR images cannot be formed. A distributed setup of transmitters and receivers can be useful in such a scenario and may also offer additional spatial diversity for target imaging. In a multistatic system using a mix of coherent and incoherent signal processing, a 3D image could be formed using tomographic principles of “reconstruction by projections” [9], as illustrated in Figure 5.2.

Hardware issues can also be a driving factor; in some instances, a narrowband operation may be more advantageous than wideband. It can be shown that the signal-to-noise ratio (SNR) after pulse compression is independent of the bandwidth of the signal. However, classical radar algorithms need the bandwidth to achieve fine range resolution. Using a higher bandwidth may not be the best system option overall.

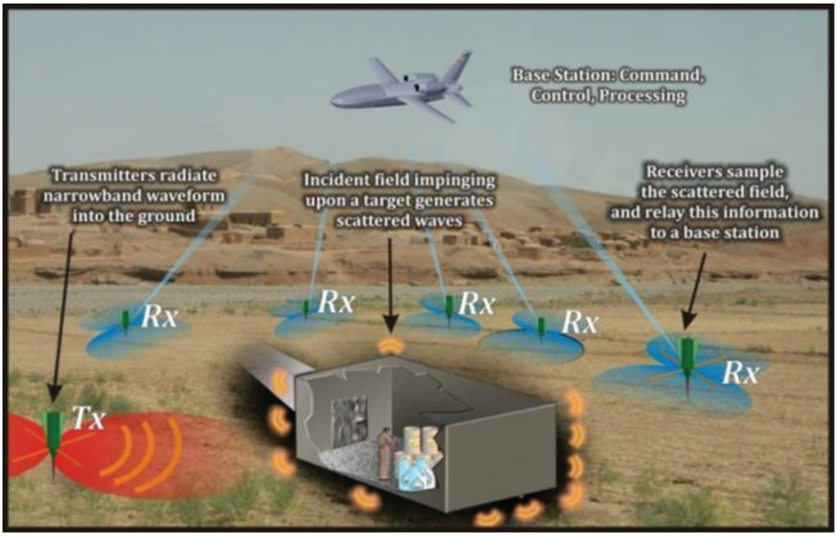
Base Station: Command, Control, Processing
Transmitters radiate narrowband waveform into the ground
Incident field impinging upon a target generates scattered waves
Receivers sample the scattered field, and relay this information to a base station
Rx
Rx
Rx
Rx
Rx
Tx

Figure 5.3 Illustration of tomography as applied to underground imaging of tunnels and caches [11]

For instance, wideband signals may require wideband ADC/DAC, wideband RF design, and, most of all, high-throughput signal processing. These requirements may increase cost, size, weight, and power. Furthermore, the dynamic range of wideband receivers is usually inferior than for narrowband receivers. Also, high-power transmitters are more efficient and easier to construct when operating at narrowband.

Narrowband operation, especially when combined with frequency hopping, may contribute to a capability of low probability of intercept and hence may constitute an electronic protection feature. Narrowband operation may also be dictated by the propagation medium. Imaging of underground networks, such as tunnels or bunkers, is limited to the few narrow frequency windows that are able to penetrate the ground. For instance, tunnels below 20–30 m can be “seen” only with a signal having frequencies up to the few MHz range [10]. Figure 5.3 depicts such an example with a distributed system of unattended sensors on the ground, which relay the received signals to a common platform for processing. Similarly, foliage penetration and building penetration are better achieved using the very high frequency/ultra high frequency (VHF/UHF) frequency regime, where the attenuation losses are minimal.

Narrowband imaging could be extended to passive imaging [12], as illustrated in Figure 5.4. The radiated waveform from sources of opportunity may have poor correlation properties so that pulse compression may generate high sidelobes. As it will be evident later, a distributed system using tomographic principles will be able to reconstruct images with less dependence on the correlation properties of the waveform, since image resolution is in principle determined predominantly by the wavelength of the carrier frequency. Some of the theoretical developments of passive distributed ISAR are discussed elsewhere in this book.

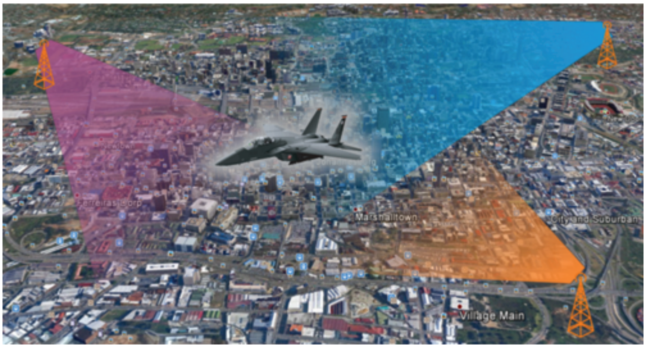

Figure 5.4 Tomography as a possible means to image using illuminators of opportunity

In most applications, the overriding promise of RT is that both spatial and spectral diversities are exploited as resources for target imaging, relaxing the requirement on spectral bandwidth, which means when spectral bandwidth is not available or inhibited, generally a 3D spatial distribution of either the transmitters or receivers or both may be used, or the radar platform maneuvering around the target, or the target itself undergoing a sufficient rotational motion or change of aspect.

In terms of system performance, there are at least three desirable characteristics that make RT very promising in a future practical radar imaging system: adaptability, modularity, and graceful degradation.

5.1.1 Adaptability

In some inaccessible or remote areas, sensors may need to be ejected at a stand-off distance and their placement on the ground is somewhat arbitrary. A distributed imaging system should be able to operate even when the sensor distribution is random, within some predictable limitations. In some instances, randomization of sensor locations could even be beneficial by reducing sidelobes in the reconstructed image.

5.1.2 Modularity

The imaging system would be intrinsically modular, i.e., the addition/removal of active elements is easily implemented: there is no prior requirement of the number of active elements, and the image quality is somewhat directly related to their number, in addition to their location. This implies that the failure of a set of transponders does not compromise the overall system but may affect the accuracy and resolution of the image reconstructions.

5.1.3 Graceful degradation

Distributed imaging should provide the user with a situational awareness of the scene. Particularly, the persistence is guaranteed by the multitude of sensors, and the unintentional (obstruction) or intentional (sabotage) failure of some Tx/Rx units does not preclude the overall image reconstruction process.

The rest of this chapter aims to provide a cohesive and comprehensive theory of multistatic RT, its various forms, and discusses its current and potential applications.

5.2 Tomographic image formation

The processing chain to transform a received radar dataset into a focused target image is commonly called "image formation" or "image reconstruction." To describe this processing chain, a mathematical signal model is required which captures the nature of the transmit signals, the generally multistatic system geometry, target motion, and the received signals. The signal processing algorithms are also required to devise the signal model to process the received data and extract the spatial locations of scatterers. The resulting radar image of a target is essentially an estimation of the spatial distribution of its reflectivity as "seen" by the radar system under a particular condition.

The problem formulation has been covered in various texts, such as [13,14]. Here, we present a different and more general perspective.

5.2.1 Signal models

In this chapter, bold symbols represent 3D vectors, and caret symbols represent unit norm 3D vectors. For simplicity, let us first consider a *planar multi-bistatic* system geometry as illustrated in Figure 5.5, which consists of *one* transmitter denoted as Tx and located at $\boldsymbol{r}_{Tx}$ and M receivers denoted as $Rx_0, Rx_1, \ldots, Rx_{M-1}$ and located at $\boldsymbol{r}_{Rx0}, \boldsymbol{r}_{Rx1}, \ldots, \boldsymbol{r}_{Rx(M-1)}$, respectively, with corresponding bistatic angles $\beta_0\,(=0), \beta_1, \ldots, \beta_{M-1}$ as indicated in the figure. In the special planar geometry, the target, transmitter, and receivers all lie a common plane. In more general geometries to be discussed later, the transmitter and all receivers may be located anywhere in a 3D space and may undergo relative motion as well; their location vectors are all expressed relative to the target-fixed reference frame described later.

A "target" in RT is quite arbitrary; it can be a localized object such as a space object, aircraft or vehicle, or a rotor such as helicopter rotor blades, or it can be an extended object like a large patch of ground on the Earth's surface; each can be roughly characterized by its "size" and the intrinsic motions. For targets that do not undergo their own rotational motion, such as a patch of ground or a vehicle, a local Cartesian frame, denoted as $\mathscr{T}_x$, with axes (x, y, z) and an origin at the *focus point* is sufficient for the imaging formulation. For targets with intrinsic rotational motion, such as a satellite or helicopter rotor, an additional nonrotating frame denoted here as $\mathscr{T}_y$ is necessary, with one of its Cartesian axes chosen to align with the radar line of sight (LOS).* $\mathscr{T}_y$ shares the same origin (or focus point) with $\mathscr{T}_x$ and is the frame to define the rotational velocity vector $\boldsymbol{\Omega}$ of the target. $\mathscr{T}_x$ is the frame for image focusing, fixed to the target, with its z-axis aligned along $\boldsymbol{\Omega}$. For a noncooperative

---

*As will be evidently later, it is convenient to choose the LOS from the radar transmitter.

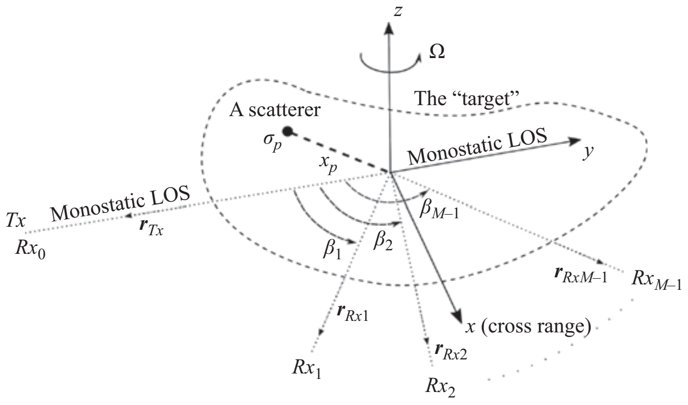

Figure 5.5 System geometry for a planar multi-bistatic scenario, with one transmitter Tx and M receivers Rx_0, Rx_1, …, Rx_{M-1}

target, $\boldsymbol{\Omega}$ (and hence the axis of rotation) is not known a priori, so is the (x, y) plane. For presentational clarity, Figure 5.5 illustrates a special case when $\boldsymbol{\Omega}$ is orthogonal to LOS, and the y-axis is defined to align with LOS at time $t = 0$ (a selected reference time). The general case of unknown $\boldsymbol{\Omega}$ translates to unknown directions of the vectors $\boldsymbol{r}_{Tx}$ and $\boldsymbol{r}_{Rxm}$ which may be inside or outside the (x, y) plane of $\mathscr{T}_x$.

Regardless of $\boldsymbol{\Omega}$, an arbitrary point scatterer (with index p) of the target is supposed to be located at $\boldsymbol{x}_p$, relative to $\mathscr{T}_x$, with a corresponding reflectivity function of $\sigma(\boldsymbol{x}_p)$. The reflectivity function may be defined virtually everywhere in the 3D space; areas or regions that do not have scatterers or reflecting components will simply have $\sigma(\boldsymbol{x}_p) = 0$. As part of the ubiquitous point-scatterer model, σ is assumed isotropic and independent of radar waveform polarization. In the current context, image focusing is relative to the origin of $\mathscr{T}_x$, hence this may also be described as "focusing to a point" (as distinct from "focusing to a line"—a well-known concept in SAR imaging) [15].

The transmit and receive signals can be expressed in either the time domain, or the temporal-frequency domain, or the spatial frequency domain. However, in most applications of RT, the spatial frequency domain is especially useful due to the centrally important role of the PST [1]. Consider a known time-domain transmit signal $s_{Tx}(t)$, which is related to its "temporal spectrum" $S_{Tx}(f)$ and spatial frequency "k-spectrum" $S_{Tx}(k)$ through

$$s_{Tx}(t) = \int S_{Tx}(f) \exp(j2\pi ft)\, df = \int S_{Tx}(k) \exp(jkct)\, dk, \tag{5.1}$$

where

$$k = 2\pi f / c = 2\pi / \lambda \tag{5.2}$$

is the classical scalar "wave number," i.e., angular form of spatial frequency f/c. The transmitter is assumed to radiate a waveform of finite or very narrow bandwidth, corresponding to *wideband* or *narrowband/ultra-narrowband* operations. Without loss of generality, the radiated and scattered waveforms can be considered spherical waves (i.e., isotropic radiators). The phase shift and amplitude attenuation measured at an observation point due to an illuminating source can be mathematically described through Green's functions for time-harmonic fields. In its simplest form, the Green's function relating the illuminator at $\boldsymbol{r}_{Tx}$ with the observation point at $\boldsymbol{x}_p$ is [16]

$$G(\boldsymbol{r}_{Tx}, \boldsymbol{x}_p, k) = \frac{\exp\{-jk|\boldsymbol{r}_{Tx} - \boldsymbol{x}_p|\}}{4\pi\,|\boldsymbol{r}_{Tx} - \boldsymbol{x}_p|}. \tag{5.3}$$

The incident field at the point scatterer at $\boldsymbol{x}_p$ is simply $S_{Tx}(k)G(\boldsymbol{r}_{Tx}, \boldsymbol{x}_p, k)$. By cascading the effect of the Green's function on the scattered path, the signal received at a receiver at $\boldsymbol{r}_{Rxm}$ is

$$\begin{aligned} S_{Rxm}(k) \;&=\; S_{Tx}(k)\sigma(\boldsymbol{x}_p)\left(\frac{\exp\{-jk|\boldsymbol{r}_{Tx} - \boldsymbol{x}_p|\}}{4\pi\,|\boldsymbol{r}_{Tx} - \boldsymbol{x}_p|}\right) \\ &\quad \times \left(\frac{\exp\{-jk|\boldsymbol{x}_p - \boldsymbol{r}_{Rxm}|\}}{4\pi\,|\boldsymbol{x}_p - \boldsymbol{r}_{Rxm}|}\right) \end{aligned} \tag{5.4}$$

in the k-domain, which represents the forward electromagnetic model used in RT.

Strictly speaking, (5.4) involves several simplifying assumptions, even at this early stage of the theoretical formulation: it does not account for the polarization of the wave, does not include the antenna radiation pattern, and, most of all, assumes that $\sigma(\boldsymbol{x}_p)$ is independent of the illumination and observation angles, i.e., the "point-scatterer model." In the real world, these assumptions may not hold; they are nevertheless useful as a first approximation which can yield at least initial insights into the more realistic and complex problems.

A *fully multistatic* geometry involving *multiple transmitters* may be modeled as a number of such multi-bistatic systems, with the transmitters employing orthogonal waveforms as in the case of MIMO radar systems. Then, (5.4) would remain the same except that the quantities $\boldsymbol{r}_{Tx}, S_{Tx}(k)$ and receive signals $S_{Rxm}(k)$ require indexing also with respect to the transmitters, leading to an extra degree of complexity in the signal model (refer to Section 5.2.2.2).

Equations of the form (5.4) lead to two broad classes of imaging methods, namely *Fourier-based* methods and *matrix-based* methods. The first class makes use of the *far-field approximation*, also known as "Fraunhofer approximation," which assumes that the illuminated target dimension is small compared to both transmitter and receiver ranges. This class can allow for computationally very efficient algorithms to compute images based on the Fourier transform, which is critical when dealing with large volumes of data in real time. It also gives rise to the theoretically elegant concept of k-spaces. The second class of matrix methods does not assume such an approximation and, hence, is inherently more exact and is most applicable in *near-field* conditions, i.e., when the target is an extended target at relatively close range to the radar antennas and the plane-wave assumption does not hold.

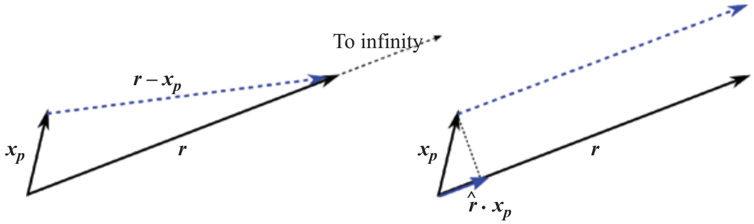

Figure 5.6 Near-field (left) and far-field (right) geometries. Here, $\boldsymbol{r}$ *denotes either* $\boldsymbol{r}_{Tx}$ *or one of the* $\boldsymbol{r}_{Rxm}$ *vectors*

The abovementioned class separation is approximate; some well-known reports on near-field radar imaging, such as in [15], have been based also on Fourier analysis. We will return to this point later in Section 5.2.3.

5.2.2 Fourier-based methods

Fourier-based methods involve some form of linearization to simplify the analysis; in this case, linearization is applied to the modulus factors of the Green's functions of (5.3). This section discusses the far-field approximation, the fast-time k-space, and the various effects imposed on the resulting imagery by radar waveform, system geometry, and relative target motion.

5.2.2.1 The far-field approximation

Figure 5.6 illustrates the single-path geometry for this approximation. For the phase factor in the numerator of (5.3), the scatterer range on the transmit path is approximated as

$$|\boldsymbol{r}_{Tx} - \boldsymbol{x}_p| \approx |\boldsymbol{r}_{Tx}| - \hat{\boldsymbol{r}}_{Tx} \cdot \boldsymbol{x}_p, \tag{5.5}$$

while for the denominator, which affects only the amplitude of the signal return, $|\boldsymbol{r}_{Tx} - \boldsymbol{x}_p| \approx |\boldsymbol{r}_{Tx}|$. Here, $\hat{\boldsymbol{r}}_{Tx}$ is a unit vector in the direction of $\boldsymbol{r}_{Tx}$. Analogous expressions can be written for $|\boldsymbol{r}_{Rxm} - \boldsymbol{x}_p|$ for the receive paths. The Green's functions then take a simpler form

$$G(\boldsymbol{r}, \boldsymbol{x}_p, k) \approx \frac{\exp\{-jk|\boldsymbol{r}|\}}{4\pi|\boldsymbol{r}|} \exp\{jk\hat{\boldsymbol{r}} \cdot \boldsymbol{x}_p\}, \tag{5.6}$$

which will significantly simplify the receive signals. Equation (5.6) also *separates* the bulk translational motion (the first range-dependent phase factor) from the target's local geometry and rotational motion (the second phase factor); the separability embellishes the power of the far-field approximation.

5.2.2.2 Multistatic fast-time *k*-space and image inversion

Again, let us first consider a single-transmitter system. Substituting (5.6) into (5.4), the receive signals become

$$\begin{aligned} S_{Rxm}(k) &= S_{Tx}(k)\sigma(\boldsymbol{x}_p)\,\frac{\exp\{-jk(|\boldsymbol{r}_{Tx}|+|\boldsymbol{r}_{Rxm}|)\}}{16\pi^2|\boldsymbol{r}_{Tx}|\,|\boldsymbol{r}_{Rxm}|} \\ &\quad \times \exp\left\{jk(\hat{\boldsymbol{r}}_{Tx}+\hat{\boldsymbol{r}}_{Rxm})\cdot\boldsymbol{x}_p\right\}. \end{aligned} \tag{5.7}$$

The factors

$$A_m(k) \equiv \frac{\exp\{-jk(|\boldsymbol{r}_{Tx}|+|\boldsymbol{r}_{Rxm}|)\}}{16\pi^2|\boldsymbol{r}_{Tx}|\,|\boldsymbol{r}_{Rxm}|} \tag{5.8}$$

in (5.7), for $m = 0, 1, \ldots, M-1$, capture the translational motion of the target as a whole and attenuation effects of bistatic ranges, while the next phase term captures the structure and rotational motion of the target, relative to the mth bisector.

The fast-time k-space

Generally, the 3D vector

$$\begin{aligned} \boldsymbol{k}_m &= -k(\hat{\boldsymbol{r}}_{Tx}+\hat{\boldsymbol{r}}_{Rxm}) \\ &= -2k\cos(\beta_m/2)\,\hat{\boldsymbol{r}}_{bis,m} = -(4\pi/\lambda)\,\cos(\beta_m/2)\,\hat{\boldsymbol{r}}_{bis,m} \end{aligned} \tag{5.9}$$

is defined as the *bistatic* ***k****-vector* for the mth receiver, where β_m is the corresponding bistatic angle and

$$\hat{\boldsymbol{r}}_{bis,m} = \frac{(\hat{\boldsymbol{r}}_{Tx}+\hat{\boldsymbol{r}}_{Rxm})}{\|\hat{\boldsymbol{r}}_{Tx}+\hat{\boldsymbol{r}}_{Rxm}\|_2}$$

is the unit vector along the mth bisector direction. Two remarks could be made:

- The minus sign in (5.9) is selected only for convention, so that the final formulas resemble the ones commonly used in spotlight SAR and computer tomography. (This arises from the choice of $\hat{\boldsymbol{r}}_{Tx}$, $\hat{\boldsymbol{r}}_{Rxm}$, and $\boldsymbol{x}_p$ being expressed relative to the local target frame.)
- The magnitude of a fast-time k-space vector is $2\cos(\beta_m/2)$ times the scalar wavenumber k. (See Section 5.2.4.2 for a comparative discussion with the slow-time k-space.)

With the definition in (5.9), the centrally important phase factor in (5.7) for target imaging simplifies to $\exp\left\{-j\boldsymbol{k}_m\cdot\boldsymbol{x}_p\right\}$ which directly and simply indicates $\boldsymbol{k}_m$ as a *spatial frequency space*, as $\boldsymbol{x}_p$ is a spatial domain we wish to estimate. At each target aspect, signal bandwidth (or an equivalent interval of k) defines a 1D spatial frequency support, called a "1D k-space."

If the target rotates around a *constant axis* of rotation relative to $\hat{\boldsymbol{r}}_{bis,m}$, the $\boldsymbol{k}$-vectors would sweep out a general conic surface in 3D k-space, with the vertex at the origin of $\mathscr{T}_x$. In the special case of $\boldsymbol{\Omega}$ orthogonal to LOS, the surface is reduced to a 2D k-space, as illustrated [17] in Figure 5.7. The diagram on the left of Figure 5.7 illustrates the support from a single receiver, for several discrete frequencies, as an

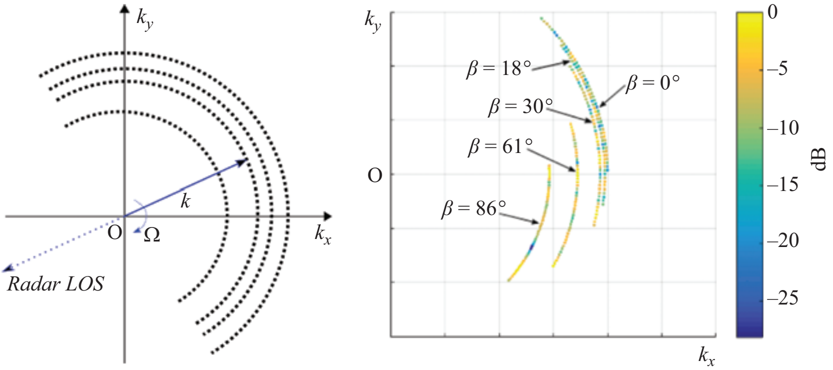

Figure 5.7 Illustration of the 2D fast-time k-space for (left) one receiver and several discrete frequencies, and (right) five receivers and one frequency

example, while the diagram on the right shows a typical support populated by five receivers at various bistatic angles, for a single frequency (for clarity) [18]. A radar waveform with finite contiguous bandwidth would replace the circular traces with an annulus (or part of) as the support.

If the target rotates around a *nonconstant* axis of rotation, or if there are multiple antennas viewing at the target from different aspects, the $\boldsymbol{k}$-vectors generally form a region in 3D k-space. Regardless of dimensionality, these regions in k-space are also called *k-space supports* of the imaging radar system.

More precisely, these are *fast-time k*-spaces since k in this formulation is defined only by the carrier frequency f and the bistatic radar LOS direction, and their axes are aligned with the target-fixed local frame defined earlier.

Populating a fast-time k-space

We refer to signals populating a k-space support as (derived) “measurement signals” or “measurement samples” if a target image can be obtained with an inverse FT applied on them. Let us consider the possible forms of such signals.

Substituting (5.8) and (5.9) into (5.7), we obtain

$$S_{Rxm}(\boldsymbol{k}_m) = S_{Tx}(k)A_m(k)\sigma(\boldsymbol{x}_p)\exp\left(-j\boldsymbol{k}_m \cdot \boldsymbol{x}_p\right). \tag{5.10}$$

Under the Born (single-bounce, or “linearized inverse scattering”) approximation, the scattered field from a distributed target having reflectivities $\sigma(\boldsymbol{x}_p)$ defined over a 3D volume V is simply the linear superposition of its point scatterers, i.e.,

$$S_{Rxm}(\boldsymbol{k}_m) = S_{Tx}(k)A_m(k) \iiint_V \sigma(\boldsymbol{x}_p)\, \exp\left(-j\boldsymbol{k}_m \cdot \boldsymbol{x}_p\right)\, d\boldsymbol{x}_p. \tag{5.11}$$

The factors $S_{Tx}(k)$ and $A_m(k)$, respectively, represent the effects of radar waveform and system motion, which need to be known or estimated. Theoretically,

$$S'_{Rxm}(\boldsymbol{k}_m) = S_{Rxm}(\boldsymbol{k}_m)/S_{Tx}(k)A_m(k) \tag{5.12}$$

$$= \iiint_V \sigma(\boldsymbol{x}_p)\ \exp\big(-j\boldsymbol{k}_m \cdot \boldsymbol{x}_p\big)\ d\boldsymbol{x}_p \tag{5.13}$$

represents the ideal measurement signals we seek, since the left-hand side of (5.13) is a measurable slice of the FT of $\sigma(\boldsymbol{x}_p)$ at $\boldsymbol{k}_m$, and the PST tells us that by assembling those slices in the k-space over a $\boldsymbol{k}_m$ support, $\sigma(\boldsymbol{x}_p)$ can be obtained by an inverse transform. However, the division operation in (5.12) is *numerically unstable*, making $S'_{Rxm}(\boldsymbol{k}_m)$ an unpractical choice.

A more practical and robust option is to use *matched filtering* and *translational motion compensation* (TMC) processing and compute

$$S''_{Rxm}(\boldsymbol{k}_m) = S_{Rxm}(\boldsymbol{k}_m)\,S^*_{Tx}(k)\ \exp\{-j\phi_m(k)\}, \tag{5.14}$$

where $\phi_m(k)$ is the phase function of $A_m(k)$, assumed known or estimated. The factor $S_{Tx}(k)$ would have its phase negated and affect the measurement signals only as an "amplitude weighting window," $|S_{Tx}(k)|^2$. The values of $S''_{Rxm}(\boldsymbol{k}_m)$ are then placed at k-space locations given by (5.9), which can also be interpreted as the Fourier transform of the target's estimated *range profile* at the aspect of $\boldsymbol{k}_m$.

An estimation of the reflectivity function, i.e., the theoretical target image, can be obtained via an image inversion

$$\sigma(\boldsymbol{x}_p) = \iiint_{V_k} \big\{\cup_m S''_{Rxm}(\boldsymbol{k}_m)\big\}\ \exp\big(j\boldsymbol{k} \cdot \boldsymbol{x}_p\big)\ d\boldsymbol{k}, \tag{5.15}$$

where the $\cup_m$ symbol represents a union (co-population) in k-space of samples from all M receivers. This theoretical expression is simply a classical 3D *inverse Fourier transform*, with V_k denoting the combined 3D k-space support. It also justifies the term "Fourier-based methods" used for this class of methods.

In the particular case of spotlight SAR, for example, the sweeping of $\boldsymbol{k}$ may be achieved by maneuvering the radar receiver (or transmitter) platform over some trajectory around the target. Under the Fraunhofer approximation, no multi-bounce scattering assumption and no depolarization effects (i.e., scalar electric fields) are included, and there exists a simple Fourier relation between the measured data over a prefixed collection trajectory and its associated image, as illustrated in Figure 5.8.

Extension to a full multistatic geometry

Full multistatics means the radar system generally comprises more than one transmitter and more than one receiver. As mentioned in Section 5.2.1, the following changes (arising from transmitter indexing) are required. For the 3D vectors: $\boldsymbol{r}_{Tx} \rightarrow \boldsymbol{r}^{(n)}_{Tx}$, $\hat{\boldsymbol{r}}_{Tx} \rightarrow \hat{\boldsymbol{r}}^{(n)}_{Tx}$, $\hat{\boldsymbol{r}}_{bis,m} \rightarrow \hat{\boldsymbol{r}}^{(n)}_{bis,m}$, and $\boldsymbol{k}_m \rightarrow \boldsymbol{k}^{(n)}_m$. For the bistatic angles: $\beta_m \rightarrow \beta^{(n)}_m$. For the signals: $S_{Tx}(k) \rightarrow S^{(n)}_{Tx}(k)$, $S_{Rxm}(\boldsymbol{k}_m) \rightarrow S^{(n)}_{Rxm}(\boldsymbol{k}^{(n)}_m)$, and $A_m(k) \rightarrow A^{(n)}_m(k)$. Most

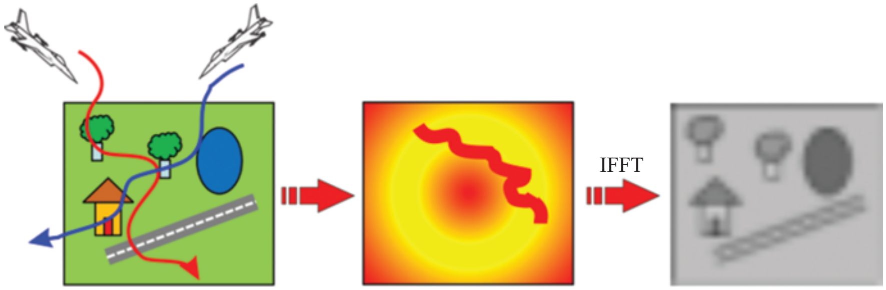

Measuring scattered fields

Filling k-space

Image domain

Figure 5.8 Illustration of relationship between image domain and k-space

quantities are augmented with an additional dimension, except for the scatterer location vectors $\boldsymbol{x}_p$ which are referenced to its own target-fixed coordinate system.

Note that all 3D vectors are expressed with respect to the $\mathscr{T}_x$ frame, which is aligned with the transmitter Tx, chosen to be the "reference transmitter"; the directional offset of an additional transmitter leads to a corresponding angular offset in the common k-space, which in turn may provide a larger volume of support for generally 3D target imaging [19]. The inversion in (5.15) may be generalized to

$$\sigma(\boldsymbol{x}_p) = \iiint\limits_{V_k} \left\{ \cup_{m,n} S''^{(n)}_{Rxm}\left(\boldsymbol{k}^{(n)}_m\right) \right\} \exp\left(j\boldsymbol{k}\cdot\boldsymbol{x}_p\right)\, d\boldsymbol{k}. \tag{5.16}$$

Here, the symbol $\cup_{m,n}$ represents a union of measurements from all available transmitter–receiver channels.

5.2.2.3 Image focusing controls

"Image focusing controls" (IFCs) refer mainly to three different processing algorithms: matched filtering, motion compensation, and channel synchronization, which affect the focusing of a target image. While a thorough discussion of these topics is beyond the scope of this chapter, a general description is given as follows.

In most radar imaging systems, *matched filtering* and *TMC*, in one form or another, are a necessary and integral part of a complete image focusing process; channel synchronization is necessary only for multichannel systems.

Matched filtering is highlighted by the product $S_{Rxm}(\boldsymbol{k}_m)S^*_{Tx}(k)$ in (5.14) which is applicable to all received signals from all transmitters; the effect of a nonideal (non-impulse) waveform is reduced to a numerically robust amplitude weighting window on the k-space support. For active radars in general, this is quite straightforward, since the transmit waveform is precisely known and readily available to the radar receiver. Interestingly, otherwise "mismatched filtering" can sometimes be useful as a detector of phenomena of interest, such as of vibrating targets [20]. Vibrational motion is a type of micro-Doppler motion which could manifest itself as a "fuzzy ball" in a SAR image, which could be masked in the k-space. For passive radars, $S_{Tx}(k)$ may be measured through the reference channel of the system by pointing the reference antenna directly at the transmitter; risks of signal contamination by the environment, however, do exist.

TMC processing to estimate the phase factor $\exp\{-j\phi_m(k)\}$, on the contrary, may not be so straightforward, even when platform motion is under the radar operator's control; errors in the inertial motion units can be significant enough to require sophisticated algorithms for accurate compensation. Noncooperative target motions in generally multistatic scenarios could be even more challenging, especially in the presence of complex 3D target motion. When wide changes of target aspect exist, which affect also the *locations* of the measurement samples in k-space, sufficiently accurate estimation of the rotational motion is necessary.

Channel synchronization includes accurate time stamping across the channels, correction for propagation phase differences, and errors in the bistatic angles $\beta_m^{(n)}$, to ensure that the placements of the measurement samples are at the correct locations in the combined k-space referenced to single instant in time. Errors in these estimates can have a significant impact on image focusing; a discussion for the narrowband cases of these effects is given in [18].

5.2.2.4 System diversities

We have noted that tomographic imaging performance measures generally depend on the "size" of the k-space support which can be generated by both signal bandwidths, i.e., spectral diversity and the total extent of target aspect (or rotational motion), i.e., spatial diversity. The definition of a general bistatic fast-time $\boldsymbol{k}$-vector in (5.9) namely

$$\boldsymbol{k} = -\left(\frac{4\pi}{c}\right) f \cos\left(\frac{\beta}{2}\right) \hat{\boldsymbol{r}}_{bis}, \tag{5.17}$$

succinctly captures the *equivalence* of these two types of system diversity. At a single radar frequency f and a bistatic angle β, the effective radar frequency is $f\ \cos(\beta/2)$, which implies that cross-range motions of the transmit or receive antennas (which result in changes in the bistatic angle during a coherent processing interval (CPI)) can be used to generate an equivalent signal bandwidth.

Figure 5.9 illustrates a simple example in which the radar is monotone at 10 GHz and the transmitter and receiver maneuvers are symmetric such that the bisector direction at the target remains fixed, $\hat{\boldsymbol{r}}_{bis}$ is constant, and $\boldsymbol{k}$ traces out an interval corresponding to a bandwidth between 9 GHz and 100 MHz. In such case, the received samples may be used to form *one* range profile with resolution $\delta r = c/(2 \times 8.999 \times 10^9) \approx 17$ cm.

More general variations of β in this example would have $\hat{\boldsymbol{r}}_{bis}$ changing direction as well, leading to some circular-trace population of the samples in the k-space [13,14]. In fact, in the previous example, if (say) the transmitter "stays" at the same direction while the receiver maneuvers around the target to the other side, the linear trace in the k-space in Figure 5.9 would be replaced by an exact semicircular trace, as illustrated in Figure 5.10, which projects the generated effective bandwidth on *both* range and cross-range dimensions. When β is fixed while the target itself is rotating relatively to the radar, a circular arc similar to those in Figure 5.7 is formed

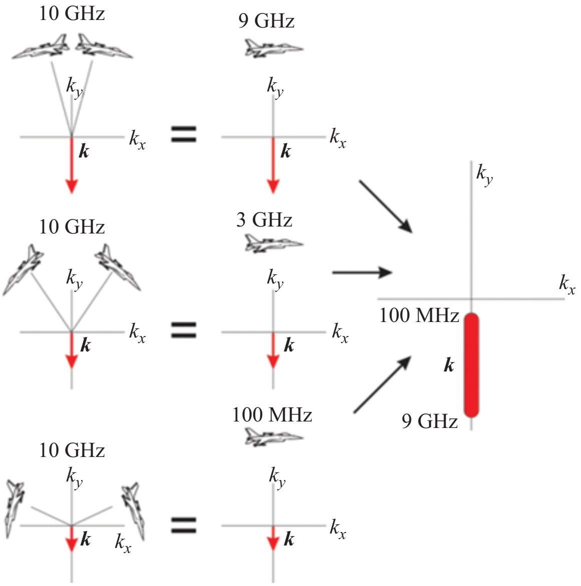

Figure 5.9 Transmitter and receiver motions can generate an effective wide bandwidth for a radar of single frequency

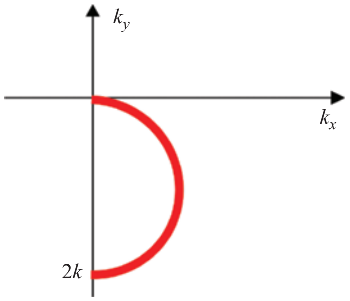

Figure 5.10 A semicircular trace as the k-space support is formed when the transmitter stays fixed at one aspect while the receiver maneuvers to the opposite side

in the k-space. When both target rotation and radar maneuvering exist, a trace with arbitrary shape may be expected. Finally, when a nonzero bandwidth also exists in the transmit and receive signals, the curvilinear trace is replaced with a 2D support with a corresponding "thickness" in the radial k dimension. The fast-time k-space is indeed a very convenient tool to describe the equivalence of the spectral and spatial diversities: they are two dimensions of the same space.

The radial component (i.e., along a bisector direction) of the target's translational motion needs to be estimated and compensated—the objective of TMC processing discussed earlier. The orthogonal (cross-range) component, on the other hand, can *induce* a rotational velocity useful for imaging. For the simpler case of a monostatic radar, this is given by

$$\boldsymbol{\Omega}_{tr} = (\hat{\boldsymbol{r}} \times \boldsymbol{v})/|\boldsymbol{r}|, \tag{5.18}$$

where $\boldsymbol{v}$ is the target's translational velocity. Hence, translational motion can be the *source* of induced (or effective) rotational motion—a system diversity for imaging.

Finally, orthogonal waveform diversity, as in MIMO radar systems, can be useful in creating separate channels in a fully multistatic system, with their separate corresponding matched filtering and TMC processing, to broaden the combined k-space. Each type of diversity can be used to enhance the "total imaging performance" of the imaging radar system, with an appropriate additional computational cost.

5.2.2.5 The nonuniform FFT for image inversion

The inverse transform operation in (5.15) or (5.16) depends on two factors: how uniformly (or nonuniformly) the samples are populated in the measurement k-space and the overall shape of the support V_k. As implied in the definition of a $\boldsymbol{k}$-vector in (5.9), the k-space reference frame is fixed to the target, whereas the direction of $\boldsymbol{k}$-vector is that of the radar LOS, the measurement samples can thus be irregular in angle and the shape of V_k can be strongly non-rectangular.

First, for a single-receiver system, when target view extents are more than a few degrees, the support V_k necessarily takes on a polar (non-rectangular) format. Second, when target's change of aspect (or effective rotation motion) is nonuniform, which is very likely in practice, the angular spacing of the samples is also nonuniform. Third, in a multi-bistatic geometry, a bistatic angle β_m, which may be arbitrary, can rotate and "shrink" the locations of the samples by a corresponding arbitrary $\cos(\beta_m/2)$ factor. Finally, due to possible lack of relative motion, V_k is most likely to be very different from a perfect circular support in 2D or a perfect spherical support in 3D. Any of these factors can disrupt the regularity of the samples and remove any symmetry of the support V_k of a k-space; the inverse transform for image inversion cannot always rely on the traditional Fourier transform or FFT.

It is possible to bridge the gap by performing a data interpolation to a regular grid prior to a discrete Fourier transform. Several techniques can be used for interpolation; however, the procedures are computationally intensive. A more efficient alternative is to use the nonuniform FFT (NUFFT) [21]. This is a recent development that is paving the way for tomography to become a technique suitable for real-time processing. NUFFTs still have a computational cost on the order of $N \log_2 N$ and can handle nonuniformly spaced samples very efficiently.

The NUFFT has been used in many fields of science, such as medical imaging, subsurface sensing, and recently radar imaging [22–24]. In fact, there are two types of NUFFT: Type 1 evaluates a nonuniformly sampled Fourier series to a regular mesh; this is the typical transformation used to construct an image from k-space data. Type 2 evaluates a regularly spaced Fourier series at irregular target points; this is a transformation that is useful to determine the k-space for a given image. It finds applications for simulating environments as well as for special iterative techniques aimed at reducing the sidelobes of the final image.

The NUFFT is used also for the companion slow-time k-space described in Section 5.2.4.2, for similar reasons.

5.2.2.6 Image resolution and contrast

Assuming that IFCs have been processed for all receive signals, then imaging performance depends on how "fully and broadly" the k-space support is populated. Basic properties of the Fourier transform generally imply the following:

- The broader the k-space in both radial (spectral bandwidth) and angular (rotation angle) directions, the higher (finer) the image resolution. In other words, image resolution can be improved by collecting many range profiles at diverse target aspects and/or using waveforms with higher bandwidths.
- A sparser sample population corresponds to higher sidelobes, hence lower image contrast, but it does not significantly impact image resolution.

2D k-space

Consider the simpler case of 2D imaging, which results when all $\boldsymbol{k}$-vectors are coplanar. A numerical example is shown in Figure 5.11, for a hypothetical radar with signal bandwidth extending from zero to some maximum frequency, and a full cycle of target rotation (i.e., a *full view* of the target). Image resolution is determined by the extent of the k-space, not by the number of samples. Here, two k-spaces have the same extent but different sample densities. The PSFs have approximately the same main lobe width, i.e., same resolution, but different sidelobe levels, and hence different image contrast.

A detailed characterization of this 2D case is presented in [17] and summarized in Figure 5.12. A radar waveform with finite bandwidth typically spans over a certain frequency range, giving rise to a donut shape in k-space, with k ranging between $k_{\min} \geq 0$ and $k_{\max}$. The PSF in this case is available in closed form, in terms of the Bessel function of the first order (J_1),

$$g_\sigma(r) = \frac{2\pi}{r}\left[k_{\max} J_1(k_{\max} r) - k_{\min} J_1(k_{\min} r)\right], \tag{5.19}$$

where r is a radial deviation from the position of a scatterer. In the limit of $k_{\min} = 0$, the PSF has the lowest sidelobe levels, hence optimal image contrast. The normalized response function $J_1(z)/z$, where $z = k_{\max} r$, has a shape as shown by the blue solid curve in Figure 5.12, with the first zero at $z_1 \approx 3.84$. If the first null is used as a measure of image resolution, then

$$r_{\min} \approx \frac{3.84}{k_{\max}} \approx \frac{\lambda_{\min}}{3.27} \tag{5.20}$$

is the mainlobe radius of the PSF, a sub-wavelength resolution performance. Note that $k_{\max} = 4\pi/\lambda_{\min}$, and the first (power) sidelobe (at $z \approx 5.2$) is -17.7 dB. A "two-sided 3-dB resolution" measure, also known as the "full width at half maximum," may be defined as $\Delta r \approx r_{\min}$.

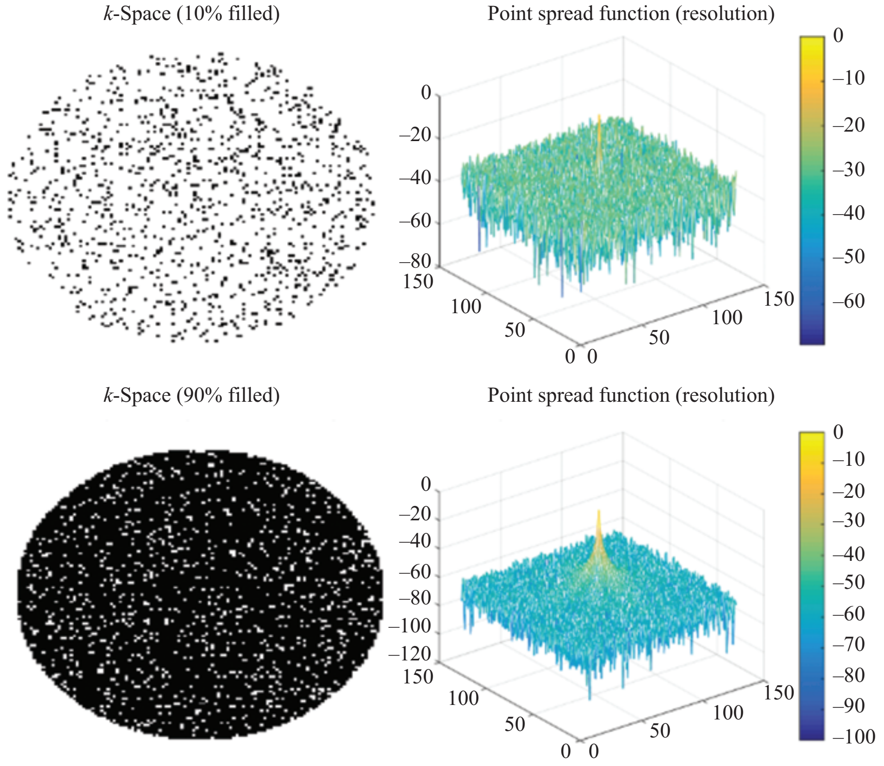

Figure 5.11 A simulation to illustrate the factors affecting image qualities. Upper: "thinned" k-space population leading to low image contrast; lower: denser population, same support, leading to same image resolution and improved image contrast

In the narrowband limits of $k_{\min} \approx k_{\max}$, (5.19) tends to be a simpler form involving the Bessel function of zero order, J_0,

$$g_\sigma(r) \propto k_{\max} J_0(k_{\max} r) \tag{5.21}$$

a normalized form which is illustrated by the dotted curve in Figure 5.12: the first zero of the narrowband response narrows down to $z_1 \approx 2.41$, while the first (power) sidelobe level increases to approximately -8.0 dB at $z \approx 3.84$. Thus, the response mainlobe actually reduces but sidelobe levels significantly increase, leading to a "grainy and noisy" look in resulting images. This prediction agrees with the observation in Figure 5.11.

In cases of *limited view* of the target, i.e., partial target rotations or aspects, circular symmetry of the k-space is broken, the exact PSF is generally not expressible in any closed form, and image resolution is generally not isotropic. However, it can be heuristically predicted that target resolution in a certain direction is generally and approximately determined by the overall extent of the k-space in that direction, while

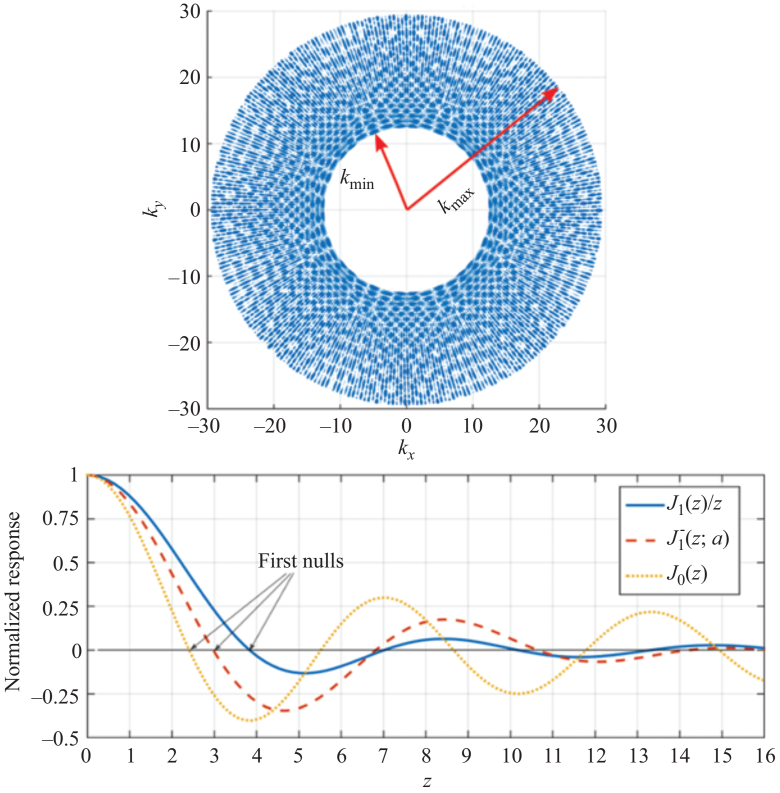

Figure 5.12 A 2D k-space support (top) and possible mainlobe responses. Blue solid curve: $k_{min} = 0$, orange curve: $k_{min} = k_{max}$. Here, $z = k_{max}r$

the density of the populating samples determines sidelobe levels and hence image contrast.

3D k-space

This case arises when the ***k***-vectors are not coplanar. In the ideal cases of *full view*, the k-space support would generally take the form of a hollow 3D sphere, while resolution and sidelobe performance predictions can be expected to be analogous to the 2D case. In the practically more likely cases of *limited view*, numerical analysis offers probably the viable means to assess imaging performance.

Details of derivations on resolution limits in both 2D and 3D cases are included in Appendix A.

5.2.2.7 An experimental demonstration

3D measurements would be ideal to demonstrate the full capability of RT; nevertheless, 2D measurements can still be useful for concept demonstration in the reduced cases of 2D imaging.

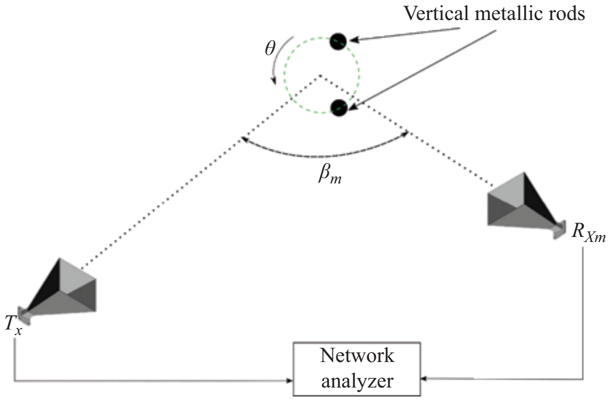

Figure 5.13 Diagram of the experimental setup showing the location of the two vertical metallic rods in a bistatic arrangement

Here, the experimental investigation reported in [18] is summarized in the current notation. The datasets were collected in the Mumma Radar Laboratory at the University of Dayton, Ohio, USA. The laboratory was an anechoic chamber, with transmit and receive horn antennas mounted on separate robotic arms which could be oriented and positioned with high precision. The experimental target consisted of two vertical metallic rods, separated by 19 cm, emulating two point scatterers which rotated around a vertical pedestal, as illustrated in Figure 5.13. A wideband waveform at X-band was used with stepped-frequency pulses between 8 and 12 GHz, over 101 regular frequency steps. For each transmitter–receiver configuration, the antennas were kept stationary whilst the target was rotated through 360°, at 1° steps. At each step, an rectangular single-frequency pulse was transmitted and one sample was taken of the received pulse. These samples thus represent the direct frequency-domain measurements $S_{Rxm}(\boldsymbol{k}_m)$. The nominal values of the bistatic angles were 0° (monostatic), 25°, 35°, 60°, and 90°. These angles, and the propagation phases of the $A_m(k)$ factors in (5.11), require some "self-focusing tuning" prior to image processing.

First, TMC processing and removal of extraneous clutter components specific to the lab environment. This was achieved by transforming the frequency-domain data to range profile domain and a phase factor $\phi_m(k)$ such that the center of the sinusoid traces is shifted to the center of the range window—a "crude" form of TMC processing, which is sometimes called "range alignment." Then, signal values in range bins outside those occupied by the sinusoidal traces are set to zero—most of the clutter is removed, as indicated in Figure 5.14. The data is then converted back to the frequency domain, which can be used for investigations on both wideband and narrowband tomographic imaging.

Next, estimations of the bistatic angles β_m. This could be achieved via either comparing the crossing points of sinusoidal traces in range profile domain between the monostatic and bistatic configurations or by image contrast. Without going into details [18], the refined bistatic angles used in particular this experiment were found to be 0°, 18°, 30°, 61°, and 86°.

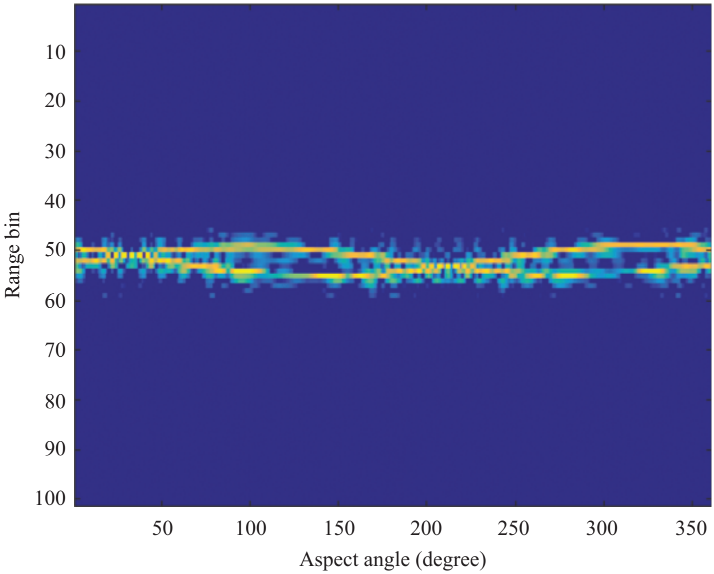

Figure 5.14 Range profiles after laboratory clutter removal and before range alignment

The final step is populating the preprocessed samples and image inversion, using the NUFFT. Some of the results are presented in Figure 5.15, ranging from using all frequencies available (widest k-space support) to more limited cases in sample densities and support extent.

5.2.2.8 Numerical methods for image optimization

When the k-space support is finite and irregular, a *weighting window* may be designed for a desirable balance between mainlobe width and sidelobe levels of the PSF, i.e., a balance between image resolution and image contrast. Such a weighting window would be multiplied with the samples in the k-space support prior to the inverse FT processing for image inversion.

One approximate but promising method for 2D imaging is the "alternate projection" method or "projections onto convex sets (POCS)" [25–28]. As explained in [27], for example, POCS involves a set theoretic formulation—finding a solution as an intersection of "property sets" rather than by a minimization of a cost function. Each property set is constructed in such a way that it contains all solutions to the problem obeying one particular property; an intersection of all property sets, if it exists, obeys all of the properties selected.

In the present context, one such property is the band-limited nature of the received signal—the frequency samples outside the available frequency support are set to zero or near zero. The second property is the (iteratively) modified PSF to be within a certain tolerance of the desired modified response.

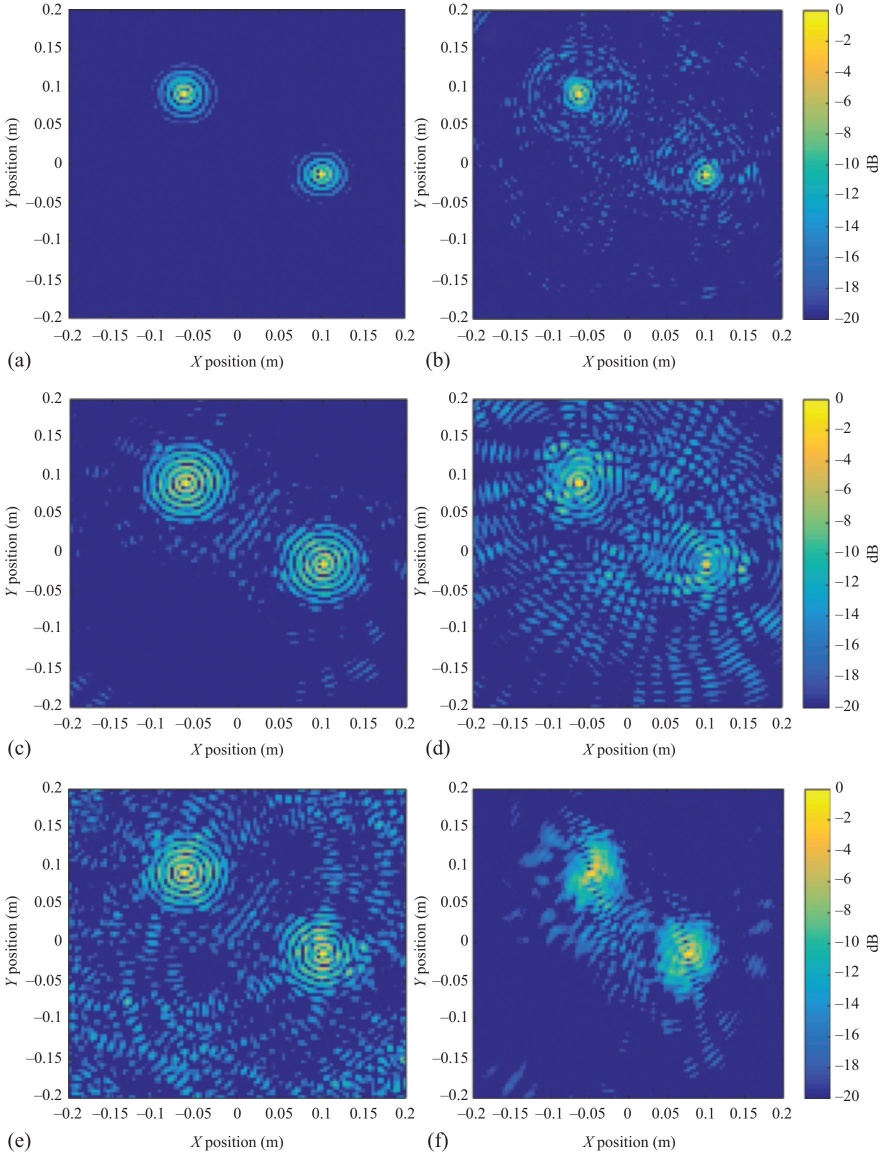

Figure 5.15 *Experimental results: (a) using all frequencies and all five receivers; (b) with 8, 10, and 12 GHz, and all five receivers; (c) with 8, 8.5, and 9 GHz, and all five receivers; (d) with a single frequency 8 GHz and all five receivers; (e) with 8, 8.5, 9 GHz, all five receivers, with samples spaced 6° apart; (f) same as in (c) but only with half cycle of the target's rotation*

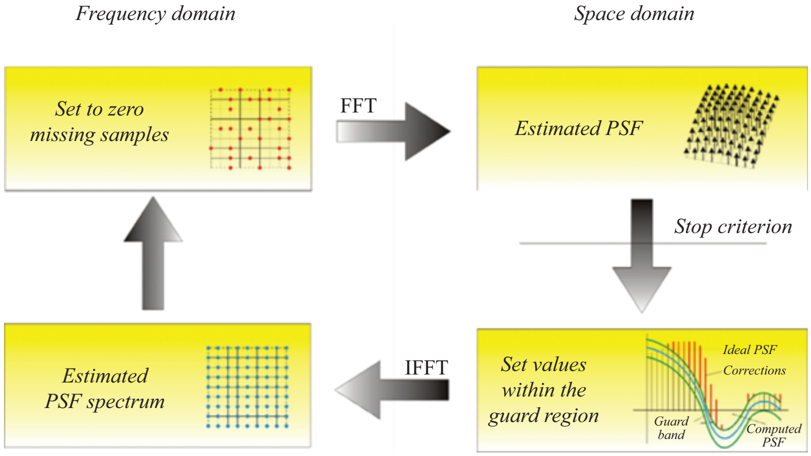

Figure 5.16 An illustration of the POCS algorithm

POCS methods are iterative. In radar imaging, a POCS algorithm to compute the weighting window is illustrated in Figure 5.16 and can be summarized as follows:

1. Preset or define the desired modified nonideal PSF (the airy function calculated at the carrier frequency is a possible choice);
2. Set the initial value of all weights in the available k-space support to unity;
3. Perform an inverse FT (either uniform or nonuniform) of the incomplete data. The result of this operation is the PSF specific to the transmitter/receiver geometry. Generally, the initial PSF may be smeared;
4. For those values of this evolving PSF that are outside a certain margin of the desired PSF, set them to those of the desired PSF. This operation is called a "mask";
5. The adjusted PSF is transformed back to the k-space domain using a FT, either uniform or nonuniform. If the uniform FFT is selected, then all the samples in the k-spaces that cannot exist (due to the geometry) shall be set to zero;
6. The resulting k-space is then transformed back to the image domain, and a new mask with more restrictive margins is applied;
7. These FT/inverse FT iterations are repeated until the designed PSF is contained within some tolerances in the mask.

5.2.3 Matrix-based methods

The Fourier-based methods for image formation are valid especially in the far-field approximation given by (5.5), or equivalently when the target dimension (or area of interest) is bounded relative to its range as given by (5.49). Beyond that limit—when the target is well within the near field—the $\boldsymbol{k}$-vector as in (5.9) cannot be linearly coupled with a scatterer's position as $(\boldsymbol{k}_m \cdot \boldsymbol{x}_p)$. A "range curvature" exists which must be fully taken into account [15] (and references therein). In such cases, matrix-based methods may be useful, which are closely related to the back-projection algorithm (BPA).

In terms of nomenclature, matrix-based methods are, strictly speaking, not tomography; the fundamental PST of tomography does not apply, and there are no k-spaces. Nevertheless, in the sense of spatial diversity and the aim of reconstructing a 3D target image from multiple spatially distributed receivers, one may again use the term "tomography" or "tomographic" for Fourier-based methods.

5.2.3.1 Near-field problem formulation

Recall the original forward signal model in (5.4), namely:

$$S_{Rx}(k) = S_{Tx}(k)\sigma(\boldsymbol{x}_p)\left(\frac{\exp\{-jk|\boldsymbol{r}_{Tx} - \boldsymbol{x}_p|\}}{4\pi|\boldsymbol{r}_{Tx} - \boldsymbol{x}_p|}\right)\left(\frac{\exp\{-jk|\boldsymbol{x}_p - \boldsymbol{r}_{Rx}|\}}{4\pi|\boldsymbol{x}_p - \boldsymbol{r}_{Rx}|}\right),$$

for a single transmitter–receiver channel. The right-hand side of this equation can be decomposed in two factors:

$$S_{Rx}(\boldsymbol{r}_{Tx}, \boldsymbol{r}_{Rx}, k) = \sigma(\boldsymbol{x}_p)\, G(\boldsymbol{r}_{Tx}, \boldsymbol{r}_{Rx}, \boldsymbol{x}_p, k), \tag{5.22}$$

where $\sigma(\boldsymbol{x}_p)$ is unknown, and

$$\begin{aligned} G(\boldsymbol{r}_{Tx}, \boldsymbol{r}_{Rx}, \boldsymbol{x}_p, k) \;=\; & S_{Tx}(k)\left(\frac{\exp\{-jk|\boldsymbol{r}_{Tx} - \boldsymbol{x}_p|\}}{4\pi|\boldsymbol{r}_{Tx} - \boldsymbol{x}_p|}\right) \\ & \times\left(\frac{\exp\{-jk|\boldsymbol{x}_p - \boldsymbol{r}_{Rx}|\}}{4\pi|\boldsymbol{x}_p - \boldsymbol{r}_{Rx}|}\right) \end{aligned} \tag{5.23}$$

is "known," at least in theory because all the parameters defining it are either known transmitter/receiver locations or selectable from a grid.

Strictly speaking, $S_{Rx}(\boldsymbol{r}_{Tx}, \boldsymbol{r}_{Rx}, k)$, $G(\boldsymbol{r}_{Tx}, \boldsymbol{r}_{Rx}, \boldsymbol{x}_p, k)$, and $\sigma(\boldsymbol{x}_p)$ are all continuous functions, but in actuality, one can assume that

1. there exist only P discrete point scatterers on the target, i.e., the target's reflectivity distribution is *discretized* into P *pixels* or *voxels*, indexed by p;
2. there exist only N possible locations of the transmitters, indexed by n;
3. there exist only M possible locations of the receivers, indexed by m;
4. there exists only a finite number F of transmit frequencies, indexed by f. In this context, f is an integer.

These assumptions approximate continuous domains by discrete quantities—the elements of a matrix-based formulation.

Consider a single nth transmitter, mth receiver, and fth frequency of operation. The received signal can be expressed as the superposition of scattered signals from all point scatterers, with amplitude given by their respective reflectivity coefficient. In other words, for a given set of $(\boldsymbol{r}_n, \boldsymbol{r}_m, k_f)$, we have:

$$S_{Rx}(\boldsymbol{r}_n, \boldsymbol{r}_m, k_f) = \sum_{p=1}^{P} \sigma(\boldsymbol{x}_p) G(\boldsymbol{r}_{Tx}, \boldsymbol{r}_{Rx}, \boldsymbol{x}_p, k), \tag{5.24}$$

which can also be interpreted as an inner dot product of two vectors $\boldsymbol{\sigma}$ and $\boldsymbol{G}$ indexed over the scatterers (or pixels) with index p, for one set of (n, m, f). When these indices are considered over the full ranges, the one-liner equations in (5.24) can be *stacked vertically* in matrix form, to become

$$\begin{bmatrix} S_{1,1,1} \\ \vdots \\ S_{1,1,F} \\ S_{1,2,1} \\ \vdots \\ S_{1,M,F} \\ S_{2,1,1} \\ \vdots \\ S_{N,M,F} \end{bmatrix} = \begin{bmatrix} G_{1,1,1,1} & \cdots & G_{1,1,P,1} \\ \vdots & \cdots & \vdots \\ G_{1,1,1,F} & \cdots & G_{1,1,P,F} \\ G_{1,2,1,1} & \cdots & G_{1,2,P,1} \\ \vdots & \cdots & \vdots \\ G_{1,M,1,F} & \cdots & G_{1,M,P,F} \\ G_{2,1,1,1} & \cdots & G_{2,1,P,1} \\ \vdots & \cdots & \vdots \\ G_{N,M,1,F} & \cdots & G_{N,M,P,F} \end{bmatrix} \times \begin{bmatrix} \sigma_1 \\ \sigma_2 \\ \vdots \\ \sigma_P \end{bmatrix}, \tag{5.25}$$

or simply as

$$\boldsymbol{S} = \boldsymbol{G}\boldsymbol{\sigma}. \tag{5.26}$$

To paraphrase this slightly differently, the "simple" matrix form of the technique class arises from the *4D* nature of the problem listed earlier: the P pixels (or voxels) of the target set the number of columns of $\boldsymbol{G}$; and the N transmitters, M receivers, and F frequencies of the system create the $N \times M \times F$ rows of the matrix, which is also equal to the length of the stacked-up receive signal $\boldsymbol{S}$. Furthermore, each element of $\boldsymbol{G}$ is the value of the product of the Green function and the transmit waveform, given by (5.23).

Note the important difference between Fourier-based and matrix-based methods regarding the vectors $\boldsymbol{x}_p$: in the former class, $\boldsymbol{x}_p$ is treated as a continuous variable, as indicated by (5.11) or (5.15); in the latter class, it is a finite set of location vectors of the image *pixels/voxels*, which may or may not contain a scatterer or be part of a "scattering center."

General solution approaches

The target image can then be obtained with a matrix inversion operation in (5.26):

$$\boldsymbol{\sigma} = \text{inverse}(\boldsymbol{G})\boldsymbol{S}. \tag{5.27}$$

Here, the term "inverse" is used in a symbolic sense, because the type of inversion strategy depends on the application, nature of the received signal, and the computational complexity.

First, the classical definition of matrix inverse cannot be applied, because $\boldsymbol{G}$ is very likely to be not square, and its inverse $\boldsymbol{G}^{-1}$ may not exist. Also, calculating the inverse of a matrix is computationally very intensive, and is usually done only for very specific applications, or when real-time processing is not critical.

In radar applications, where the volume of data, number of pixels, and refresh rates can be very high, fast and perhaps suboptimal algorithms are preferred over the high-quality, highly demanding inversion methods. The most common approach is to use the BPA, in which the image is formed by calculating

$$\boldsymbol{\sigma} = \boldsymbol{G}^H \boldsymbol{S}, \tag{5.28}$$

where superscript H denotes the Hermitian matrix transpose. This operation is simply a *generalized matched filter*.

As common for matched filters, the limitations of the BPA approach include the following:

1. The maximization is with respect to SNR; it does not control the extent and intensity of the sidelobes. As such, back projection is prone to high sidelobes.
2. Differently from the Fourier-based approaches, where the inverse FT of an FT output will return its original values, the "forward projection" operation will not reverse the back projection. As such, iterative techniques exploiting contrast optimization cannot be used explicitly.

Inherent challenges

The discretization in matrix-based methods gives rise to several quite unique problems, the first of which is the so-called off-grid scatterer problem: the nominal location vector $\boldsymbol{x}_p$ of an *image pixel* (or voxel) may not exactly correspond to a real scatterer (if any) and may require a number of "atoms" to represent a single real scatterer, causing possible image blur effects. Many authors, such as in [29,30], have attempted to address this challenge.

Another problem is the possible errors in the location/range vectors $\boldsymbol{r}_{Tx}$ and $\boldsymbol{r}_{Rxm}$ in practical scenarios, especially when the target is a noncooperative one; these range vectors must still be estimated prior to the set-up of matrix $\boldsymbol{G}$. In other words, the target's translational motion is mathematically not separable from the rotational component; yet, its estimation is still required. System run time is another major problem: algorithms involving large matrices, caused by the multidimensional nature of the problem, may be computationally exhaustive.

5.2.3.2 Rigorous inversions

The matrix inversion problem can be recast in terms of an optimization (i.e., minimization of a cost function). Such optimizations may be preferred for the following reasons:

1. They attempt to *deconvolve* the received signal rather than maximizing its SNR as in matched filtering. In other words, if $\boldsymbol{\sigma}$ is the unknown reflectivity distribution, $\boldsymbol{G\sigma}$ is its convolved representation, $\boldsymbol{s}$ is the observed convolved signal, matrix inversions tend to find the (deconvolved) $\boldsymbol{\sigma}$ such that $\boldsymbol{G\sigma} - \boldsymbol{s} = 0$. Ideally, deconvolution provides the actual value of $\boldsymbol{\sigma}$, rather than a modified version given by back projection.
2. They can appropriately weigh the importance of the collected data. For instance, some view angles may be very sensitive to errors, so their contribution should be minimal to prevent a small error causing wild variations in the image.
3. They provide additional flexibility of the "type" of image that is sought. For instance, one can promote a solution of $\boldsymbol{\sigma}$ that is sparse (has few peaks) if the target

is known to be sparse. Otherwise, one can promote an image that is "connected" rather than a sparse collection of points. Matrix methods also allow for adaptive schemes aimed at reducing specific interferences, such as direct-path coupling.

A brief summary of commonly used matrix inversion approaches is described later. They usually start by defining the minimization objective function, and for many of these objectives, a closed form is found.

Tikhonov regularization

The Tikhonov regularization method [31] seeks a solution as the global minimum of the following minimization problem

$$\hat{\boldsymbol{\sigma}} = \arg\min_{\sigma} \left\{ \|\boldsymbol{G}\boldsymbol{\sigma} - \boldsymbol{s}\|_2^2 + \beta\|\boldsymbol{\sigma}\|_2^2 \right\}, \tag{5.29}$$

in its simpler form. Here, β is the *regularization* parameter that needs to be appropriately selected, and the addition of the $\beta\|\boldsymbol{\sigma}\|_2^2$ constraint physically means that among all possible solutions, the one with minimum ℓ_2 norm, i.e., minimum "energy," is selected. By manipulating (5.29), an analytical solution is obtained:

$$\hat{\boldsymbol{\sigma}} = (\boldsymbol{G}^H\boldsymbol{G} + \beta\boldsymbol{I})^{-1}\boldsymbol{G}^H\boldsymbol{s}. \tag{5.30}$$

This is a linear projection of the received signal $\boldsymbol{s}$ and hence can be computationally efficient—an attractive advantage of the method.

Truncated singular value decomposition (SVD)

Another important regularized inversion method is the truncated singular value decomposition (SVD) method [32]. Basically, $\boldsymbol{G}$ can be decomposed in its singular values as

$$\boldsymbol{G} = \boldsymbol{U}\boldsymbol{S}\boldsymbol{V}^H, \tag{5.31}$$

where $\boldsymbol{U}$ and $\boldsymbol{V}$ are unitary matrices, and $\boldsymbol{S}$ is a diagonal matrix containing the *singular values* of $\boldsymbol{G}$ sorted in descending order. The matrices $\boldsymbol{U}$ and $\boldsymbol{V}$ are both orthogonal (i.e., $\boldsymbol{U}^H\boldsymbol{U} = \boldsymbol{V}^H\boldsymbol{V} = \boldsymbol{I}$) and complete (i.e., $\boldsymbol{U}\boldsymbol{U}^H = \boldsymbol{V}\boldsymbol{V}^H = \boldsymbol{I}$). The diagonal values of $\boldsymbol{S}$, normalized with respect to the first (largest) singular value s_1, are referred to as pseudospectrum, usually expressed in dB. In many inverse scattering problems including the one at hand, the pseudospectrum exhibits a plateau for large values (with null or low dynamical range), followed by a sharp decay, but rarely equaling the zero value due to numerical approximations. Singular values that are very small compared to s_1 represent the sensitive directions of $\boldsymbol{G}$: along these directions, a small amount of noise or clutter in the sampled field leads to a large (undesired) deviation of $\boldsymbol{\sigma}$.

When the SVD is performed on $\boldsymbol{G}$, an ideal matrix structure occurs:

$$\boldsymbol{G} = [\boldsymbol{U}_\Gamma \ \boldsymbol{U}_0] \begin{bmatrix} \boldsymbol{S}_\Gamma & 0 \\ 0 & 0 \end{bmatrix} \begin{bmatrix} \boldsymbol{V}_\Gamma^H \\ \boldsymbol{V}_0^H \end{bmatrix}, \tag{5.32}$$

where Γ is the number of singular values that are nonzero, $\boldsymbol{U}_\Gamma$ and $\boldsymbol{V}_\Gamma$ are the collected eigenvectors that are spanned by the singular values in $\boldsymbol{S}_\Gamma$, $\boldsymbol{U}_0$ is made of vectors that do not belong to the range of $\boldsymbol{G}$, and $\boldsymbol{V}_0$ is made of vectors belonging to the null space of $\boldsymbol{G}$.

Through the SVD of $\boldsymbol{G}$, the scattered field may be expressed as

$$\boldsymbol{s} = \boldsymbol{U}_\Gamma \boldsymbol{S}_\Gamma \boldsymbol{V}_\Gamma^H \boldsymbol{\sigma}. \tag{5.33}$$

By exploiting the properties of $\boldsymbol{U}$ and $\boldsymbol{V}$, inverting (5.33) gives:

$$\hat{\boldsymbol{\sigma}} = \boldsymbol{V}_\Gamma \boldsymbol{S}_\Gamma \boldsymbol{U}_\Gamma^H \boldsymbol{s}. \tag{5.34}$$

The strategy commonly referred to as truncated SVD [33] consists simply of *selecting* the singular values to be retained in $\boldsymbol{S}_\Gamma$: generally, in the truncated SVD, the singular values to be retained are related to the SNR.

The SVD is helpful also for the fast computation of the Tikhonov regularization scheme. In fact, by decomposing (5.30) in its singular values, one obtains:

$$\begin{aligned}\hat{\boldsymbol{\sigma}} &= (\boldsymbol{G}^H\boldsymbol{G} + \beta\boldsymbol{I})^{-1}\boldsymbol{G}^H\boldsymbol{s} \\ &= (\boldsymbol{V}\boldsymbol{S}^H\boldsymbol{U}^H\boldsymbol{U}\boldsymbol{S}\boldsymbol{V}^H + \beta\boldsymbol{V}\boldsymbol{I}\boldsymbol{V}^H)^{-1}\boldsymbol{V}\boldsymbol{S}^H\boldsymbol{U}^H\boldsymbol{s} \\ &= \boldsymbol{V}(\boldsymbol{S}^H\boldsymbol{S} + \beta\boldsymbol{I})^{-1}\boldsymbol{S}^H\boldsymbol{U}^H\boldsymbol{s} = \boldsymbol{V}\,\mathrm{diag}\left(\frac{s_i}{s_i^2+\beta}\right)\boldsymbol{U}^H\boldsymbol{s}.\end{aligned} \tag{5.35}$$

The interesting feature is that the optimal selection of $\boldsymbol{\sigma}$ by varying the parameter β is obtained just by a relatively fast matrix multiplication, rather than a formal matrix inversion.

The notable work in [34,35] applied both Tikhonov regularization and truncated SVD to Wi-Fi-based "radio tomographic imaging" of moving objects based on *changed attenuation* in a scene, rather than the scattering reflectivity distribution.

5.2.3.3 Sparse regularization

As has been discussed by many authors, such as in [36] and references therein, high sidelobes, especially for limited view angles, can make it difficult for an analyst to identify the type of target or scene, or it may stress the ATR capabilities. An image with fewer sidelobes may help both analysis and ATR algorithms. Sidelobe reduction may be obtained using sparse regularization techniques, where the underlying assumption is that $\boldsymbol{\sigma}$ is composed of a relatively small number of scatterers:

$$\hat{\boldsymbol{\sigma}} = \arg\min \|\boldsymbol{\sigma}\|_0 \quad \text{subject to} \quad \|\boldsymbol{G}\boldsymbol{\sigma}\|_2^2 < \epsilon, \tag{5.36}$$

where the ℓ_0 norm of a vector returns just the number of nonzero elements. Unfortunately, such minimization is of the type *NP*-hard and practically impossible to solve for the dimension of our problem. The intractable ℓ_0 norm can be replaced with similar norms that have lower computational complexity, leading to several efficient techniques as summarized later.

ℓ_1-norm minimizations

A good candidate norm to minimize is the ℓ_1 norm,

$$\hat{\boldsymbol{\sigma}} = \arg\min \|\boldsymbol{\sigma}\|_1 \quad \text{subject to} \quad \|\boldsymbol{G}\boldsymbol{\sigma}\|_2 < \delta. \tag{5.37}$$

This particular minimization is called *quadratically constrained* ℓ_1. The positive-valued δ can be estimated on the basis of the noise level on data. The case of $\delta = 0$ corresponds to the classical *basis pursuit* minimization, although it is not adequate for noisy problems.

Alternatively, one can set up a similar minimization procedure,

$$\hat{\boldsymbol{\sigma}} = \arg\min_{\sigma} \left\{ \lambda \|\boldsymbol{\sigma}\|_1 + \|\boldsymbol{G\sigma} - \boldsymbol{s}\|_2^2 \right\} \tag{5.38}$$

where λ is a regularization parameter that needs to be appropriately chosen. This minimization is called *basis pursuit de-noising*.

Similarly, another minimization procedure can be instated:

$$\hat{\boldsymbol{\sigma}} = \arg\min_{\sigma} \|\boldsymbol{G\sigma} - \boldsymbol{s}\|_2 \quad \text{subject to} \quad \|\sigma\|_1 < \tau. \tag{5.39}$$

This type of minimization is also called the *Least Angle Shrinkage and Selection Operator* technique [37].

Mathematically, these three problems are all different ways of arriving at the same set of solutions. In fact, the solution to any one of these problems is characterized by a triplet of values (δ, λ, τ) which renders the same $\hat{\boldsymbol{\sigma}}$, although finding the values that return the same image is not trivial. Reconstructed images using sparse regularization are usually too "peaky," reducing extended objects into points, or missing small target features. To overcome these problems, two other extensions of sparse regularization algorithms have been introduced.

Mixed norm minimizations

A more effective minimization scheme leading to enhanced image quality is

$$\hat{\boldsymbol{\sigma}} = \arg\min \left\{ \|\boldsymbol{G\sigma} - \boldsymbol{s}\|_2^2 + \alpha \|\boldsymbol{\sigma}\|_1 + \beta \|\boldsymbol{\sigma}\|_2^2 \right\}. \tag{5.40}$$

In fact, the previous minimization problem incorporates both the energy-stabilizing effect due to the ℓ_2 penalty (which encourages extended targets) and the sparsity-promoting effect due to the ℓ_1 penalty (which reduces the number of required samples and decreases sidelobes and artifacts). This minimization scheme could be solved using more classical methods, but there exists a faster minimization procedure usually named fast iterative shrinking thresholding algorithm [38].

Finally, another very useful imaging scheme exploits the *total variation* norm. One example could be [39]

$$\begin{aligned} \hat{\boldsymbol{\sigma}} &= \arg\min \left\{ \|\boldsymbol{G\sigma} - \boldsymbol{s}\|_2^2 + \alpha \|\boldsymbol{\sigma}\|_{1S} + \beta \|\boldsymbol{\sigma}\|_{TVS} \right\}, \\ &\quad \text{subject to} \quad \tau_{\min} \le |\sigma_i| \le \tau_{n\max}, \quad i = 1, \ldots, K, \end{aligned} \tag{5.41}$$

where α, β are the regularization parameters, $\tau_{\min}, \tau_{n\max}$ represent the minimum/maximum absolute values that the contrast function can have, and σ_i denotes the ith element of $\boldsymbol{\sigma}$, and K is the length of the $\boldsymbol{\sigma}$ vector. In (5.41), the operators $\|\cdot\|_{1S}$ and

$\|\cdot\|_{TVS}$ are the smoothed ℓ_1 norm and the smoothed total variation norm, respectively, defined as

$$\|\boldsymbol{\sigma}\|_{1S} = \sum_{i=1}^{K} \sqrt{\sigma_i^2 + \epsilon}, \quad \|\boldsymbol{\sigma}\|_{TVS} = \sqrt{(D|\boldsymbol{\sigma}|)^2 + \epsilon}, \quad \epsilon > 0. \tag{5.42}$$

where D is the discrete approximation to the gradient operator, and ϵ is a small constant.

The minimization problem in (5.41) incorporates several advantages as follows:

- The total variation penalty promotes solutions that are clustered and not fragmented. The addition of ϵ relaxes the minimization problem.
- The ℓ_1 penalty promotes solutions having a small number of nonzero elements.
- The condition on the elements of $\boldsymbol{\sigma}$ guarantees realistic values of the contrast functions and distributes the energy of the image to weaker voxels.

The solution of (5.41) is obtained by implementing the Cetin algorithm [38].

A comprehensive literature review on general sparsity techniques could also be found in [40,41].

5.2.4 Multistatic Doppler–radar tomography

Doppler processing is a classical narrowband concept; a Doppler shift is a frequency change to a single-carrier-frequency waveform induced by the "radial" motion of a scatterer as seen by a receiver. DRT is a narrowband form of RT which exploits a target's rotational motion and the direct dependence of Doppler shift on a scatterer's cross range.

This section revisits the Fourier-based methods in Section 5.2.2 to describe a novel development in this class of methods for narrowband radars. The definition of a $\boldsymbol{k}$-vector, such as in (5.17), implies that effective bandwidth for target imaging can be generated with relative rotational motion, even when f is a single frequency. In the fast-time k-space, this would correspond to the formation of a 1D curvilinear support spanning in both range and cross-range dimensions, as discussed in Section 5.2.2.4. Image resolution may be fine, though may not be practically useful, because of possible high sidelobes and hence poor image contrast; see Section 5.2.2.6. DRT is a promising approach to address this limitation, exploiting a companion k-space known as the "*slow-time* k-space" [17,42].

The rest of this section introduces related fundamental concepts of cross-range bandwidth and resolution, and the slow-time k-space, reviews the theory of standard monostatic DRT, describes its extension to multistatics, and explains how high-resolution imaging may be achieved with a generally multistatic narrowband radar system and *augmented* k-spaces. Finally, the section concludes with some experimental demonstrations.

5.2.4.1 Cross-range bandwidth and resolution

In the fast-time k-space, phase functions $\boldsymbol{k}_m \cdot \boldsymbol{x}_p$, such as in (5.10), are treated as "snapshots," due to the existence of k over a finite bandwidth; variations over slow time points t_k (i.e., on the target motion time scale) are ignored. In narrowband imaging, the effects over slow time are exploited. Given the definition of $\boldsymbol{k}$ in (5.17), the phase function could be expanded as [17]

$$\boldsymbol{k}_m(t_k)\cdot\boldsymbol{x}_p = \frac{4\pi}{c}\cos\left(\frac{\beta_m}{2}\right)\left(fx_2 + x_1 f\Omega_e t_k - \frac{1}{2}x_2 f\Omega_e^2 t_k^2 + \cdots\right), \tag{5.43}$$

where x_1 and x_2 are the cross-range and down-range components of $\boldsymbol{x}_p$ which we wish to estimate, and Ω_e is an effective rotational speed (rad/s). We have also assumed that $\Omega_e \approx \Omega$ so that the effects of scatterer height x_3 are negligible.

A "narrowband" signal implies that an interval on f is not available to directly estimate x_2 of the zeroth-order term; however, the varying slow time t_k in the *first*-order term of (5.43) suggests that a *cross-range bandwidth*,

$$B_{\perp,m} = f\,\cos\left(\frac{\beta_m}{2}\right)\Omega_e T_{CPI} = f\,\cos\left(\frac{\beta_m}{2}\right)\Delta\theta, \tag{5.44}$$

for the mth receiver channel may be defined, which can be used to estimate x_1. Assuming the rotation angle $\Delta\theta = \Omega_e T_{CPI}$ is sufficiently small such that the second and higher order terms in (5.43) are negligible. The corresponding cross-range resolution is

$$\Delta x_{1m} = \frac{c}{2B_{\perp,m}}, \tag{5.45}$$

which is the same form that range resolution is conventionally expressed in terms of spectral bandwidth B: $\Delta x_2 = c/2B$. Cross-range bandwidth $B_{\perp,m}$ determines the image *resolution* performance of DRT algorithms, as discussed in Section 5.2.4.3.

Note that $B_{\perp,m}$ depends only on carrier frequency f, the bistatic angle, and total rotation angle $\Delta\theta$ of a CPI, as indicated in (5.44), not on target dimension, or rotation speed, or types of translational motion; it is related to a target's Doppler frequency span or extent, or "Doppler bandwidth" (a term used by some authors), but not the same. "Doppler bandwidth" does not determine imaging resolution.

5.2.4.2 The slow-time *k*-space

The slow-time k-space arises from considerations of resolution of cross-range profiles in Doppler processing. For the mth channel at bistatic angle β_m, and the cross-range resolution Δx_{1m} given in (5.45), the extent of cross-range spatial frequency $f_{s\perp}$ is $1/\Delta x_{1m} = 2B_{\perp,m}/c$, which symmetrically spans the interval $(-B_{\perp,m}/c, B_{\perp,m}/c)$. Making use of (5.44), the interval for k_s $(= 2\pi f_{s\perp})$ is thus

$$k_{s,m} \in \cos\left(\frac{\beta_m}{2}\right)\left(-\frac{2\pi f}{c}\Delta\theta, \frac{2\pi f}{c}\Delta\theta\right),$$

as illustrated by the radial dashed lines in Figure 5.17.

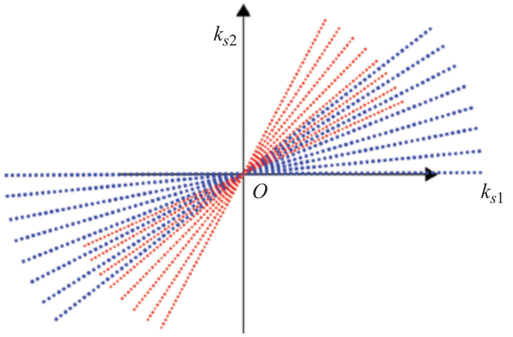

Figure 5.17 Illustration of the combined support from two receivers in the slow-time k-space. Blue: monostatic; red: bistatic

When forming the cross-range profile with the FFT, which is a computationally efficient choice, the number of samples in time domain and frequency domain is equal to K. Hence, the (discretized) slow-time $\boldsymbol{k}$-vectors $\boldsymbol{k}_{s,m}$ corresponding to each cross-range projection can be defined as

$$\boldsymbol{k}_{s.m} = \frac{2\pi f}{c} \cos\left(\frac{\beta_m}{2}\right) k'(\Omega_e T_{PRI})\, \hat{\boldsymbol{r}}_{bis,m\perp}, \tag{5.46}$$

where

$$k' = -K, -K+2, \ldots, -2, 0, 2, \ldots, K-2;$$

$$T_{PRI} = \frac{T_{CPI}}{K},$$

and $\hat{\boldsymbol{r}}_{bis,m\perp}$ is the cross-range unit vector and is perpendicular to $\hat{\boldsymbol{r}}_{bis,m}$.

Each CPI produces one radial dashed line (see Figure 5.18), leading to a fan-shape collection of such lines for a data block from the mth receiver. (Refer to the DRT algorithm in Section 5.2.4.3 for further details.) The total angular extent of the collection equals to the total rotation angle of the target over the data block. The total support from M receivers (and one transmitter) is a union of such collections, rotated by half of their angular separation, as illustrated in Figure 5.17 for two receivers. Note that the supports from the separate receivers may partially overlap.

Finally, for a full multistatic system with N transmitters and M receivers, the combined slow-time k-support is a union of such unions for a single transmitter, rotated by the appropriate angles between the additional transmitters and the reference transmitter Tx_0.

For additional insight, a few points of comparison between the fast and slow time k-spaces are provided in Table 5.1. A key characteristic is that the maximum extent of a slow-time k-space is only a factor $\Delta\theta \cos(\beta/2)$ of the wavenumber k, as compared to $2\cos(\theta/2)$ of the fast-time case; hence, augmentation processing, as will be described later, may be necessary for a comparable resolution performance.

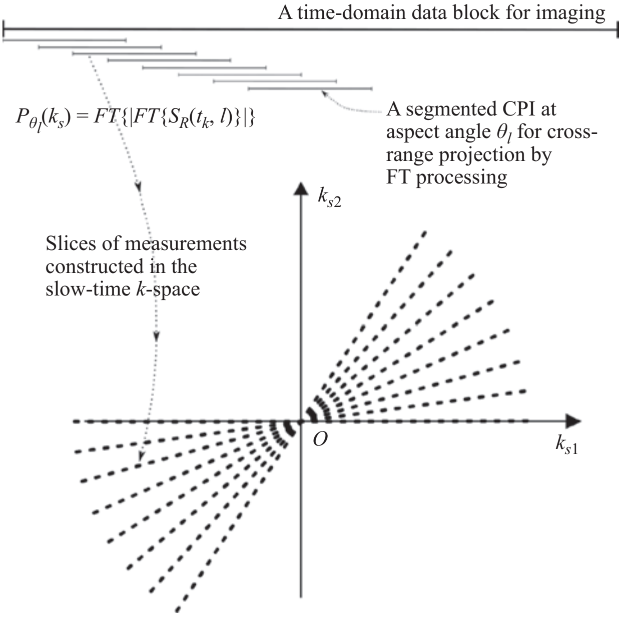
A time-domain data block for imaging
$P_{\theta_l}(k_s) = FT\{|FT\{S_R(t_k, l)\}|\}$
A segmented CPI at aspect angle θ_l for cross-range projection by FT processing
Slices of measurements constructed in the slow-time k-space
k_{s2}
O
k_{s1}

Figure 5.18 Illustration of the DRT algorithm in the slow-time k-space

Table 5.1 Comparison between the fast- and slow-time k-spaces

	Fast-time *k*-space	**Slow-time *k*-space**
Fourier-pair	(Down) range y	Cross-range x
Max extent	$2k\cos\beta$	$k\Delta\theta\cos\beta$
k-Space support shape	Annular (or "flat donut") shape or "hollow" ring	Filled fan shape, always symmetric about the origin
Augmentability	No	Yes
Computation	Lighter	Heavier

5.2.4.3 The DRT algorithms

Several variants of DRT exist: traditional monostatic standard DRT, augmented DRT, multistatic DRT, or some combination of these variants.

Using standard Doppler processing, the single-channel DRT algorithm [5] builds successive cross-range profiles and exploits the fundamental PST of tomography to estimate both x_1 and x_2 components of a scatterer's location vector $\boldsymbol{x}_p$. The algorithm, modified for a single-channel bistatic geometry, is illustrated in Figure 5.18, which consists of the following steps:

1. First, the set of all N samples $s_{Rx}(t_n)$ in the received data block is segmented into L overlapping CPIs $s_{Rx}(t_k, l)$, each of length K and with an overlap factor η. Here,

$k = 0, 1, \ldots, K-1$; $l = 1, 2, \ldots, L$; and $0 \leq \eta \leq 1$. The target aspect angle at the midpoint of such a segment is denoted as θ_l.

2. Next, compensation for any translational motion is applied to each CPI, by multiplying the signal with a linear phase factor $\exp(j2\pi \nu t_k)$, to shift the Doppler line of known nonrotating components to zero Doppler frequency. Here, ν is the target's translational velocity projected onto the bisector of bistatic angle and is assumed to be known or estimated by other methods. A standard Fourier transform, denoted as $\mathscr{F}\{\cdot\}$, is then applied to all segments, with a circular shift to place the zero Doppler frequency at the center of the spectrum. Denote the magnitude of the output as

$$p_{\theta_l}(x_1) = \left|\mathscr{F}\{s_{Rx}(t_k, l)\ \exp(j2\pi \nu t_k)\}\right| \tag{5.47}$$

   for the cross-range profiles. Accumulate all such cross-range profiles, along with the corresponding aspect angles θ_l, available from the data block.
3. The spatial Fourier transform of $p_{\theta_l}(x_1)$ namely

$$P_{\theta_l}(f_s) = \mathscr{F}\{p_{\theta_l}(x_1)\} \tag{5.48}$$

   is then used as the "measurement samples" at aspect angle θ_l to populate the slow-time k-space *at locations defined by* (5.46). As the target rotates, the measurements "fan out" as indicated in Figure 5.18.

   Note that the k_{s2} and k_{s1} axes here describe components of $\boldsymbol{k}_s$ as defined in (5.46) and are, respectively, aligned with the initial range and cross-range directions in the image domain. Note also that the measurement population always starts close to the k_{s1}-axis because $p_{\theta_l}(x_1)$ are cross-range profiles.
4. The final step is an application of the NUFFT to the populating samples over the entire support, to obtain a target image.

Extension to multistatics

To extend the previous algorithm to a multi-bistatic or full multistatic geometries, the steps of a–c are processed separately for each channel, taking into account the different bistatic angles, the angular offsets between the transmitters, the possibly different projections of the target's translational velocity onto the various bisectors, and combining all measurements from all channels in the k-space, before applying the final step d.

5.2.4.4 An example

This section summarizes a simulation study reported in [42]. A simple point-scatterer target as depicted in Figure 5.19(top) is used. Five scatterers of various radial distances from the origin O rotate around it at 300 RPM. The radar transmitter transmits a single-frequency waveform at 10 GHz. Five receivers are located at $\beta_m = 0, \pm 70, \pm 140$; each samples the scattered signals at 50 kHz, for a full cycle of target rotation. On each receive channel, the length of a segmented CPI corresponds to an angular extent of approximately 4.6° of target rotation, with an overlapping factor of 0.7.

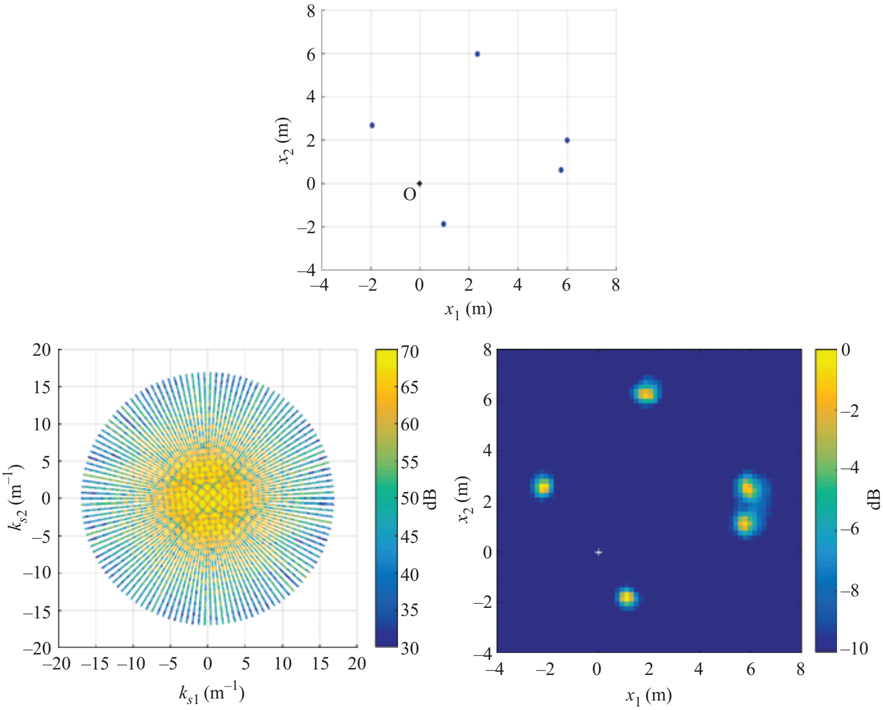

Figure 5.19 Top: A point-scatterer target model, rotating at 300 RPM around the origin denoted by the small cross (+) symbol. The two scatterers closest to one another are separated by approximately 1.5 m. Bottom: full slow-time k-space support and corresponding DRT image

If full target data is available, a result as shown in Figure 5.19(bottom) is obtained, which is reasonably close to the truth data. When partial data is used, typical results are as in Figure 5.20.

Standard DRT has relatively short CPIs (and rotation angles accordingly) such that (5.43) is valid only up to the first-order term, resulting in relatively low imaging resolution. On the contrary, (5.44) and (5.45) imply that higher DRT resolution requires larger rotation angles $\Delta\theta$. The conflicting requirements can be resolved by compensating for higher order terms in (5.43)—this is the basis of "augmented DRT" and the aim and rationale of *k-space augmentation techniques* to be discussed next.

5.2.4.5 Augmentation of the slow-time *k*-space

"Augmentation" refers to the process of re-partitioning the original time-domain data and using overlapping CPIs that are *longer* than in standard DRT for cross-range profile formation, compensating for nonlinear effects of rotation, and thus enlarging the slow-time *k*-space support, as illustrated in Figure 5.21. Augmentation is *not*

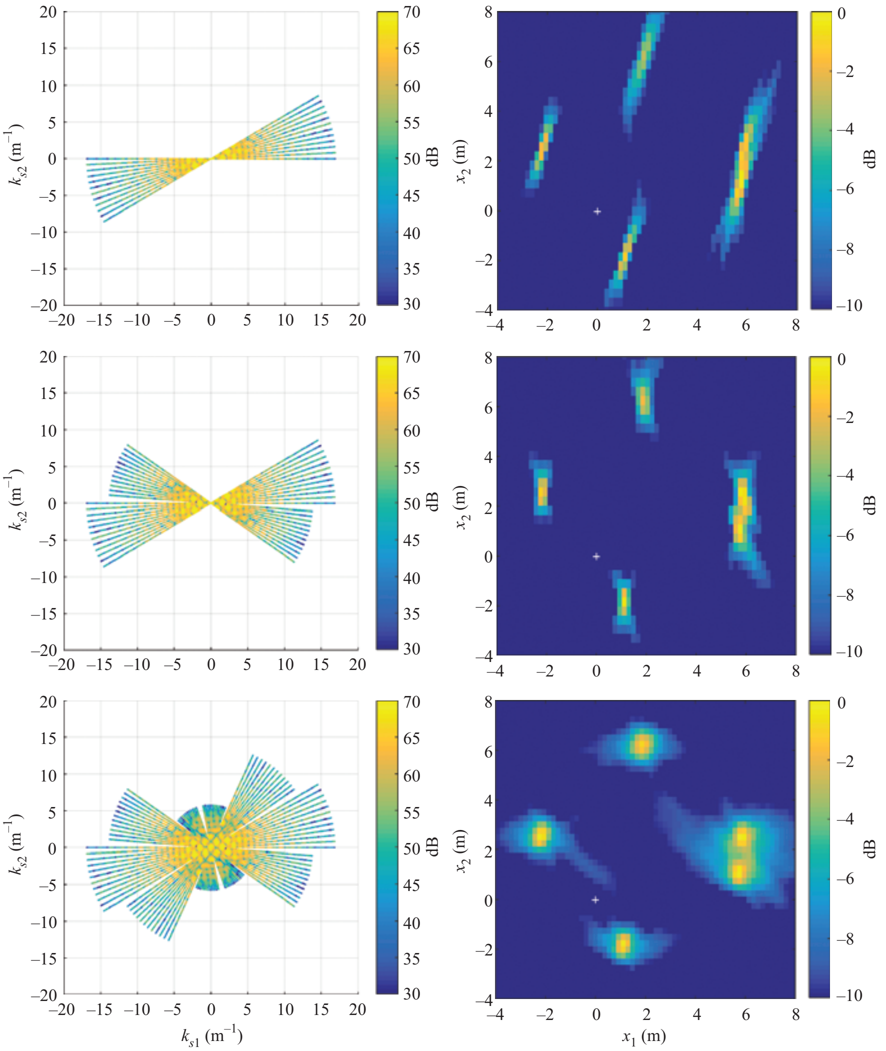

Figure 5.20 Top: Imaging result for the Rx$_0$ receiver, 30° target rotation, with k-space support and corresponding DRT image; middle: for the Rx$_0$ and Rx$_1$ receivers, same extent of rotation; bottom: all five receivers

possible in the traditional fast-time *k*-space and represents a key advantage of the slow-time *k*-space.

The topic is currently in early stages of development. Nevertheless, at least one technique called "FrFTS augmentation" has been proposed; this involves a combination of the fractional Fourier transform (FrFT), the *S*-method, and a CLEAN algorithm.

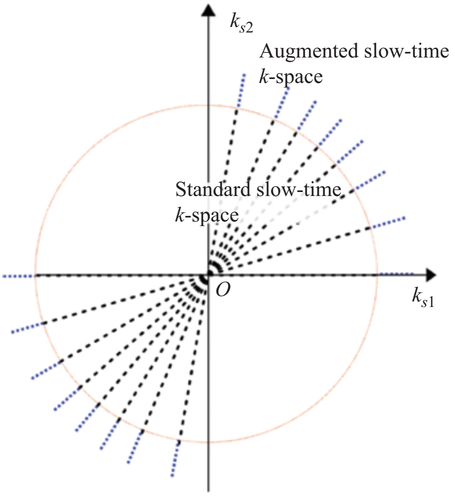

Figure 5.21 Conceptual illustration of the augmentation of the slow-time k-space. The circle indicates the boundary of support in standard DRT

FrFTS augmentation

This technique was first reported in [43]. Without describing all the related details, it suffices here to mention that FrFTS augmentation is essentially a CLEAN technique in which the individual chirp components in each CPI are detected sequentially, in the order of decreasing strength, and extracted from the signal, which are then compressed separately by the S-method. The individually compressed spectra are then summed to obtain a final focused cross-range profile for DRT processing.

The FrFT is a generalized Fourier transform in which a linear chirp signal can be rotated in time-frequency space through an angle determined by the chirp rate to become a single-tone signal and hence can be used as a chirp detector. The S-method is a computationally efficient version of the Wigner–Ville distribution that also minimizes the spurious cross terms. Once cross-range projections are focused with this processing, the DRT algorithm is applied as in standard DRT algorithm.

A numerical example is shown in Figure 5.22: the target consists of ten point scatterers orientated around an ellipse shape and is offset from the center of rotation (top-left). The smear-free standard DRT image, top-right, shows the locations of the scatterers, at low resolution. Using a longer integration time with standard DRT processing, the bottom-left sub-figure features a smearing effect which is increasingly more severe at longer radial distances from the rotation center. Finally, the bottom-right image demonstrates the higher resolution and effectiveness of the FrFTS augmentation method.

Other augmentation techniques, such as those based on sparse signal representation, are possible; we expect such techniques to be reported in the near future.

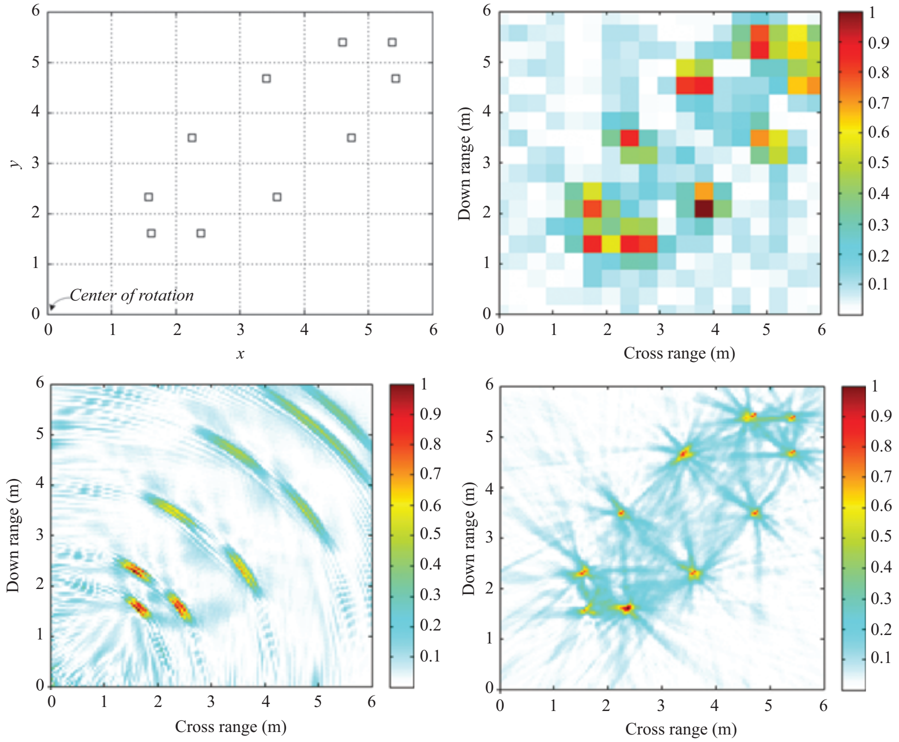

Figure 5.22 An example of slow-time k-space augmentation with simulated data. Top-left: true point-scatterer target rotating around (0,0); top-right: standard DRT image; bottom-left: standard DRT on long CPIs; bottom-right: DRT image with FrFTS processing

5.3 Practical considerations

This section discusses several aspects in practical exercises to collect receiver data and populate it in a k-space. Such tasks are obviously application dependent; nevertheless, general guidance can be gleaned from equations such as (5.14) and (5.15) and the related k-spaces.

5.3.1 Considerations with system geometry

The following considerations are most applicable to spotlight SAR and circular SAR applications.

5.3.1.1 Minimum distance

Fourier tomographic reconstruction requires the far-field approximation, i.e., the distance $\boldsymbol{r}$ from the radar antenna to the "target center" is large relative to the size of the target or scene patch so that the curvature of the waveform front is negligible: when the patch area becomes too large, a quadratic phase term appears, leading to defocused images. The Fraunhofer approximation states that to avoid unacceptable image degradation, the maximum size D of the target must be [4]

$$D \ll \sqrt{\frac{2r}{\lambda}}. \tag{5.49}$$

For a modest region of 10 m × 10 m and a carrier frequency of merely 3 GHz, for example, this condition requires that all transmitters and receivers must be more than 4 km away from the target center. The dilemma becomes whether to image larger scenes (and accept defocusing) or to confine the imaging algorithm to a focused region and accept additional clutter folding in the patch area due to ambiguities.

5.3.1.2 Image extent and aliasing

As well known in Fourier analysis, the maximum unambiguous size of the image depends on the discretization steps, δk, used in the k-space grid. Therefore, a finer grid will cover for a larger unambiguous extent of the image. Approximately, the unambiguous size of the image is related to the spacing in the k-space as

$$\Delta r = \frac{2\pi}{\delta k}.$$

The system design needs to take the maximum size of the target into account; this expression can then be used to determine the minimum spacing of the grid in the k-space. If the grid spacing is larger than the minimum required, aliasing (fold-overs) in the image domain may occur. On the other hand, having the k-spacing too small may unnecessarily increase the computational cost or distort the sidelobe distributions in undesirable manners.

Furthermore, suppose that there exists a point scatterer or target at a distance greater than Δr: due to the properties of the FFT, this point target will appear inside the reconstructed image, or "wrapped around," according to the principles of aliasing. Therefore, there must be a pre-filtering strategy to ensure that no signal is collected from regions outside of the area of interest.

5.3.1.3 Receiver platform flight paths

For optimum results of SAR-type imaging, a typical radar tomographic imaging mission may consist of the following:

- Flying the radar platform along an *arbitrary path*, possibly having large azimuth and elevation variations. Using a wideband radiated signal with sufficiently high pulse sampling rates would increase the size of the k-space support and density of measurement samples and, therefore, optimizing on image resolution and lowering sidelobe levels; it is, however, not an absolute requirement.
- At each azimuth and elevation angle, radiating a pulse and coherently detecting the complex-signal-based range profile, and performing and recording its FFT.

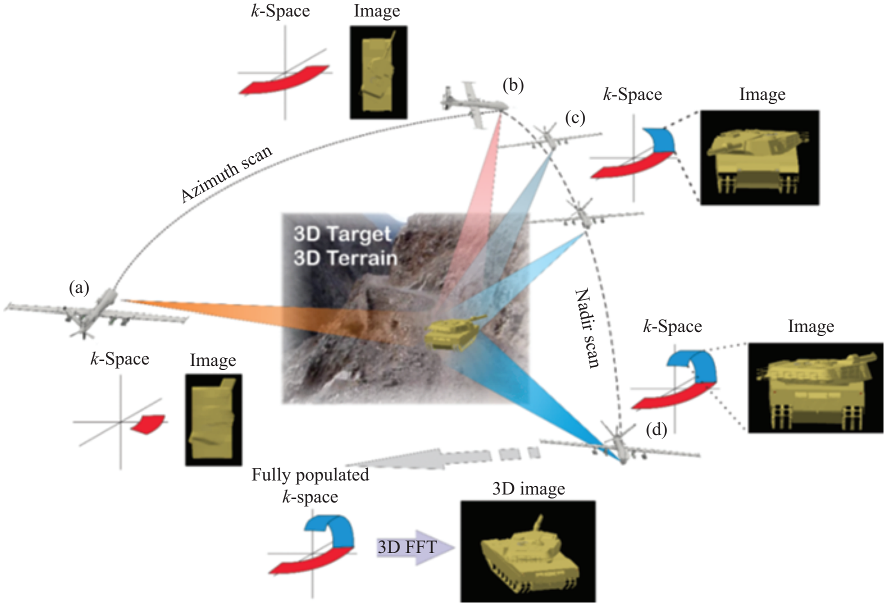

Figure 5.23 A possible flight maneuver optimizing the 3D resolution

- Storing the FFT data for long integration times (typically seconds or tens of seconds, depending on the platform speed and distance from the target). The stored data contains the information of the 3D k-space of the scene.
- Performing a 3D-inverse NUFFT to obtain a 3D reconstruction of the scene.

Tomographic SAR processing [3] does not assume any specific flight path around the target of interest. RT can in principle automatically and optimally weight the collected data to form a 3D image of the scene having the best theoretically possible resolution.

One can achieve adequate range and cross-range resolution regardless of the bandwidth of the signal, provided that sufficiently wide observation angles in 3D space are accessible. As shown in Appendix A, the resolution limit of a tomographic system is approximately $\lambda/3$, where λ is the wavelength of the carrier signal. In principle, sub-wavelength resolution can be achieved using even ultra-narrowband signals. In Ku-band, RT may provide a 3D spatial resolution less than 1 cm, independently of the signal bandwidth.

RT can provide a 3D image regardless of the flight path, but there exist preferred routes which may provide better 3D image resolution. Again, Figure 5.11 shows that resolution is governed by covering the maximum extents of the k-space and not by the density or number of points. Flight paths can be constructed to ensure maximum coverage of the k-space extent optimized for some applications. One of the most effective flight maneuvers is depicted in Figure 5.23. In simple terms, the joint circular-azimuth/nadir scan of the area of regard will increase both the horizontal and vertical resolutions. Other favorable flight maneuvers are high-altitude multiple circular scans (nadir-looking) or bistatic SAR systems flying in opposite directions.

5.3.2 Considerations for signal processing

Tomography is inherently and traditionally a frequency-domain technique, whilst receiver data is necessarily collected in the time domain, except for special cases where the two domains are the same. Such a case is the stepped-frequency waveform: each sample received from each stepped-frequency pulse can also be regarded as the target's frequency response at that frequency. In general, preprocessing of the receiver data is necessary.

Particular processing tasks may depend on particular types of waveform; nevertheless, some of these are listed as follows:

- For each (wideband) radar pulse, a start time t_0 and end time t_{end} should be selected—these times are relative to the rising edge of the transmit pulse—for the data collection, and they should be approximately centered in the range where the target is expected to be. If the target range is totally unknown, then one can set t_0 to the earliest sampling time in the PRI (corresponding to the first range bin) and $t_{end} = PRI$ (last range bin), assuming that there are N samples (or range bins) in between. Let the sampling interval be $\tau = 1/f_s$, where f_s is sampling frequency, and the total collection time is T.
- Collect the time-domain data and store it in a vector $s_{Rx}[t]$. Then, perform a FT on such data to obtain $S_{Rx}[f]$, as described by (5.11). According to properties of the Fourier transform, the frequency span will be $\pm 1/(2\tau)$, and the frequency stepsize is $1/T$. Strictly speaking, the frequency data also involves a phase factor of $\exp(-j2\pi f t_0)$, which needs to be either removed or accounted for when populating the k-space.
- Apply matched filtering and TMC as discussed in Section 5.2.2.3. Moving over to the k-space, the corresponding scale in k-space is simply $k = (2\pi/c)f$.
- Channel synchronization. Even for a single transmitter and a single receiver, synchronization is necessary to estimate the bistatic angle, which affects the *locations* of the processed signals populating the k-space and hence imaging performance measures. For multiple receivers, a multidimensional parameter optimization is necessary to focus on the image [42]. Lastly, for multiple transmitters, the complexity increases, and MIMO type of processing is necessary.

5.4 Concluding remarks

Making optimal use of spatial diversity is the key characteristic of RT, without ignoring other types of diversities: spectral diversity is seamlessly incorporated in the fast-time k-space; so is "waveform diversity," which can be captured as the arbitrary "transmit waveform" $S_{Tx}(k)$ of (5.7) or (5.10), as long as it is available (or accurately reconstructed) for matched filtering by a radar receiver.

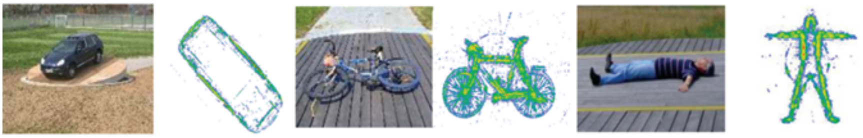

Figure 5.24 Turntable tomographic experiments showing that the shape of targets is retained after the coherent image formation [44]

One of the main criticisms to tomographic approaches, for single-channel systems, is that the phase coherence of the target's point scatterers sharply decreases after a few degrees of change in the observation angle. Theoretically, since SAR images must be formed by adding coherent data, the short coherence interval will restrict the length of the synthetic aperture, which ultimately will affect the resolution. Some of the counterarguments to this claim are as follow:

- **Coherent and incoherent image registration.** In some circumstances for SAR, the whole data can be divided into several subsets where the scatterers' phase appears coherent. Each subset will be processed coherently to form images. These images are then added incoherently to reconstruct the 3D scene.
- **Preserved phase coherence.** Optics theory states that the phase coherence of a collection of point targets improves when (1) the wavelength of the probing waveform becomes larger and (2) the bandwidth of the signal is reduced. This suggests that the use of narrowband signals may improve the phase coherency while affecting minimally the overall resolution (which is proportional to the RF carrier wavelength). This also suggests that lower frequency applications, such as foliage penetration, may provide a better degree of coherence, leading to better, sharper image reconstructions.
- **Nonpoint-scatterer models.** By using scattering models other than the point scatterer, it may be possible to predict the angular extent of the coherence and hence the k-space support available for tomographic radar processing, or even to reformulate the theory of RT.
- **Experimental confirmation.** Full 360° 2D tomographic ISAR imaging has shown that multipath, shadowing, and decreased degree of coherence pose only a minor loss in resolution and image quality, as evident in Figure 5.24. This is compelling evidence that tomographic algorithms can be applied to image realistic targets.

For multichannel multistatic systems, synchronization across the channels and accurate TMC for each channel are required for a coherent population of measurements in the combined k-space support. This requirement may impose significant practical challenges and warrant further attention from the research communities and system designers.

In conclusion, this chapter summarizes some of the currently known methods and applications of RT, with the promising potential of offering very high-resolution target imaging without the requirement of wideband hardware. Issues with tomographic data collection, image formation methods, and the special case of Doppler RT have been discussed in detail.

Given the current trends of operational requirement and developments for radar imaging technologies, RT can be expected to play an ever increasingly important role in the foreseeable future.

Appendix

A Theoretical image resolution limits

This appendix shows details of derivation leading to resolution limits, such as that indicated in (5.19) for the 2D case. Circular symmetry and an ideal band-limited frequency-domain signal populating the annular support (denoted as V_k) are assumed. Without loss of generality, we may set $S(\boldsymbol{k}) = 1$ over the support V_k (and 0 elsewhere). The PSF is the inverse FT

$$\begin{aligned} g_\sigma(x,y) &= \mathscr{F}^{-1}\{S(\boldsymbol{k})\} = \iint_{V_k} S(\boldsymbol{k}) \exp\{j(k_x x + k_y y)\}\, dk_x\, dk_y \\ &= \iint_{V_k} \exp\{j(k_x x + k_y y)\}\, dk_x\, dk_y \\ &= \int_{k_{\min}}^{k_{\max}} \left(\int_0^{2\pi} \exp\{jkr\ \cos\varphi\} d\varphi \right) k\, dk \\ &= 2\pi \int_{k_{\min}}^{k_{\max}} J_0(kr)\, k\, dk. \end{aligned} \tag{A.1}$$

where (k, φ) is the polar form of (k_x, k_y), $r = (x^2 + y^2)^{1/2}$ the radial deviation from true scatterer location, $(k_{\min}, k_{\max})$ is the k-space equivalent of the signal's lower and upper frequencies, and $J_0(\cdot)$ is the Bessel function of the first kind and zero order. Using the indefinite integral result

$$\int u\, J_0(u) = u\, J_1(u),$$

where $J_1(\cdot)$ is Bessel function of first order, (A.1) leads to

$$g_\sigma(r) = \frac{2\pi}{r} \left[k_{\max}\, J_1(k_{\max} r) - k_{\min}\, J_1(k_{\min} r)\right], \tag{A.2}$$

as shown in (5.19).

In the 3D case, the result in (A.2) is replaced with

$$g_\sigma(r) = \left(\frac{2\pi}{r}\right)^{3/2} \left[k_{\max}^{3/2}\, J_{3/2}(k_{\max} r) - k_{\min}^{3/2}\, J_{3/2}(k_{\min} r)\right]. \tag{A.3}$$

References

[1] Kak AC, and Slaney M. Principles of Computerized Tomographic Imaging. Philadelphia, PA, USA: Society for Industrial and Applied Mathematics; 2001.

[2] Dictionary check for ‘tomography’. Accessed: October 2018. Available from: https://www.thefreedictionary.com/tomography.

[3] Munson DC, O’Brien JD, and Jenkins WK. A tomographic formulation of spotlight-mode synthetic aperture radar. Proceedings of the IEEE. 1983;71(8): 917–925.

[4] Jakowatz CV, Wahl DE, Eichel PH, *et al.* Spotlight-Mode Synthetic Aperture Radar: A Signal Processing Approach. Springer, New York, USA; 1996.

[5] Mensa DL, Halevy S, and Wade G. Coherent Doppler tomography for microwave imaging. Proceedings of the IEEE. 1983;71(2):254–261.

[6] Soumekh M. Reconnaissance with slant plane circular SAR imaging. IEEE Transactions on Image Processing. 1996;5(8):1252–1265.

[7] Moreira A, Prats-Iraola P, Younis M, *et al.* A tutorial on synthetic aperture radar. IEEE Geoscience and Remote Sensing Magazine. 2013;1(1):6–43.

[8] Chen V, and Martorella M. Inverse Synthetic Aperture Radar Imaging. Scitech Publishing, Edison, NJ; 2014.

[9] Brisken S, Martorella M, Mathy T, *et al.* Motion estimation and imaging with a multistatic ISAR system. IEEE Transactions on Aerospace and Electronic Systems. 2014;50(3):1701–1714.

[10] Wicks MC. RF Tomography With Application to Ground Penetrating Radar. In: 2007 Conference Record of the Forty-First Asilomar Conference on Signals, Systems and Computers; 2007. pp. 2017–2022.

[11] Monte LL, Erricolo D, Soldovieri F, *et al.* Radio frequency tomography for tunnel detection. IEEE Transactions on Geoscience and Remote Sensing. 2010;48(3):1128–1137.

[12] Olivadese D, Giusti E, Petri D, *et al.* Passive ISAR with DVB-T Signals. IEEE Transactions on Geoscience and Remote Sensing. 2013;51(8):4508–4517.

[13] Griffiths HD, and Baker CJ. Fundamentals of Tomography and Radar. In: Advances in Sensing With Security Applications; 2005. pp. 171–187.

[14] Griffiths HD, and Baker CJ. Imaging Radar for Combatting Terrorism. In: Imaging for Detection and Identification; 2007. pp. 29–48.

[15] Lopez-Sanchez JM, and Fortuny-Guasch J. 3-D radar imaging using range migration techniques. IEEE Transactions on Antennas and Propagation. 2000;48(5):728–737.

[16] Balanis CA. Advanced Engineering Electromagnetics, 2nd Edition. Wiley, Hoboken, NJ, 1040 pp. 2012.

[17] Tran H, and Melino R. The slow-time k-space of radar tomography and applications to high-resolution target imaging. IEEE Transactions on Aerospace and Electronic Systems. 2018;54(6):3047–3059.

[18] Tran H, Heading E, Monte LL, *et al.* An Experimental Study of Radar Tomographic Imaging in a Multi-bistatic Scenario. In: 2017 IEEE Radar Conference (RadarConf); 2017. pp. 0419–0424.

[19] Knaell KK, and Cardillo GP. Radar tomography for the generation of three-dimensional images. IEE Proceedings – Radar, Sonar and Navigation. 1995; 142(2):54–60.

[20] Blacknell D, Andre D, Finch C, *et al.* Life in the Frequency Domain: SAR CCD over Mountains and the Physics of Vibrating Targets. In: Proceedings of the Defense Applications of Signal Processing (DASP'11); 2011.

[21] Greengard L, and Lee J. Accelerating the nonuniform fast Fourier transform. SIAM Review. 2004;46(3):443–454. Available from: https://doi.org/10.1137/S003614450343200X.

[22] Dutt A, and Rokhlin V. Fast Fourier transforms for nonequispaced data, II. Applied and Computational Harmonic Analysis. 1995;2(1): 85–100. Available from: http://www.sciencedirect.com/science/article/pii/S106352038571007X.

[23] Sun S, Zhu G, and Jin T. Novel methods to accelerate CS radar imaging by NUFFT. IEEE Transactions on Geoscience and Remote Sensing. 2015;53(1):557–566.

[24] Ferrara M. Implement 1D-3D NUFFTs via 'Fast Gaussian Gridding'. Accessed: November 2018. Available from: https://ww2.mathworks.cn/matlabcentral/fileexchange/25135-nufft-nfft-usfft.

[25] Cetin AE, and Ansari R. Iterative procedure for designing two-dimensional FIR filters. Electronics Letters. 1987;23(3):131–133.

[26] Combettes PL. The foundations of set theoretic estimation. Proceedings of the IEEE. 1993;81(2):182–208.

[27] Stasinski R, and Konrad J. POCS-Based Image Reconstruction From Irregularly-Spaced Samples. In: Proceedings 2000 International Conference on Image Processing (Cat. No.00CH37101). vol. 2; 2000. pp. 315–318.

[28] Wang B. An efficient POCS interpolation method in the frequency-space domain. IEEE Geoscience and Remote Sensing Letters. 2016;13(9): 1384–1387.

[29] Nguyen NH, Doğançay K, Tran HT, *et al.* An image focusing method for sparsity-driven radar imaging of rotating targets. Sensors. 2018;18:1840.

[30] Nguyen NH, Dogancay K, Tran HT, *et al.* Nonlinear Least-Squares Post-Processing for Compressive Radar Imaging of A Rotating Target. In: 2018 International Conference on Radar; 2018.

[31] Shalev-Shwartz S, and Ben-David S. Understanding Machine Learning: From Theory to Algorithms. Cambridge University Press, New York; 2014.

[32] Bertero M, and Boccacci P. Introduction to Inverse Problems in Imaging. Institute of Physics Publishing, Bristol, UK; 1998.

[33] Hansen PC. The truncated SVD as a method for regularization. BIT Numerical Mathematics. 1987;27(4):534–553. Available from: http://dx.doi.org/10.1007/BF01937276.

[34] Wilson J, Patwari N, and Vasquez OG. Regularization Methods for Radio Tomographic Imaging. In: 2009 Virginia Tech Symposium on Wireless Personal Communications; 2009.

[35] Wilson J, and Patwari N. Radio tomographic imaging with wireless networks. IEEE Transactions on Mobile Computing. 2010;9(5):621–632.

[36] Potter LC, Ertin E, Parker JT, *et al.* Sparsity and compressed sensing in radar imaging. Proceedings of the IEEE. 2010;98(6):1006–1020.

[37] Tibshirani R. Regression shrinkage and selection via the lasso. Journal of the Royal Statistical Society Series B (Methodological). 1996;58(1):267–288. Available from: http://www.jstor.org/stable/2346178.

[38] Beck A, and Teboulle M. A fast iterative shrinkage-thresholding algorithm for linear inverse problems. SIAM Journal on Imaging Sciences. 2009;2(1):183–202. Available from: https://doi.org/10.1137/080716542.

[39] Cetin M, and Karl WC. Feature-enhanced synthetic aperture radar image formation based on nonquadratic regularization. IEEE Transactions on Image Processing. 2001;10(4):623–631.

[40] Nguyen NH, Tran HT, Dogancay K, *et al.* A Review of Sparsity-Based Methods for Analysing Radar Returns from Helicopter Rotor Blades. Defence Science and Technology Group; 2016. DST-Group-TR-329.

[41] Nguyen NH, Dogancay K, Berry PE, *et al.* Convex Relaxation Methods: A Review and Application to Sparse Radar Imaging of Rotating Targets. Defence Science and Technology Group; 2017. DST-Group-RR-0444.

[42] Tran HT, Heading E, and Ng B. Multi-Bistatic Doppler Radar Tomography for NonCooperative Target Imaging. In: 2018 International Conference on Radar; 2018.

[43] Tran HT, and Melino R. Application of the Fractional Fourier Transform and S-Method in Doppler Radar Tomography. Defence Science and Technology Group; 2010. DSTO-RR-0357.

[44] Essen H, Biegel G, Sommer R, *et al.* High Resolution Tower-Turntable ISAR with the Millimetre Wave Radar COBRA (35 / 94 / 220 GHz). In: 7th European Conference on Synthetic Aperture Radar; 2008. pp. 1–4.

This page intentionally left blank

Chapter 6

Multistatic PCL–SAR

Diego Cristallini[1], Philipp Wojaczek[1] and
Ingo Walterscheid[2]

In this chapter, the attention is turned toward multistatic passive radar systems on airborne platforms for the purpose of synthetic aperture radar (SAR) image creation. A passive radar system is a special type of bistatic radar that exploits noncooperative transmitters as its source of illumination.

This chapter begins with an overview and introduction to passive SAR. By referring to the widely used digital video broadcast-terrestrial (DVB-T) standard as illuminator, we describe the complete signal processing chain in order to create a passive SAR image. This includes (i) preprocessing, which involves the synchronization, and the estimation of the reference signal; (ii) range compression, specifically addressing the time-varying waveform characteristics; (iii) the image formation stage, basically residing on back projection; and finally (iv) the issues related to mitigation of co-channel interference (CCI) arising in airborne passive radars.

One big drawback of passive SAR is the relatively poor-range resolution, due to the limited bandwidth of the transmitted signal. To overcome this issue, we propose the exploitation of multistatic passive SAR. Specifically, the multistatic received signal model is presented in the **K**-space, and optimal platform trajectories are presented which lead to constant range resolution improvement over the synthetic aperture.

Finally, the current experimental passive-radar activities for SAR imaging are presented along with the results.

6.1 Introduction

The expression passive coherent location (PCL) indicates a class of bistatic radar systems that do not send a dedicated electromagnetic signal but instead they exploit electromagnetic signals emitted by other sources for other purposes [1,2]. Such sources are usually referred to as illuminators of opportunity (IOs), and they can be other radars, communication systems, and broadcast systems for public utility,

[1] Department of PSR, Fraunhofer FHR, Wachtberg, Germany
[2] Department of ARB, Fraunhofer FHR, Wachtberg, Germany

such as frequency modulation (FM) radio or digital television (DVB-T), and so on. PCL radar systems have gained renewed interest over the last decades, thanks to the advantages coming from not having a dedicated transmitter, namely, (i) they can be considered “green radars,” not introducing further electromagnetic pollution in the environment; (ii) they are generally low cost, as they only need a receiver, whose hardware is usually easily found on the commercial market; and (iii) they work in covert operation as they do not emit a dedicated signal, thus their position is hard to be estimated.

The idea of adapting the PCL to obtain (inherently bistatic) SAR, namely, PCL–SAR or passive SAR, has been analyzed in different works over the last few decades. First, PCL–SAR exploiting satellite illuminators has been investigated. Specifically, [3] introduced the idea of satellite-based passive SAR. Namely, geostationary broadcast illuminators were proposed with the receiver mounted on a geosynchronous satellite. Integration times of several hours are foreseen to achieve adequate signal-to-noise ratio (SNR). Cherniakov *et al.* [4] adapt the previous idea but resorting to low Earth orbit satellites and stationary ground-based receivers so to enhance the SNR, while in [5], an experimental validation is presented. Later, also global navigation satellite system (GNSS) illuminators, such as global positioning system (GPS) and Galileo, have been considered, and experimental verification has been conducted [6–9]. GNSS also offers the possibility to have multiple dislocated transmitters (namely, the different satellites of the constellation), which can be used in a multistatic passive SAR configuration to improve range resolution as shown in [10]. The concept of airborne passive radar exploiting terrestrial illuminators is presented in [11]. In [12–14], ground-based passive SAR exploiting orthogonal frequency division modulation (OFDM)-based signals, such as worldwide interoperability for microwave access (WiMAX), is addressed and demonstrated in a small-scale experimental setup. The authors focus their work on the analysis of the WiMAX bistatic ambiguity function. In the same work, the range compression stage is addressed, which aims at obtaining phase histories of targets by matched filtering. In [15], a similar approach is extended to other OFDM-based IO, such as long-term evolution (LTE) [16], digital audio broadcast (DAB), and DVB-T. In the same paper, a *partially* matched filter (MF) is also applied for range compression that exploits only known signal features. Mulgrew in [17] formulates the passive SAR imaging as a linear regression. In the same work, also the principle of exploiting geometry diversity through multiple transmitters to ameliorate resolution is proposed. Different works set an analytical approach to passive radar imaging based on various forms of back projection for the bistatic and for the multistatic scenario [18–21]. References [22–27] show experimental results of passive SAR exploiting DVB-T as IO.

As is apparent, miniaturized and real-time operation of PCL radar systems is becoming available so that installation of PCL systems on moving platforms is becoming reality. In addition, also constellations of low-cost light-weight receivers will become an extremely appealing solution for surveillance and reconnaissance in the near future. It is, therefore, highly advisable to investigate techniques and strategies to exploit at best the potentialities of such constellations. In fact, the reduced costs of passive and covert operation would be extremely appealing features for any imaging radar. In this context, one of the main drawbacks of PCL systems is that the transmitted signal is not under the control of the radar designer, as it is designed for other purposes. As a consequence, the transmitted signal does not exhibit characteristics typical of a radar signal. For instance, if analog-modulated waveforms are exploited, then the signal is likely to have time-varying spectral characteristics, which directly affect the corresponding PCL radar performance [28]. Although digital transmissions usually show features much nicer for radar use (e.g., OFDM signals have flat constant spectrum), their overall bandwidth is still limited to few MHz. The limited signal bandwidth is a significant obstacle toward the use of PCL–SAR. In fact, the range resolution of an imaging radar is inversely proportional to the signal bandwidth. In contrast, the cross-range resolution of an imaging radar is mainly limited by the along-track synthetic aperture, so that fine cross-range resolution values are theoretically achievable also by a PCL–SAR.

The range resolution of a PCL–SAR can be improved by simultaneous processing of multiple adjacent received signals (for instance adjacent DVB-T channels), or by exploiting a constellation of PCL receivers observing the same area on ground illuminated by a single IO. The first approach is not always viable since there might not be multiple available signals so close that a coherent combination is possible. In contrast, the second approach might define an interesting multistatic PCL–SAR (shortened to multi-PCL–SAR in the following) constellation. The problem of defining multiple trajectories that improve SAR range resolution has been already addressed for the conventional active radar case [29–32]. In [33,34], also the impact of trajectory errors is analyzed. In addition, in [35], the idea has been applied to simultaneous operation of a constellation of multiple PCL receivers, where the geometry is defined by resorting to the **K**-space occupancy of the multiple bistatic received signals.

In this chapter, it is shown that the **K**-space signal occupancy changes (in general) over the acquisition (i.e., slow-time) and over an extended scene, and consequently also the range pulse response characteristics vary. This occurs also for the simple case of rectilinear trajectories. In this work, the effects of range pulse response of multi-PCL–SAR for rectilinear trajectories are analyzed. Also, it will be demonstrated that circular trajectories can guarantee an unvarying **K**-space signal occupancy over the acquisition.

This chapter is organized as follows: in Section 6.2, the required signal processing for PCL–SAR is addressed with particular attention to the DVB-T-based case. In addition, the imaging steps to achieve PCL–SAR as well as the main issues arising from airborne operation of a PCL system are addressed. Section 6.3 is devoted to the analysis of multistatic PCL–SAR configurations for improved range resolution. Section 6.4 presents some results of the PCL–SAR activities conducted at Fraunhofer FHR. Finally in Section 6.5, we draw our conclusions.

6.2 Signal processing for PCL–SAR based on DVB-T

DVB-T is probably the most used transmitter worldwide for illumination among all transmitters exploited for passive radar. It is a standardized and almost worldwide used transmission type in order to provide audio and video broadcast [36].

For the passive radar community, it offers some advantages, e.g., it has usually a high transmit power, the occupied bandwidth is reasonably broad (approximately 8 MHz) thus providing (monostatic) range-resolution possibilities in the order of 20 m. On land, it is available almost everywhere, thus providing a good coverage which makes it attractive for PCL. The main advantage is, however, the possibility of recovering the transmitted waveform and the constant bandwidth due to the digital modulation. Therefore, it is possible to get a clean copy of the transmitted signal for range compression without introducing any errors due to correlation with a defective reference signal. For these advantages, we focus on DVB-T transmitters as IOs.

6.2.1 Structure of DVB-T signal

The DVB-T signal is transmitted as continuous wave signal. It constitutes in time-domain of so-called symbols, each of duration T_{OFDM} [36]. Each symbol consists of a useful part of duration T_U and of a guard interval (also called cyclic prefix) of duration T_{CP}: $T_{OFDM} = T_U + T_{CP}$. The guard interval is a copy of the last part of the useful part and copied before it so that cyclic convolution is enabled and inter-symbol interference (ISI) is reduced. In frequency domain, the DVB-T signal utilizes the OFDM modulation scheme, which means that each symbol comprises M separately modulated carriers, where the frequency of each carrier is separated by $1/T_U$, which creates the orthogonality. The carriers are indexed with $m = 0, \ldots, M - 1$, and they can be divided in two groups: payload data carriers (nondeterministic) and pilot carriers (deterministic). The pilot carriers are transmitted with 3 dB higher power level compared to the average power level. They can be further subdivided in two groups, the *scattered* pilot carriers and the *continual* pilot carriers. The positions $\mathbf{m}_{CP}$ of the continual pilots are constant for each symbol, while the positions $\mathbf{m}_{SP}$ of the scattered pilots are shifted by three from symbol to symbol, i.e., the positions $\mathbf{m}_{SP}$ are the same for each fourth symbol.

Due to their deterministic nature, the pilot carriers enable synchronization in frequency and time, as well as channel estimation.

6.2.2 Received DVB-T signal model

Broadcast signals, such as DVB-T, FM, or DAB, are usually transmitted by networks of transmitters. Those networks are organized either in multifrequency networks (MFNs) or single frequency networks (SFNs). In an MFN, which is normally the case for FM broadcast networks, an FM radio station broadcasts on a particular carrier frequency from one transmitter. That same carrier frequency is not reused by another transmitter unless it is suitably outside of the coverage region of the first transmitter. This is to prevent CCI and as a result, the frequency reuse factor in FM broadcasting is low. In theory, a receiver in a particular coverage region should only be influenced by the signal received from the transmitter, which is exploited as IO. The reception should not be disturbed by a different signal, which is transmitted from another radio station on the same carrier frequency.

On the other hand, if an SFN broadcasting type is employed, a number of transmitters are grouped to an SFN. Each transmitter belonging to a particular SFN is synchronized in time and frequency and radiates the same signal on the same carrier frequency. However, any SFN directly adjacent will transmit on a different carrier frequency, while the primarily used carrier frequency can be reused in the next but one SFN. This is because a ground-based receiver will most likely not receive (or at least receive the signal considerably attenuated) the transmission of the next but one SFN due to shadowing by landscape, man-made buildings and attenuation due to free-space loss, etc. In order to prevent ISI from transmitters from the same SFN, guard intervals are introduced in the transmission. As a consequence, SFNs offer a significant improvement in frequency reuse.

In a single transmitter environment, the complex envelope of the received signal at the passive radar surveillance channel can be written as a function of time t as (including motion compensation of the receiving platform)

$$r(t) = A_{dir}s(t) + \sum_{q=1}^{N_R} \int_{\Phi_q} A_q(\phi)s(t - t_q) \exp(j2\pi f_{q,\phi}t)d\phi + e(t) \qquad 0 \leq t \leq T \tag{6.1}$$

where T is the global observation time, $s(t)$ is the transmitted signal and A_{dir} is its corresponding complex amplitude at the surveillance antenna, N_R is the range extent of the observed scene (expressed in range gates), Φ_q is the azimuthal angular sector of the illuminated scene, $A_q(\phi)$ is the complex amplitude of the echo received with time delay $t_q = R_q/c_0$ (c_0 is the speed of light) from azimuth angle ϕ, R_q is the bistatic range of the qth range gate, and $e(t)$ is the additive white Gaussian noise (AWGN) generated in the receiver. Finally, $f_{q,\phi} = (V_R/\lambda)\cos\phi\cos\psi_q$ is the bistatic Doppler frequency for the stationary echo received in the qth range gate observed under off-nadir angle ψ_q and under azimuth angle ϕ (λ being the carrier wavelength). Please note that the aforementioned expression for the Doppler frequency is valid only for stationary transmitter and moving receiver (with velocity V_R assumed in the along-track direction) and for stationary echoes.

The signal model introduced in (6.1) refers (for simplicity) to the MFN case, but it can be readily extended to the SFN case by summing up the contributions for each transmitter in the network.

6.2.3 Synchronization and reference signal reconstruction

Digitally coded OFDM broadcast signals, in contrast to analog broadcast signals, generally provide synchronization features, which enable the receivers to synchronize on the data stream and identify the beginning and end of data symbols to be interpreted by the receiver.

As stated in Section 6.2.1, for DVB-T signals, this is provided by the pilot carriers, which also enable channel transfer function (CTF) estimation. This basically enables two processing schemes: (i) using a dedicated reference channel for the acquisition of the direct signal and (ii) by reconstructing the direct signal through signal demodulation and remodulation enabled by knowledge of the deterministic pilot carrier positions and modulations. Corresponding block diagrams for the two approaches

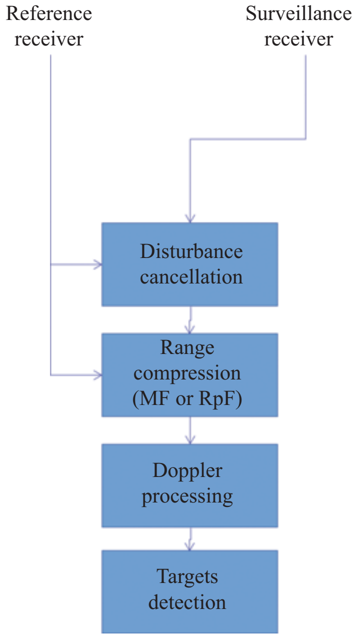

Figure 6.1 Basic PCL processing block diagram using a dedicated reference channel

are sketched in Figures 6.1 and 6.2, respectively. In both cases, the processing block *disturbance cancellation* refers to the removal of the interfering direct signal. This is usually done by exploiting adaptive temporal cancellation approaches such as those in [37]. In the following, we will refer to the second approach. In fact, since in PCL systems the direct signal is generally the strongest contribution, its decoding is generally possible and the second approach offers the possibility to reduce the number of receiving channels. The reconstruction of reference signal in DVB-T is based on (i) synchronization on the start of a DVB-T symbol in the received data stream (as any other DVB-T receiver should do, not only a PCL receiver); (ii) decoding of the synchronized signal according to the DVB-T standard down to the sequence of bits; and (iii) the remodulation of the bit sequence according to the DVB-T standard. This processing step is represented by the block *direct signal reconstruction* in Figure 6.2. At the end of this processing, a replica of the transmitted signal is available, which is free of multipath echoes and multiple transmitter contributions, so that it can be used as the reference signal for further processing of the received target echo signals.

In DVB-T standard, synchronization features are provided by the scattered and continuous pilot carriers within the signal. Specifically, since the position, amplitude, and phase of these carriers are known, a comparison of their received values with the expected ones is used to determine the CTF and thus calculates through carrier interpolation the complete signal, as it was transmitted. In a first step, the received signal after sampling at Nyquist rate is synchronized using a reference sequence. This sequence is a synthesized segment of four DVB-T symbols containing only the known

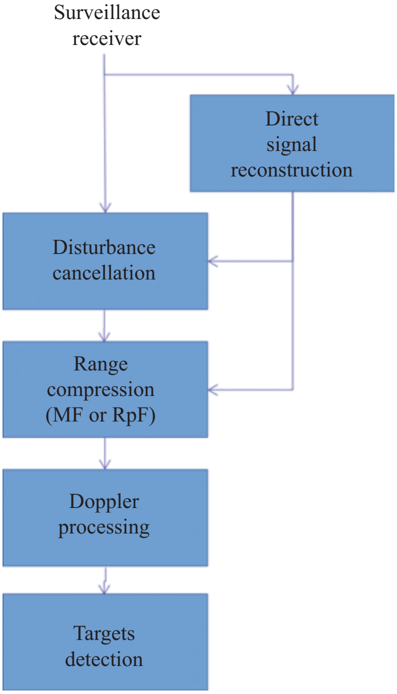

Figure 6.2 Digital PCL processing block diagram where the direct signal is extracted from the surveillance channel

modulation of the scattered and continual pilots. Correlating both signals results in a detection statistic that has a dominant peak at the synchronization position, i.e., at the beginning of four consecutive symbols with different positions of the scattered pilots in each symbol. The received signal can, therefore, be considered synchronized to the transmitter with an accuracy equals to half the sampling rate, so that the correct location m of each carrier within the received OFDM symbol can be determined. By recalling (6.1) and by referring only to the direct signal contribution, the received signal $r(t)$ in (6.1) is first sampled at Nyquist rate obtaining the sequence $r[l]$, where $t = l/f_s$ (f_s being the sampling frequency). After synchronization on the start of a DVB-T symbol, the sequence $r[l]$ is then partitioned in $N = \lfloor T/T_{OFDM} \rfloor$ sequences (or batches) each having the length $L_{OFDM} = T_{OFDM} \times f_s$ of an OFDM symbol that is $r[l] = \sum_{n=1}^{N} r_n[l - nL_{OFDM}]$. After discrete Fourier transform (DFT) in frequency domain $r_n[l]$ (i.e., $R_n[m] = DFT\{r_n[l]\}$), one gets:

$$\begin{aligned} R_n[m] &= \sum_{l=1}^{M} r_n[l] e^{-(j2\pi mn/M)} \qquad m = 1, \ldots, M \\ &= S_n[m] \cdot W_n[m] + E[m] \end{aligned} \tag{6.2}$$

where $W_n[m]$ denotes the channel response function for the nth OFDM symbol, and $E[m] = DFT\{e[l]\}$ is the DFT of the AWGN contribution.

The CTF W_n can be estimated at the known pilot carrier positions $m_p \in [\mathbf{m}_{SP}, \mathbf{m}_{CP}]$ by using:

$$W_n[m_p] = \frac{R_n[m_p]}{S_n[m_p]} \qquad \forall\, m_p \tag{6.3}$$

as $R_n[m_p]$ are the received pilot carrier values and $S_n[m_p]$ are the pilot carrier values modulated according to the DVB-T standard [36]. The characteristics of the CTF at the remaining carriers can be estimated using an interpolation. Applying the CTF on the received signal using:

$$S_n^{(e)}[m] = \frac{R_n[m]}{W_n[m]} \qquad \forall\, m_p \tag{6.4}$$

gives a preliminary estimate $S_n^{(e)}$ of the transmitted signal. The carrier values of $S_n^{(e)}$ then have to be remapped to the actual values of the constellation map, which results in a "clean" (i.e., non-noisy, but not necessarily correct) estimation $\hat{S}_n$ of the transmitted signal S_n.

It has to be noted here that CTF estimation is possible due to the orthogonality of the carriers and time-invariance of the CTF. While this holds for a stationary receiver, this is not necessarily the case for a moving receiver, as due to Doppler-shifted multipath, the CTF is not time invariant anymore. However, the DVB-T standard is very robust against time-varying channels as stated in [38] and which has been confirmed in a trial campaign on an airborne receiver [39].

6.2.4 Range compression in PCL–SAR

According to the block diagram presented in Figure 6.2, the following processing step is the *range compression*.

Given the employed waveforms of opportunity in PCL systems, the resulting pulse response after range compression shows a generally high side-lobe level. Basically, clutter echoes generated at a given range cell are likely to affect, through their side lobes, the response of targets appearing at other cells even in the presence of a large range/Doppler separation. To better understand the effects of this phenomenon, let us consider a conventional signal processing based on the exploitation of an MF at the range compression stage.

In this work, we assume that this is performed on batches of length L_{OFDM} corresponding to a single OFDM symbol, namely, $r_n[l]$. Each single batch is then processed separately as far as the range compression stage is concerned. The output of the corresponding range compression stage can be written as

$$x_n[l] = r_n[l] \circledast h_n[l] \qquad n = 1, \ldots, N \tag{6.5}$$

where $\circledast$ indicates the convolution operator, and $h_n[l]$ is the range compression filter for the nth batch. In order to build up this filter, we assume a perfect reconstruction of the transmitted signal based on the signal collected either at the Rx surveillance antenna or at a separate dedicated antenna element [40,41]. By applying an MF in the range compression in (6.5), we obtain:

$$h_n[l] = h_n^{(MF)}[l] = \kappa s_n^*[-l + nL_{\mathrm{OFDM}}] \qquad n = 1, \ldots, N \tag{6.6}$$

where κ is a multiplicative constant, and "$*$" indicates complex conjugation. After application of the MF as in (6.6), the range compressed signal $x_n[l]$ in (6.5) can be written as

$$x_n^{(MF)}[l] = s_n[l - nL_{\mathrm{OFDM}}] \circledast h_n^{(MF)}[l] = \kappa \mathrm{IDFT}\{|S_n[m]|^2\} \qquad n = 1, \ldots, N \tag{6.7}$$

being $S_n[m]$ the DFT of $s_n[l]$, and indicating with IDFT$\{\cdot\}$ the inverse discrete Fourier transform (IDFT) of its argument. Since the signal changes from batch to batch, the shape of $x_n^{(MF)}[l]$ varies with n. We emphasize that the considered signal model is valid only for echo delays smaller than the cyclic prefix T_G of the OFDM symbol, otherwise a border effect should be taken into account. An example of possible realization of $x_n^{(MF)}[l]$ is reported in Figure 6.3. Notice that some high side peaks appear due to the presence of pilots in the DVB-T OFDM symbol [42,43]. These represent the deterministic components of the generic OFDM symbol and usually show periodic repetitions across consecutive OFDM symbols within a frame [36]. In addition, a quite constant background level is apparent that is basically due to the random sequences of bits transmitted on data subcarriers.

Aiming at removing the impact of the signal information content on the range pulse response, an approach based on the use of the reciprocal filter (RpF) for the range compression stage can be considered. The use of RpF filter has been first introduced for a passive radar system based on OFDM transmissions by Glende in [44]. This performs a spectral equalization of the input signal, thus generating waveform-independent compressed output signals. In this case, the filter $h_n[l]$ in (6.6) becomes:

$$h_n[l] = h_n^{(RpF)}[l] = \kappa' IDFT \left\{ S_n[m]^{-1} \exp\left(\frac{j2\pi mn}{N}\right) \right\} \qquad n = 1, \ldots, N \tag{6.8}$$

where κ' is a multiplicative constant. Correspondingly, the output of the range compression stage for the generic signal batch becomes:

$$x_n^{(RpF)}[l] = s_n[l - nL_{OFDM}] \circledast h_n^{(RpF)}[l] = k' L_{OFDM} \delta[l] \qquad n = 1, \ldots, N \tag{6.9}$$

which is clearly independent of the information content transmitted in the specific signal fragment. For instance, the output of the RpF is reported in Figure 6.4 for the same OFDM symbol considered in Figure 6.3, where we limit the application of the RpF to nonzero subcarriers (i.e., data and pilot subcarriers) in order to avoid possible overweighting caused by the RpF [44]. Following the application of the RpF, all the side peaks appearing in Figure 6.3 have been removed and the side-lobe decay has been restored to a digital sinc function typical of chirp signals after range compression.

6.2.5 Image formation

After range compression, the last processing step to achieve PCL–SAR is the *image formation*. Please note that this slightly differs from the block diagram presented in Figure 6.2, being that related to a more general PCL system and not specific for PCL–SAR.

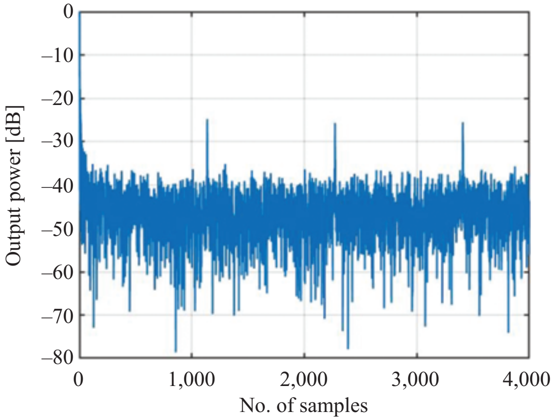

Figure 6.3 Output of the range compression stage for a single DVB-T symbol after matched filter. © 2019 IEEE. After, with permission, from [45]

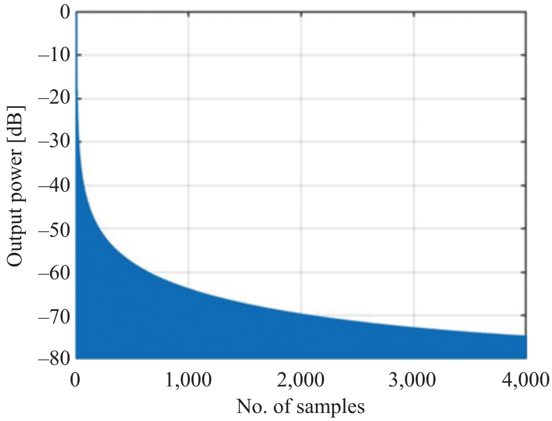

Figure 6.4 Output of the range compression stage for a single DVB-T symbol after reciprocal filter. © 2019 IEEE. After, with permission, from [45]

A classical monostatic SAR is a type of radar, where transmitter and receiver are colocated on a moving platform such as a satellite or an aircraft. Typically, the antennas are arranged in a side-looking configuration so that a scene is illuminated while the platform is in motion. In contrast to a conventional beam-scanning radar, a SAR synthesizes a large antenna array in along-track direction by periodically transmitting a pulse, receiving the echoes and storing the sampled data. The following coherent processing of the collected data allows for a very fine resolution in flight direction. The cross-track resolution is mainly determined by the bandwidth of the emitted waveform. This two-dimensional image formation process can be done using frequency-domain or time-domain focusing algorithms.

The PCL–SAR case differs from the classical airborne SAR in some characteristics. First, the PCL transmitter (e.g. DVB-T) is stationary, where the antenna is usually mounted at a tall mast at an exposed location. Second, the transmit waveform and pulse repetition interval (symbol length) are specified by the IO, and third, a complex preprocessing of the data is necessary to get a data matrix with well-synchronized range-compressed echoes over time. Furthermore, the flight track of the PCL receiver may not necessarily be linear so that an acquisition geometry as sketched in Figure 6.5 is assumed.

Due to the bistatic acquisition geometry and an arbitrary flight path of the receiver, the use of a back projection algorithm (time-domain processor) is favorable. In contrast to frequency-domain methods, the back projection can model the ideal SAR MF even for a curved flight path and is invariant to the imaging mode, which means that the same algorithm can be used for stripmap and spotlight modes. Further, bi- or multistatic imaging geometries where the transmit and receive antenna are widely separated do not represent a focusing problem, because the back projection algorithm produces a pixel-by-pixel varying MF. It only requires the precise knowledge of the acquisition geometry, which means the exact knowledge of the antenna positions over time relative to the three-dimensional position of the scatterers in the ground-plane of the scene. While for PCL–SAR the position of the transmitter is well known and fixed, the position of the receive antenna is usually estimated with an inertial measurement unit (IMU) on board the platform. The height of the scatterers in the

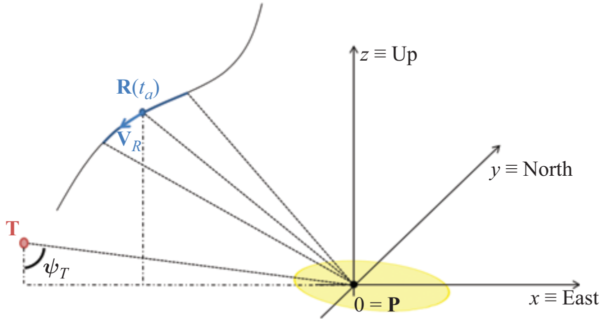

Figure 6.5 PCL–SAR geometry with a fixed transmitter and a moving receiver

scene can be estimated using a digital elevation map. In the past, the back projection algorithm was less significant for standard SAR processing, because it is more computationally expensive than the frequency domain methods. But nowadays, the state-of-the-art computer technology is so sophisticated that multiple operations can be executed simultaneously. The back projection algorithm is highly parallelizable so that it profits from parallel computing, for example, using general-purpose computing on graphics processing units.

The image formation process can be separated into two parts. In the first part, the compression of the received signal is done as already described in Sections 6.2.3 and 6.2.4. The range compressed OFDM symbols $x_n[l]$ can be interpreted as range compressed echoes of a standard pulse radar with a pulse repetition interval equal to the length of an OFDM symbol and n the pulse index. In the second part, the azimuth compression is performed using the back projection algorithm [46] for the reasons stated earlier. The algorithm works in such a way that for each position on ground (image pixel), the appropriate contributions in the echoes are coherently added. This coherent summation for a given position **P** can be described by

$$I(\mathbf{P}) = \sum_{n \in \mathcal{N}} x_n[d_n(\mathbf{P})]\, e^{jkd_n(\mathbf{P})} \tag{6.10}$$

where n is the slow-time pulse index, $\mathcal{N}$ is the set of all pulses contributing to the pixel at position **P**, $k = 2\pi f_0/c_0$ is the wavenumber with f_0 the local frequency in the receiver and c_0 the speed of light, and $d_n(\mathbf{P})$ is the bistatic range for a given scatterer at position **P** with the receiver position according to the pulse index n. The bistatic range is calculated by

$$d_n(\mathbf{P}) = d^{Tx}(\mathbf{P}) + d_n^{Rx}(\mathbf{P}) = |\mathbf{T} - \mathbf{P}| + |\mathbf{R}(n\, T_{\mathrm{OFDM}}) - \mathbf{P}| \tag{6.11}$$

where **T** is the time-invariant transmitter position, $\mathbf{R}(t_a)$ is the time-variant receiver position, and **P** is the position of the scatterer. It is important to note that the argument of $x(\cdot)$ in (6.10) is no longer fast time (or fast time index) but range. The conversion is given by $t = lT_s = d_n/c_0$. Furthermore, it is crucial to upsample the range compressed echo so that during the coherent summation, the residual phase error is low.

6.2.6 Challenges for airborne PCL

Among the challenges resulting from hijacking of a noncooperative transmitter, the challenge of the so-called CCI is maybe one of the most severe challenges for airborne passive radar. CCI describes the phenomenon of receiving more than one signal on the same carrier frequency f_C, where the interfering signals result from transmitters either emitting a different signal content or—if the same signal content is transmitted—arrive at the receiver with a delay which is longer than the guard interval. In the latter case, this is called self-interference and happens only in SFNs. Unlike intentional broadband (noise) jamming, the CCI is not a willful act, as the interfering signals are transmitted from other broadcast transmitters with the purpose of providing full coverage with their broadcasting. A ground-based receiver will most likely not be affected by the reception of interfering signals, as a line of sight (LOS) between receiver and transmitter does not exist, due to shadowing by landscape, man-made objects, etc. However, an airborne receiver has an increased radar horizon due to its higher altitude. In [47], the phenomenon of CCI and its influence was analyzed by means of simulations. For ultra-high frequency (UHF), the signal reception on an airborne platform is mostly attenuated only by free-space loss.

The broadcast operators intend to transmit the signal to the ground, as the customer is generally on the ground. The directive transmission can usually be achieved by transmit antenna tilting and antenna beamforming. However, the antenna tilting and type and number of employed antenna elements are usually not publicly available. Therefore, the power level of received interfering signals cannot be estimated precisely. Furthermore, diffraction on hills or on man-made buildings can lead to multipath reception. Although the simultaneous reception of the long distance traveling UHF signals might be advantageous for airborne moving target detection, for PCL–SAR operations, it is severely disadvantageous, as the interfering signals can drastically increase the noise level, thus limiting the dynamic range.

As it is independent of the transmitter infrastructure, i.e., SFN or MFN, CCI is generally everywhere possible. However, since signals in MFNs are usually transmitted with a higher power (to achieve coverage at edges of the service area [48]), the power level of the interfering signals might be higher for MFNs than compared to SFNs.

The spectrum usage is restricted and reserved for particular usage only based on international law. Therefore, only signals which are generated according to the same standard are transmitted on the frequency which is exploited for PCL–SAR. That means, CCI is usually hard to be detected, as the interfering signals coincide with the exploited signal in terms of bandwidth, synchronization features, etc. This is especially true for standardized signals as DVB-T or DAB, where the standard does not allow exceptions, e.g., in occupied bandwidth. A cancellation via, e.g., spatial nulling is usually only possible if the positions of all transmitters are precisely known to the receiver. However, for the new published standard DVB-T2, variations in terms of synchronization features, bandwidth, carrier spacing, etc. are possible in order to increase the data throughput and to be more flexible and adaptive on the service area, e.g., cities, small towns, and countrysides [49]. Specifically, DVB-T2 allows to use an extended bandwidth compared to DVB-T. This fact gives the chance to detect an interfering signal and to analyze its influence, provided the signal with smaller bandwidth is received with higher power.

For a duration of few years, Germany was in the state of soft-switching from DVB-T to DVB-T2. That means, transmitters providing cities and dense populated areas with television were switched to DVB-T2 first, while transmitters serving the countryside and less populated areas will switch to DVB-T2 with a delay. In order to have an increased data rate for high populated areas, the DVB-T2 transmitters make use of the possibility to transmit on an extended bandwidth $B_W^{(2)} = 7.77\,\text{MHz}$, while the DVB-T standard only allows a fixed bandwidth $B_W^{(1)} = 7.61\,\text{MHz}$, that is, the non-overlapping part of the bandwidth amounts approximately $B_W^{(2)} - B_W^{(1)} \approx 0.16\,\text{MHz}$. This can be proven by real data from a measurement campaign, see Figure 6.6. This figure shows the enlarged view of a recorded DVB-T signal interfered with one or many DVB-T2 signals. The left border of the recorded DVB-T channel is shown,

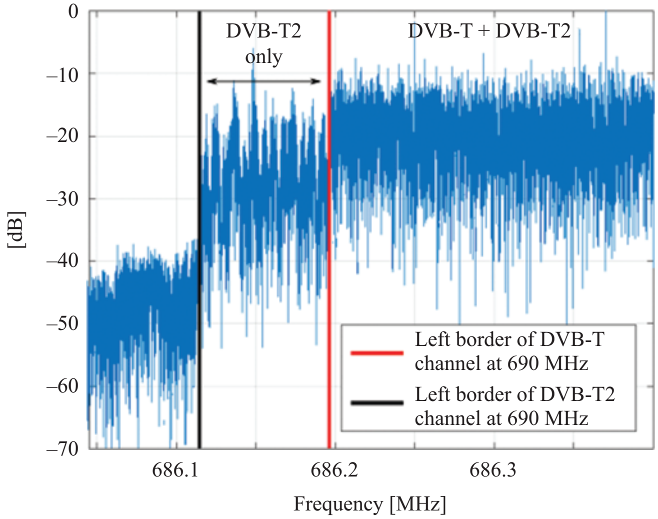

Figure 6.6 Enlarged view of recorded DVB-T with interfering DVB-T2 signal(s). View shows the left border of DVB-T channel at 690 MHz, where one or more DVB-T2 signals at 690 MHz are interfering with the DVB-T signal. The DVB-T signal is the exploited signal from the IO

where the red line indicates its border. The black line indicates the left border of the interfering DVB-T2 signal, which has a bandwidth $B_W^{(2)} = 7.77\,\text{MHz}$. It is easily possible to see the increased power level of the DVB-T2 signal, which severely limits the reference signal reconstruction possibilities and reduces the dynamic range.

Details to the measurement campaign and to the interfering signal sources are provided in Section 6.4. To demonstrate the impact of CCI on reference signal estimation and on increased noise floor, an initial attempt at estimating the reference signal without any prior CCI suppression was performed. The first estimation is done with the received signal $Y^{(1)}(f)$ from antenna 1. During the estimation of a transmitted symbol, so-called constellation maps can be produced. In Figure 6.7, the constellation maps for four DVB-T symbols are shown. The considered transmitter (Eifel) uses 16-quadrature amplitude modulation (QAM), but this constellation format cannot be recognized in Figure 6.7. A range–Doppler map for a coherent processing interval of 512 DVB-T symbols is shown in Figure 6.8. One can see the returns of strong clutter sources, but overall the range–Doppler map is covered with a high noise.

This is for two reasons: one reason is due to the CCI, which increases the noise level. The other reason is an indirect consequence of the CCI: the CCI impedes reference signal estimation. Performing a range compression with a nonideal, erroneous reference signal does not equalize the spectral characteristic of the waveform, which leads to a noncoherent noise floor on the range–Doppler map, compared to the result of MF application [45].

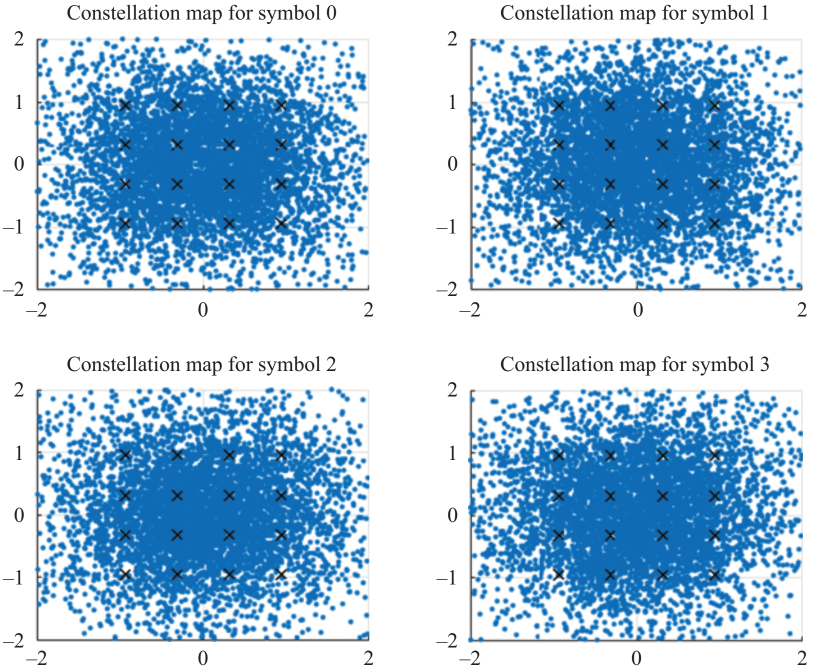

Figure 6.7 Constellation map of four OFDM symbols before CCI suppression. The black crosses indicate the positions of the ideal constellation points

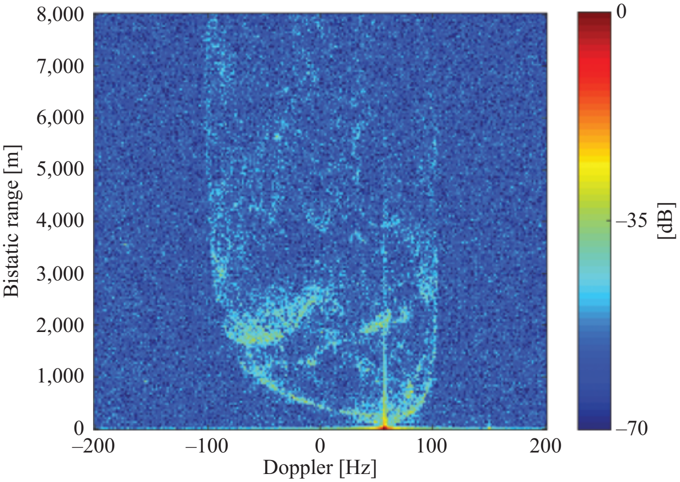

Figure 6.8 Range–Doppler map before CCI suppression

To improve the reference signal estimation, we show a first approach to suppress the CCI using multiple antennas on receive. The received signal $Y^{(n)}(f)$ on antenna $n = (1, 2)$ can be described in frequency domain as

$$Y^{(n)}(f) = H^{(n)}(f)X(f) + H_I^{(n)}(f)X_I(f) + N^{(n)}(f) \tag{6.12}$$

where $X(f)$ defines the transmitted DVB-T signal from transmitter Eifel and $X_I(f)$ defines the CCI source, i.e., the transmitted DVB-T2 signal. $H^{(n)}(f)$ and $H_I^{(n)}(f)$ define the CTFs for the DVB-T signal and the interfering DVB-T2 signal at antenna n, respectively. $N^{(n)}(f)$ defines AWGN.

The transmission of DVB-T2 in extended bandwidth gives us the opportunity to suppress the DVB-T2 signal, using the subcarriers on frequencies occupied only by the DVB-T2 signal. By formulating a minimization problem, one can use these subcarriers and both antennas to estimate suitable values to suppress the CCI.

The domains and codomains of $X(f)$ and $X_I(f)$ are defined in (6.13) and (6.14):

$$X(f) = \begin{cases} \neq 0, & \text{for} f \in F_E \\ = 0, & \text{for} f \notin F_E \end{cases} \tag{6.13}$$

$$X_I(f) = \begin{cases} \neq 0, & \text{for} f \in F_I \\ = 0, & \text{for} f \notin F_I \end{cases} \tag{6.14}$$

where

$$\begin{aligned} F_{BW} &= \left[-\frac{7{,}168}{2T_{U_D}}, \frac{7{,}168}{2T_{U_D}}\right], \quad F_E = \left[-\frac{K-1}{2T_{U_D}}, \frac{K-1}{2T_{U_D}}\right], \\ F_I &= \left[-\frac{K_I-1}{2T_{U_I}}, \frac{K_I-1}{2T_{U_I}}\right], \quad F_E \subsetneq F_I \subsetneq F_{BW} \end{aligned} \tag{6.15}$$

$K = 6{,}817$ and $T_{U_D} = 896 \cdot 10^{-6}$ s define the number of carriers and the duration of the useful symbol part for a DVB-T symbol. $K_I = \{13{,}921, 27{,}841\}$ and $T_{U_I} = \{1{,}792, 3{,}584\} \cdot 10^{-6}$ s define the number of carriers and the duration of the useful symbol part of the extended bandwidth of a DVB-T2 symbol transmitted using the 16k and 32k mode, respectively. Equation (6.15) defines frequency sets: F_{BW} defines the set of frequencies in the complete 8 MHz bandwidth. F_E defines the set of frequencies in the bandwidth occupied by the subcarriers from DVB-T. F_I defines the set of frequencies occupied by DVB-T2, where F_E and F_I overlap at the DVB-T subcarriers. The set of frequencies occupied from DVB-T2 only is defined by $F_T = F_I \setminus F_E$.

The minimization problem is then

$$\underset{z \in \mathbb{C}}{\text{minimize}} \sum_{f_T \in F_T} |Y^{(1)}(f_T) - zY^{(2)}(f_T)|^2 \tag{6.16}$$

where z is a complex number: $z = r \exp(j\varphi)$. z is then applied on $Y^{(2)}(f_E)$ on the subcarriers at the frequencies $f_E \in F_E$ in order to suppress the interfering signal by calculating the difference of $Y^{(1)}(f_E)$ and $zY^{(2)}(f_E)$:

$$Y_m(f_E) = Y^{(1)}(f_E) - zY^{(2)}(f_E) \tag{6.17}$$

The described process was done for each OFDM symbol individually.

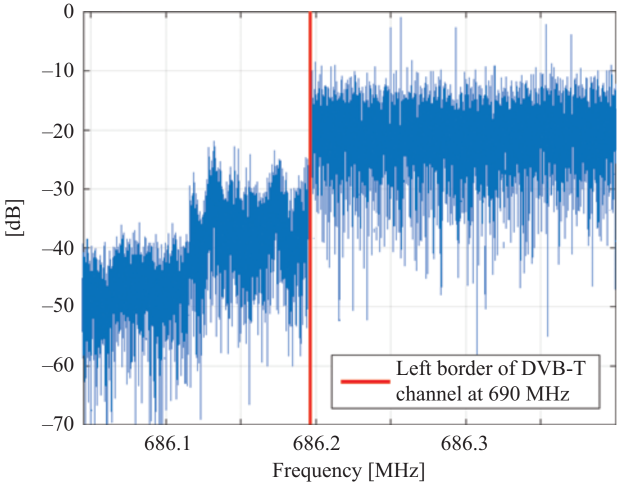

Figure 6.9 Left side of the spectrum of the DVB-T channel after CCI suppression

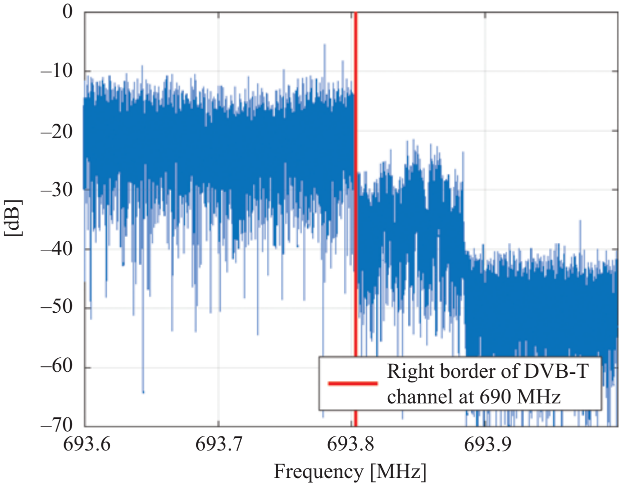

Figure 6.10 Right side of the spectrum of the DVB-T channel after CCI suppression

Figures 6.9 and 6.10 show the spectrum at the left and right edges of the DVB-T signal after the CCI suppression. The DVB-T2 signal is reduced by approximately 10 dB when compared to Figure 6.6.

Assuming that by using (6.16) and (6.17), the CCI in $Y_m(f_E)$ is sufficiently suppressed while the signal of opportunity $X(f_E)$ is preserved, an estimation of the transmitted DVB-T signal $X(f_E)$ can be achieved. Constellation maps of four estimated DVB-T symbols acquired during the process of reference signal estimation are

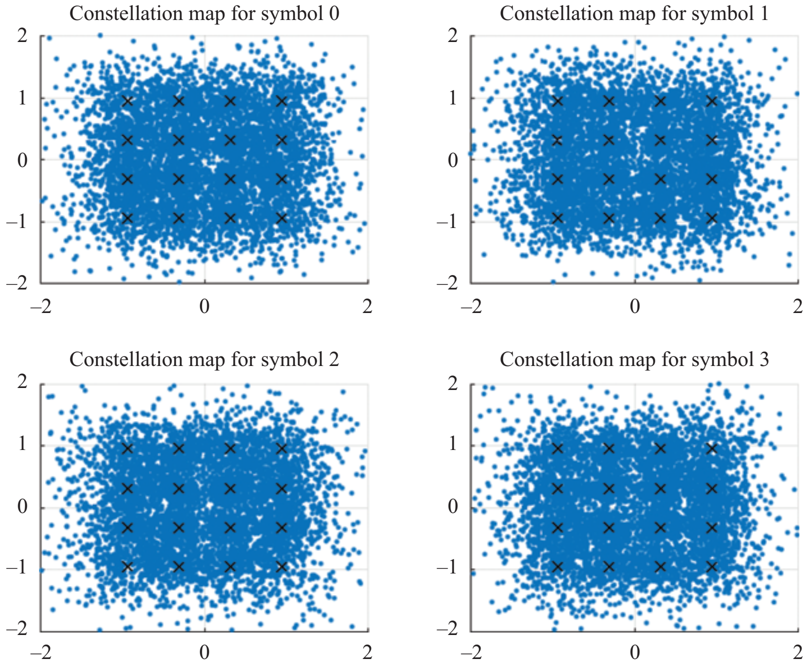

Figure 6.11 Constellation map of four OFDM symbols after CCI suppression. The black crosses indicate the positions of the ideal constellation points

shown in Figure 6.11. Each symbol is still noisy, but the structure of the 16-QAM is now recognizable.

A range–Doppler map of the data with suppressed CCI is shown in Figure 6.12. The estimated reference signal was used for range compression.

Comparing Figure 6.12 with Figure 6.8, the improvement is visible due to the overall reduced noise floor. A reduction of noise N_{red} in the exo-clutter region was calculated using

$$N_{red} = 10 \log 10 \left(\frac{\sum_{f_D \in F_D} \sum_{r \in R_g} |R^{(a)}(f_D, r)|^2}{\sum_{f_D \in F_D} \sum_{r \in R_g} |R^{(b)}(f_D, r)|^2} \right) \tag{6.18}$$

where F_D are Doppler frequencies $F_D = [120, 195]$ Hz and R_g is a set of bistatic ranges $R_g = [750{,}7{,}060]$ m. $R^{(a)}$ and $R^{(b)}$ define the range–Doppler maps after and before CCI suppression. The calculated value of N_{red} is approximately -9.6 dB.

Suppressing the CCI allows for an improved estimate of the reference signal. The better the estimate of the reference signal is, the better are ambiguities and side lobes of the exploited waveform removed. This effect in combination with the suppression of the CCI leads to the reduction in noise floor and in conclusion to a better target detection performance.

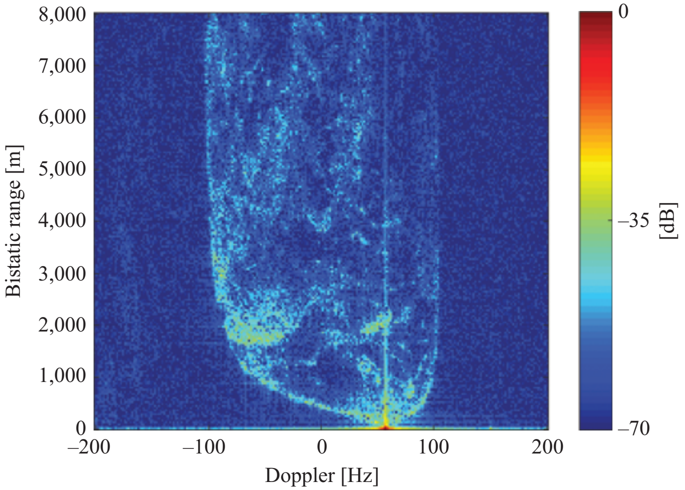

Figure 6.12 Range–Doppler map after CCI suppression

6.3 Multi-PCL–SAR for improved range resolution

The range resolution of a PCL–SAR can be improved by exploiting a constellation of PCL receivers observing the same area on ground illuminated by a single IO. This approach defines a multi-PCL–SAR constellation. The idea of defining multiple trajectories that improve SAR-range resolution can be taken from the conventional active radar case, where multiple authors already addressed the topic [29–34]. In this section, we will define a simultaneous operation of a constellation of multiple PCL receivers, starting from the simple case of two receivers. In particular, the multistatic geometry will be defined by resorting to the **K**-space occupancy of the multiple bistatic received signals.

6.3.1 Range resolution improvement principle

Let us consider an east–north–up (ENU) Cartesian coordinate system (where x-axis being aligned with the east direction, y-axis with the north direction, and z-axis with the vertical direction perpendicular to x–y plane), and let us indicate with $\mathbf{T} = [x_T, y_T, z_T]^\dagger$ the position of an IO (e.g., DVB-T transmitter), and with $\mathbf{R}_i(t_a) = \left[x_{R,i}(t_a), y_{R,i}(t_a), z_{R,i}(t_a)\right]^\dagger$ the time-varying positions of multiple PCL receivers observing the same area illuminated by the IO ($i = 1, 2$ in the simplest case), where t_a indicates the slow-time, and the subscript † indicates the transpose operation. Without loss of generality, we can assume the transmitter $\mathbf{T}$ to be located on the x-axis, that is having $y_T = 0$. In addition, let us indicate with $\mathbf{P}_1$ the position of the scene center, which, for simplicity and without loss of generality, is assumed to be located in the origin of the considered Cartesian coordinate system. The geometry is sketched in Figure 6.13.

Indicating with $\hat{u}_T$ the LOS unit vector from $\mathbf{T}$ to $\mathbf{P}_1$, and with $\hat{u}_{R,i}(t_a)$ the LOS unit vectors from $\mathbf{R}_i(t_a), (i = 1, 2)$ to $\mathbf{P}_1$, each bistatic observation can be equivalently represented by a monostatic one acquired on the corresponding bistatic bisectors [51]. That is, from position:

$$\mathbf{B}_i(t_a) = \frac{1}{2}(\mathbf{T} + \mathbf{R}_i(t_a)) \qquad i = 1, 2 \tag{6.19}$$

As a consequence, the two following equivalent monostatic LOS vectors can be defined:

$$\hat{u}_{B,i}(t_a) = \frac{1}{2}\left(\hat{u}_T + \hat{u}_{R,i}(t_a)\right) \qquad i = 1, 2 \tag{6.20}$$

Recalling [52], the $\mathbf{K}$-space occupancy for the two bistatic signals can be defined as

$$\mathbf{K}_{B,i}(t_a) = \left\{ k\hat{u}_{B,i}(t_a) : k \in \left[\frac{2\pi}{\lambda_{\max}}, \frac{2\pi}{\lambda_{\min}}\right]\right\} \qquad i = 1, 2 \tag{6.21}$$

where k represents the wavenumber spanned by the DVB-T signal bandwidth, and $\lambda_{\min}$ and $\lambda_{\max}$ are the minimum and the maximum carrier wavelengths within the transmitted signal, respectively. Given the close dependency between $\mathbf{K}$-space occupancy in (6.21) and the signal bandwidth (represented by the wavelength span $[\lambda_{\min}, \lambda_{\max}]$), it is easy to assess an inverse proportionality between $\mathbf{K}_{B,i}(t_a)$ in (6.21) and the achievable bistatic range resolution. Specifically, for SAR purposes, the ground-range resolution is of interest, which directly derives from the projection of the $\mathbf{K}$-spaces $\mathbf{K}_{B,i}(t_a)$ onto the (x, y)-plane [52]. By doing so, one gets:

$$\mathbf{K}_{B,i}^{(xy)}(t_a) = \mathbf{\Gamma}^{(xy)}\mathbf{K}_{B,i}(t_a) \tag{6.22}$$

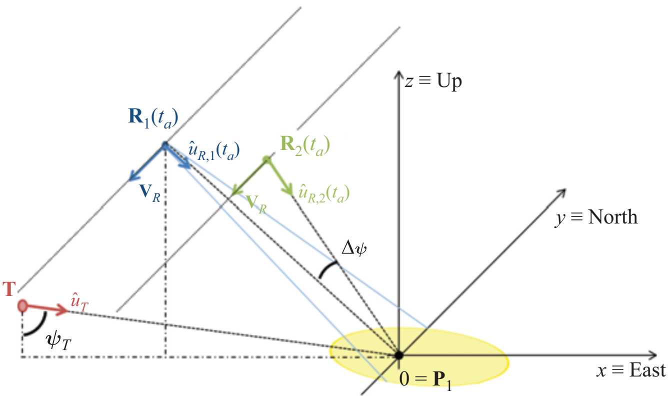

Figure 6.13 Sketched geometry for a multi-PCL–SAR with sensors moving along rectilinear trajectories. © 2017 Elsevier. After, with permission, from [50]

where $\mathbf{\Gamma}^{(xy)} = \mathbf{I} - \mathbf{z}\mathbf{z}^{\dagger}$ is the projection onto the (x, y)-plane, $\mathbf{z}$ indicates the unit vector along the z-axis, and $\mathbf{I}$ is the identity matrix. To better understand (6.22), let us refer to a simplified two-dimensional geometry like the one sketched in Figure 6.14. Please note how this simplified geometry can be considered as a particular case of the general situation depicted in Figure 6.13 for a specific slow-time instant $t_a = t_{a,0}$ (also referred to as mid-acquisition slow-time instant later on in the manuscript), where both receivers $\mathbf{R}_1$ and $\mathbf{R}_2$ lay on the $y = 0$ plane. Namely,

$$\begin{aligned}
\mathbf{R}_1(t_{a,0}) &= \begin{bmatrix} -r_{R,1}\sin(\psi_{R,1}) \\ 0 \\ r_{R,1}\cos(\psi_{R,1}) \end{bmatrix} \\
\mathbf{R}_2(t_{a,0}) &= \begin{bmatrix} -r_{R,2}\sin(\psi_{R,2}) \\ 0 \\ r_{R,2}\cos(\psi_{R,2}) \end{bmatrix}
\end{aligned} \tag{6.23}$$

where $r_{R,i}$ $(i = 1, 2)$ indicates the ranges of the two receivers from the origin of the considered Cartesian reference system, and $\psi_{R,i}$ $(i = 1, 2)$ indicates the corresponding incident angles. In the simplified two-dimensional geometry of Figure 6.14, the equivalent monostatic unit vectors $\hat{u}_{B,1}$ and $\hat{u}_{B,2}$ can be defined as

$$\hat{u}_{B,i} = \frac{1}{2}(\hat{u}_T + \hat{u}_{R,1}) = \frac{1}{2}\left(\begin{bmatrix} u_{T,x} \\ u_{T,y} \\ u_{T,z} \end{bmatrix} + \begin{bmatrix} -\sin(\psi_{R,i}) \\ 0 \\ \cos(\psi_{R,i}) \end{bmatrix}\right) \qquad i = 1, 2 \tag{6.24}$$

Consequently, the $\mathbf{K}$-space signal occupancies $\mathbf{K}_{B,1}(t_{a,0})$ and $\mathbf{K}_{B,2}(t_{a,0})$ for the two bistatic acquisitions (shown in blue and green in Figure 6.14, respectively) can be written from (6.21).

In the simplified two-dimensional geometry, the ground projection in (6.22) becomes:

$$\mathbf{K}^{(x)}_{B,i}(t_{a,0}) = \mathbf{\Gamma}^{(x)}\mathbf{K}_{B,i}(t_{a,0}) \tag{6.25}$$

where $\mathbf{\Gamma}^{(x)} = \mathbf{I} - \mathbf{z}\mathbf{z}^{\dagger}$. As is apparent (cf. (6.21) and (6.24)), the $\mathbf{K}$-space signal occupancy in (6.25) is only dependent on the transmitter characteristics (position and signal wavelengths) and on the incident angles of the two receivers $\psi_{R,1}$ and $\psi_{R,2}$. Given that we do not usually have control over the characteristics of the transmitter, the incident angles $\psi_{R,1}$ and $\psi_{R,2}$ are the only degrees of freedom we have to correctly locate the two received signals in the $\mathbf{K}$-space. Specifically, we want to locate them adjacent one to the other such that a wider $\mathbf{K}$-space signal occupancy is achieved (see $\mathbf{K}^{(x)}_{B,(1+2)}$ in orange in Figure 6.14).

In other words, the range resolution can be improved if the (x)-plane projection of the $\mathbf{K}$-space interval spanned by the first signal (namely $\mathbf{K}^{(x)}_{B,1}(t_{a,0})$) is adjacent without gaps to the (x)-plane $\mathbf{K}$-space projection spanned by the second signal (namely, $\mathbf{K}^{(x)}_{B,2}(t_{a,0})$), as sketched in Figure 6.14 for a simplified two-dimensional geometry. It

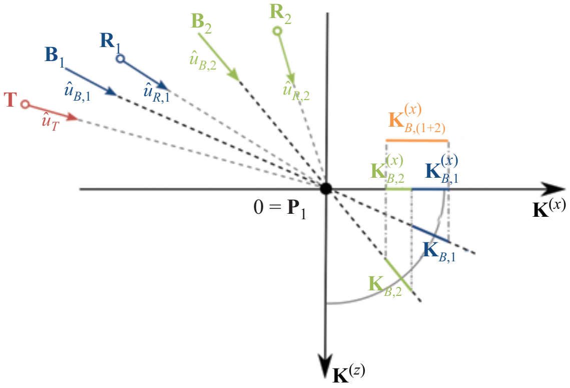

Figure 6.14 Two-dimensional representation of **K***-space signal occupancy and its geometrical dependency in the bistatic case. This two-dimensional geometry corresponds to the three-dimensional geometry of Figure 6.13, for the instant $t_a = t_{a,0}$ where relations in (6.23) apply. The dependency on $t_{a,0}$ has been removed to simplify the figure.* *© 2017 Elsevier. After, with permission, from [50]*

is easy to show that a maximum range resolution improvement can be achieved by setting the following constraint:

$$\frac{2\pi}{\lambda_{\max}}\boldsymbol{\Gamma}^{(x)}\hat{u}_{B,1}(t_{a,0}) = \frac{2\pi}{\lambda_{\min}}\boldsymbol{\Gamma}^{(x)}\hat{u}_{B,2}(t_{a,0}) \tag{6.26}$$

This guarantees a perfect contiguity between $\mathbf{K}^{(x)}_{B,1}(t_{a,0})$ and $\mathbf{K}^{(x)}_{B,2}(t_{a,0})$ without overlap or gaps (see the contiguity in the **K**-space projection $\mathbf{K}^{(x)}_{B,(1+2)}(t_{a,0})$ in Figure 6.14 for the simplified two-dimensional case). This point of perfect spectral contiguity is also referred to as *critical baseline* in SAR interferometry, see [53].

By plugging in (6.24) and (6.25) into (6.26), one gets:

$$\begin{aligned}
\frac{2\pi}{\lambda_{\max}}\boldsymbol{\Gamma}^{(x)}\hat{u}_{B,1}(t_{a,0}) &= \frac{2\pi}{\lambda_{\min}}\boldsymbol{\Gamma}^{(x)}\hat{u}_{B,2}(t_{a,0})\\
\frac{2\pi}{\lambda_{\max}}\left[\tfrac{1}{2}\left(u_{T,x} - \sin(\psi_{R,1})\right)\right] &= \frac{2\pi}{\lambda_{\min}}\left[\tfrac{1}{2}\left(u_{T,x} - \sin(\psi_{R,2})\right)\right]\\
\frac{u_{T,x} - \sin(\psi_{R,1})}{\lambda_{\max}} &= \frac{u_{T,x} - \sin(\psi_{R,2})}{\lambda_{\min}}\\
\sin(\psi_{R,2}) &= \frac{\lambda_{\min}}{\lambda_{\max}}\left(-u_{T,x} + \sin\psi_{R,1}\right) + u_{T,x}
\end{aligned} \tag{6.27}$$

which provides a direct expression to set the incidence angle of the second receiver once the transmitter and the incident angle of the first receiver are given.

The same approach can be readily extended to general three-dimensional geometry of Figure 6.13. By doing so, the time dependency in (6.26) can be removed, since there is no need for perfect alignment in the $y = 0$ plane between transmitter and receiver for the slow-time instant $t_a = t_{a,0}$. In fact, slightly shifted trajectories in the long-track direction can be compensated and re-synchronized using simple Doppler processing. The approach here proposed for the simple case of two receivers can be readily extended to more than two receivers, with subsequent direct improvement in range resolution. It is worth mentioning that this approach has already been proposed and validated in the case of monostatic SAR with real data of a multiple pass acquisition of the European remote sensing (ERS) radar satellite ERS-1, see [29], and in a multipass airborne SAR scenario in [54]. A multiple input–multiple output variation of the same approach has also been proposed in [32,55].

6.3.2 Scenario for multi-PCL–SAR

Figure 6.13 depicts a typical geometry multi-PCL–SAR using airborne platforms, where each platform is equipped with a PCL receiver. The two platforms are supposed to fly with same velocity $\mathbf{V}_{R,1} = \mathbf{V}_{R,2} = \mathbf{V}_R$ along rectilinear trajectories observing the scene in a pure side-looking configuration. Main geometry and system parameters are reported in Table 6.1.

Assuming the transmitter and the two receivers to be aligned in the x-axis at slow-time instant $t_{a,0}$, the optimum geometry constraint for range resolution in (6.26) applies.

The resulting multistatic geometry is obtained from (6.27), leading to the parameters in Table 6.1. As is apparent, for this sample realistic scenario, the receivers incident angles $\psi_{R,1}$ and $\psi_{R,2}$ vary less than 2°. As a consequence, a reasonable assumption on the coherence of the target backscattering between the two acquisitions can be made.

Table 6.1 Case study geometry

Parameter	**Value**
Illuminator of opportunity	DVB-T (8k mode)
Carrier frequency f_C	600 MHz
Signal bandwidth B	7.61 MHz
Transmitter incident angle ψ_T	89.9°
Height of transmitter	10 m
Distance transmitter to scene center $\lvert\mathbf{T} - \mathbf{P}_1\rvert$	12,000 m
Altitude of receivers	5,000 m
Receivers trajectory	Rectilinear
Velocity of receivers $\lvert\mathbf{V}_R\rvert$	65 m/s
Bistatic geometry	
Receivers incident angles $\psi_{R,1},\ \psi_{R,2}$	47.98°, 46.13°
Angular separation of receivers $\Delta\psi$	1.85°

As shown in Figures 6.13 and 6.14, it would be convenient to define a geometry where the transmitter is in the back lobe of both PCL surveillance antennas. This would not only attenuate the direct signal in the surveillance channel but it would also create a "quasi-monostatic" geometry, where the signal from the area of interest is basically backscattered to both receivers. As a result, the bistatic iso-ranges and the bistatic iso-Dopplers will almost be orthogonal to each other, thus creating a favorable configuration for imaging purposes, see [51] page 61. From a PCL point of view, it is interesting to notice how such a configuration would permit PCL radar imaging using a single channel receiver (i.e., one receiver per platform),by using the DVB-T signal decoding and reconstruction principle described in [56]. In order this approach to be feasible, the direct signal (albeit attenuated) should be still strong enough to allow low bit error rate DVB-T digital stream decoding and signal reconstruction, and CCI should be negligible.

6.3.3 Simulation of DVB-T range pulse response

In this section, the DVB-T range pulse response for a multi-PCL–SAR system is analyzed. First, the analysis will be conducted for the scene center $\mathbf{P}_1$, and then the effects over an extended scene will be addressed. In both these two cases, the analysis will be confined to the mid-acquisition slow-time instant $t_{a,0}$. Finally, the behavior over an extended scene and for a rectilinear acquisition will be investigated.

6.3.3.1 Scene center $\mathbf{P}_1$ at mid-acquisition $t_{a,0}$

Figure 6.15 shows the spectrum in the **K**-space of the backscattered signal from a point target located in $\mathbf{P}_1$ received by the two receivers at slow-time instant $t_{a,0}$. As one can see, the spectra are shifted such that no gaps between the spectra are present,

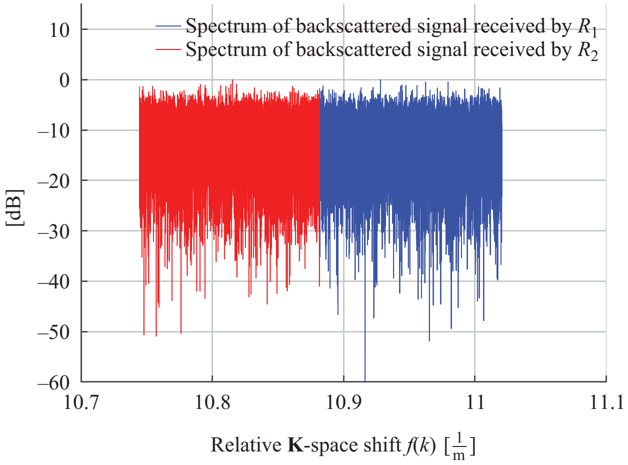

Figure 6.15 ***K**-space spectra of the two backscattered signals from scatterer in $\mathbf{P}_1$ at time $t_{a,0}$ projected onto (x,y)-plane [dB]. © 2017 Elsevier. After, with permission, from [50]*

as expected from setting the constraint in (6.26) and (6.27). After range compressing the signal receiver from the solely first PCL sensor, the pulse response shown as the red solid line in Figure 6.16 is obtained. On the other hand, by coherently combining the two signals, after range compression, one gets the pulse response shown as the solid black plot in Figure 6.16. The range resolution improvement is apparent, by observing the corresponding widths of the pulse response main lobes. Table 6.2 reports the theoretical and measured resolutions for the single and the combined cases, respectively.

6.3.3.2 Extended scene at mid-acquisition $t_{a,0}$

It is worth to mention that the constellation geometry (and hence the **K**-space shift) is calculated using (6.26) for the single point $\mathbf{P}_1$ on ground. Adjacent points will exhibit slightly different LOS unit vectors and, therefore, slightly different spectral shifts in the **K**-space, given that the constraint in (6.27) will not be fulfilled anymore. This will create a gap or an overlap between the two spectra (cf. Figure 6.15). This effect

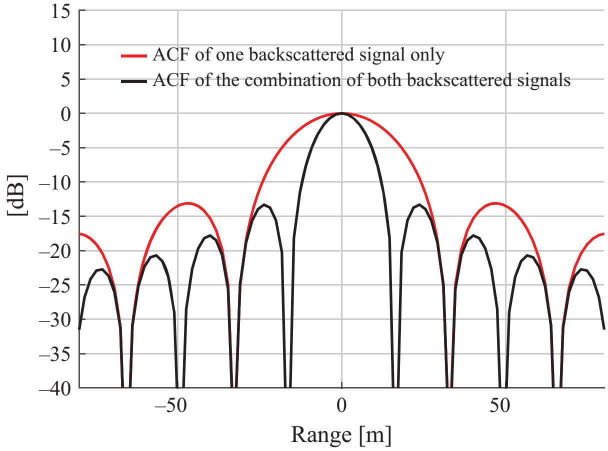

Figure 6.16 Range pulse response (autocorrelation function (ACF)) for scatterer in $\mathbf{P}_1$ at time $t_{a,0}$: single sensor in red; two sensors combined in black [dB]. © *2017 Elsevier. After, with permission, from [50]*

Table 6.2 Measured range resolutions for scatterer in $\mathbf{P}_1$ at instant $t_{a,0}$

Range resolution	**Value [m]**	**Side-lobe level [dB]**
Single sensor	18.8	−13.35
Combined sensors	9.4	−13.25

has been already investigated in [54], where the variations of the wavenumber shift under strong variations of the incident angle have been analyzed.

Figure 6.17 shows a heatmap of **K**-space signal shifts in top view of an extended scene in Cartesian coordinates. In particular, the x-axis is aligned to the along-track direction of the two platforms, and the y-axis is the ground range (see also geometry in Figure 6.13). Compared to Figure 6.13, not only one scatterer was simulated but multiple point-like targets were considered. Three points are highlighted in Figure 6.17: $\mathbf{P}_1$, $\mathbf{P}_2$, and $\mathbf{P}_5$, whose coordinates can be found in Table 6.4. For every simulated scatterer $\mathbf{P}_n$, its relative **K**-space shift between both spectra is calculated as in the following equation:

$$\Delta f(\mathbf{P}_n) = \left(\frac{2\pi}{\lambda_{\max}} \mathbf{\Gamma}^{(xy)} \hat{u}_{B,1}(t_{a,0}) - \frac{2\pi}{\lambda_{\min}} \mathbf{\Gamma}^{(xy)} \hat{u}_{B,2}(t_{a,0}) \right)_{\mathbf{P}_n} \tag{6.28}$$

For each scatterer, there are three possibilities of the outcome of (6.28):

1. $\Delta f(\mathbf{P}_n) = 0$: This means a perfect alignment of both spectra as shown in Figure 6.15, and hence a fulfillment of (6.27).
2. $\Delta f(\mathbf{P}_n) < 0$: This means an overlap of both spectra.
3. $\Delta f(\mathbf{P}_n) > 0$: In this case, there is a gap between both spectra.

In the first case, there is an optimum in range resolution improvement achievable, whereas the second and third cases result in a degradation of the performance.

Figure 6.17 depicts $\Delta f(\mathbf{P}_n)$ color coded as a heatmap. Two regions separated by a line can be identified: a region with overlapping spectra $R_{overlap}$ and a region R_{gap} with noncontiguous spectra. The regions are separated by a line l_0 depicted by black crosses. l_0 is the locus of points with optimum **K**-space spectra shift, that is neither

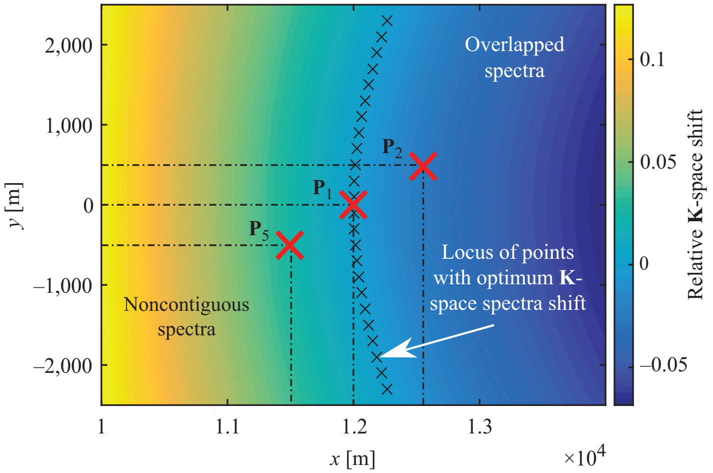

Figure 6.17 ***K**-space shift evaluated for the mid-acquisition slow-time instant $t_{a,0}$ over an extended scene. © 2017 Elsevier. After, with permission, from [50]*

gap nor overlap between both spectra. As an example, for the coordinates of $\mathbf{P}_1$ in Figure 6.17, it holds $\mathbf{P}_1 \in l_0$; therefore, $\Delta f(\mathbf{P}_1) = 0$.

$\mathbf{P}_2$ is situated in the region of the overlapping spectra, $\mathbf{P}_2 \in R_{overlap}$; therefore, $\Delta f(\mathbf{P}_2) < 0$, whereas for $\mathbf{P}_5$, $\Delta f(\mathbf{P}_5) > 0$ holds as it is situated in the region of the noncontiguous spectra, $\mathbf{P}_5 \in R_{gap}$. It is here important to notice that the effects of a noncontiguous spectrum in the **K**-space manifest as increased side lobes in the scatterer range pulse response, while an overlapped spectrum leads to a suboptimal range resolution value. Given a maximum tolerated pulse response side-lobe level and a loss in the range resolution improvement, Figure 6.17 allows to define a maximum area which can be imaged.

As also stated in [54], the different incident angles over the observed scene give rise to different signal shifts in the **K**-space. The effects on the pulse response are clearly visible in Figures 6.18–6.21, where a gap between the spectra produces increase in the side lobes, and a spectra overlap leads to a non-optimum improvement of the range resolution. Achievable ground-range resolutions and side-lobe levels measured for the scatterers in $\mathbf{P}_2$ and $\mathbf{P}_5$ at instant $t_{a,0}$ are reported in Table 6.3. This analysis should clearly show which effects a relative shift in the **K**-space create in the resulting range pulse response. In the following, we will then directly refer to the **K**-space signal shift.

A final comment is in order. The relative **K**-space spectral shift has been derived under the hypothesis of a flat terrain. Any topography in the scene would locally alternate the **K**-space occupancy of the corresponding echoes, thus directly affecting the relative **K**-space signal shift. This effect has been considered also in [54]. Unfortunately, the **K**-space signal occupancy cannot be corrected by the topography, even

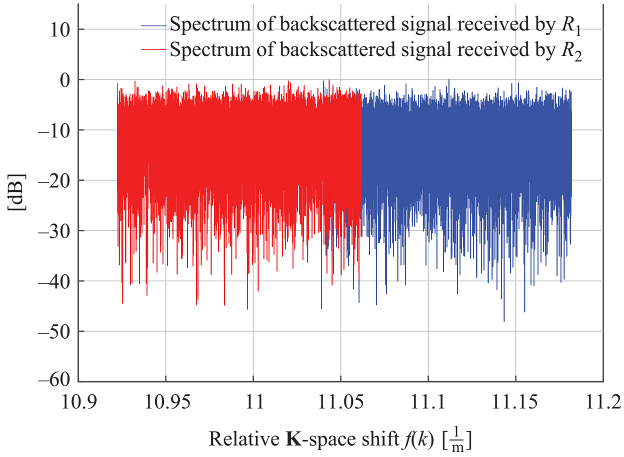

Figure 6.18 ***K**-space spectra of the two backscattered signals from scatterer in $\mathbf{P}_2$ at time $t_{a,0}$ projected onto (x,y)-plane [dB]. © 2017 Elsevier. After, with permission, from [50]*

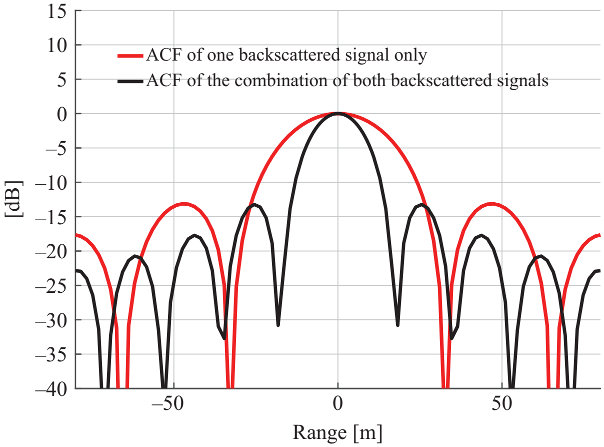

Figure 6.19 Range pulse response (autocorrelation function (ACF)) for scatterer in $\mathbf{P}_2$ *at time* $t_{a,0}$*: single sensor in red; two sensors combined in black [dB].* © *2017 Elsevier. After, with permission, from [50]*

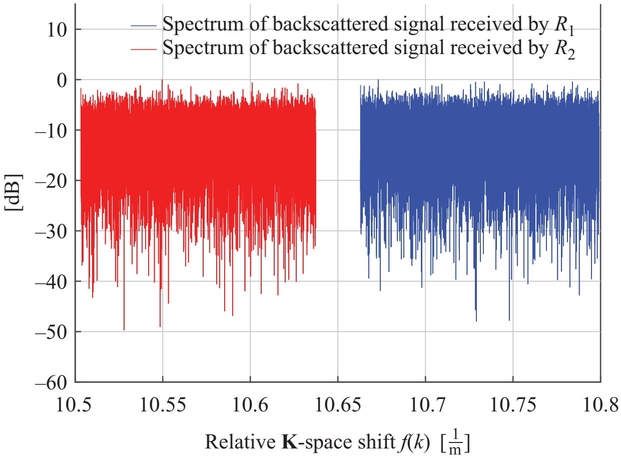

Figure 6.20 ***K****-space spectra of the two backscattered signals from scatterer in* $\mathbf{P}_5$ *at time* $t_{a,0}$ *projected onto (x,y)-plane [dB].* © *2017 Elsevier. After, with permission, from [50]*

if known, and this directly affects the range pulse response characteristics (similarly to what we see happening with $\mathbf{P}_2$ and $\mathbf{P}_5$).

6.3.3.3 Extended scene over entire acquisition

By flying a rectilinear trajectory, the optimum contiguity constraint in (6.26) cannot be kept during the entire acquisition. That is, the contiguity constraint can be set

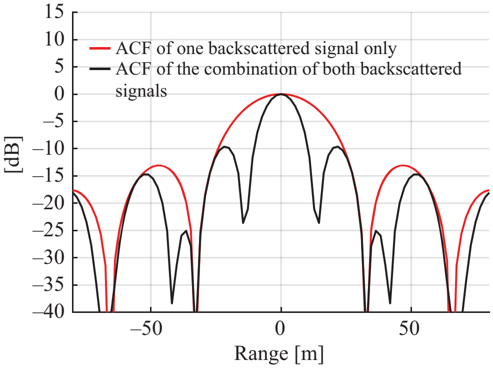

Figure 6.21 Range pulse response (autocorrelation function (ACF)) for scatterer in $\boldsymbol{P}_5$ at time $t_{a,0}$: single sensor in red; two sensors combined in black [dB]. © 2017 Elsevier. After, with permission, from [50]

Table 6.3 Measured range resolutions for scatterers in $\boldsymbol{P}_2$ and $\boldsymbol{P}_5$ at instant $t_{a,0}$

Range resolution	Value [m]	Side-lobe level [dB]
$\mathbf{P}_2$ single sensor	19.72	−13.38
$\mathbf{P}_2$ combined sensors	10.74	−13.32
$\mathbf{P}_5$ single sensor	19.72	−13.29
$\mathbf{P}_5$ combined sensors	8.62	−9.66

for one specific slow-time instant (for instance for the mid-acquisition instant $t_{a,0}$ as in (6.27)), but this will not be fulfilled as the platforms move along rectilinear trajectories with constant velocity. An example of this is shown in Figure 6.22 for the five different point scatterers located in Table 6.4. In particular, the **K**-space shift between the two bistatic signals is shown during an acquisition corresponding to 90° of azimuth aspect angle variation. As one can see, for the scene center $\mathbf{P}_1$ and for the mid-acquisition point ($t_a = t_{a,0} = 0$), the optimum contiguity constraint is met, but the constraint deviates as the scatterer position changes or as the platform moves, leading to a gap or to an overlap between the spectra. The most annoying aspect is that the relative **K**-space shift is jointly a function of the slow-time t_a and of the azimuth position of the scatterers.

By observing Figure 6.22, we can see that the constraint is never met when regarding the points $\mathbf{P}_4$ and $\mathbf{P}_5$, as they are situated in the region R_{gap} of noncontiguous spectra, compared to Figure 6.17. At the beginning of the acquisition, the gap is at one of its maxima (for the duration of this acquisition); the size of the gap decreases while both receivers are moving until the minimum is reached for $t_a = t_{a,0} = 0$. The gap increases again for $t_a > 0$. The **K**-space shifts of points $\mathbf{P}_2$ and $\mathbf{P}_3$ show similar

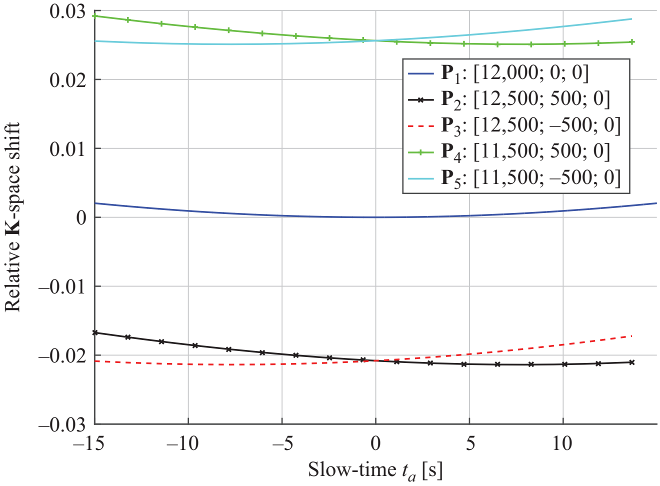

Figure 6.22 Relative ***K****-space shift for five point-like scatterers over entire acquisition: rectilinear trajectories case. © 2017 Elsevier. After, with permission, from [50]*

Table 6.4 Positions of the five point-like scatterers in ENU

Scatterer	**Position [m]**
$\mathbf{P}_1$	[12,000; 0; 0]
$\mathbf{P}_2$	[12,500; 500; 0]
$\mathbf{P}_3$	[12,500; −500; 0]
$\mathbf{P}_4$	[11,500; 500; 0]
$\mathbf{P}_5$	[11,500; −500; 0]

characteristics of their appearance, but now the relative **K**-space shift is negative, which means, there is an overlap between both resulting spectra. For a longer rectilinear trajectory, the amount of overlap of both spectra of $\mathbf{P}_2$ and $\mathbf{P}_3$ will decrease, until the optimum contiguity constraint will be met. From then on, the **K**-space shift will be positive, which results in a gap between both spectra.

As one can see, the constraint in (6.27) is met only once during the acquisition (not only for the scene center $\mathbf{P}_1$), when a rectilinear trajectory is flown. The variation of the relative **K**-space shift for a given scatterer position leads to a varying range pulse response characteristic (namely, range resolution and side-lobe level) during the slow-time. A varying range resolution over slow-time would remain even after complete SAR processing, leading to a nonuniform resolution over the final focused image. This contrasts with common SAR images requirements that impose constant uniform resolutions (not only in range but also between range and azimuth dimensions) to improve visual understanding of the scene to be imaged.

Therefore, in the next section, a new trajectory will be defined.

6.3.4 Optimal trajectories for multi-PCL–SAR

It will be first considered the trajectory of a single platform, let us say the one indicated with $\mathbf{R}_1(t_a)$ in Figure 6.13. It will be shown that, to guarantee a constant width of $\mathbf{K}_{B,1}^{(xy)}$ over the slow-time t_a (that is a constant ground-range resolution), the platform's trajectory must lay on a cone surface centered in $\mathbf{P}_1$. By setting the additional constraint of a constant flying altitude, the circular trajectory will be derived.

Second, given the first platform trajectory to be circular, the trajectory of the second platform will be derived by imposing the constraint in (6.26) for the whole slow-time t_a. That is, by imposing $\Delta f(\mathbf{P}_1) = 0 \; \forall \; t_a$.

6.3.4.1 Derivation of a circular trajectory for the first platform

For simplicity, we will hereon neglect the dependency on the slow-time t_a. The locus of points $\mathbf{B}_1$ (compare (6.19)) that ensures a constant ground-range resolution for the scene center point $\mathbf{P}_1$ is given as the focus of points where the corresponding $\mathbf{K}$-space projections $\mathbf{K}_{B,1}^{(xy)} = 2\pi/\lambda \left[u_{B,1}^{(x)}, u_{B,1}^{(y)}, 0\right]^{\dagger}$ ($\lambda \in [\lambda_{\min}, \lambda_{\max}]$) have constant width. The squared distance between the two edges of $\mathbf{K}_{B,1}^{(xy)}$ can be written as:

$$d_{B,1}^{(xy)}(\lambda_{\min}, \lambda_{\max})^2 = \left(\frac{2\pi}{\lambda_{\min}} u_{B,1}^{(x)} - \frac{2\pi}{\lambda_{\max}} u_{B,1}^{(x)}\right)^2 + \left(\frac{2\pi}{\lambda_{\min}} u_{B,1}^{(y)} - \frac{2\pi}{\lambda_{\max}} u_{B,1}^{(y)}\right)^2 \qquad (6.29)$$

By setting:

$$d_{B,1}^{(xy)}(\lambda_{\min}, \lambda_{\max})^2 = C_1 \qquad (6.30)$$

being C_1 a constant greater than 0, and by indicating:

$$\hat{u}_{B,1} = -\frac{1}{r_{B,1}} \cdot \left[x_{B,1}, y_{B,1}, z_{B,1}\right]^{\dagger} \qquad (6.31)$$

and with:

$$r_{B,1} = \sqrt{x_{B,1}^2 + y_{B,1}^2 + z_{B,1}^2} \qquad (6.32)$$

(6.30) becomes:

$$x_{B,1}^2(1 - C_2) + y_{B,1}^2(1 - C_2) - C_2 z_{B,1}^2 = 0 \qquad (6.33)$$

with $C_2 = C_1/2\pi((1/\lambda_{\max}) - (1/\lambda_{\min}))^2$. The locus of points described in (6.33) represents a cone, and specifically it states the position of the "equivalent monostatic acquisition" $\mathbf{B}_1$. From the locus of points in (6.33), it is possible to derive the locus of points of the receiver $\mathbf{R}_1$. To do this, let us consider a second Cartesian coordinate system (x'_T, y'_T, z'_T) centered in the position of the transmitter. The linear transformation from $(x_{B,1}, y_{B,1}, z_{B,1})$ to (x'_T, y'_T, z'_T) is given by

$$\begin{aligned} x'_T &= x_{B,1} - x_T \\ y'_T &= y_{B,1} - y_T \\ z'_T &= z_{B,1} - z_T \end{aligned} \tag{6.34}$$

The cone in (6.33) can be expressed in (x'_T, y'_T, z'_T) as

$$(x'_T + x_T)^2(1 - C_2) + (y'_T + y_T)^2(1 - C_2) - C_2(z'_T + z_T)^2 = 0 \tag{6.35}$$

We then notice that, by construction (see (6.20)), in (x'_T, y'_T, z'_T), the coordinates of $\mathbf{R}_1$ are simply doubled of those of $\mathbf{B}_1$. As a consequence, the locus of points for the receiver $\mathbf{R}_1$ that ensures a constant ground-range resolution can be written (in $(x'_{R,1}, y'_{R,1}, z'_{R,1})$) as

$$\left(\frac{x'_{R,1}}{2} + x_T\right)^2 (1 - C_2) + \left(\frac{y'_{R,1}}{2} + y_T\right)^2 (1 - C_2) - C_2\left(\frac{z'_{R,1}}{2} + z_T\right)^2 = 0 \tag{6.36}$$

which is also a cone. By setting the flight altitude of $\mathbf{R}_1$ constant, one gets a circular trajectory for the receiver $\mathbf{R}_1$.

6.3.4.2 Derivation of second platform trajectory

For analogy with the first platform, it is clear that also the second platform trajectory should lay onto a cone, if the constant ground-range resolution constraint has to be met. Here, in addition, it is derived the trajectory of the second platform $\mathbf{R}_2$ as a function of the first platform trajectory. To do this, the optimum contiguity constraint in (6.26) has to be set, leading to

$$\begin{aligned} x_{R,2} &= \left[\frac{\lambda_{\min}}{\lambda_{\max}}\left(\frac{x_T}{r_T} + \frac{x_{R,1}}{r_{R,1}}\right) - \frac{x_T}{r_T}\right] \cdot r_{R,2} \\ y_{R,2} &= \left[\frac{\lambda_{\min}}{\lambda_{\max}}\left(\frac{y_T}{r_T} + \frac{y_{R,1}}{r_{R,1}}\right) - \frac{y_T}{r_T}\right] \cdot r_{R,2} \end{aligned} \tag{6.37}$$

where $r_T = |\mathbf{T}|$, $r_{R,1} = |\mathbf{R}_1|$, and $r_{R,2} = |\mathbf{R}_2|$. Clearly, due to the circular nature of both trajectories, $r_{R,1}$ and $r_{R,2}$ are constant (Table 6.5).

6.3.4.3 Extended scene over entire acquisition

Figure 6.24 shows results of the relative $\mathbf{K}$-space shift for five point-like scatterers when both receivers are flying a circular trajectory. A top-view of the geometry is shown in Figure 6.23. The $\mathbf{K}$-space is evaluated for the slow-time $t_a = [-15,\ldots,+15]$ [s]. $t_a = 0$ refers to the point of acquisition where $y_{R,1} = y_{R,2} = 0$, that is, the scenario described in Section 6.3.1. The solid line in Figure 6.23 depicts the receivers' trajectory flown during this time interval. For illustration purposes, the trajectory is extended with a dashed line.

First, the trajectory of receiver $\mathbf{R}_2$ with reference to the point scatterer $\mathbf{P}_1$ at (12,000 ; 0) [m] was created. Based on this trajectory, the path of receiver $\mathbf{R}_1$ according to (6.37) was calculated. When comparing Figure 6.24 to Figure 6.22, one can

Table 6.5 Optimum trajectory parameters

Parameter	**Value**
Illuminator of opportunity	DVB-T (8k mode)
Carrier frequency f_C	600 MHz
Signal bandwidth B	7.61 MHz
Transmitter incident angle ψ_T	89.9°
Height of transmitter	10 m
Distance transmitter to scene center	12,000 m
Altitude of receivers	5,000 m
Receivers trajectory	Circular
Velocity of receiver 1 $\lvert\mathbf{V}_{R,1}\rvert$	68.778 m/s
Velocity of receiver 2 $\lvert\mathbf{V}_{R,1}\rvert$	65 m/s
Bistatic geometry	
Receivers incident angles $\psi_{R,1}$, $\psi_{R,2}$	47.98°, 46.13°
Angular separation of receivers $\Delta\psi$	1.85°

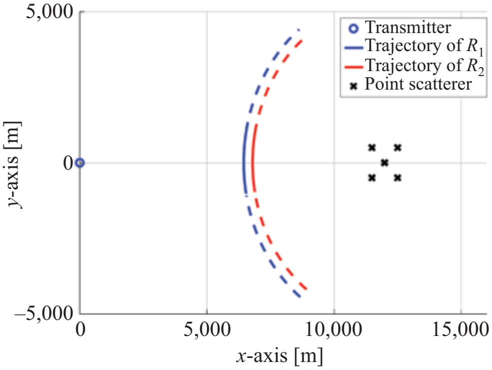

Figure 6.23 Sample case study geometry for multi-PCL–SAR with circular trajectories (top view). The position of the transmitter is marked by a circle, the crosses mark the positions of the scatterers. © 2017 Elsevier. After, with permission, from [50]

clearly see that the relative **K**-space shift holds $\Delta f(\mathbf{P}_1) = 0$ for the complete time of acquisition for the circular trajectories. This is obvious, as $\mathbf{P}_1$ is the point of reference for this simulation, thus confirming (6.36) and (6.37). When comparing the relative **K**-space shifts for the points $\mathbf{P}_2$ to $\mathbf{P}_5$, one notices $\Delta f(\mathbf{P}_n)$, $n \in \{2, 3, 4, 5\}$ is almost constant, although it deviates from the optimal value $\Delta f(\mathbf{P}_n) = 0$. The dependencies of the relative **K**-space shift upon (i) the azimuth position of the scatterers and (ii) the slow-time t_a are now significantly reduced (compare Figure 6.22). The advantage coming from a non-varying relative **K**-space shift between the spectra is evident for

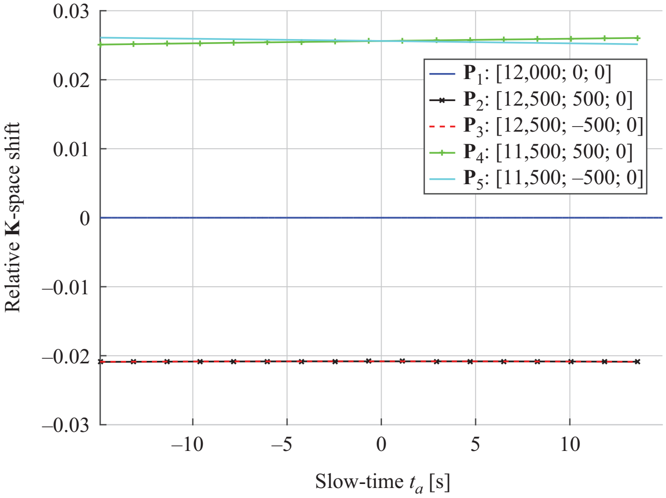

*Figure 6.24 Relative **K**-space shift for five point-like scatterers over entire acquisition: circular trajectories case. © 2017 Elsevier. After, with permission, from [50]*

the range as for the subsequent azimuth SAR processing. Specifically, a constant relative **K**-space shift during the acquisition, which only depends upon the position of the scatterer, allows defining a maximum area which can be imaged, according to the requirements on range resolution improvement degradation and side-lobe level increase (see last comment in Section 6.3.3.2). Basically, by exploiting circular trajectories, the results of Figure 6.17 (which were obtained for the single mid-acquisition instant $t_{a,0}$) are now valid for the entire acquisition. On the other hand, a varying relative **K**-space shift during the acquisition affects the overall signal occupancy in the wavenumber domain (or equivalently **K**-space and Doppler domain). This clearly impacts the subsequent azimuth processing, as the characteristics of the azimuth pulse response of a given scatterer are directly affected.

In [50], an analysis is conducted evaluating the **K**-space shifts for realistic trajectories.

6.4 Experimental verification

6.4.1 Scenario definition

6.4.1.1 Location of the measurement campaign

A measurement campaign site in the countryside of western Germany was chosen. A number of SFNs cover the western part of Germany as well as France, Netherlands, Luxembourg, and Belgium. Regarding the digital television status, Germany is in the progress of soft-switching from DVB-T to the new version of the standard DVB-T2 [49], which means, DVB-T stations in densely populated and metropolitan areas were switched to DVB-T2 first, while stations serving the countryside will follow later. Figure 6.25 shows a map of the measurement campaign site and the surrounding region with annotations to mark the exploited transmitter of opportunity and some surrounding SFNs. The SFNs are labeled with SFN A1, A2, and B1, where the letter indicates SFNs using common frequencies, and the cypher indicates a running number in order to differentiate between distributed SFNs. Close to the center of Figure 6.25, one Tx (Eifel) is marked with SFN A1—IO, which is regarded as the transmitter of opportunity transmitting DVB-T signals at carrier frequencies $f_C = \{674, 690\}$ MHz using 16-QAM. A zoom into the region around Tx Eifel is provided in the upper right corner of Figure 6.25. The white arrows define the trajectories of the airborne receiver. A single DVB-T channel occupies a bandwidth of 8 MHz of which it uses 7.61 MHz to transmit on 6,817 subcarriers in the 8k mode [38]. The SFN in the northern part of the map (labeled as SFN A2) is transmitting at the same frequencies as SFN A1. It is located in and around the densely populated area of Dusseldorf. In fact, there are more SFNs transmitting at the mentioned frequencies around the considered IO in all directions, but in order to show the principle and to keep Figure 6.25 clear, only the closest SFN is depicted in Figure 6.25. The SFN around the city Dusseldorf is transmitting a DVB-T2 signal in either the extended 16k or 32k mode, which means it occupies 13,921 or 27,841 carriers in the bandwidth of 8 MHz [49]. By doing so, it extends the occupied bandwidth by 0.16 MHz compared to the 8k mode of DVB-T. As the DVB-T2 SFNs transmit in extended mode, we have the chance to differentiate between the DVB-T and the DVB-T2 signals in frequency domain and, therefore, it

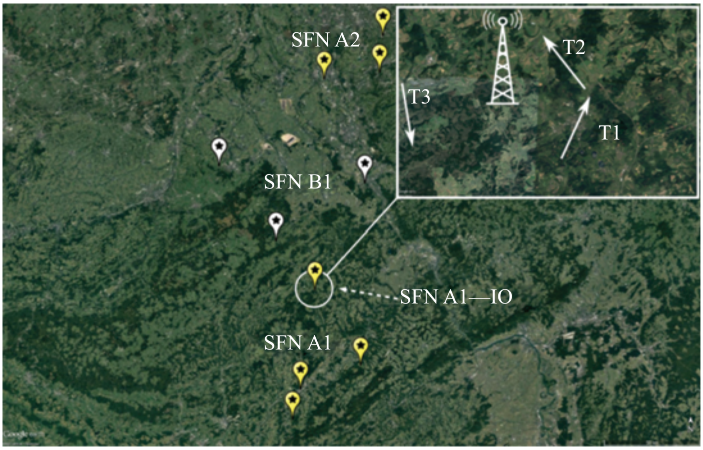

Figure 6.25 Map of the region with some annotated SFNs. The IO is marked with SFN A1—IO. A zoom into the region around the IO is shown in the upper right corner where the trajectories of the airborne receiver are labeled with T1, T2, and T3. Image source: Google Earth

gives us the possibility to indicate the strength of CCI in UHF as long as the DVB-T2 is weaker than the DVB-T signal. But as the measurement's location is closer to the DVB-T Tx Eifel, the DVB-T signal should be the stronger one.

6.4.1.2 Description of the receiving system

The receiving system used in the airborne measurement consisted of a front-end and a back-end. The back-end is a two channel software-defined radio radar receiver, which is able to sample two receiving channels at a sampling frequency $f_s = 64$ MHz with an effective bandwidth of 32 MHz. The front-end consisted of two antennas. Each antenna was connected to one of the two receive channels. Furthermore, a GPS-aided IMU was included providing accurate platform-position truth data.

The front-end was integrated in a pod, which can be mounted beneath the wing of an ultralight aircraft. The usage of an ultralight aircraft limits the weight that can be carried additionally. Also, as the pod is mounted outside of the ultralight aircraft, the pod's dimensions are very restricted as its shape influences the ultralight aircraft's aerodynamics and flight characteristics. The pod together with equipment mounted inside of it is shown in Figure 6.26. It shows both antennas at the bottom, the IMU in the center of the pod, and radar-absorbing material (RAM) mounted on the opposite side, which was used to achieve a signal attenuation toward the IO in order to prevent damaging of the hardware equipment due to an expected strong direct signal from the IO. A strong direct signal was expected due to the close range to the Tx Eifel; and the exact strength of the direct signal could not be determined due to the unknown tilting of the transmit antennas. The RAM was not matched to the UHF wavelengths, but due to the restricted size of the pod, the space for mounting the equipment was limited. The limited space inside the pod is as well the reason for choosing discone omnidirectional antennas: generally, it is preferred to use directive antennas with a

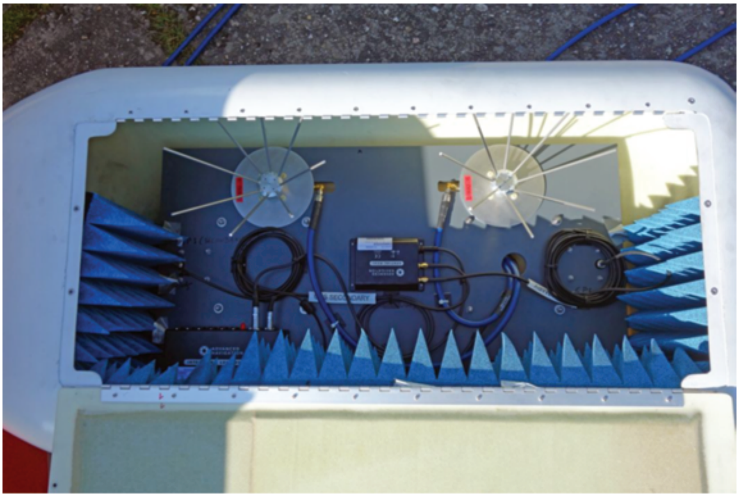

Figure 6.26 Front-end integrated in a pod

higher gain, such as Yagi–Uda antennas. However, these antennas have usually greater dimensions compared to the ones, thus not fitting into the pod. The equipment is mounted on a plate consisting of plastic material, and the plate is mounted inside the pod. In between the ground plate and the pod, a gap of approximately 5 cm was left in order to have space for two GNSS antennas needed for the IMU. Figure 6.26 shows the pod upside-down, which means the pod was flipped around the longitudinal axis to be mounted on the bottom of the airplane's wing. The ultralight aircraft with the pod mounted below the wing is shown in Figure 6.27. The receiver was flying on a circular-like path around the Tx and recorded data when flying on trajectories marked by the white arrows which are labeled with T1, T2, and T3 in Figure 6.25.

6.4.2 Image results of PCL–SAR

The data for the image results shown in this paragraph have been collected on leg T2 (see Figure 6.25). The velocity of the aircraft was 40–50 m/s and height above ground was about 680 m. The right side-looking PCL–SAR system described in Section 6.4.1 was used to acquire the direct and ground-reflected DVB-T signal. The DVB-T transmitter Eifel was about 5–6 km away from the radar and the antenna mast height is approximately 300 m. The parameters of the transmitter are summarized in Table 6.6.

The individual processing steps to focus the radar raw data are shown in the block diagram in Figure 6.28. In a first step, the output of the two-channel analog-to-digital converter is individually preprocessed. Then, the CCI suppression as described in Section 6.2.6 is performed, which is absolutely necessary if interfering signals from other SFNs (transmitting at the same frequency) are present. The next steps include the synchronization to the transmitter, decoding of the signal according to the DVB-T standard [36] and the remodulation. At the end of these steps, a replica of the transmitted signal is available, which can be used as a reference signal for range compression. The range compression itself is done using a RpF as described

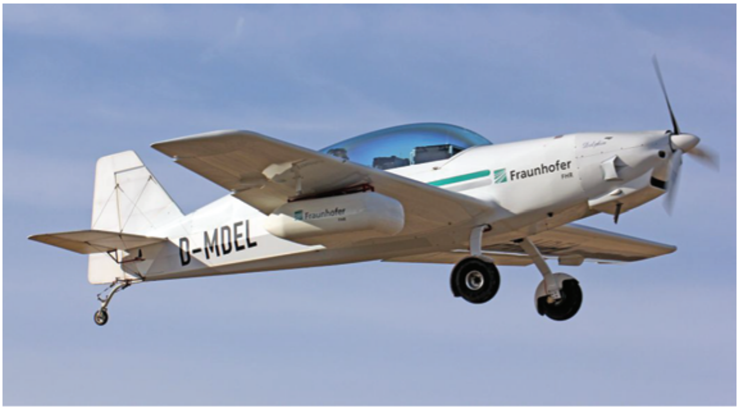

Figure 6.27 Ultralight aircraft with a pod under the right wing for PCL–SAR measurements

Table 6.6 Parameters of the DVB-T transmit signal

Parameter	**Value**
Center frequency	690 MHz
Bandwidth	7.61 MHz
Power (ERP)	50 kW
Number of carriers	6,817
Polarization	H
Symbol length (PRI)	1.12 ms
Modulation	16-QAM (8k mode)

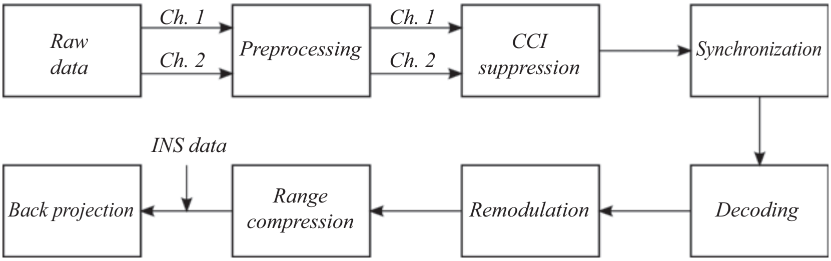

Figure 6.28 Processing steps

in Section 6.2.4, which is able to eliminate unwanted DVB-T signal characteristics, e.g., ambiguities and side lobes, which are responsible for a higher noise level. The last step is the azimuth compression using the bistatic back projection algorithm as described in Section 6.2.5.

Figure 6.29 shows a Google Earth image of the scene, where the area of the processed SAR image is visually accentuated. The grazing angle from a point in the center of the scene to the transmitter is only 4° and to the receiver 19°, which means a bistatic angle of 15°. According to this geometry and the available signal bandwidth, the expected ground-range resolution is about 20 m. The cross-range resolution mainly depends on the processing angle used for the azimuth focusing. It was about 10° resulting in a cross-range resolution of about 2.5 m.

In order to illustrate the effect of CCI suppression on the image results, the image in Figure 6.30(a) was calculated using the processing steps sketched in Figure 6.28 but without CCI suppression, whereas the image in Figure 6.30(b) was calculated applying the suggested CCI approach. The enhancement in SNR is remarkable. Many details in Figure 6.30(b) become visible only due to the CCI suppression. The pixel spacing in both images is 4 m × 4 m. Due to the hilly terrain (which is not visible in the Google Earth image), there are some regions with no direct LOS to the transmitter. Nevertheless, it seems that reflections within these regions are visible in the

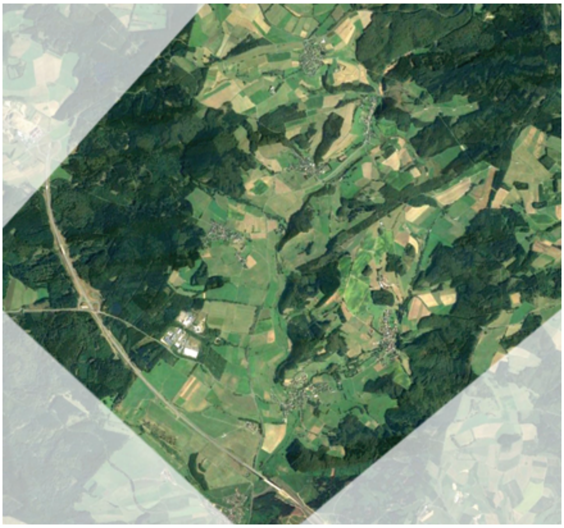

Figure 6.29 Google Earth image of the area shown in the radar images in Figure 6.30

SAR image. Therefore, effects like shadowing, diffraction, and foliage penetration require further investigation. The SAR images show especially strong reflections from wooded areas so that they can be clearly distinguished from grassland, see e.g., the region around ($x = 0, y = 0$) of Figure 6.30(b). The highway, which is nearly parallel to the flight track, is also clearly visible.

6.5 Conclusions

This chapter addressed the problem of multistatic PCL–SAR (multi-PCL–SAR). The work introduced a model for PCL–SAR raw received signals together with a signal processing scheme. In addition, the exploitation of multiple receivers is addressed in order to increase the range resolution of the multi-PCL–SAR system. In particular, it was shown by simulation how PCL–SAR acquisitions over the same area taken with different elevation angles result in shifted signal supports when the data are projected onto the **K**-space, and how this can be exploited to increase the resulting ground-range resolution. The behavior of the **K**-space shift between two acquisitions was also analyzed over an extended area and over the synthetic aperture for two different classes of platform trajectories, namely rectilinear and circular. The chapter concludes with an overview of the current PCL–SAR experimental activities performed over the last years at Fraunhofer FHR.

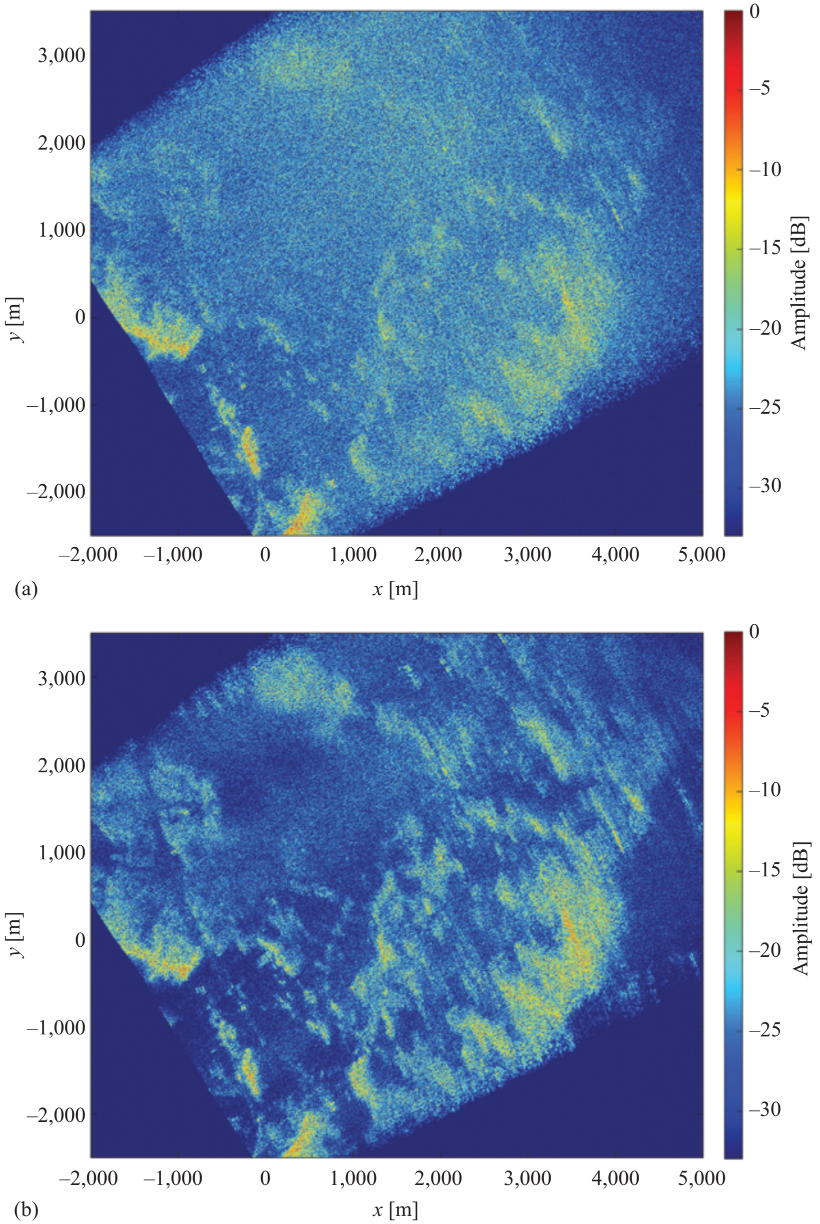

Figure 6.30 Airborne PCL–SAR image (a) without and (b) with co-channel interference suppression. © 2018 VDE VERLAG, Berlin, Offenbach. After, with permission, from [57]

Acknowledgments

The authors would like to acknowledge Prof. Pierfrancesco Lombardo and Prof. Fabiola Colone from University of Rome La Sapienza, Italy, and Ashley Summers from DST Group, Australia, for the fruitful discussions on removal of the time-varying characteristics of DVB-T signal and on removing of CCI.

Glossary

The following list includes the acronyms used in this chapter:

ACF	autocorrelation function
AWGN	additive white Gaussian noise
CCI	co-channel interference
CTF	channel transfer function
DAB	digital audio broadcast
DOF	degrees of freedom
DVB-T	digital video broadcast-terrestrial
DVB-T2	digital video broadcast-terrestrial 2
ENU	east north up
ERS	European remote sensing
FM	frequency modulation
GNSS	global navigation satellite system
GPS	global positioning system
IDFT	inverse discrete Fourier transform
IMU	inertial measurement unit
IO	illuminator of opportunity
ISI	inter-symbol interference
LOS	line of sight
MF	matched filter
MFN	multifrequency network
OFDM	orthogonal frequency division modulation
PCL	passive coherent location
QAM	quadrature amplitude modulation
RAM	radar absorbing material
RpF	reciprocal filter
Rx	receiver
SAR	synthetic aperture radar
SFN	single frequency network
SNR	signal-to-noise ratio
Tx	transmitter
UHF	ultrahigh frequency

References

[1] P. E. Howland, D. Maksimiuk, and G. Reitsma, “FM radio based bistatic radar,” *IEE Proceedings – Radar, Sonar and Navigation*, vol. 152, no. 3, pp. 107–115, 2005.

[2] P. Howland, “Editorial: Passive radar systems,” *IEE Proceedings – Radar, Sonar and Navigation*, vol. 152, no. 3, pp. 105–106, 2005.

[3] C. Prati, F. Rocca, D. Giancola, and A. M. Guarnieri, “Passive geosynchronous SAR system reusing backscattered digital audio broadcasting signals,” *IEEE Transactions on Geoscience and Remote Sensing*, vol. 36, no. 6, pp. 1973–1976, 1998.

[4] M. Cherniakov, K. Kubik, and D. Nezlin, “Bistatic synthetic aperture radar with non-cooperative LEOS based transmitter,” in *IGARSS 2000. IEEE 2000 International Geoscience and Remote Sensing Symposium. Taking the Pulse of the Planet: The Role of Remote Sensing in Managing the Environment. Proceedings (Cat. No.00CH37120)*, vol. 2, July 2000, pp. 861–862.

[5] L. Cazzani, C. Colesanti, D. Leva, *et al.*, “A ground-based parasitic SAR experiment,” *IEEE Transactions on Geoscience and Remote Sensing*, vol. 38, no. 5, pp. 2132–2141, 2000.

[6] M. Antoniou and M. Cherniakov, “GNSS-based bistatic SAR: a signal processing view,” *EURASIP Journal on Advances in Signal Processing*, vol. 2013, no. 1, p. 98, 2013. [Online]. Available: https://doi.org/10.1186/1687-6180-2013-98.

[7] M. Antoniou, Z. Zeng, L. Feifeng, and M. Cherniakov, “Experimental demonstration of passive BSAR imaging using navigation satellites and a fixed receiver,” *IEEE Geoscience and Remote Sensing Letters*, vol. 9, no. 3, pp. 477–481, 2012.

[8] F. Santi, M. Antoniou, D. Pastina, D. Tzagkas, M. Bucciarelli, and M. Cherniakov, “Passive multi-static SAR with GNSS transmitters: first theoretical and experimental results with point targets,” in *Proceedings of EUSAR 2014; 10th European Conference on Synthetic Aperture Radar*, June 2014, pp. 1–4.

[9] F. Santi, M. Bucciarelli, D. Pastina, M. Antoniou, and M. Cherniakov, “Passive multistatic SAR with GNSS transmitters and using joint bi/multi-static CLEAN technique,” in *2016 IEEE Radar Conference (RadarConf)*, May 2016, pp. 1–6.

[10] H. Ma, M. Antoniou, and M. Cherniakov, “Passive GNSS-based SAR resolution improvement using joint Galileo E5 signals,” *IEEE Geoscience and Remote Sensing Letters*, vol. 12, no. 8, pp. 1640–1644, 2015.

[11] K. Kulpa, M. Malanowski, P. Samczynski, and B. Dawidowicz, “The concept of airborne passive radar,” in *2011 Microwaves, Radar and Remote Sensing Symposium*, August 2011, pp. 267–270.

[12] J. R. G. del Arroyo and J. A. Jackson, “SAR imaging using WiMAX OFDM PHY,” in *2011 IEEE RadarCon (RADAR)*, May 2011, pp. 129–134.

[13] J. R. G. del Arroyo and J. A. Jackson, "Collecting and processing WiMAX ground returns for SAR imaging," in *2013 IEEE Radar Conference (RadarCon13)*, April 2013, pp. 1–6.

[14] J. R. G. D. Arroyo and J. A. Jackson, "WiMAX OFDM for passive SAR ground imaging," *IEEE Transactions on Aerospace and Electronic Systems*, vol. 49, no. 2, pp. 945–959, 2013.

[15] A. Evers and J. A. Jackson, "Experimental passive SAR imaging exploiting LTE, DVB, and DAB signals," in *2014 IEEE Radar Conference*, May 2014, pp. 0680–0685.

[16] European Telecommunications Standards Institute Std., *LTE: Evolved Universal Terrestrial Radio Access (E-UTRA), Physical Channel and Modulation*. European Telecommunications Standards Institute Std., 2010. Rev. v. 9.1.0 Release 9. [Online]. Available: http://www.etsi.org/deliver/etsi_ts/136200_136299/136211/09.01.00_60/ts_136211v090100p.pdf.

[17] B. Mulgrew, "Algorithms for passive SAR imaging," in *2006 International Waveform Diversity Design Conference*, January 2006, pp. 1–6.

[18] C. E. Yarman, B. Yazici, and M. Cheney, "Bistatic synthetic aperture hitchhiker imaging," in *2007 IEEE International Conference on Acoustics, Speech and Signal Processing – ICASSP '07*, vol. 1, April 2007, pp. I-537–I-540.

[19] L. Wang, I.-Y. Son, and B. Yazici, "Passive imaging using distributed apertures in multiple-scattering environments," *Inverse Problems*, vol. 26, no. 6, p. 065002, 2010. [Online]. Available: http://stacks.iop.org/0266-5611/26/i=6/a=065002.

[20] C. E. Yarman, L. Wang, and B. Yazici, "Passive synthetic aperture radar imaging with single frequency sources of opportunity," in *2010 IEEE Radar Conference*, May 2010, pp. 949–954.

[21] L. Wang and B. Yazici, "Passive imaging of moving targets with sparsely distributed receivers," in *2011 IEEE RadarCon (RADAR)*, May 2011, pp. 073–078.

[22] L. M. H. Ulander, P. Frölind, A. Gustavsson, R. Ragnarsson, and G. Stenström, "VHF/UHF bistatic and passive SAR ground imaging," in *2015 IEEE Radar Conference (RadarCon)*, May 2015, pp. 0669–0673.

[23] L. M. H. Ulander, P. Frölind, A. Gustavsson, R. Ragnarsson, and G. Stenström, "Airborne passive SAR imaging based on DVB-T signals," in *2017 IEEE International Geoscience and Remote Sensing Symposium (IGARSS)*, July 2017, pp. 2408–2411.

[24] P. Frölind, A. Gustavsson, A. Haglund, R. Ragnarsson, and L. M. H. Ulander, "Analysis of a ground target deployment in an airborne passive SAR experiment," in *2017 IEEE Radar Conference (RadarConf)*, May 2017, pp. 0273–0278.

[25] D. Gromek, P. Samczynski, K. Kulpa, P. Krysik, and M. Malanowski, "Initial results of passive SAR imaging using a DVB-T based airborne radar receiver," in *2014 11th European Radar Conference*, October 2014, pp. 137–140.

[26] D. Gromek, K. Kulpa, and P. Samczynski, "Experimental results of passive SAR imaging using DVB-T illuminators of opportunity," *IEEE Geoscience and Remote Sensing Letters*, vol. 13, no. 8, pp. 1124–1128, 2016.

[27] D. Gromek, P. Krysik, K. Kulpa, P. Samczynski, and M. Malanowski, "Ground-based mobile passive imagery based on a DVB-T signal of opportunity," in *International Radar Conference (Radar), 2014*, October 2014, pp. 1–4.

[28] P. E. Howland, H. D. Griffiths, and C. J. Baker, *Passive Bistatic Radar Systems*. John Wiley & Sons, Ltd, 2008, pp. 247–313. [Online]. Available: http://dx.doi.org/10.1002/9780470985755.ch7.

[29] C. Prati and F. Rocca, "Improving slant-range resolution with multiple SAR surveys," *IEEE Transactions on Aerospace and Electronic Systems*, vol. 29, no. 1, pp. 135–143, 1993.

[30] H. Zhong and X. Liu, "A new combination technique for improving slant resolution in constellation SAR system," in *IEEE International Conference on Geoscience and Remote Sensing Symposium, 2006, IGARSS 2006*, July 2006, pp. 3152–3155.

[31] M. Graziano and M. D'Errico, "Novel constellation design method for space-borne/airborne bistatic SAR systems," *IEEE Transactions on Aerospace and Electronic Systems*, vol. 50, no. 3, pp. 2082–2095, 2014.

[32] D. Cristallini, D. Pastina, and P. Lombardo, "Exploiting MIMO SAR potentialities with efficient cross-track constellation configurations for improved range resolution," *IEEE Transactions on Geoscience and Remote Sensing*, vol. 49, no. 1, pp. 38–52, 2011.

[33] A. Liu, G. Liao, L. Ma, and Q. Xu, "An array error estimation method for constellation SAR systems," *IEEE Geoscience and Remote Sensing Letters*, vol. 7, no. 4, pp. 731–735, 2010.

[34] A. Liu, G. Liao, Q. Xu, and L. Ma, "An improved array-error estimation method for constellation SAR systems," *IEEE Geoscience and Remote Sensing Letters*, vol. 9, no. 1, pp. 90–94, 2012.

[35] D. Cristallini, P. Wojaczek, and M. Ummenhofer, "Range resolution improvement for multiple PCL radar systems on moving platforms," in *Proc. of IEEE RadarConf 2015*, 2015.

[36] ETSI Std., *Digital Video Broadcasting (DVB); Framing Structure, Channel Coding and Modulation for Digital Terrestrial Television*. ETSI Std. Rev. v1.5.1, 06 2004. [Online]. Available: http://www.etsi.org/deliver/etsi_en/300700_300799/300744/01.05.01_40/en_300744v010501o.pdf.

[37] C. Schwark and D. Cristallini, "Advanced multipath clutter cancellation in OFDM-based passive radar systems," in *2016 IEEE Radar Conference (RadarConf)*, May 2016, pp. 1–4.

[38] ETSI, *ETSI TR 102 401 V1.1.1 – Digital Video Broadcasting (DVB); Transmission to Handheld Terminals (DVB-H); Validation Task Force Report*, ETSI, Sophia Antipolis Cedex, France, May 2015.

[39] C. Berthillot, A. Santori, O. Rabaste, D. Poullin, and M. Lesturgie, "BEM Reference Signal Estimation for an Airborne Passive Radar Antenna Array,"

IEEE Transactions on Aerospace and Electronic Systems, December 2017, vol. 53, no. 6, pp. 2833–2845.

[40] S. Searle, S. Howard, and J. Palmer, "Remodulation of DVB-T signals for use in passive bistatic radar," in *2010 Conference Record of the Forty Fourth Asilomar Conference on Signals, Systems and Computers*, November 2010, pp. 1112–1116.

[41] D. Poullin, "Passive detection using digital broadcasters (DAB, DVB) with COFDM modulation," *IEE Proceedings – Radar, Sonar and Navigation*, vol. 152, no. 3, pp. 143–152, 2005.

[42] J. E. Palmer, H. A. Harms, S. J. Searle, and L. Davis, "DVB-T passive radar signal processing," *IEEE Transactions on Signal Processing*, vol. 61, no. 8, pp. 2116–2126, 2013.

[43] F. Colone, D. Langellotti, and P. Lombardo, "DVB-T signal ambiguity function control for passive radars," *IEEE Transactions on Aerospace and Electronic Systems*, vol. 50, no. 1, pp. 329–347, 2014.

[44] M. Glende, "PCL-signal-processing for sidelobe reduction in case of periodical illuminator signals," in *2006 International Radar Symposium*, May 2006, pp. 1–4.

[45] P. Wojaczek, F. Colone, D. Cristallini, and P. Lombardo, "Reciprocal filter-based STAP for passive radar on moving platforms," *IEEE Transactions on Aerospace and Electronic Systems*, April 2019, vol. 55, no. 2, pp. 967–988.

[46] M. Soumekh, *Synthetic Aperture Radar Signal Processing with MATLAB Algorithms*. Wiley-Interscience, New York, NY, USA, 1999.

[47] W. C. Barott and B. Himed, "Cochannel interference in ATSC passive radar," in *2015 IEEE Radar Conference*, May 2015, pp. 1270–1275.

[48] ETSI, *ETSI TR 101 190 V1.3.2 – Digital Video Broadcasting (DVB); Implementation Guidelines for DVB Terrestrial Services; Transmission Aspects*, ETSI, Sophia Antipolis Cedex, France, May 2011.

[49] ETSI, *ETSI EN 302 755 V1.4.1 – Digital Video Broadcasting (DVB); Frame Structure Channel Coding and Modulation for a Second Generation Digital Terrestrial Television Broadcasting System (DVB-T2)*, ETSI, Sophia Antipolis Cedex, France, July 2015.

[50] P. Wojaczek and D. Cristallini, "Optimal trajectories for range resolution improvement in multi-PCL SAR," *AEU – International Journal of Electronics and Communications*, vol. 73, pp. 173–182, 2017. [Online]. Available: http://www.sciencedirect.com/science/article/pii/S1434841117300821.

[51] N. Willis, *Bistatic Radar, Second Edition*. Institution of Engineering and Technology, Stevenage, 2005.

[52] I. Walterscheid, J. Klare, A. R. Brenner, J. H. G. Ender, and O. Loffeld, "Challenges of a bistatic spaceborne/airborne SAR experiment," in *Proc. EUSAR 2006*, 2006.

[53] R. Bamler and P. Hartl, "Synthetic aperture radar interferometry," *Inverse Problems*, vol. 14, no. 4, pp. R1–R54, 1998.

[54] S. Guillaso, A. Reigber, L. Ferro-Famil, and E. Pottier, "Range resolution improvement of airborne SAR images," *IEEE Geoscience and Remote Sensing Letters*, vol. 3, no. 1, pp. 135–139, 2006.

[55] D. Cristallini, D. Pastina, and P. Lombardo, "Efficient configurations of SAR sensors for improved range resolution," in *IEEE International Conference on Geoscience and Remote Sensing Symposium, 2009, IGARSS 2009*, vol. 1, July 2009, pp. I-52–I-55.

[56] S. Searle, J. Palmer, L. Davis, D. W. O'Hagan, and M. Ummenhofer, "Evaluation of the ambiguity function for passive radar with OFDM transmissions," in *2014 IEEE Radar Conference*, May 2014, pp. 1040–1045.

[57] I. Walterscheid, P. Wojaczek, D. Cristallini, and A. Summers, "Challenges and first results of an airborne passive SAR experiment using a DVB-T transmitter," in *EUSAR 2018; 12th European Conference on Synthetic Aperture Radar*, June 2018, pp. 1–4.

Chapter 7

Sparsity-driven multistatic ISAR image reconstruction

Stefan Brisken[1]

The conventional, monostatic way of producing inverse synthetic aperture radar (ISAR) images leaves the user with significant problems in the image interpretation. An ISAR image is the estimate of a two-dimensional (2D) projection of the target's three-dimensional (3D) reflectivity distribution. The image projection plane (IPP) is usually unknown. To recognise a target, e.g. for non-cooperative identification (NCI), the image (or features extracted from the image) has to be compared against a database that contains all possible projections of all possible targets. Obviously, the creation of such databases is very cumbersome and in fact one of the main reasons why automatic NCI has not found widespread application yet. Figure 7.1 illustrates the problem.

It is true that the problem of the IPP exists for optical images, too. The interpretation of ISAR images is – apart from the lower resolution – anyway more difficult for two other reasons. For once, in ISAR, the targets are usually only illuminated from one side. This consequence is that a large fraction of the target is shadowed and the image looks incomplete. In optical images, if there is illumination at all, this illumination is typically scattered light from many directions. Furthermore, the surface roughness of imaged objects is often on a larger or a similar scale compared to optical wavelengths. This leads to diffuse scattering which causes the same part of a target being visible from very different aspect angles. At radar wavelengths, scattering on surfaces of typical ISAR targets is specular, and the scattering behaviour of well-defined geometrical shapes depends strongly on incident and observation angle. This means that a database for ISAR-based NCI does not only need to contain data for all possible IPPs but also for all possible aspect angles, and eventually even for all possible bistatic angles. For optical images, on the other hand, the aspect angle is directly related to the IPP and does not represent an additional degree of freedom.

This chapter, therefore, presents a method that approaches this problem by combining measurements from distributed radars. The illumination of the target is more uniform in this case, the resulting images can hence be expected to look more complete. Furthermore, the new method pursues a 3D reconstruction, which ultimately solves the problem of the IPP. Relative scatterer positions as well as target features,

---

[1] Department of Passive Radar and Anti-Jamming Techniques, Fraunhofer FHR, Wachtberg, Germany

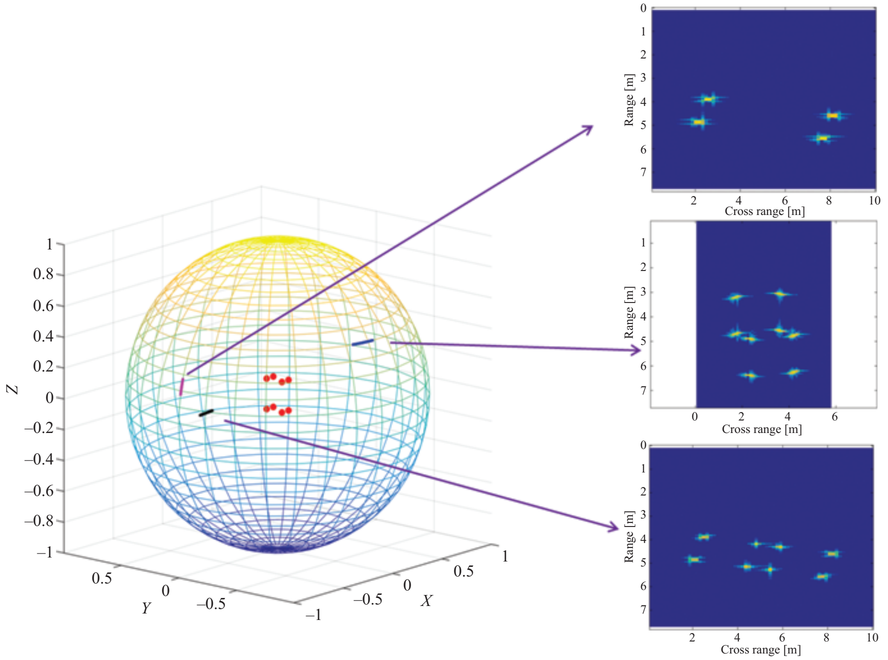

Figure 7.1 Conventional monostatic ISAR imaging of 3D objects leads to 2D projections that can have very different appearance. The simulation in this figure includes eight isotropic point scatterers, represented by the red dots. After radial motion compensation, the trajectories of sensors in the target fixed coordinate system can be displayed as lines on the surface of a sphere. Every possible line corresponds to a possible IPP that has to be included in NCI databases

such as length and width, become invariant under aspect angle changes. The effort to create NCI databases can, therefore, be greatly reduced. Moreover, the combined image is on the same grid for all sensors. This allows to conclude back onto the angular dependence of the reflectivity of single scatterers. In theory, this information could be used to conclude on the respective scattering mechanism.

A small number of papers deal with the possibility of combining the data from different spatially distributed radars (e.g. [1–3]). This idea, however, faces two severe constraints, explained in the following section. The technique presented in this chapter sets itself apart from previous work in that it respects both constraints.

7.1 Constraints

7.1.1 Spatial decorrelation

A straightforward approach to ISAR image combination would be to add up the complex images from different receivers. Unfortunately, the isotropic point scatterer

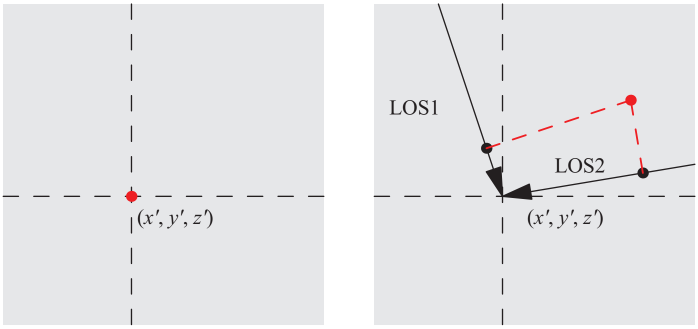

(a) (b)

Figure 7.2 Reflectivity distribution for two different scenes, colour coded in red: (a) isotropic point scatterer on the grid and (b) isotropic point scatterer off the grid

assumption, which is used for monostatic ISAR, does not hold for the case where the aspect angles of the radars are very different. Figure 7.2 supports the explanation of this fact. In Figure 7.2(a), there is a single point scatterer q in the scene, which coincides with a point $\vec{r}$ on the image grid. The received noise-free, range-compressed frequency domain signal in this case would be

$$Y(f,T) = |S(f,T)|^2 \, A_q \cdot e^{-i4\pi(f/c)\left|\vec{r}-\vec{R}(T)\right|}, \tag{7.1}$$

where $S(f,T)$ is the transmitted frequency domain signal at frequency f and transmit time (macro time) T. $\vec{R}(T)$ is the position of the radar at T. Applying a matched filter for each image pixel $\vec{r}$ would yield

$$\begin{aligned} \hat{A}(\vec{r}) &= \sum_T \sum_f |S(f,T)|^2 A_q \cdot e^{-i4\pi(f/c)\left|\vec{r}-\vec{R}(T)\right|} \cdot e^{i4\pi(f/c)\left|\vec{r}-\vec{R}(T)\right|} \\ &= \sum_T \sum_f |S(f,T)|^2 \, A_q e^0 \end{aligned} \tag{7.2}$$

and the point $\vec{r}$ on the grid would get appointed the phase $\phi = 0$, regardless from the position of the sensor. In Figure 7.2(b), however, a single point scatterer is off the regarded grid point, at a coordinate $\vec{r}_q$ and (7.2) becomes

$$\hat{A}(\vec{r}) = \sum_T \sum_f |S(f,T)|^2 A_q \cdot e^{-i4\pi(f/c)\left(\left|\vec{r}_q-\vec{R}(T)\right|-\left|\vec{r}-\vec{R}(T)\right|\right)}. \tag{7.3}$$

The phase term in (7.3) contains the range difference between grid point and point scatterer. From Figure 7.2(b), it can be seen that this difference depends clearly on the aspect angle. This means that phase and amplitude of $\hat{A}(\vec{r})$ do not correspond if observed from different angles. More generally, it becomes clear from (7.3) that any reflection from a point in the vicinity of a grid point causes an aspect angle-dependent contribution to the grid point's amplitude and phase value.

The point scatterer model furthermore neglects the fact that for real targets, the continuous points that constitute the target surface interact with each other via currents and multi-bounce. This introduces an additional dependence on aspect angle, bistatic angle and polarisation into the received signal.

Due to this mismatch between the discrete point scatterer assumption and reality, it cannot be assumed that complex values of the same grid point will add up constructively if the corresponding observations result from very different aspect angles.

This effect is called *spatial decorrelation*. The magnitude of this effect with varying aspect/bistatic/polarisation angle is different from target to target and from grid point to grid point and empirical values are missing in the open literature. Available data exist from investigations in the field of interferometric synthetic aperture radar (InSAR) [4], where the effect is also important. However, scattering properties of the surfaces regarded in InSAR are fundamentally different from the targets of interest in ISAR. The results are, therefore, not portable. The bottom line of the above-mentioned analysis is that all methods of image combination that assume coherent image reconstructions under very different aspect/bistatic/polarisation angles are ruled out in reality.

7.1.2 Foreshortening effect

The second important constraint is derived from the fact that radars and target are usually distributed in all three spatial dimensions and the scatterers on the target are also distributed in 3D. A scatterer that does not lie in the IPP will not appear at its orthogonal projection, but at the intersection between its iso-range and the IPP. For sensors in different positions, this intersection falls into different points in the IPP. Figure 7.3 displays this effect, which in the radar terminology is named *foreshortening*.

To quantify the effect, regard a scene like in Figure 7.3, with a radar located at a height z_p above the IPP and a scatterer q located at a horizontal distance x_q and a vertical (relative to the IPP) distance z_q from the radar. For the iso-range $|r|$ applies

$$|r|^2 = x_q^2 + z_q^2 = x_p^2 + z_p^2. \tag{7.4}$$

The foreshortening $\Delta x = x_p - x_q$, horizontally to the IPP in the direction towards the respective sensor, is, therefore, given by

$$\Delta x = \sqrt{x_q^2 + z_q^2 - z_p^2} - x_q. \tag{7.5}$$

The approach to fuse images in the 2D domain is, therefore, limited to the rare case, where all scatterers coincide to lie in the IPP. Thus, resolving the target in three dimensions is not only a benefit but is mandatory for forming a combined image from distributed sensors.

7.2 Problem formulation

As a consequence from the restrictions due to spatial decorrelation and foreshortening, this chapter presents a method that fuses the image data in the 3D spatial

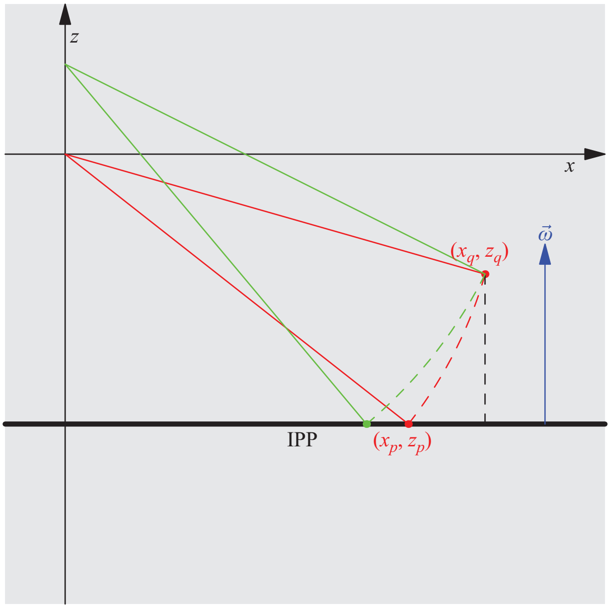

Figure 7.3 *Foreshortening effect: a scatterer with coordinates* (x_q,z_q) *is projected into the IPP at coordinates* (x_p,z_p). *The projection coincides with the intersection of the iso-range and the IPP. Hence, the same scatterer is projected onto different positions (always following the iso-range) in the IPP if observed from different positions (represented by the different origins of the red and green lines)*

domain and does not require coherence between different receivers. For this purpose, a sparse reconstruction method is utilised, namely the block orthogonal matching pursuit (OMP) (BOMP) [5]. Recently, BOMP was proposed as a tool to increase the resolution in passive SAR images [6] and for sensor fusion in passive coherent location [7]. Other reconstruction methods, for example the combined ℓ_1/ℓ_2 optimisation, which are also mentioned in [7], could be used for the same purpose, but BOMP is chosen because it is computationally very efficient for high sparsity levels. As the reconstruction method itself is able to handle arbitrary target motions, it is also suited to form multi-aspect ISAR images.

Regard a setup in which L radar sensors labelled $l = 1, \ldots, L$ observe a common target. A sensor can be a monostatic or a bistatic radar. In the multistatic set-up, l always refers to one combination of transmitter and receiver. Assume that the complete target motion is known and that the coordinates of the sensors can be transformed into a target-fixed coordinate system, where the coordinate of sensor l at time $T_m, m = 1, \ldots, M$ is labelled $\vec{R}_m^{(l)}$.

The task is to reconstruct the reflectivity distribution of the target. For this purpose, a grid of points is defined for which the reflectivity is evaluated. Let $\vec{r}_n$ be the coordinate of the image point indexed with $n = 1, \ldots, N$. In conventional image reconstruction with compressive sensing, the reflectivity of $\vec{r}_n$ is written by its respective entry in a vector $\mathbf{x} = (x_1, x_2, \ldots, x_N)^T$. This notation is eligible for the monostatic case but does not respect the fact that the phase and amplitude of the reflectivity are aspect angle dependent.

For the multistatic case, the notation is, therefore, modified and the complex reflectivity $\mathbf{x}^{(l)}$ towards sensor l is defined as

$$\mathbf{x}^{(l)} = (x_1^{(l)}, x_2^{(l)}, \ldots, x_N^{(l)})^T, \tag{7.6}$$

where the index n again relates to a point $\vec{r}_n, n = 1, \ldots, N$ on the 3D image grid.

The range-compressed receive signal vector in the frequency domain $\mathbf{y}^{(l)}$, as observed by a single sensor l, is sorted by frequency $f_k, k = 1, \ldots, K$ and by slow time $T_m, m = 1, \ldots, M$:

$$\mathbf{y}^{(l)} = \begin{pmatrix} y^{(l)}\left(f_1^{(l)}, T_1\right) \\ \vdots \\ y^{(l)}\left(f_K^{(l)}, T_1\right) \\ y^{(l)}\left(f_1^{(l)}, T_2\right) \\ \vdots \\ y^{(l)}\left(f_K^{(l)}, T_M\right) \end{pmatrix}. \tag{7.7}$$

The signal model used for the reconstruction can be described by L linear equation systems, respectively, written in the form

$$\mathbf{y}^{(l)} = \mathbf{A}^{(l)}\mathbf{x}^{(l)} + \mathbf{n}^{(l)}, \tag{7.8}$$

where $\mathbf{n}^{(l)}$ is the noise contribution and $\mathbf{A}^{(l)}$ is a sensing matrix:

$$\mathbf{A}^{(l)} = \begin{pmatrix} A(f_1^{(l)}, T_1, \vec{r}_1) & \cdots & A(f_1^{(l)}, T_1, \vec{r}_N) \\ \vdots & & \vdots \\ A(f_K^{(l)}, T_1, \vec{r}_1) & \cdots & A(f_1^{(l)}, T_1, \vec{r}_N) \\ A(f_1^{(l)}, T_2, \vec{r}_1) & \cdots & A(f_1^{(l)}, T_2, \vec{r}_N) \\ \vdots & & \vdots \\ A(f_K^{(l)}, T_M, \vec{r}_1) & \cdots & A(f_K^{(l)}, T_M, \vec{r}_N) \end{pmatrix}. \tag{7.9}$$

The elements of $\mathbf{A}^{(l)}$ are defined as

$$A^{(l)}(f_k^{(l)}, T_m, \vec{r}_n) = P^{(l)}(f_k^{(l)})e^{-i2\pi f_k^{(l)} d^{(l)}(T_m, \vec{r}_n)/c} \tag{7.10}$$

given that the total distance from transmitter to target to receiver:

$$d^{(l)}(T_m, \vec{r}_n) = \left|\vec{R}_T'^{(l)}(T_m) - (\vec{r}_n)\right| + \left|\vec{R}_R'^{(l)}(T_m) - (\vec{r}_n)\right|, \tag{7.11}$$

where $\vec{R}_T^{\prime(l)}(T_m)$ and $\vec{R}_R^{\prime(l)}(T_m)$ are the coordinates of transmitter and receiver belonging to sensor l, respectively. $P^{(l)}(f_k^{(l)})$ means the point spread function of sensor l in the frequency domain. If a matched filter is used for range compression, the point spread function is given by $P^{(l)}(f_k^{(l)}) = |S^{(l)}(f_k^{(l)})|^2$, where $S^{(l)}(f_k^{(l)})$ is the transmit signal in the frequency domain.

In this problem formulation, the different $\mathbf{y}^{(l)}$ can have different length. Obviously, the sensor positions $\vec{R}^{\prime(l)}(T_m)$ are different for different sensors, but also the frequencies $f_k^{(l)}$ and point spread functions $P^{(l)}(f_k^{(l)})$ are not required to correspond. Hence, this signal model is well suited to fuse ISAR data from heterogeneous sensors. As the objective is to form a combined image, the grid coordinates $\vec{r}_n$ should be the same for each sensor. Nevertheless, this signal model does not assume that scatterers observed by separated radars must have the same phase or amplitude.

7.3 Reconstruction

Although scatterers do not have the same complex reflectivity towards different radars, they may still appear on the same position $\vec{r}_n$ on the grid, at least for some of the observing sensors. To use this feature, first construct an N-by-L matrix $\mathbf{X}$, by writing the reflectivity distributions $\mathbf{x}^{(l)}$ in adjacent columns:

$$\mathbf{X} = \begin{pmatrix} x_1^{(1)} & x_1^{(2)} & \cdots & x_1^{(L)} \\ x_2^{(1)} & x_2^{(2)} & \cdots & x_2^{(L)} \\ \vdots & \vdots & & \vdots \\ x_N^{(1)} & x_N^{(2)} & \cdots & x_N^{(L)} \end{pmatrix}. \tag{7.12}$$

Each row in $\mathbf{X}$ corresponds to a point on the grid, each entry within a row to this point's complex reflectivity towards the different sensors. Subsequently, construct a vector $\boldsymbol{\xi}$, which is the ℓ_2-norm of the rows of $\mathbf{X}$:

$$\boldsymbol{\xi} = \begin{pmatrix} \ell_2(x_1^{(1)} & x_1^{(2)} & \cdots & x_1^{(L)}) \\ \ell_2(x_2^{(1)} & x_2^{(2)} & \cdots & x_2^{(L)}) \\ \vdots & \vdots & & \vdots \\ \ell_2(x_N^{(1)} & x_N^{(2)} & \cdots & x_N^{(L)}) \end{pmatrix}. \tag{7.13}$$

The ℓ_2-norm of a vector is the square root of the sum of the absolute squares of its entries, hence:

$$\ell_2(x_n^{(1)}, x_n^{(2)}, \ldots, x_n^{(L)}) = \sqrt{\sum_{l=1}^{L} |x_n^{(l)}|^2}. \tag{7.14}$$

A central assumption for the reconstruction of the $\mathbf{x}^{(l)}$ is that $\boldsymbol{\xi}$ has only a small number s of non-zero entries. This property is usually referred to as *block sparsity*. Other than for SAR, in ISAR, this can be considered to be realistic after the removal of eventual clutter. Note the analogy to conventional sparse reconstruction methods, such as OMP [8], which require the sparsity of $\mathbf{x}$. Another precondition relates to the coherence properties of the sensing matrix. To characterise the convergence properties of the BOMP algorithm, [5] defines two quantities, namely *block-coherence* μ_B and *sub-coherence* ν. The block coherence is defined as

$$\mu_B = \max_{l,r \neq l} \frac{1}{L} \rho(\mathbf{B}[l,r]), \tag{7.15}$$

where $\mathbf{B}[l,r] = \mathbf{A}^{(l)\dagger}\mathbf{A}^{(r)}$ and $\rho(\mathbf{B})$ means the spectral norm, defined as

$$\rho(\mathbf{B}) = \sqrt{\lambda_{\max}(\mathbf{B}^{\dagger}\mathbf{B})}, \tag{7.16}$$

with $\lambda_{\max}$ being the largest eigenvalue of a matrix $\mathbf{B}^{\dagger}\mathbf{B}$. The definition of the sub-coherence is

$$\nu = \max_{l} \max_{i,j \neq i} |\mathbf{a}_i^{\dagger}\mathbf{a}_j|, \tag{7.17}$$

where a_i and a_j are columns of $\mathbf{A}^{(l)}$. Per definition, it is $\nu = 0$ for $L = 1$.

These quantities are required to be small, which sets a lower limit on the grid spacing. Eldar *et al.* [5] furthermore derive a sufficient convergence criterion for BOMP for the noiseless case, which relates sparsity level s, block length L, block coherence and sub-coherence to

$$sL < \frac{1}{2}\left(\mu_B^{-1} + L - (L-1)\frac{\nu}{\mu_B}\right). \tag{7.18}$$

Note that for $L = 1$, (7.18) becomes

$$s < \frac{\mu^{-1} + 1}{2} \tag{7.19}$$

which is exactly the condition for OMP.

Fang *et al.* [9] present the conditions under that the signal can be recovered correctly in the presence of noise. Both articles, [5,9], derive sufficient convergence conditions, but experience has shown that a correct or nearly correct solution for the $\mathbf{x}^{(l)}$ can be obtained very often, even though the aforementioned criteria are not strictly met. A statistical analysis that relates the quantities in (7.18) to a recovery probability is – to the author's knowledge – still missing.

The reconstruction strategy of BOMP is similar to the conventional OMP: in each iteration *it* of a loop, the algorithm

1. estimates the matched filter bank response $\hat{\mathbf{m}}^{(l)} = \mathbf{A}^{(l)\dagger}\tilde{\mathbf{r}}^{(l)it}$ for a residual signal $\tilde{\mathbf{r}}^{(l)it}$ (initially $\tilde{\mathbf{r}}^{(l)0} = \tilde{\mathbf{y}}^{(l)}$),
2. constructs a vector

$$\hat{\boldsymbol{\zeta}} = \begin{pmatrix} \ell_2(\hat{m}_1^{(1)} & \hat{m}_1^{(2)} & \cdots & \hat{m}_1^{(L)}) \\ \ell_2(\hat{m}_2^{(1)} & \hat{m}_2^{(2)} & \cdots & \hat{m}_2^{(L)}) \\ \vdots & \vdots & & \vdots \\ \ell_2(\hat{m}_N^{(1)} & \hat{m}_N^{(2)} & \cdots & \hat{m}_N^{(L)}) \end{pmatrix}$$

(the construction of $\hat{\boldsymbol{\zeta}}$ from $\hat{\mathbf{m}}^{(l)}$ is completely analogue to the construction of $\boldsymbol{\xi}$ from $\mathbf{x}^{(l)}$),

3. finds the index $\hat{n}_{\max}$ of the maximum entry of $\hat{\boldsymbol{\zeta}}$ (thereby identifying the pixel on the grid, from which the most energy was received) and merges $\hat{n}_{\max}$ into an index set $\hat{I}^{it} = \hat{I}^{it-1} \cup \left\{\hat{n}_{\max}\right\}$ (initially $\hat{I}^{0} = \emptyset$),
4. constructs a partial sensing matrix $\mathbf{E}^{(l)}$, which is constituted only by the columns of $\mathbf{A}^{(l)}$ listed in $\hat{I}^{it}$,
5. calculates the complex weights

   $$\hat{\mathbf{w}}^{(l)} = \left(\mathbf{E}^{(l)\dagger}\mathbf{E}^{(l)}\right)^{-1}\mathbf{E}^{(l)\dagger}\tilde{\mathbf{y}}^{(l)}$$

   which is the linear least square estimator that minimises $\left|\tilde{\mathbf{y}}^{(l)} - \mathbf{E}^{(l)}\mathbf{w}^{(l)}\right|^{2}$ with respect to the vectors $\mathbf{w}^{(l)}$ that list only the reflectivities of the scene points found in the index set $\hat{I}^{it}$,
6. calculates the updated residual signal by $\hat{\mathbf{r}}^{(l)it+1} = \tilde{\mathbf{y}}^{(l)} - \mathbf{E}^{(l)}\hat{\mathbf{w}}^{(l)}$,

until the energy in the residual signal $\tilde{\mathbf{r}}^{(l)it}$ falls below a threshold value or a maximum number of iterations are reached. The resulting reflectivity of the scene $\hat{\mathbf{x}}^{(l)}$ for the individual sensors l is obtained by setting the elements of $\hat{\mathbf{x}}^{(l)}$ that are included in the final index set to $\hat{\mathbf{x}}^{(l)}_{I^{it}} = \hat{\mathbf{w}}^{(l)}$ and the other coefficients to zero.

The combined image is then represented by the resulting $\hat{\boldsymbol{\xi}}$ constructed from the $\hat{\mathbf{x}}^{(l)}$s. Note that constructing $\boldsymbol{\xi}$ and $\boldsymbol{\zeta}$ are the only steps in which data resulting from different sensors are associated. In the construction of both vectors, the phases are discarded by the absolute squares and the distribution of the amplitudes towards the individual sensors is omitted by summing up. Thus, in steps 2 and 3, the requirement for coherence between the sensors is eliminated, while steps 1, 4, 5 and 6 are processed individually for each sensor.

For the reconstruction, no assumption on the form of target motion was made. The applicability of the proposed method is, therefore, not limited to special cases. Furthermore, the different sensors may work with totally different frequencies and signal forms.

BOMP and the underlying OMP have often been criticised for the difficulty to set the termination criterion a priori. If the termination threshold on the residual energy is too high, (B)OMP will miss to select scatterers that exist on the target. If the threshold is set too low, (B)OMP selects false scatterers due to noise contributions. This is in fact a problem if one is interested in a 100% correct solution. In the ISAR case, false scatterers can be accepted if their reflectivity level is significantly below that of the dominant real scatterers. In principal, the same problem occurs for any imaging algorithm where one is confronted with selecting the threshold of the dynamic range presented in the image. Some small spurious contributions are usually accepted in the image in order to not suppress too many weak scatterers.

The problem of the termination criterion could also be addressed from the application point of view. If it is known how many scatterers are necessary for a particular task, the algorithm could be terminated after this preset number of iterations. It is then on the radar system to provide sufficient SNR to accomplish the task for a given range.

Table 7.1 Simulated intensity and phase as seen by the different sensors

Scatterer no.	**1**	**2**	**3**	**4**	**5**	**6**
		Relative scatterer intensity [dB]				
Sensor 1	−6	0	−10	−24	−8	−30
Sensor 2	−26	−39	−12	−6	−22	−21
Sensor 3	−7	−16	−22	−14	−15	−11
Sensor 4	−9	−10	−6	−22	−97	−26
Sensor 5	−48	−36	−4	−9	−25	−15
		Relative scatterer phase [rad]				
Sensor 1	2.5	−2.7	2.4	−1.2	0.9	−2.6
Sensor 2	−0.2	−1.1	−1.9	3.0	1.5	−2.1
Sensor 3	1.6	−2.1	1.4	−3.1	2.7	−2.0
Sensor 4	0.8	−2.8	−1.9	−0.3	0.0	1.7
Sensor 5	−2.3	0.4	−0.9	1.1	2.5	−0.8

7.4 A simulated example

The image reconstruction shall now be demonstrated in a simulation. The simulated target consists of independent scatterers distributed in three dimensions. The individual scatterers are not isotropic but have different random amplitudes and phases for different sensors. The realisations of these random values for the simulation displayed here are denoted in Table 7.1.

The target moves as a rigid body along a fraction of a Euler spiral, whose parameters have been created via Monte Carlo simulation. The velocity is set to 1 m/s. A top view of the target motion is depicted in Figure 7.4. The orientation of the target follows the velocity vector, as is often the case for ground targets.

The sensors are distributed around the target at different heights. Transmitter and receiver of each sensor are co-located. The locations of the sensors are listed in Table 7.2, and a top view of the simulated geometry is displayed in Figure 7.5.

The radars transmit chirp signals of 800 MHz bandwidth at a centre frequency of 8.9 GHz. The pulse repetition frequency is set to 100 Hz, the coherent processing interval is 5 s. The full signal for each sensor $\mathbf{y}_{Full}^{(l)}$ therefore has 128,000 samples, of which 3,000 were chosen randomly for the reconstruction, along with the corresponding entries in $\mathbf{A}^{(l)}$. White Gaussian noise is added to the signal with a level of −30 dB relative to the strongest scatterer (see Table 7.1), after range compression.

Figure 7.6 shows the aggregated images projected into the *Y*–*Z*, *X*–*Z* and *X*–*Y* plane. The purple circles represent the true location of scatterers. Obviously, the algorithm has reconstructed the target's reflectivity distribution with high accuracy. The locations of reflectivity peaks largely coincide with the real position of the scatterers. Furthermore, some additional non-zero entries are visible, which are the result of spurious noise contributions. For additional iterations, more noise contributions

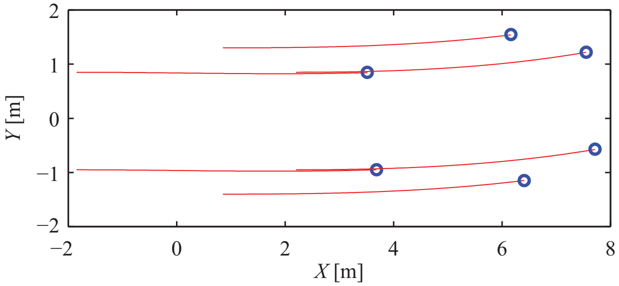

Figure 7.4 *Top view of the trajectory of the simulated target. The blue circles represent the end point of the trajectory (red) of the individual scatterers*

Table 7.2 *Simulated positions of the sensors*

x	y	z
20	−110	40
−100	−155	0
5	10	−310
−155	100	−50
90	200	120

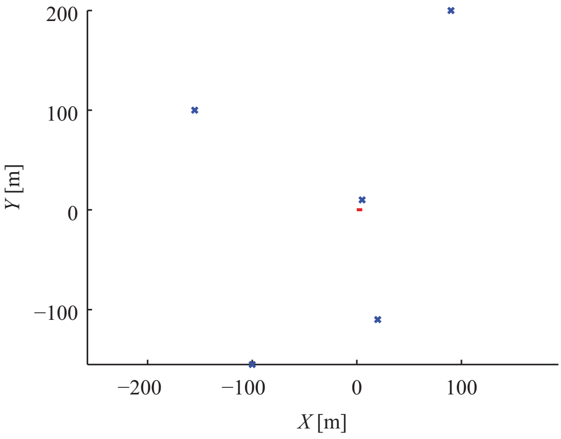

Figure 7.5 *The blue crosses indicate the X and Y coordinates of the sensors, relative to the target (red) starting at (0, 0, 0). For the Z coordinates please refer to Table 7.2*

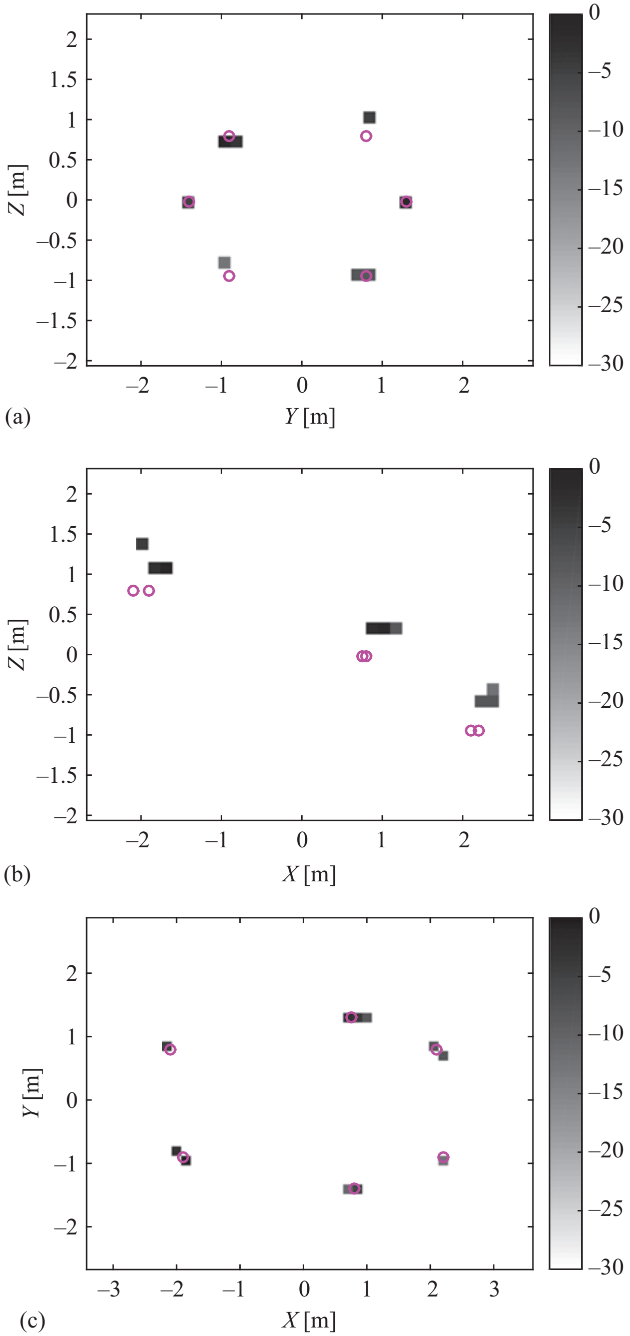

Figure 7.6 Orthogonal projections of the reconstructions of the target reflectivity with BOMP. (a) Y–Z projection, (b) X–Z projection, (c) X–Y projection

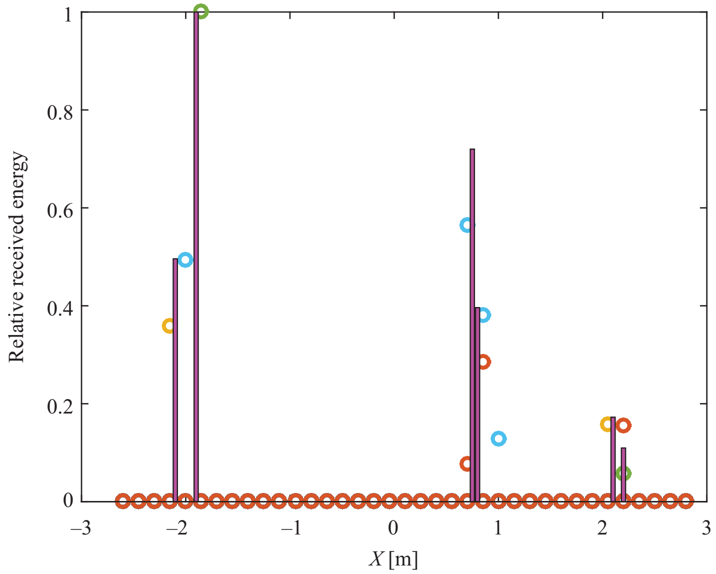

Figure 7.7 Relative scatterer energy, associated to their position on the x-axis. The magenta bars indicate the true values. The circles indicate the estimate values. Different colours indicate different y-positions

can be expected, but on a level below that of those already included in the image. The relative strength of true and reconstructed scatterers can be better compared in Figure 7.7. It shows the reconstructed reflectivity values as circles and the true values as magenta bars, both assigned to their respective x-position. The main reason why the reconstruction is not perfect is because the simulated scatterers do not exactly coincide with the grid points. This problem is often called the *off-grid problem* and well known in compressive sensing. The problem is not addressed here, but subject of several dedicated papers (e.g. [10–12]).

7.5 Experimental results

The applicability of the algorithm shall now be tested on real data, collected by the Fraunhofer Institute for High Frequency Physics and Radar Techniques in Wachtberg, Germany. The software-defined radar LabRadOR [13] serves as transmitter and co-located receiver. The target (Figure 7.9(b)) is placed on a turntable with adjustable and well-known rotation vector. The horizontal distance from the centre of the turntable to the radar was measured with a laser distance measurement system to be 87.5 m. A scissor lift elevated the radar antennas to a height of 3.90 m. The height of the target is roughly estimated to be 3 m. The IPP is set to $z = 2$ m. Instead of employing multiple

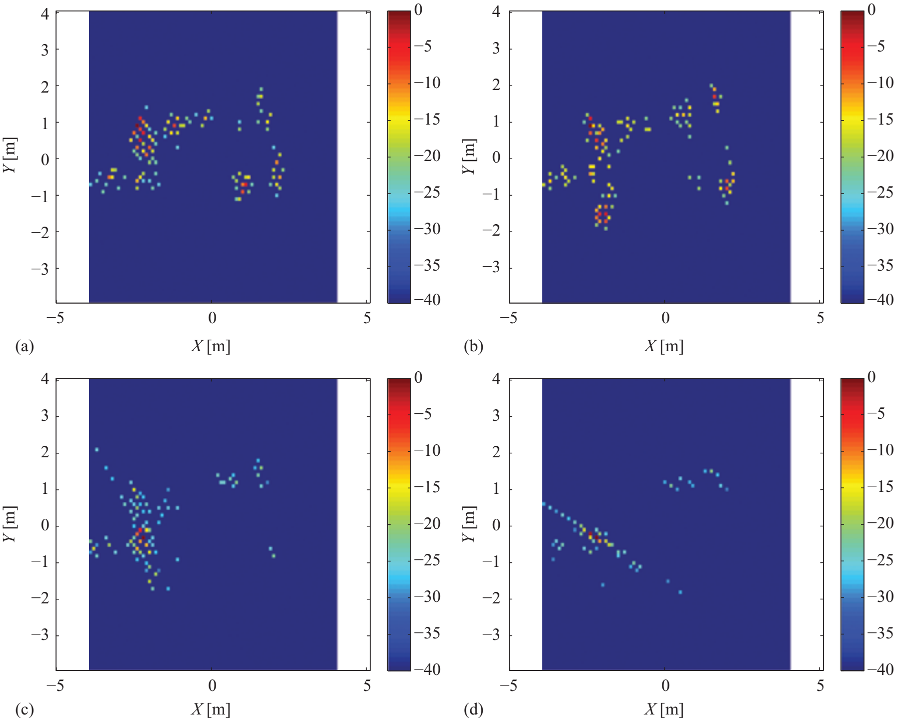

Figure 7.8 Turntable images from different azimuth aspect angles: (a) 0°, (b) 30°, (c) 60° and (d) 90°

radars, data sets from different aspects (here 0°, 30°, 60° and 90° azimuth rotation) are used to emulate a multistatic radar. In the literature, this technique is often called *multi-look*.

Obviously, this geometry represents the special case where all emulated radars and the target are almost coplanar. On the one hand, this means that the target cannot be resolved in 3D. In the words of compressive sensing, the coherence of the sensing matrix would be too high. On the other hand, it means that the foreshortening effect is very limited. For the given geometry, according to (7.5), the displacement of a scatterer in two images does not exceed 5 cm. Consequently, for this data set, a 2D grid has to be used. The pixel size is set to 10 cm in both dimensions, twice the value of the maximum expected foreshortening. Figure 7.8 shows the individual images, produced with the OMP algorithm. The combined image, produced with BOMP, is displayed in Figure 7.9(a). If compared to the optical image in Figure 7.9(b), it comes clear that the combined image represents the outline of the target better than the individual images.

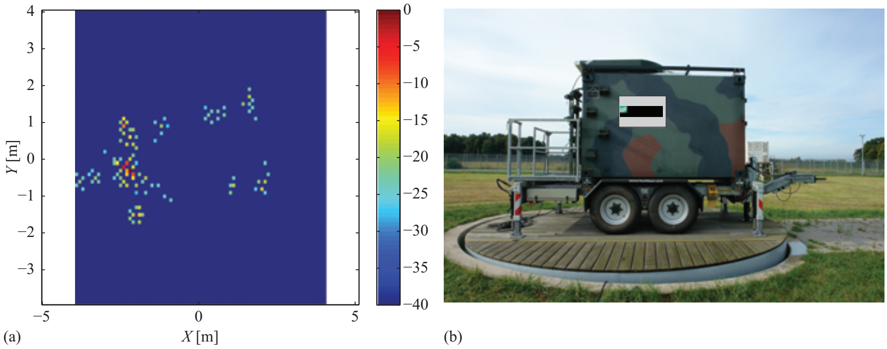

[redacted]

Figure 7.9 (a) Combined image resulting from four (emulated) radars situated at 0°, 30°, 60° and 90° azimuth angle and (b) optical image of the target on the turntable

7.6 Conclusion

The simulation proves that BOMP can be used to eliminate the requirement of a coherent return signal in 3D multi-aspect ISAR. This, of course, is only one of the several criteria for the applicability to real scenarios. Apart from the convergence conditions already mentioned in the chapter, the performance of the technique in reality furthermore depends on

- noise properties
- motion estimation errors
- system accuracy (antenna positions and system delays)
- imaging geometry
- target scattering properties.

The noise properties in ISAR images often deviate from the white Gaussian noise model, which was used to derive the convergence conditions in [9]. Therefore, this condition might not be exactly portable to this application.

The response of BOMP to motion estimation errors and system accuracy is still to be quantified. Experience indicates that greedy algorithms, such as BOMP or OMP, react significantly more sensitive to inaccurate sensing matrices than the classic matched filter does. In principle, an image quality-based autofocus algorithm could be applied to the combined 3D image, in order to estimate the target's motion parameters and optimise the image quality. Let $\boldsymbol{\chi}$ be a vector of motion parameters that is used to construct the sensing matrices $\mathbf{A}^{(l)}(\boldsymbol{\chi})$. Then an estimator for $\boldsymbol{\chi}$ could be

$$\hat{\boldsymbol{\chi}} = \arg\min_{\boldsymbol{\chi}}\{\ell_1(\hat{\boldsymbol{\xi}}(\boldsymbol{\chi}))\}, \tag{7.20}$$

where $\hat{\xi}$ is constructed like in Section 7.3. However, computing $\hat{\xi}$ is already very time consuming. Iterating this step in an optimisation algorithm is, therefore, regarded as a very interesting task for future research and will require a fast computer.

An imaging geometry that is not appropriate to resolve the target in three dimensions will directly be indicated by a high coherence of the sensing matrix. Thus, the requirements to the imaging geometry are implicitly included in (7.18).

The scattering properties of the target obviously affect the value of the block sparsity. Furthermore, if shadowing or anisotropy of a scatterer effects that it is only visible to a single sensor, it might be allocated to a wrong position, but the contribution of this scatterer to the signal would still be subtracted correctly. Therefore, the progress of the algorithm is not disturbed. However, such behaviour can be expected to degrade the performance of classification algorithms applied to the image.

References

[1] Brisken S, Matthes D, Mathy T, *et al.* Spatially Diverse ISAR Imaging for Classification Performance Enhancement. International Journal of Electronics and Telecommunications. 2011;57(1):15–21.

[2] Pastina D, Bucciarelli M, and Lombardo P. Multi-platform distributed ISAR for surveillance and recognition. In: Radar Conference – Surveillance for a Safer World, 2009. RADAR. International; 2009. pp. 1–6.

[3] van Dorp P, Otten MPG, and Verzeilberg JMM. Coherent multistatic ISAR imaging. In: Radar Systems (Radar 2012), IET International Conference on; 2012. pp. 1–6.

[4] Lee H, and Liu JG. Analysis of Topographic Decorrelation in SAR Interferometry Using Ratio Coherence Imagery. IEEE Transactions on Geoscience and Remote Sensing. 2001;39(2):223–232.

[5] Eldar YC, Kuppinger P, and Bolcskei H. Block-Sparse Signals: Uncertainty Relations and Efficient Recovery. IEEE Transactions on Signal Processing. 2010;58(6):3042–3054.

[6] Mao X, Zhang YD, and Amin MG. Two-stage multi-static passive SAR imaging with reduced complexity. In: Radar Conference, 2014 IEEE; 2014. pp. 0340–0343.

[7] Ender JHG. A compressive sensing approach to the fusion of PCL sensors. In: Signal Processing Conference (EUSIPCO), 2013 Proceedings of the 21st European; 2013. pp. 1–5.

[8] Pati YC, Rezaiifar R, and Krishnaprasad P. Orthogonal matching pursuit: Recursive function approximation with applications to wavelet decomposition. In: Signals, Systems and Computers, 1993. 1993 Conference Record of The Twenty-Seventh Asilomar Conference on. IEEE; 1993. pp. 40–44.

[9] Fang J, and Li H. Block-sparsity pattern recovery from noisy observations. In: Acoustics, Speech and Signal Processing (ICASSP), 2012 IEEE International Conference on; 2012. pp. 3321–3324.

[10] Chi Y, Scharf LL, Pezeshki A, *et al.* Sensitivity to Basis Mismatch in Compressed Sensing. IEEE Transactions on Signal Processing. 2011;59(5): 2182–2195.

[11] Tang G, Bhaskar BN, Shah P, *et al.* Compressed Sensing Off the Grid. IEEE Transactions on Information Theory. 2013;59(11):7465–7490.

[12] Chen Y, and Chi Y. Robust Spectral Compressed Sensing via Structured Matrix Completion. IEEE Transactions on Information Theory. 2014;60(10): 6576–6601.

[13] Brisken S. Motion Estimation and Imaging with Multistatic Inverse Synthetic Aperture Radar. Fraunhofer FHR; 2017. Available from: http://publica.fraunhofer.de/documents/N-461344.html.

This page intentionally left blank

Part II

Practical feasibility and applications

This page intentionally left blank

Chapter 8

Rotor blade parameter estimation with multichannel passive radar

Marcin Kamil Bączyk[1] *and Jacek Misiurewicz*[1]

8.1 Introduction

This chapter is dedicated to the radar measurements of rotary-wing aircraft parameters. It concerns primarily helicopters as targets; however, the considerations presented herein are also valid, at least in part, for a wider class of aircraft, including multicopter drones. The chapter focuses mainly on blade echo detection and the estimation of blade parameters, as the presence of a rotor with moving blades is a common distinguishing feature specific for this class of targets.

8.1.1 Problem formulation

The classification of helicopters not only raises an important problem in itself but is also closely related to the detection process. Any copter poses challenges as a radar's target due to its relatively low speed (possibly as low as zero when hovering) and typically low flight altitude (i.e. on its way down to hide behind various land forms). Thus, recognition of specific echo properties that differentiate the helicopter from other (unimportant) objects usually constitutes a part of helicopter detection algorithms. In general, the copter already detected can be classified by its most prominent features, usually with rotor blade parameters first in line. The same features can also be used for the recognition of the copter's type. The helicopter echo consists of several components [1,2], typically with the fuselage echo as the strongest one. Weaker components come from the copter's two rotors: the main and tail rotors. Each rotor echo consists of echoes from its blades and the rotor's hub as well. The fuselage echo is not considered a distinctive element, since it cannot be easily differentiated from echoes of various objects, such as a car, building or a fixed-wing aircraft. In the case of blade echo, the useful property is the blade movement. It enables the employment of Doppler-based techniques first to recognize the blade and then to measure its parameters [1,3,4].

A significant number of works have been published on the subject of helicopter detection and classification with active radars – namely pulsed radars [5] or FMCW

---

[1] Warsaw University of Technology, Institute of Electronic Systems, Warsaw, Poland

radars [6,7]. A passive radar, however, as is the case with CW radars, differs from classical radars significantly in the transmit–receive geometry, as well as in the properties of the illumination signal and the processing chain (long integration time being one of the most important processing characteristics). In the last 10 years, several theoretical studies of helicopter detection and classification with passive radar have been presented [8,9], some of them backed up with simulations [10,11], others with live signal experiments [12–17]. In addition, active radar experiments with bistatic geometry and noise-like modulation have also been conducted [7,18]. The results of these experiments are also valuable for the passive radar due to the similar properties of the illuminating signal.

8.1.2 Methods for helicopter classification

Typically, target classification with radar is based on a high resolution image of the target. Such an image may be one- or two-dimensional. The former – in the range dimension (i.e. a high-resolution range (HRR) profile) – requires appropriate wideband illumination, the latter entails combining HRR with special processing in the cross-range dimension. Following appropriate processing, the image obtained can be classified with many available techniques, ranging from simple size measurements to artificial intelligence methods.

The cross-range processing choices primarily include the following:

- Synthetic aperture radar (SAR) imaging with stationary targets: This requires the radar's transmitter and/or receiver to be in motion.
- Inverse synthetic aperture radar (ISAR) imaging with targets moving in the cross-range direction: This calls for the predictable movement of the target.

Both these techniques have, however, poor applicability to a helicopter's fuselage imaging since not only is it a moving target but also its movement is rather slow and difficult to predict. A natural way to obtain the cross-range dimension of the image of a helicopter-type target is the use of the ISAR technique based on the rotor movement [14].

It is a convenient approach, as the rotor movement is relatively fast and predictable. Moreover, the simple processing of the rotor image can yield straightforward and distinctive parameters for helicopter classification and recognition, such as the number and/or length of the rotor's blades, as well as the rotor's angular velocity. Similar parameters can be derived from the image of the tail rotor (if it is present). Distinctive features of the helicopter's rotor can also be extracted without creating an image of the rotor, because the unique physical rotor properties create a visible signature in the time and Doppler domains. Such an approach for a pulsed radar was theoretically analysed in [3] and then experimentally validated in [19,20]. The practical implementation of a helicopter detector in a working radar device was described in [21]. A high-resolution FMCW radar signature of a helicopter was studied in [6], and the classification using such a signature was undertaken in [22]. A bistatic continuous-wave radar with code modulation was used for similar experiments, as described in [7] and [18].

8.1.3 Recognition of the propeller aircraft or other rotary-wing aircraft

Rotor echo recognition, followed by the estimation of the basic rotor parameters, is also useful for differentiating between a helicopter, propeller aircraft and jet aircraft. Due to the relatively large size of the helicopter's rotor with respect to the size of its fuselage, the presence of a strong rotating blade echo component indicates a helicopter echo, whereas any target with a weaker blade component is likely to be a propeller aircraft. Moreover, the rotation speed of any rotor or propeller is approximately inversely proportional to their respective sizes, which enables a rough size estimation, indicating the aircraft's type. A jet aircraft's engine may exhibit a signature of its turbine's rotor similar in nature to the one given by the helicopter's rotor. In the literature, the effect of jet engine reflection is referred to as jet engine modulation (JEM). The JEM echo may be differentiated from the echo of the helicopter's rotor by its higher harmonic content in the Doppler domain. Another type of aircraft which may exhibit a similar signature is a multirotor drone (multicopter). Two distinct properties of this aircraft class are the presence of several unsynchronized high-speed rotors and variations in the rotor speed controlled by the flight stabilization system. The latter comes from the fact that a typical multicopter employs fixed-pitch rotors and changes in the rotor speed affect the flight control and stabilization (the rotor tilt is also varied at times). It must be noted that a drone's rotor is typically small with respect to a radar wavelength, so a flash from the blade analysed in Section 8.3.2 is not as prominent as it is in the case of a large helicopter's blades.

8.2 A geometric model of the helicopter

In this section, a geometric model of a helicopter is considered. This model is applied to understand the structure of the echo signal reflected from a hovering helicopter. In the geometric modelling, for most air objects, it is assumed that with a sufficiently high accuracy, they can be represented by rigid bodies. All reflective points from any rigid body do not change their positions in relation to the determined centre of mass of the object and to the fixed orientation associated with this object. In this case, only the trajectories of the object are considered, taking into account both a displacement relative to the determined point representing the origin of the coordinate system and the change of orientation with respect to this system. Plainly, such assumption cannot be met in the case of the rotary-wing aircraft, whose rotating elements (at least one) change their orientations in relation to the aircraft's fuselage. In the following subsections, the individual components of the geometric model under consideration are presented and described. A model of the considered helicopter type is shown in Figure 8.1.

8.2.1 The echo of the helicopter's fuselage

The main non-rotating elements in the model under consideration are the parts of the helicopter's fuselage: the hull and the tail. In a simplified way, the copter's fuselage

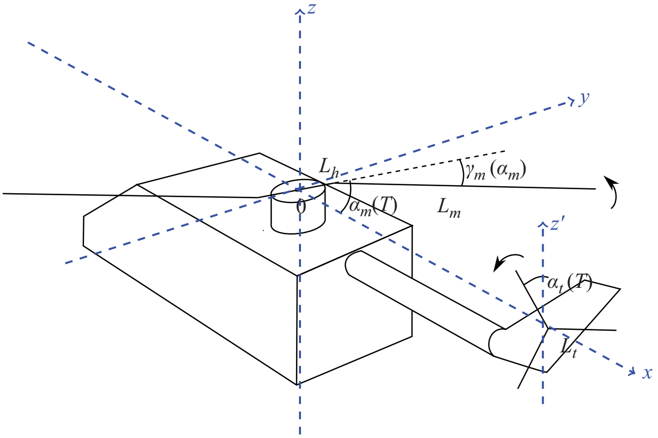

Figure 8.1 A simplified model of the helicopter

can be modelled as a cuboid with a cylinder placed at its back wall, see Figure 8.1. Both the displacement and rotation of the helicopter's hull with its tail can be easily represented by an equation based on the movement model. The helicopter typically either moves along a selected trajectory or remains in a hover. In both cases, the orientation of its hull in the space changes slightly. Depending on the kind of motion, the helicopter's hull is oriented horizontally if it is in a hover or is tilted in the direction, in which it is moving at a given moment. The occurring inclination is associated with a different lifting force acting on the blade in various deflections. In this way, the helicopter's pilot decides which direction the machine will move.

8.2.2 The main rotor

The main rotor generates an aerodynamic lifting force that supports the copter's weight. Each rotorcraft's blade, like the wing of an aircraft, generates a lifting force as a result of its rotational motion. The value of this lifting force depends on the blade's construction, angle of attack and the angular velocity of the rotor. Most helicopters are characterized by the constant angular velocity of the rotor due to their design constraints. This limitation is primarily caused by the adverse consequences of moving with the speed of propagation of mechanical waves in a given medium. Since the linear velocity of the individual blade fragments increases with the distance from the rotor centre, and none of its points can exceed the value of about 334 m/s, the angular velocity of the blade is limited to approximately $((334\ \mathrm{m/s})/(L_h + L_m))\ \mathrm{rd/s}$.

The power transmitted directly to the main rotor balances the total air resistance (drag) of each blade. This resistance depends on the angle of attack; the wider the angle, the greater the air resistance and lifting force generated by the blade in a given deflection. If all blades have the same angle of attack and assuming calm weather, the helicopter remains in a hover or moves vertically. Any imbalance of lifting forces within the main rotor causes the helicopter to tilt in a given direction and move towards the inclination (see Figure 8.2).

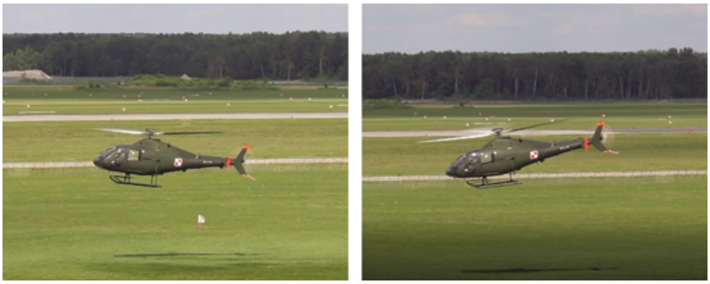

Figure 8.2 Helicopter in a hover (left) and moving forwards (right)

The copter's main rotor is responsible for generating the lifting force, setting the rotorcraft in a progressive speed and creating control moments. The central part of the main rotor is the rotor itself, and each blade is attached to it. The rotor is also responsible for the correct transfer of control; namely, it works as a setting device to correct the angles of attack of individual blades. The actual element responsible for changing the angle of the attack of the blades is a swashplate. It consists of one non-rotating disc, and another rotating together with the whole rotor. Both discs face each other in such a way that they always remain parallel to each other. The lower fixed shield is set by the copter's pilot by means of appropriate gears. Another disc sets the angle of the attack of all blades by means of joints and connectors (see Figure 8.3).

The main rotor's hub reflection properties are usually derived from a simplified hub model, a cylinder with randomly distributed reflecting points in the entire volume of the cylinder, because it consists of a large number of different elements capable of reflecting the electromagnetic wave (see Figure 8.1).

The motion of the rotor's blade, and therefore its geometrical model, is much more complex than the rotor model. As mentioned previously, the blade carries out a circular motion around its own axis in order to periodically change the angle of attack and, as a result, creates a thrust vector in the direction in which the helicopter moves. The constant angle of attack of the blade occurs only when the helicopter stays still or moves vertically.

The aerodynamics of a copter's blades is much more complex than the aerodynamics of an aircraft's wing. This is due to the fact that different parts of the blade move at a different linear speed. If the blade had an identical aerofoil over its entire length, an uneven distribution of the lifting force would cause significant stresses. This effect is called the asymmetry of lift, and in modern designs, it is responsible for varying the blade's aerodynamic profile along its length. In addition, it also affects the wing, which is not flat but slightly twisted so that its tip is characterized by a lower coefficient of lift.

The blade is mounted to the rotor at a distance from the rotation centre of the entire rotor. Due to the significant air resistance, the blade is tilted in the opposite direction to its movement, changing the load-bearing force acting on the blade. The blade can be mounted to the rotor's hub in one of the three possible configurations:

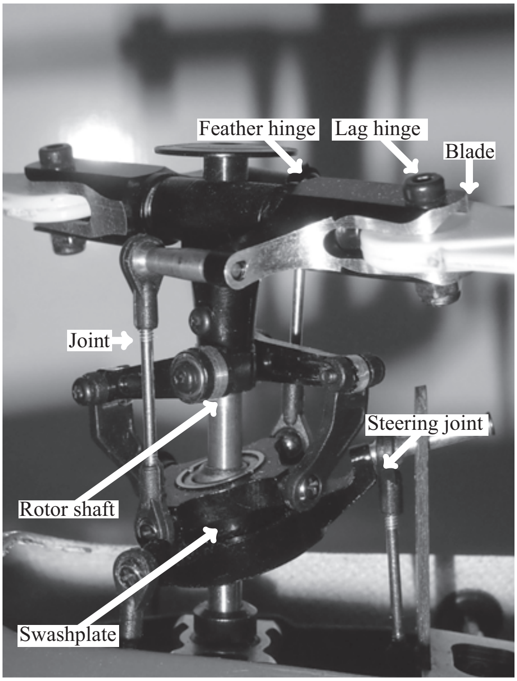

Figure 8.3 The photo of the rotor's hub of the small radio-controlled (RC) helicopter

fully articulated, semi-rigid and rigid. These terms relate to the degree of the relative independence of the blades from the rotor's hub.

In a fully articulated rotor system, the blades have the highest degree of freedom relative to the centre of rotation. The freedom of adjustment allows for the turning of the blade around its axis. The freedom of 'flapping' allows the blade to move perpendicularly to the rotor's disc. Lag/lead allows the blade to swing in the plane of the rotor's disc over the rotation period. A model of the fully articulated system is presented in Figure 8.4.

In a semi-rigid rotor system, the blades are fixed relative to the blade deflection assembly in the lead/lag plane. However, the semi-rigid system does not prevent 'flapping'. An example of a semi-rigid rotor system is presented in Figure 8.3.

A rigid rotor system is the simplest configuration: the blades are fixed rigidly in relation to the centre of rotation. Displacement of the blade against the rotor hub is not possible.

Bearing in mind the complexity of the main rotor design and the complex nature of the movement of each blade, the construction of a universal movement model seems to be impossible. Taking into account the wavelength used in the passive radar, the authors assumed that the helicopter's blade can be modelled as a metal rod of the length L_m mounted on an arm with the length L_h at a $\gamma(\alpha_m)$ angle, where α_m denotes the blade orientation in relation to the tail. The α_m angle takes the value 0 when the

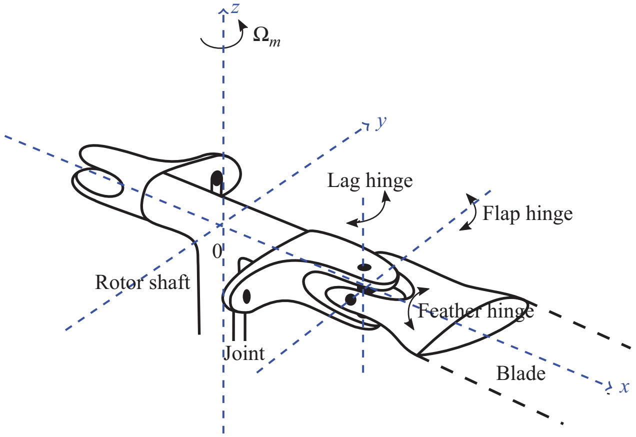

Figure 8.4 A model of the fully articulated rotor system

blade is parallel to the helicopter's tail. Values from 0 to 180 degrees mean that the blade moves towards the front of the helicopter and from 180 to 360 degrees towards its tail. Deflection angle γ depends on many factors, and its value does not exceed several degrees. In addition, the adopted model assumes that the rotor disc is oriented horizontally perpendicular to the gravitational force vector (see Figure 8.1).

8.2.3 The tail rotor

In the most popular Sikorski design, the tail rotor is one of the main components of the structure, responsible for both counteracting the torque of the copter's main rotor and controlling the helicopter's rotational movement around the rotation axis of the rotor.

As with the rotor, the control is carried out by changing the angle of the attack of the tail rotor's blades. The mechanism for controlling this angle is much simpler because the angle of the attack (pitch) of the blade is the same for all blades.

In helicopters, the diameter of the tail rotor is usually several times smaller than that of the main rotor, and its stroke (and thus the thrust) is controlled separately to compensate for and control the rotational movement of the entire machine. A tail rotor shaft is positioned transversely to the main symmetry axis of the helicopter. The tail rotor model under consideration is made of N_t metal rods of the length L_t. Each blade is mounted at the point around which the rotation occurs. The geometry of the rear rotor is shown in Figure 8.1.

It is worth noting that there are also several other ways to counteract the torque coming from the rotor, which do not require the use of the tail rotor. These are all types of double systems (Flettner, Piasecki and Kamov rotor systems) as well as NOTAR systems. The reflection of the double system follows the general idea presented in this chapter; however, it differs because of the presence of additional reflection components and the absence of tail rotor reflections.

8.2.4 The rotor parameters

A database of helicopter rotor parameters may allow for the classification of a detected helicopter. Key parameters, which may enable the differentiation between models, are

- the number of rotor blades
- blade length
- the rotation speed of the rotor.

If a tail rotor is detectable for a given helicopter model, the tail rotor parameters should also be entered into the database. By estimating these parameters from radar observations, it is possible to recognize the type of helicopter. The estimation methods for these parameters, as well as imaging methods for the main rotor, will be presented further in this chapter.

8.3 A model of the received echo signal

In this section, based on the helicopter geometry model, a model of the helicopter echo is derived from data obtained by the radar in a bistatic configuration. It is assumed that the helicopter under consideration has two rotors: the main and tail rotors. The second assumption of this model-building construction is that the copter remains in a hover, and the only movable elements are both its rotors.

8.3.1 A generic model of the echo signal

It is assumed that both the transmitters emitting an electromagnetic wave which illuminates the observed object and the receiver recording the signals are in the far field. In such a case, the illuminating signal can be treated as a plane wave. Next, it is also assumed that the object under consideration is made of metal elements that perfectly reflect the electromagnetic radiation. Consequently, the electromagnetic wave does not penetrate the surface of the individual elements of the model.

The signal illuminating the object is treated as a narrowband signal, as its bandwidth is 10% of the carrier frequency value at most. In the first approximation, the assumption is that the distance resolution cell resulting from the signal bandwidth is greater than the size of the object under consideration, so the object echo is contained in one range cell. This assumption is correct for most signals widely used in passive radar. The expression given in the following:

$$\delta r = \frac{c}{2B\cos(\beta/2)} \tag{8.1}$$

defines the range resolution's relation to bandwidth. As an example, the resolution of a passive radar using terrestrial digital TV (DVB-T) signals is 18 m in the monostatic case ($\beta = 0$).

Another assumption is that the polarization of the transmitted signal is excluded in the reflection model, so the model itself is compliant with the Huygens–Fresnel principle. This simplification does not significantly affect the signal model under consideration, especially since the horizontal polarization coincides with the orientation of the main rotor's blades for the DVB-T signals used.

8.3.2 A model of the main rotor blade echo

Figure 8.5 presents a model of the main rotor's blade. Let the helicopter's main axis coincide with the 0x axis of the coordinate system. Two angles, β_{Tx} and β_{Rx}, denote the angles formed by the 0 axis with two lines that connect, respectively, the transmitter and receiver with point 0 located in the centre of the main rotor. The 0x axis determines the positive direction of the coordinate system.

Let l denote the distance of the given blade's fragment dl from the blade's beginning. The bistatic range of the dl element of the rotor's blade is expressed by the following equation:

$$r(l,\alpha_m) = ||R_{Tx} - R_{dl}(l,\alpha_m)|| + ||R_{Rx,n} - R_{dl}(l,\alpha_m)|| \tag{8.2}$$

where $R_{Tx} = r_{Tx} \cdot [\cos(\beta_{Tx})\ \sin(\beta_{Tx})\ 0]^T$ and $R_{Rx,n} = r_{Rx} \cdot [\cos\left(\beta_{Rx,n}\right)\ \sin\left(\beta_{Rx,n}\right)\ 0]^T$ are the transmitter and receiver positions, respectively. The position $R_{dl}(l,t)$ of the given dl element is expressed by the following expression:

$$R_{dl}(l,\alpha_m) = M(\alpha_m) \cdot [l\cos(\gamma(\alpha_m)) + L_h l\sin(\gamma(\alpha_m))\ \ 0]^T \tag{8.3}$$

where $M(\alpha_m)$ denotes a rotation matrix around the z-axis, and L_h is the length of blade grip. By substituting the previous expressions, (8.2) can be rewritten as

$$\begin{aligned} r(l,\alpha_m) \ = \ & \sqrt{\begin{matrix} ((r_{Tx}\cos(\beta_{Tx}) - (l\cos(\gamma(\alpha_m)+\alpha_m) + L_h\cos(\alpha_m)))^2 \\ +\,(r_{Tx}\sin(\beta_{Tx}) - (l\sin(\gamma(\alpha_m)+\alpha_m) + L_h\sin(\alpha_m)))^2 \end{matrix}} \\ & + \sqrt{\begin{matrix} ((r_{Rx}\cos(\beta_{Rx}) - (l\cos(\gamma(\alpha_m)+\alpha_m) + L_h\cos(\alpha_m)))^2 \\ +\,(r_{Rx}\sin(\beta_{Rx}) - (l\sin(\gamma(\alpha_m)+\alpha_m) + L_h\sin(\alpha_m)))^2 \end{matrix}} \end{aligned} \tag{8.4}$$

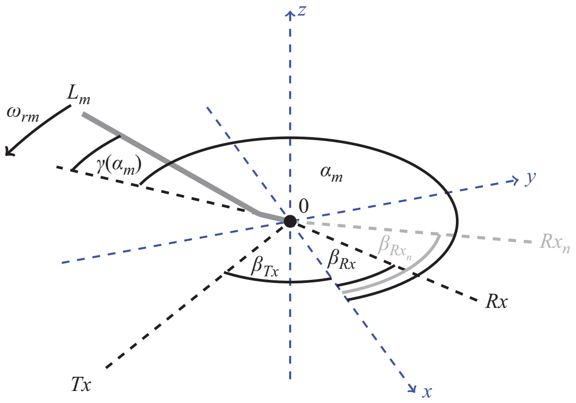

Figure 8.5 Main rotor blade geometry

Assuming $r_{Tx} \gg L_m + L_h$ and $r_{Rx,n} \gg L_m + L_h$ where L_m is the length of the main rotor's blade, using the Taylor series of $\sqrt{1+x}$ about $x = 0$ and simple trigonometric identities, (8.4) is given by

$$\begin{aligned} r(l,\alpha_m) = {} & r_{Tx} + r_{Rx,n} - \cos\left(\frac{\beta_{Tx} - \beta_{Rx}}{2}\right) \\ & \cdot \left[l\cos\left(\gamma(\alpha_m) + \alpha_m - \frac{\beta_{Tx} + \beta_{Rx}}{2}\right) \right. \\ & \left. + L_h \cos\left(\alpha_m - \frac{\beta_{Tx} + \beta_{Rx}}{2}\right)\right] \end{aligned} \tag{8.5}$$

Equation (8.5) is similar to the equations presented in [12–14]. In many publications, this is simplified to the case with no blade grip and a fully rigid blade mount, which corresponds to no lead/lag phenomena.

Equation (8.5) describes the bistatic range of any point of the blade (modelled as a metal rod). The signal registered by the receiver is the sum of all signals reflected from all points of the given blade, the whole rotor or, in general, the entire helicopter.

When constructing an echo signal model for a single rotor's blade, it can be assumed that:

$$s_{echo}(t) = e^{j\phi_0} \int_0^{L_m} \rho(l) s(t - \tau(l,t)) dl \tag{8.6}$$

where $\rho(l)$ denotes the reflectivity of the given blade part, $s(t)$ denotes the signal emitted by the transmitter and $\tau(l,t) = (r(l,\alpha_m(t))/c)$ denotes a delay resulting from the finite speed of light corresponding to the bistatic range of the given blade's point. The factor $e^{j\phi_0}$ that appears before the integral sign denotes a random phase of the signal at the beginning of its registration.

It is worth noting that the model of the echo signal given by (8.6) does not depend on the envelope of the probing (sounding) signal. In order to obtain synthetic information, the echo signal is compressed. Typical sounding waveforms and methods of their compression are described in Section 8.1.1.

A pulse compression provides synthetic information about the echo structure of the observed scene. Since all objects can be assumed to be stationary during compression, the 'stop and go' approach can be used. Then, a single range profile of the main rotor's blade at time T can be represented as

$$r(T,t) = e^{j\phi_0} \int_0^{L_m} \rho(l) \delta(t - \tau(l,T)) e^{-j\omega_c \tau(l,T)} dl \tag{8.7}$$

Its spectrum after substituting the expression (8.5) can be presented by

$$\begin{aligned} R(T,\omega) = {} & e^{j\phi_0} \cdot e^{-j((\omega_c+\omega)/c)\cdot(r_{Tx}+r_{Rx,n})} \cdot e^{j((\omega_c+\omega)/c)\cdot L_h \cdot B_m(T)} \\ & \cdot \int_0^{L_m} \rho(l) \cdot e^{j((\omega_c+\omega)/c)\cdot l \cdot A_m(T)} dl \end{aligned} \tag{8.8}$$

where

$$\begin{aligned} A_m(T) &= \cos\left(\gamma(\alpha_m(T)) + \alpha_m(T) - \frac{\beta_{Tx}+\beta_{Rx}}{2}\right)\cos\left(\frac{\beta_{Tx}-\beta_{Rx}}{2}\right) \\ B_m(T) &= \cos\left(\alpha_m(T) - \frac{\beta_{Tx}+\beta_{Rx}}{2}\right)\cos\left(\frac{\beta_{Tx}+\beta_{Rx}}{2}\right) \end{aligned} \tag{8.9}$$

Next, after calculating the integral in (8.9), compensating for the coefficient $e^{-j((\omega_c+\omega)/c)\cdot(r_{Tx}+r_{Rx,n})}$ and assuming the same reflections for the whole rod, it takes the following form:

$$\begin{aligned} R(T,\omega) \;=\; & \rho\cdot e^{j\phi_0}\cdot e^{j((\omega_c+\omega)/c)\cdot L_h\cdot B_m(T)}\cdot L_m\cdot e^{j\cdot((\omega_c+\omega)/c)\cdot(L_m/2)\cdot A_m(T)} \\ & \operatorname{sinc}\left(\frac{\omega_c+\omega}{c}\cdot\frac{L_m}{2}\cdot A_m(T)\right) \end{aligned} \tag{8.10}$$

Subsequently, when considering the model of the signal reflecting from the main rotor's blade, cyclic changes in the amplitude of the recorded signal can be noticed. The sinc() function takes the maximum value for the argument of 0. Because the argument of this function according to the expression $A_m(T)$ changes its value periodically, the maxima of function $R(T,\omega)$ also occur in cycles. To determine these moments, in which the expression (8.10) takes the maximum values, the expression describing the function argument sinc() should be equal to 0:

$$\begin{aligned} \frac{\omega_c+\omega}{c}\cdot\frac{L_m}{2}\cdot A_m(T) = 0 \Leftrightarrow \\ \cos\left(\gamma(\alpha_m(T)) + \alpha_m(T) - \frac{\beta_{Tx}+\beta_{Rx}}{2}\right) = 0 \vee \\ \cos\left(\frac{\beta_{Tx}-\beta_{Rx}}{2}\right) = 0 \Leftrightarrow \\ \gamma(\alpha_m(T)) + \alpha_m(T) - \frac{\beta_{Tx}+\beta_{Rx}}{2} = \frac{\pi}{2} + k\pi, k\in Z \vee \\ \frac{\beta_{Tx}-\beta_{Rx}}{2} = \frac{\pi}{2} + k\pi, k\in Z \end{aligned} \tag{8.11}$$

Based on (8.11) and the assumptions made, it can be concluded that the function (8.10) takes a maximum value, when the main rotor's blade is perpendicular to the bisector of the bistatic angle between the transmitter-helicopter and receiver-helicopter planes, or when such a bistatic angle is 180 degrees. The latter corresponds to forward scattering phenomena and will not be discussed in this chapter.

The cyclic amplitude variation of the signal received results in a phenomenon called 'blade flashes'. As can be noticed, the bistatic angle strongly influences the amplitude of the received signal during the slow time – T. The small bistatic angle denotes short and strong flashes, while the wider bistatic angle corresponds to the wider but weaker peaks of the signal amplitude.

Figure 8.6(a) shows the amplitude of (8.10) function determined for simulated signals. The simulation geometry was quasi-monostatic. Both β_{Tx} and β_{Rx} were set

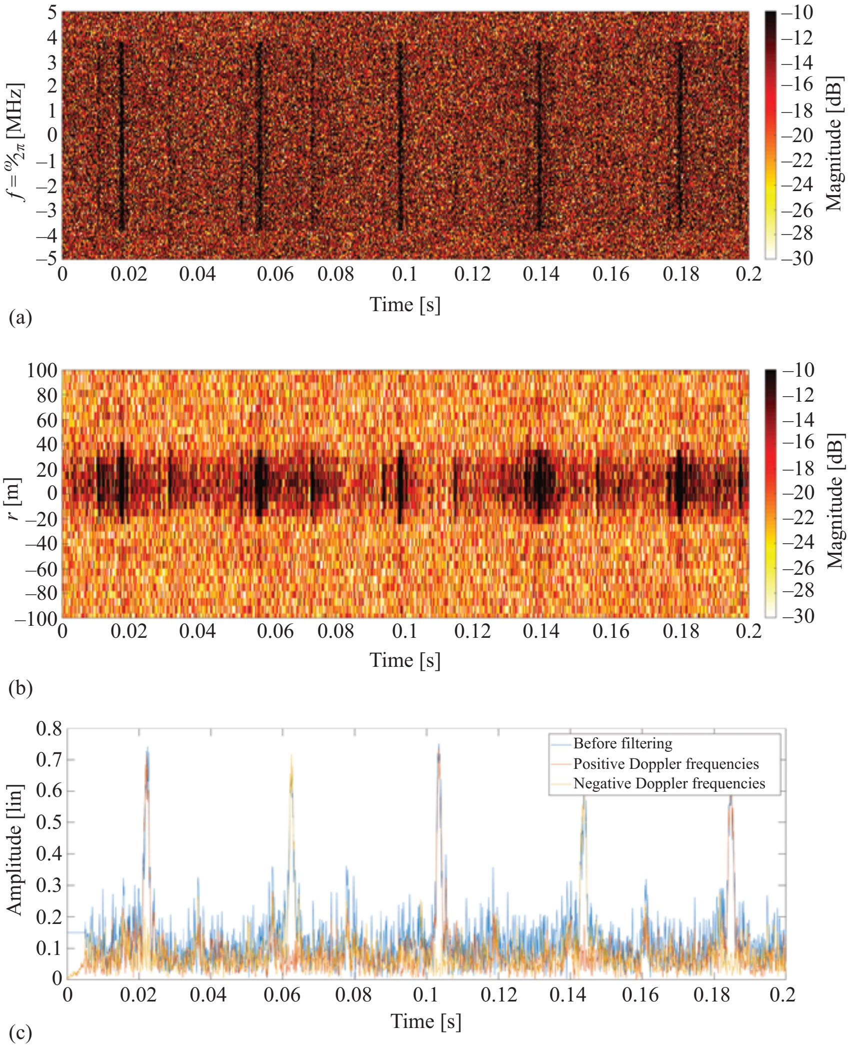

Figure 8.6 Simulation results for Mi-2 helicopter model: (a) function |R(T, ω)| for the simulated signal, (b) function |r(T, t)| for the simulated signal and (c) a single range slice of the function |r(T, t)| for the real signal

to 0. The frequency and bandwidth of the simulated signals were 610 and 7.6 MHz, respectively. The simulations only include moving parts of the observed objects, such as the hubs and blades of both the main and tail rotors. Although from the point of view of the observer the movement of both rotors takes place on various planes (horizontal for the main rotor and vertical for the tail one), only changes in the distance between the blade and the radar are noticeable. In the simulations performed, a geometric

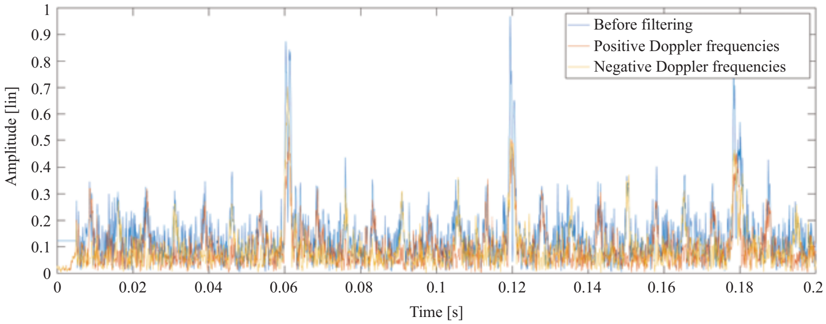

Figure 8.7 A single range slice of the function |r(T, t)| for the real signal for W3-Sokół helicopter model

reflection model was adopted. Each element of the simulated rotor model consisted of all-round reflecting points. The density of the points was chosen so that at least ten points were at the wavelength. The signal-to-noise ratio was set at −20 dB.

The Mi-2 helicopter rotor model was used for the simulation. The length of the rotor's blade was 7.8 m and its rotational speed was about 246 rpm. In turn, the length of the tail rotor's blade was 1.3 m, and its rotational speed was equal to 1,445 rpm which was about six times higher than the main rotor. The main rotor of the simulated object consists of three blades, and the tail's rotor of two.

Figure 8.6(b) presents the signal after range compression, evaluated by applying a Fourier transform over the coordinate ω, which is shown in Figure 8.6(a). After demodulation, the target echo is placed at a distance equal to 0. At this stage, the main rotor flashes are clearly visible, because the energy of the echo is focused in several range cells. Other features of the signal structure, such as the tail's rotor flashes or the fuselage echo, are recognizable as well.

Figure 8.6(c) shows a single slice of the plot presented in Figure 8.6(b) for a single range cell, in which the simulated object is located. Additionally, two more signals are presented in this figure. One is received after removing negative frequencies from the echo signal, and the other after removing the relative positive components. They correspond to the movement of the blades, respectively, towards the radar and in the opposite direction.

Based on the analysis of the results presented in Figure 8.6(c), it can be stated that every second blade flash consists of positive or negative frequencies; hence, the observed/simulated model of the helicopter has an odd number of main rotor blades.

Figure 8.7 shows the result of simulating a different type of helicopter. In this case, the W3-Sokół model of helicopter was used. The length of the rotor blade was 7.85 m, and its rotational speed was about 254 rpm. In turn, the length of the tail rotor blade was 1.65 m, and its rotational speed was equal to 1,342 rpm. The main rotor of the simulated object consists of four blades, and the tail rotor of three.

Similarly, based only on the analysis of the presented results, it can be easily stated that the observed/simulated model of the helicopter has an even number of main rotor

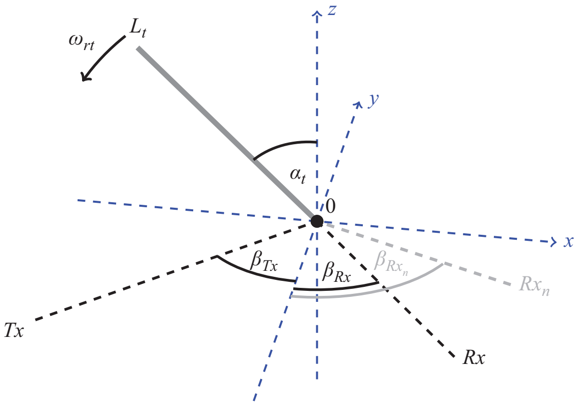

Figure 8.8 Tail rotor blade geometry

blades. Every rotor blade flash consists of both positive and negative frequencies. Approaching and receding blades flash mostly at the same moment.

8.3.3 A tail rotor blade echo model

A model of the echo signal of the tail rotor's blade can be created in a similar manner. However, in this case, the rotor rotates in a different plane than in the case described earlier. To determine the orientation, let us assume that the blade rotates in the $0xy$ plane. Let the zero deflection of the blade mean that its direction and return are consistent with the direction of the positive $0z$ axis (Figure 8.8). In addition, let us assume that (8.2) is also valid for the tail's rotor.

The position $R_d l(l, \alpha_t)$ of any given dl element is expressed by the following expression:

$$R_{dl}(l, \alpha_t) = M(\alpha_t) \cdot [l \;\; 0 \;\; 0]^T + [r_t \;\; 0 \;\; 0]^T \tag{8.12}$$

where r_t and $M(\alpha_t)$ denote a displacement of the tail's rotor related to the centre of the main rotor and a rotation matrix around the y-axis, respectively. By substituting the previous expressions, (8.2) for the tail's rotor can be rewritten as

$$\begin{aligned} r(l, \alpha_t) = & \sqrt{\begin{array}{l} r_{Tx} \cdot \cos(\beta_{Tx}) - l \cdot \cos(\alpha_t) - r_t^2 \\ + (r_{Tx} \cdot \sin(\beta_{Tx}))^2 + (l \cdot \sin(\alpha))^2 \end{array}} \\ & + \sqrt{\begin{array}{l} r_{Rx} \cdot \cos(\beta_{Rx}) - l \cdot \cos(\alpha_t) - r_t^2 \\ + (r_{Rx} \cdot \sin(\beta_{Rx}))^2 + (l \cdot \sin(\alpha))^2 \end{array}} \end{aligned} \tag{8.13}$$

Similarly, assuming $r_{Tx} \gg L_t + r_t$ and $r(Rx, n) \gg L_t + r_t$ where L_t is the length of the tail rotor's blade, (8.13) is given by

$$\begin{aligned} r(l, \alpha_t) = {} & r_{Tx} + r_{Rx,n} - 2 \cdot \cos\left(\frac{\beta_{Tx} - \beta_{Rx}}{2}\right) \cos\left(\frac{\beta_{Tx} + \beta_{Rx}}{2}\right) \\ & \cdot (r_t + l \cdot \cos(\alpha_t)) \end{aligned} \tag{8.14}$$

Likewise, for the main rotor, the model of the resulting signal can be expressed as

$$\begin{aligned} R(T, \omega) = {} & \rho \cdot e^{j\phi_0} \cdot L_t \cdot e^{j((\omega_c + \omega)/c) \cdot r_t \cdot B_t(T)} \\ & \cdot e^{j \cdot ((\omega_c + \omega)/c) \cdot (L_t/2) \cdot A_t(T)} \mathrm{sinc}\left(\frac{\omega_c + \omega}{c} \cdot \frac{L_t}{2} \cdot A_t(T)\right) \end{aligned} \tag{8.15}$$

where $A_t(t) = \cos((\beta_{Tx} - \beta_{Rx})/2) \cos((\beta_{Tx} + \beta_{Rx})/2) \cdot L_t \cdot \cos(\alpha_t)$ and $B_t(T) = \cos((\beta_{Tx} - \beta_{Rx})/2) \cos((\beta_{Tx} + \beta_{Rx})/2)$. Equation (8.15) slightly differs from (8.10). A chief dissimilarity is that typical flashes for rotating blades cannot be observed either for a forward scattering configuration corresponding to $\cos((\beta_{Tx} - \beta_{Rx})/2) = 0$ or in the instances, when $\cos((\beta_{Tx} + \beta_{Rx})/2) = 0$. This happens when the bisector of the bistatic angle is perpendicular to the plane of the tail's rotor or, in other words, when a bistatic equivalent monostatic radar observes the helicopter from one side. For other cases, the amplitude of the signal reflected from the rotating tail rotor's blade varies in time according to the $\cos(\alpha_t)$ component.

In addition, the tail rotor's echo can also be missing, because the tail's rotor is often shaded by the helicopter's fuselage.

Figure 8.9(a) and (b) presents the echo of the tail's rotor, when the echo of the main rotor is removed by subtracting the main rotor signal modelled by the equation from the total echo signal. Similarly, the echo signal of the tail's rotor, after extracting and filtering, is also presented in the same figure. It can be noticed that the flashes of the tail rotor's blades are much more frequent than the ones of the main rotor. This is because the tail rotor's blade is much shorter. In addition, for both helicopter models applied in the simulation, the real linear velocities of the blade tips of both rotors are almost the same being about 200 m/s. Regardless of this feature, applying the same method as in the case of the main rotor is an easy way to verify whether the tail's rotor has an even or an odd number of blades. Thus, based on the analysis of Figures 8.9(a) and (b), it can be stated that there is an even (more precisely 2) and odd (more precisely 3) number of blades, respectively.

8.4 Method for determining rotor parameters

In the process of helicopter classification, the estimation of the main rotor parameters (and if possible, also the parameters of the tail's rotor) plays a decisive role. Key parameters in this respect are the angular velocity of the main rotor, the length of the blade and the number of rotary wings. Table 8.1 presents a summary of these parameters for several popular types of helicopters. It is worth noting that not all models are characterized by a constant rotor speed.

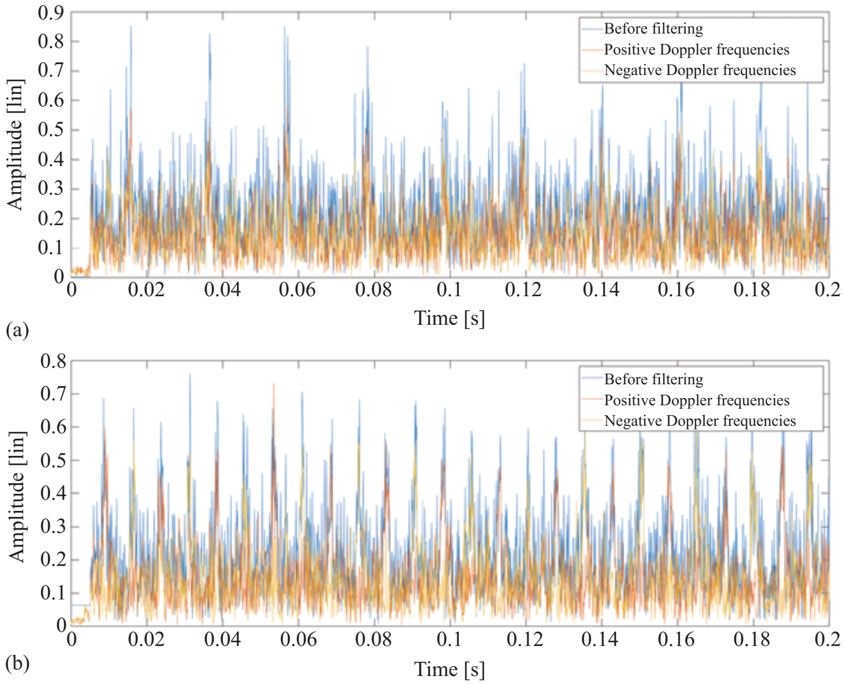

Figure 8.9 A single range slice of the function |r(T, t)| for the simulated signals of tail rotor echo: (a) simulation results for Mi-2 helicopter model and (b) simulation results for M3-Sokół helicopter model

Table 8.1 Rotor parameters of typical helicopters

Helicopter type	**No. of blades**	**Rotation rate [*r*/min]**	**Main rotor blade length [m]**	**Linear velocity of the tip of blade [m/s]**	**Flash interval [ms]**	**Flash duration at S-band [ms]**
Bell 206 B (JetRanger)	2	374–394	5.08	199–210	78	0.24
Bell 209 (Cobra)	2	294–324	6.70	206–227	97	0.23
Robinson R22	2	491	3.85	198	61	0.25
MI-2	3	246	7.80	207	40	0.53
PZL W-3 (Sokół)	4	254	15.65	214	59	0.23
Eurocopter EC-120	3	406	5.00	213	25	0.47
Sikorsky S434 Schweizer	4	471	4.19	206	32	0.24
Bell 430	4	348	6.40	233	43	0.21
Bell 412EP	4	314	7.01	230	48	0.22

The basic mechanism for determining the rotor parameters is to analyse the echo signal reflected by this rotor in both time and frequency domains. Based on the analysis of (8.10) and (8.15), it is possible to associate characteristic flashes denoting an increase in the amplitude of the echo signal with the orientation of the given blade relative to the transmitter and the receiver.

To obtain information on the frequency spectrum of the echoes of the single rotor's blade, the Fourier transform in a dimension corresponding to the slow time should be applied:

$$S(\omega_D, \omega) = F_{T \to \omega_D}(R(T, \omega)) \tag{8.16}$$

8.4.1 Main rotor parameters

The determination of the exact analytic function representing the spectrum of the blade echo signal might be difficult due to an entangled function of time, thus some simplifications should be introduced.

A significant part of the power of the blade echo is recorded during a very short flash. This flash occurs when the cosine of the angle between the rotary blade $\alpha_m(T) + \gamma(\alpha_m(T))$ and the bisector of the bistatic angle $((\beta_{Tx} + \beta_{Rx})/2)$ is equal to 0. Assuming a constant and slight delay of the blade $\gamma(\alpha_m(T)) = \gamma$ and also that $\alpha_m(T) = \alpha_0 + \Omega_m T$, where Ω_m denotes the angular velocity of the main rotor, at the moment of the flash the parameters $A_m(T)$ and $B_m(T)$ in (8.10) can be presented in the following form:

$$\begin{aligned} A_m(T) &\approx \left(\gamma + \Omega_m T - \frac{\beta_{Tx} + \beta_{Rx}}{2} + \frac{\pi}{2}\right)\cos\left(\frac{\beta_{Tx} - \beta_{Rx}}{2}\right) \\ B_m(T) &\approx \left(\Omega_m T - \frac{\beta_{Tx} + \beta_{Rx}}{2} + \frac{\pi}{2}\right)\cos\left(\frac{\beta_{Tx} - \beta_{Rx}}{2}\right) \end{aligned} \tag{8.17}$$

After substituting these values to (8.10) and determining the spectra of the echo signal of the single blade flash, the amplitude of this spectrum can be expressed as

$$S(\omega_D, \omega) = \rho \cdot e^{jk_0} \cdot L_m \cdot \frac{\pi}{k_2} \sqcap \left(\frac{k_1 - \omega_D}{2k_2}\right) e^{-j(k_3/k_2)(k_1 - \omega_D)} \tag{8.18}$$

where k_xs denotes corresponding coefficients:

$$\begin{aligned} k_0 &= \phi_0 + \frac{\omega_c + \omega}{c} \cdot \left[\left(L_h + \frac{L_m}{2}\right) \cdot \left(\frac{\pi}{2} - \frac{\beta_{Tx} + \beta_{Rx}}{2}\right) + \frac{L_m}{2} \cdot \gamma\right] \cos\left(\frac{\beta_{Tx} - \beta_{Rx}}{2}\right), \\ k_1 &= \frac{\omega_c + \omega}{c} \cdot \left(L_h + \frac{L_m}{2}\right) \cdot \cos\left(\frac{\beta_{Tx} - \beta_{Rx}}{2}\right) \cdot \Omega_m, \\ k_2 &= \frac{\omega_c + \omega}{c} \cdot \frac{L_m}{2} \cdot \cos\left(\frac{\beta_{Tx} - \beta_{Rx}}{2}\right) \cdot \Omega_m \text{ and} \\ k_3 &= \frac{\omega_c + \omega}{c} \cdot \frac{L_m}{2} \cdot \cos\left(\frac{\beta_{Tx} - \beta_{Rx}}{2}\right) \cdot \left(\gamma - \frac{\beta_{Tx} + \beta_{Rx}}{2} + \frac{\pi}{2}\right) \end{aligned} \tag{8.19}$$

Based on the analysis of (8.19), the width of the Doppler spectrum occupied by the single blade during the flash can be determined. The width is related to the length of the blade, the angular velocity of the main rotor, the distance of the blade from the rotor's centre and the bistatic angle between the transmitter, the observed object and the receiver:

$$\omega_{D,\max,\min} \approx \pm \frac{\omega_c}{c} \cdot (L_h + L_m) \cdot \cos\left(\frac{\beta_{Tx} - \beta_{Rx}}{2} \right) \cdot \Omega_m \tag{8.20}$$

In the case of echo signal analysis, a simplified model can be adopted with the blade's length measured from the beginning of the rotation axis to its end. However, the width of the measured spectrum allows only for the maximum linear speed of the blade's tip to be determined. This particular value depends on the product of the blade's length and the angular velocity of the rotating blade. In conclusion, there is no direct method of estimating blade parameters based on the single flash echo analysis.

Figure 8.10(a)–(c) presents the spectrum of the helicopter echo for several bistatic angles. It can be noticed that the wider the transmitter–target–receiver angle, the narrower the spectrum of the echo received. This phenomenon has to be taken into account when the parameters of the main rotor's blade are evaluated.

The blade, when modelled as a rod, has an echo that generates two flashes over a full blade's rotation. One flash occurs when the blade rotates away from the observer, the other occurs when it reappears and rotates towards the observer. As the analysis of (8.18) shows, each of the flashes has a different spectrum. Depending on the direction of blade movement, its echo is characterized by smaller or larger Doppler frequencies than the fuselage's Doppler frequency, corresponding to the bistatic speed of the entire helicopter.

By measuring the time between individual flashes, it is simple to estimate the product of the blade's angular velocity and the number of blades: $\Omega_m \cdot N_m$. Each helicopter's rotor has at least two blades mounted symmetrically on opposite sides. In general, the number of blades of the copter's rotor varies from two to eight, and each blade generates flashes separately. Interestingly, the even number of blades decreases the number of independent flashes in time because of the overlapping of flashes emanating from the opposite blades. This effect is easy to notice by analysing the spectrum of each flash, when the spectrum extension goes on in both directions.

Although determining whether the number of blades of the given rotor is even or odd is relatively easy (by analysing the spectrum of individual impulses), estimating the exact number of blades is not so simple.

For this purpose, the multistatic nature of passive radar can be explored as each receiver observes the object from a different angle. Therefore, for each radar, a flash occurs for a different deflection of the rotor's blade $\alpha_m(T)$.

As was stated in the previous sections, due to the Doppler effect, it is possible to separate the individual flashes of each blade by applying the accurate filter. In each separate data set, there are N flashes observed for each rotation of the main rotor. The time between flashes is expressed by the following equation:

$$|\Delta T| = \frac{2\pi}{\Omega_m N} \Leftrightarrow \Omega_m N = \frac{2\pi}{|\Delta T|} \tag{8.21}$$

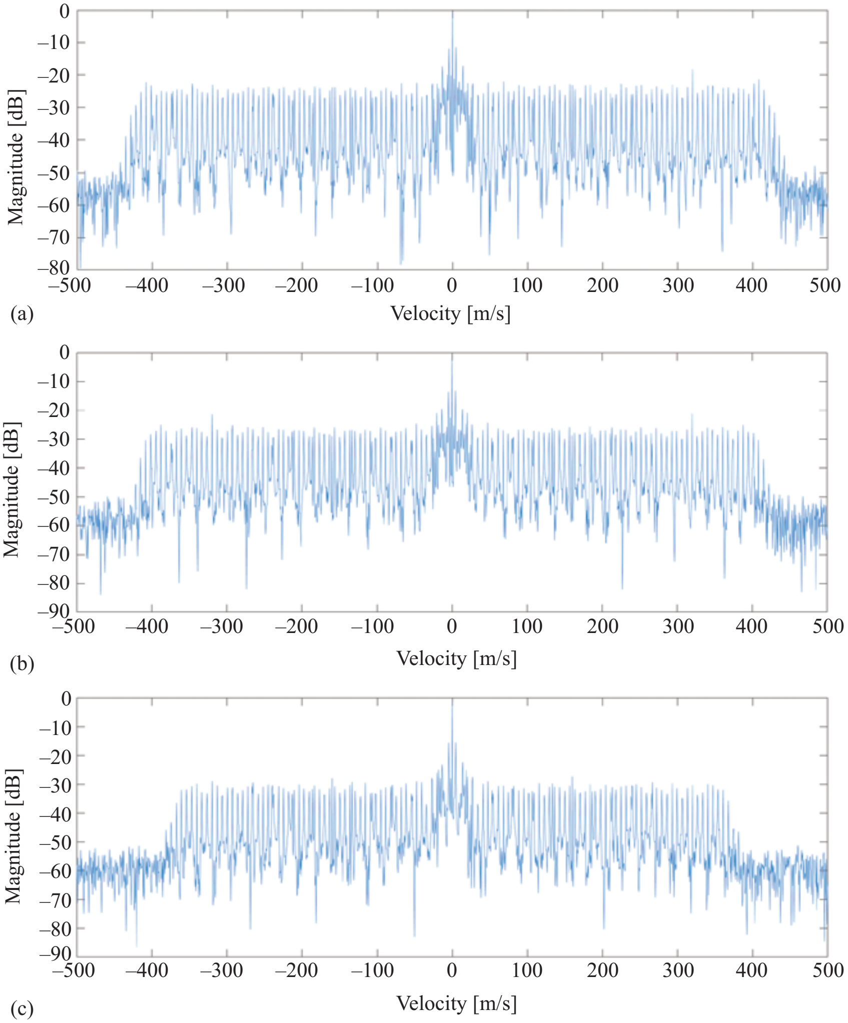

Figure 8.10 Spectrum of the Mi-2 helicopter model echo for several bistatic angles between transmitter target and receiver: (a) $\beta_{Tx} - \beta_{Rx} = 0$, (b) $\beta_{Tx} - \beta_{Rx} = \pi/6$ and (c) $\beta_{Tx} - \beta_{Rx} = \pi/3$

Equation (8.21) combines two unknowns: Ω_m and N; hence, measuring the time between two consecutive flashes only allows for the estimation of the product of these values. Let us assume that each radar cooperating in the multistatic scenario observes the helicopter at a different angle, as appointed by a bisector of the bistatic angle. Thus, each receiver registers the blade flash at a different time according to the angular movement of the main rotor. By comparing the flashes' timestamps with the observation angles, the angular velocity of the main rotor Ω_m can be estimated as

$$\alpha_m(T_1) - \alpha_m(T_2) = \Omega_m(T_1 - T_2) = \frac{\beta_{Rx,1} - \beta_{Rx,2}}{2} \tag{8.22}$$

Considering (8.22), two scenarios require particular attention. The first is the simpler of the two: when the angle denoted by $((\beta_{Rx,1} - \beta_{Rx,2})/2)$ is smaller than the minimum possible angle between two blades. In this case, the flashes coming from the same blade can be identified for each receiver. Thus, the angular velocity and the number of the main rotor's blades can be estimated using (8.21) and (8.22), respectively. The second scenario, requiring a more complex solution, is when the difference in the observing angle by each radar is wide. Because two consecutive flashes registered by two receivers cannot be associated with the same rotor's blade, a deeper analysis has to be carried out.

Let δT denote the minimal time between two consecutive flashes registered in the multistatic system, regardless of whether they are registered by a single or multiple receivers. Due to the periodic nature of flashes, and the number of the main rotor's blades being unknown, δT might be expressed as

$$\delta T = \frac{\mathrm{mod}(\beta_{Rx,1} - \beta_{Rx,2}, (2\pi/N))}{2\Omega_m} \tag{8.23}$$

where $\mathrm{mod}(x, y)$ denotes the modulo operation. The minimal time between two flashes depends on the angle of observation, the number of rotor blades and the angular velocity. Comparing (8.21) and (8.23) leads to the expression for the number of blades:

$$N = \frac{4\pi\delta T}{\Delta T \cdot \mathrm{mod}(\beta_{Rx,1} - \beta_{Rx,2}, (2\pi/N))} \tag{8.24}$$

Equation (8.24) does not, however, render the precise number of the rotor's blades. Still, given that the possible number of blades falls between two and eight inclusive, the previous equation can be easily solved by the trial-and-error technique.

In the rare case, when the difference of observing angles is close to an integer multiple of the value $2\pi/N$, the estimation of the number of the blades might be hindered or impossible. As an effective way of tackling this risk, another transmitter–receiver pair should be used, if available. Otherwise, the angles will change when the helicopter moves. Also, the higher the number of independent measurements from various radars, the more accurate the estimation of the number of the rotor's blades.

Figure 8.11 presents two consecutive flashes of the main rotor's blade from three separate receivers. The aspect angle of each receiver differs, resulting in the different arrival time of the blade flash. The bistatic angles between the transmitter, target and each receiver are 0, 30 and 60 degrees, respectively.

By knowing the number of blades and the time between consecutive flashes, the angular velocity of the main rotor can be estimated, which allows one to determine the length of the blade based on the Doppler widening of the rotor echo.

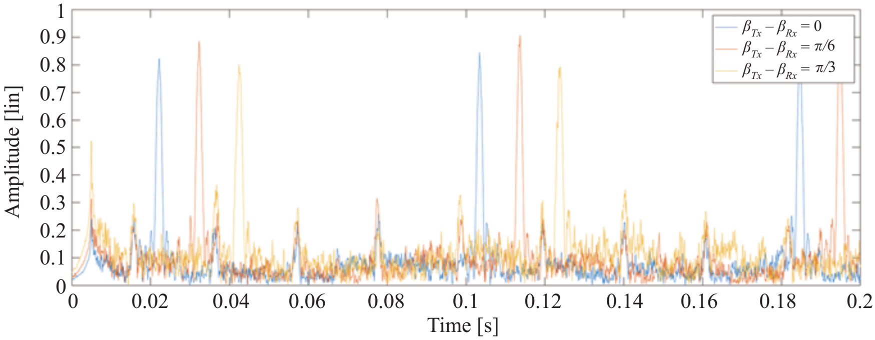

Figure 8.11 Two consecutive flashes of the main rotor for three separate receivers observing the helicopter at different aspect angles

8.4.2 Tail rotor parameters

The estimation of tail rotor parameters is much more difficult than it is in the case of the main rotor. First of all, the tail's rotor may be invisible to the observer, and the reasons for this invisibility can vary. For example, the tail's rotor can be either covered by the fuselage or integrally housed within the tail. However, since the tail rotor echo is observed quite often, some parameters can be estimated.

The main problem in the evaluation of the tail rotor parameters relates to the fact that the echo of the tail rotor's blades is characterized by a relatively weak power. Consequently, the echo signals may remain invisible in relation to other echo components of the helicopter and, thus, be difficult to estimate by automatic methods. To address this situation, first, the echo components covering the tail rotor's echo have to be removed from the signal received. For this purpose, the CLEAN method, commonly used to detect weak signals against strong ones, might be adopted.

Then, having all the parameters of the main rotor echo, the echo signal model can be built and subtracted from the helicopter echo. Next, the same can be done with the fuselage echo. As a result, the measured signal should contain only the tail rotor's echo and the noise.

However, it is impossible to reconstruct all the geometrical parameters of the tail's rotor based solely on the analysis of the echo signal of the flashes. Usually, it is because all receivers are located roughly at the same level, and even in the multistatic scenario, most receivers observe the flashes at the same moment. Thus, although it is not feasible to estimate the angular velocity of the tail's rotor, the number of flashes per second can be measured. As a result, a ratio of the number of the tail rotor's flashes to the main rotor ones might yield a parameter useful for a more accurate identification of the helicopter.

8.5 Main rotor imaging algorithm based on the target echo spectrogram

By analysing the echo signal of the helicopter under observation, basic parameters of the main rotor, such as the number of blades, their length and the angular velocity of the rotor, can be estimated. Also, after extracting the echo signal of the tail's rotor, some signal properties of this echo, for example the frequency of flashes or the maximum speed of the tip of the rotor's blade, can also be estimated.

This section presents an imaging method of the helicopter's main rotor, which is done by applying the spectral analysis of the signal recorded by the receiver. Such an image can provide additional information, even though it is essentially based on the estimation of the main rotor parameters.

In general, radar imaging of the copter's main rotor provides synthetic information about this rotor. Key parameters, including the number of blades and their length, also contain information on the distribution of the blade reflectivity along its main axis. The latter is of particular importance, given that the blade profiles are individually designed for each copter. Such synthetic information in an image format can be used for a more accurate classification based on a comparison of data patterns from historical measurements.

Let us consider a short interval of a recorded signal with the single blade flash registered. Then, by applying a two-dimensional transform, any signal derived from the model given by (8.15) can be transformed into a range–Doppler (RD) map. This map is generally used for target detection and tracking, and it might be treated as an unscaled ISAR image. To scale this image properly, knowledge of angular velocity (or even the motion model, in general) is required. As shown in the previous sections, this constitutes a sufficient base for combining and rescaling the consecutive images and, hence, provides an easy way to the relevant parameter estimation.

After the translational motion compensation, the main rotor echo is mainly focused in a single range bin. Only the echo of the blade's tip might change the range bin over time, if the range resolution is high enough:

$$\frac{c}{2B} < L_m \tag{8.25}$$

Assuming a single range bin, the echo signal of the single rotor's blade can be presented as

$$R(T) = \rho \cdot e^{j\phi_0} \cdot L_t \cdot e^{j(\omega_c/c)\cdot r_t \cdot b(T)} \cdot e^{j\cdot(\omega_c/c)\cdot(L_t/2)\cdot a(T)}\,\mathrm{sinc}\left(\frac{\omega_c}{c}\cdot\frac{L_t}{2}\cdot a(T)\right) \tag{8.26}$$

Equation (8.26) shows how the amplitude of the echo signal changes. For a higher number of blades, local maxima are more frequent.

A more detailed analysis of the helicopter echo can be done by determining the short-time Fourier transform with the following expression:

$$X_R(\tau, \omega) = \int_{-\infty}^{\infty} R(T) \cdot W(T - \tau) e^{-j\omega T} dT \tag{8.27}$$

where $W(T)$ denotes the window function.

Two window parameters, namely width and shape, constitute key STFT parameters. Usually, a Gaussian window is adopted, with its width several times wider than a magnitude of the step used for determining the function given by the expression (8.27).

Figure 8.12(a) and (b) presents spectrograms evaluated for the signals shown in Figures 8.6(c) and 8.7, respectively. A brief analysis of these results indicates clearly the helicopter with an even or odd number of blades of the main rotor.

Each blade produces two flashes per cycle, so one of them can be removed. Choosing either the positive or negative Doppler frequencies related to the Doppler frequency of the helicopter centre allows the data to be presented in polar coordinates. This results in a spectrogram-based ISAR image, which enables the integration of the input data incoherently over several cycles. Thus, the signal-to-noise ratio of the image

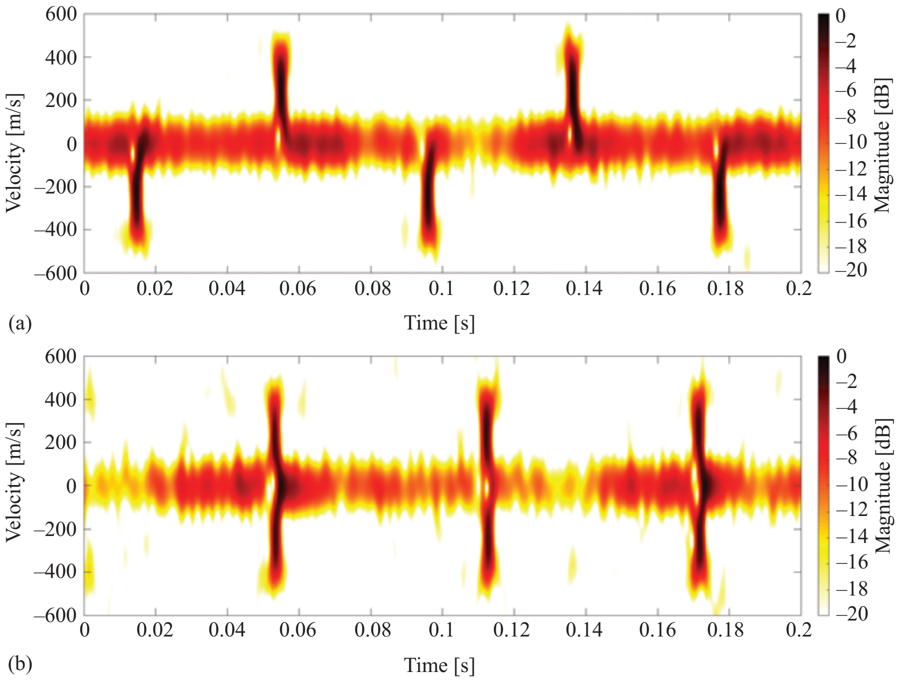

Figure 8.12 Spectrogram of the simulated helicopter echo signal: (a) Mi-2 helicopter model and (b) W3-Sokół helicopter model

obtained increases in relation to a comparable ratio of the regular spectrogram. The spectrogram-based ISAR image can be perceived as a combination of several RD images obtained for short-time intervals. In short, to produce such a combination, each RD image should be rotated according to the angular motion of the main rotor and then accumulated with other images alike. Figure 8.13(a) and (b) presents the final ISAR images obtained for the simulated signals.

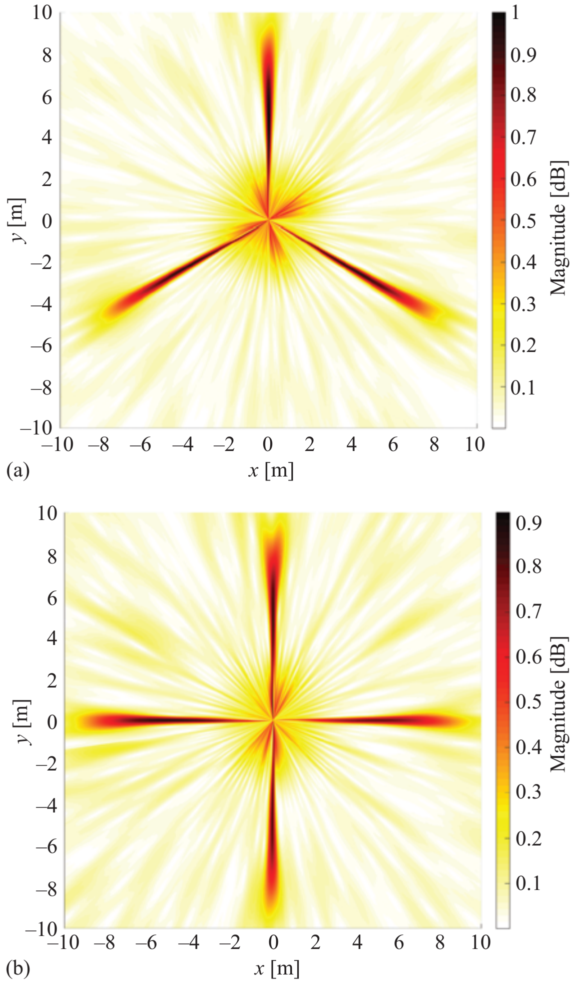

Figure 8.13 Spectrogram-based ISAR images of the main rotors of simulated helicopter models: (a) Mi-2 helicopter model and (b) W3-Sokół helicopter model

8.6 Live signal processing experiment

8.6.1 Measurement campaign

In order to illustrate the previous considerations, real data were processed. All signals were recorded on the coast of Livorno (Italy) during a measurement campaign organized in 2014 within the framework of the NATO-SET 196 Group. The measuring system applied to record the signals consisted of five physical channels, each built in the form of a Yagi–Uda antenna mounted on a low mast with a wideband UVHF amplifier, a recorder and the necessary cables. Two National Instruments PXIe-5663 receivers synchronized via a Global Positioning System signal constituted the signal recording system.

The measurement scenario is shown in Figure 8.14. Three physical channels were installed in the receiver placed on a rooftop of the building. One channel was dedicated to picking up the reference signal, while two others connected to the antenna were directed towards the object's location. Another receiver, placed near the seafront, was connected to two antennas receiving the object's echoes. The DVB-T transmitter was located at a distance of 30 km from the observation spot. A non-cooperating target – the helicopter under observation – was about 1 km away from the receiver. The measurement scenario was quasi-monostatic; therefore, its actual parameters are unknown. However, its type can be ascertained based on the results obtained.

8.6.2 Data pre-processing

The recorded data were processed offline in the MATLAB environment. The recording was done with a sampling rate equals to 48 MS/s. To avoid inter-frequency channel interferences, the first step of the calculations was to isolate each DVBT channel for separate processing. Also, prior to the micro-Doppler analysis, to prevent the

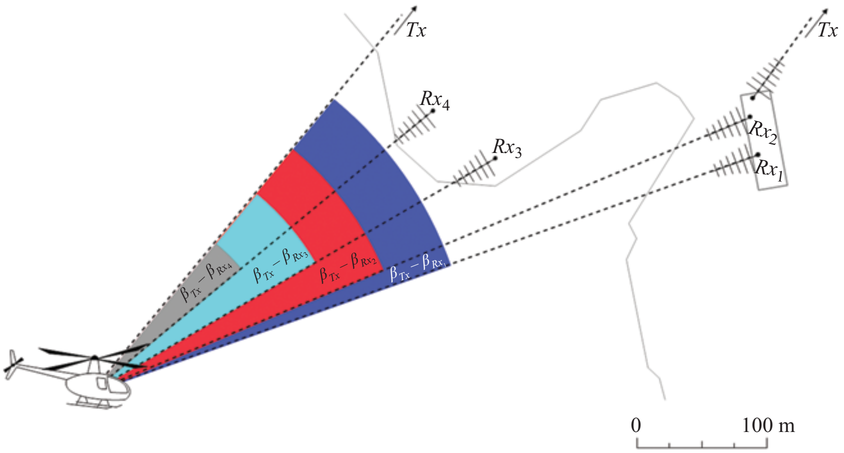

Tx
Tx
Rx_4
Rx_3
Rx_2
Rx_1
$\beta_{Tx}-\beta_{Rx_4}$
$\beta_{Tx}-\beta_{Rx_3}$
$\beta_{Tx}-\beta_{Rx_2}$
$\beta_{Tx}-\beta_{Rx_1}$
0
100 m

Figure 8.14 Measurement scenario

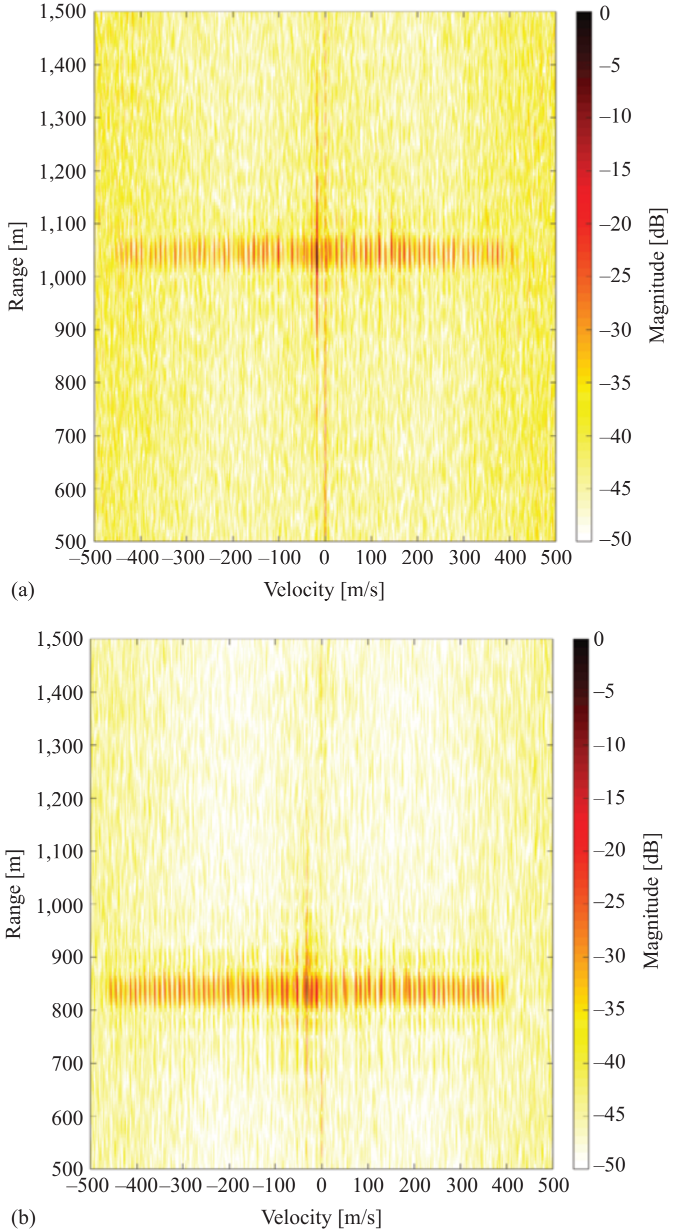

Figure 8.15 Cross ambiguity function evaluated for measured signals: (a) Rx_1 and (b) Rx_4

influence of the direct signal and ground returns, the direct signal and stationary clutter echoes were removed using lattice filtering, as described in [23]. The carrier frequency and the bandwidth of the signal used for the calculations were 610 and 7.6 MHz, respectively. In order to find out the exact parameters of the object to be observed, first it was necessary to determine its position. For this purpose, the cross-ambiguity functions of the surveillance and reference signals were evaluated. Figure 8.15(a) and (b) presents sections of these functions (with a magnitude of $R(T, \omega)$) designated for two receivers. The object was localized based on the measured bistatic range of the observed object, evaluated for each pair of the receiver–transmitter. The exact target position was marked in Figure 8.14 by the helicopter pictogram. All these steps constitute a viable way to determine the aspect angles of each receiver.

8.6.3 Results

All figures shown in this subsection were obtained by reprocessing data and results already presented in [14].

Figure 8.16 presents a single slice of the received signal for the range equals to 0 after it was filtered to extract the echoes of approaching and receding blades. It is worth noting that in the presented case, both echoes – one with a positive Doppler frequency and the other with a negative Doppler frequency originating from the receding and approaching blades, respectively – generate the blade flashes almost at the same moment. This means that the observed helicopter has an even number of main rotor blades. It is also interesting that the amplitude of the ‘approaching’ blade is stronger, which is related to its shape. The leading edge (an oval) of the aerofoil has a much larger effective radar cross-section than the trailing (sharpened) edge has. In addition, the tail’s rotor echo is clearly visible.

Figure 8.17 presents the echo of the tail’s rotor when the echo of the main rotor is removed by filtrating. The received signal contains the blade echo clearly visible only for the positive Doppler frequencies. Such a phenomenon may occur for many reasons. For instance, the tail’s rotor might be partially covered by other parts of the

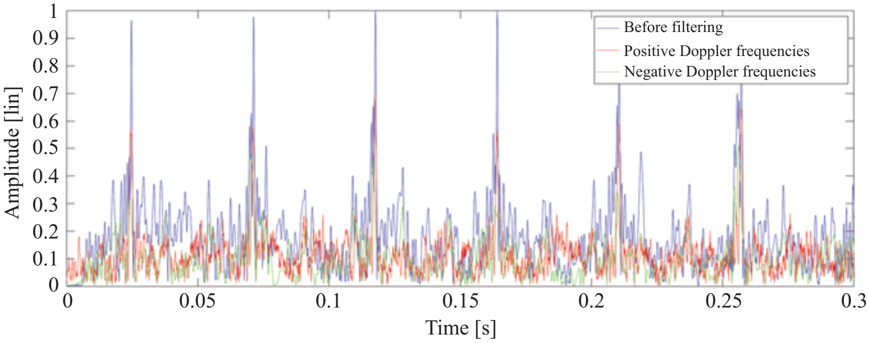

Figure 8.16 A single range slice of the function $|r(T, t)|$ for the real signal

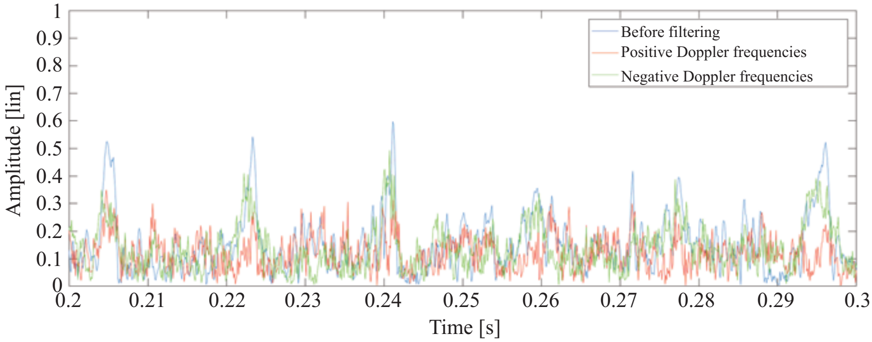

Figure 8.17 A single range slice of the function |r(T, t)| for the real signal of tail rotor echo

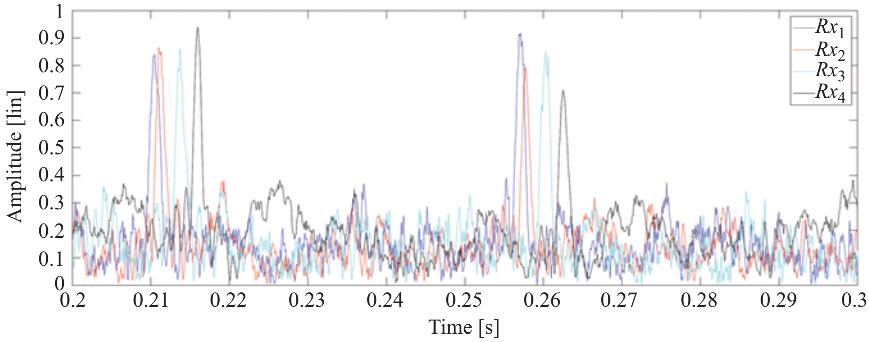

Figure 8.18 Two consecutive flashes of the main rotor for four separate receivers observing the helicopter in motion

helicopter, or the radar cross-section of the trailing edge of the tail rotor's blade is too small to detect the signal flashes generated by this edge.

Figure 8.18 presents two consecutive flashes of the main rotor's blade from four separate receivers. The aspect angle of each receiver differs resulting in a different arrival time of the blade flash. The relevant measurement scenario is presented in Figure 8.14. The aspect angle of each receiver is denoted by a coloured arc.

Figure 8.19 shows a spectrogram evaluated for the signal presented in Figure 8.16. Here, it is again clearly visible that the flashes from two separate blades occur at the same moment. This leads to the conclusion that the number of the main rotor's blades is even.

Before determining the $X_R(\tau, \omega)$ values, the data were not filtered. Thus, the echo of the tail's rotor is also visible in this figure. The spectrogram presented clearly shows that the observed helicopter has a bistatic velocity lower than zero, which should be interpreted as it moves towards smaller biostatic distances. In the presented case, the helicopter moved towards the passive radar receiver (see Figure 8.14). Figure 8.20 presents the spectrogram-based ISAR image generated from the data recorded by four

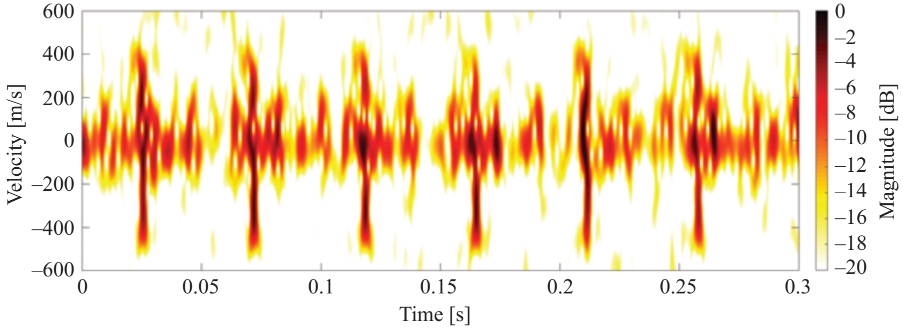

Figure 8.19 Spectrogram of the signal presented in Figure 8.16

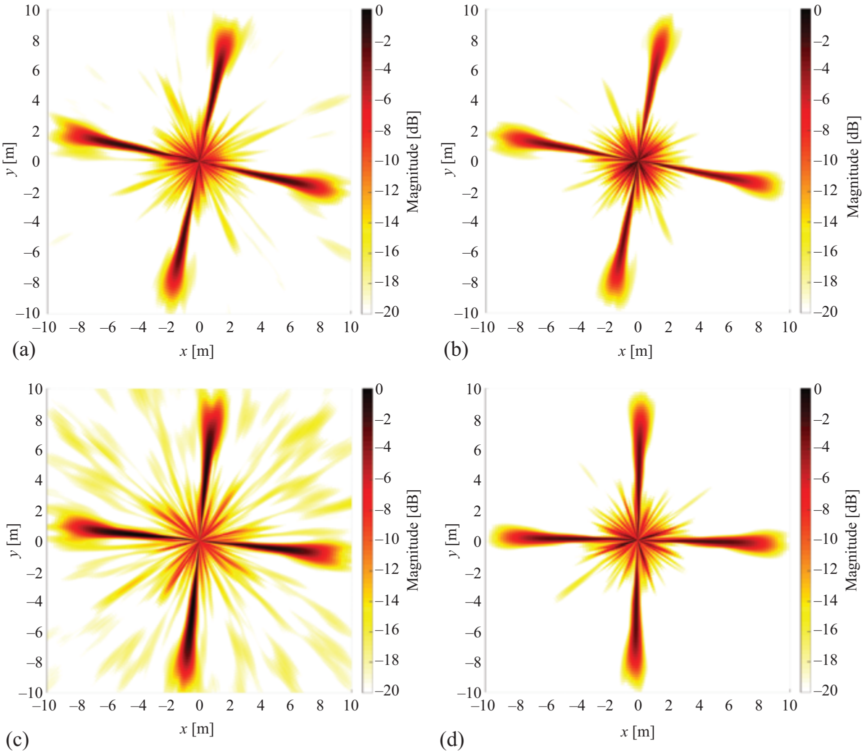

Figure 8.20 Spectrogram-based ISAR image of the main rotor evaluated for the same moment for each receiver: (a) Rx_1, (b) Rx_2, (c) Rx_3 and (d) Rx_4

separate passive radars at the very same moment. The rotation angle for each image is different because their observation angles vary.

8.7 Conclusions and result discussion

This chapter presents modern techniques of helicopter detection and classification employing the characteristic features of the rotor's blade echo. The echo properties, derived analytically, form a basis for the design of signal processing algorithms. The proposed solution is based on the time–frequency analysis of the echo signal received with a multistatic passive radar system. During the radar observation, a helicopter object cannot be treated as a rigid body, with a response focused both in time and in frequency. Elements, such as the main rotor and tail rotor, remain in constant motion relative to the fuselage. Due to the complex aerodynamics of the helicopter, in general, this movement cannot be described easily. However, using a few additional assumptions, it is possible to show the motion of the blade of both the main and tail rotors by a function dependent on several parameters, such as the number of rotor blades, the length of a single blade and the angular velocity of the rotor. These parameters allow the size and class of the observed helicopter to be determined, which is sufficient in a significant number of cases.

In order to illustrate the issues discussed, simulations of two different helicopters with different parameters of both rotors were performed. On the basis of the presented results, it was shown how to estimate each main rotor parameter and how to use the multistatic nature of passive radar to resolve the ambiguity in determining the number of main rotor blades. It was also shown that the constructed, simplified model of the main rotor echo can be used to remove the echo of this rotor from the signal recorded by the radar. This procedure makes it possible to analyse the tail rotor echo signal if it is visible to the radar.

In this chapter, the method of obtaining ISAR images of the main rotor is also presented. A database built upon this information can be used for accurate determination of the model or type of the observed helicopter.

The proposed method was also confirmed by the analysis of the real echoes of a helicopter recorded during a measurement campaign carried out as part of the NATO SET-196 group activity. The presented results correspond to the analyses carried out for simulated signals, which confirm both the correctness of the performed simulations and the presented method of estimation of helicopter rotor parameters.

References

[1] Bullard BD, and Dowdy PC. Pulse Doppler signature of a rotary-wing aircraft. IEEE Aerospace and Electronic Systems Magazine. 1991;6(5):28–30.
[2] Misiurewicz J, Kulpa K, and Czekala Z. Multichannel detection of the helicopter echo. In: Proceedings of the International Radar Symposium 1998; 1998. pp. 829–838.

[3] Rotander CE, and Von Sydow H. Classification of helicopters by the L/N-quotient. In: IET Radar 97 Conf. 449; October 1997. pp. 629–633.

[4] Yoon SH, Kim B, and Kim YS. Helicopter classification using time–frequency analysis. Electronics Letters. 2000;36(22):1871–1872.

[5] Kulpa K, Misiurewicz J, Gajo Z, *et al.* A simple robust detection of weak target in noise radars. In: 2007 European Radar Conference; 2007. pp. 275–278.

[6] Burgos-Garcia M, Perez-Martinez F, and Menoyo JG. Radar signature of a helicopter illuminated by a long LFM signal. IEEE Transactions on Aerospace and Electronic Systems. 2009;45(3):1104–1110.

[7] Johnsen T, Olsen KE, and Gundersen R. Hovering helicopter measured by bi-/multistatic CW radar. In: Proceedings of the 2003 IEEE Radar Conference (Cat. No. 03CH37474); 2003. pp. 165–170.

[8] Clemente C, and Soraghan JJ. Passive bistatic radar for helicopters classification: A feasibility study. In: 2012 IEEE Radar Conference; 2012. pp. 0946–0949.

[9] Clemente C, and Soraghan JJ. GNSS-based passive bistatic radar for micro-Doppler analysis of helicopter rotor blades. IEEE Transactions on Aerospace and Electronic Systems. 2014;50(1):491–500.

[10] Lesturgie M. Use of dynamic radar signature for multistatic passive localisation of helicopter. IEE Proceedings – Radar, Sonar and Navigation. 2005; 152(6):395–403.

[11] Clemente C, and Soraghan JJ. Application of the singular spectrum analysis for extraction of micro-Doppler signature of helicopters. In: IET International Conference on Radar Systems (Radar 2012); 2012. pp. 1–5.

[12] Bączyk MK, Misiurewicz J, Gromek D, *et al.* Analysis of recorded helicopter echo in a passive bistatic radar. In: 2013 European Radar Conference; 2013. pp. 243–246.

[13] Bączyk MK, Krysik P, Samczyński P, *et al.* Identification of helicopter rotor parameters using multistatic passive radar. In: 2015 IEEE Radar Conference (RadarCon); 2015. pp. 1464–1467.

[14] Bączyk MK, Samczyński P, Kulpa K, *et al.* Micro-Doppler signatures of helicopters in multistatic passive radars. IET Radar, Sonar Navigation. 2015;9(9):1276–1283.

[15] Clemente C, Parry T, Galston G, *et al.* GNSS based passive bistatic radar for micro-Doppler based classification of helicopters: Experimental validation. In: 2015 IEEE Radar Conference (RadarCon); 2015. pp. 1104–1108.

[16] Vorobev E, Veremyev V, and Kutuzov V. Recognition of propeller-driven aerial targets in DVB-T2 passive bistatic radar. In: 2018 19th International Radar Symposium (IRS); 2018. pp. 1–8.

[17] Tikkinen J, Hiltunen K, and Martikainen K. Utilization of long coherent integration time in helicopter recognition by passive coherent location (PCL) radar. In: 2013 European Radar Conference; 2013. pp. 247–250.

[18] Lie-Svendsen Ø, Olsen KE, and Johnsen T. Measurements and signal processing of helicopter micro-Doppler signatures. In: 2014 11th European Radar Conference; 2014. pp. 121–124.

[19] Misiurewicz J, Kulpa K, and Czekala Z. Analysis of recorded helicopter echo. In: Radar 97 (Conf. Publ. No. 449); 1997. pp. 449–453.

[20] Misiurewicz J, Kulpa K, and Czekala Z. Analysis of radar echo from a helicopter rotor hub. In: 12th International Conference on Microwaves and Radar. MIKON-98. Conference Proceedings (IEEE Cat. No.98EX195). vol. 3; 1998. pp. 866–870.

[21] Czekała Z, Misiurewicz J, and Kulpa K. Practical implementation and performance of a hovering helicopter detection system in a search radar. In: International Radar Symposium India 2005; 2005. pp. 18–21.

[22] Munoz-Ferreras J, Perez-Martinez F, and Burgos-Garcia M. Helicopter classification with a high resolution LFMCW radar. IEEE Transactions on Aerospace and Electronic Systems. 2009;45(4):1373–1384.

[23] Haykin S. Adaptive Filter Theory, Third Edition. Pearson, Upper Saddle River, NJ; 1996.

Chapter 9

Multistatic 3D ISAR imaging of maritime targets

Federica Salvetti[1]*, Elisa Giusti*[1]*, Daniele Staglianò*[2]
and Marco Martorella[1,2]

The increase of legal (commercial and passenger traffic) and illegal maritime traffic demands for strengthened maritime surveillance and security both offshore and within the harbours. It is progressively becoming more important to monitor the vessel movements in order to avoid collisions and prevent possible environmental damages other than keeping watch over the maritime traffic situation. Currently, maritime traffic control is performed via the vessel traffic service (VTS), which is a system established by harbour or port authorities that exploits the information provided by the automatic identification system (AIS). The AIS is installed on board of cooperative vessels and provides important information, such as their global positioning system (GPS) position over time, their distinctive identification, course and speed. VTS is usually supported by a coastal surveillance radar that offers the possibility to detect targets 24/7 at long distances and in all weather conditions.

An important step forward for improving maritime surveillance and security may be the use of radar systems with three-dimensional (3D) imaging capabilities. Having available 3D images of targets enables new functionalities, such as effective automatic non-cooperative target identification, recognition and classification (NCTI/R/C). 3D radar systems could be of great help both in civil and military applications for maritime monitoring, security and surveillance even in dense operational environments. If installed on board, 3D radars can provide situational awareness and aided navigation.

3D interferometric inverse synthetic aperture radar (InISAR) imaging has proven to be an effective tool to produce accurate 3D images of the target. The concept of 3D InISAR is shown in Figure 9.1. The idea is to expand the 2D space of the ISAR image to a volume, where the brighter scatterers extracted from the 2D ISAR image are mapped according to their estimated height.

3D InISAR can overcome a number of limitations of the 2D ISAR technique, which has been deeply investigated in the last few decades as it provides some means for automatic target classification and recognition of non-cooperative targets. The reader may refer to Chapter 2 for more details on 3D InISAR concept and theory.

[1] National Laboratory of Radar and Surveillance Systems (RaSS) – CNIT, Pisa, Italy
[2] Department of Information Engineering, University of Pisa, Pisa, Italy

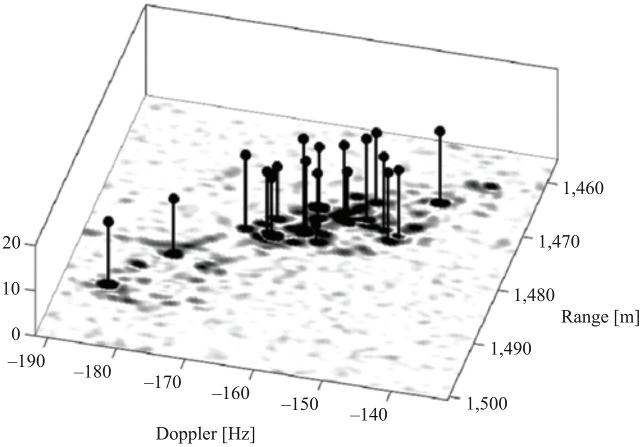

Figure 9.1 3D InISAR concept

Although many features can be extracted from a 2D ISAR image, the 2D image quality depends on the target's dynamics other than the radar's position. Depending on the radar-target geometry, ISAR images can be difficult to interpret due to the fact that the 3D reflectivity of the target is projected onto an image plane, which is not known a priori. Non-cooperative target recognition via 2D-ISAR may be complex as theoretically infinite number of 2D target's 'views' could be collected, thus leading to very large and most possibly incomplete databases. In addition, monostatic 2D ISAR suffers from self-occlusion issues, it is not very robust to jammers and stealthy targets cannot be imaged.

In addition to the single sensor 3D capability, a valuable cutting-edge response to the demand of increased level of monitoring and security is the use of several spatially distributed low-weight/low-power active InISAR systems. There are many advantages of a multistatic ISAR configuration that makes this approach appealing:

- Defeat stealthy targets: Some targets are made stealthy against monostatic radars, but they are detectable by bistatic/multistatic radars. Therefore, bistatic/multistatic radar imaging of stealthy targets may be possible.
- Avoid geometrically adverse cases: Some targets may deliberately fly directly at the radar, therefore generating a geometrical case where no aspect angle variation is generated by the target.
- Improve target visibility: With a single configuration, there is a significant risk that the target may not be visible due to the presence of obstacles.
- Reduce/suppress shadowing effects: In monostatic ISAR, parts of the target may be shadowed by other parts of the target itself.
- Image projection plane (IPP): The IPP depends on the target's effective rotation vector orientation and on the sensor position; by varying the sensor position, a number of possible IPPs can be obtained. The availability of multiple sensors increases the chance to obtain a desired IPP.

- Time to image: In some simple geometrical cases, multiple sensors may be used to form ISAR images (coherent and incoherent multi-ISAR image formation).
- Image fusion: ISAR images obtained by single sensors can be post-processed and fused to form more detailed images and/or images with higher resolution.
- Multiperspective radar imaging for classification and recognition: Multiple-aspect ISAR images can be used to improve classification and recognition performances (both in the cases of template-matching and feature-based approaches).

The joint use of the information from each 3D InISAR system can be exploited also in the framework of the new generation of smart harbours at the purpose of more effective collision avoidance, docking facilitator and improved monitoring against illegal activities.

More in general, the 3D information collected at each sensor could provide fundamental features, such as the vessel size and type and, more importantly, could greatly improve automatic NCTI/R/C performances.

However, a challenging issue that should be addressed is how to combine the data from each sensor.

Some papers have been proposed in the recent literature that address the problem of how to combine data of a net of distributed radars [1–3]. Fusion may be implemented either at raw-data level or at image level. The first one, however, requires a high degree of coherence (both in frequency and in phase), which may be difficult to reach in a net of spatially distributed radars.

In the following, the multiview fusion algorithm proposed in [1] is described, which can handle data collected from multitemporal and multiperspective configurations to form more detailed and complete 3D reconstructions.

The remainder of the chapter is organized as follows. Section 9.1 describes the multiview fusion technique. Section 9.2 presents experimental results obtained by using real data. Finally, concluding remarks are drawn in Section 9.3.

9.1 Multiview 3D InISAR image fusion

Reliable monostatic 3D InISAR reconstructions are typically composed of a small number of scatterers for several reasons:

- Variations of signal to noise ratio (SNR): The correct positioning of the extracted scattering centres is affected by the SNR associated to each of them. Then, reliable point clouds are often sparsely populated.
- Self-occlusion: Parts of the illuminated object might be covered depending on the specific radar-target geometry. This limits the amount of scatterers that can be extracted and then located in the 3D space.
- Undesirable radar-target geometries: 2D ISAR images with little or no Doppler extension might be generated from received data corresponding to specific target's dynamics [4–6]. In this case, the standard range–Doppler image formation processing practically produces 1D ISAR images instead of 2D images and no scatterers can be extracted.

As a consequence, monostatic reconstructions might not carry enough information about the target for it to be identified or even for its overall dimensions to be estimated.

Having available a number of spatially distributed interferometric sensors can then be of great advantage in order to obtain a densely populated, accurate 3D reconstruction by fusing the information from each node of the network. However, a significant issue is how to combine this information. The data fusion can be performed either at raw-data level (coherent fusion) or at image level (incoherent fusion). The coherent fusion approach typically consists of coherently combining the received signals in the spatial frequency domain. However, some critical aspects make it difficult to implement this class of systems in practice:

1. Increased system complexity.
2. Required accurate time and phase synchronization between the radars in the network.
3. Required a priori knowledge or estimation of both the target's aspect angle and the target's rotation vector in order to map the signal in the 3D Fourier space, namely the full 3D spatial frequencies domain.
4. Required coherence of the target's return signal over the multistatic angles.

Data fusion can be also performed at the image level, which means that the outputs of each radar processing are incoherently combined in the image domain. However, 2D ISAR images cannot be easily combined. In fact, each radar produces a 2D ISAR image, which describes a particular projection of the target's reflectivity, according to the specific radar-target geometry. As an example, let's consider the case in Figure 9.2, where the radars produce three ISAR images, each of which is the projection of the 3D target reflectivity function onto different 2D planes, arbitrarily oriented in the 3D space.

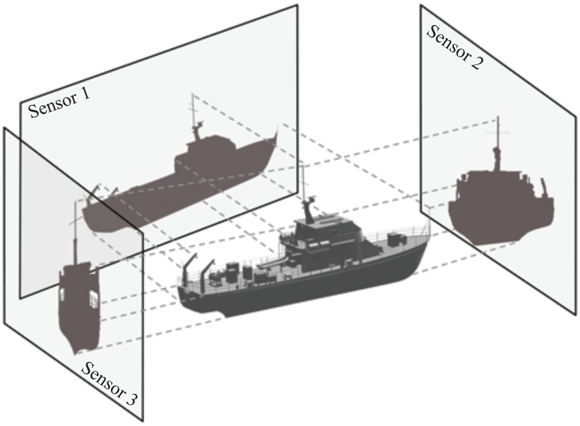

Figure 9.2 ISAR IPPs

An efficient way to overcome such a limitation is to use a number of InISAR systems instead of conventional ISAR systems [7,8], in order to obtain 3D models of the target from each sensor and then incoherently join them together. This method, although less accurate with respect to the fusion performed at raw data level, is less sensitive to phase coherence, angular decorrelation and target's motion estimation errors. In addition, it does not require frequency/time/phase synchronization among radars. The great advantage of this method is that a 3D target reconstruction can be collected either at different acquisition times or from a generic number of spatially distributed interferometric sensors and then merged independently. The block scheme of the proposed algorithm is shown in Figure 9.3.

More specifically, the 3D fusion algorithm can handle the following:

- Multitemporal data: Batches of received data selected at different times. This is a cost-effective solution, as information about the target can be added by using a single interferometric system. Scintillation effects of the scattering centres generally cause 2D images of a multitemporal sequence to show different scatterers. These images, collected during a short or a long temporal baseline, in turn, generate different 3D reconstructions that can be incoherently joined together to increase information about the target. Short temporal baseline data consist of a set of 3D images formed by processing data acquired at relatively close time intervals, also within a single acquisition. Long temporal baseline data can be collected if a target does not change its characteristics in time. In this case, multiple 3D reconstruction may be obtained from data collected at very distant times (days, weeks and months). The implication is that databases can be updated when another acquisition of the same target occurs. In an ATR scenario, a database should always be updated when possible. Therefore, when a target identification is confirmed, the

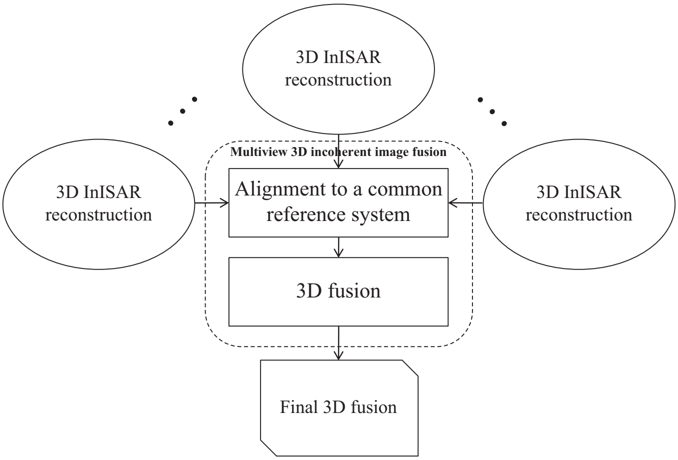

Figure 9.3 Multiview 3D fusion concept

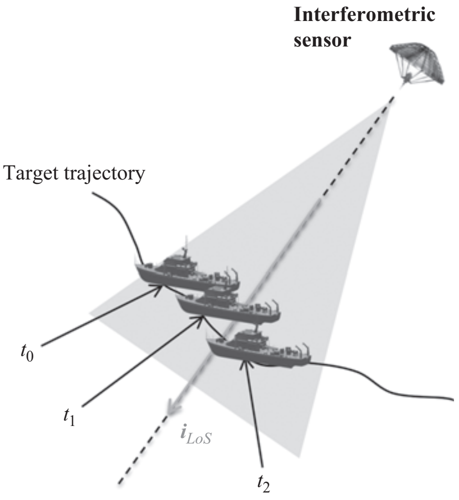

Figure 9.4 Multitemporal configuration

same data used to identify the target can be used to update the database via a 3D fusion.

A pictorial representation of a multitemporal configuration is shown in Figure 9.4.

- Multistatic data: These are gathered by spatially distributed sensors. This method allows to obtain a 3D fusion that is a collection of 3D reconstructions obtained at different aspect angles. This may reduce or completely solve shadowing issues, other than resulting in a more complete and detailed final reconstruction. Multistatic 3D reconstruction may become available if multiple InISAR systems are in place. One of the main advantages of a multistatic configuration is that multiple 3D reconstructions can be simultaneously available for 3D fusion, therefore reducing the time needed to obtain a satisfactory 3D reconstruction. Also, a number of sensors may be positioned strategically to defeat the problems of self-occlusion and stealthy targets.

  A pictorial representation of a multistatic configuration is shown in Figure 9.5.
- A combination of multitemporal and multiperspective data. A pictorial representation of a multiview configuration is shown in Figure 9.6.
- 3D InISAR fusions: 3D clouds of points that are already obtained by fusing 3D ISAR images.

9.1.1 3D fusion

It is worth noting that each 3D image is formed by estimating the three spatial coordinates of each scatterer with respect to a given image plane, which is generally not the same for all the sensors. For this reason, a pre-alignment stage as first a step in order to align the 3D reconstructions with respect to a common reference

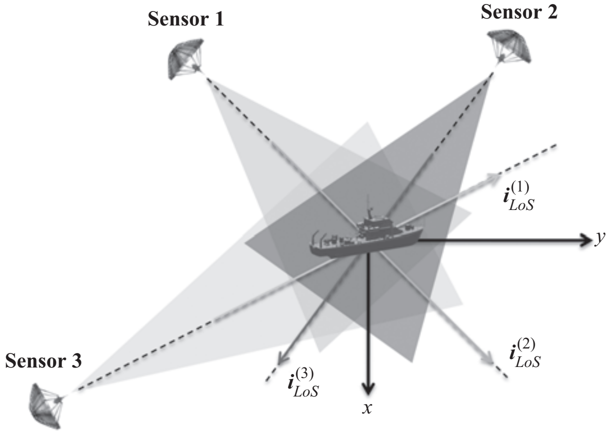

Figure 9.5 Multistatic configuration

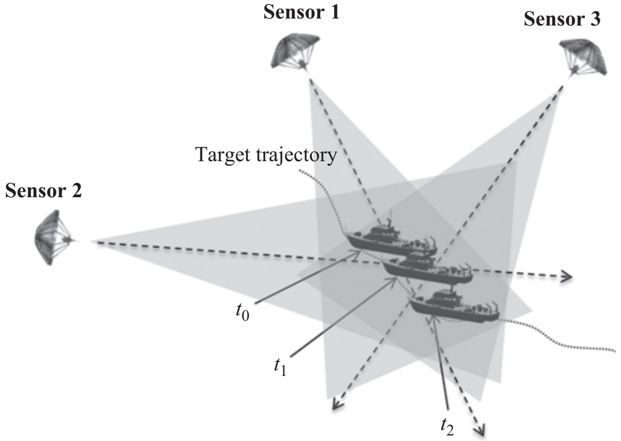

Figure 9.6 Multiview configuration

system is necessary. First, each 3D reconstruction is rotated by its estimated angle $\hat{\phi}$ to eliminate the dependence from the specific IPP. Then, supposing that the positions of the nodes of the net are known, it is possible to rotate all the reconstructions with respect to a fixed reference system. However, the 3D image formed at each sensor can be affected by shadowing effects and inaccurate estimation of ϕ. These effects can cause misalignments, and for this reason, it is necessary to perform a further alignment, which is the fundamental step of the 3D fusion algorithm.

The 3D image fusion algorithm [9] works iteratively between pairs of 3D reconstructions and is structured in the following steps. Among the two 3D reconstructions of interest, let us identify one 3D image as the reference, composed of N scatterers. The other 3D image is composed of M scatterers.

- The height error is computed between the nth scatterer of the reference and all the M scatterers of the other reconstruction in order to identify possible matches. The height error is defined as

$$\varepsilon_{nm} = |h_n - h_m| \tag{9.1}$$

- The height error is compared to a threshold Λ. A match $m_k(n)$ for the nth scatterer is confirmed when the height error is lower than the threshold, where $k = 1, \ldots, K_n$ and K_n is the number of matches for the specific scatterer of the reference.
- The reference and the other reconstruction are aligned by overlapping the match to the nth scatterer, for all the matches.
- The Euclidean distance is used to compute the number of scatterers that the two 3D images have in common in this particular position, denoted as $cs_k(n)$. A mean matching distance is also calculated as a reliability indicator and is expressed as follows:

$$mmd_k(n) = \frac{1}{C} \sum_{i=1}^{C} d_i(k) \tag{9.2}$$

  where C is the number of common scatterers and $d_i(k)$ is the ith Euclidean distance between the associated scatterers.
- For that particular nth scatterer of the reference, among all the alignments obtained by overlapping each of the possible matches to the considered scatterer, the best alignment is selected based on the maximum number of common scatterers $cs_k(n)$. If several alignments have the same maximum number of common scatterers, the best alignment is chosen based on the minimum mean matching distance $mmd_k(n)$.

These operations are repeated for all the N scatterers and the best final alignment is chosen between the best alignments of each scatterer based on the maximum number of common scatterers and the minimum mean matching distance. The block diagram of the 3D fusion algorithm is detailed in Figure 9.7.

It can be noticed that the exhaustive search of the best alignment is performed for each of the N scatterers of the reference. Then, it is important to choose as the reference the 3D reconstruction composed of the smallest number of scatterers, that is $N < M$, in order to reduce the computational costs.

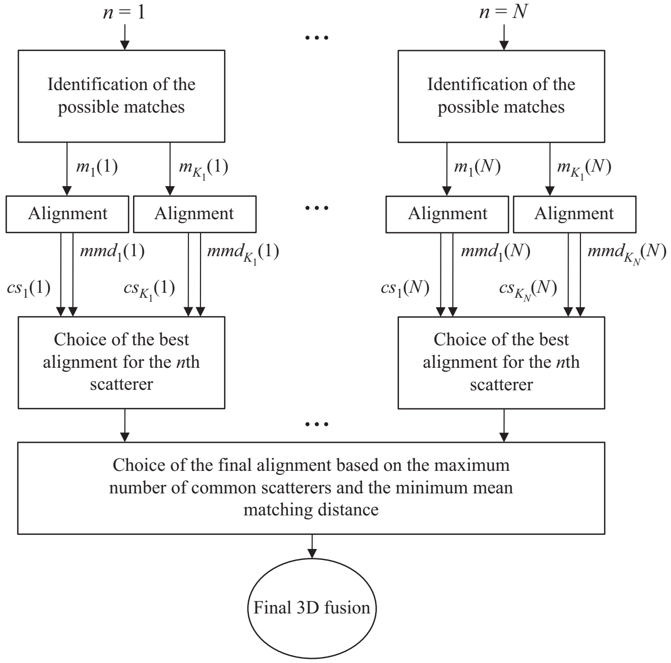
n = 1
n = N
Identification of the possible matches
Identification of the possible matches
m1(1)
mK1(1)
m1(N)
mK1(N)
Alignment
Alignment
Alignment
Alignment
mmd1(1)
mmdK1(1)
mmd1(N)
mmdKN(N)
cs1(1)
csK1(1)
cs1(N)
csKN(N)
Choice of the best alignment for the nth scatterer
Choice of the best alignment for the nth scatterer
Choice of the final alignment based on the maximum number of common scatterers and the minimum mean matching distance
Final 3D fusion

Figure 9.7 3D fusion block diagram

9.2 Multiview 3D InISAR image fusion in experimental scenarios

Results of the multiview 3D InISAR image fusion technique applied to real data are detailed hereafter to show the capability and versatility of this approach in experimental scenarios. The data were acquired during the NATO Set 196 joint trials on 'Multichannel/Multistatic Radar Imaging of Non-cooperative Targets', where a number of heterogeneous sensors were deployed in order to investigate multichannel/multistatic radar imaging as a feasible solution to the current limitations of NCTI/NCTR based on single channel radars. The trials were run in Livorno from 29 September to 3 October 2014 and the radar systems were used to simultaneously acquire data of a number of cooperative maritime and air targets [10,11] equipped with GPS/IMU (inertial measurement unit) systems to measure their position and velocity. With the purpose of 3D InISAR imaging and incoherent fusion, three ground-based radars, such as HABRA1, HABRA2 and PIRAD, were used to observe the scenario from different aspect angles. The two HABRA interferometric sensors are a metasensing BV manufacture, while the PIRAD prototype has borne from a collaboration between the Department of Information Engineering, University of Pisa, and the Radar and Surveillance System national laboratory. Both the HABRA and the PIRAD systems are frequency-modulated continuous wave interferometric radars. Each of their antenna system consists of a transmitting element and three receivers arranged in an L-shape but spaced differently according to the system characteristics. The beampatterns of the antennas have a beam width of 60° along the azimuth direction and of 20° along the elevation. The PIRAD system is horizontally polarized and makes the use of an X-band Fabry–Pérot resonator, while the HABRA system is vertically polarized and uses a microstrip patch flat panel antenna. Finally, a GPS PPS and a reference clock at 10 MHz of the GPS-DO system were installed on board the radars in order to reach time and phase synchronization between the systems. The campaign set-up is depicted in Figure 9.8, while the main parameters of the HABRA and PIRAD systems are detailed in Figures 9.9 and 9.10, respectively.

The analysed data were collected on 3 October 2014. The training ship of the Italian Navy, Astice, was crossing the illuminated area with a number of non-cooperative targets. Astice is shown in Figure 9.11 with its CAD and Astice's dimensions are specified in Table 9.1.

9.2.1 Application of multiview 3D to multitemporal data

Multitemporal results shown hereinafter refer to the training ship Astice when illuminated by the interferometric sensor PIRAD.

Three batches of data from a single PIRAD acquisition interval were elaborated to form three 3D reconstructions that will be joined together throughout the multiview technique. The range–Doppler maps corresponding to the different time intervals t_0, $t_1 = t_0 + 2$ s and $t_2 = t_0 + 3$ s are shown in Figure 9.12. Astice is highlighted by the red box and the selected time intervals are detailed in Table 9.2.

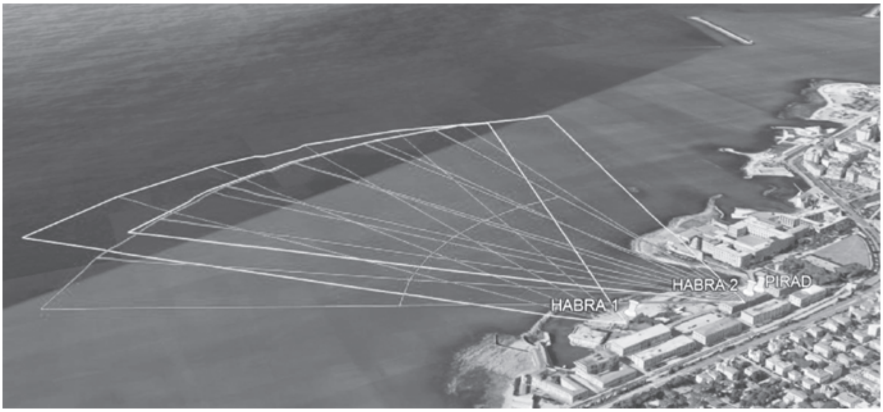

Figure 9.8 Measurement campaign set-up

Description	Value
Waveform	FMCW
Transmitted frequency (X-band)	9.6 GHz
Band	300 MHz
Antenna elevation beamwidth (–3 dB)	20°
Antenna azimuth beamwidth (–3 dB)	60°
Transmitted power	Up to 37 dB m
Polarization	V
PRF	1.22 kHz
Vertical/horizontal baseline	0.54/0.35 m

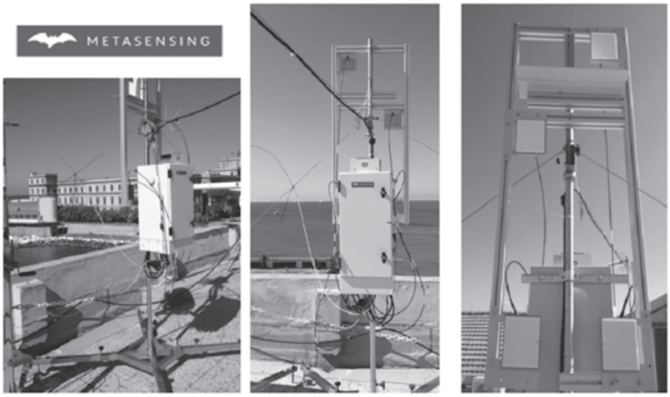

Figure 9.9 HABRA main parameters

Description	Value
Waveform	FMCW
Transmitted frequency (X-band)	10.7 GHz
Band	300 MHz
Antenna elevation beamwidth (–3 dB)	20°
Antenna azimuth beamwidth (–3 dB)	60°
Transmitted power	Up to 33 dB m
Polarization	H
PRF	500 Hz
Vertical/horizontal baseline	0.47/0.41 m

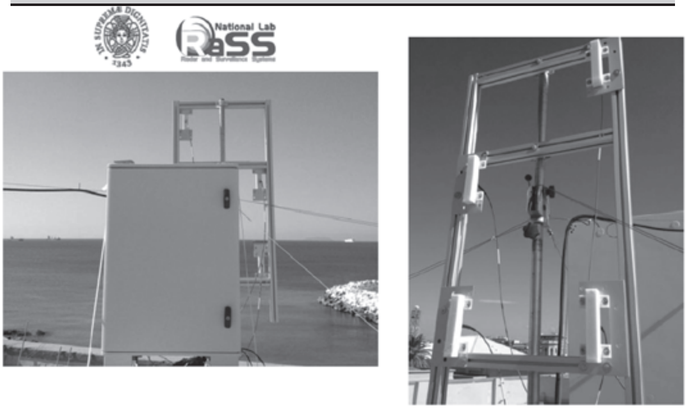

Figure 9.10 PIRAD main parameters

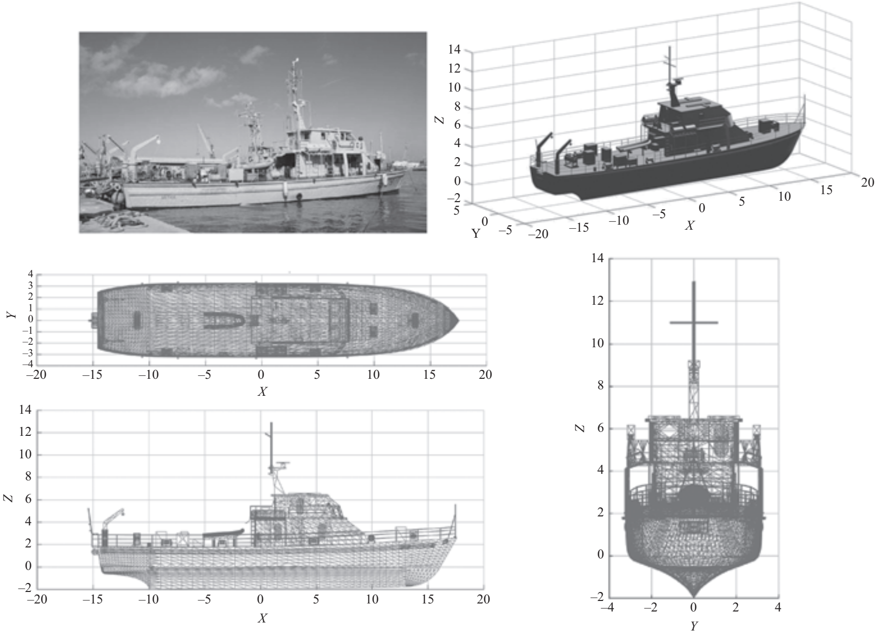

Figure 9.11 Training ship Astice

Table 9.1 Size of Astice

Length	32.4 m
Width	6.47 m
Deckhouse height	≃4.5 m
Main mast height	≃8 m

As expected, the data processed at different time intervals produce different 2D ISAR images due to the target's complex motion. Figure 9.13 illustrates the 2D ISAR images of each time step and the scatterers extracted by means of the MC-CLEAN technique described in Chapter 2.

Figures 9.14–9.16 show the output of the 3D InISAR processing for the three time intervals before the prealignment stage.

The output of the prealignment block is depicted in Figures 9.17 and 9.18, where the 3D images are rotated by the estimated rotation angle ϕ and located in a common reference system with their centroids in $[0, 0, 0]$. Again, shadowing effects and possible incorrect estimation of the rotation angle cause misalignments and the overall

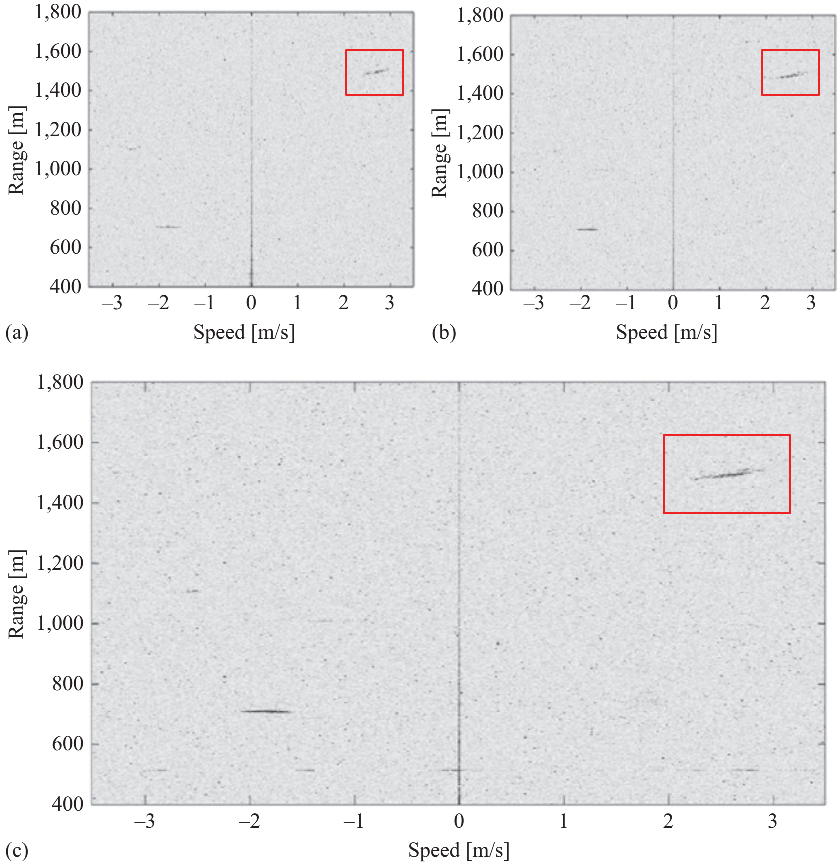

Figure 9.12 Range–Doppler maps of PIRAD at times (a) t_0, (b) $t_1 = t_0 + 2$ s and (c) $t_2 = t_0 + 3$ s. The training ship Astice is highlighted in the red box

Table 9.2 Selected time intervals – 3 October 2014 – Astice

	Acquisition time **[hh:mm:ss]**	T_{obs} **[s]**
t_0	13:02:40	0.9
t_1	13:02:42	0.9
t_2	13:02:43	0.8

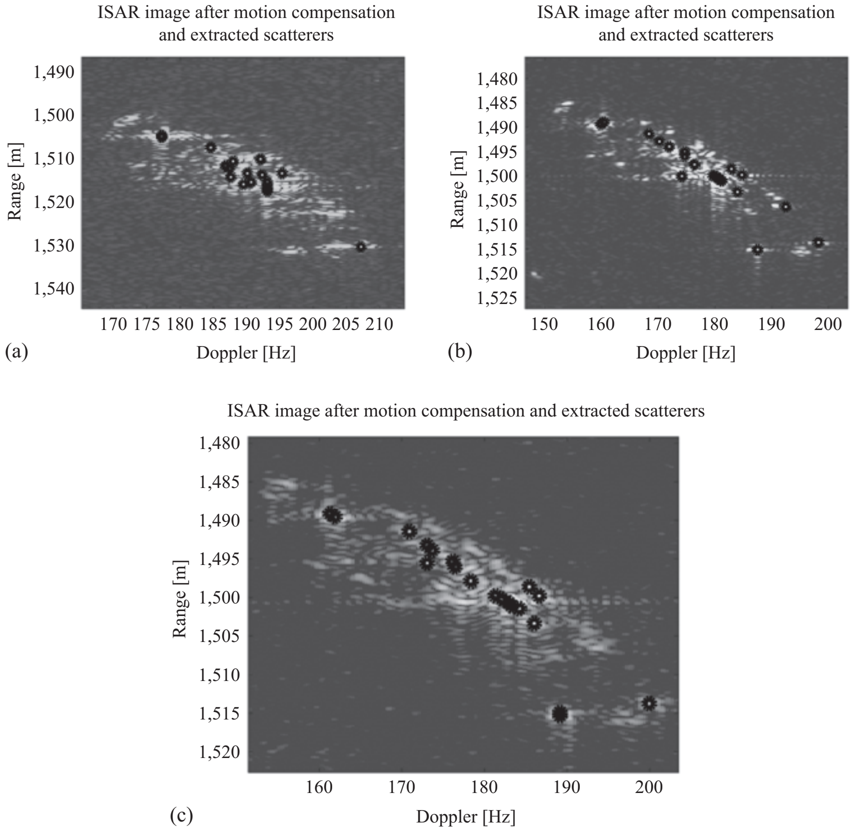

Figure 9.13 2D ISAR images of the target collected at PIRAD at times (a) t_0, (b) $t_1 = t_0 + 2$ s and (c) $t_2 = t_0 + 3$ s. The black circles denote the scatterers extracted by means of the MC-CLEAN technique – Astice.

size of the ship cannot be inferred. The 3D fusion algorithm aligns the monostatic 3D reconstructions by exploiting the scatterers height and the Euclidean distance. The resulting final fusion is shown in Figures 9.19 and 9.20, while Table 9.3 details the estimated target dimensions for the monostatic cases and for the multitemporal fusion compared with the actual size of the training ship Astice.

It is worth pointing out that the multitemporal 3D reconstruction contains the joint information from the three time intervals and consequently, it improves 3D target reconstruction. As an example, it can be noted that after the multitemporal fusion, the main structures of the ship as the bow, the deckhouse, the mast and the stern are more easily distinguishable with respect to the single monostatic cases. This is because, even if similar, each monostatic 3D reconstruction derives from the analysis of temporally diverse data batches and thus adds information to a single acquisition.

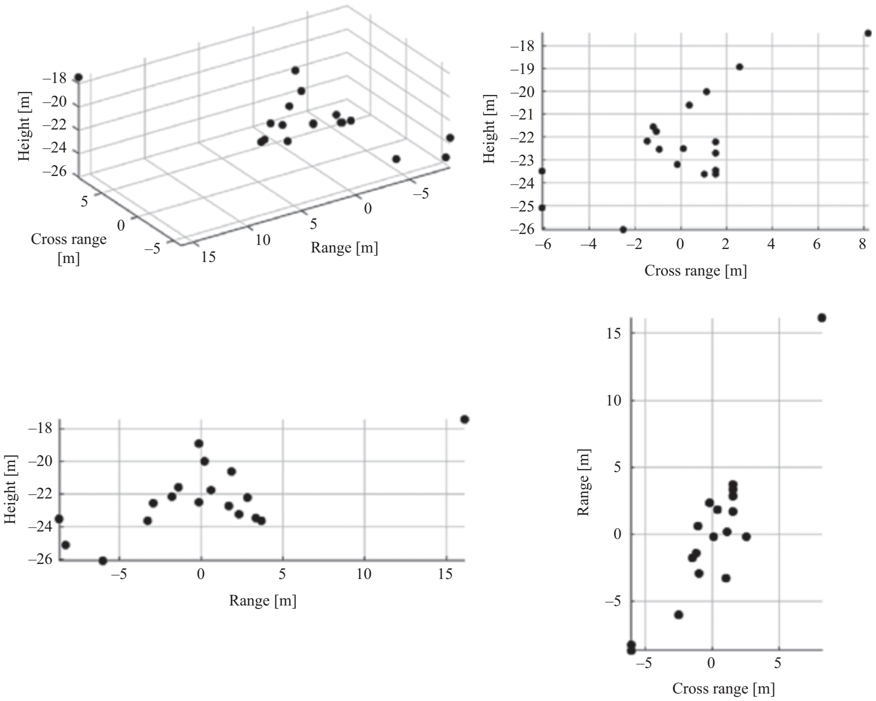

Figure 9.14 InISAR 3D reconstruction relative to time t_0 – Astice

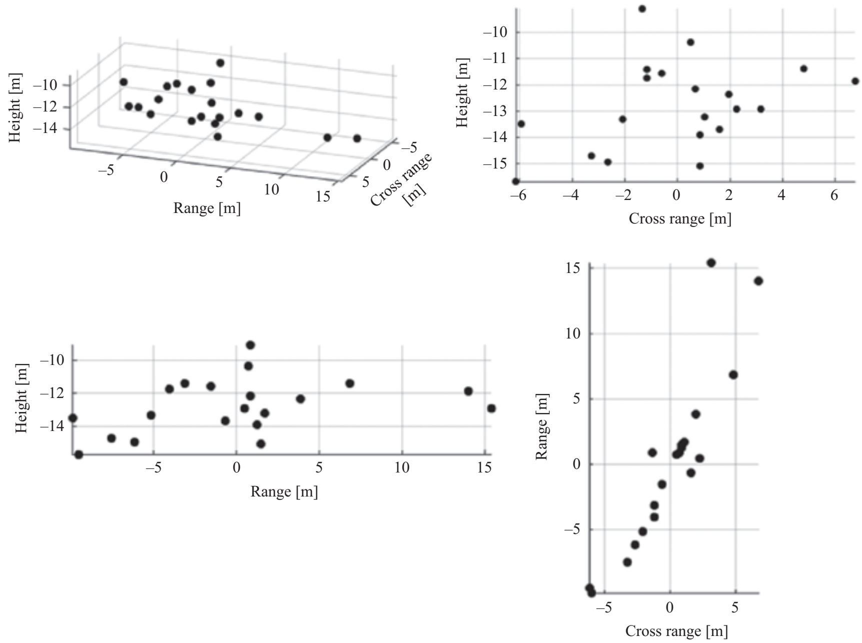

Figure 9.15 InISAR 3D reconstruction relative to time $t_1 = t_0 + 2$ s – Astice

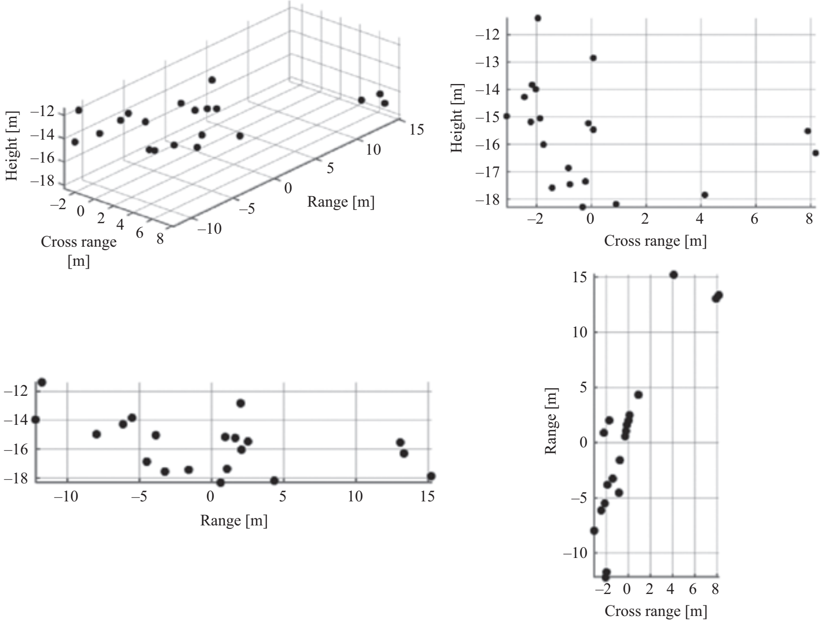

Figure 9.16 InISAR 3D reconstruction relative to time $t_2 = t_0 + 3$ s – Astice

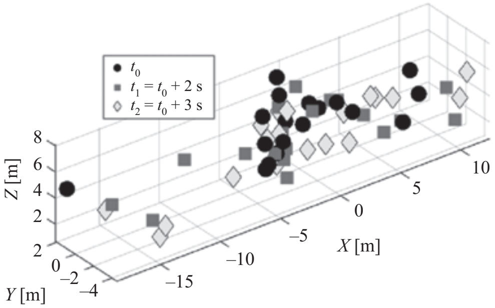

Figure 9.17 Results of the prealignment step – multitemporal data set – 3D view – Astice

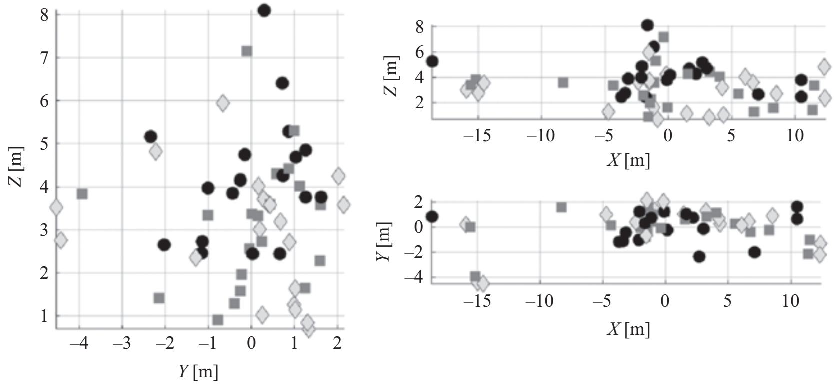

Figure 9.18 Results of the prealignment step – front view (left), side view (top-right), top-view (bottom-right) – multitemporal data set – Astice

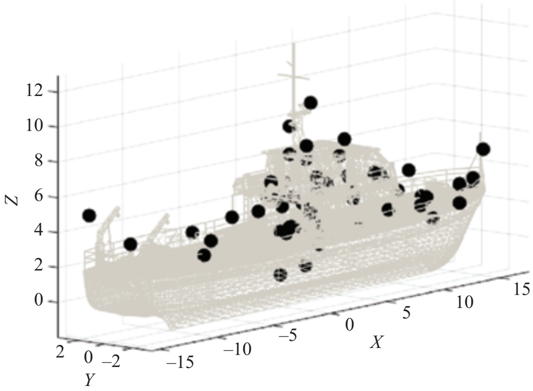

Figure 9.19 Multitemporal final fusion – Astice – 3D view

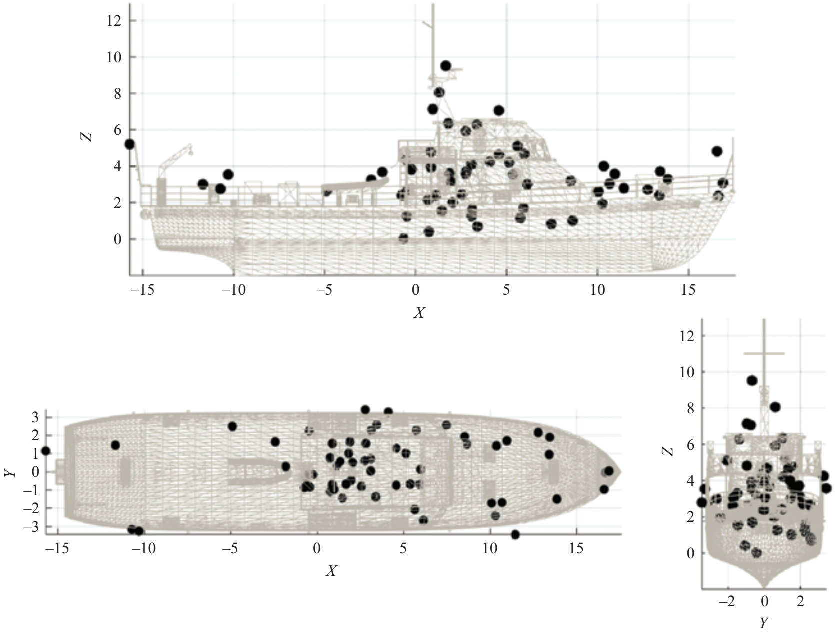

Figure 9.20 Multitemporal final fusion – Astice – projections – side view (top), top-view (bottom-left) and front-view (bottom-right)

Table 9.3 Estimated dimensions – multitemporal case – Astice

	Length [m]	**Width [m]**	**Height [m]**
Actual size	32.4	6.47	12.5
t_0	29.14	3.96	5.6
t_1	21.77	5.95	9.5
t_2	28.32	6.67	5.24
Final fusion	32.5	6.8	9.5

9.2.2 Application of multiview 3D to multistatic data

This approach takes advantages from the spatial diversity, which exploits different aspect angles and consequently generates multiperspective data sets. Results of the multistatic processing that are shown here are related to sensors HABRA 1, HABRA 2 and PIRAD illuminating the training ship Astice on 3 October 2014. Table 9.4 describes the selected sensors and the processed time intervals.

As a result of the prealignment processing, the 3D images are aligned as shown in Figures 9.21 and 9.22.

The output of the 3D fusion algorithm is shown in Figures 9.23 and 9.24, which illustrates the final 3D multistatic fusion obtained by incoherently fusing the three monostatic reconstructions obtained by HABRA 1, HABRA 2 and PIRAD.

Table 9.5 details the estimated ship dimensions for the monostatic cases and the multistatic fusion against the actual size.

Also in this case, the final 3D cloud of points results more dense and the target's shape is reconstructed. In addition, the estimation of the target length, width and height is more accurate with respect to the monostatic cases.

Table 9.4 Selected sensors and time intervals – 3 October 2014 – Astice

	Acquisition time [hh:mm:ss]	**T_{obs} [s]**
HABRA 1	13:02:38	0.9
HABRA 2	13:02:38	0.9
PIRAD	13:02:42	0.9

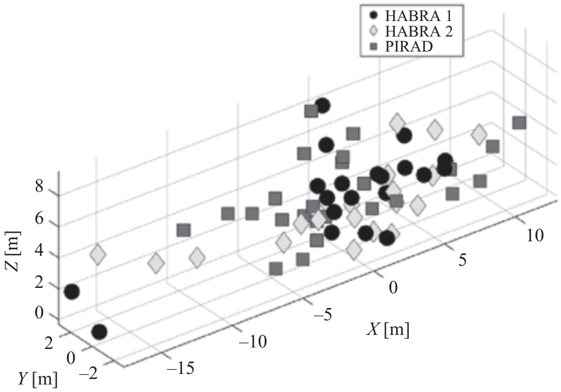

Figure 9.21 Results of the prealignment step – multiperspective set – Astice – 3D view

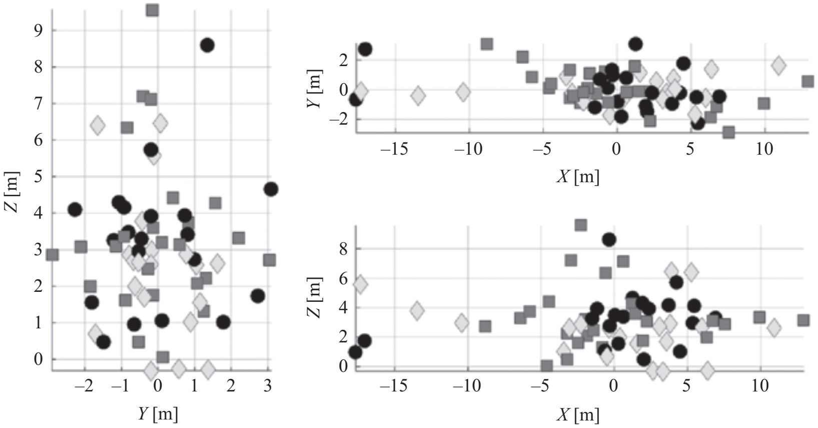

Figure 9.22 Results of the prealignment step – multiperspective set – Astice – projections – front-view (left), top-view (top-right) and side-view (bottom-right)

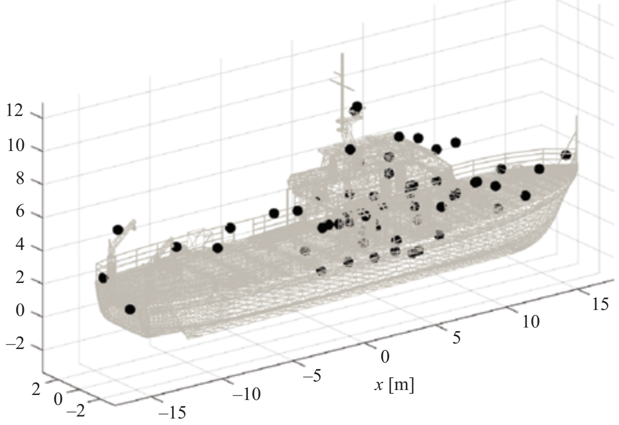

Figure 9.23 Multistatic final fusion – Astice – 3D view

9.2.3 Application of multiview 3D to a combination of multistatic and multitemporal data

Further information to the final image can be added by combining multitemporal and multiperspective data. The availability of both these configurations gives the opportunity to use a larger number of 3D reconstructions as input to the 3D fusion algorithm and consequently to obtain a more complete and more detailed 3D image of the target.

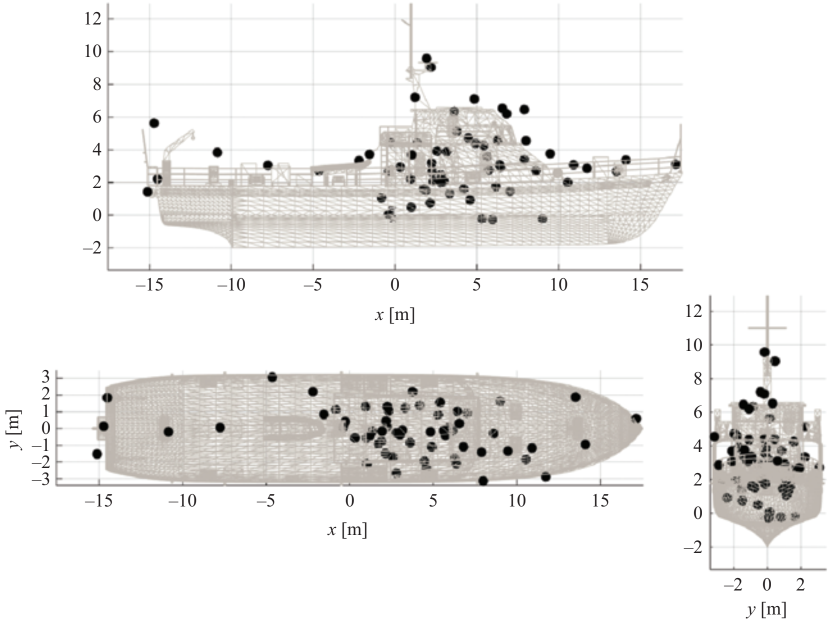

Figure 9.24 Multistatic final fusion – Astice – projections – side view (top), top-view (bottom-left) and front-view (bottom-right)

Table 9.5 Estimated dimensions – multistatic case – Astice

	Length [m]	**Width [m]**	**Height [m]**
Actual size	32.4	6.47	12.5
HABRA 1	24.6	5.4	8.1
HABRA 2	28.3	3.3	6.8
PIRAD	21.8	6	9.5
Final fusion	32.2	6.2	9.8

The multitemporal and the multistatic reconstructions of the training ship Astice are fused by means of the 3D fusion algorithm in order to exploit both the space and time diversity of the received data. Multitemporal and multistatic data are used to form a final 3D reconstruction by means of the 3D fusion technique and are depicted in Figures 9.25 and 9.26. The cloud of points that is located in a 3D space is highly populated and best highlights the main structures of the target. Moreover, the multitemporal/multistatic fusion accurately estimates the target dimensions, as detailed in Table 9.6.

The availability of a wider set of information, that is the combination of both multitemporal and multiperspective data, suggests that the resulting multiview 3D

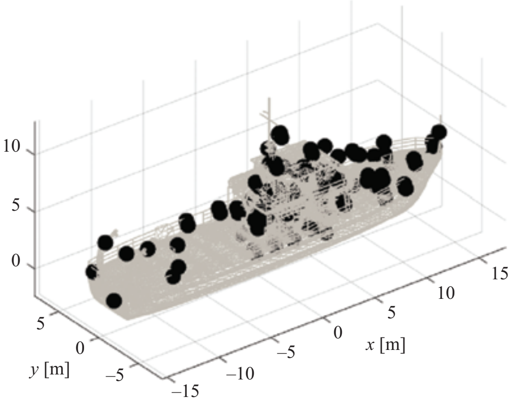

Figure 9.25 Multiview final fusion – Astice – 3D view

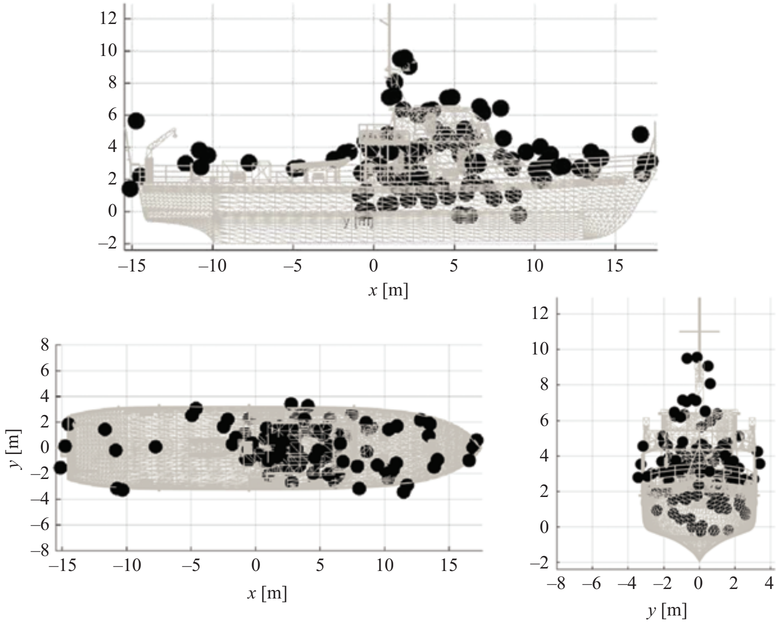

Figure 9.26 Multiview final fusion – Astice – projections – side view (top), top-view (bottom-left) and rear-view (bottom-right)

reconstruction will be in most cases the most complete with respect to the configurations described in the previous paragraphs. As expected, in this case, the multiview 3D reconstruction best describes the target shape and size, which is very important for ATR/ATC systems, as observed in Table 9.6.

Table 9.6 Estimated dimensions – multiview case – Astice

	Length [m]	**Width [m]**	**Height [m]**
Actual size	32.4	6.47	12.5
Multitemporal final fusion	32.58	6.84	9.5
Multistatic final fusion	32.2	6.2	9.8
Multiview final fusion	32.8	6.8	9.8

9.3 Conclusion

In this chapter, it has been shown that 3D image reconstruction using multiple views greatly enhances the system capability to reconstruct 3D non-cooperative target images effectively. The fusion of 3D point clouds obtained by using several temporal and a number of node acquisitions creates a more densely populated point cloud that better represents the target of interest and allows for important features to be extracted more accurately and reliably. In fact, every single 3D fusion may add important information about the target with respect to a single reconstruction. Moreover, new information about the target of interest can be uploaded, when available, in order to update recognition and classification databases based on 3D InISAR imaging systems. Although the implementation of ATR systems that make use of 3D reconstructions is still not in place, the results shown here are a strong encouragement to use this new technology to strengthen radar image-based ATR.

References

[1] Salvetti F, Giusti E, Staglianò D, *et al.* Incoherent fusion of 3D InISAR images using multi-temporal and multi-static data. In: 2016 IEEE Radar Conference (RadarConf); 2016. pp. 1–6.

[2] Brisken S, and Ender J. Block-sparse 3-D ISAR image reconstruction in a non-coherent multistatic scenario. In: 2015 IEEE Radar Conference (RadarCon); 2015. pp. 0265–0269.

[3] van Dorp P, Otten MPG, and Verzeilberg JMM. Coherent multistatic ISAR imaging. In: IET International Conference on Radar Systems (Radar 2012); 2012. pp. 1–6.

[4] Ausherman DA, Kozma A, Walker JL, *et al.* Developments in radar imaging. IEEE Transactions on Aerospace and Electronic Systems. 1984;AES-20(4): 363–400.

[5] Wehner DR. High-Resolution Radar. Artech House Radar Library. Artech House; 1995. Available from: http://books.google.it/books?id=SaFjQgAACAAJ.

[6] Martorella M, Berizzi F, and Haywood B. Contrast maximisation based technique for 2-D ISAR autofocusing. IEE Proceedings – Radar, Sonar and Navigation. 2005;152(4):253–262.

[7] Martorella M, Salvetti F, and Staglianò D. 3D target reconstruction by means of 2D-ISAR imaging and interferometry. In: 2013 IEEE Radar Conference (RadarCon13); 2013. pp. 1–6.

[8] Salvetti F, Martorella M, Giusti E, *et al.* Multi-view three-dimensional interferometric inverse synthetic aperture radar. IEEE Transactions on Aerospace and Electronic Systems. 2018;55(2):718–733.

[9] Salvetti F, Giusti E, Staglianò D, *et al.* Multistatic 3D ISAR image reconstruction. In: 2015 IEEE Radar Conference (RadarCon); 2015. pp. 0640–0645.

[10] Salvetti F, Giusti E, Staglianò D, *et al.* Multistatic 3D InISAR imaging. In: NATO SET-228 Specialists Meeting on Radar Imaging for Target Identification; 2015.

[11] Martorella M, Staglianò D, Lischi S, *et al.* multi-static/multichannel radar imaging in practice: the NATO SET-196 trials. In: NATO SET-228 Specialists Meeting on Radar Imaging for Target Identification; 2015.

This page intentionally left blank

Chapter 10

Challenges of semi-cooperative bi/multistatic synthetic aperture radar (SAR) using Cosmo-SkyMed as an illuminator

Claire Stevenson[1]*, Matthew Nottingham*[1]*, Darren Muff*[1]
and David Blacknell[1]

10.1 Introduction

There has been a recent surge in activity related to bistatic synthetic aperture radar (SAR) systems. This is, in part, due to recent advances in hardware making such systems more attainable and the fact that the approach itself has the potential to provide the following unique properties:

1. Defeating counter-measures (such as jamming).
2. Improving detection performance by reduction of 'spiky' clutter [1].
3. Investigation of complex radar phenomenology (e.g. analysis of complex scattering environments, such as the inside of buildings).

A SAR image is typically formed by having a moving radar system (e.g. on a spacecraft or an aeroplane) which transmits a series of pulses illuminating an area of the ground and records the energy reflected from the ground. It is then possible to combine these recorded reflected pulses into a map of radar cross section (RCS) as a function of 2D position within the illuminated area. More details of the basic principles of SAR image formation can be found in [2–4].

Here, we investigate the bistatic case whereby transmitter and receiver are spatially separated by a significant distance. There are a number of ways to implement a bistatic SAR system, with either a moving transmitter, a moving receiver or both transmitter and receiver moving. Exploiting illumination sources designed for SAR image formation has a number of advantages, including desirable waveform ambiguity functions and suitable power spectral density on the ground. Previous studies have demonstrated successful bistatic SAR image formation using space-based SAR systems as illumination sources and ground or airborne receivers [5,6]. In this work, we explore the case of a space-based SAR system (Cosmo-SkyMed) as an illumination source and static ground-based receivers.

[1] Cyber and Information Systems Division, Defence Science and Technology Laboratory (DSTL), Porton Down, Salisbury, UK

The bistatic imaging geometry is itself a subset of the more general imaging geometry – multistatic. A multistatic imaging geometry allows for N-transmitters and M-receivers all working simultaneously. For the investigation of complex radar phenomenology, a multistatic configuration is the preferred solution as it provides the required diversity of collection in the spatial, frequency and polarimetric domains necessary for characterising the underlying complex scattering matrix. In order to fully exploit the dataset, phase must be comparable across all receivers such that the system is coherent at the frequency of operation. Coherent multistatic data collection, for single pass volumetric or single pass multi-aspect imaging, for example, places more stringent requirements on the hardware used for transmission and reception than a bistatic collection [7,8] as coherency between pairs also needs to be maintained. This work provides a general overview of some of the challenges faced when expanding from a bistatic to a multistatic configuration. There is a focus on the specific application of semi-cooperative bi/multistatic imaging using Cosmo-SkyMed as an illuminator. The impact of errors in transmitter location is addressed and the resulting spatially variant geometric distortions in imagery explored.

10.2 Semi-cooperative bi/multistatic data collection

A multistatic system is considered as a series of bistatic pairs, which can be combined coherently. There are several ways of achieving coherence in a bistatic system; previous work has investigated the use of both specially modified transmitter–receiver pair, such that timing for synchronisation is shared between the pair [1,9] and an unmodified transmitter with a receiver which captures signals from both the reflected path and directly from the transmitter [10]. The second method has the advantage that it allows the use of transmitters of opportunity, e.g. DTV, to be exploited as illumination sources and for the multistatic case, it does not require modification of multiple sensors.

In this work, the following assumptions are made about the general hardware and collection parameters:

- The multistatic array is formed ad hoc from an illuminator of opportunity (in this case Cosmo-SkyMed) and available receivers are capable of operating bistatically (i.e. with two channels for digitisation of direct and reflected path) but not necessarily designed to operate as a distributed coherent network, as might be the case when pooling of hardware resources between research groups.
- For simplicity, the receivers are stationary.
- The required distance between receiver locations to provide desired imagery of a target area prohibits cabling for synchronisation links.
- The receivers have no transmit capability. This allows for completely passive operation in RF dense environments, where transmission licences may be difficult to acquire.

The imaging geometry for a single bistatic pair is illustrated in Figure 10.1.

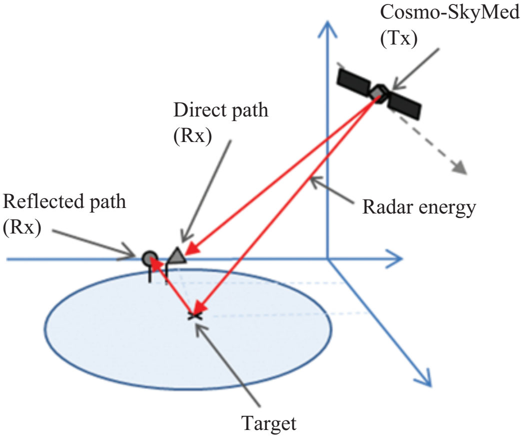

Figure 10.1 The bistatic imaging geometry used for an unmodified spaceborne transmitter (Tx); in this case, Cosmo-SkyMed, and a static two-channel ground-based receiver (Rx). The direct and reflected path antennas of the receiver are shown within the main beam of the transmitter, with the two paths of radar energy given by red arrows

10.3 Hardware considerations

If, as described previously, coherence between transmitter and receiver is achieved through digitisation of both direct and reflected path, then, for the multistatic array, only the coherence between the receivers needs to be considered.

Ideally, the receivers would all digitise the incoming signal at precisely the same sample times so that coherence is maintained across the array. However, there are some practical reasons why this might not be possibly outlined as follows:

10.3.1 Analogue-to-digital convertors (ADCs): bulk delay offset

As shown in Figure 10.2, the time between triggering the ADC, the sampling edge of the clock and the instant when the sample of the input analogue signal is taken is known as the bulk delay offset. Even for ADCs sharing a clock, sampling does not typically start at precisely the same time due to jitter on the time between clock edge and sample taking. Typically, the jitter is very small in comparison to the delay (on the order of femtoseconds [11]). However, the bulk delay offset between different ADCs running on separate clocks may be significant; on the order of ~200 ms has been seen between ADCs of different models.

If one considers that the pulse repetition frequency (PRF) of Cosmo-SkyMed is, at a minimum, 3,148 Hz during spotlight mode [12], 200 ms equates to 629 pulses difference in start of digitisation between receivers. This presents a problem in realigning the data across a multistatic array to achieve coherence. If digitisation

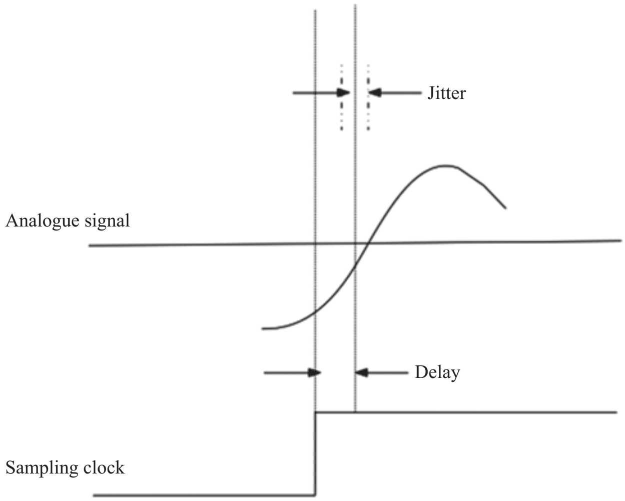

Figure 10.2 Delay offset and jitter shown with respect to the sampling clock edge

does not start some time before the illumination window to ensure that the first pulse is clearly identifiable in all receivers discerning which individual pulses have been digitised is problematic.

In most cases, GPS data can be used to provide a coarse realignment followed by cross correlation to provide a finer estimate of delay between pulses. However, this does place additional hardware requirements on the available receivers that GPS data is also digitised alongside the SAR data.

10.3.2 Clock drift

Accurate synchronisation of the clocks on-board the distributed set of receivers is necessary for coherent combination of the data. Oscillator (or clock) noise can broadly be broken down into two main components; a low-frequency linear drift over time and a random high-frequency component, which is parameterised by the Allan deviation [13].

In a bistatic pair with an unmodified transmitter, differences between the on-board clocks are avoided by digitisation of the direct path from the transmitter and using that as the reference function to cross correlate with the reflected path for pulse compression. In that case, both the reference pulse and the pulse to be compressed are sampled using the same clock. For a multistatic system with M unmodified receivers, the problem becomes more complicated as M free running clocks will digitise a different instantiation of the direct and reflected paths, as depicted in Figure 10.3.

The impact of oscillator noise on bistatic SAR has been investigated in detail in [14], and the reader is referred to the paper for a qualitative discussion on the impact on the resultant image. To summarise the findings, the main lobe impulse response

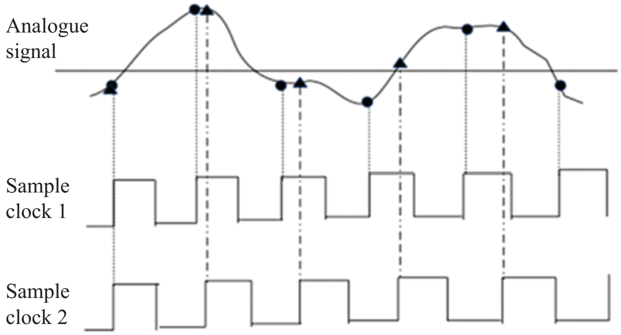

Figure 10.3 Effect of clock drift between two receiver clocks on analogue signal sample times. Circles represent sample times of receiver 1 running sample clock 1 and triangles show sample times of receiver 2 running sample clock 2

function of the compressed pulse is found to broaden, sidelobes become asymmetric and sidelobe contribution increases. With increasing clock drift, peaks undergo an offset in range and azimuth defocussing.

Digitisation of the illuminator Cosmo-SkyMed, which operates at 9.6 GHz, places particularly stringent requirements on clock stability. For coherent combination, we pose the constraint of stability on the order of one-tenth of a wavelength over the collection aperture, at 9.6 GHz with a 7-s aperture that gives a required Allan deviation of $<1.48\text{e}-12$ s over the period of 1 s. Therefore, given sufficiently stable clocks in all receivers (hydrogen masers can achieve $<1\text{e}-13$ s in 1 s), coherent combination of data should not be an issue. However, such technologies can be prohibitive, both in terms of cost and size, weight and power. In these cases, a data-driven clock-recovery post-processing technique is required.

Given a sufficient signal-to-noise ratio in the digitised data, phase offset can be directly measured between two channels using cross-correlation techniques. Phase offset of all receivers with respect to a ‘master’ receiver can be computed, and the appropriate phase corrections applied to the data. This may be problematic for the reflected path channel of a bistatic receiver where signal-to-noise ratio can be a challenge; however, in these cases, the direct path measurements can be used to estimate and remove the low-frequency component of clock drift followed by a contrast maximisation technique applied to the final image to provide finer resolution corrections.

10.4 Semi-cooperative bistatic SAR signal processing

In addition to hardware considerations, there are a number of signal-processing factors to be taken into account when considering the quality of the resulting bi/multistatic image when formed semi-cooperatively. The theory for processing data using a two-channel receiver to achieve coherence with the transmitter and a semi-cooperative illumination source is developed later.

Considering the transmission of a single pulse with a signal of $S(t)$, the received signal, $Q(t)$, will be

$$Q(t) = A_{direct} S(t - T_{direct}) + \sum_{i=0}^{alltargets} A_i S(t - T_i) \tag{10.1}$$

where A is the amplitude due to the RCS of the target (i), the strength of the transmitted pulse and the RF characteristics of the receiver (antenna gains in the direction of target, cable losses, amplifier characteristics, etc.) and T is the time delay due to the total path length, i.e.

$$T_i = \frac{|\vec{P}_{tx} - \vec{P}_i| + |\vec{P}_{rx} - \vec{P}_i|}{c} \tag{10.2}$$

where $\vec{P}$ is the vector position of the object, for example in ECEF coordinates, and c is the speed of light. For the direct path signal delay, T_{direct}, $\vec{P}_{rx} = \vec{P}_i$, hence $T_{direct} = |\vec{P}_{tx} - \vec{P}_{rx}|/c$.

For (10.1) and (10.2), it can be seen that a signal recorded by the receiver Q will be a time delayed copy of the transmitted signal followed (in time) by the reflected copies from all the targets in the scene. If Q is now the range compressed to form Q' (by using, e.g., a suitable matched filter), then the positions and phase of the reflected signals can be determined from the difference to the phase and position of the direct path return. The direct path signal will always be the first return for a given pulse and typically the brightest return making it simple to synchronise to this return.

In order to process the received data into an image, it is necessary to convert the stream of continuously recorded data into a series of pulses that can then be supplied to a generic SAR image-formation processor. The processing in this work was undertaken semi-cooperatively meaning that there was no a priori information available about transmitter timings and locations. As such, some assumptions have to be made about the nature of the transmitter, these are as follows:

1. The PRF is fixed, i.e. the nth pulse will be transmitted at a time $T_0 + nT_{PRI}$, where T_{PRI} (pulse repetition interval, PRI) is 1/PRF, T_0 is the date and time of the first pulse and n is the pulse index.
2. The position of the transmitter can be accurately estimated.

In this case, having a satellite-based transmitter, its position can be estimated using the SGP4 algorithm [15]. SGP4 refers to a simplified perturbations model, which allows for the calculation orbital state vectors of satellites relative to the Earth-centred inertial coordinate system. Using two-line element (TLE) data from Celestrak (http://celestrak.com/publications/AIAA/2006-6753. [Online]), the position of the satellite can be estimated such that:

$$\vec{P}_{tx} = SGP4(T_0 - nT_{PRI}) \tag{10.3}$$

Due to the specification of the TLE data format and limitations in the SGP4 model, there will be errors in the absolute position of a satellite to a couple of kilometres (see [15] for details). In the geometry, we are considering here with a static ground-based receiver, P_{rx} is known to a high accuracy. The effects of the error in position of the transmitter, P_{tx}, are discussed later in this chapter.

Combining (10.2) and (10.3) with a known P_{rx} and derived T_0 (from the arrival time of the first pulse and allowing for the time of flight) means that it is now possible to split the recorded data stream into pulses, which can be processed by a standard bistatic SAR image formation algorithm [9]. This process is performed by identifying the range-compressed data in the direct path return for a given pulse, shifting the whole (i.e. including a suitable swath width to include the target area of interest) of that pulse such that the direct path return is now located at a fixed range cell, applying a phase correction such that the direct path signal now has a fixed (between pulses) phase. The effect of this process is to stabilise the data to the fixed receiver position so that for a given target and pulse:

$$\begin{aligned}\Delta R(n,i) &= |SGP4(T_0 - nT_{PRI}) - \vec{P}_i| + |\vec{P}_{rx} - \vec{P}_i| \\ &\quad -|SGP4(T_0 - nT_{PRI}) - \vec{P}_{rx}| \end{aligned} \tag{10.4}$$

where ΔR is the difference in path length from the direct path signal. This form of stabilised data is the same as is typically produced by a dechirp-on-receive radar [2] and so it can be processed by a standard image formation algorithm as we have effectively caused data associated with the P_{rx} position to have zero range (for each pulse) and zero rate of change of phase (between pulses).

10.5 Effect of errors in transmitter position

As described in the previous section, due to the semi-cooperative nature of these data collection activities, transmitter locations were predicted using a TLE and SGP4 orbit propagator. However, there may be significant errors in the positions the TLE predicts [15]. In order to consider the effect of these uncertainties of the transmitter position on the quality of the output image, an expression for the magnitude of these errors is developed later.

If, at the centre of aperture time, the transmitter has a positional error R_{err} in the direction of P_{tx}–P_{rx}, then the stabilisation process described previously would estimate the value of T_0 incorrectly by a value of R_{err}/c, which in turn would lead to an additional error in the along-track direction of $\sim V_{orb}R_{err}/c$ due to the orbital motion. If we assume an error of 1 km, this orbital error would be of the order of 3 cm (assuming $V_{orb} = 7.5$ km/s). As a first approximation, this additional error will be ignored as it is much less than the 1-km positional error.

The positional error will manifest itself as a phase error, which can be investigated by adding an additional term into (10.5).

$$\begin{aligned}\Delta R(n,i) &= |SGP4(T_0 - nT_{PRI}) + \vec{P}_{err} - \vec{P}_i| + |\vec{P}_{rx} - \vec{P}_i| \\ &\quad -|SGP4(T_0 - nT_{PRI}) + \vec{P}_{err} - \vec{P}_{rx}| \end{aligned} \tag{10.5}$$

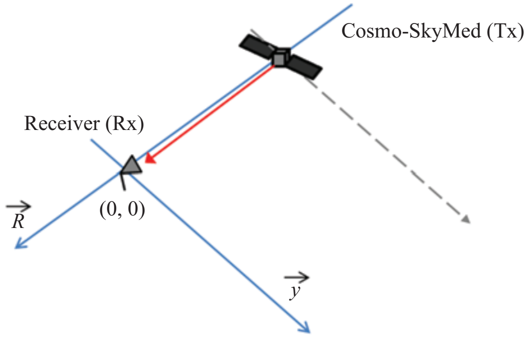

Figure 10.4 The simplified 2D model geometry is shown with the receiver at the origin of the (R, Y) space

From (10.5), it can be seen that an analytical expression for a general case is difficult to determine. To simplify we make the assumption of a linear track in a coordinate system of slant range, $\hat{r}$, and along-track position, $\hat{y}$, originating at the receiver location and with a transmitter position error that is only in $\hat{r}$ as shown in Figure 10.4.

$$\begin{aligned}\Delta R_{err}(n,i) &= |R_0\hat{r} + (y_0 + n\Delta y)\,\hat{y} + R_{err}\hat{r} - \vec{P}_i| + |\vec{P}_i| \\ &\quad -|R_0\hat{r} + (y_0 + n\Delta y)\,\hat{y} + R_{err} - 0\hat{r}| \qquad (10.6)\end{aligned}$$

The vector $\vec{P}_i$ has components $\left(P_i^{\hat{y}}, P_i^{\hat{r}}\right)$ in the $\hat{r}$ and $\hat{y}$ directions, respectively. Assuming that $R_0 \gg R_{err}, y_0, P_i, n\Delta y$ and that terms of R_0^{-4} and smaller can be ignored, it can be shown using a binomial expansion that the difference between the assumed ΔR and the actual ΔR_{err} is the important quantity as that will show the mismatch in the expected phase history to the actual phase history. It can be shown that:

$$\begin{aligned}E(n,i) &= \Delta R(n,i) - \Delta R_{err}(n,i) = \frac{R_{err}P_i^{\hat{y}}}{R_0^2}\left(n\Delta y + \frac{P_i^{\hat{y}}}{2} + y_0\right) \\ &\quad - \frac{R_{err}}{R_0^3}\left(P_i^{\hat{r}}\,(n\Delta y)^2 + P_i^{\hat{y}2}\left(\frac{R_{err}}{2} + P_i^{\hat{r}}\right) + P_i^{\hat{r}}y_0^2\right. \\ &\quad \left. - n\Delta y\left(R_{err}P_i^{\hat{y}} + P_i^{\hat{r}}P_i^{\hat{y}}\right) + y_0\left(2n\Delta y P_i^{\hat{r}} + R_{err}P_i^{\hat{y}} + 2P_i^{\hat{r}}P_i^{\hat{y}}\right)\right) \\ &\quad + \frac{\dots}{R_0^4} \qquad (10.7)\end{aligned}$$

If suitable values are used, e.g. R_0 (800 km), n ($-10{,}000$ to $+10{,}000$), Δy gives the position between pulses, so assuming an orbital velocity of 7.5 km/s and a 3-kHz PRF Δy (7,500/3,000 = 2.5 m), y_0 (0 m), P_i (100.0, 100.0), then a graph of the range error vs pulse can be formed and is shown in Figure 10.5.

The error manifests itself as a very small offset in range (~10 μm) and an approximate linear range ramp over the aperture. This linear range ramp will have the

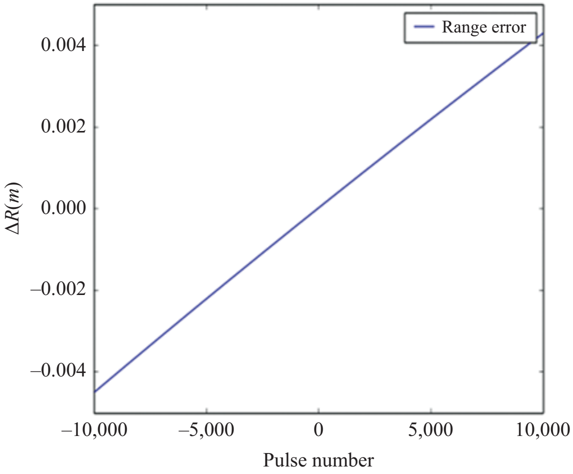

Figure 10.5 Graph showing the amount of range error over the course of the imaging aperture computed from (10.6) using representative values. The centre of aperture point is given as pulse number 0

effect of causing a linear phase ramp over the aperture, which will cause an azimuthal shift. However, due to the small amplitude of this phase ramp, the azimuthal shift will be quite small. As the magnitude of P_i increases, the effects of the error become larger as shown in Figure 10.6.

As can be seen from Figure 10.6, as the magnitude of P_i increases, the size of the error also increases and also becomes more non-linear. The non-linearity will have a defocussing effect on the created image. From Figure 10.6, it can also be seen that the size of the error increases more rapidly with increases in displacement in the along-track position than it does with increases in the transmitter–receiver displacement.

Unfortunately, due to the mathematical derivation used to form (10.6), it is impossible to use larger values of P_i or R_{err} without encountering significant numerical errors. Further work will be undertaken to improve the error model and to incorporate along-track errors from the transmitter.

10.6 Image formation

The typical algorithms used for SAR image formation are the polar format algorithm (PFA), the range migration algorithm (RMA, also known as omega-K) and the back-projection algorithm (also known as time domain processing) [2,3].

There are advantages and disadvantages to each of these algorithms, which are summarised in the following table. Due to the nature of the imaging geometry used with near-range returns from targets close to the receiver and with the inherent wide

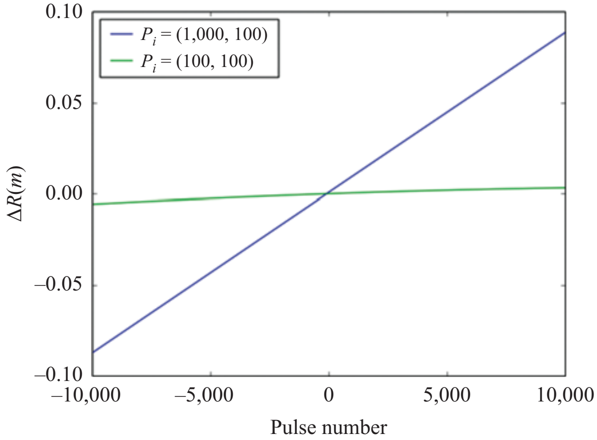

Figure 10.6 Graph showing the variation in range error as a function of target position. As the distance increases between the target and the receiver, the range error becomes larger and more non-linear. Vector $\vec{\boldsymbol{P}}_i$ *has components* $(\boldsymbol{P}_i^{\hat{y}}, \boldsymbol{P}_i^{\hat{r}})$

Table 10.1 A comparison of image formation techniques for bistatic SAR

Algorithm	**Advantages**	**Disadvantages**
PFA	Speed (fast) Low memory requirements	Assumes planar wavefronts
RMA	No planar wavefront assumption	Large memory requirements
Back-projection	No assumptions	Speed (slow)

significant angular spread of target positions, this makes it more likely that there will be significant wavefront curvature. This can be noticed when an image is formed using PFA on such an imaging geometry as it will show significant distortions in areas of the scene close to the receiver. From Table 10.1, it can be seen that the back-projection algorithm is the preferred choice, especially if there are no time constraints.

The implementation of the back-projection algorithm that has been used to process data in this report had been written to exploit the ‘embarrassingly parallel’ inherent nature of the back-projection algorithm. In order to fully exploit the performance available in modern computing devices, it had been coded to run using the OpenCL environment and can exploit the hundreds of threads (execution units) available on modern GPU cards.

10.7 Experimental validation of semi-cooperative bistatic SAR signal processing

In order to demonstrate the concept of performing bistatic image formation from a fixed receiver using a space-based SAR system as an illuminator and to validate the output of the transmitter location error work, a semi-cooperative bistatic data collection activity was undertaken. Cosmo-SkyMed was used as the semi-cooperative space-based transmitter, and a fixed ground-based receiver was deployed in the main beam in the Portsmouth region of the United Kingdom.

An overview of the system used for collections is given in Table 10.2.

The Cosmo-SkyMed SAR constellation [12] was used in enhanced spotlight mode on a descending pass and used horizontal polarisation.

An example of bistatic image formed using an accurate TLE model is shown in Figure 10.7(b). There is some roll off in SNR towards the edges of the beam; however, it can be seen that the image is well focussed throughout the swath (the receiver is located in the top right corner of the image).

The optical image is shown in Figure 10.7(a) for comparison and it can be seen that there is a good correspondence between features in the bistatic and the optical images. Although well focussed, there is a small range offset in the bistatic image (Figure 10.7(b)) compared to the true underlying scatterers. This range error increases with distance from the receiver as described in previous sections. This can be attributed to minor errors in the TLE model used to derive transmitter locations. Further work is required to understand the extent to which these errors may impact coherent combination of datasets.

A bistatic image formed using a TLE several weeks ahead of the collect and SGP4 to propagate forward to predict transmitter locations is shown in Figure 10.7(c). It has been shown [15] that errors in orbit predictions using TLEs increase the further ahead in time one estimates the orbit. The spatially variant geometric distortions due to errors in transmitter location can clearly be seen in Figure 10.7. The amount of defocus and displacement increases with distance from the receiver as predicted. The phase errors introduced due to transmitter location error also impact on the

Table 10.2 Overview of receiver system used for bistatic collection of Cosmo-SkyMed illumination

Disposition	Stationary ground-based receiver
Frequency band of operation	X-band (8–12 GHz)
Number of Rx nodes	1 receiver node
• *channels per node*	• 2 coherent channels
• *digitisation*	• 8 bits real at 2G samples/s
• *IMU*	• N/A
Number of Tx nodes	0 transmit nodes
Synchronisation	Rubidium frequency standard
Coverage	~30 degrees beam width
Size and weight	0.7 × 0.6 × 0.8 m box ~30 kg

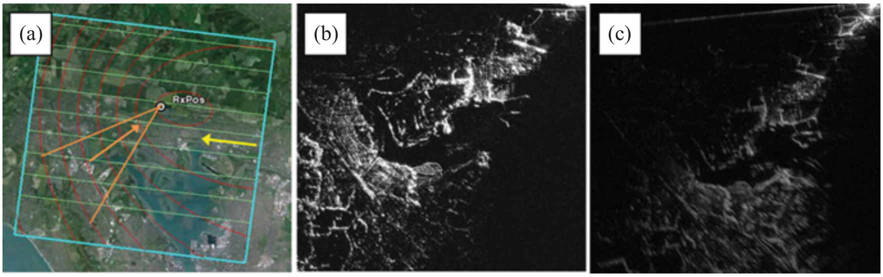

Figure 10.7 (a) Collection geometry overlaid on a satellite image of the region, the yellow arrow shows the direction of incoming energy and the orange arrow indicates reflected energy from the target area to the receiver, iso range and iso-Doppler lines are shown in red and green, respectively, (b) example bistatic image formed with an accurate TLE model for transmitter location prediction, (c) example bistatic image formed using a TLE several weeks ahead of the collect for transmitter location prediction. Image formed on a 4,096 × 4,096 grid with 1 m post-spacing

contrast-to-noise ratio of the image as energy from a single scattering body becomes spread across many resolution cells. Autofocus was not used in this image formation process; however, such a technique may help in both focussing defocussed images and determining transmitter position more accurately. Currently, images are formed using back-projection onto a regularly spaced grid covering the area of interest. The application of autofocus techniques would require the image formation to be carried out on a range-Doppler grid and is an area for future study.

It may be possible, given a known receiver position and an accurate digital elevation model of the local terrain to use tie points on the ground and an iterative approach to determine the precise location of the transmitter, analogous to the rigorous-range-Doppler method. This would allow for appropriate phase correction terms to be derived for each bistatic image formed. Future work will look to implement such a method and demonstrate the reduction in phase errors.

Such geometric distortions and phase errors will impact on the success of coherent combination of multiple datasets to form a multistatic image. The precision required in knowledge of transmitter location and pulse timings increases and the number of datasets for coherent combination increases. Future work will determine the required transmitter position precision as a function of N multistatic datasets for coherent combination.

10.8 Conclusions

Semi-cooperative bistatic SAR has been demonstrated using Cosmo-SkyMed as an illuminator of opportunity and a static two-channel ground-based receiver. A general discussion of hardware considerations to be taken into account when expanding to a multistatic scenario has been presented. A simple error model for predictions in transmitter location has been derived and the impact of such errors has been shown in example imagery. Defocussing and range migration are the main effects when large errors exist in the predicted transmitter location. Further work is required to extend the error model and to determine the required precision to allow coherent combination of bistatic datasets.

References

[1] G.A. Yates. *Bistatic Synthetic Aperture Radar.* s.l.: PhD Thesis, University College London, London, January 2005.

[2] W. Carrara, R. Goodman, and R. Majewski. *Spotlight Synthetic Aperture Radar.* s.l.: Artech House, Norwood, United States, 1995. ISBN 0-89006-728-7.

[3] C. Jakowatz, D. Wahl, P. Eichel, D. Ghiglia, and P. Thompson. *Spotlight-Mode Synthetic Aperture Radar: A Signal Processing Approach.* s.l.: Springer, New York, United States, 1996. ISBN 0-7923-9677-4.

[4] G. Stimson, H. Griffiths, C. Baker, and D. Adamy. *Introduction to Airborne Radar.* s.l.: IET, New York, United States, 2014. ISBN 978-1-61353-022-1.

[5] I. Walterscheid, T. Espeter, A.R. Brenner, *et al.* Bistatic SAR experiments with PAMIR and TerraSAR-X – setup, processing and image results. *IEEE Transactions on Geoscience and Remote Sensing.* 2010, Vol. 58, 8: pp. 3268–3279.

[6] P. Krysik, L. Maslikowski, P. Samczynski, and A. Kurowska. *Bistatic ground-based passive SAR imaging using TerraSAR-X as an illuminator of opportunity.* Adelaide: IEEE 2013 International Conference on Radar, 2013. ISBN 978-1-4673-5177-5.

[7] S. Guillaso, A. Reigber, L. Ferro-Famil, and E. Pottier. Range resolution improvements of airborne SAR images. *IEEE Geoscience and Remote Sensing Letters*. 2006, Vol. 3, 1: pp. 135–139.

[8] C. Prati, and F. Rocca. Improved slant-range resolution with multiple SAR surveys. *IEEE Transactions on Aerospace and Electronic Systems*. 1993, Vol. 29, 1: pp. 135–143.

[9] G. Yates, A.M. Horne, A.P. Blake, and R. Middleton. Bistatic SAR image formation. *IEE Proceedings of Radar and Sonar Navigation*. 2006, Vol. 153, 3: pp. 208–213.

[10] G.E. Smith, K. Chetty, C.J. Baker, and K. Woodbridge. Extended time processing for passive bistatic radar. *IET Radar, Sonar and Navigation*. 2013, Vol. 7, 9: pp. 1012–1018.

[11] R. Reeder, W. Green, and R. Shillito. *Analog-to-Digital Converter Clock Optimization: A Test Engineering Perspective*. 02, s.l.: Analog Dialog, Norwood, United States, 2008, Vol. 42.

[12] Italian Space Agency COSMO-SkyMed Mission. *COSMO-SkyMed SAR Products Handbook*. Rev.2 09/06/09, 2009.

[13] D. Allan. Statistics of atomic frequency. *Proceedings of the IEEE*. 1966, Vol. 54, 2: pp. 221–230.
[14] G. Krieger, and M. Youmis. Impact of oscillator noise in bistatic and multistatic SAR. *IEEE Geoscience and Remote Sensing Letters*. 2006, Vol. 3, 3: pp. 424–428.
[15] D.A. Vallado, P. Crwaford, R. Hujsak, and T.S. Kelso. *Revisiting spacetrack report #3*. s.l.: AIAA/AAS Astrodynamics Specialist Conference, Keystone, CO, 2006 August 21–24.

Chapter 11

Lesson learnt from NATO SET-196 RTG on 'multichannel/multi-static radar imaging of non-cooperative targets'

Marco Martorella[1] *and David Greig*[2]

Research is carried out at different levels, from basic to applied research, and within a variety of bodies, which span from academia to industry and government institutions. NATO has its own organisation that deals with science and technology, namely the Science and Technology Organisation. Within such an organisation, a number of research-related activities are carried out. In particular, the Collaborative Support Office is in charge of fostering and supporting research collaboration among NATO and NATO-friendly nations. It is within this framework that the Research Task Group (RTG) NATO SET-196 on 'Multichannel and Multi-static Radar Imaging of Non-Cooperative Targets' was created and where more than ten nations have contributed to the results that have been presented in this book.

11.1 The role and impact of NATO SET-196 RTG within and outside NATO

NATO SET-196 has dedicated all its effort in trying to study algorithms and systems that make use of multiple channels and multiple nodes to improve imaging capabilities of non-cooperative targets. This aspect is a fundamental importance to NATO and the Alliance as it provides the basis for improving target classification. Target classification is one of the pillars of intelligence surveillance and reconnaissance, which represents the basic input to tactical and strategic command and control. The results obtained by SET-196 have been recognised within NATO as a step forward in this direction and follow-on activities have spun off it, such as the SET-250 RTG on 'Multidimensional Radar Imaging'. It is also important to highlight the impact of SET-196 on the open literature and scientific community. In fact, releasable results have been published in various journals and conferences and then reviewed and collected in this

[1] Department of Information Engineering, University of Pisa and Radar and Surveillance Systems, CNIT, Pisa, Italy
[2] Leonardo, Edinburgh, UK

book, which is offered as well to the open literature. Other than producing relevant and solid results, SET-196 has provided an outstanding platform for interaction and collaboration among more than ten nations and has fostered several collaborations outside the NATO framework.

11.2 Progress made by NATO SET-196 within multidimensional radar imaging

Imaging radars are of great importance in the increasing complex operational environment of the modern military world where it is necessary to not only detect but also recognise and identify objects of interest quickly and with a high level of confidence. Radar imagery gives a view of the world at radio frequencies driven by the resolution achievable within the bandwidth of the receiver, so it does not look like optical imagery requiring a high degree of expertise and experience to interpret visually. This has led to the development of Automatic (or sometimes Aided) Target Recognition (ATR) algorithms which present a classification of type of target imaged by the radar to the operator. ATR algorithms are well advanced for recognition of medium and large air and maritime targets and are reasonably mature for static ground targets imaged by high-resolution synthetic aperture radar (SAR). Nevertheless, they are less mature for smaller targets and moving ground targets and, in general, there is no ATR algorithm which could not be improved by higher probability of correct target recognition and/or lower false target recognition. ATR performance is driven by the quality of the imagery input to the process. Increasing resolution of radar imaging puts demands on bandwidth and processor throughput which may be difficult and expensive to meet. There are also physical limitations on what resolution can be meaningfully achieved related to the wavelength of the imaging radar, lower frequency radars having fundamentally lower resolution capability (which has to be traded off against their inherently longer range and wider area coverage). In terms of system design, therefore, the addition of other dimensions to 2-d radar imagery may be more easily achieved than increasing resolution and can offer enhanced ATR performance from a classifier which exploits the unique features of the target measured in the additional dimensions of the data. Moving from 2-d to 3-d imaging is the obvious approach (as in Chapters 2, 5 and 9). The additional dimensions could be more abstract also, such as variation in frequency (Chapter 7), exploiting features unique to certain targets (Chapter 8) or removing signals which reduce image quality (Chapter 3). Introducing multidimensional imaging to a radar system will have an impact on systems design. Increasing the number of channels and/or antennas on a system introduces complexity which can be difficult and expensive to implement unless it maps onto existing architectures. Using multiple simultaneous sources of data to form multidimensional images is the alternative, which would increase the overall cost of a system unless existing signals can be exploited for the purpose. This is why the use of passive radar (Chapters 4, 6 and 10) is strongly connected with viable methods of multidimensional imaging. Multidimensional imaging techniques are most likely to be adopted if they can be applied in existing operational radar systems rather than require the development and procurement of bespoke systems. For multichannel imaging algorithms, the techniques which can produce a performance benefit with a low number of channels (2, 3 or 4 typical of monopulse radars) are those which can be considered for immediate exploitation. Cooperative and coherent uses of multiple radars along a horizontal or vertical baseline or reconstruction of multidimensional data from multiple passes of a scene are alternative systems set ups to support imaging. In particular, vertically separated radar channels or antennas allow for the measurement of target height via interferometry (Chapters 2 and 9). Such methods could potentially be implemented in radars with elevation monopulse channels enabled, but if a wider baseline is required for the method to achieve the desired accuracy in height, then two antennas or multiple passes at varying height will be required.

Although it may sound obvious that either adding channels (multichannel, multifrequency or fully polarimetric) to a radar imaging system or operating simultaneously a number of similar radar imaging systems (multi-static systems, multiple nodes) would improve the system performance, it is not so obvious what the quantitative advantage would be and at what cost. Furthermore, adding channels or nodes provides extra degrees of freedom to the overall systems, which brings in the additional problem of how to optimise it. The state-of-the-art before SET-196 did not provide straight answers to these questions. SET-196 has made significant effort to fill scientific and technological gaps and provide some answers to such questions. In summary, the contribution of SET-196 may be summarised as follows:

- Multichannel and multi-static radar imaging systems have been defined in order to provide a precise collocation within standard definitions in radar imaging and to avoid ambiguities and misuse of technical nomenclature.
- An extensive review of the state-of-the-art has been made to report on the latest scientific and technological advancement in multi-static and multichannel radar imaging. A deep analysis has also been conducted and reported that identifies gaps that should be filled in order to enable effective multichannel and multi-static radar imaging.
- Spatial/angular decorrelation effects have been studied and the point-like target model has been extended with a wire model, to account for spatial-angular decorrelation effects.
- A thorough analysis has been carried out at a system level to identify the key aspects to enable multichannel and multi-static radar imaging at operational level.
- Multichannel and multi-static radar imaging algorithms have been developed theoretically, implemented and tested on simulated and real data.
- System demonstrators have been built to prove the concept and demonstrate the improvement achievable with multichannel and multi-static radar imaging systems.
- Simulators have been developed and simulations have been run to generate data for phenomenological analysis and for testing algorithms.
- Trials have been organised and run to collect a large and extensive amount of data to be distributed among the SET-196 participants.

- Extensive data analysis has been run on the amount of data collected during the NATO SET-196 trials and on additional data made available by members of the RTG.

11.3 Lesson learnt and open issues

NATO SET-196 has taught us a great deal concerning the use of multidimensional radar imaging system, specifically when dealing with multiple channels and multiple nodes. Developing and optimising a multichannel/multi-static radar imaging is not only a fascinating challenge but also a very hard one, also considering the costs that are associated with radar imaging systems. Nevertheless, the joint effort of more than ten nations has allowed for quite a lot of questions to be answered, and not just theoretically. Scaled and affordable demos have been developed and built in order to analyse the quantitative effects. Real, although scaled, systems have highlighted issues and complexity that were not entirely foreseen theoretically and by making use of simulation, such as synchronisation effects, target decorrelation effects to not mention the amount of data to be processed by multichannel and multi-node systems. It should be mentioned that NATO SET-196 was somehow limited in its analysis as it did not go through the alley of analysing performances at a classification level. Involving the entire classification process was beyond reach given the available resources and the time. Nevertheless, in some cases, the results clearly indicated the quantitative advantage of multichannel and multi-static vs single-channel/single-node systems.

As for much of the analysis presented here, post-processing of data collected by individual sensors is immediately applicable for intelligence gathering and reconnaissance. For real-time, distributed and multidimensional imaging systems, the ability to communicate data around the nodes must be considered. Issues related to synchronisation and secure data transfer have not been addressed completely by NATO SET-250 and they will require further effort to be solved.

11.4 The way ahead for multidimensional radar imaging systems

NATO SET-196 provided some answers to questions that were posed prior to the beginning of the RTG. Nevertheless, some of such answers cannot be stated as complete. Moreover, some additional questions have arisen that need to be answered, more specifically, the role of other dimensions, such as frequency and polarisation, in addition to multichannel and multi-static. Is there an optimal configuration that sees the use of multidimensional radar within a cost–benefit paradigm? Is this scenario/application dependent? Also, how important is flexibility compared to fixed configurations? Some ideas of the future of multidimensional radar imaging are given in the next sections.

11.4.1 Towards affordable multidimensional radar imaging systems

NATO SET-196 has produced a significant advancement in multidimensional imaging techniques some of which can be considered for immediate exploitation. Techniques which do not map immediately to enhancements of current systems can be used to inform requirements for emerging and future systems. The design of a multichannel system is based around the requirements for established multichannel techniques, such as mono-pulse, adaptive beam forming (ABF) and space time adaptive processing (STAP). Multichannel imaging methods need to be considered when specifying a new system. If channelisation for imaging, STAP and ABF can be met by a common set of system requirements, then there is a reduction in the complexity (and thus the cost) of the system which makes the adoption of multichannel imaging into the system more likely. Note that for an operational system, the calibration of channels needs to be considered which may have to be an embedded process to allow for system variations in operation (e.g. operating temperature). In designing multi-node, multidimensional imaging techniques are likely to drive the requirements on the data which must be shared between nodes, both the volume of data and the maximum time allowable to transfer it which defines the bandwidth of the communication method applied. The lack of available bandwidth in communications may be the limiting factor in the implementation of multidimensional imaging, in which case some adaptation of imaging algorithms to remain effective with lower bandwidth communications may have to be considered. Robustness to the loss of data from one or more nodes of the system must also be considered. If multi-node system fails to be effective with the loss of a single node, then the operational value of the system is greatly reduced and the argument for procuring such a system is made harder. This is especially true if each of the nodes is of a similar cost and complexity as a typical mono-static (one-dimensional) imaging system. Passive radar is an attractive concept for system designers. The need to transmit from a radar is a major contributor to the size, weight and power of the system. Finding a slot in an increasingly crowded spectrum where your waveform can fit becomes more problematic every year, especially for imaging radars which require a high bandwidth. Given that RF signals are now so ubiquitous, why not exploit the energy that is already in the environment than generate your own? Despite the obvious advantages, passive radar is being introduced as an operational capability slowly. This is partly due to a lack of maturity in the signal processing techniques for passive radar, the work presented in Chapters 4, 6, 8 and 10 will help address this capability gap. There are also operational restrictions in the deployment of passive radars. If the signals being exploited are not under friendly control, they could be switched off or corrupted as a defensive measure. This would likely limit the use of non-cooperative passive radar over hostile territory to a secondary capability or for covert surveillance. Passive SAR or ISAR may, however, be the only realistic method of performing airborne imaging at long wavelengths by exploiting low-frequency illumination sources (e.g. DVB-T as in Chapter 4) as the size weight and power requirements of active low frequency radars are generally prohibitive. For defence and security in friendly territory, the availability of signals can be assumed, though the coverage provided by sources of illumination which can be exploited does introduce further restrictions on the deployment of passive radars. In populated areas, radio, television and communication signals are pervasive, not so in remote sparsely populated regions over in the open sea away from land ('blue water' operations). Passive ISAR, as discussed in Chapter 4, is more applicable to the defence of friendly harbours or coastlines than imaging ships in international waters. It is also the case that most commercial broadcasters are intended to be used by ground-based users, hence their signals are directed downwards. This is useful for imaging of ground and sea targets (close to shore), less so for high flying air targets. Helicopters and smaller unmanned aerial vehicle (UAVs) operate at lower altitudes making the measurement of micro-Doppler signatures discussed in Chapter 8 operationally viable. Satellite systems provide global coverage and thus are potentially cooperative or non-cooperative sources of illumination. The various networks of global positioning satellites provide all pervasive coverage of the planet; unfortunately, their signals are so weak that they are difficult to exploit without unfeasible integration times. Earth imaging radar systems, such as Cosmo-SkyMed, are a far more feasible source of illumination, as demonstrated in Chapter 10. There are only a few of these systems available, meaning that their time is much in demand and coverage requires awaiting them being in the right part of their orbit at the right time. A potential solution to this shortcoming may be found in the use of in-orbit ad-hoc illuminators, therefore enabling specific and optimised illumination from space.

11.4.2 Clusters and swarms

Small satellites which can be launched more cheaply into low-Earth orbit are an emerging technology which have applications in sensing and communications. Compared to a system like Cosmo-SkyMed, these 'micro' or 'cube' satellites have a much lower payload and much lower power available on then as well as short lifespan (months rather than years). Their much lower cost, however, would increase the possibility of a larger number of cheaper smaller satellites being launched to provide particular capability in a particular region for a limited period of time. One such application could be for a cluster of small satellites to be used to provide radar imaging capability for Persistent Wide Area Surveillance. Size, weight and power restrictions mean that conventional monostatic imaging radars cannot be installed as a payload on these small systems. Novel technology, such as folding antennas, may allow the aperture of a satellite radar to be increased, but this only partly compensates for the lack of power. Even in low-Earth orbit, the range to the fourth power fall-off for monostatic radars means that much of the available power aperture of the radar used up simply by the signal reaching the surface of the Earth. If these systems were used as illumination sources, this becomes a range squared fall off which could provide enough illumination for passive radars operating much closer to the area to be imaged. Knowledge of where the satellite clusters are is needed for cooperative operation, the infrastructure for satellite communications is well established and would only require narrowband communication of position, waveform and timing information which puts less demand on the limited resources on the satellite than downlinking imagery from space would.

Examples may be found at lower altitudes (not in space) when considering swarms of small UAVs which operate cooperatively and combine information so that a larger number of smaller, less capable sensors can emulate or exceed the performance of a smaller number of more capable but larger, more expensive (and more vulnerable) sensors. Like small satellites, small UAVs suffer from significant size, weight and power restrictions. They must also be disposable if they can be recovered or returned so much the better but this cannot be relied upon. This means that any RF sensor on a small UAV must be very low power (so almost certainly passive), very low cost and compact. The requirement to be passive means relying on an illuminator of opportunity like a television signal or a cooperative illuminator like a satellite cluster. The requirement to be compact will restrict the antenna size meaning that small high-frequency antennas are best suited as a payload. Unfortunately, this is unlikely to be compatible with the lower frequency signals from the illumination sources previously mentioned. There is also the need for the sensor to instantaneously transmit its data to the central hub to be combined to form a radar image. A likely intermediate step to UAV swarms is for larger numbers or lower cost sensor systems to be deployed on medium-sized UAVs. Such systems are still much smaller and cheaper than current large, high-value surveillance assets and may be deployed in larger numbers as part of a network-enabled capability but offer more size, weight and power for sensors and communications with respect to small UAVs. Such platforms would not be disposable but could be considered as semi-expendable, the occasional loss of one would not reduce capability or incur a major expense in replacing. Cooperative use of such platforms with both passive and active radar systems would still require the combination of data from multiple platforms to enhance overall sensing capability. The multidimensional imaging techniques discussed in this book would readily find an outlet to make networks the performance of a network of smaller, cheaper, passive and active radars greater than the sum of its parts.

This page intentionally left blank

Index

adaptive beam forming (ABF) 329
additive white Gaussian noise (AWGN) 23, 193
aerodynamics of copter's blades 259
airborne PCL, challenges for 200–7
analogue-to-digital convertors (ADCs) 313–14
antenna system 131
Astice 125–8, 296, 298
  multistatic final fusion 305–6
  multitemporal final fusion 303
  multiview final fusion 307
augmentation techniques 176–9
augmented DRT 143
Automatic (or Aided) Target Recognition (ATR) algorithms 326
automatic identification system (AIS) 132, 287
azimuth compression 200

back-projection algorithm (BPA) 165, 200, 320
backscattered signal 32
basis pursuit de-noising 170
best frame selection algorithm 119, 132
bidimensional fast Fourier transform (2D-FFT) 53
bistatically equivalent monostatic (BEM) radar 94, 116
bistatic imaging geometry 312–13
bistatic ISAR theory 110
blade flashes 265
block coherence 242
block orthogonal matching pursuit (BOMP) 239, 242, 249
block sparsity 241
bounding box (BB) 112
broadcast signals 192
bulk delay offset 313–14

Cartesian reference system 209
channel transfer function (CTF) 193, 196
CLEAN technique 21
clock drift 314–15
clusters and swarms 330–1
clutter Doppler shift 57
clutter model 55–60
clutter range dependence 56, 68, 98
co-channel interference (CCI) 189
coherent fusion approach 290
coherent processing interval (CPI) 54, 119
commercial off-the-shelf (COTS) 109
compression rate (CR) 134
compression sensing (CS) 110, 121
  -based ISAR imaging 121–3
  -based ISAR reconstruction algorithm 134, 138
conventional ISAR imaging 119–21
Cosmo-SkyMed 315, 321
cross-ambiguity function (CAF) 110
"cross-range scaling" algorithm 132

data fusion 290
"detection and tracking" block 112
digital elevation model (DEM) 89
digitally coded OFDM broadcast signals 193

digital video broadcast-terrestrial (DVB-T) signal 110, 189, 192
  received DVB-T signal model 192–3
  simulation of DVB-T range pulse response 212–19
    extended scene at mid-acquisition 213–16
    extended scene over entire acquisition 216–19
    scene center at mid-acquisition 212–13
direction of arrival (DoA) 57
discrete Fourier transforming (DFT) 195
Doppler–radar tomography (DRT), multistatic 171–9
  cross-range bandwidth and resolution 171–2
  Doppler–radar tomography (DRT) algorithms 174–5
  slow-time *k*-space 172–4, 176
    FrFTS augmentation 178–9
doubled weight vector 69

earth imaging radar systems 330
echo signal 262
  generic model of 262–3
  main rotor blade echo model 263–8
  tail rotor blade echo model 268–9
European remote sensing (ERS) 211

far-field approximation 150
fast Fourier transform (FFT) 119, 142
fast-time *k*-space 151–2
  populating 152–3
flight paths 181
foreshortening 238
Fourier-based methods 150–64
  experimental demonstration 160–2
  far-field approximation 150
  fast-time *k*-space 151–2
  full multistatic geometry, extension to 153–4
  image focusing controls (IFCs) 154–5
  image resolution and contrast 158
    3D *k*-space 160
    2D *k*-space 158–60
  nonuniform FFT for image inversion 157
  numerical methods for image optimization 162–4
  populating a fast-time *k*-space 152–3
  system diversities 155–7
fractional Fourier transform (FrFT) 177
Fraunhofer approximation 149, 180
frequency modulation (FM) radio 190
FrFTS augmentation 177–8
full multistatics 153
full width at half maximum 158
fully articulated rotor system 260–1

geostationary broadcast illuminators 190
global navigation satellite system (GNSS) 190
global positioning system (GPS) 190, 124, 287, 314
Google Earth image 226–7
Green's functions 149–50
ground clutter 105

HABRA interferometric sensors 295
HABRA main parameters 297
height error 30, 32–3
  standard deviation of 34
helicopter
  geometric model of 257
    echo of helicopter's fuselage 257–8
    main rotor 258–61
    rotor parameters 262
    tail rotor 261
  lifting force of 259
  methods for classification of 256
  simplified model of 258
helicopter echo 255, 269
high-resolution range (HRR) 256
Huygens–Fresnel principle 262

illuminators of opportunity (IOs) 123, 189
image contrast (IC) 119
image contrast (IC)-based autofocus (ICBA) algorithm 54, 119
image focusing controls (IFCs) 154
image formation 55, 147, 200
image projection plane (IPP) 15, 235, 288
image reconstruction 147, 244
independent and identically distributed (IID) assumption 55–6, 68
inertial measurement unit (IMU) 199
interferometric ISAR (InISAR) system 15–17
inter-symbol interference (ISI) 192
inverse Fourier transform (IFT) 112
inverse synthetic aperture radar (ISAR) 5, 15, 109
  algorithm description 17
    multichannel CLEAN algorithm 21–3
    multichannel ISAR signal model 18
    received signal modelling 18–21
    system geometry 18
    3D reconstruction processing 23–7
  Compressive sensing (CS)-based ISAR imaging 121–3
  conventional ISAR imaging 119–21
  experimental results 37–42
  image pre-processing algorithm 111
  performance analysis 28
    performance indicators 29–30
    scatterers realignment 28–9
    soft assignment 29
  processing 53–4
    cross-range scaling 55
    image formation 55
    motion compensation 54
    time window selection 54
  from SAR techniques 110
  simulated results 30–6
"ISAR pre-processing" block 111
Italian National Inter-University Consortium for Telecommunications (CNIT) 123

jet aircraft's engine 257
jet engine modulation (JEM) 257

K-space 208, 215

LabRadOR, software-defined radar 247
Least Angle Shrinkage and Selection Operator technique 170
least square error (LSE) approach 134
line of sight (LoS) 16, 200
live signal processing experiment 279
  data pre-processing 279–81
  measurement campaign 279
  results 281–4
long-term evolution (LTE) 190

main rotor 258–61
  spectrogram-based ISAR image of 283
main rotor blade echo model 263–8
main rotor echo 276
main rotor imaging algorithm based on target echo spectrogram 276–8
mask 164
match filter (MF) 68, 154, 190
matrix-based methods 164–71
  near-field problem formulation 165–7
  rigorous inversions 167–9
  sparse regularization 169
    $$-norm minimizations 169–70
    mixed norm minimizations 170–1
matrix inversion problem 167
measurement campaign set-up 296
Mi-2 helicopter rotor model 267
monostatic 3D InISAR reconstructions 289
motion compensation technique 54

Moving Target Indicator (MTI) techniques 47
multichannel CLEAN (MC-CLEAN) technique 17, 21–3
  block diagram 22
multichannel ISAR signal model 48–51
multichannel/multi-static ISAR systems 15, 18
multichannel radar imaging systems 6
multichannel range–Doppler (MRD) processing 74
multidimensionality 5
multifrequency networks (MFNs) 192
multi-frequency radar imaging systems 7–8
multi-frequency systems, use of 7
multi-pass SAR 143
multi-PCL–SAR for improved range resolution 207
  digital television (DVB-T) range pulse response 212–19
    extended scene at mid-acquisition 213–16
    extended scene over entire acquisition 216–19
    scene center at mid-acquisition 212–13
  optimal trajectories for 219–22
    derivation of a circular trajectory for the first platform 219–20
    derivation of second platform trajectory 220
    extended scene over entire acquisition 220–2
  range resolution improvement principle 207–11
  scenario for 211–12
multiple radars, cooperative uses of 327
multi-polarisation radar imaging systems 7
multistatic and multitemporal data, application of multiview 3D to combination of 305–8
multistatic configuration 292–3, 312
multistatic data 292
  application of multiview 3D to 304–5
multistatic fast-time k-space and image inversion 151–3
multistatic imaging 6
multistatic imaging geometry 312
multistatic radar-imaging systems 5–6
multistatic systems 8
multitemporal 3D reconstruction 300
multitemporal configuration 292
multitemporal data 291
  application of multiview 3D to 296–303
multiview 3D, application of
  to combination of multistatic and multitemporal data 305–8
  to multistatic data 304–5
  to multitemporal data 296–303
multiview 3D InISAR image fusion technique 289–95
multiview configuration 293
multiview fusion algorithm 289

narrowband operation 145
“narrowband” signal 172
NATO SET-196 RTG 325
  multidimensional radar imaging systems 328
    affordable 329–30
    clusters and swarms 330–1
  open issues 328
  role and impact of 325–6
  within multidimensional radar imaging 326–8
natural scenes, classification of 7
near-field problem formulation 165–7
non-cooperative identification (NCI) 235
noncooperative moving targets, high-resolution imaging of 51
  ISAR processing 54
    cross-range scaling 55
    image formation 55
    motion compensation 54
    time window selection 54

non-cooperative target identification, recognition and classification (NCTI/R/C) 287
nonuniform FFT (NUFFT) 157

operational radar systems 9
optics theory 183
orthogonal frequency division modulation (OFDM) 190, 192
orthogonal waveform diversity 157

P92 128–30
passive bistatic radar (PBR) 110
passive coherent location (PCL) 189
passive coherent location (PCL)–synthetic aperture radar (SAR) 189
  image results of 225–7
  multi-PCL–SAR 207
    digital television (DVB-T) range pulse response 212–19
    optimal trajectories for 219–22
    range resolution improvement principle 207–11
    scenario for 211–12
  scenario definition 222–5
    description of the receiving system 224–5
    location of the measurement campaign 222–4
  signal processing for 191
    airborne PCL, challenges for 200–7
    digital video broadcast-terrestrial (DVB-T) signal, structure of 192
    image formation 198–200
    range compression 196–7
    received DVB-T signal model 192–3
    synchronization and reference signal reconstruction 193–6
passive inverse synthetic aperture radar (P-ISAR) technique 109
  cooperative targets – WUT system 123
    Astice 125–8
  data pre-processing 111
    merging of RD maps and ISAR data formation 115–18
    target extraction 112–15
  ISAR image processing 119
    compression sensing (CS) -based ISAR imaging 121–3
    conventional ISAR imaging 119–21
  non-cooperative targets – SMARP 130–7
passive radars (PRs) 109, 329–30
PIRAD system 37–9, 296–7
  2D ISAR images of 300
  Range–Doppler maps of 299
Point scatterer model 238
point spread function (PSF) 22, 143
polar format algorithm (PFA) 319
POLCLEAN technique 22
projection-slice theorem (PST) 141
projections onto convex sets (POCS) 162, 164
propeller aircraft, recognition of 257
PR processing 110
pseudo-ground truth 88
pseudospectrum 168
pulse repetition frequency (PRF) 58, 313

16-quadrature amplitude modulation (QAM) 202
“quasi-monostatic” geometry 212

radar-absorbing material (RAM) 224
Radar and Surveillance System (RaSS) 123
radar cross section (RCS) 311
radar image projection plane 3
radar imaging 109, 141
radar polarimetry 7
radar tomography (RT) 141

  - adaptability 146
  - advantage of 143
  - graceful degradation 146–7
  - modularity 146
  - signal processing, considerations for 182
  - system geometry, considerations with 179–82
    - image extent and aliasing 180
    - minimum distance 179–80
    - receiver platform flight paths 180–2
  - tomographic image formation 147
    - Fourier-based methods 150–64
    - matrix-based methods 164–71
    - multistatic Doppler–radar tomography 171–9
    - signal models 147–50
- radio-controlled (RC) helicopter
  - rotor's hub of 260
- range–Doppler (RD) map 39, 202, 204, 276, 296, 299
- range-Doppler (RD) technique 20, 55, 121
- range migration algorithm (RMA) 53, 319
- range resolution improvement principle 207–11
- reciprocal filter (RpF) 197
- reflectivity function 148
- Research Task Group (RTG) NATO SET-196 325
- rotary-wing aircraft parameters, radar measurements of 255
  - helicopter, geometric model of 257
    - helicopter's fuselage, echo of 257–8
    - main rotor 258–61
    - rotor parameters 262
    - tail rotor 261
  - helicopter classification, methods for 256
  - live signal processing experiment 279
    - data pre-processing 279–81
    - measurement campaign 279
    - results 281–4
  - main rotor imaging algorithm based on target echo spectrogram 276–8
  - method for determining rotor parameters 269
    - main rotor parameters 271–5
    - tail rotor parameters 275
  - problem formulation 255–6
  - propeller aircraft, recognition of 257
  - received echo signal, model of 262
    - generic model of 262–3
    - main rotor blade echo, model of 263–8
    - tail rotor blade echo model 268–9
- rotor echo recognition 257

- sample matrix inversion (SMI) 55
- SAR raw data simulator 89
- satellite systems 330
- scatterers realignment 28–9
- scatterers' height estimation error 30
- scattering centre extraction 17
- self-occlusion 4
- semi-cooperative bi/multistatic SAR 311, 315–17
  - experimental validation of 321–2
  - hardware considerations 313
    - analogue-to-digital convertors (ADCs) 313–14
    - clock drift 314–15
  - image formation 319–21
  - transmitter position, effect of errors in 317–19
- SET-250 RTG 5
- SGP4 algorithm 316
- signal-to-clutter ratio (SCR) 79
- signal-to-noise ratio (SNR) 144, 190
- single frequency networks (SFNs) 192, 223
- singular value decomposition (SVD) 168
- slow-time *k*-space 171–4
- SMARP system 130–7

smear-free standard DRT image 178
soft assignment method 29
space Doppler adaptive processing (SDAP) 60
  filtering process 66
space–time adaptive processing (STAP), for clutter suppression 60
  E-SDAP ISAR results 88–104
  joint E-SDAP ISAR 68–73
    optimum processing 68–70
    suboptimum processing 70–3
  joint SDAP ISAR 61–7
    optimum processing 61–5
    suboptimum processing 65–7
  SDAP–ISAR results 73–88
sparse regularization 169
  $$-norm minimizations 169–70
  mixed norm minimizations 170–1
sparsity-driven multistatic ISAR image reconstruction 235
  constraints 236
    foreshortening effect 238
    spatial decorrelation 236–8
  experimental results 247–9
  problem formulation 238–41
  reconstruction 241–4
  simulated example 244–7
spatial decorrelation 236–8
spatial diversity 142
synchronization signal generator 131
synthetic aperture radar (SAR) 5, 189
systems design considerations 8–9

tail rotor 261
tail rotor blade echo model 268–9
tail rotor blade geometry 268
tail rotor’s blade 268–9
“target extraction” block 112
3D fusion algorithm 291, 300
3D fusion block diagram 295
3D image fusion algorithm 294
3D interferometric ISAR (InISAR) imaging 287
3D *k*-space 160
3D radar systems 287
3D reconstruction processing 23–7, 41–2
  flowchart 17
Tikhonov regularization method 168
time window selection 54
tomographic image formation 147
  Fourier-based methods 150–64
    experimental demonstration 160–2
    far-field approximation 150
    image focusing controls (IFCs) 154–5
    image resolution and contrast 158–60
    multistatic fast-time *k*-space and image inversion 151–4
    nonuniform FFT for image inversion 157
    numerical methods for image optimization 162–4
    system diversities 155–7
  matrix-based methods 164–71
    near-field problem formulation 165–7
    rigorous inversions 167–9
    sparse regularization 169–71
  multistatic Doppler–radar tomography 171–9
    augmentation of the slow-time k-space 176–9
    cross-range bandwidth and resolution 171–2
    DRT algorithms 174–5
    example 175–6
    slow-time *k*-space 172–4
  signal models 147–50
tomography 141, 182
  illustration of 145–6
translational motion compensation (TMC) 153, 161
transmitter position, effect of errors in 317–19
truncated singular value decomposition (SVD) 168
2D-ISAR image 16

2D *k*-space 158
two-line element (TLE) data 316

ultra-high frequency (UHF) 201
ultralight aircraft 224–5
Universal Mobile Telecommunications System (UMTS) 110

vessel traffic service (VTS) 287
VHF/UHF band 137
vibrational motion 154

W3-Sokół model 267
Warsaw University of Technology (WUT) 73, 123
weighting window 162
worldwide interoperability for microwave access (WiMAX) 190

Yagi–Uda antennas 225
ϒ convex function 27

Multidimensional Radar Imaging

Synthetic aperture radar and inverse synthetic aperture radar (SAR/ISAR) images have been largely used for monitoring small to large areas and more specifically for target recognition/identification. However, the technology has limitations due to the use of classical monostatic, single channel, single frequency and single polarization systems. To overcome these limitations, solutions have been proposed that show the benefit of using multiple frequencies, spatial channels, polarisations and perspective, in one word multi-dimensional radar imaging systems when dealing with non-cooperative targets.

Multidimensional Radar Imaging introduces a new framework within which to address the problem of radar imaging and target recognition as it jointly looks at optimising the use of multiple channels to significantly outperform classical radar imaging systems.

It has been used in the military within NATO for the last few years and the technology is now declassified.

Topics covered include three-dimensional ISAR; STAP-ISAR; wide-band multi-look passive ISAR; radar tomography; multistatic PCL-SAR; fusion of multistatic ISAR images with large angular separation; rotor blade parameter estimation with multichannel passive radar; multistatic 3D ISAR imaging of maritime targets; challenges of semi-cooperative bi/multistatic SAR using Cosmo SkyMEd as an illuminator; and lessons learnt from the NATO SET-196 RTG on multi-channel/multi-static radar imaging of non-cooperative targets.

About the Editor

Marco Martorella is an Associate Professor at the Department of Information Engineering of the University of Pisa, Italy, and Director of the Radar and Surveillance Systems National Laboratory of the Italian Inter-University Consortium for Telecommunications (CNIT). He is author of about 200 international journal and conference papers, thirteen book chapters, and two books on radar technologies. He is currently a member of the IEEE Radar Systems Panel, a member of the NATO Sensors and Electronics Technology Panel and has chaired four NATO Research Task Groups since 2012. His research interests are mainly in the field of radar imaging and multichannel radar signal processing.

ISBN 978-1-78561-807-9

9 781785 618079 >

Radar, Sonar & Navigation

SciTech Publishing an imprint of the IET/The Institution of Engineering and Technology • www.theiet.org
978-1-78561-807-9